ERDC TR-24-11

Engineer Research and Development Center

U.S. ARMY

US Army Corps of Engineers®

ERDC

Navigation Systems Research Program

Hydraulic Load Definitions for Use in Load and Resistance Factor Design (LRFD) Analysis, Including Probabilistic Load Characterization, of 10 Hydraulic Steel Structures

Report Number 1

John E. Hite, Jr., Robert M. Ebeling, and Barry C. White

May 2024

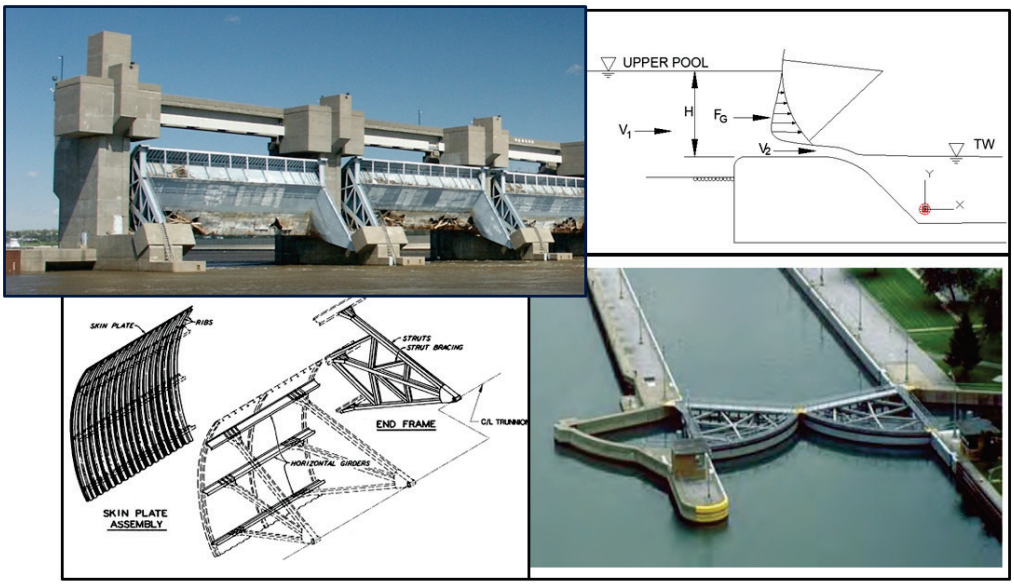

Distribution Statement A. Approved for public release: distribution is unlimited.

The US Army Engineer Research and Development Center (ERDC) solves the nation's toughest engineering and environmental challenges. ERDC develops innovative solutions in civil and military engineering, geospatial sciences, water resources, and environmental sciences for the Army, the Department of Defense, civilian agencies, and our nation's public good. Find out more at www.erdc.usace.army.mil.

To search for other technical reports published by ERDC, visit the ERDC online library at https://erdclibrary.on.worldcat.org/discovery.

ERDC TR-24-11
May 2024

Hydraulic Load Definitions for Use in Load and Resistance Factor Design (LRFD) Analysis, Including Probabilistic Load Characterization, of 10 Hydraulic Steel Structures

Report Number 1

John E. Hite Jr.

US Army Engineer Research and Development Center (ERDC)
Coastal and Hydraulics Laboratory (CHL)
3909 Halls Ferry Road
Vicksburg, MS 39180-6199

Robert M. Ebeling and Barry C. White

US Army Engineer Research and Development Center (ERDC)
Information Technology Laboratory (ITL)
3909 Halls Ferry Road
Vicksburg, MS 39180-6199

Final Technical Report (TR)

Distribution Statement A. Approved for public release: distribution is unlimited.

Prepared for Headquarters, US Army Corps of Engineers
Washington, DC 20314-1000

Under Funding Account Code U4388265, AMSCO Code 031391

Abstract

In the past, allowable stress design (ASD) was used to design steel structures. The allowable stresses used were determined from previous practice, with limited understanding of the reliability and risk performance provided by the structure. Engineering methods based on Load and Resistance Factor Design (LRFD) provide more accurate lifetime models of structures by providing risk-based load factors. Besides improved safety, cost savings can be provided through improved performance and, in some cases, by delaying rehabilitation. This research project develops LRFD-based engineering procedures for the evaluation and design of hydraulic steel structures (HSS).

Hydraulic loads are a key element to the LRFD analysis. This report identifies the primary hydraulic loads and describes procedures that can be used to determine these hydraulic loads. Existing design guidance for HSS is described and presented in the individual chapters. The appendixes to the report provide examples of the procedures used to compute the hydrostatic, wave, and hydrodynamic loads.

A new approach for determining wind-induced wave loads was developed. Design guidance for computing the hydrodynamic load was limited for many of the HSS. Additional research is recommended to improve capabilities for computing hydraulic loads. Details on these recommendations can be found in this report.

DISCLAIMER: The contents of this report are not to be used for advertising, publication, or promotional purposes. Citation of trade names does not constitute an official endorsement or approval of the use of such commercial products. All product names and trademarks cited are the property of their respective owners. The findings of this report are not to be construed as an official Department of the Army position unless so designated by other authorized documents.

DESTROY THIS REPORT WHEN NO LONGER NEEDED. DO NOT RETURN IT TO THE ORIGINATOR.

Contents

Abstract ii

Figures and Tables xiv

Preface xxx

1 Introduction 1

1.1 Background 1
1.2 Objective 2
1.3 Approach 2
1.4 Report Contents 4

2 Loadings Applied to Spillway Tainter Gates (STGs) 13

2.1 Existing Guidance for STG Design 13
2.1.1 Engineer Transmittal Letter (ETL) 1110-2-584, *Design of Hydraulic Steel Structures*, and Engineer Manual (EM) 1110-2-2702, *Design of Spillway Tainter Gates* (Rescinded) 13
2.1.2 EM 110-2-1603, *Hydraulic Design of Spillways* 16
2.1.3 EM 1110-2-1605, *Hydraulic Design of Navigation Dams* 17
2.1.4 STG Operation—Navigation Dam 17
2.1.5 STG Load Cases 17
2.1.5.1 Usual 18
2.1.5.2 Unusual 18
2.1.5.3 Extreme 18
2.1.5.4 Load Combinations 19
2.1.5.5 Cyclic and Noncyclic Loading 19
2.2 Hydraulic Data Collection and Statistical Data Reduction for Mean Loading 20
2.2.1 Upper Pool Elevation (El) 20
2.2.2 Tailwater 20
2.2.3 Flow Regimes 21
2.2.3.1 Free Uncontrolled Flow 22
2.2.3.2 Submerged Uncontrolled Flow 23
2.2.3.3 Free Controlled Flow 24
2.2.3.4 Submerged Controlled Flow 24
2.3 Hydraulic Loading for STGs 26
2.3.1 Hydrostatic Load for STGs 26
2.3.2 Wave Load for STGs 33
2.3.2.1 *Shore Protection Manual* (SPM) Guidance 34
2.3.2.2 Wind-Wave Generation on Restricted Fetches 35
2.3.2.3 Simplified Forecasting Method of Wind Waves and Swell 36
2.3.2.4 Converting a Trapezoidal Pressure Distribution Acting on a Discrete Segment of the STG into End Point Forces 42
2.3.2.5 Significant Wave Height Selection for Inland Structures 44
2.3.2.6 Wind Speed for Extreme Value Estimation 45
2.3.2.7 Type 1 Gumbel Distribution 47
2.3.3 Hydrodynamic Load for STGs 51

2.3.3.1 Hydrodynamic Load for STGs with Tailwater Higher than the Gate Opening 52
2.3.3.2 Hydrodynamic Load for STGs with Tailwater Less than the Gate Opening 58
2.3.3.3 Location for Resultant Hydrodynamic Force with Tailwater above the Gate Opening 71
2.3.4 Combined Hydrostatic and Wave Loads for STGs 74
2.3.5 Combined Hydrodynamic and Wave Loads for STGs 75
2.3.6 Summary of Hydraulic Loads for STGs 75
2.4 Probabilistic Characterization of the Hydrostatic and Hydrodynamic Loads for the STG 76
2.4.1 Probabilistic Characterization of the Hydrostatic Load 76
2.4.2 Probabilistic Characterization of the Hydrodynamic Load 79
2.5 Other Loadings for STGs 80
2.5.1 Barge Impact 80
2.5.2 Debris Impact 81
2.5.3 Ice Impact 81
2.5.4 Operational Loadings 81
2.5.4.1 Trunnion and Bearing Friction 82
2.5.4.2 Side Seal Friction 82
2.5.4.3 Gate Binding 82
2.5.5 Flow-Induced Vibration (Design or Operational Counter Measures) 82
2.6 Summary and Conclusions 83

3 Loadings Applied to Vertical-Lift Gates 85
3.1 Existing Guidance for Vertical-Lift Gate Design 85
3.1.1 ETL 1110-2-584, *Design of Hydraulic Steel Structures* 85
3.1.2 EM 110-2-1603, *Hydraulic Design of Spillways* 88
3.1.3 EM 1110-2-1605, *Hydraulic Design of Navigation Dams* 89
3.1.4 Spillway Vertical-Lift Gate Operation—Navigation Dam 89
3.1.5 Vertical-Lift Gate Load Cases 90
3.2 Hydraulic Data Collection and Statistical Data 90
3.2.1 Upper Pool El 90
3.2.2 Tailwater 90
3.2.3 Flow Regimes for Vertical-Lift Gates 91
3.2.3.1 Free Controlled Flow 91
3.2.3.2 Submerged Controlled Flow 93
3.3 Hydraulic Loading for Vertical-Lift Gates 93
3.3.1 Hydrostatic Load for Vertical-Lift Gates 94
3.3.2 Wave Load for Vertical-Lift Gates 95
3.3.3 Hydrodynamic Load for Vertical-Lift Gates 96
3.3.3.1 Hydrodynamic Load for a Vertical-Lift Gate with Tailwater 96
3.3.3.2 Hydrodynamic Load for a Vertical-Lift Gate with No Tailwater 100
3.3.3.3 Flow-Induced Vibration 101
3.3.4 Combined Hydrostatic and Wave Loads for Vertical-Lift Gates 102
3.3.5 Combined Hydrodynamic and Wave Loads for Vertical-Lift Gates 102
3.3.6 Summary of Hydraulic Loads for Vertical-Lift Gates 102

3.4 Probabilistic Characterization of the Hydrostatic and Hydrodynamic Loads for the Vertical-Lift Gate 103
3.4.1 Probabilistic Characterization of the Hydrostatic Load for the Vertical-Lift Gate 103
3.4.2 Probabilistic Characterization of the Hydrodynamic Load for the Vertical-Lift Gate 103
3.5 Other Loadings for Vertical-Lift Gates 103
3.6 Summary and Conclusions 104

4 Loadings Applied to Roller Gates 105
4.1 Existing Guidance for Roller Gate Design 105
4.1.1 ETL 1110-2-584, *Design of Hydraulic Steel Structures* 106
4.1.2 EM 1110-2-1605, *Hydraulic Design of Navigation Dams* 107
4.1.3 Roller Gate Load Cases 107
4.2 Hydraulic Data Collection and Statistical Data Reduction for Mean Loading and Dispersion for Spillway Roller Gates 108
4.2.1 Upper Pool El 108
4.2.2 Tailwater 108
4.2.3 Flow Regimes for Spillway Roller Gates 109
4.2.3.1 Free Controlled Flow 109
4.2.3.2 Submerged Controlled Flow 109
4.3 Hydraulic Loading for Spillway Roller Gates 110
4.3.1 Hydrostatic Load for Spillway Roller Gates 110
4.3.2 Wave Load for Spillway Roller Gates 112
4.3.3 Hydrodynamic Load for Spillway Roller Gates 112
4.3.4 Combined Hydrostatic and Wave Loads for Spillway Roller Gates 115
4.3.5 Combined Hydrodynamic and Wave Loads for Spillway Roller Gates 116
4.3.6 Summary of Hydraulic Loads for Spillway Roller Gates 116
4.4 Probabilistic Characterization of the Hydrostatic and Hydrodynamic Loads for the Roller Gate 116

5 Loadings Applied to Sector Gates 118
5.1 Existing Design Guidance for Sector Gates 118
5.1.1 ETL 1110-2-584, *Design of Hydraulic Steel Structures* 118
5.1.2 EM 1110-2-1604, *Hydraulic Design of Navigation Locks* 119
5.1.3 EM 1110-2-2703, *Lock Gates and Operating Equipment* 120
5.1.4 EM 1110-2-2610, *Mechanical and Electrical Design for Lock and Dam Operating Equipment* 121
5.2 Hydraulic Data Collection for Sector Gates 121
5.3 Hydraulic Loading for Sector Gates 122
5.3.1 Hydrostatic Load for Sector Gates 122
5.3.2 Wave Load for Sector Gates 123
5.3.3 Hydrodynamic and Hydrostatic Load for Sector Gates 123
5.3.4 Probabilistic Characterization of the Hydrostatic and Hydrodynamic Loads for the Sector Gate 125
5.3.4.1 Probabilistic Characterization of the Hydrostatic Load for the Sector Gate 125

5.3.4.2 Probabilistic Characterization of the Hydrodynamic Load for the Sector Gate 126
5.3.5 Summary of Hydraulic Loads for the Sector Gate 126

6 Loadings Applied to Lock Miter Gates 127

6.1 Existing Guidance for Miter Gates 127
6.1.1 ETL 1110-2-584, *Design of Hydraulic Steel Structures* 128
6.1.2 EM 1110-2-1604, *Hydraulic Design of Navigation Locks* 128
6.1.3 EM 1110-2-2703, *Lock Gates and Operating Equipment* 129
6.1.4 EM 1110-2-2602, *Planning and Design of Navigation Locks* 131
6.1.5 EM 1110-2-2610, *Mechanical and Electrical Design for Lock and Dam Operating Equipment* 131
6.2 Hydraulic Data Collection and Statistical Data Reduction for Mean Loading and Dispersion for the Miter Gate 132
6.2.1 Upper Pool El 132
6.2.2 Tailwater or Lower Pool El 133
6.3 Hydraulic Loading for the Lock Miter Gate 133
6.3.1 Hydrostatic Load for the Miter Gate 133
6.3.2 Wind-Induced Wave Load for the Miter Gate 135
6.3.3 Temporary Hydraulic Wave Load for Miter Gates 135
6.3.4 Combined Hydrostatic, Wind-Induced Wave Loads, and Temporary Loads for Miter Gates 136
6.3.5 Hydrodynamic Loads for Miter Gates 136
6.3.6 Probabilistic Characterization of the Hydrostatic and Hydrodynamic Loads for the Miter Gate 137
6.3.6.1 Probabilistic Characterization of the Hydrostatic Load 137
6.3.6.2 Probabilistic Characterization of the Hydrodynamic Load 138
6.3.7 Summary of Hydraulic Loads for Miter Gates 138

7 Loadings Applied to Submergible Tainter Gates for Locks 139

7.1 Existing Design Guidance for Submergible Tainter Gates for Locks 139
7.1.1 ETL 1110-2-584, *Design of Hydraulic Steel Structures* 139
7.1.2 EM 1110-2-1604, *Hydraulic Design of Navigation Locks* 142
7.1.3 Submergible Tainter Operations—Navigation Locks 142
7.1.4 Submergible Tainter Gate Load Cases 143
7.2 Hydraulic Data Collection for Submergible Tainter Gates 143
7.3 Hydraulic Loading for Submergible Tainter Gates 144
7.3.1 Hydrostatic Load for Submergible Tainter Gates 144
7.3.2 Wave Load for Submergible Tainter Gates 145
7.4 Probabilistic Characterization of the Hydrostatic Load for the Submergible Tainter Gate 145

8 Loadings Applied to Bulkheads 146

8.1 Existing Guidance for Bulkheads 146
8.1.1 ETL 1110-2-584, *Design of Hydraulic Steel Structures* 146
8.1.2 EM 110-2-1603, *Hydraulic Design of Spillways* 148
8.1.3 EM 1110-2-1605, *Hydraulic Design of Navigation Dams* 148
8.1.4 EM 1110-2-2702, *Design of Spillway Tainter Gates* (Rescinded) 148

8.1.5 EM 1110-2-2607, *Planning and Design of Navigation Dams* 148
8.1.6 Bulkhead Load Cases 149
8.2 Hydraulic Data Collection and Statistical Data Reduction for Mean Loading and Dispersion for Bulkheads 149
8.2.1 Upper Pool El 149
8.2.2 Tailwater 150
8.2.3 Flow Regimes for Bulkheads 150
8.3 Hydraulic Loading for Bulkheads 152
8.3.1 Hydrostatic Load for Bulkheads 152
8.3.2 Wave Load for Bulkheads 153
8.3.3 Hydrodynamic Load for Bulkheads 153
8.3.4 Combined Hydrostatic and Wave Load for Bulkheads 157
8.3.5 Combined Hydrodynamic and Wave Load for Bulkheads 157
8.3.6 Summary of Hydraulic Loads for Bulkheads 157
8.4 Probabilistic Characterization of the Hydrostatic and Hydrodynamic Loads for Bulkheads 158
8.4.1 Probabilistic Characterization of the Hydrostatic Load for the Bulkhead 158
8.4.2 Probabilistic Characterization of the Hydrodynamic Load for Bulkheads 158
8.5 Summary and Conclusions 159

9 Loadings Applied to Rolling Gates 160
9.1 Existing Guidance for Rolling Gates 160
9.1.1 ETL 1110-2-584, *Design of Hydraulic Steel Structures* 160
9.1.2 Rolling Gate Load Cases 162
9.2 Hydraulic Data Collection and Statistical Data Reduction for Mean Loading and Dispersion for Rolling Gates 162
9.2.1 Flood-Side Water Level 163
9.2.2 Wave Load 163
9.3 Hydraulic Loading for Rolling Gates 163
9.3.1 Hydrostatic Load for the Rolling Gate 163
9.3.2 Wave Load for Rolling Gates 164
9.3.3 Combined Hydrostatic and Wave Load for Rolling Gates 165
9.3.4 Probabilistic Characterization of the Hydrostatic Load for the Rolling Gate 165
9.3.5 Summary of Hydraulic Loads for Rolling Gates 165

10 Loadings Applied to Needle Dam / Girder Beams (ND/GB) 166
10.1 Existing Guidance for ND/GB 166
10.1.1 ETL 1110-2-584, *Design of Hydraulic Steel Structures* 169
10.1.2 ND/GB Load Cases 169
10.2 Hydraulic Data Collection and Statistical Data Reduction for Mean Loading and Dispersion for the ND/GB 170
10.2.1 Upper Pool El 170
10.2.2 Tailwater Elevation (TW El) 170
10.3 Hydraulic Loading for ND/GB 170
10.3.1 Hydrostatic Load for the ND/GB 171
10.3.2 Wave Load for ND/GB 172

10.3.3 Probabilistic Characterization of the Hydrostatic Load for the ND/GB.....172
10.3.4 Combined Hydrostatic and Wave Load for ND/GB.....173
10.3.5 Summary of Hydraulic Loads for ND/GB.....173

11 Loadings Applied to Reverse Tainter Valves.....174
11.1 Existing Guidance for Reverse Tainter Valves.....175
11.1.1 ETL 1110-2-584, *Design of Hydraulic Steel Structures*.....175
11.1.2 EM 1110-2-1610, *Hydraulic Design of Lock Culvert Valves*.....175
11.1.2.1 Horizontally Framed Valve.....176
11.1.2.2 Double Skin Plate Reverse Tainter Valve.....177
11.1.2.3 Vertically Framed Reverse Tainter Valve.....179
11.1.2.4 Performance Comments.....180
11.1.3 EM 1110-2-1604, *Hydraulic Design of Navigation Locks*.....181
11.1.4 EM 1110-2-2602, *Planning and Design of Navigation Locks*.....181
11.1.5 EM 1110-2-2610, *Mechanical and Electrical Design for Lock and Dam Operating Equipment*.....181
11.2 Hydraulic Data Collection and Statistical Data Reduction for Mean Loading and Dispersion for the Reverse Tainter Valve.....182
11.2.1 Forebay El.....182
11.2.2 TW El.....182
11.3 Hydraulic Loading for Reverse Tainter Valves.....182
11.3.1 Hydrostatic Load for the Reverse Tainter Valve.....182
11.3.2 Hydrodynamic Load for Reverse Tainter Valves.....184
11.3.3 Probabilistic Characterization of the Hydrostatic and Hydrodynamic Loads for the Reverse Tainter Valve.....185
11.3.3.1 Probabilistic Characterization of the Hydrostatic Loads for the Reverse Tainter Valve.....186
11.3.3.2 Probabilistic Characterization of the Hydrodynamic Load for the Reverse Tainter Valve.....186
11.3.4 Summary of Hydraulic Loads for Reverse Tainter Valves.....186

12 Summary, Conclusions, and Recommendations.....187
12.1 Report Summary.....187
12.2 Conclusions and Recommendations.....187

References.....189

Appendix A: Example Hydraulic Load Computations for the Melvin Price Locks and Dam (MPLD) Spillway Tainter Gate (STG).....195
A.1 The 30 yr Record of Hydrologic Data of the Tailwater for MPLD.....195
A.2 Hydrostatic Load for MPLD without Tailwater Effect.....201
A.3 Wave Load Based on Wave Height and Period for MPLD.....202
A.3.1 Wind Speed and Fetch.....202
A.3.2 Wind Speed Analyses.....205
A.3.3 Extreme Value Estimation based on US Army Corps of Engineers, St. Paul District (USACE-MVP), Project Using Maximum Yearly Values of Wind Speed for MPLD.....207
A.3.4 Wind Frequency Based on Gumbel Type 1 Distribution with Gringorten's Method Using Maximum Yearly Values of Wind Speed for MPLD.....211

A.3.5 Extreme Value Estimation Based on the USACE-MVP Project Using Maximum 2 hr Average Yearly Value of Wind Speed for MPLD 212
A.3.6 Wind Frequency Based on Gumbel Type 1 Distribution with Gringorten's Method Using Maximum 2 hr Average Yearly Values of Wind Speed for MPLD 216
A.3.7 Wave Height and Period from Smith (1991) and Ebeling et al. (2023) 224
A.3.8 Wave Load from Goda 226
A.4 Hydrodynamic Loads for MPLD 232
A.4.1 Average Hydrodynamic Load on STGs Based on Average Tailwater Elevation (TW El) 232
A.4.2 Hydrodynamic Loads for Different Gate Operations 235
A.5 Probabilistic Characterization of the Hydrostatic and Hydrodynamic Loads for the MPLD STG 238
A.5.1 Statistical Analysis of Hydrostatic Loads for MPLD 238
A.5.2 Statistical Analysis of Hydrodynamic Loads for MPLD with Tailwater Higher than the Gate Opening 239
A.5.3 Statistical Analysis of Hydrodynamic Loads for MPLD with Tailwater Lower than the Gate Opening 260

Appendix B: Example Hydraulic Load Computations for the McNary Lock and Dam (MLD) Vertical-Lift Gate 261

B.1 A 30 yr Record of Hydrologic Data for MLD for Forebay Statistics 261
B.2 Hydrostatic Load for MLD without Tailwater Effect 265
B.3 Wave Load Based on Wave Height and Period for MLD 266
B.3.1 Wind Speed and Fetch for MLD 266
B.3.2 Wind Speed Analyses for MLD 268
B.3.3 Extreme Value Estimation Using Maximum 1 hr Average Yearly Values of Wind Speed for MLD 269
B.3.4 Wind Frequency Based on Gumbel Type 1 Distribution with Gringorten's Method Using Maximum Yearly Values of Wind Speed for MLD 270
B.3.5 Wave Height and Period from NARFET Model 272
B.3.6 Wave Load from Goda for MLD 273
B.4 Hydrodynamic Loads for MLD Spillway Vertical-Lift Gate 280
B.4.1 Average Hydrodynamic Load on Spillway Vertical-Lift Gates Using the Conservation of Momentum Procedure 280
B.4.2 Hydrodynamic Load on Spillway Vertical-Lift Gates Using Kim's (2007) Procedure 282
B.5 Probabilistic Characterization of the Hydrostatic and Hydrodynamic Loads for the MLD Spillway Vertical-Lift Gate 284
B.5.1 Statistical Analysis of Hydrostatic Loads for the McNary Vertical-Lift Gate 284
B.5.2 Statistical Analysis of Hydrodynamic Loads for the McNary Vertical-Lift Gate 285
B.6 Summary of Hydraulic Loads for MLD 289

Appendix C: Example Hydraulic Load Computations for R. C. Byrd Locks and Dam (RCBLD) Spillway Roller Gate 291

C.1 Record for Hydrologic Data for RCBLD 291
C.1.1 Upper Pool El Statistics for RCBLD 292

C.1.2 Tailwater Statistics for RCBLD....295
C.2 Hydrostatic Load for RCBLD without Tailwater Effect for RCBLD....297
C.3 Wave Load Based on Wave Height and Period for RCBLD....298
C.3.1 Wind Speed and Fetch for RCBLD....298
C.3.2 Wind Speed Analyses for RCBLD....299
C.3.3 Extreme Value Estimation Using Maximum 0.3 hr Average Yearly Values of Wind Speed for RCBLD....300
C.3.4 Wind Frequency Based on Gumbel Type 1 Distribution with Gringorten's Method Using Maximum Yearly 0.3 hr Average Values of Wind Speed....301
C.3.5 Wave Height and Period from NARFET Model for RCBLD....303
C.3.6 Wave Load from Goda for RCBLD....304
C.4 Hydrodynamic Loads for RCBLD....310
C.5 Probabilistic Characterization of the Hydrostatic and Hydrodynamic Loads for the R. C. Byrd Spillway Roller Gate....314
C.5.1 Probabilistic Characterization....314
C.5.2 Probabilistic Characterization....315
C.6 Summary of Hydraulic Loads for RCBLD....316

Appendix D: Example Hydraulic Load Computations for Calcasieu Lock East Sector Gate....317
D.1 Hydrologic Data for Calcasieu River East Sector Gate....317
D.2 Hydrostatic Load for Calcasieu Lock East Sector Gate with Maximum Head on the Sector Gate....320
D.3 Wave Load Based on Wave Height and Period for the Calcasieu Lock East Sector Gate....321
D.3.1 Wind Speed and Fetch for the Calcasieu Lock East Sector Gate....322
D.3.2 Wind Speed Analyses for the Calcasieu Lock East Sector Gate....323
D.3.3 Extreme Value Estimation Using Maximum 0.5 hr Average Yearly Values of Wind Speed for the Calcasieu Lock East Sector Gate....324
D.3.4 Wind Frequency Based on Gumbel Type 1 Distribution with Gringorten's Method Using Maximum Yearly Values of Wind Speed....325
D.3.5 Wave Height and Period from the NARFET Model....328
D.3.6 Wave Load from Goda for the Calcasieu Lock East Sector Gate....329
D.4 Hydrodynamic Loads on Sector Gates for the Calcasieu Lock East Sector Gate....335
D.5 Probabilistic Characterization of the Hydrostatic and Hydrodynamic Loads for the Calcasieu Lock East Sector Gate....336
D.5.1 Probabilistic Characterization of the Hydrostatic Load on the East Sector Gate....336
D.5.2 Probabilistic Characterization of the Hydrodynamic Load on the East Sector Gate....338
D.6 Summary of Hydraulic Loads for the Calcasieu Lock East Sector Gate....338

Appendix E: Example Hydraulic Load Computations for the Barkley Lock Miter Gates....339
E.1 The 30 yr Record of Hydrologic Data for the Barkley Lock and Dam (BLD)....339
E.1.1 Forebay Statistics for the Barkley Lock Upper Miter Gate....341
E.1.2 Tailwater Statistics for the Barkley Lock Lower Miter Gate....343
E.2 Hydrostatic Load for the Barkley Lock Gates....345

E.2.1 Hydrostatic Load for the Barkley Upper Lock Gate 345
E.2.2 Hydrostatic Load for the Barkley Lower Lock Gate 346
E.3 Wave Load Based on Wave Height and Period for the Barkley Lock Gates 347
E.3.1 Wind Speed and Fetch for the Barkley Upper Lock Gate 347
E.3.2 Wind Speed Analyses for the Barkley Lock Upper Gate 348
E.3.3 Extreme Value Estimation Using Maximum 1 hr Average Yearly Values of Wind Speed for the Barkley Lock Upper Gate. 350
E.3.4 Wind Frequency Based on Gumbel Type 1 Distribution with Gringorten's Method Using Maximum Yearly 1 hr Average Values of Wind Speed for the Barkley Lock Upper Miter Gate. 350
E.3.5 Wave Height and Period from the NARFET Model for the Barkley Lock Upper Miter Gate 352
E.3.6 Wave Load from Goda for the Barkley Lock Upper Miter Gate 353
E.3.7 Wind Speed and Fetch for the Barkley Lower Lock Gate 359
E.3.8 Wind Speed Analyses for the Barkley Lock Lower Gate 360
E.3.9 Extreme Value Estimation Using Maximum 0.25 hr Average Yearly Values of Wind Speed for the Barkley Lock Lower Gate. 361
E.3.10 Wind Frequency Based on Gumbel Type 1 Distribution with Gringorten's Method Using Maximum Yearly 0.25 hr Average Values of Wind Speed for the Barkley Lock Lower Miter Gate. 361
E.3.11 Wave Height and Period from the NARFET Model for the Barkley Lock Lower Miter Gate 363
E.3.12 Wave Load from Goda for the Barkley Lock Lower Miter Gate 364
E.4 Hydrodynamic Loads for the Barkley Lock Gates 369
E.5 Probabilistic Characterization of the Hydrostatic and Hydrodynamic Loads for the Barkley Lower Lock Gate 371
E.5.1 Probabilistic Characterization of the Hydrostatic Load for the Lower Lock Gate 371
E.5.2 Probabilistic Characterization of the Hydrodynamic Load for the Lower Lock Gate 372
E.6 Summary of Hydraulic Loads for the BLD Miter Gates 373

Appendix F: Example Hydraulic Load Computations for the Ice Harbor Lock Upper Submergible Tainter Gate 374

F.1 A 30 yr Record of Hydrologic Data for the Ice Harbor Lock and Dam 374
F.2 Hydrostatic Load for the Ice Harbor Submergible Tainter Gate 377
F.3 Wave Load Based on Wave Height and Period for the Submergible Tainter Gate 378
F.3.1 Wind Speed and Fetch for the Submergible Tainter Gate 378
F.3.2 Wind Speed Analyses for the Submergible Tainter Gate 380
F.3.3 Extreme Value Estimation Using Maximum 0.5 hr Average Yearly Values of Wind Speed for the Submergible Tainter Gate 381
F.3.4 Wind Frequency Based on Gumbel Type 1 Distribution with Gringorten's Method Using Maximum Yearly 0.5 hr Average Values of Wind Speed for the Submergible Tainter Gate 382
F.3.5 Wave Height and Period from the NARFET Model for the Submergible Tainter Gates 384
F.3.6 Wave Load for the Ice Harbor Lock Submergible Tainter Gate 385

F.4 Probabilistic Characterization of the Hydrostatic Load for the Ice Harbor Lock Submergible Tainter Gate. 391
F.5 Summary of Hydraulic Loads for Submergible Tainter Gates 391

Appendix G: Example Hydraulic Load Computations for the BLD Spillway Bulkhead 393
G.1 A 30 yr Record of Hydrologic Data for the BLD 393
G.1.1 Forebay Statistics for the BLD 396
G.1.2 Tailwater Statistics for the BLD 398
G.2 Hydrostatic Load for the BLD Bulkhead without Tailwater Effects 400
G.3 Wave Load Based on Wave Height and Period for the BLD 400
G.3.1 Wind Speed and Fetch for the BLD 401
G.3.2 Wind Speed Analyses for the BLD 402
G.3.3 Extreme Value Estimation Using Maximum 1 hr Average Yearly Values of Wind Speed for the BLD 403
G.3.4 Wind Frequency Based on Gumbel Type 1 Distribution with Gringorten's Method Using Maximum Yearly 1 hr Average Values of Wind Speed for the BLD 404
G.3.5 Wave Height and Period from the NARFET Model for the BLD 406
G.3.6 Wave Load from Goda for the BLD 407
G.4 Hydrodynamic Loads for the BLD 412
G.5 Probabilistic Characterization of the Hydrostatic and Hydrodynamic Loads for the Barkley Spillway Bulkhead 413
G.6 Summary of Hydraulic Loads for the BLD 415

Appendix H: Example Hydraulic Load Computations for the Williams Boulevard Rolling Gate 416
H.1 Flood Protection System Description 416
H.2 Hydrostatic Load for Rolling Gates 419
H.3 Wave Load Based on Wave Height and Period for Rolling Gates 420
H.3.1 Wind Speed and Fetch for Rolling Gates 420
H.3.2 Wind Speed Analyses for Rolling Gates 420
H.3.3 Wave Load from Goda for Rolling Gates 420
H.4 Probabilistic Characterization of the Hydrostatic Load for the Williams Boulevard Rolling Gate 425
H.5 Summary of Hydraulic Loads for Rolling Gates 425

Appendix I: Example Hydraulic Load Computations for the Chickamauga Lock Needle Dam / Girder Beams (ND/GB) 427
I.1 Characterization of Hydraulic loads in the Upper Lock Approach for the Chickamauga Lock and Dam ND/GB 427
I.1.1 A 31 yr Record of Hydrologic Data for the Chickamauga Lock and Dam Forebay El 427
I.1.2 Hydrostatic Load for the Upper ND/GB 430
I.1.3 Wave Load Based on Wave Height and Period for the ND/GB in the Upper Lock Approach 431
I.1.3.1 Wind Speed and Fetch for the ND/GB in the Upper Lock Approach 431
I.1.3.2 Wind Speed Analyses for the Upper ND/GB 433

I.1.3.3 Extreme Value Estimation Using Maximum 0.9 hr Average Yearly Values of Wind Speed for the Upper ND/GB 434
I.1.3.4 Wind Frequency Based on Gumbel Type 1 Distribution with Gringorten's Method Using Maximum Yearly 0.9 hr Average Values of Wind Speed for the Upper ND/GB 435
I.1.3.5 Wave Height and Period from the NARFET Model for Upper ND/GB 437
I.1.3.6 Wave Load from Goda for the Upper ND/GB 438
I.1.4 Summary of Hydraulic Loads for the Upper ND/GB 444
I.2 Characterization of Hydraulic Loads in the Lower Lock Approach for the Chickamauga Lock and Dam ND/GB 444
I.2.1 A 31 yr Record of Hydrologic Data for the Chickamauga Lock and Dam Lower Approach 444
I.2.2 Hydrostatic Load for the Lower ND/GB 447
I.2.3 Wave Load Based on Wave Height and Period for the ND/GB in the Lower Lock Approach 447
I.2.3.1 Wind Speed and Fetch for the ND/GB in the Lower Lock Approach 448
I.2.3.2 Wind Speed Analyses for the Lower ND/GB 448
I.2.3.3 Extreme Value Estimation Using Maximum 0.2 hr Average Yearly Values of Wind Speed for the Lower ND/GB 449
I.2.3.4 Wind Frequency Based on Gumbel Type 1 Distribution with Gringorten's Method Using Maximum Yearly 0.2 hr Average Values of Wind Speed for the Lower ND/GB 450
I.2.3.5 Wave Height and Period from the NARFET Model for the Lower ND/GB 452
I.2.3.6 Wave Load from Goda for the Lower ND/GB 453
I.2.4 Probabilistic Characterization of the Hydrostatic Load for the Chickamauga Lock ND/GB 459
I.2.4.1 Probabilistic Characterization of the Hydrostatic Load for the Chickamauga Lock Upper Pool ND/GB 459
I.2.4.2 Probabilistic Characterization of the Hydrostatic Load for the Chickamauga Lock Lower Pool ND/GB 459
I.2.5 Summary of Hydraulic Loads for the Lower ND/GB 460

Appendix J: Example Design for Determining Hydrostatic Loads for the Dalles Lock Reverse Tainter Valve 461

J.1 A 50 yr Record of Hydrologic Data for the Dalles Lock and Dam 461
J.1.1 Forebay Statistics for the Dalles Lock Reverse Tainter Valve 462
J.1.2 Tailwater Statistics for the Dalles Project 464
J.2 Hydrostatic Load for the Dalles Reverse Tainter Valve 466
J.3 Hydrodynamic Load for the Dalles Reverse Tainter Valve 467
J.3.1 Dynamic Amplification Factor (DAF) 467
J.3.2 Vibration and Fatigue Analysis 468
J.4 Probabilistic Characterization of the Hydrostatic Load for the Dalles Lock Reverse Tainter Valve 468
J.5 Summary of Hydrostatic Loads for the Dalles Lock Reverse Tainter Valve 469

Abbreviations 470

Report Documentation Page (SF 298) 473

Figures and Tables

Figures

1. Melvin Price Dam spillway tainter gate (STG), looking upstream. 5
2. McNary Dam spillway vertical-lift gate, looking upstream. 6
3. View of a spillway roller gate looking across the downstream side of the dam. (Image reproduced from US Army Corps of Engineers, Huntington District [USACE-LRH], files.) 7
4. Satellite imagery showing an aerial view of Calcasieu Lock on the Gulf Intracoastal Waterway (GIWW). (Map data: Landsat/Copernicus, n.d.) 8
5. View of the frame side of the Barkley Lock lower miter gate, looking upstream. 8
6. View of the Ice Harbor Lock submergible tainter gate. 9
7. A 1:15-scale model of the Barkley Dam spillway bulkhead. (Image reproduced from Hite and Pickering 1983, Figure 6. Public domain.) 10
8. View of a rolling gate stored behind a floodwall. 11
9. View of needle dam / girder beams (ND/GB) being installed in the Chickamauga Upper Lock approach. 12
10. View of Dalles Lock double skin plate reverse tainter valve removed for repairs. 12
11. Structural components of STGs from Engineer Manual (EM) 1110-2-2702 (rescinded). (Image reproduced from HQUSACE 2000, 3-2. Public domain.) 14
12. Flow regimes for STGs. (Image reproduced from USACE 1987, 5-10. Public domain.) 22
13. Discharge coefficients for submerged controlled flow. (Image reproduced from EM 1110-2-1605, HQUSACE 1987, 5-16. Public domain.) 25
14. Hydrostatic pressure distribution for a closed STG with no tailwater effects. 29
15. Schematic for hydrostatic force computations. (Image adapted from Roberson and Crow 1985.) 30
16. Schematic for hydrostatic force computations on a curved surface. (Image adapted from Roberson and Crow 1985.) 30
17. Illustration of terms in Goda's (1974) pressure formulation. (Image reproduced from Ebeling et al. 2023, 112. Public domain.) 38
18. Goda's (2010) wave pressure distribution adapted for an STG. 41
19. Distribution of stress acting normal to a discrete segment, *k*: (*a*) trapezoidal pressure distribution and (*b*) equivalent nodal point forces. (Image reproduced from Ebeling et al. 2016, 46. Public domain.) 43
20. Internal shear and moment at node *i+2* for segment *k+1*: (*a*) trapezoidal pressure distributions and (*b*) equivalent nodal point forces. (Image reproduced from Ebeling et al. 2016, 47. Public domain.) 43
21. Generalized extreme value (GEV) type 1 Gumbel distribution peak annual 2 min wind data for Fargo, North Dakota, used in the *Oxbow-Hickson-Bakke (OHB) Levee Wind-Wave Analysis* (USACE-MVP 2014). ACE is annual chances of exceedance. 46
22. Estimation of wind speed using the extreme value method for Saint Charles County (SCC) airport near the Melvin Price Locks and Dam (MPLD) project. 47

23. Wind frequency curve from Gumbel type 1 distribution with Gringorten's method for the St. Louis Regional (SLR) and SCC airports data using annual peak values. 49
24. Wind frequency based on maximum 2 hr average wind speed for the combined airport data. 51
25. Schematic of the pressure distribution on a tainter gate with the gate open and with no tailwater effects. 52
26. Schematic for terms used in Equation (84). 55
27. Discharge coefficients (C_{gs}) for submerged controlled flow. (Graph adapted from EM 1110-2-1605, HQUSACE 1987.) 56
28. Spillway rating curve for MPLD. (Graph provided by USACE, St. Louis District [USACE-MVS], Hydraulics Branch.) 57
29. Example of hydrodynamic forces computed for the MPLD STG for varying gate openings and tailwater with constant upper pool el. 58
30. Schematic of the pressure distribution on a sluice gate with an opening of height *a* and an illustration of parameters to compute the pressure distribution. (Image adapted from Kim 2007.) 60
31. Maximum, minimum, and average values. (Graph adapted from the data presented in Kim 2007, Figure 8.) 63
32. Fit equations for data from Kim (2007, Figure 8) in the present study. 66
33. Pressure distribution developed from Kim (2007) data with a 5 cm gate opening. 66
34. Pressure distribution from Kim (2007) data with a 5 cm gate opening approximated using two triangles and a rectangle. 67
35. Ratio of z_2 and z_3 locations to z_M for a/E_1 from 0.1 to 0.6. 69
36. Comparison of hydrodynamic force determined from coarse and fine resolution curves. 70
37. Hydrodynamic pressure distribution developed for the MPLD spillway gate open 1 ft and no tailwater effects. 72
38. Hydrodynamic pressure distribution developed for the MPLD spillway gate open 1 ft for no tailwater effects and a tailwater elevation (TW El) of 395. 72
39. Hydrostatic pressure distribution for upper pool els +6σ and −6σ around the mean upper pool. 77
40. Hydrostatic pressures computed for the MPLD spillway gate for upper pool els +6σ and −6σ around the normal upper pool and the mean upper pool. 79
41. Structural components of spillway vertical-lift gate. (Image adapted from Engineer Transmittal Letter [ETL] 1110-2-584, HQUSACE 2014.) 86
42. Schematic for parameters used in Equation (104). (Image reproduced from HQUSACE 1990, plate 6-4. Public domain.) 92
43. Discharge coefficients for vertical-lift gates on a spillway. (Image reproduced from HQUSACE 1990, plate 6-4. Public domain.) 93
44. Hydrostatic pressure distribution for vertical-lift gate. 95
45. Goda's (2010) wave pressure distribution adapted for a vertical-lift spillway gate. 95
46. Schematic for terms used in Equation (84) for a vertical-lift gate with tailwater. 99
47. Discharge coefficients (C_{gs}) for a submerged controlled flow vertical-lift gate. (Image adapted from EM 1110-2-1605, HQUSACE 1987.) 100

48. Schematic of pressure distribution on a vertical-lift gate with the gate open and no tailwater. 100
49. Schematic for terms used in Equation (105) for a vertical-lift gate with no tailwater. 101
50. Roller gate at the R. C. Byrd Locks and Dam (RCBLD) project. (Image reproduced from USACE-LRH files.) 105
51. Roller gate at the Upper Mississippi River project. (Image reproduced from USACE, Rock Island District [USACE-MVR], files.) 106
52. Comparison of discharge coefficients for the RCBLD spillway roller gate and those in EM 1110-2-1605 (HQUSACE 1987) for submerged controlled flow. 110
53. Hydrostatic pressure distribution for the roller gate. 111
54. Wave pressure distribution adapted from Goda (2010) for a spillway roller gate. 112
55. Schematic of hydrodynamic pressure distribution on an open roller gate. 113
56. Schematic for terms used in Equation (84) for a roller gate with tailwater. 115
57. Plan view of a sector gate lock. (Image reproduced from HQUSACE 2006, 3-8. Public domain.) 118
58. Sector gate used as a lock gate. (Image reproduced from HQUSACE 2014, B-7. Public domain.) 119
59. Plan view of the typical structural members of a sector gate. (Image reproduced from HQUSACE 2006, B-5. Public domain.) 120
60. Hydrostatic pressure distribution for a sector gate. 123
61. Head versus pintle torque for Type A1 sector gate design with a 12 ft deep lower pool and gate openings (G_O) of 5 and 7 ft. (Image adapted from Oswalt and Murphy 1971.) 125
62. View of the upper miter gate during construction of the new McAlpine Lock. 127
63. Upstream elevation and sectional view of a miter gate. (Image reproduced from EM 1110-2-1604, HQUSACE 2006, B-3. Public domain.) 129
64. Schematic of a horizontally framed miter gate in the mitered position and the symbols used to describe the reactions. 130
65. Section view of the hydrostatic pressure distribution normal to the skin plate of the upper gate in the mitered position. 134
66. Section view of the hydrostatic pressure distribution normal to the skin plate of the lower gate in the mitered position. 135
67. Cross section of a submergible tainter gate used as an upper lock gate. (Image reproduced from HQUSACE 2014, D-48. Public domain.) 140
68. End frame and lock recess for a submergible tainter gate. (Image reproduced from HQUSACE 2014, D-49. Public domain.) 141
69. Hydrostatic pressure distribution for a submergible tainter gate. 145
70. Structural components of a one-piece bulkhead. (Image reproduced from ETL 1110-2-584, HQUSACE 2014, B-8. Public domain.) 147
71. Dewatering bulkhead in lower lock approach. (Image reproduced from ETL 1110-2-584, HQUSACE 2014, B-8. Public domain.) 150
72. Vertical hydraulic forces from a model study of the Barkley Bulkhead. (Image reproduced from Hite and Pickering 1983, Plate 13. Public domain.) 151
73. Hydrostatic pressure distribution for a bulkhead. 153
74. Schematic of flow around a submerged bulkhead. 154

75. Schematic of pressure distribution on a bulkhead with flow over and under the bulkhead. 154
76. Comparison of Eschler (1958) and Melsheimer and Murphy (1961) results for deployment of an individual closure gate....155
77. Hite and Pickering (1983) results adapted for deployment of an individual closure gate....156
78. Rolling gate with two lines of wheels. (Image reproduced from HQUSACE 2014, F-12. Public domain.)....161
79. Rolling gate with L-frame design. (Image reproduced from HQUSACE 2014, F-12. Public domain.) 162
80. Hydrostatic pressure distribution on the rolling gate. 164
81. Side view of the ND/GB for the upper end of the lock. (Image reproduced from USACE, Nashville District [USACE-LRN], files.) 167
82. Side view of the ND/GB for the lower end of the lock. (Image reproduced from USACE-LRN files.)....168
83. Looking upstream at the ND/GB closure structure for the upper end of the Chickamauga Lock....169
84. Hydrostatic pressure distribution and the location of the resultant hydrostatic force for the ND/GB at the upper end of the lock. 172
85. Side view of a reverse tainter valve (flow is left to right). (Image reproduced from Bislip-Morales and Hite 2013, 7. Public domain.)....175
86. Photo of a scale model of a horizontally framed reverse tainter valve, which reproduced the structural members shown in the section view. (Image reproduced from EM 1110-2-1610, HQUSACE 1975, 3-9. Public domain.)....176
87. Photo of a scale model of a double skin plate reverse tainter valve, which reproduced the structural members shown in the section view. (Image reproduced from EM 1110-2-1610, HQUSACE 1975, 3-9. Public domain.)....178
88. Double skin plate tainter valve at the Dalles Lock removed for repair. 179
89. Photo of a scale model of a vertically framed reverse tainter valve, which reproduced structural members shown in the section view. (Image reproduced from EM 1110-2-1610, HQUSACE 1975, 3-9. Public domain.)....180
90. Hydrostatic pressure distribution and the location of the resultant hydrostatic force for a reverse tainter valve in a lock....183
91. Illustration of flow conditions around a reverse tainter valve that cause downpull and uplift forces. (Image reproduced from HQUSACE 1975, 3-13. Public domain.)...184
92. Total hoist loads from EM 1110-2-1610 used as design guidance. (Image reproduced from HQUSACE 1975, 3-14. Public domain.)....185
A-1. Melvin Price Locks and Dam (MPLD) spillway and basin elevations. 196
A-2. Average, maximum, and minimum tailwater hydrographs used in the design of MPLD. 197
A-3. Histogram of average daily tailwater elevation (TW El) from 1939 through 1969. 198
A-4. Probability density function (PDF) from histogram of average daily tailwater. 198
A-5. Cumulative distribution function (CDF). 199
A-6. Standard deviation determined from (maximum – minimum)/6....200
A-7. Standard deviation for the TW El (σTW El) versus Δ*H*. 200

A-8. Satellite imagery showing the wind speed and direction data collection sites for MPLD. (Map data: Google Earth 2014.) 202
A-9. Wind speed from the St. Louis Regional (SLR) airport data for a storm event....204
A-10. Fetch and wind direction determined for the MPLD project....204
A-11. Wind speed data using the weighting procedure for the storm event from the SLR airport....207
A-12. Extreme wind speed estimation for the SLR airport based on peak annual values of wind speed. 208
A-13. Extreme wind speed estimation for the Saint Charles County (SCC) airport based on maximum yearly values of wind speed. 210
A-14. Wind frequency from Gumbel type 1 distribution with Gringorten's method for the SLR airport using the peak annual values....211
A-15. Wind frequency from Gumbel type 1 distribution with Gringorten's method for the SCC airport using the peak annual values. 212
A-16. Wind speed data for the SLR airport used to determine the maximum 2 hr average for a maximum storm event in 2005. 213
A-17. Extreme wind speed estimation for the SLR airport based on maximum 2 hr average annual values of wind speed. 215
A-18. Extreme wind speed estimation for the SCC airport based on maximum 2 hr average annual values of wind speed. 215
A-19. Wind frequency from Gumbel type 1 distribution with Gringorten's method for the SLR airport using the maximum yearly 2 hr average wind speed values. 217
A-20. Wind frequency from Gumbel type 1 distribution with Gringorten's method for the SCC airport using the maximum yearly 2 hr average wind speed values. 217
A-21. Wind frequency from Gumbel type 1 distribution with Gringorten's method for the combined SLR and SCC airports using the maximum yearly 2 hr average wind speed values. 219
A-22. Wind frequency curves based on peak yearly 2 hr average wind speed for the SLR airport data bounded by plus and minus 1 and 2 standard deviations. 222
A-23. Wind frequency curves based on peak yearly 2 hr average wind speed for the SCC airport data bounded by plus and minus 1 and 2 standard deviations. 222
A-24. Wind frequency curves based on peak yearly 2 hr average wind speed for the SLR and SCC airport data bounded by plus and minus 1, 2, and 3 standard deviations...223
A-25. Wave height versus wind speed from Smith's NARFET model. 225
A-26. Wave height versus wind speed using Goda's (2010) procedure....227
A-27. Goda wave pressure distribution adapted for the spillway tainter gate (STG). 231
A-28. Definition of wave pressure moment arm terms on an STG. 231
A-29. Schematic of parameters used for MPLD in Equation (82). 235
A-30. Hydrodynamic force on STGs for varying gate openings and tailwater (upper pool el 419). 236
A-31. TW El PDF histogram. 241
A-32. PDF for hydrodynamic force per foot of gate for 1 ft gate opening. 242
A-33. PDF for hydrodynamic force per foot of gate for 2 ft gate opening. 242
A-34. PDF for hydrodynamic force per foot of gate for 3 ft gate opening. 243
A-35. PDF for hydrodynamic force per foot of gate for 4 ft gate opening. 243

A-36. PDF for hydrodynamic force per foot of gate for 5 ft gate opening. 244
A-37. PDF for hydrodynamic force per foot of gate for 6 ft gate opening. 244
A-38. PDF for hydrodynamic force per foot of gate for 7 ft gate opening. 245
A-39. PDF for hydrodynamic force per foot of gate for 8 ft gate opening. 245
A-40. PDF for hydrodynamic force per foot of gate for 9 ft gate opening. 246
A-41. PDF for hydrodynamic force per foot of gate for 10 ft gate opening. 246
A-42. Fitted spillway rating curves for the gate openings from 1 to 10 ft. 247
A-43. Maximum hydrodynamic force (per foot of gate) occurring on the gate for gate openings from 1 to 10 ft 248
A-44. Maximum total hydrodynamic force for the median and mean TW Els and the minimum and maximum TW Els for each of the 1–10 ft gate openings and a gate width of 110 ft 250
A-45. Median hydrodynamic force for each of the 1–10 ft gate openings and standard deviation ranges for –σ to +σ (*orange*), −2σ to + 2σ (*green*), and −3σ to +3σ (*blue*) 252
A-46. Comparison of σ ranges to collected data range from TW El. 253
A-47. Median hydrodynamic force for each of the 1–10 ft gate openings and reduced 6-sigma standard deviation ranges for –σ to +σ (*orange*), −2σ to +2σ (*green*), and −3σ to +3σ (*blue*). 254
A-48. Comparison of reduced 6-sigma standard deviation ranges to collected data range from TW El. 255
A-49. Comparison of PDFs for a narrow normal distribution for the hydrodynamic force distribution per foot of gate to a broader step PDF distribution from average tailwater data for a gate opening of 1 ft. 257
A-50. (*A*) Stages upstream and (*B*) stages downstream from Lock and Dam 5a on the Mississippi River between 16 March and 1 April 2011. 258
A-51. (*A*) Stages upstream and (*B*) stages downstream from James W. Trimble Lock and Dam on the Arkansas River between 21 and 27 May 2019 259
A-52. (*A*) Stages upstream and (*B*) stages downstream from McAlpine Lock and Dam on the Ohio River between 16 and 26 February 2011. 260
B-1. McNary Lock and Dam (MLD) spillway vertical-lift gate. (Image reproduced from US Army Corps of Engineers, Walla Walla District [USACE-NWW], files.) 262
B-2. Looking upstream at McNary spillway vertical-lift gates. 263
B-3. Histogram of forebay el for MLD from 1989 through 2020. 264
B-4. PDF from histogram of forebay el for MLD. 264
B-5. CDF of forebay el for MLD. 265
B-6. Satellite imagery of the wind speed and direction data collection site for MLD. (Map data: Google Earth 2013.) 267
B-7. Fetch and wind direction determined for the McNary project. 268
B-8. Extreme wind speed estimation for Hermiston Municipal (HM) airport based on maximum 1 hr average annual values of wind speed. 270
B-9. Wind frequency from Gumbel type 1 distribution with Gringorten's method for the HM airport using the maximum 1 hr average annual wind speed. 271
B-10. Wind frequency curves based on peak yearly 1 hr average wind speed for the HM airport data. 272

B-11. Wind speed versus wave height from Smith's NARFET model for MLD.....273
B-12. Wind speed versus significant wave height from Goda's (2010) procedure for the McNary project.....274
B-13. Goda wave pressure distribution adapted for vertical-lift gates.....278
B-14. Definition of wave pressure moment arm terms on a vertical-lift gate.....279
B-15. Discharge versus gate opening for McNary spillway bay 10.....281
B-16. Hydrodynamic force on gate versus gate opening for McNary spillway bay 10.....281
B-17. Hydrodynamic pressure distribution determined using Kim's (2007) procedure for the MLD spillway vertical-lift gate with 1 ft gate opening and normal upper pool el...284
B-18. Resultant hydrostatic force per foot of gate width for range of upper pool els for the MLD spillway vertical-lift gate.....285
B-19. Magnitude and location of resultant hydrodynamic force for +6σ, mean, and −6σ upper pool els for the McNary vertical-lift gate with a 1 ft gate opening.....289
C-1. R. C. Byrd Lock and Dam (RCBLD) spillway section view. (Image reproduced from USACE, Huntington District [USACE-LRH] files.)....292
C-2. Histogram of upper pool el from 1999 through 2020.....293
C-3. PDF from histogram of upper pool el.....294
C-4. CDF for upper pool el.....294
C-5. Histogram of TW El between 1993 and 2020.....295
C-6. PDF from histogram of TW El.....296
C-7. CDF for TW El.....296
C-8. Satellite imagery of the wind speed and direction data collection site in relation to R. C. Byrd Spillway. (Map data: Google Earth 2016.)....298
C-9. Satellite imagery showing the fetch and wind direction determined for the RCBLD project. (Map data: Google Earth 2015.).....299
C-10. Extreme wind speed estimation for Point Pleasant Airport (PPA) based on max 0.3 hr average annual values of wind speed.....301
C-11. Wind frequency from Gumbel type 1 distribution with Gringorten's method for the PPA using the maximum 0.3 hr average annual wind speed.....302
C-12. Wind frequency curves based on peak yearly 0.3 hr average wind speed for the PPA data.....303
C-13. Wave height versus wind speed from Smith's NARFET model for the R. C. Byrd roller gate.....304
C-14. Wave height versus wind speed from Goda's (2010) procedure for the R. C. Byrd roller gate.....305
C-15. Schematic for terms used in Equation (82) for a roller gate with tailwater.....311
C-16. Spillway rating curves for the R. C. Byrd roller gate, redrawn from original curves provided by USACE-LRH.....313
C-17. Hydrodynamic force per foot of gate for the R. C. Byrd roller gate.....313
C-18. Hydrostatic pressure distribution for the RCBLD roller gate with an upper el of 537.918 (mean), 538.5 (+6σ), and 537.336 (−6σ).....315
D-1. Satellite imagery of Calcasieu Lock on the Gulf Intracoastal Waterway (GIWW). (Map data: Landsat/Copernicus, n.d.).....318
D-2. Histogram of head on the Calcasieu Lock east sector gate, 2004 through 2020.....319

D-3. PDF from histogram of head on sector gate.....319
D-4. CDF for head on east sector gate.....320
D-5. Satellite imagery of the wind speed and direction data collection site. (Map data: Landsat/Copernicus, n.d.).....322
D-6. Satellite imagery of fetch and wind direction determined for the Calcasieu Lock east sector gate. (Map data: Landsat/Copernicus, n.d.).....323
D-7. Extreme wind speed estimation for the Lake Charles (LCH) airport based on maximum 0.5 hr average annual values of wind speed.....325
D-8. Wind frequency from Gumbel type 1 distribution with Gringorten's method for the LCH airport using the maximum 0.5 hr average annual wind speed. 326
D-9. Wind frequency curves based on peak yearly 0.5 hr average wind speed for the LCH airport data.....328
D-10. Wind speed versus wave height from Smith's NARFET model for the Calcasieu Lock east sector gate. 329
D-11. Wind speed versus wave height from Goda's (2010) procedure for the Calcasieu Lock east sector gate.....330
E-1. Looking upstream at the frame side of the upper Barkley Lock miter gate. 340
E-2. Looking upstream at the frame side of the Barkley Lock lower miter gate. 341
E-3. Histogram of forebay el from 1989 through 2020 for the upper lock gate. 342
E-4. PDF from histogram of forebay el for the upper lock gate.....342
E-5. CDF for forebay el for the upper lock gate.....343
E-6. Histogram of TW El between 1989 and 2020 for the lower lock gate.....344
E-7. PDF from the histogram of TW El for the lower lock gate. 344
E-8. CDF for TW El for the lower lock gate.....345
E-9. Satellite imagery showing the wind speed and direction data collection site in relation to the Barkley Lock. (Map data: Landsat/Copernicus 2002.).....347
E-10. Fetch and wind direction determined for the Barkley upper miter gate. 348
E-11. Extreme wind speed estimation for Barkley Regional Airport (PAH) based on maximum 1 hr average annual values of wind speed and used for the Barkley Lock upper miter gate. 350
E-12. Wind frequency from Gumbel type 1 distribution with Gringorten's method for PAH using the maximum 1 hr average annual wind speed and used for the Barkley Lock upper miter gate. 351
E-13. Wind frequency curves based on peak yearly 1 hr average wind speed for the PAH data and used for the Barkley Lock upper miter gate. 352
E-14. Wave height versus wind speed from Smith's NARFET model for the Barkley Lock upper miter gate. 353
E-15. Wave height versus wind speed from Goda's (2010) procedure for the Barkley Lock upper miter gate.....354
E-16. Fetch and wind direction determined for the Barkley lower miter gate.....359
E-17. Extreme wind speed estimation for PAH based on maximum 0.25 hr average annual values of wind speed and used for the Barkley Lock lower miter gate.....361
E-18. Wind frequency from Gumbel type 1 distribution with Gringorten's method for PAH using the maximum 0.25 hr average annual wind speed and used for the Barkley Lock lower miter gate. 362

E-19. Wind frequency curves based on peak yearly 0.25 hr average wind speed for the PAH data and used for the Barkley Lock lower miter gate. 363
E-20. Wave height versus wind speed from Smith's NARFET model for the Barkley Lock lower miter gate. 364
E-21. Wave height versus wind speed from Goda's (2010) procedure for Barkley Lock lower miter gate. 365
E-22. Hydrostatic force illustration for the Barkley lock lower gate. 372
F-1. Ice Harbor Lock submergible tainter gate. 375
F-2. Histogram of forebay el from 1962 through 2020. 376
F-3. PDF from histogram of forebay el for the Ice Harbor submergible tainter gate. 376
F-4. CDF for forebay el for the Ice Harbor submergible tainter gate. 377
F-5. Satellite imagery of the wind speed and direction data collection site in relation to Ice Harbor Lock. (Map data: Google Earth 2012.) 379
F-6. Satellite imagery of the fetch and wind direction determined for the Ice Harbor Lock and Dam project. (Map data: Google Earth 2012.) 380
F-7. Extreme wind speed estimation for Pasco / Tri Cities (PSC) based on maximum 0.5 hr average annual values of wind speed. 382
F-8. Wind frequency from Gumbel type 1 distribution with Gringorten's method for the PSC using the maximum 0.5 hr average annual wind speed. 383
F-9. Wind frequency curves based on peak yearly 0.5 hr average wind speed for the PSC data. 384
F-10. Wave height versus wind speed from Smith's NARFET model for the submergible tainter gate. 385
F-11. Wave height versus wind speed from Goda's (2010) procedure for a submergible tainter gate. 386
G-1. Barkley Dam spillway section view. (Image reproduced from USACE, Nashville District [USACE-LRN], files.) 394
G-2. Pictures of 1:15-scale model of Barkley spillway bulkheads. (Image reproduced from Hite and Pickering 1983, Figure 6. Public domain.) 395
G-3. Histogram of forebay el from 1989 through 2020. 396
G-4. PDF from histogram of forebay el. 397
G-5. CDF for forebay el. 397
G-6. Histogram of TW El between 1989 and 2020 398
G-7. PDF from histogram of TW El. 399
G-8. CDF for TW El. 399
G-9. Satellite imagery of the wind speed and direction data collection site in relation to the Barkley Spillway. (Map data: Landsat/Copernicus 2002.) 401
G-10. Satellite imagery of the fetch and wind direction determined for the Barkley project. (Map data: Landsat/Copernicus 2002.) 402
G-11. Extreme wind speed estimation for PAH based on maximum 1 hr average annual values of wind speed. 404
G-12. Wind frequency from Gumbel type 1 distribution with Gringorten's method for the PAH airport using the maximum 1 hr average annual wind speed 405
G-13. Wind frequency curves based on peak yearly 1 hr average wind speed for the PAH data. 406

G-14. Wave height versus wind speed from Smith's NARFET model for the Barkley bulkhead. 407
G-15. Wave height versus wind speed from Goda's (2010) procedure for the Barkley bulkhead. 408
G-16. Hydrostatic pressure distributions for the range of upper pool els for the Barkley spillway bulkhead....414
G-17. Resultant hydrostatic force for range of upper pool els for the Barkley spillway bulkhead....414
H-1. Location of Williams Boulevard Rolling Gate. (Image reproduced from USACE-MVN 2011, sheet G-002. Public domain.) 417
H-2. Plan schematic of rolling gate location. (Image reproduced from USACE-MVN 2011, sheet S-101. Public domain.)....418
H-3. Partial elevation view of rolling gate. (Image reproduced from USACE-MVN 2011, sheet S-108. Public domain.)....418
I-1. Chickamauga needle dam / girder beams (ND/GB) being installed in upper approach (view is looking upstream). 428
I-2. Histogram of forebay el from 1989 through 2020. 429
I-3. PDF from histogram of forebay el for ND/GB. 429
I-4. CDF for forebay el for ND/GB. 430
I-5. Satellite imagery of the wind speed and direction data collection site in relation to Chickamauga Lock ND/GB. (Map data: Google Earth 2013.)....432
I-6. Satellite imagery of the fetch and wind direction determined for the Chickamauga Lock ND/GB project. (Map data: Google Earth 2013.)....433
I-7. Extreme wind speed estimation for Chickamauga Lock Lower ND/GB based on maximum 0.9 hr average annual values of wind speed....435
I-8. Wind frequency from Gumbel type 1 distribution with Gringorten's method for the Chickamauga Lock upper lock approach using the maximum 0.9 hr average annual wind speed....436
I-9. Wind frequency curves based on peak yearly 0.9 hr average wind speed for the Chattanooga/Lovell Airport (CHA) data. 437
I-10. Wave height versus wind speed from Smith's NARFET model for Chickamauga Lock upper ND/GB....438
I-11. Wave height versus wind speed from Goda's (2010) procedure for the upper ND/GB....439
I-12. Histogram of TW El from 1989 through 2020....445
I-13. PDF from the histogram of TW El for the lower ND/GB. 446
I-14. CDF for TW El for the lower ND/GB. 446
I-15. Extreme wind speed estimation for Chickamauga Lock lower ND/GB based on maximum 0.2 hr average annual values of wind speed....450
I-16. Wind frequency from Gumbel type 1 distribution with Gringorten's method for the Chickamauga Lock lower ND/GB using the maximum 0.2 hr average annual wind speed. 451
I-17. Wind frequency curves based on peak yearly 0.2 hr average wind speed for the CHA data. 452
I-18. Wave height versus wind speed from Smith's NARFET model for Chickamauga Lock lower ND/GB. 453

I-19. Wave height versus wind speed from Goda's (2010) procedure for the lower ND/GB. 454
J-1. Satellite aerial view of the Dalles Lock and Dam. (Map data: Google Earth 2020.)....462
J-2. Histogram of the Dalles forebay el from 1967 through 2021. 463
J-3. PDF from histogram of the Dalles forebay el. 463
J-4. CDF for the Dalles forebay el. 464
J-5. Histogram of the Dalles TW El between November of 1966 and August of 2021....465
J-6. PDF from histogram of TW El for the Dalles project. 465
J-7. CDF for TW El for the Dalles project. 466

Tables

1. Hydraulic steel structure (HSS) types, project example, and loads. 4
2. Load factors for tainter gates. (Table adapted from Engineer Transmittal Letter [ETL] 110-2-584, HQUSACE 2014, D-10.)....15
3. *K* values for submerged uncontrolled flow. (Table adapted from EM 1110-2-1605, HQUSACE 1987.) 24
4. Minimum wind duration times (t_{min}) to obtain significant wave height at MPLD. 50
5. Minimum, maximum, and average values obtained from Figure 31. 63
6. Parameters used to compute hydrodynamic pressures from the Kim (2007) data with a 5 cm gate opening. 65
7. The simplified three shapes, pseudo-static hydrodynamic pressure diagram components, and lever arm used to determine location, h_{Lat}, of the resultant hydrodynamic force acting on a sluice gate with a 5 cm gate opening. 68
8. Hydrodynamic pressure distribution with no tailwater effects and a TW El of 395 for the MPLD spillway gate with 1 ft gate opening. 73
9. Hydrostatic gate force per foot of gate run for the upper pool els +6σ and −6σ around the mean upper pool for the MPLD STG. 77
10. Load factors for spillway crest vertical-lift gates. (Table adapted from ETL 1110-2-584, HQUSACE 2014, Table E-2.)....87
11. Load factors for miter gates. (Table adapted from ETL 1110-2-584, HQUSACE 2014, C-3.) 128
A-1. Sample of wind speed and direction data for station number 724395 99999, latitude 38.883, longitude −90.033, elevation 166. 203
A-2. Peak annual wind speed values at the SLR airport for the 1983 to 2005 observation period. 209
A-3. Peak annual wind speed values at the Saint Charles County (SCC) airport for the 1998 to 2019 observation period. 209
A-4. Minimum wind duration times to obtain significant wave height. 213
A-5. Maximum 2 hr average annual wind speed values at the SLR airport for the 1983 to 2005 observation period. 214
A-6. Maximum 2 hr average annual wind speed values at the SCC airport for the 1999 to 2019 observation period. 216

A-7. Maximum 2 hr average annual wind speed values at the SLR and SCC airports for the 1983 to 2019 observation period. 218
A-8. Results from wind speed analyses for MPLD. 224
A-9. Example wave height and wave period computed using the NARFET model. 225
A-10. Significant wave height and wave period using Goda's formulations. 226
A-11. Parameters used in example wave force calculation (imperial and metric units included) 227
A-12. Goda's (2010) procedure for wave height, period, and wavelength for combined airport data. 232
A-13. Wave force and pressure distribution computations using Goda's (2010) procedure for data in Table A-12. 232
A-14. Hydrodynamic loads for varying tailwater and gate openings from 1–10 ft. 237
A-15. Exit area used for calculations in Table D-14. 237
A-16. Hydrostatic gate force per foot of gate run for the upper pool els +6σ and −6σ around the mean upper pool for the Melvin Price STG. 239
A-17. Tailwater statistics from average daily values 249
A-18. Results of computations using the 6-sigma method; total hydrodynamic force values on the 110 ft wide gate given minimum and maximum forces for each of the 10 gate openings. 251
A-19. Results of computations using the reduced 6-sigma method, total hydrodynamic force values on a 110 ft wide gate given a range in minimum and maximum forces at 10 gate openings. 254
A-20. Summary of ranges in total hydrodynamic forces about the median hydrodynamic force value on a 110 ft wide gate using the reduced 6-sigma method for the 10 gate openings. 256
B-1. Maximum yearly 1 hr average wind speed for wind directions between 60° and 100° at the HM airport for the 1999 to 2020 observation period. 268
B-2. Results from the wind speed analysis for MLD. 270
B-3. Wave height, period, and wavelength computed using the NARFET model for the McNary project. 273
B-4. Significant wave height, period, and wavelength from Goda's (2010) formulations for the McNary project. 274
B-5. Parameters used in example wave force calculation (imperial and metric units included) for McNary project for a wind speed of 33.7 mph 275
B-6. Wave force and pressure distribution computations using Goda's (2010) procedure for the McNary project. 279
B-7. Hydrodynamic loads for gate openings from 1–15 ft using the conservation of momentum procedure. 282
B-8. Parameters used to compute hydrodynamic pressures from the Kim (2007) procedure for the MLD spillway vertical-lift gate with a 1 ft gate opening. 283
B-9. Hydrostatic gate force per foot of gate run for the upper pool els +6σ and −6σ around the mean upper pool for the McNary vertical-lift gate. 285
B-10. Parameters used to compute hydrodynamic pressures using the Kim (2007) procedure for the MLD spillway vertical-lift gate with a 1 ft gate opening and an upper pool el of 342.21 286

B-11. Parameters used to compute hydrodynamic pressures using the Kim (2007) procedure for the MLD spillway vertical-lift gate with a 1 ft gate opening and an upper pool el of 335.37....287
B-12. Parameters used to compute hydrodynamic pressures using the Kim (2007) procedure for the MLD spillway vertical-lift gate with a 1 ft gate opening and an upper pool el of 338.79....288
B-13. Example hydraulic loads for the McNary spillway vertical-lift gate....289
C-1. Maximum yearly 0.3 hr average wind speed for a wind directions between 340° and 20° at the Point Pleasant Airport (PPA) for the 2005 to 2020 observation period....300
C-2. Results from the wind speed analysis for the R. C. Byrd roller gate....302
C-3. Wave height, wave period, and wavelength computed using the NARFET model for the R. C. Byrd roller gate....303
C-4. Significant wave height, wave period, and wavelength from Goda's formulations for the R. C. Byrd roller gate....305
C-5. Parameters used in example wave force calculation (imperial and metric units included) for the R. C. Byrd project for a wind speed of 16.2 mph....306
C-6. Wave force and pressure distribution computations using Goda's (2010) procedure for data in Table C-4....309
C-7. Hydrostatic force statistics for the R. C. Byrd spillway roller gate for a range of upper pool els from −6σ (537.336) to +6σ (538.5) about the mean of 537.918....314
C-8. Hydrodynamic force statistics for the R. C. Byrd spillway roller gate with 1 ft gate opening, normal upper pool el of 538, and TW El range from −3σ (511.3) to +3σ (533.83)....315
C-9. Example hydraulic loads for the RCBLD spillway roller gate....316
D-1. Maximum yearly 0.5 hr average wind speed for wind directions between 110° and 150° at LCH for the 1990 to 2021 observation period....324
D-2. Results from wind speed analysis for the Calcasieu Lock east sector gate....327
D-3. Wave height, period, and wavelength computed using the NARFET model for the Calcasieu Lock east sector gate....328
D-4. Significant wave height, period, and wavelength using Goda's (2010) formulations for the Calcasieu Lock east sector gate....329
D-5. Parameters used in example wave force calculation (imperial and metric units included) for the Calcasieu Lock east sector gate for a wind speed of 42.5 mph....331
D-6. Wave force and pressure distribution computations using Goda's (2010) procedure for the Calcasieu Lock east sector gate....334
D-7. Hydrostatic forces computed for the Calcasieu Lock east sector gate for the range of heads from +3σ to −3σ around the mean head....337
D-8. Example hydraulic loads for the Calcasieu Lock east sector gate....338
E-1. Maximum yearly 1 hr average wind speed for wind directions between 140° and 180° at the Barkley Regional Airport (PAH) for the observation period from 1991 and 2020 and used for the Barkley Lock upper miter gate....349
E-2. Results from wind speed analysis for the Barkley Lock upper miter gate....351
E-3. Wave height, wave period, and wavelength computed using the NARFET model for the Barkley Lock upper miter gate....353

E-4. Significant wave height, wave period, and wavelength using Goda's (2010) formulations for the Barkley Lock upper miter gate. 354
E-5. Parameters used in example wave force calculation (imperial and metric units included) for the Barkley Lock upper miter gate for a wind speed of 36.3 mph. 355
E-6. Wave force and pressure distribution computations using Goda's (2010) procedure for data in Table E-4 for the Barkley Lock upper miter gate. 358
E-7. Maximum yearly 0.25 hr average wind speed for wind directions between 320° and 360° at PAH for the 1991 to 2020 observation period and used for the Barkley Lock lower miter gate. 360
E-8. Results from wind speed analysis for the Barkley Lock lower miter gate. 362
E-9. Wave height, wave period, and wavelength computed using the NARFET model for the Barkley Lock lower miter gate. 363
E-10. Significant wave height, wave period, and wavelength using Goda's (2010) formulations for the Barkley Lock lower miter gate. 364
E-11. Parameters used in the example wave force calculation (imperial and metric units included) for the Barkley Lock lower miter gate for a wind speed of 36.3 mph. 366
E-12. Wave force and pressure distribution computations using Goda's (2010) procedure for data in Table E-4 for the Barkley Lock lower miter gate. 369
E-13. Maximum operating forces for the Barkley Lock lower gate machinery with 35 ft submergence from USACE-LRN (1958). 370
E-14. Hydrostatic forces computed for the Barkley lower lock gate beam for the range of heads from +3σ to −3σ around the mean head of 42.26 ft. 371
E-15. Example hydraulic loads for the Barkley Lock miter gates. 373
F-1. Maximum yearly 0.5 hr average wind speed for wind directions between 50° and 90° at the Pasco / Tri Cities (PSC) airport for the 1990 to 2020 observation period. 381
F-2. Results from wind speed analysis for the Ice Harbor submergible tainter gate. 383
F-3. Wave height, wave period, and wavelength computed using the NARFET model for the submergible tainter gate. 385
F-4. Significant wave height, wave period, and wavelength using Goda's (2010) formulations for submergible tainter gates. 386
F-5. Parameters used in the example wave force calculation (imperial and metric units included) for a submergible tainter gate with a wind speed of 36.3 mph. 387
F-6. Wave force and pressure distribution computations using Goda's (2010) procedure for data in Table F-4 for the Ice Harbor project. 391
F-7. Hydrostatic forces computed for the Ice Harbor Lock submergible tainter gate for the range of upper pool els from +3σ to −3σ around the mean upper pool el of 438.68. 391
F-8. Example hydraulic loads for the Ice Harbor Lock and Dam submergible tainter gate. 392
G-1. Maximum yearly 1 hr average wind speed for wind directions between 140° and 180° at PAH for the 1991 to 2020 observation period. 403
G-2. Results from wind speed analysis for the Barkley bulkhead. 405
G-3. Wave height, wave period, and wavelength computed using the NARFET model for the Barkley bulkhead. 406

G-4. Significant wave height, wave period, and wavelength using Goda's (2010) formulations for the Barkley bulkhead. 407
G-5. Parameters used in the example wave force calculation (imperial and metric units included) for the Barkley project for a wind speed of 36.3 mph. 409
G-6. Wave force and pressure distribution computations using Goda's (2010) procedure for data in Table G-4 for the Barkley project. 412
G-7. Example hydraulic loads for the Barkley Lock and Dam (BLD) spillway bulkhead.....415
H-1. Significant wave height, wave period, and wavelength using Goda's (2010) formulations for a rolling gate with a 5 mi fetch. 421
H-2. Parameters used in the example wave force calculation (imperial and metric units included) for the rolling gate for a wind speed of 80 mph. 421
H-3. Wave force and pressure distribution computations using Goda's (2010) procedure for data in Table H-2 for the rolling gate example with a wind speed of 80 mph. 425
H-4. Hydrostatic forces computed for the Williams Boulevard rolling gate for a range of surge heights from +3σ to −3σ around the assumed mean surge height el of 13.25. 425
H-5. Example hydraulic loads for the Williams Boulevard rolling gate. 425
I-1. Maximum yearly 0.9 hr average wind speed for wind directions between 70° and 110° at Chattanooga/Lovell Airport (CHA) for the upper ND/GB at Chickamauga Lock for the 1970 to 2020 observation period. 434
I-2. Results from wind speed analysis for CHA for the Chickamauga upper ND/GB. 436
I-3. Wave height, wave period and wavelength computed using the NARFET model for upper ND/GB. 437
I-4. Significant wave height, significant wave period, and significant wavelength from Goda's (2010) formulations for the upper ND/GB. 438
I-5. Parameters used in the example wave force calculation (imperial and metric units included) for ND/GB for a wind speed of 28.0 mph. 440
I-6. Wave force and pressure distribution computations using Goda's (2010) procedure for data in Table I-4 for the Chickamauga Lock upper ND/GB project. 443
I-7. Example hydraulic loads for the Chickamauga Lock upper ND/GB. 444
I-8. Maximum yearly 0.2 hr average wind speed for wind directions between 250° and 290° at CHA for the lower ND/GB at Chickamauga Lock for the 1970 to 2020 observation period. 449
I-9. Results from the wind speed analysis for CHA for the Chickamauga lower ND/GB. 451
I-10. Wave height, wave period, and wavelength computed using the NARFET model for lower ND/GB. 452
I-11. Significant wave height, wave period, and wavelength computed using Goda's (2010) formulations for the lower ND/GB. 453
I-12. Parameters used in the example wave force calculation (imperial and metric units included) for lower ND/GB for a wind speed of 28.0 mph. 455
I-13. Wave force and pressure distribution computations using Goda's (2010) procedure for data in Table I-11 for the Chickamauga Lock lower ND/GB project 458
I-14. Hydrostatic forces computed for the Chickamauga Lock needle dam / girder beams (ND/GB) for the range of upper pool els from +3σ to −3σ around the mean upper pool el of 679.80. 459

I-15. Hydrostatic forces computed for the Chickamauga Lock ND/GB for the range of lower pool els from +3σ to −3σ around the mean lower pool el of 637.02. 459
I-16. Example hydraulic loads for the Chickamauga Lock lower ND/GB.....460
J-1. Hydrostatic forces computed for the Dalles Lock reverse tainter valve for the range of heads from +3σ to −3σ around the mean head of 80.57 ft. 468
J-2. Example hydrostatic loads for the Dalles Lock reverse tainter valve.....469

Preface

This study and report were prepared for Headquarters, US Army Corps of Engineers (HQUSACE), under the Load and Resistance Factor Design for Hydraulic Steel Structures (LRFD for HSS) work unit of the Navigation Systems Research Program, Funding Account Code U4388265, AMSCO Code 031391. Ms. Morgan M. Johnston, US Army Engineer Research and Development Center, Coastal and Hydraulics Laboratory (ERDC-CHL), was the program manager for the Navigation Systems Research Program while most of this research was conducted. At the time of preparation of this report, Mr. Kareem S. El-Naggar was the HQUSACE Navigation Business Line manager.

This research was performed by the Navigation Branch, Navigation Division, ERDC-CHL. At the time of publication, Mr. Benjamin C. Burnham was chief of the Navigation Branch, and Ms. Ashley E. Frey was chief of the Navigation Division. Mr. Charles E. Wiggins was the Navigation technical director. The deputy director of ERDC-CHL was Mr. Keith Flowers, and the director was Dr. Ty V. Wamsley. The research was also performed by the Information Technology Laboratory (ITL), and Dr. Robert M. Ebeling (retired) of the ERDC-ITL was the principal investigator (PI) for the LRFD for HSS work unit until March 2022. Mr. Barry C. White of ERDC-ITL became the PI after March 2022. Mr. David C. Stuart was chief of the Computational Analysis Branch, Dr. Jeffrey L. Hensley was chief of the Computational Science and Engineering Division, Dr. Jacqueline S. Pettway was deputy director of ERDC ITL, and Dr. David A. Horner was director of ERDC ITL at the time of publication.

Numerous USACE team members provided valuable data and advice during preparation of this report. Mr. Edward Brauer and Mr. Steven Hobbs (St. Louis District); Mr. Marcus Palmer, Mr. Byran Mason, Mr. Shawn Nelson, Mr. Martin Ahmann, Mr. Martin Ahmann, Jr., and Ms. Willow Walker (Walla Walla District); Mr. Aaron Litzenberg (Portland District); Mr. Dan Coz (Lakes and Rivers Division); Mr. Ted Hamb, Mr. Rodney Cremeans, Mr. Steve Foster, and Mr. Fred McCallister (Huntington District); Mr. Ben Rohbach, Mr. James Bilbrey, Mr. Cory Morgan, Mr. Charlie Thomason, Mr. Clint Neel, Mr. Rob Baulsir, III, Ms. Britt Henderson, and Mr. Michael Murphy (Nashville District); Mr. Kent Hokens (St. Paul District); Mr. Clyde Barré, Mr. Charles Brandstetter, and Mr. Denis Hoerner, Jr. (New Orleans District); Mr. Ben Johnson and Mr. Frederick Sheffield

(Kansas City District); and Dr. Shubhra Misra, Mr. Coraggio Maglio, Mr. Dave Lovett, Mr. Patrick Corbitt Kerr, and Ms. Amanda Hafemeister (Galveston District) all provided information or data for this research effort.

COL Christian Patterson was commander of ERDC, and Dr. David W. Pittman was the director.

This page intentionally left blank.

1 Introduction

1.1 Background

In the past, the US Army Corps of Engineers (USACE) relied on the allowable stress design (ASD) when building steel structures. The allowable stresses were determined from previous experience and did not include quantification of the reliability and risk performance provided by the structure. However, the Load and Resistance Factor Design (LRFD) approach was adopted by the industry and is reflected in industry standards for the design of buildings and bridges. LRFD-based engineering methods provide more accurate lifetime models of structures by providing risk-based load factors. Structures designed using LRFD provide more consistent, tolerable, and understood risk performance.

USACE is currently transitioning to LRFD, which can also be used to evaluate existing structures by incorporating the uncertainty of the load and limit-state capacity of the structure. An advantage of LRFD is that it considers the variability in the load and resistances separately. Besides improved safety, improved performance and, in some cases, delayed rehabilitation can provide cost savings. USACE first incorporated LRFD into the design of hydraulic steel structures (HSS) in 1993, but with specific development of LRFD only for lock miter gates.

Currently, the primary guidance document used for the design of HSS is Engineer Transmittal Letter (ETL) 1110-2-584, *Design of Hydraulic Steel Structures* (HQUSACE 2014). This document refers to the American Institute of Steel Construction's (AISC; 1980) steel construction manual to compute member capacity for design. ETL 1110-2-584 contains load factors that have not been fully calibrated. In addition, loads encountered in HSS environments have not been fully developed. Therefore, the total reliability and risk provided by HSS design with this guidance is uncertain. The primary guidance document used for the evaluation of HSS (Engineer Manual [EM] 1110-2-6054, *Inspection, Evaluation, and Repair of Hydraulic Steel Structures*; USACE 2001) is absent of any guidance on loads, load factors, load combinations, or the influence of condition. This report, therefore, presents the results of the hydraulic loadings that are applicable to USACE HSS. The report is the first in a series that will describe the methodologies for the application of LRFD to HSS and contains the hydraulic loading determined for the 10 HSS selected for the research.

1.2 Objective

The overall research effort will develop LRFD methodologies for application to different types of USACE HSS, with an emphasis on providing the risk-based load factors that are a key contributor for the most cost-effective design. The devised relationship will result in load factors that are consistent with resistance factors contained in the AISC manual and other relevant design standards such that a minimum level of reliability is assured for HSS. The devised reliability based procedure will need to take the following into account: the design life that is unique to USACE HSS, with its consequent reliability index β target value; the need to establish a safety margin ratio of load factor to the resistance factor that is consistent with the target reliability index value; and the appropriate procedure to be used to define a load factor that is calculated with appropriate consideration of the required safety margin ratio and given an AISC-defined resistance factor.

The primary goal of this work unit is to create an LRFD risk-based engineering methodology for the analysis and design of the different types of HSS in USACE's inventory to determine a value for the load factors that are consistent with resistance factors contained in AISC and other relevant design standards such that a minimum level of reliability is assured for HSS.

Because HSS designs are dominated by hydraulic loading, a key data input in the development of a hydraulic load factor is the statistical dispersion about the mean hydraulic load estimate. This dispersion in hydraulic loading will be different for each respective HSS type. Application of reliability theory and probability theory requires the formal statistical characterization (i.e., mean, standard deviation, and distribution type) of the hydraulic load.

1.3 Approach

USACE has a broad portfolio of different types of HSS systems that are used for multiple purposes. For this research, the hydraulic structures were placed in categories of (1) spillway gates, (2) lock gates, (3) closure structures, and (4) reverse tainter lock valves. Within each of these categories, the structural community has initially identified 10 HSS that need LRFD guidance and engineering-based reliability methodologies or procedures.

The 10 HSS that need LRFD guidance and engineering-based reliability methodologies are listed here, separated according to their categories:

- Spillway gates

    1. Tainter gates
    2. Vertical-lift gates
    3. Roller gates

- Lock gates

    4. Sector gates
    5. Miter gates
    6. Submergible tainter gates

- Closure structures

    7. Bulkheads
    8. Rolling gates
    9. Needle dam / girder beams (ND/GB)

- Reverse tainter lock valves

    10. Reverse tainter valve

For each HSS, a site-specific project with a gate type from the list was chosen to demonstrate the procedures and computations used to characterize the hydraulic loads. Table 1 contains project examples and the hydraulic loads associated with the particular gate type.

Because of the unique nature of gate operations and the specifics of hydraulic flow conditions encountered by each gate type, differing hydraulic loadings can be applied to the 10 different HSS. The loads on a spillway tainter gate (STG) are primarily hydrostatic and hydrodynamic, while a lock valve is subjected to these loads in addition to flow-induced vibrations. A miter gate is vulnerable to loads that result from machinery, lock valve failures, and impacts from vessels in the chamber. Therefore, one reliability based methodology will not fit all HSS. An appropriate and consistent reliability based procedure of analysis or design will be devised for each of the 10 gate types, with consideration given first to those gates that are most widely used on USACE projects.

Table 1. Hydraulic steel structure (HSS) types, project example, and loads.

Gate Type	Gate Feature	Project Example	Loads
Spillway gates	Tainter gate	Melvin Price Locks and Dam on the Ohio River, St. Louis District	H_s, H_d, W-W
	Vertical-lift gate	McNary Lock and Dam, Columbia River, Portland District	H_s, H_d, W-W
	Roller gate	R. C. Byrd Locks and Dam on the Ohio River, Huntington District	H_s, H_d, W-W
Lock gates	Miter gate	Barkley Lock on the Cumberland River, Nashville District	H_s, H_d, W-W
	Sector gate	Calcasieu Lock East Sector Gate on the Gulf Intracoastal Waterway (GIWW), New Orleans District	H_s, H_d, W-W
	Submergible tainter gate	Ice Harbor Lock on the Snake River, Walla Walla District	H_s, W-W
Closure structures	Bulkhead	Barkley bulkhead, BLD on the Cumberland River, Nashville District	H_s, W-W
	Rolling gate	Williams Blvd Floodgate, on Lake Pontchartrain, New Orleans District	H_s, W-W
	Needle dam / girder beam	Chickamauga Lock on the Tennessee River, Nashville District	H_s, W-W
Lock valve	Reverse tainter valve	The Dalles Lock on the Columbia River, Portland District	H_s, H_d

Note: H_s designates design for hydrostatic water loading. H_d designates a dynamic flow condition. A pseudo-static dynamic water design force load definition is required. This definition will include the dynamic water force, its point of action, and a corresponding pseudo-static dynamic pressure distribution for use in design. W-W designates design for wind-induced wave loading.

Many of USACE's HSS are in complex flow environments, which makes estimating the hydraulic loads a challenge. The hydrostatic loads are usually straightforward and can be determined analytically. Determining the hydrodynamic loads is complicated because of the rapidly varying and unsteady flow. Computational fluid dynamics (CFD) modeling has been used to determine the flow field for many hydraulic problems, but it has limitations in a near-field, rapidly varying flow environment. In this report, the authors provide guidance on how to determine hydraulic loads using some simplified techniques. As the capability of CFD modeling advances, better estimates of these loads may be possible.

1.4 Report Contents

This report contains primarily the hydraulic loads associated with the 10 HSS listed in Section 1.3. The chapters are presented according to the groups shown in Table 1. The spillway gates are addressed in Chapters 2, 3, and 4. Lock gates are addressed in Chapters 5, 6, and 7. Closure

structures are in Chapters 8, 9, and 10. The lock valve is covered in Chapter 11. A brief description of the contents of each chapter is listed here:

- Chapter 2 describes the STG and the hydraulic loads associated with this type of gate. It also includes a limited discussion of other loads that will be addressed in separate reports in the overall research effort.
- Chapter 3 presents the hydraulic loads for the vertical-lift gate.
- Chapter 4 presents the hydraulic loads for the spillway roller gate.
- Chapter 5 presents the hydraulic loads for the sector gate.
- Chapter 6 presents the hydraulic loads for the lock miter gate.
- Chapter 7 presents the hydraulic loads for the submergible tainter gate used as an upper lock gate.
- Chapter 8 presents the hydraulic loads for bulkheads.
- Chapter 9 presents the hydraulic loads for the rolling gate.
- Chapter 10 presents the hydraulic loads for the ND/GB used for lock dewatering.
- Chapter 11 presents the hydraulic loads for the reverse tainter valve used for lock filling and emptying operations.
- Chapter 12 presents a summary, conclusions, and recommendations.

Each of the chapters is paired with an example project in the appendixes that details the procedures for developing hydraulic loads. Appendix A contains an example of the procedures for developing hydraulic loads for an STG. The Melvin Price Locks and Dam (MPLD), on the Mississippi River in the USACE, St. Louis District (USACE-MVS; Figure 1), was selected for use in this example.

Figure 1. Melvin Price Dam spillway tainter gate (STG), looking upstream.

Appendix B shows an example of how to determine the hydraulic loads on a spillway vertical-lift gate. McNary Lock and Dam (MLD), on the Columbia River in the USACE, Walla Walla District (USACE-NWW; Figure 2), was selected for this example.

Figure 2. McNary Dam spillway vertical-lift gate, looking upstream.

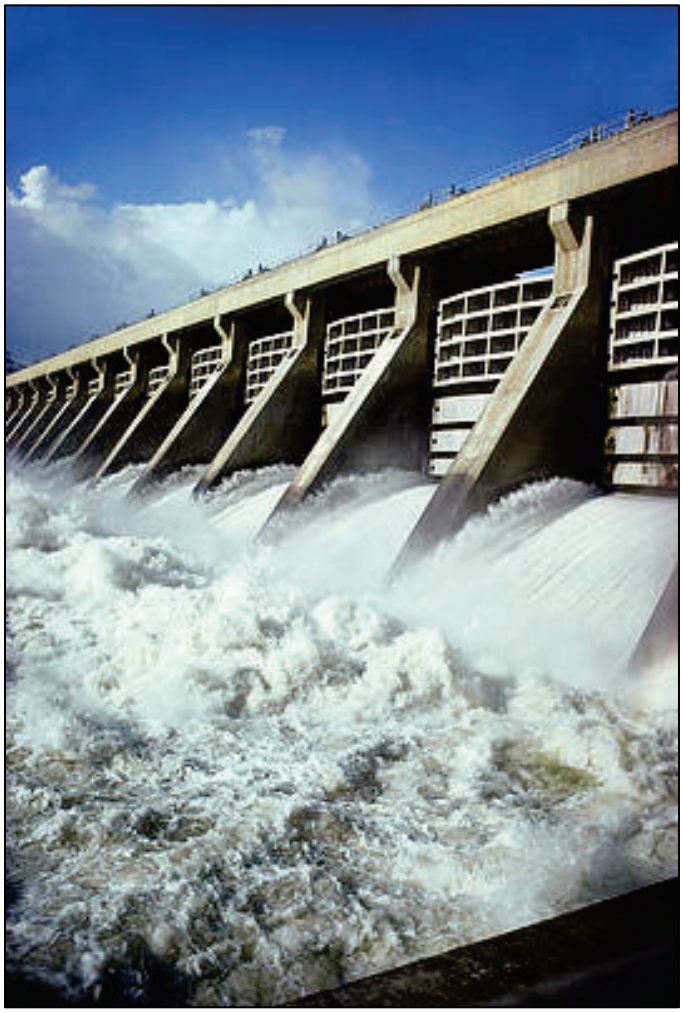

Appendix C presents the hydraulic loads determined for the spillway roller gate. The R. C. Byrd Locks and Dam (RCBLD), on the Ohio River in the USACE, Huntington District (USACE-LRH), was selected for the example. Figure 3 shows a view of a spillway roller gate looking across the downstream side of the dam.

Figure 3. View of a spillway roller gate looking across the downstream side of the dam. (Image reproduced from US Army Corps of Engineers, Huntington District [USACE-LRH], files.)

Appendix D presents the hydraulic loads determined for the sector gate. The project selected to serve as an example was the east sector gate at the Calcasieu Lock on the Gulf Intracoastal Waterway (GIWW) near Lake Charles, Louisiana, in the USACE, New Orleans District (USACE-MVN). Figure 4 shows an aerial view of the project. New sector gates are proposed for the project.

Figure 4. Satellite imagery showing an aerial view of Calcasieu Lock on the Gulf Intracoastal Waterway (GIWW). (Map data: Landsat/Copernicus, n.d.)

Appendix E presents the hydraulic loads determined for the lock miter gate. For this example, the Barkley Lock miter gate on the Cumberland River in the USACE, Nashville District (USACE-LRN), was selected. Figure 5 shows the frame side of the lower miter gate, looking upstream.

Figure 5. View of the frame side of the Barkley Lock lower miter gate, looking upstream.

Appendix F presents the hydraulic loads determined for the submergible tainter gate used as an upper lock gate. The project selected for the example was the Ice Harbor Lock and Dam on the Snake River in the USACE-NWW. Figure 6 is a view of the Ice Harbor Lock submergible tainter gate, looking across the upper sill of the lock.

Figure 6. View of the Ice Harbor Lock submergible tainter gate.

Appendix G describes the hydraulic loads determined for a bulkhead used as a closure structure. The project selected for the example was the Barkley Lock and Dam (BLD) project on the Cumberland River in the USACE-LRN. Figure 7 shows a 1:15-scale model of the Barkley Dam spillway bulkhead.

Figure 7. A 1:15-scale model of the Barkley Dam spillway bulkhead. (Image reproduced from Hite and Pickering 1983, Figure 6. Public domain.)

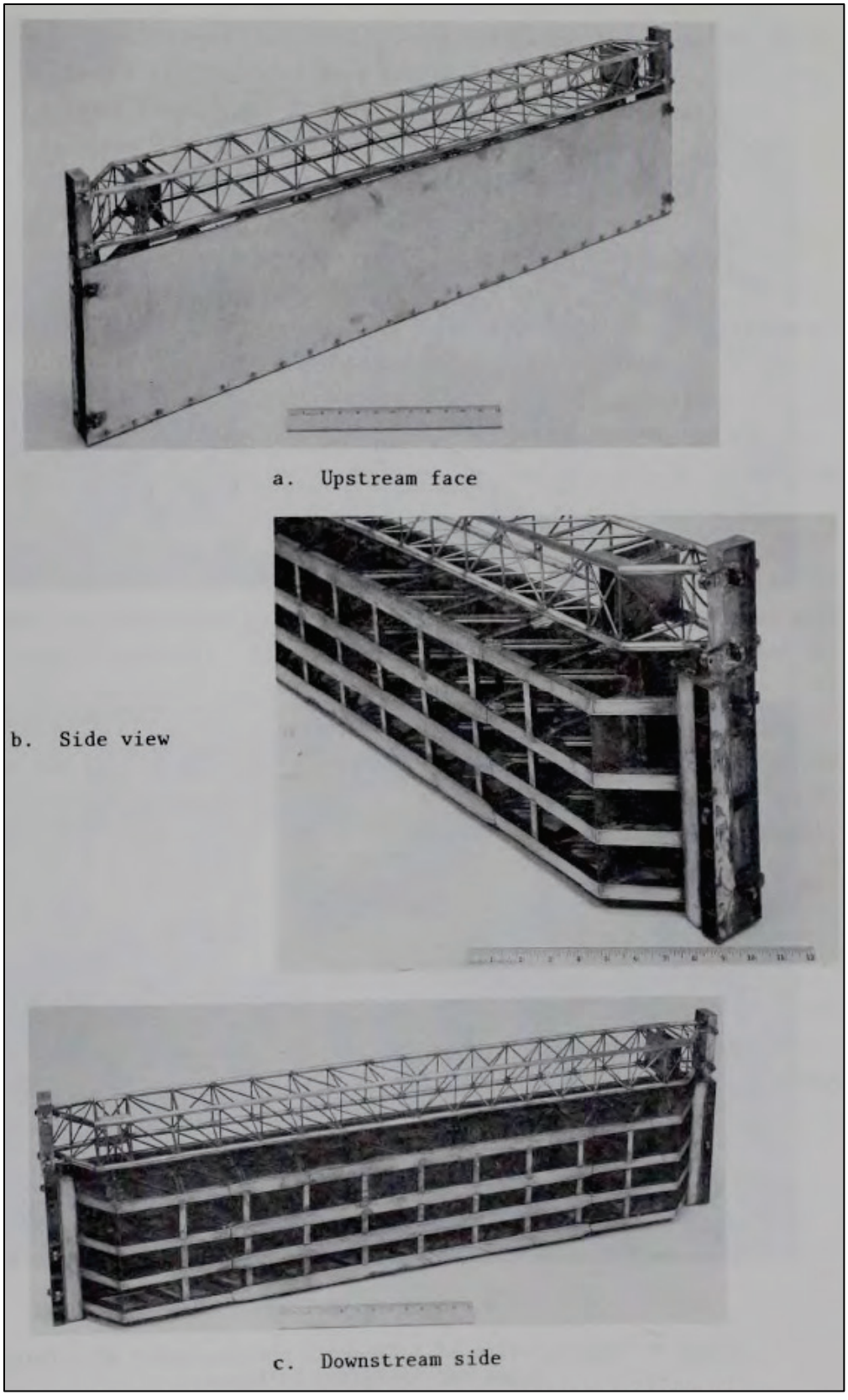

Appendix H presents the hydraulic loads determined for a rolling gate. The Williams Boulevard Floodgate in Kenner, Louisiana, in the USACE-MVN, was chosen as the example project. Figure 8 shows a rolling gate used as a closure structure for a floodwall. The gate is stored behind the floodwall.

Figure 8. View of a rolling gate stored behind a floodwall.

Appendix I presents the hydraulic loads determined for the ND/GB structure used for lock dewatering. The project selected for the example was the Chickamauga Lock and Dam on the Tennessee River in the USACE-LRN. Figure 9 shows the placement of one of the needles. The needles are installed one at a time and are secured to girder beams that span the width of the lock approach.

Appendix J presents the hydraulic loads determined for the reverse tainter valve used for lock filling and emptying operations. The project chosen as the example was the Dalles Lock and Dam project on the Columbia River in the USACE, Portland District (USACE-NWP). Figure 10 shows the double skin plate reverse tainter valve removed from operation for repair.

Figure 9. View of needle dam / girder beams (ND/GB) being installed in the Chickamauga Upper Lock approach.

Figure 10. View of Dalles Lock double skin plate reverse tainter valve removed for repairs.

2 Loadings Applied to Spillway Tainter Gates (STGs)

This chapter describes the loads associated with STGs, focusing primarily on hydraulic loads, and summarizes the dispersion in these applied loads and the distribution of pressures.

2.1 Existing Guidance for STG Design

The main purposes of inland navigation projects are to provide water depths sufficient for safe travel upstream and downstream from the project and a method or structure that allows the vessel to transit through the project. Water levels are controlled by spillway gates. The four steel spillway gate designs used for most USACE projects are the tainter (most common), vertical-lift, roller, and rolling.

2.1.1 Engineer Transmittal Letter (ETL) 1110-2-584, *Design of Hydraulic Steel Structures*, and Engineer Manual (EM) 1110-2-2702, *Design of Spillway Tainter Gates* (Rescinded)

A spillway gate design is selected based on the operational requirements of the spillway. Because the tainter gate is the most common spillway gate, the initial research on LRFD for HSS focused on this structure. The tainter gate has an inexpensive first cost and a low cost of operation and maintenance. A typical gate consists of a skin plate assembly and a framework of vertical and horizontal members. Figure 11 shows the primary components of the tainter gate.

The skin plate assembly is the damming surface for the water above the spillway crest and is designed as a cylindrical segment with radial struts that transfer the hydraulic load to the trunnion. The skin plate is concentric to the trunnion, so the resultant hydrostatic force passes through the trunnion; there is no moment from this force that has to be overcome by the gate hoisting mechanism. The vertical and horizontal members generally consist of curved vertical ribs attached to the skin plate and horizontal girders that span the gate width. The horizontal girders are supported by the end frames, which contain the radial struts and strut bracing.

Figure 11. Structural components of STGs from Engineer Manual (EM) 1110-2-2702 (rescinded). (Image reproduced from HQUSACE 2000, 3-2. Public domain.)

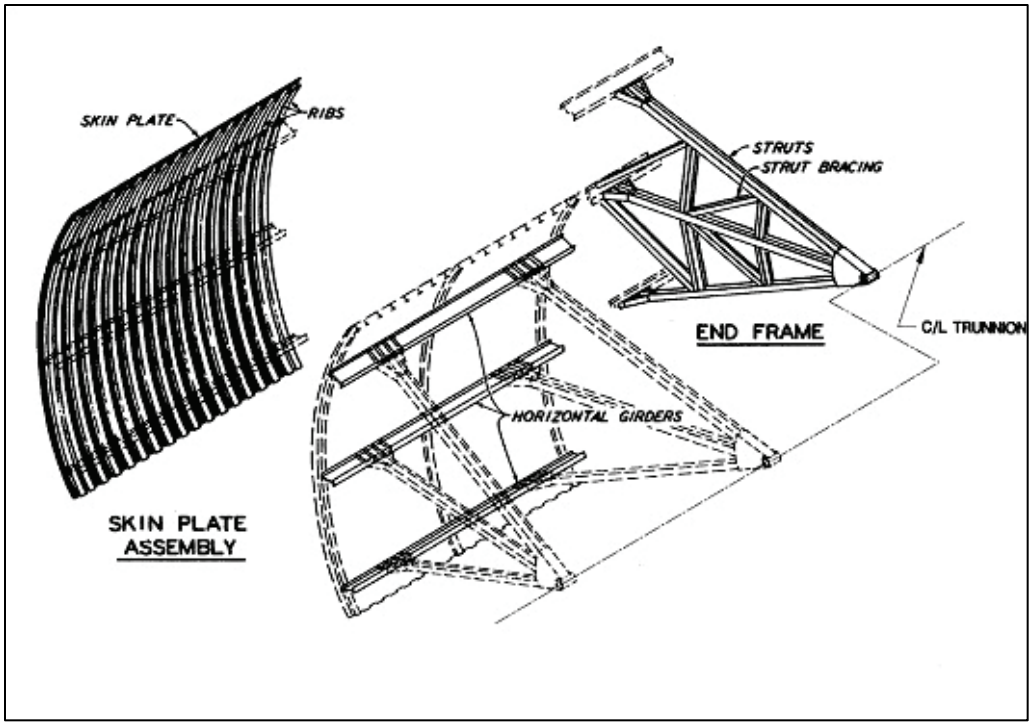

ETL 1110-2-584 (HQUSACE 2014) provides guidance for designing new HSS and conducting major rehabilitation of existing HSS using LRFD. The design philosophy for HSS is to achieve the objectives of constructability, safety, and serviceability for the specified limit states while considering inspections and economics. The ETL states, "The structural system of an HSS shall be proportioned and detailed to ensure the development of significant and visible inelastic deformations at the strength and extreme event limit states before failure" (2-1). Limit states applicable to HSS are strength, serviceability, fatigue, and fracture. The design life of HSS is assumed to be 100 yr.

ETL 1110-2-584 (HQUSACE 2014, Sections 3.2.3.1, 3.2.3.2, C3.2.3.1, and C3.2.3.2) describes the hydrostatic and hydrodynamic loads to be considered. Section 3.2.3.1 of the ETL states that loads caused by the hydrostatic head differential (i.e., no flowing water) across the HSS, with due consideration from any tailwater effects, should be considered. Section C3.2.3.1 states, "While considered a hydrostatic load, the hydraulic head can be a function of hydrodynamic conditions, particularly by the tailwater, under flowing conditions. A Hydraulic Engineer should be consulted to quantify tailwater effects" (HQUSACE 2014, 3-2).

ETL 1110-2-584 (HQUSACE 2014, Appendix D) provides design information for STGs, and Section D.2.4 states, "Hydrostatic loads consist of hydrostatic pressure on the gate considering both upper and lower pools. Three levels of hydrostatic loads are considered as described in ETL 1110-2-584 Section 3.2.3.1." (D-7). Section D.2.4, states, "The primary hydrodynamic load considered in design is the wave load (WA). See Section 3.2.3.2 of ETL 1110-2-584 for information on determining wave loads. Flow-induced vibration shall be limited, as discussed in Section 3.2.3.2 and in this Appendix" (D-8). Table 2 shows the load factors for tainter gates. The load factor is designated with the Greek symbol γ in this table.

Table 2. Load factors for tainter gates. (Table adapted from Engineer Transmittal Letter [ETL] 110-2-584, HQUSACE 2014, D-10.)

Load Cases			Loads/Load Factors							
			D	*G*	*Hs*	*Hd*	*Q*	EV	IM	EQ
Limit State	Description	Case	γD	γG	γHs	γHd	γQ	γEV	γIM	γEQ
Strength I	Gate closed	1	1.2	1.6	1.4Hs2	0	1.2Q1	0	0	0
Strength I	Gate closed	1	1.2	1.6	1.4Hs2	1.2(1)	1.2Q2	0	1.6(1)	0
Strength II	Usual operation	2.a	1.2	1.6	1.4Hs3	0	1.4QFs2+ 1.0QFt2	0	0	0
Strength II	Usual operation	2.b	1.2	1.6	1.4Hs2	1.2(1)	1.4QFs2+ 1.0QFt2	0	1.6(1)	0
Strength II	Unusual operation	3	1.2	1.6	1.4Hs2	0	1.4QFs2+ 1.0QFt2	0	0	0
Extreme I	Gate closed	4.a	1.2	1.6	1.4Hs3	0	1.2Q2	0	0	0
Extreme I	Gate closed	4.b	1.2	1.6	1.4Hs1	0	0	0	0	1.0EQ
Extreme I	Gate jammed	5	1.2	1.6	1.4Hs2	0	1.2Q3	0	0	0
Extreme I	Gate opened	6	γD2(2)	γG2(2)	0	0	1.2Q3(1)	1.3W(1)	0	1.0EQ(1)

Note: (1) Select one at a time. (2) Use max or min values, whichever produces maximum effects.
γ = load factor; *D* = self-weight (dead load); G = gravity load, which includes weight of the gate (*D*), mud weight (*M*), and ice weight (*I*); *Hs* = hydrostatic load; *Hd* = wave load; *Q* = machinery load; EV = wind load; IM = ice-impact load; EQ = earthquake load

EM 1110-2-2702 (HQUSACE 2000, Chapter 3, Section 3-4, rescinded), describes the three levels of hydrostatic loads that are considered in the design of tainter gates: the maximum hydrostatic load, H_1, which is defined as the maximum net hydrostatic load that will ever occur; the design hydrostatic load, H_2, which is defined as the maximum net hydrostatic load for conditions up to a 10 yr* flood event; and the normal hydrostatic load, H_3, which is defined as the net load from the upper and lower pool levels

* For a full list of the spelled-out forms of the units of measure used in this document and their conversions, please refer to *US Government Publishing Office Style Manual*, 31st ed. (Washington, DC: US Government Publishing Office, 2016), 248–252, https://www.govinfo.gov/content/pkg/GPO-STYLEMANUAL-2016/pdf/GPO-STYLEMANUAL-2016.pdf.

that exist up to 50% of the time during the year. There is no description of the hydrodynamic loads that need to be considered.

These hydrostatic loads are highly dependent on the lower pool el (elevation), also referred to as the *tailwater el* (TW El). The maximum possible net hydrostatic head would occur if the upper pool el were at the top of the gate with no effect from the TW El. For many navigation projects with STGs, there is usually tailwater on the downstream (i.e., back) side of the gate. Typical STGs are designed with the top of the gate a few feet above the normal upper pool el. H_1 is then at the top of gate el when closed (i.e., spillway gate seat el). The spillway gate seat el (also referred to as *gate sill el*) is generally the same as the spillway crest el. This condition occurs if the gate operating mechanism fails because, under normal operating conditions at a navigation project, the gate is raised with an upper pool level higher than the normal pool.

H_3 is usually higher than H_2 because a 10 yr flood event requires the gates to be open. If there were a failure of the gate operating mechanism with this flood event, the 10 yr upper pool level would be checked against the top gate el when closed.

2.1.2 EM 110-2-1603, *Hydraulic Design of Spillways*

EM 1110-2-1603 (HQUSACE 1990) states the following:

> The hydraulic design of crest gates involves the determination of the hydrostatic and hydrodynamic forces acting on the gate and crest in the immediate vicinity of the gate; the design and evaluation of gate seals, seats, and slots with respect to flow-induced vibrations and cavitation-related problems; the determination of the rate of flow from partially open gates; and the evaluation of gate seat locations, the trunnion elevation, and other hydraulics-related structural features. (6-1)

EM 1110-2-1603 (HQUSACE 1990, Appendix D) shows computations for the design of a spillway, but there is no procedure presented for determining the hydrodynamic loads on an STG.

2.1.3 EM 1110-2-1605, *Hydraulic Design of Navigation Dams*

EM 1110-2-1605 by HQUSACE (1987) states, "The current most commonly used and recommended control gate is the tainter gate" (Chapter 5, Section 5-12, 5-35). It also describes many advantages of using a tainter gate. Cox (1972) present gate designs and mounting arrangements for 176 USACE projects, and some of them are included in EM 1110-2-1605. EM 1110-2-1605 provides design guidance for tainter gates (Chapter 5, Section 5-14, paragraphs a–h). There is no information on hydrodynamic loads. However, flow regimes experienced by STGs are described, and the equations presented are used in subsequent sections of this report.

2.1.4 STG Operation—Navigation Dam

A typical navigation dam STG with no overflow operates in a manner that maintains the navigation pool with the gate openings as small as possible to pass the river discharge. Tainter gates used for navigation projects are designed to maintain a pool for navigation and to minimize resistance during flood events. To avoid interference during flood events, the trunnions for the gates need to be high, and the gate arms need to be long.

The gate sills for low-head projects (i.e., those with heads less than 30 ft) are placed near the channel invert, and the gate provides the damming surface for normal flows. Most of the gates are usually closed for normal flows, and the ones that are open provide the discharge for maintaining the normal upper pool and minimum flow requirements. Therefore, the highest hydrostatic load occurs with the gate closed, and the head is the difference between the upper pool el and the gate sill el, assuming no tailwater effects. The gate is raised as the upper pool rises, and the hydrostatic force is reduced. As flow increases, the gates are raised until the difference in the upper pool and tailwater is small, and as the flow continues to increase, the gates are raised completely out of the flow. With unusual and extreme flow events, the hydraulic forces on the STG are minimal because they are out of the flow.

2.1.5 STG Load Cases

EM 1110-2-2702 (HQUSACE 2000, rescinded) states that all loads that HSS will be subjected to must be considered in the design. These loads include gravity (e.g., weight, ice, and mud), hydrostatic, hydrodynamic, operational and machinery, floating and thermal ice, debris, vessel impacts,

and environmental (e.g., typically wind and temperature). Frequency of loading is considered in the design for the three load categories described in the sections that follow and is specified in terms of frequency of occurrence. The load information that follows was taken directly from ETL 1110-2-584 (HQUSACE 2014, 2-5 and 2-6).

2.1.5.1 Usual

The usual loading category represents daily or frequent operational conditions that require highly reliable performance. The design criteria for the usual loading category apply to load cases with the predominant load (or joint loads) having a mean return period (*Tr*) between 1 and 10 yr. This load category is typically associated with the service and fatigue limit states. These loads should not cause damage. Steel should remain within the elastic state, and fatigue cracking should be avoided or limited to non-critical size. Damage may accumulate due to normal degradation (operational wear and tear) over the service life of the project.

2.1.5.2 Unusual

The unusual loading category represents infrequent operational conditions that require a defined level of performance and that can be reasonably expected to occur within the service life of the project. The design criteria for the unusual loading category apply to load cases with the predominant (or joint loads) having a mean return period (*Tr*) between 10 and 300 yr. This load category is typically associated with the strength and fracture limit states. These loadings should not cause significant damage or disruption of service. Localized yielding is acceptable (i.e., stresses may exceed the yield limit in localized areas). Damage may accumulate due to normal degradation (operational wear-and-tear) over the service life and may require major rehabilitation or restoration after 50 yr of service.

2.1.5.3 Extreme

The extreme loading category represents possible conditions that are not likely to occur within the service life of the project. The design criteria for extreme load cases are applicable if the predominant load (or joint load) has a mean return period (*Tr*) greater than 300 yr. This load category is associated with the extreme limit state. Significant damage may result from these loads in the form of plastification, buckling, tearing, fracture, or other damage, but sufficient redundancy exists to redistribute the loads

and prevent catastrophic collapse. Limited operational capability may also be required to maintain minimal project function (i.e., maintain pool) until corrective measures can be implemented.

2.1.5.4 Load Combinations

Loads are combined to produce maximum effects for a given limit state under the varying load frequencies. Several load combinations are defined and varying load factors applied to achieve a consistent level of reliability. Load combinations are based on probabilistic load modeling and a survey of reliabilities inherent in traditional design practice. Specific load combinations are based on the notion that the maximum combined load effect occurs when one of the time-varying loads is at the maximum lifetime value and the remaining loads are taken at an arbitrary point in time. The likelihood that two or more loads, excluding self-weight, are at their maximums coincidently is remote. Load factors are calibrated accordingly to reflect the arbitrary nature of loading events.

2.1.5.5 Cyclic and Noncyclic Loading

Cyclically loaded structures are those that repeatedly undergo significant changes in stresses during operation. Noncyclically, or statically, loaded structures are defined as those that do not repeatedly undergo significant changes in stresses in the process of operating. Noncyclically loaded structures may experience changes in applied stresses from loading and unloading during the normal use of the structure, but those changes only occur for a relatively small number of operating cycles throughout the service life of the structure. For most HSS, the changes in stress are induced through changes in position, primarily under specific operating cycles (opening and closing), changes in the loading (e.g., changes in hydraulic head), or both. Two components used to define cyclically loaded structures are (1) the magnitude of the imposed stress-range cycles, and (2) the frequency of the application of those cycles. The implications of cyclic versus noncyclic loading are largely related to fatigue cracking. There is a practical lower limit of stress cycles to consider whether an HSS is cyclically loaded or not (e.g., where fatigue cracking is not likely but is dependent on the magnitude of stress range and number of cycles). Design life and material strength are also considerations, as are high-frequency vibration and high stress / low cycle conditions. Given an expected number of stress cycles over the life of the HSS, and live load stress range at a detail, the fatigue strength of a detail can easily be determined and the results used to

designate a member as cyclically loaded or not. STGs, miter gates, and lock valves are examples of cyclically loaded HSS. Dewatering bulkheads, stop logs, and closure structures are noncyclically loaded HSS.

2.2 Hydraulic Data Collection and Statistical Data Reduction for Mean Loading

The reliability analysis for the STG requires that the mean and standard deviation of the loads be determined, and hydraulic data are needed to develop these values. The discharge, upper pool el, gate setting, and TW El are needed to determine hydraulic loads. Historical data are necessary to develop the samples and statistical data required for the analysis.

As mentioned previously, these deviations from the mean can result from a number of factors. Changes in head near the gate could be caused by wind waves, ice, debris, approach flow, and tailwater effects. Approach flow asymmetry could result from having adjacent gates set at different openings and pier contractions. The pier or abutment contractions would reduce the water level upstream at the edges of the gate. Empirical coefficients are used to account for these contractions. Because gate operations usually consist of keeping adjacent gates at similar openings, the gate openings adjacent to a closed gate would be small (probably less than 2 ft). The primary parameters that cause changes in the hydraulic load for an STG are wind waves and tailwater.

2.2.1 Upper Pool Elevation (El)

A navigation project is operated to maintain a near constant upper pool. This is accomplished by raising the gates as the discharge increases. The nominal loads needed for the statistical analysis will generally occur with a near constant upper pool el. The mean and standard deviation for the upper pool need to be determined. The first design example chosen for this report was the MPLD project located near Alton, Illinois, on the Mississippi River. Appendix A contains the methodology used to determine the hydraulic data and the statistical data reduction.

2.2.2 Tailwater

The tailwater is a primary variable affecting the load on a tainter gate for most navigation projects, especially low-head projects. The tailwater reduces the head across the gate once it begins to submerge the downstream

side of the gate. A record of tailwater stages in time is also needed to develop the hydraulic forces. Most navigation projects east of the Mississippi River have tailwater effects. In the design example shown in Appendix A, a 31 yr record for tailwater stages was used to determine the mean and standard deviation for the tailwater.

2.2.3 Flow Regimes

The STG is used to control the discharge to maintain desired upper pool levels. To account for factors that affect the quantity of flow under the gate, empirical relationships have been developed. The very basic weir equation,

$$Q = CLH^{1.5}, \quad (1)$$

is expanded to account for factors that affect discharge. In this equation,

Q = the discharge over the weir,
C = the discharge coefficient,
L = the weir length, and
H = the total head on the weir.

The discharge coefficient accounts for uncertainties in head loss. The orifice equation shown here is used to determine flow under the gate:

$$Q = CbG_o\sqrt{2gH}, \quad (2)$$

where

b = the gate width,
G_o = the gate opening taken as the minimum distance from the gate lip to crest boundary,
H = the head on the gate, and
g = the acceleration due to gravity.

The four flow regimes that STGs are subjected to are free uncontrolled flow, submerged uncontrolled flow, free controlled flow, and submerged controlled flow (Figure 12). These schematic profiles were taken from EM 1110-2-1605 (HQUSACE 1987).

Figure 12. Flow regimes for STGs. (Image reproduced from USACE 1987, 5-10. Public domain.)

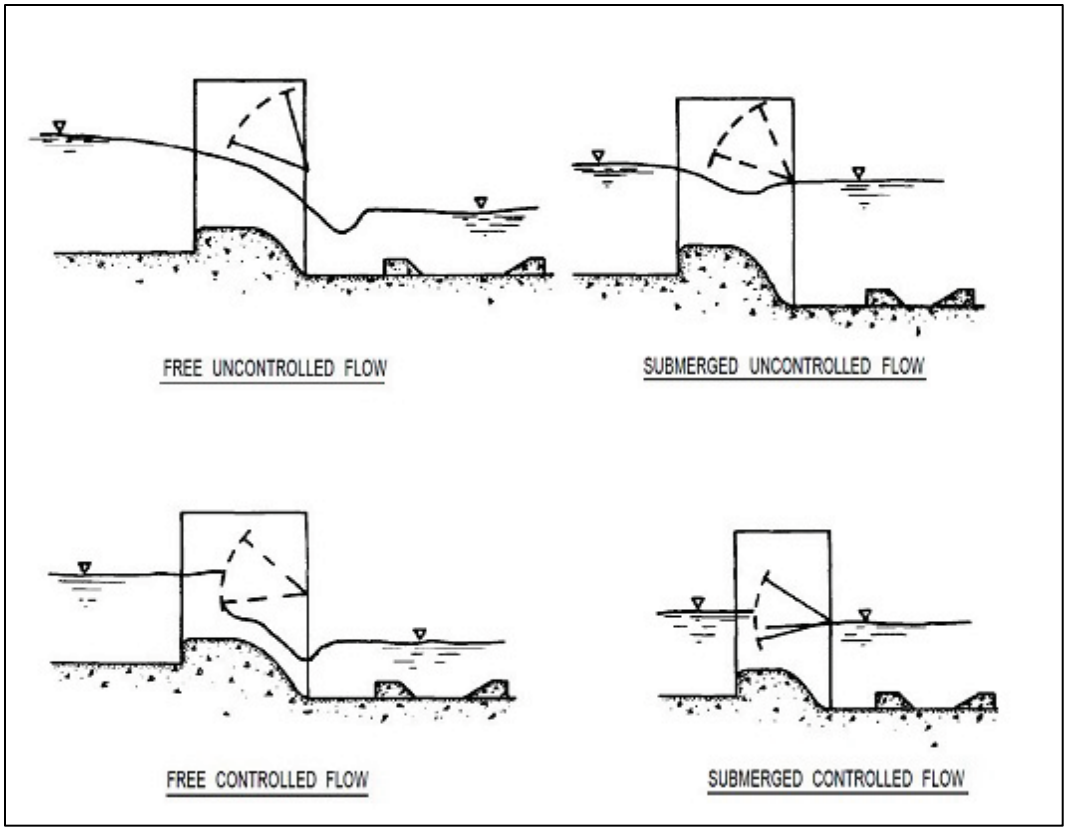

2.2.3.1 Free Uncontrolled Flow

Free uncontrolled flow occurs when the gates are completely out of the flow and the tailwater does not affect the upper pool. EM 1110-2-1605 (HQUSACE 1987) presents a version of the weir equation (Equation 1) and provides guidance for the selection of the discharge coefficient. The equation

$$Q = C_F L H^{1.5}, \tag{3}$$

is used, and C_F, a discharge coefficient for free uncontrolled flow, is selected from Figure 5.9 in EM 1110-2-1605. The crest length, L, is reduced to account for abutment contraction to give L_{eff}, as shown in Equation (4):

$$L_{eff} = L - 2KH, \tag{4}$$

which gives

$$Q = C_F L_{eff} H^{1.5}. \tag{5}$$

The abutment contraction coefficient, *K*, is selected from chart 111 of USACE Waterways Experiment Station (WES; 1980), *Hydraulic Design Criteria* (HDC). Because the discharge coefficients in Figure 5.9 of EM 1110-2-1605 (HQUSACE 1987, 5-13) already account for pier effects, the abutment contraction coefficient should be one-half of the value selected from HDC Chart 111. The hydraulic load on the STG is insignificant in this flow regime.

2.2.3.2 Submerged Uncontrolled Flow

In this flow regime, the gates are completely out of the water, and the tailwater is high enough above the spillway crest el to affect the discharge. There are several equations and procedures that have been developed to compute the discharge coefficient. One method is simply to use the weir equation (Equation 1) and then to use a coefficient that accounts for submergence, C_s, instead of C. The equation, then, becomes

$$Q = C_s L H^{1.5}. \tag{6}$$

EM 1110-2-1605 (HQUSACE 1987) presents the guidance needed to select C_s. C_s was determined from model data. Another equation used to determine submerged uncontrolled flow is known as the d' Aubuisson equation (Equation 7):

$$Q = KLH\sqrt{[2g(H-h)+V^2}, \tag{7}$$

where

K = the spillway coefficient of contraction (Table 3),
L = the crest length = the number of spillway bays times the bay width,
V = the spillway approach velocity,
H = the total head upstream of the spillway, and
h = the difference in elevation between the tailwater and the spillway crest.

The suggested *K* values shown in Table 3 vary with bay width and have been derived empirically from experience with prototype structures (HDC 111-4, WES 1980; Grace 1964).

Table 3. *K* values for submerged uncontrolled flow. (Table adapted from EM 1110-2-1605, HQUSACE 1987.)

Bay Width (ft)	K
40	0.8
60	0.85
80	0.9
100	0.95

These coefficients were developed from prototype data. Equation (7) is only recommended for preliminary development of a discharge rating. The hydraulic forces on the STG in this flow regime are also considered insignificant.

2.2.3.3 Free Controlled Flow

For this flow regime, the gates control the flow, and there is no tailwater effect on the discharge. Equation (8) can be used to determine the discharge:

$$Q = C_g L G_o \sqrt{2gH}, \tag{8}$$

where

C_g = the discharge coefficient for free controlled flow, and
G_o = the gate opening.

Guidance for selecting C_g is presented in EM 1110-2-1605 (HQUSACE 1987) for heads up to 30 ft and gate openings up to 14 ft. Guidance on C_g outside these ranges is provided in HDC (WES 1980). When viewing this guidance, be aware that the symbols and equations that are presented can differ.

2.2.3.4 Submerged Controlled Flow

For this flow regime, the gates are partially open, and the discharge (and upper pool el) is controlled by the gate opening and submergence effect. The equation typically used to determine the discharge is as follows:

$$Q = C_{gs} L h \sqrt{2g\Delta H}, \tag{9}$$

where

C_{gs} = the discharge coefficient for submerged controlled flow, and
ΔH = the difference in the total head upstream and the TW El.

Figure 13 shows a plot of h/G_o versus C_{gs} that was obtained from EM 1110-2-1605 (HQUSACE 1987). The prototype data in Figure 13 was obtained at dams 2, 5A, and 26 on the Mississippi River. B is the vertical distance from the spillway crest to the spillway apron.

Figure 13. Discharge coefficients for submerged controlled flow. (Image reproduced from EM 1110-2-1605, HQUSACE 1987, 5-16. Public domain.)

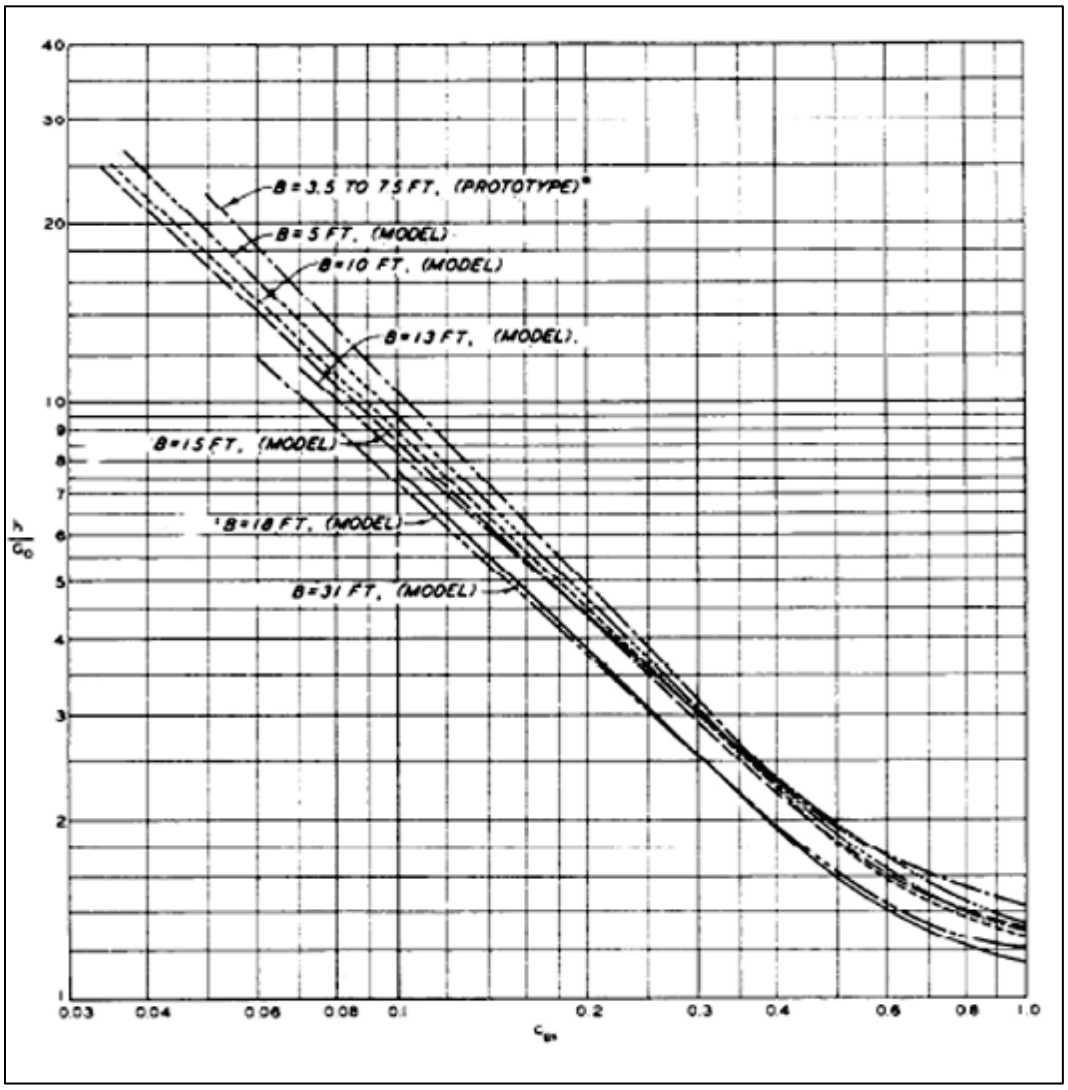

Free controlled flow and submerged controlled flow are the flow regimes that affect the hydraulic loads on the STG. The hydrodynamic loads for these regimes will be described in Sections 2.3.2 through 2.3.5.

2.3 Hydraulic Loading for STGs

Hydraulic loads consist of all loads due to water. These include hydrostatic (i.e., weight of water), hydrodynamic (i.e., load due to flowing water), and wave action. These are the primary hydraulic loads, in terms of magnitude and frequency, experienced by HSS. Vibrations caused by flowing water, constricted flow, and water hammer are also considered hydraulic loads.

2.3.1 Hydrostatic Load for STGs

The hydrostatic load is due to the hydraulic head across the STG. The load on the gate results from the hydrostatic pressure acting on the gate. If tailwater is present, it will affect the hydrostatic load. The maximum hydrostatic load occurs when the tainter gate is closed and there is no tailwater effect on the gate. This condition generally happens during minimum discharges. The deviations from the mean hydrostatic load need to be developed and will be discussed in Section 2.4. These deviations can result from a number of factors. As mentioned previously, changes in head near the gate are caused primarily by wind-induced waves or tailwater effect. Approach flow asymmetry could result from having adjacent gates set at different openings and pier contractions, although the changes in head caused from these conditions would likely be minimal and are not considered in this analysis.

The hydrostatic pressure on a closed gate is typically expressed as γH, where γ is the unit weight of water, and H is the total head on the closed gate. An illustration of the hydrostatic pressure distribution on an imaginary vertical section in front of a closed STG is shown in Figure 14. When the gate is closed, H represents the difference between the upper pool el and the spillway crest el when the tailwater is lower than the crest el. Equation (10) is a conventional equation that can be found in many fluid mechanics and hydraulics textbooks and is used to compute the hydrostatic pressure (p). As stated previously, γ is the unit weight of water, and y is the vertical distance from the water surface to the location of the hydrostatic pressure of interest (Figure 15):

$$p = \gamma y. \tag{10}$$

The value of hydrostatic pressure, p, at depth y is isotropic. The maximum hydrostatic pressure (Equation 11) on the gate would be at the bottom of the gate, which is the spillway crest el:

$$p_{max} = \gamma H. \tag{11}$$

The hydrostatic pressure acting along the vertical imaginary plane in Figure 15 is integrated over depth to obtain the resultant horizontal hydrostatic force, H_s. H_s is the resultant force computed from the triangular pressure distribution acting on the gate area. In most cases, a unit gate width is used to compute the gate area, resulting in Equation (12), which is the hydrostatic force per unit width of the gate. The location of the horizontal resultant force is $H/3$ above the spillway crest when H is the head on the gate (Figure 15):

$$H_s = \frac{1}{2}\gamma H^2. \tag{12}$$

Figures 15 and 16 are also used for the following discussion, which was adapted from Roberson and Crow (1985), to determine the resultant forces on a curved surface. The distance from the axis *o-o* through the centroid of the area is noted as $\bar{y}$. The distance from *o-o* to the differential area, dA, is y. The pressure on the differential area can be computed if the y distance is known. The differential force on the differential area is, then,

$$dH_s = p\ dA. \tag{13}$$

Substituting for p gives

$$dH_s = \gamma y\ dA. \tag{14}$$

The total force on the area is determined by integrating the differential over the entire area:

$$H_s = \int p\ dA, \tag{15}$$

and again substituting for p,

$$H_s = \int \gamma y\ dA. \tag{16}$$

Because γ is a constant, Equation (16) then becomes

$$H_s = \gamma \int y\ dA. \tag{17}$$

The integral in Equation (17) is the first moment of the area about axis *o-o*, so ydA can be replaced with its equivalent $\bar{y}A$. Equation (17) becomes

$$H_s = \gamma \bar{y} A. \tag{18}$$

As shown in Figure 15, $\gamma\bar{y}$ is the pressure at the centroid of the area. Equation (18) demonstrates that the magnitude of the resultant hydrostatic force on a plane surface is the product of the pressure at the centroid of the surface and the area of the surface and can be written as

$$H_s = \bar{p}A. \tag{19}$$

Because the resultant hydrostatic force on the STG is primarily due to water pressure that increases with depth, the location of the line of action lies below the centroid. This location is determined by taking moments of the pressure forces about the horizontal axis *o-o*. The point where the resultant intersects the surface is noted as the center of pressure. In Figure 15, the distance from axis *o-o* to the center of pressure is y_{cp}. By definition, then, the location of the resultant force and the moment equation is

$$y_{cp}H_s = \int y \, dH_s. \tag{20}$$

From Equation (13), $dH_s = pdA$, so Equation (20) can be written as

$$y_{cp}H_s = \int yp \, dA, \tag{21}$$

and because $p = \gamma y$, Equation (21) becomes

$$y_{cp}H_s = \int \gamma y^2 \, dA. \tag{22}$$

Because γ is a constant,

$$y_{cp}H_s = \gamma \int y^2 \, dA. \tag{23}$$

The integral on the righthand side of Equation (23) is the second moment, I_o, of the area about the axis *o-o* and is generally referred to as the *area moment of inertia*. It is often convenient in engineering applications to use the horizontal centroidal axis for the second moment, so using the transfer equation

$$I_0 = \bar{I} + \bar{y}^2 A, \tag{24}$$

and substituting for the integral on the righthand side of Equation (23), shown on the previous page, gives

$$y_{cp} H_s = \gamma(\bar{I} + \bar{y}^2 A). \tag{25}$$

And, further, substituting for H_s from Equation (18), gives

$$y_{cp} \gamma \bar{y} A = \gamma(\bar{I} + \bar{y}^2 A). \tag{26}$$

Solving for y_{cp} gives

$$y_{cp} = \bar{y} + \frac{\bar{I}}{\bar{y}A}, \tag{27}$$

which is rearranged to give

$$y_{cp} - \bar{y} = \frac{\bar{I}}{\bar{y}A}. \tag{28}$$

Figure 14. Hydrostatic pressure distribution for a closed STG with no tailwater effects.

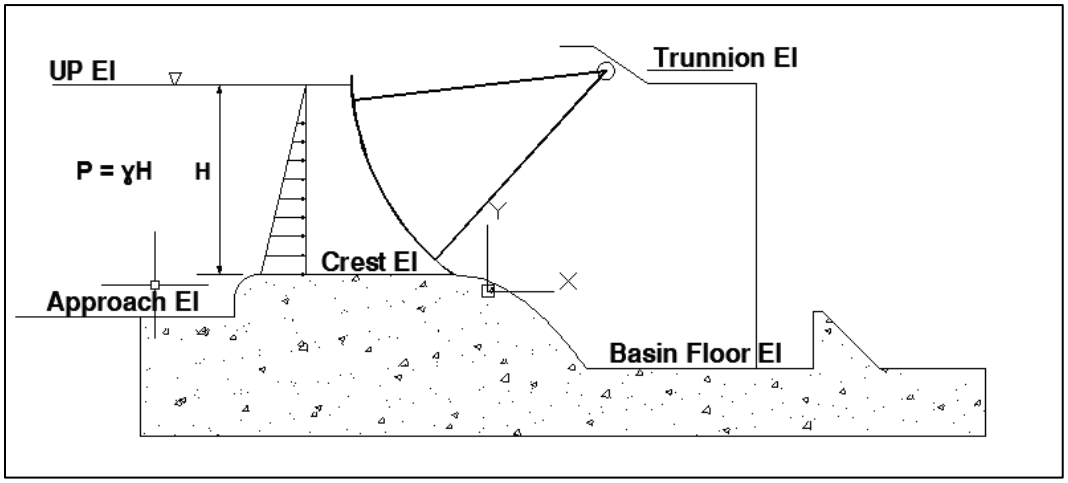

Figure 15. Schematic for hydrostatic force computations. (Image adapted from Roberson and Crow 1985.)

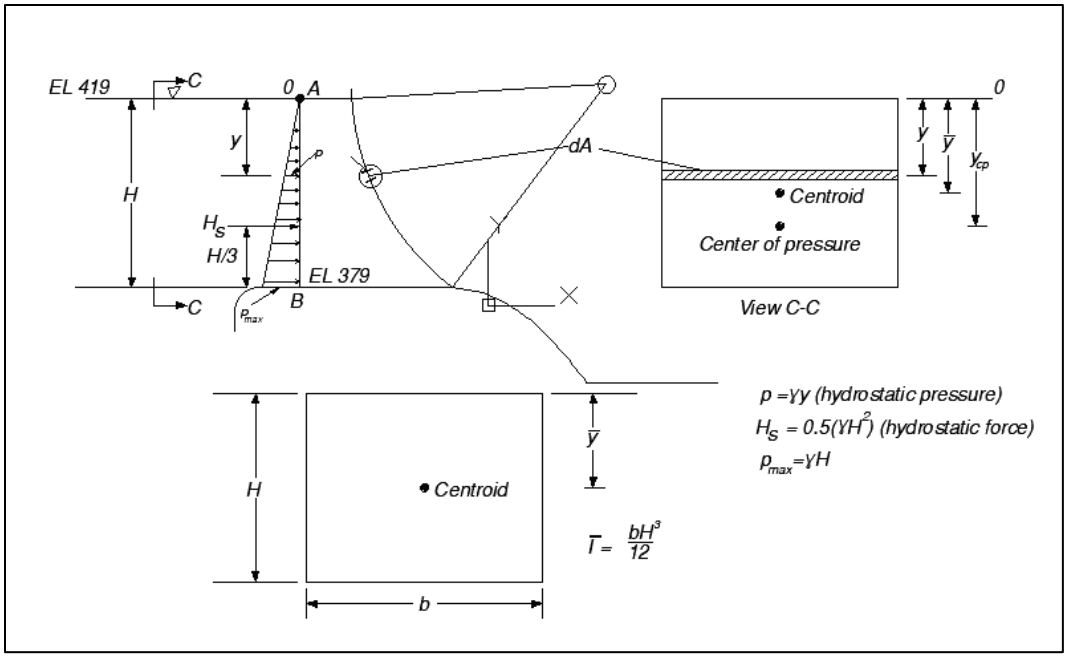

Figure 16. Schematic for hydrostatic force computations on a curved surface. (Image adapted from Roberson and Crow 1985.)

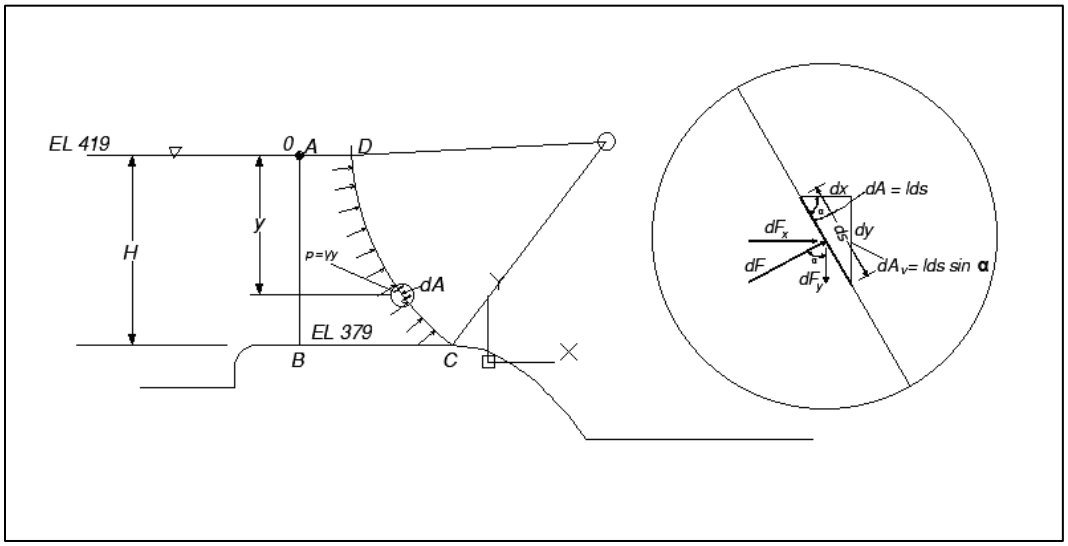

The magnitude and direction of the resultant hydrostatic force acting on the curved surface can be determined by resolving the force into horizontal and vertical components and then adding these vectorially to get the total hydrostatic force on the surface. The arrows normal to the curved surface, labeled DC in Figure 16, represent the differential pressures acting on differential areas of the surface. A representative differential area is shown

within the circle in Figure 16. The component forces can be determined from this differential. The differential dA is as follows:

$$dA = lds, \tag{29}$$

where l represents a length dimension normal to the page. The differential hydrostatic force, dH_s, can be calculated this way:

$$dH_s = \gamma ylds. \tag{30}$$

The horizontal component of this differential force is

$$dH_{s_x} = \gamma yl\ ds\ \sin\alpha, \tag{31}$$

as shown in the circle in Figure 16. The vertical projection of the differential area dA is $lds \sin \alpha$. Equation (31) can be written as

$$dH_{s_x} = \gamma y\ dA_v. \tag{32}$$

The total horizontal component of force can be determined by summing dH_{sx} over the entire surface:

$$H_{s_x} = \int \gamma y\ dA_v. \tag{33}$$

Because γ is constant, Equation (33) can be written as

$$H_{s_x} = \gamma \int y\ dA_v = \gamma\ \bar{y}_v A_v, \tag{34}$$

where $\bar{y}_v$ is the vertical distance from the water surface to the centroid of the vertical projection of the curved surface. So Equation (34) is

$$H_{s_x} = \bar{p}_v\ A_v. \tag{35}$$

Equation (35) indicates that the magnitude of the horizontal component of hydrostatic force on a curved surface is equal to the product of the pressure at the centroid of the vertical projection of the surface and the area of the vertical projection.

The location of the line of action of the horizontal component is determined by summing moments of the differential horizontal components,

dH_{sx}, and equating that to the moment of the horizontal component, H_{sx}. The moments are taken about a horizontal axis that is normal to the hydrostatic force, and for this discussion, it will be a horizontal axis that passes through point *O* in Figure 16. Therefore,

$$\int y \, dH_{s_x} = y_{cp} H_{s_x}, \tag{36}$$

where

y = the vertical distance from point O, and
y_{cp} = the vertical distance from point O to the center of pressure.

Substituting for dH_{sx} and H_{sx}, the equation becomes

$$\int y \gamma y \, dA_v = y_{cp} \gamma \bar{y}_v A_v, \tag{37}$$

where

$\bar{y}_v$ = the depth to the centroid of the vertical projection, and
A_v = the magnitude of the area of the vertical projection.

Dividing both sides of the equation by γ, then the lefthand side of Equation (37) is the second moment, or moment of inertia, of the vertical projection of the curved surface about the axis passing through O in Figure 16. Again, it is often convenient in engineering applications to use the horizontal centroidal axis for the second moment. So using the transfer equation,

$$\bar{I}_{0,v} = \bar{I}_v + \bar{y}_v^2 A_v, \tag{38}$$

where $\bar{I}_v$ = the second moment of the vertical projection about its horizontal-centroidal axis, and

$$y_{cp} \bar{y}_v A_v = I_{0,v}. \tag{39}$$

Solving for y_{cp},

$$y_{cp} = \bar{y}_v + \frac{\bar{I}_v}{\bar{y}_v A_v}. \tag{40}$$

Equation (40) is nearly the same as Equation (27), except that in Equation (40), the center of pressure is equated to the vertical projection of the curved surface.

Now, to determine the vertical component of the differential force shown in Figure 16, use

$$dH_{s_y} = \gamma y l \, ds \cos\alpha. \tag{41}$$

The cross-sectional area of the volume of water above the differential area *dA* is a prism (i.e., triangular sides times *l*). The differential volume of the prism, $d\forall$, is then

$$d\forall = yl ds \cos\alpha. \tag{42}$$

Therefore,

$$dH_{s_y} = \gamma d\forall, \tag{43}$$

and it follows that

$$H_{s_y} = \int \gamma d\forall = \gamma\forall. \tag{44}$$

Equation (44) shows that the vertical component of force acting on the curved surface is equal to the weight of water located vertically above the surface. The line of action of the vertical component of force acts through the centroid of the volume of water lying above the curved surface.

To summarize the forces acting on a curved surface, the horizontal component of force is equal to the force acting on a vertical projection of that surface, both in magnitude and line of action. The magnitude of the vertical component of force is equal to the sum of all vertical forces acting on the surface. The lines of action of these vertical components are used to determine the line of action of the resultant vertical force.

2.3.2 Wave Load for STGs

Wave loads are project specific and are considered for projects that experience significant wind and fetch.

2.3.2.1 Shore Protection Manual *(SPM) Guidance*

Development of wave loading is shown in the *Shore Protection Manual* (SPM; Coastal Engineering Research Center 1984b). The waves considered in this discussion are driven by large-scale pressure gradients in the atmosphere that have been in a nearly steady state. The two variables that need to be determined to start the analysis are the wind speed and fetch. The general definition for fetch is a region in which the wind speed and direction are fairly constant. For most inland-water-related projects, a narrow fetch is appropriate. This generally means an adjustment is needed to develop an effective fetch.

Water depth is a factor in wave generation. Wave heights will be smaller and wave periods shorter if generation takes place in transitional or shallow water rather than in deep water. Shallow-water wave forecasting procedures have been developed. The SPM (Coastal Engineering Research Center 1984a, Chapter 3, Section VI, 3-55) provides a process for determining the wave height and period. Curves were developed based on the following equations for wave height and period:

$$\frac{gH}{U_A^2} = 0.283 \tanh\left[0.530 \left(\frac{gd}{U_A^2}\right)^{3/4}\right] \tanh\left\{\frac{0.00565\left(\frac{gF}{U_A^2}\right)^{1/2}}{\tanh\left[0.530\left(\frac{gd}{U_A^2}\right)^{3/4}\right]}\right\}, \quad (45)$$

and

$$\frac{gT}{U_A^2} = 7.54 \tanh\left[0.833 \left(\frac{gd}{U_A^2}\right)^{3/8}\right] \tanh\left\{\frac{0.0379\left(\frac{gF}{U_A^2}\right)^{1/3}}{\tanh\left[0.833\left(\frac{gd}{U_A^2}\right)^{3/8}\right]}\right\}, \quad (46)$$

where

g = the acceleration due to gravity,
H = the wave height,
U_A = the wind-stress factor,
d = the water depth,
F = the fetch, and
T = the period.

Once U_A and F are determined from procedures described in the SPM, H and T can be determined from Figures 3-27 to 3-36 in the SPM (Coastal Engineering Research Center 1984a, 3-56–3-65). These figures were developed based on Equations (45) and (46) in this report. The SPM figures have water depth increments every 5 ft between 5 and 50 ft.

The SPM (Coastal Engineering Research Center 1984b, Chapter 7, Section III) presented guidance on how to determine wave forces on coastal structures. The forces were classified by (1) the type of structure on which the forces act and (2) the type of wave action against the structure. According to the SPM, the coastal structures were referred to as one of three types: pile-supported structures, such as piers and offshore platforms; wall-type structures, such as seawalls, bulkheads, revetments, and some breakwaters; and rubble structures, such as groins, revetments, jetties, and breakwaters. The types of waves that can act on the structure are nonbreaking, breaking, or broken waves.

An inland navigation project would have to be treated as a seawall or bulkhead type of structure, and the wave type would most likely be a nonbreaking wave. SPM (Coastal Engineering Research Center 1984b, Chapter 7, Section III part 2) mentioned that these nonbreaking waves usually occur in protected areas where fetch is limited and when the depth at the structure is more than 1.5 times the maximum expected wave height. SPM (Coastal Engineering Research Center 1984b, 6-161–7-173) presented guidance for computing wave forces and moments. A different procedure was selected for computing wave forces in this report and will be described subsequently.

Bishop et al. (1992) reviewed the SPM and recommended that it should be revised based on investigations of steady state wave prediction. They stated that the SPM procedure overpredicts wave parameters at wind speeds greater than 5 m/sec. Other methods to predict wave heights and periods were investigated and are presented next.

2.3.2.2 Wind-Wave Generation on Restricted Fetches

Smith (1991) provided guidance on significant wave height and peak period as a function of fetch geometry and wind speed based on linear regressions of wave data collected at four different locations. Smith then developed a numerical model, called NARFET, based on concepts by Donelan (1980). Donelan proposed creating wind generation on fetch

lengths in off-wind directions. The NARFET model was updated by Dr. James Tallent of the US Army Engineer Research and Development Center Information Technology Laboratory (ERDC-ITL) using an updated computer language. The input to the model requires radial fetch lengths, the angle increment between radial measurements, wind measurement elevation, location of wind observations (over water or land), air–sea temperature difference, wind speed, wind direction, and duration. Appendix A of this report provides wave height and period results using Tallent's updated NARFET model for the MPLD project.

2.3.2.3 Simplified Forecasting Method of Wind Waves and Swell

Goda (2010) suggested using the following relationships to determine significant wave height and period:

$$\frac{gH_{1/3}}{U_{10}^2} = 0.3\left\{1 - \left[1 + 0.004\left(\frac{gF}{U_{10}^2}\right)^{1/2}\right]^{-2}\right\}, \tag{47}$$

and

$$\frac{gT_{1/3}}{U_{10}} = 8.61\left\{1 - \left[1 + 0.008\left(\frac{gF}{U_{10}^2}\right)^{1/3}\right]^{-5}\right\}, \tag{48}$$

where

g = the acceleration due to gravity,
$H_{1/3}$ = the significant wave height,
$T_{1/3}$ = the significant wave period,
U_{10} = the wind speed at the elevation of 10 m above the sea surface, and
F = the fetch.

Goda (2010) indicated that the growth of wind waves is limited by the minimum wind duration, t_{min}. He proposed the following empirical equation, which was numerically derived and experimentally validated, to determine t_{min}:

$$\frac{t_{min}U_{10}}{F} = 43\left(\frac{gF}{U_{10}^2}\right)^{-0.27}. \tag{49}$$

This equation can be rewritten as

$$t_{min} = 1.0F^{0.73}U_{10}^{-0.46}, \quad (50)$$

when t_{min} is hours, U_{10} is in meters per second, and F is in kilometers. Goda (2010) proposed the following equation for the minimum fetch length, F_{min} (in kilometers), necessary for full wave growth under a given wind duration, t(h):

$$F_{min} = 1.0t^{1.37}U_{10}^{0.63}. \quad (51)$$

Goda's (2010) procedure for computing wave height and period were also used with the MPLD parameters and are included in Appendix A. Goda conducted many investigations, both theoretical and in the laboratory, to develop a wave pressure formulation. A recent investigation by Ebeling et al. (2023) into the use of Goda's procedure to determine wave forces on structural walls was adopted for use in the development of a procedure for inland STGs. Because the hydrostatic forces on the STG are at maximum when the gate is closed, it is considered appropriate to treat the upper portion of the gate that is exposed to air as a vertical wall. Even though the gate is curved, the upper portion is nearly vertical when the gate is closed.

Goda (1974) came up with a formula for computing wave loading on vertical walls. He used his wave pressure relationships to design many of Japan's caissons, which are subject to ocean wave loading. The caisson being analyzed was subjected to both hydrostatic water pressure components acting on both vertical faces of the caisson and wave loading on the ocean side. In Goda's pressure formula, the following terms are used:

ρ = the density of seawater,
g = the acceleration due to gravity,
H_D = the design wave height,
β_D = the design approach angle,
h_{SWL} = the still water depth seaward of berm (Figure 17, also designated h in equations),
L_D = the design wave length,
H_b = the still water depth breaker height is evaluated,
d_{SWL} = the still water depth top of berm (Figure 17, also designated d in equations),
θ = the mean gradient of the seabed, and
η^* = the elevation of wave pressure action above the still water level (SWL).

Figure 17 shows the pressure relations and terms of Goda's (1974) formula. He used three pressure terms (i.e., P_1, P_2, and P_3) to define the wave pressure distribution on the vertical face of the wall and the pressure term P_U to describe the uplift pressure at the toe of the wall (Figure 17). P_1 represents the maximum wave pressure at the SWL, and P_2 and P_3 represent the reduction in wave pressure with depth.

Figure 17. Illustration of terms in Goda's (1974) pressure formulation. (Image reproduced from Ebeling et al. 2023, 112. Public domain.)

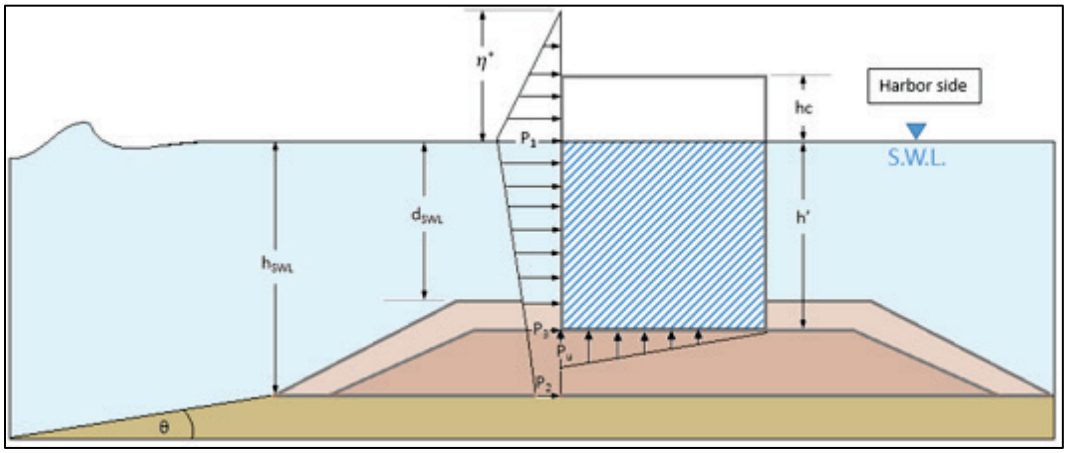

The following equations were developed for P_1, P_2, P_3, and P_U:

$$P_1 = 0.5\,(1\ + \cos\beta_D)\,(\alpha_1 + \alpha_2 * \cos^2\beta_D)\,\rho * g * H_D, \tag{52}$$

$$P_2 = \frac{P_1}{\cosh(2\pi h/L_D)}, \tag{53}$$

$$P_3 = \alpha_3 P_1, \tag{54}$$

and

$$P_U = 0.5\,(1\ + \cos\beta_D)\,\alpha_1 * \alpha_3 * \rho * g * H_D, \tag{55}$$

where α_1 and α_2 are wave pressure coefficients derived from laboratory data. The α_1 coefficient represents the average tendency of wave pressure to increase with wave length (L), and the α_2 coefficient represents the tendency of the wave pressure to increase with berm height. This α_2 term reflects the wave shoaling effect due to berm height and the impulsive pressure component. The α_3 coefficient describes the assumed linear pressure variation between P_1 and P_2. The equations to determine these coefficients are as follows:

$$\alpha_1 = 0.6 + \frac{1}{2}\left[\frac{\frac{4\pi h}{L_D}}{\sinh\left(\frac{4\pi h}{L_D}\right)}\right]^2, \quad (56)$$

$$\alpha_2 = \min\left[\frac{h_b - d}{3h_b}\left(\frac{H_D}{d}\right)^2, \frac{2d}{H_D}\right], \quad (57)$$

$$\alpha_3 = 1 - \frac{h'}{h}\left[1 - \frac{1}{\cosh\left(\frac{2\pi h}{L_D}\right)}\right]. \quad (58)$$

The Goda (1974) analysis uses a single design wave height, H_D, and length, L_D, to represent the complex spectrum of sea waves. Equations (59)–(66) show the empirical techniques used to develop the wave heights. The design wave height (H_D) of Goda's formula is described as the highest wave expected under given wave conditions; this wave height is also identified as H_{MAX}. H_{MAX} is determined as the lesser of 1.8 times the significant wave height ($H_{1/3}$) and the breaking wave height (H_b; Equations 59 and 60), where H_b is evaluated at a distance of $5H_{1/3}$ seaward of the breakwater berm. The significant wave height ($H_{1/3}$) is equal to the mean of the heights of the highest one-third waves in a wave group. The design wave length (L_D) of Goda's formula is described as the longest wave expected under given wave conditions; this wave length is also identified as L_{MAX}. In Equation (60), L_{MAX} (L_D) is approximated using first order wave theory and the significant wave period ($T_{1/3}$). Equation (59) is as follows:

$$H_D = H_{Max} = \min\{\alpha_h * H_{1/3}, H_b\}, \quad (59)$$

where α_h is typically in the range of 1.6 to 2.0. The α_h term defines the non-deterministic characteristic of the highest wave due to the random nature of sea waves. According to Goda (2010), the value of α_h is selected based on the reliability of the design for storm wave estimation, the importance of the structure, and the type and nature of the possible structural failure. Goda stated that a value of 2.0 or greater is often used for offshore structures, such as offshore oil rigs. For the design of nearshore vertical structures, Goda suggested using a value of 1.8 for α_h:

$$H_b = 0.17 * L_D\left\{1 - \exp\left[-1.5\frac{\pi h_b}{L_D}\left(1 + \sigma_S * \tan^{\frac{4}{3}}\theta\right)\right]\right\}. \quad (60)$$

Originally, Goda (1974) specified the σ_s value as a constant equal to 15, but he later recommended a value of 11 based on the work of Rattanapitikon

and Shibayama (2000). This reduction in the σ_s value accounts for an overprediction in the wave shoaling effect for steep bottom slopes (i.e., >1/10). Therefore, the authors of this report recommend using $\sigma_s = 11$ for bottom slopes greater than 1/50 and $\sigma_s = 15$ for bottom slopes that are less than 1/50:

$$h_b = h + 5 * H_{1/3} \tan\theta, \tag{61}$$

and

$$L_D = L_{MAX} = \frac{g*T_{1/3}^2}{2\pi}. \tag{62}$$

Site-specific estimates of $H_{1/3}$ and $T_{1/3}$, based on historical records, simulations, and so on, can be either obtained or calculated from historical records of deep-water surface elevation changes with time. When selecting a historical record, it is important to ensure that the record length is sufficient to include the events of interest (e.g., 100 yr storm if possible).

A second method used to approximate the $H_{1/3}$ value is based on the generally accepted premise that the distribution of wave heights in the sea can be adequately represented by a theoretical distribution function known as the Rayleigh distribution (Equation 63):

$$p(x) = \frac{\pi}{2} x \exp\left[-\frac{\pi}{4} x^2\right], \tag{63}$$

where

$$x = \frac{H}{H_{mean}}. \tag{64}$$

If the Rayleigh distribution is adopted, then the $H_{1/3}$ and $H_{1/10}$ values can be calculated as a function of the historical record's mean wave height (Equations 65 and 66):

$$H_{1/3} = 1.6 * H_{mean}, \tag{65}$$

$$H_{1/10} = 2.03 * H_{mean}. \tag{66}$$

The Goda (2010) wave pressure distribution was adapted to the STG (Figure 18). The P_1 term represents the maximum wave pressure exerted at the

upper pool el. P_3 represents the linear decay in wave pressure with depth, and P_4 represents the wave pressure at the top of the spillway gate.

Figure 18. Goda's (2010) wave pressure distribution adapted for an STG.

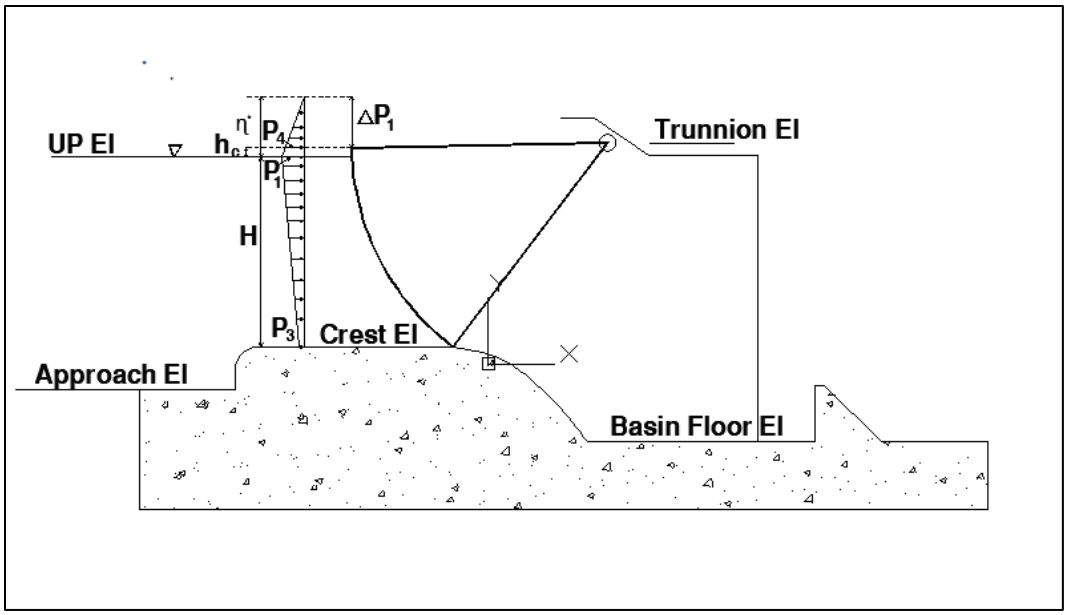

The total lateral force per linear width (F_{Lat}) on the face of the tainter gate is as follows:

$$F_{Lat} = 0.5(P_1 + P_3)H + 0.5(P_1 + P_4)h_c', \tag{67}$$

where

$$P_4 = P_1\left(1 - \frac{h_c}{\eta^*}\right), if\ \eta^* > h_c, \tag{68}$$

or

$$P_4 = 0, \text{ if } \eta^* < h_c,$$

$$\eta^* = 0.75(1 + \cos(\beta_D))H_D, \tag{69}$$

and

$$h_c' = \min\{\eta^*, h_c\}. \tag{70}$$

Appendix A contains an example procedure for computing the wave pressure on the STG using the Goda (2010) procedure for the MPLD STGs.

2.3.2.4 Converting a Trapezoidal Pressure Distribution Acting on a Discrete Segment of the STG into End Point Forces

The wave pressure distributions acting on the STG can be converted into equivalent forces using the relationships given in Ebeling et al. (2016) and described in this subsection. Most of the information in the remainder of this section is from Ebeling et al. (2016). As described in Section 2.3.1, the magnitude of the horizontal component of hydrostatic force on a curved surface is equal to the product of the pressure at the centroid of the vertical projection of the surface and the area of the vertical projection. This makes it possible to use the procedures developed for the I-Wall in Ebeling et al. (2016) for the STG. From the top of the spillway gate down to the spillway crest, gate segments are defined by each pair of adjacent nodes. Figure 19 depicts segment *k* between node *i* and node *i+1*. Figure 20 depicts the Figure 19 segment *k* and segment *k+1* between nodes *i+1* and *i+2*.

For each segment of gate, the applied pressure distribution is converted into nodal point forces (F_i^- and F_{i+1}^+) using the one-third/one-sixth computational procedure. The equivalent nodal point forces acting at node *i* and node *i+1* are computed this way:

$$F_i^- = length_k * \left[\frac{\sigma_i^-}{3} + \frac{\sigma_{i+1}^+}{6}\right], \tag{71}$$

and

$$F_{i+1}^+ = length_k * \left[\frac{\sigma_i^-}{6} + \frac{\sigma_{i+1}^+}{3}\right], \tag{72}$$

where $length_k$ is the distance from node *i* to node *i+1*, σ_i^- is the stress normal to node *i* on gate segment *k*, and σ_{i+1}^+ is the stress normal to node *i+1* on gate segment *k*. These two relationships for equivalent end forces, F_i^- and F_{i+1}^+, will exactly reflect the trapezoidal pressure diagram along its nodal pair gate segment *k*. The sum of these two forces equals the area under the trapezoidal pressure diagram. Moment equilibrium for the gate segment *k* is satisfied for the applied trapezoidal pressure distribution and these two end normal forces.

Figure 19. Distribution of stress acting normal to a discrete segment, *k*: (*a*) trapezoidal pressure distribution and (*b*) equivalent nodal point forces. (Image reproduced from Ebeling et al. 2016, 46. Public domain.)

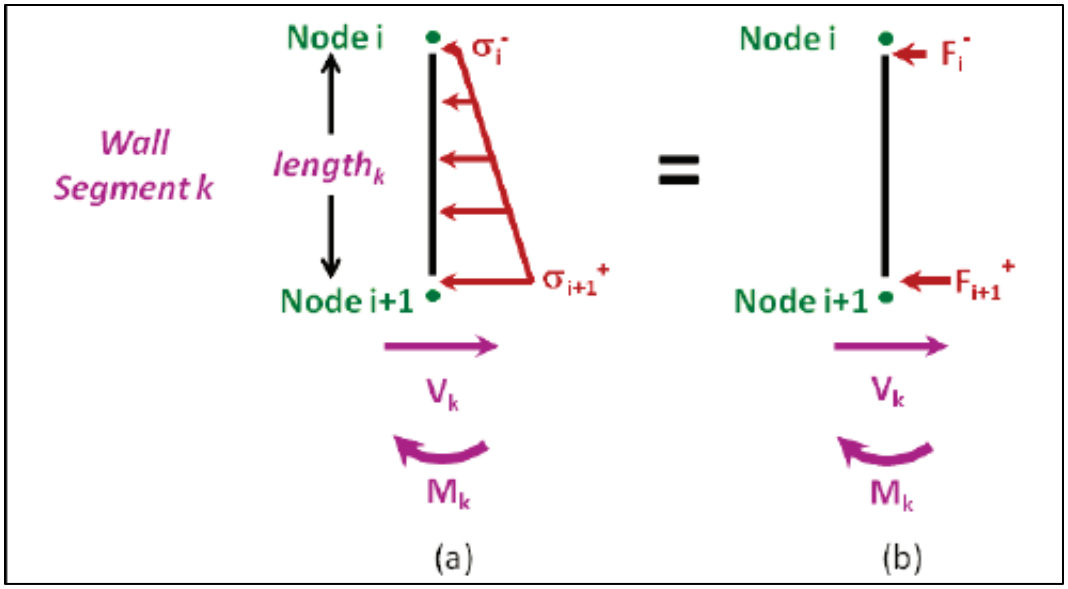

Figure 20. Internal shear and moment at node *i+2* for segment *k+1*: (*a*) trapezoidal pressure distributions and (*b*) equivalent nodal point forces. (Image reproduced from Ebeling et al. 2016, 47. Public domain.)

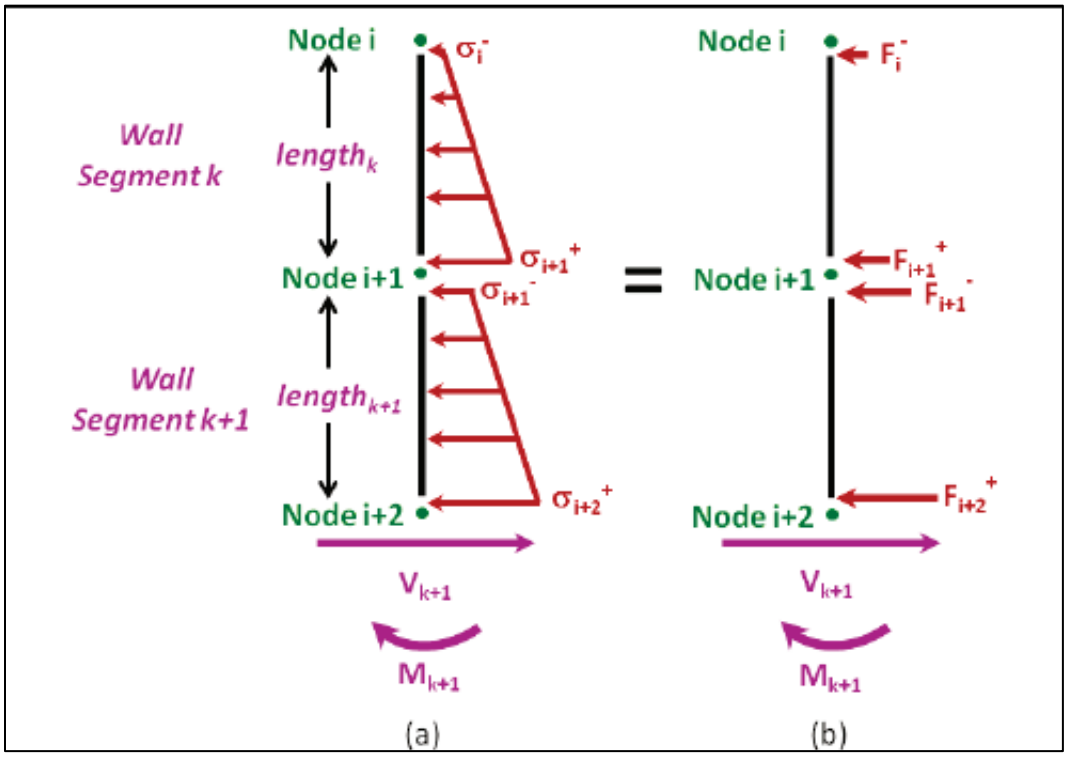

The moment M_k, located at the bottom of the Figure 19 gate segment k, is equal to the sum of forces acting on gate segment k:

$$M_k = F_i^- * length_k. \quad (73)$$

The moment M_k is assigned at the elevation of node $i+1$. The moment M_{k+1}, located at the bottom of Figure 20, gate segment $k+1$, is equal to the sum of forces acting on gate segments k and $k+1$ times their respective lever arm:

$$M_{k+1} = F_i^- * (length_k + length_{k+1}) + \{F_{i+1}^+ + F_{i+1}^-\} * (length_{k+1}). \quad (74)$$

This moment, M_{k+1}, is assigned at the elevation of node $i+2$. This procedure is followed top down for all gate segments to define the distribution of moment internal to the wall.

2.3.2.5 Significant Wave Height Selection for Inland Structures

A literature review by Ebeling et al. (2023) identified that Goda's (2010) method is generally accepted among the international coastal engineering community and can be implemented with reasonable effort. This method was established on an extensive set of laboratory data and theoretical considerations. The wave-loading-based pressure formulation was also validated for numerous case histories for different prototype caissons in several of Japan's harbors that experienced design storm events.

The Goda (2010) procedure uses the mean of the heights of the highest one-third waves in a wave group; this is known as the *significant wave* and is designated $H_{1/3}$. The selection of the appropriate wave height to use for an inland structure depends on the wind properties that generate the wave.

The current USACE guidance for determining wave load design is to use the SPM (Coastal Engineering Research Center 1984b). Smith's (1991) and Goda's (2010) procedures are more recent and are considered improvements over the SPM. The wave force computation method recommended for the LRFD for HSS is the one developed by Goda. This procedure, depending on site-specific conditions, may result in slightly higher wave forces than current USACE guidance recommends. ETL 1110-2-584 (HQUSACE 2014) provides load factors for tainter gates and recommends a factor of 1.2 for both strength limit state I with the gate closed and strength limit state II with usual operation. ETL 1110-2-584 states,

> For consistency in application of LRFD, the coincident effects of hydrostatic and hydrodynamic conditions that produce the maximum effects for each load category should be used. However, for convenience and conservatively, the individual maximum events, under each load category, can be determined separately and applied together to produce the maximum effects. (HQUSACE 2014, 3-5)

The authors of this report recommend that wind-induced wave forces be determined using the Goda (2010) design procedure and the wind-speed estimation discussed in the next section.

The wind properties needed to determine the wave heights must be determined from the available wind data. For the example presented in Appendix A, these data were obtained from the two airports closest to the project. The quality of the data may not be what is desired, but if it is the only source available, then the most appropriate processing techniques must be selected. The process used in Appendix A consisted of analyzing the highest wind events that met the criteria for t_{min} shown in Equation (50). The data were reduced to eliminate all those events with wind direction not applicable to the project fetch. The wind direction that produces the highest waves for most tainter gates occurs normal to the axis of the dam. In a companion study, Ebeling et al. (2023) developed the LRFD process for flood structures and determined the wind direction that produces the highest waves for the flood wall is parallel to the axis of the dam, assuming the flood wall is normal to the axis of the dam.

2.3.2.6 Wind Speed for Extreme Value Estimation

This first statistical analysis method investigated to determine an appropriate wind speed was to follow a procedure used by USACE-MVP (2014) in the *Oxbow-Hickson-Bakke (OHB) Levee Wind-Wave Analysis*. This study was performed to determine the levee heights required for flood protection in the OHB community. The maximum annual wind speed data were determined for the period of record. The type 1 Gumbel distribution was used for a generalized extreme value (GEV) analysis. This analysis is typically used to evaluate extreme, low probability meteorological and hydrological events. The probability of nonexceedance and wind speed are plotted, and a linear regression can be used to estimate values for extreme return periods. Figure 21 shows the plot done for the OHB wind-wave

analysis study. Probability is a double-log axis. The 50 yr (2%) return period for the wind speed was chosen for the wave analysis. Figure 21 shows the wind speed in meters per second plotted versus the double log probability (-ln(-ln(P)) for different annual chances of exceedance (ACE).

The results of an analysis performed for the MPLD project using maximum yearly wind speeds for the period 1999 to 2019 are shown in Figure 22 and also in Appendix A. These data were obtained from the Saint Charles County (SCC) airport, which is about 15 mi west of the project.

Figure 21. Generalized extreme value (GEV) type 1 Gumbel distribution peak annual 2 min wind data for Fargo, North Dakota, used in the *Oxbow-Hickson-Bakke (OHB) Levee Wind-Wave Analysis* (USACE-MVP 2014). ACE is annual chances of exceedance.

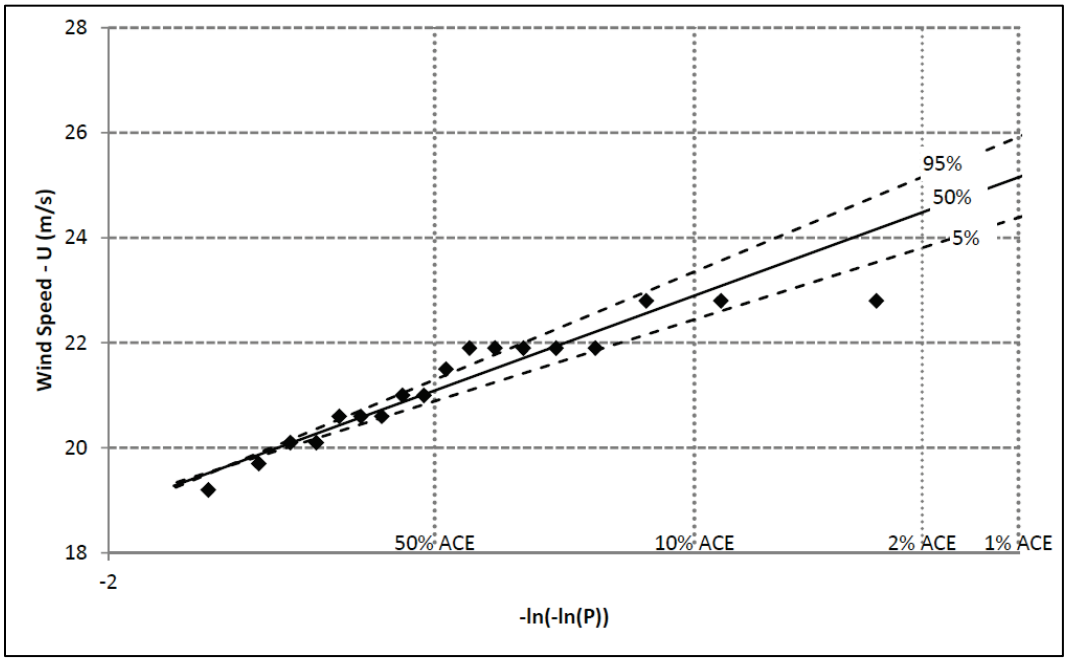

Using the equation shown in Figure 22 (i.e., wind speed (mph) = 6.7356ln[year] + 31.828), the wind speed for the 100 yr recurrence interval is 63 mph. The wind speed values from the extreme value estimation procedure for the 100 yr recurrence interval were considered too high based on the observations of wind speed collected at the St. Louis Regional (SLR) and SCC airports. A sustained wind duration (t_{min} in Equation 50) is required for full wave growth, and the data indicated that this wind duration is extremely unlikely for a 63 mph wind. The wind frequency based on the Gumbel type 1 distribution with Gringorten's plotting position formula was considered more representative of actual storm event possibilities.

Figure 22. Estimation of wind speed using the extreme value method for Saint Charles County (SCC) airport near the Melvin Price Locks and Dam (MPLD) project.

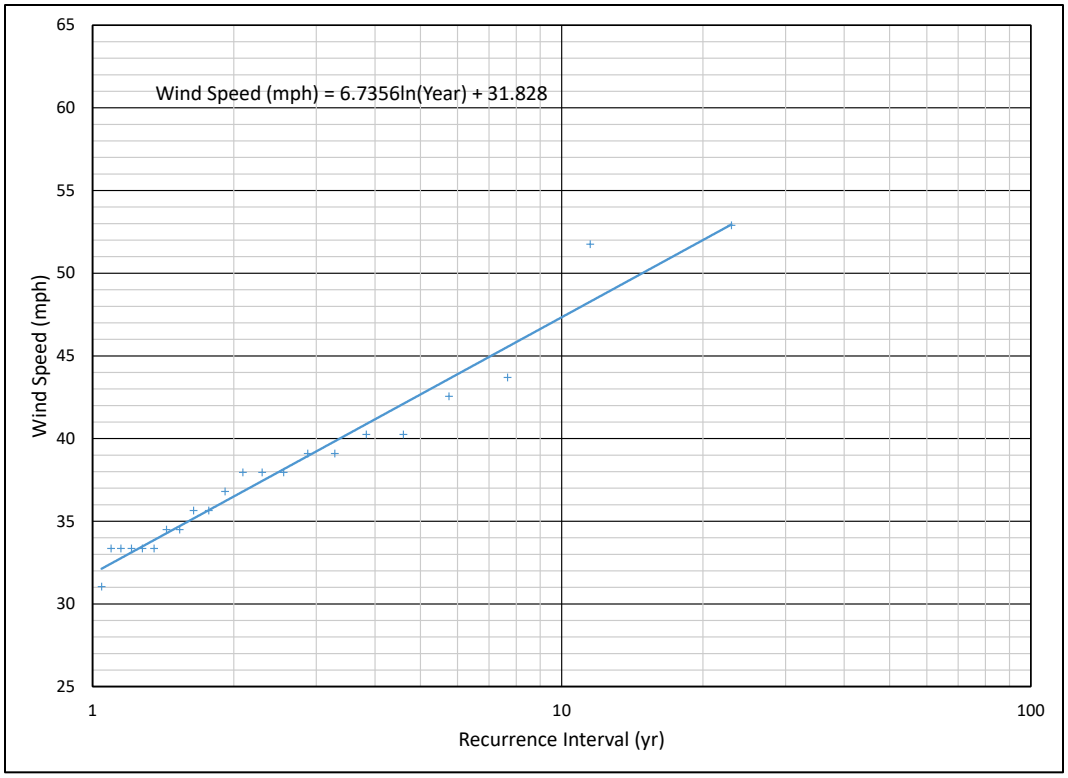

2.3.2.7 *Type 1 Gumbel Distribution*

As an alternative procedure for assessing the site-specific wind speed, the type 1 Gumbel distribution was used to determine the most appropriate wind speed for the wave height. We began by using Gringorten's (1963) plotting position formula to calculate the estimates of exceedance probabilities. This formula is shown here:

$$q_i = -\frac{i - a}{N + 1 - 2a}, \tag{75}$$

where

q_i = the exceedance probability associated with specific observation;
N = the number of annual maximal observations;
i = the rank of a specific observation, with i = 1 being the smallest to i = N being the largest; and
a = the constant for estimation = 0.44 using Gringorten's method.

The nonexceedance probability of the distribution was $1 - q_i$. The statistical definition of return period was determined next using methods described in Ebeling et al. (2023) and repeated here. If x is a random variable that has a cumulative distribution function (CDF) of $Fx(x)$, the probability that x is less than or equal to a given x_p is given as

$$F_x(x) = P\left(X \le x_p\right) = p. \tag{76}$$

The probability that this event would be exceeded was then equal to $1 - p$, and the percent exceedance was noted as $100(1 - p)$. For an event x_p, the return period corresponding to this exceedance probability was noted by T, and $T - 1/(1 - p)$.

The 100 yr return period, then, would be an event with a probability of exceedance $1 - p = 0.01$, or a nonexceedance probability of $p = 0.99$. T_p estimated represents the estimated distribution of the number of years of data and was determined using T and p_i to form $T_p = 1/(1 - p_i)$. The parameters for the Gumbel type 1 distribution were then determined. The CDF of the Gumbel type 1 distribution is given here:

$$F_x(x) = \exp\left[-\exp-\left(-\frac{x-u}{\alpha}\right)\right] = p, \tag{77}$$

where

x = the observed data,
u = a calculated parameter of the distribution, and
α = another calculated parameter of the distribution.

The theoretical value of p was then developed as follows. The value of $x - u)/\alpha$ was calculated from the values of $\overline{x}$, s_x, u, and α, which were determined from the equations that follow:

$$\overline{x} = \sum_{i=1}^{n} \frac{x_i}{n}, \tag{78}$$

$$s_x^2 = \frac{1}{(n-1)} - \sum_{i=1}^{n} (x_i - \overline{x})^2, \tag{79}$$

$$u = \overline{x} - 0.5772\alpha, \tag{80}$$

$$\alpha = \frac{\sqrt{6}s_x}{\pi}. \tag{81}$$

The value of p theoretical was then calculated from the CDF of the Gumbel distribution shown in Equation (77). Next, using the same equation used to calculate T_p estimated, we calculated T_p theoretical. Once T_p theoretical was known, the frequency analysis was finished. The wind speed frequency curve could then be constructed.

An example wind speed frequency curve for the data obtained from the SLR and SCC airports is shown in Figure 23. The curve represents the theoretical distribution, and the dots represent the fit of the annual peak wind speed with respect to a Gumbel distribution. From this curve, the wind speed values for the desired return period between 1 yr and 100 yr can be determined. The theoretical follows the estimated distribution well for low speeds and not as well for the higher theoretical distribution.

Figure 23. Wind frequency curve from Gumbel type 1 distribution with Gringorten's method for the St. Louis Regional (SLR) and SCC airports data using annual peak values.

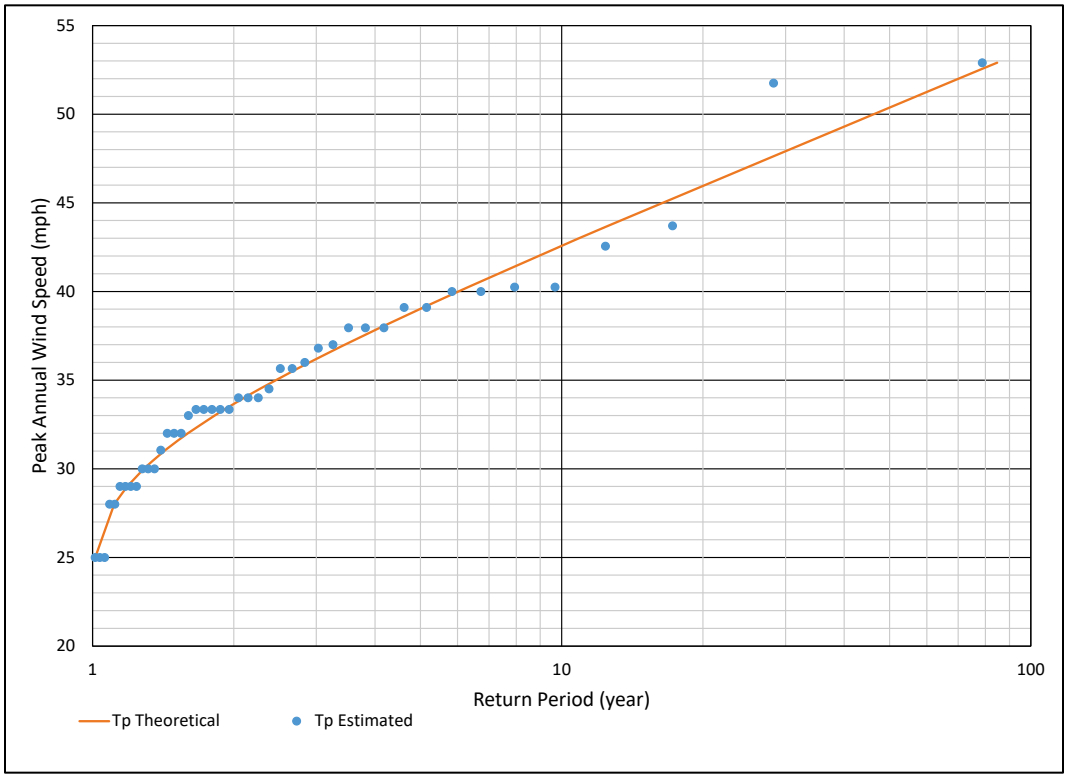

As the maximum storm event per year was being investigated for the MPLD project, it became obvious that using the maximum single value of wind speed was not truly representative for the wave height calculations. A minimum wind duration was needed to produce the significant wave height and period (Section 2.3.2.3). Based on the t_{min} values computed

from Equation (50), the minimum duration required to produce the significant wave height and wave period for wind speeds between 35 and 40 mph with a 7.72 mi fetch was about 1 hr and 40 min. Using Equation (50) gives the t_{min} values in Table 4 for wind speeds of 30, 50, 35.6, and 40 mph.

Table 4. Minimum wind duration times (t_{min}) to obtain significant wave height at MPLD.

U_{10} (mph)	t_{min} (hr)
30	1.79
50	1.51
35.6	1.69
40	1.62

Based on the t_{min} values in Table 4, the maximum 2 hr average wind speed during the highest storm event, rather than the peak annual value, was considered a more reasonable annual value for the statistical analysis. In addition, the data from both airports showed that the results from the wind frequency determined from the Gumbel type 1 distribution using Gringorten's plotting position were in good agreement and, if combined, would provide a larger sample size for statistical analysis.

A standard error procedure, described in Appendix A, was adopted to help determine statistical parameters for the wind speed data for the combined airport data. This allowed us to bound the wind speed frequency determined using the Gumbel type 1 distribution with Gringorten's plotting position. Figure 24 shows a plot of wind frequency bounded by +1, +2, and +3 and −1, −2 and −3 standard deviations that was developed using the standard error procedure.

Appendix A provides a more detailed analysis of the wind data that were obtained from both airports in the vicinity of the MPLD project and were used for estimating wave heights.

Figure 24. Wind frequency based on maximum 2 hr average wind speed for the combined airport data.

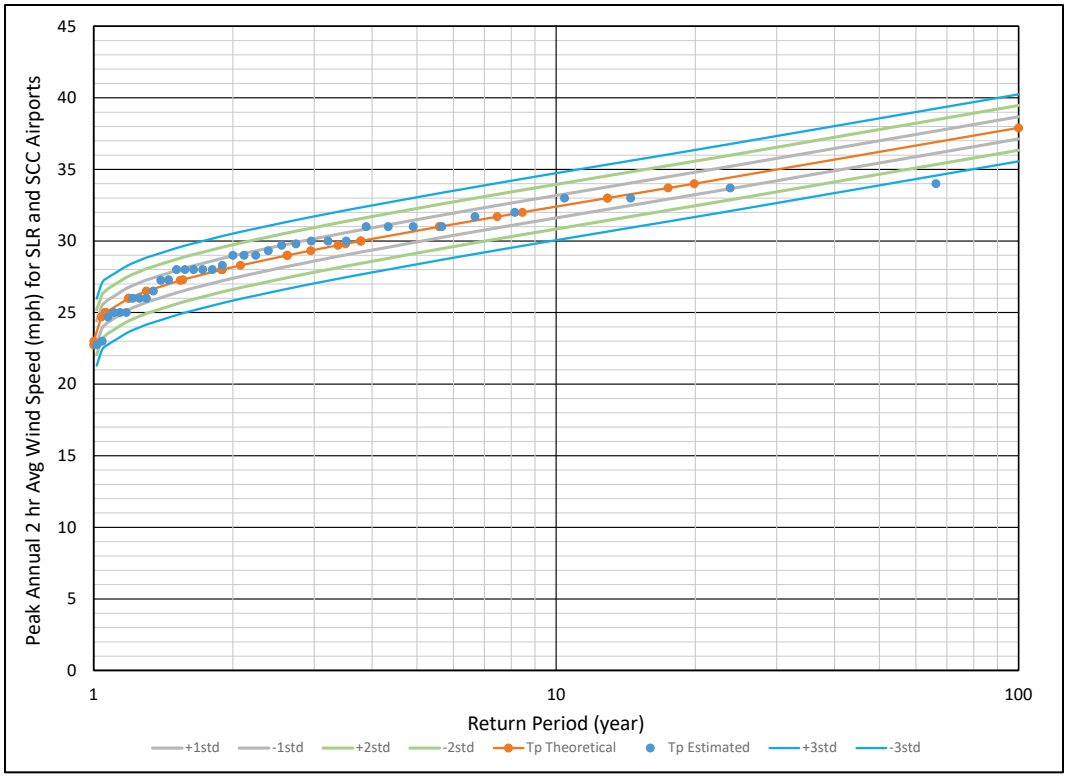

2.3.3 Hydrodynamic Load for STGs

The magnitudes of the hydrodynamic loads caused by flowing water are also a function of the usual, unusual, and extreme load category. The deviations from the mean hydrodynamic load can also result from many factors, including wind, waves, ice, debris, vessel impacts, approach flow asymmetry, gate settings, and tailwater effects. The effects of the upper pool el, the gate settings, and the TW El on the hydrodynamic loads are the main factors that contribute to deviations about the mean load.

The hydrodynamic load results from the force due to water flowing under the gate. The pressure distribution near the upper part of the gate is primarily hydrostatic because the velocity is small in this location. The velocity starts to increase with depth; near the bottom of the gate, the velocity can be large. In this area, there is a deviation from the hydrostatic pressure distribution. Figure 25 shows a schematic of a pressure distribution with no effects from tailwater. F_g is the resultant hydrodynamic force acting on the gate. The hydrodynamic pressure at the bottom is considered atmospheric. A discussion of the hydrodynamic loads on the gate, with and without effects from tailwater, is provided in the sections that follow.

Figure 25. Schematic of the pressure distribution on a tainter gate with the gate open and with no tailwater effects.

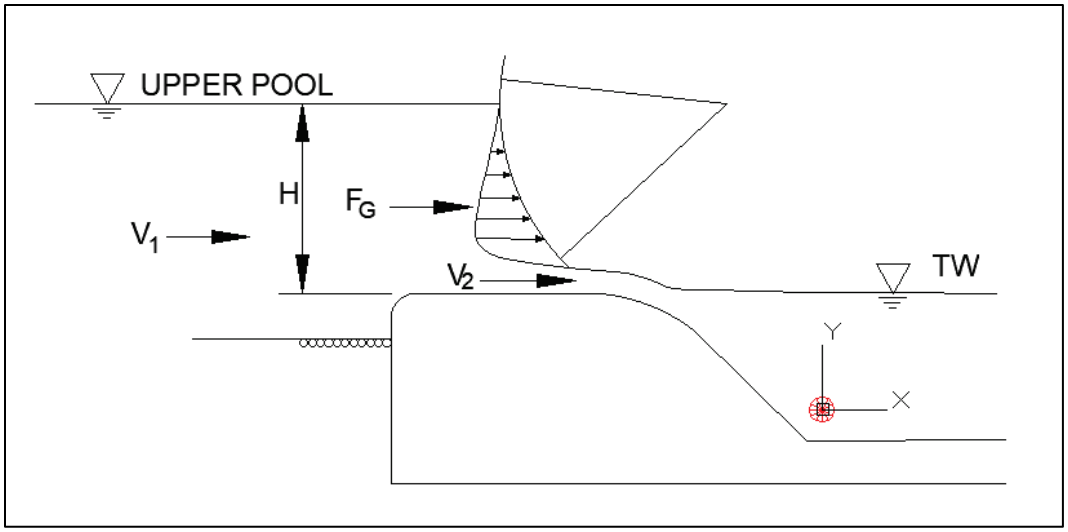

2.3.3.1 Hydrodynamic Load for STGs with Tailwater Higher than the Gate Opening

This variable pressure on the gate makes it difficult to determine the force on the gate by integrating the pressure over the gate surface. The momentum equation applied to a control volume upstream and downstream from the gate can be used to estimate the force on the gate. This is a simplified method because the flow across the control volume is assumed to be uniform and steady. The equations that follow were chosen to estimate the hydrodynamic force on the gate with tailwater higher than the gate opening.

The momentum equation from Roberson and Crowe (1985) was modified as

$$\frac{\gamma H^2 b}{2} - \frac{\gamma h^2 b}{2} + F_{GW} - F_{visc} = V_1 \rho(-V_1 H b) + V_2 \rho(V_2 h b). \quad (82)$$

Considering the viscous force (F_{visc}) is negligible and $V_1 H b = V_2 h b = Q$,

$$F_{GW} = \rho Q(-V_1) + \rho Q(V_2) - \frac{1}{2}\gamma b(H^2 - h^2). \quad (83)$$

F_{GW} is the force of the gate acting on the water in the control section. To obtain the force on the gate (F_G), F_{GW} is solved, and then the sign on F_{GW} is changed:

$$F_G = \rho Q(V_1 - V_2) + \frac{1}{2}\gamma b(H^2 - h^2), \quad (84)$$

where

Q = the discharge per gate in ft³/sec,
V_1 = the approach velocity in ft/sec,
V_2 = the velocity downstream of the gate in ft/sec,
ρ = the mass density = 1.936 slugs/ft³,
γ = the unit weight of water = 62.4 lb/ft³, and
b = the gate width in feet,

with

$$H = \text{upper pool el} - \text{spillway crest el}, \quad (85)$$

and

$$h = \text{TW El} - \text{spillway crest el}. \quad (86)$$

The solution to Equation (84) requires that Q, V_1, and V_2 are known. Figure 26 shows a schematic of some of the terms used in Equation (84). Using flow through a single gate for the discharge, Q, the approach velocity, V_1, can be determined from

$$V_1 = \frac{Q}{A_1}. \quad (87)$$

A_1 is the area upstream from the gate, and when using flow through a single gate, it can be computed from the terms shown in Figure 26 as UP El – Approach El (P) times the gate width, b, or

$$A_1 = P * b. \quad (88)$$

If tailwater is present and affects the discharge through the gate, V_2 can be determined using the submerged controlled flow equation:

$$Q = C_{gs} b h \sqrt{2g\Delta H}, \quad (89)$$

where

$$h = \text{TW El} - \text{spillway crest el}, \tag{90}$$

and the differential head, ΔH, is

$$\Delta H = H - h. \tag{91}$$

Equation (89) is often used to develop spillway rating curves that are used to set the desired gate opening. The coefficient C_{gs} in Equation (89) is obtained from Figure 5-12 in EM 1110-2-1605 (HQUSACE 1987, 5-16). The data were collected from several studies and assembled for use in the EM. As with all empirical coefficients, it is based on the information available for the analysis. This figure was reconstructed for clarity and shown as Figure 27 for B = 20 ft. This was the value for B used in the example problem in Appendix A. Figure 27 was interpolated from B = 18 ft and B = 31 ft, which are shown in Figure 5-12 in EM 1110-2-1605 (HQUSACE 1987, 5-16).

To use Figure 27, h/G_o and B are needed. Equation (90) is used to determine h, and G_o is the gate opening (Figure 26). B is given as

$$B = \text{spillway crest el} - \text{stilling basin floor el}. \tag{92}$$

C_{gs} is then chosen from Figure 5-12 of EM 1110-2-1605 (HQUSACE 1987). The discharge in Equation (89) can now be computed because b, h, ΔH, *and* C_{gs} are all known. The value of discharge determined from Equation (89) is generally used to develop the project spillway rating curve.

Typically, a spillway rating curve is used to determine what gate opening to set for a given discharge and TW El. If a spillway rating curve has been developed, the discharge, Q, is known, and one can take advantage of this information to determine V_2. Figure 28 shows the spillway rating curve for the MPLD project used as the example in Appendix A. If the discharge and TW El are known, the gate opening required to keep the upper pool near constant (i.e., el 419 at MPLD) can be determined from Figure 28.

If V_2 is assumed to be the representative velocity downstream from the gate between the tailwater and the spillway crest, it can be computed from

$$V_2 = \frac{Q}{A_2}, \tag{93}$$

where A_2 is

$$A_2 = b * h, \tag{94}$$

for a project with tailwater when Q has been computed using Equation (89) or determined from the spillway rating curve.

All the parameters in Equation (84) have now been determined, so the hydrodynamic force on the gate, F_g, can be computed. Each navigation project with STGs should have a spillway rating curve that shows the gate setting, discharge, and TW El combination required to maintain a near constant upper pool el. Appendix A illustrates how the spillway rating curve is used to determine the hydrodynamic load on the STG.

Hydrodynamic loads computed for the STG at the MPLD are shown in Appendix A. The results show the hydrodynamic loads on this gate are primarily dependent on the TW El (Figure 29). The plots show that the tailwater dominates the hydrodynamic load because there is not much change in the magnitude of the hydrodynamic force with varying gate opening.

Figure 26. Schematic for terms used in Equation (84).

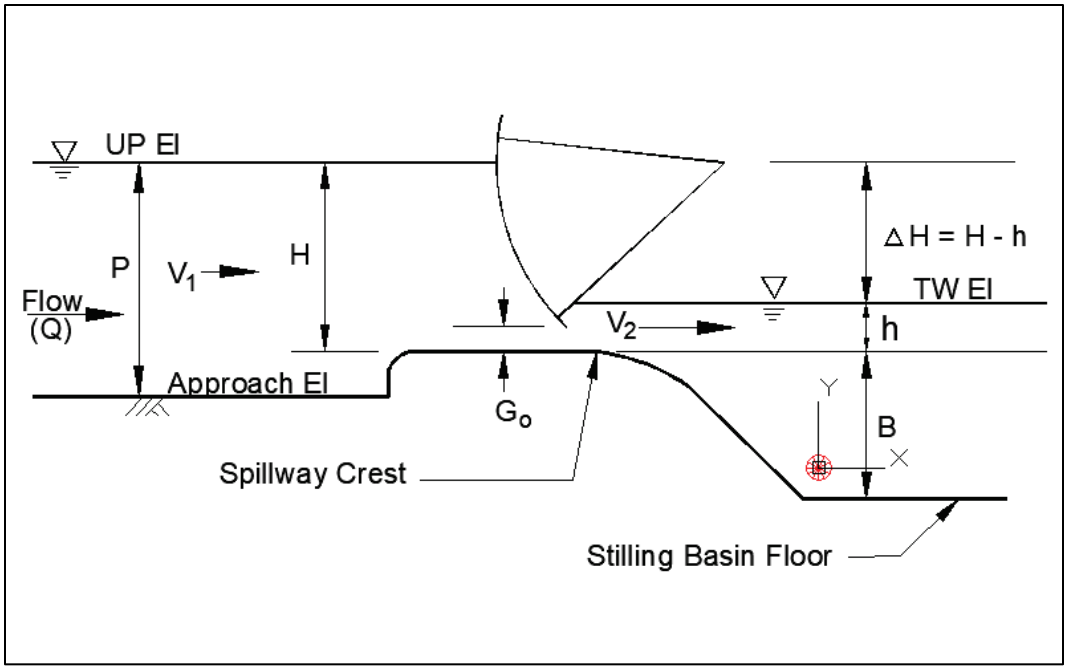

Figure 27. Discharge coefficients (C_{gs}) for submerged controlled flow. (Graph adapted from EM 1110-2-1605, HQUSACE 1987.)

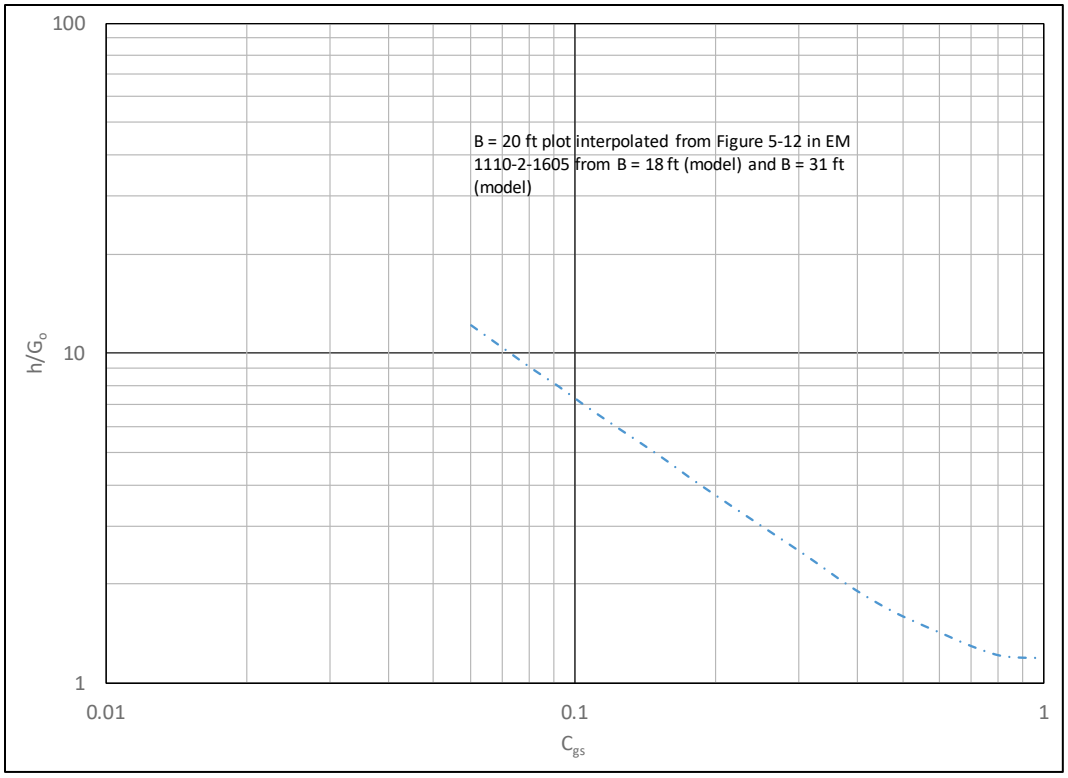

Figure 28. Spillway rating curve for MPLD. (Graph provided by USACE, St. Louis District [USACE-MVS], Hydraulics Branch.)

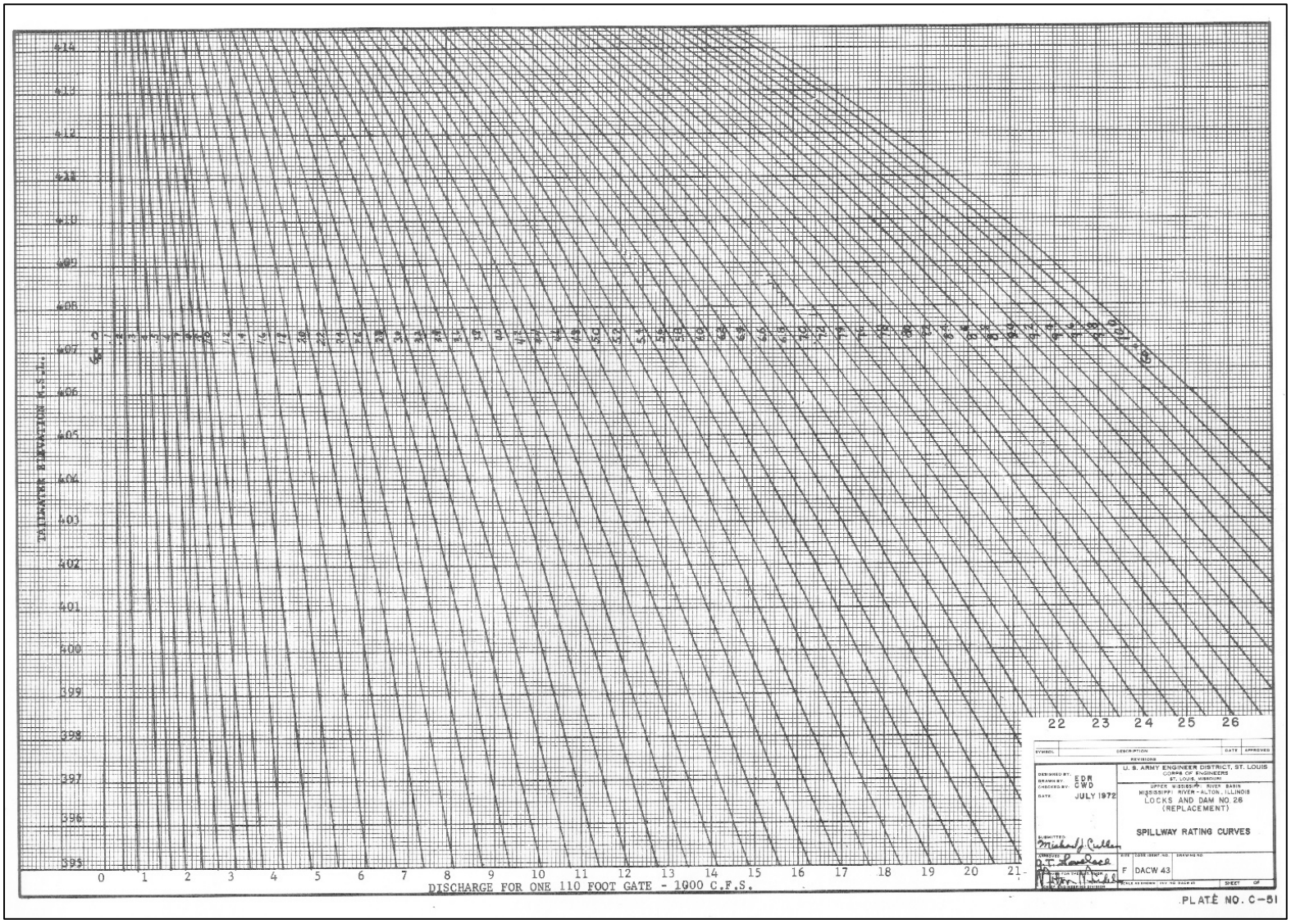

Figure 29. Example of hydrodynamic forces computed for the MPLD STG for varying gate openings and tailwater with constant upper pool el.

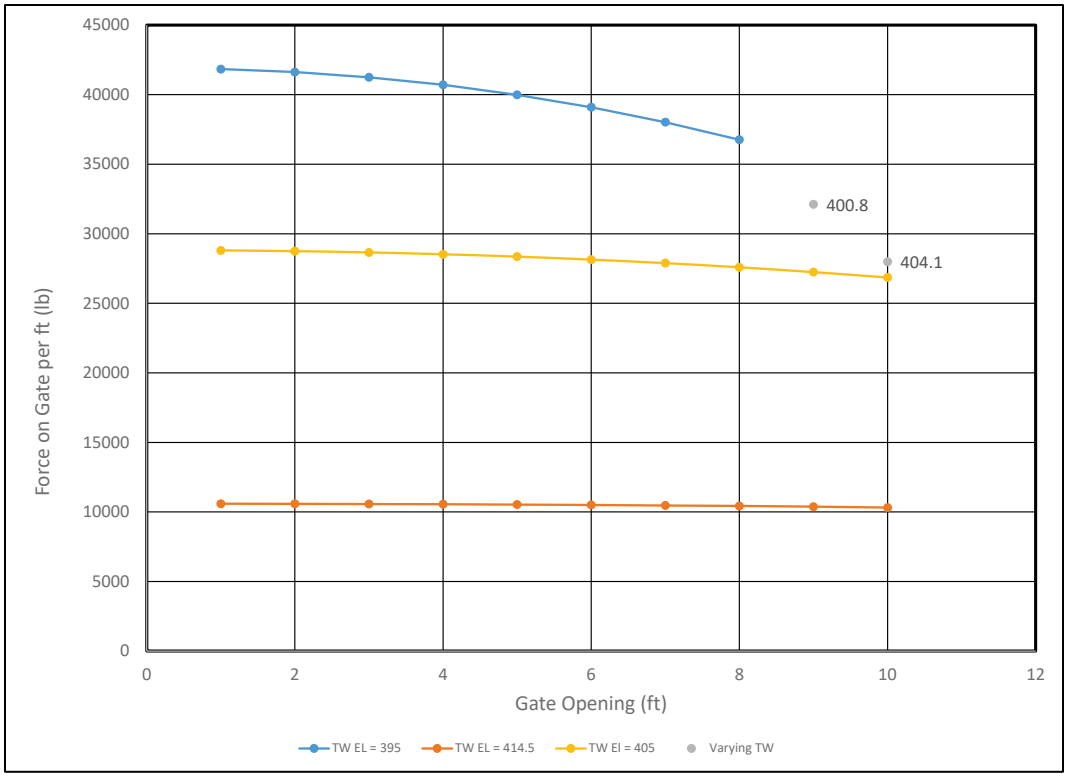

The location of the resultant hydrodynamic force computed from Equation (84) needs to be determined for the LRFD analysis. The procedure that follows was selected for the analysis of the STG when the tailwater is less than the gate opening. Similar techniques were adopted to develop the location of the resultant hydrodynamic force for an STG with tailwater greater than the gate opening; these will be discussed in Section 2.3.3.3.

2.3.3.2 Hydrodynamic Load for STGs with Tailwater Less than the Gate Opening

The location of the hydrodynamic load is needed to develop the LRFD procedures for the spillway gates. Due to turbulent flow through a gate opening, a time varying pressure exists on the gate, which makes it difficult to determine the force on the gate by integrating the pressure over the gate surface. This holds true even when the upper pool el is constant and the gate opening does not change. The procedure outlined in this subsection may be used to establish a pseudo-static hydrodynamic pressure distribution on a spillway gate with no tailwater effects.

Figure 25 shows an idealized schematic of the pressure distribution on an STG, with the hydrodynamic force denoted as F_{GW}. The area enclosed by the hydrodynamic pressure distribution is the hydrodynamic force per unit width of the gate. For the discussion that follows and the remainder of the chapters and appendixes, the hydrodynamic force will be noted as H_D to be consistent with ETL 1110-2-584 (HQUSACE 2014) and the definitions in Chapter 1.

The procedure to compute the hydrodynamic force using the conservation of momentum from Roberson and Crow (1985) described in Section 2.3.3.1 is considered more applicable to a spillway gate where the tailwater is higher than the gate opening. The procedure to determine the magnitude and location of the hydrodynamic force was investigated for use on a spillway gate where the tailwater is lower than the gate opening. This procedure was then modified to help estimate the location of the resultant hydrodynamic force when tailwater is above the gate opening.

Roth and Hager (1999) conducted experiments on flow under a sluice gate to measure velocities and pressures in the vicinity of a gate in a rectangular channel in an effort to advance the state of numerical modeling. As part of this investigation, the pressure distribution on a vertical sluice gate was measured upstream and downstream from the gate. Kim (2007) used FLOW-3D, a commercially available fluid dynamics program, to compute the pressure distribution for free flow past a sluice gate. Figure 30 contains a schematic of the parameters used by Kim (2007). The gate opening is designated a and is the vertical distance from the datum to the tip of the sluice gate. The results from Kim (2007, Figure 7) compared favorably to the laboratory results from Roth and Hager (1999).

Figure 30. Schematic of the pressure distribution on a sluice gate with an opening of height *a* and an illustration of parameters to compute the pressure distribution. (Image adapted from Kim 2007.)

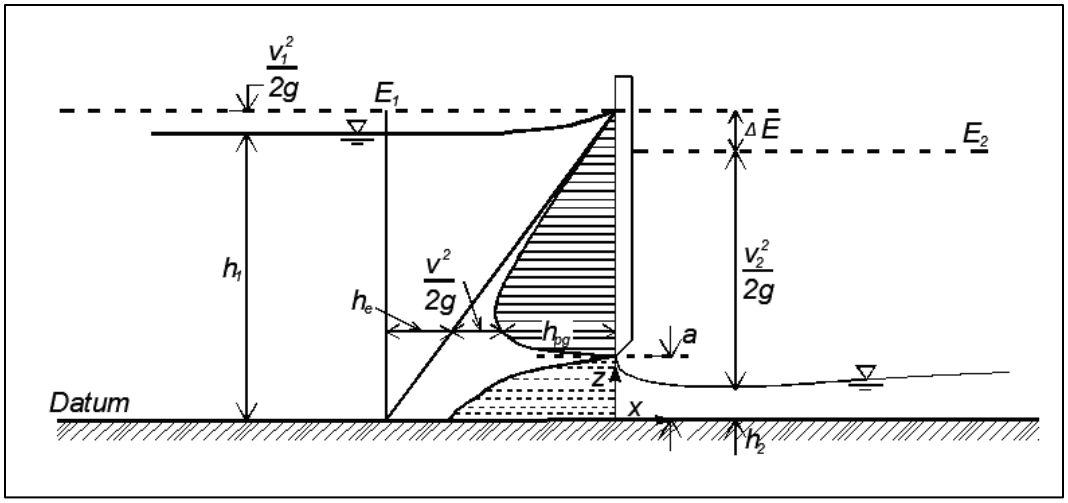

In Figure 30,

E_1 = the upstream energy, which is often referred to as the total energy head;
h_1 = the approach flow depth;
V_1 = the approach velocity;
$V_1^2/2g$ = the upstream velocity head;
ΔE = energy loss;
E_2 = the downstream energy or $E_1 - \Delta E$;
h_2 = the flow depth at the vena contracta;
V_2 = the downstream flow velocity;
$V_2^2/2g$ = the downstream velocity head;
a = the gate opening;
h_{pg} = the pressure head on the gate;
z = the vertical distance above datum and can be considered as the elevation head; and
x = the horizontal distance from upstream face of sluice gate.

The parameters all have units in terms of length. The total upstream energy head, shown as the upper dashed line labeled E_1 in Figure 30, represents the sum of the pressure head (h_p), the velocity head (h_v), and the elevation head (h_e), which is commonly presented in hydraulics as

$$E_1 = h_p + h_v + h_e = \frac{p_1}{\gamma} + \frac{v_1^2}{2g} + z_1, \quad (95)$$

where

$$\frac{p_1}{\gamma} = h_1, \tag{96}$$

and likewise for E_2, the downstream energy head,

$$E_2 = \frac{p_2}{\gamma} + \frac{v_2^2}{2g} + z_2, \tag{97}$$

where

$$\frac{p_2}{\gamma} = h_2, \tag{98}$$

and γ is the specific weight of water. The pressure head on the gate is noted as h_{pg} in Figure 30 and is calculated by dividing the simulated hydrostatic pressure on the gate by the specific weight of water. In this simplified example, the energy loss between E_1 and E_2 is ΔE and is due primarily to flow under the gate (a form loss) and some friction loss.

In Kim (2007, Figure 7), a plot of the dimensionless pressure distribution, H_{pg}/H_{pgM}, as a function of the dimensionless flow depth, Z, is shown. If h_{pg} is known, H_{pg} can be determined from Equation (99) and represents the pressure head on the gate, h_{pg}, normalized by the total approach energy, E_1, minus the gate opening, a. H_{pg} is a dimensionless term for the pressure head on the gate, and $E_1 - a$ is a quasi-representation of the energy level at the tip of the open gate:

$$H_{pg} = \frac{h_{pg}}{(E_1 - a)}. \tag{99}$$

H_{pgM} is the maximum normalized pressure head and can be determined using Kim's (2007, Figure 8) numerical study and laboratory data from Roth and Hager (1999) because a and E_1 are known. The maximum normalized pressure head is the top curve in Kim (2007, Figure 8).

Z is a dimensionless flow depth and is computed from Equation (100), where z is the vertical location above the test flume floor. When z is equal to the gate opening (a), Z is zero. Z is also normalized by the total approach energy, E_1, minus the gate opening, a:

$$Z = \frac{(z - a)}{(E_1 - a)}. \quad (100)$$

The dimensionless flow depth, Z, is measured downward from the E_1 surface and ranges from 0 at the tip of the gate, where z is equal to gate opening a, to 1 at the top of the gate, where z is equal to the E_1. Z is an expression of depth that is related to the tip of the gate rather than to the datum. The location of the maximum dimensionless pressure head on the gate, Z_m, is the bottom curve from Kim (2007, Figure 8). As seen in the figure, the location of Z_m is close to the bottom of the gate and varies from about 0.03 to 0.17 for values of a/E_1 between 0.05 and 0.6.

Figure 31 was drawn to encompass the range of data from the Kim (2007) numerical study and the Roth and Hager (1999) laboratory study. Maximum, minimum, and average curves were constructed to show that the scatter was fairly minimal considering the range of gate openings varied from approximately 20% to 60% of the approach flow energy head. These data represent a significant range in sluice gate openings and indicate how the hydrodynamic water pressure data, after normalization, collapse onto a very narrow band of normalized pressure heads. This range of gate openings covers most of the gate operations that a typical USACE project would encounter. Table 5 provides the maximum, minimum, and average values of H_{pg}/H_{pgM} for selected values of Z. The Z values that best describe the three curves were selected for Table 5. Values of Z that are between two adjacent values shown in the table can be linearly interpolated to determine the H_{pg}/H_{pgM} ratio.

Figure 31. Maximum, minimum, and average values. (Graph adapted from the data presented in Kim 2007, Figure 8.)

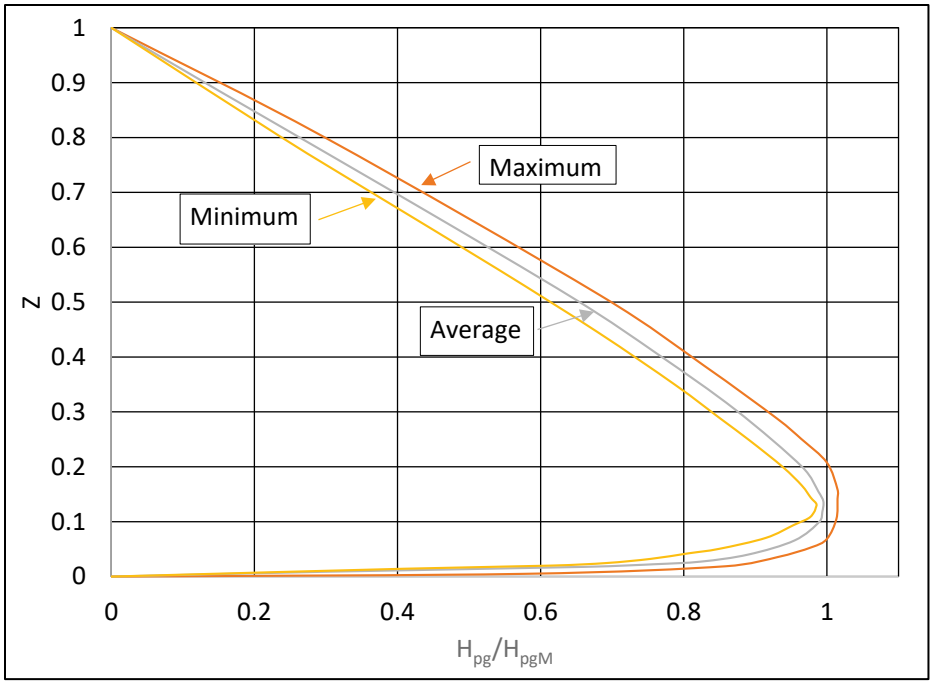

Table 5. Minimum, maximum, and average values obtained from Figure 31.

	H_{pg}/H_{pgM}		
Z	Minimum	Average	Maximum
1.00	0.000	0.000	0.000
0.90	0.120	0.130	0.150
0.80	0.240	0.260	0.300
0.70	0.360	0.390	0.434
0.60	0.490	0.525	0.570
0.50	0.615	0.655	0.695
0.45	0.675	0.715	0.760
0.40	0.730	0.770	0.815
0.35	0.790	0.825	0.865
0.30	0.840	0.875	0.920
0.25	0.890	0.925	0.965
0.20	0.940	0.965	1.000
0.17	0.965	0.985	1.010
0.13	0.985	0.995	1.015
0.10	0.970	0.993	1.010
0.07	0.915	0.960	0.995
0.05	0.850	0.920	0.970
0.02	0.580	0.760	0.875
0.00	0.000	0.000	0.000

H_{pg} can also be determined from Kim (2007, Figures 7 and 8)and then used to compute h_{pg}. A description of the procedure follows. To demonstrate this procedure, a dataset from Kim (2007) was constructed. The values for these data are shown for a = gate opening in centimeters (5 cm):

E_1 = the total energy head upstream from gate in centimeters, with a 5 cm gate opening (50.00 cm);
a/E_1 = 0.1; and
$E_1 - a$ = 45.00 cm.

H_{pgM} is determined from Kim (2007, Figure 8) once E_1 and a are known. Z is then computed throughout the range of desired vertical locations. In this example, Z was computed from z = 5 cm to z = 50.00 cm; z = 5 cm is the location of the bottom of the gate with a 5 cm gate opening, and z = 50.00 cm is the approach energy head. For this example, Z was computed at 2 cm intervals of z between 5 and 49 cm. Table 6 shows the values used in this example for the 5 cm gate opening.

Knowing Z, the average value curve from Figure 30 is used to select the H_{pg}/H_{pgM} value for the computed Z values. The Roth and Hager (1999) curve is being used in this example. The data shown in Kim (2007, Figure 8) for the present study were digitized, and fit equations were developed, as shown in Figure 32. Using the a/E_1 value of 0.10, the top equation in Kim (2007, Figure 8) was used to compute a value of 0.853 for the maximum normalized value, H_{pgM}. H_{pg} (column 4 in Table 6) can then be computed for the range of Z values. Knowing H_{pg}, h_{pg} can then be computed from Equation (99), rearranged as

$$h_{pg} = H_{pg}(E_1 - a). \tag{101}$$

Note that h_{pg} represents the pressure head on the gate in centimeters of water. To convert h_{pg} to pressure, P, it is multiplied by the unit weight of water (9.8 kN/m^3) and converted to Newtons per square centimeter. Figure 33 shows a plot of the depth versus the pressure from the Kim (2007) data for a 5 cm gate opening.

The location and magnitude of the resultant force for this pressure distribution needs to be determined. The mathematical functions contained within the 2019 version of Autodesk AutoCAD were used to compute the area enclosed by the hydrodynamic pressure distribution and the centroid.

Most spreadsheet software programs can also be used to determine these values. The results in Figure 33 show the resultant unit force to be 10.356 N/cm run of gate, acting at z = 21.793 cm.

Table 6. Parameters used to compute hydrodynamic pressures from the Kim (2007) data with a 5 cm gate opening.

Z (cm)	Z	H_{pg}/H_{pgM}	H_{pg}	h_{pg} (cm)	P_{pg} (N/cm^2)
5	0	0.000	0.0000	0	0.000
7	0.044	0.945	0.8061	36.27	0.355
9	0.089	0.995	0.8487	38.19	0.374
11	0.133	1.000	0.8530	38.39	0.376
13	0.178	0.994	0.8479	38.15	0.374
15	0.222	0.965	0.8231	37.04	0.363
17	0.267	0.935	0.7976	35.89	0.352
19	0.311	0.900	0.7677	34.55	0.339
21	0.356	0.855	0.7293	32.82	0.322
23	0.400	0.810	0.6909	31.09	0.305
25	0.444	0.765	0.6525	29.36	0.288
27	0.489	0.715	0.6099	27.45	0.269
29	0.533	0.665	0.5672	25.53	0.250
31	0.578	0.595	0.5075	22.84	0.224
33	0.622	0.540	0.4606	20.73	0.203
35	0.667	0.485	0.4137	18.62	0.182
37	0.711	0.425	0.3625	16.31	0.160
39	0.756	0.365	0.3113	14.01	0.137
41	0.800	0.295	0.2516	11.32	0.111
43	0.844	0.235	0.2005	9.02	0.088
45	0.889	0.170	0.1450	6.53	0.064
47	0.933	0.105	0.0896	4.03	0.039
49	0.978	0.035	0.0299	1.34	0.013
50	1	0.000	0.0000	0.00	0.000

Figure 32. Fit equations for data from Kim (2007, Figure 8) in the present study.

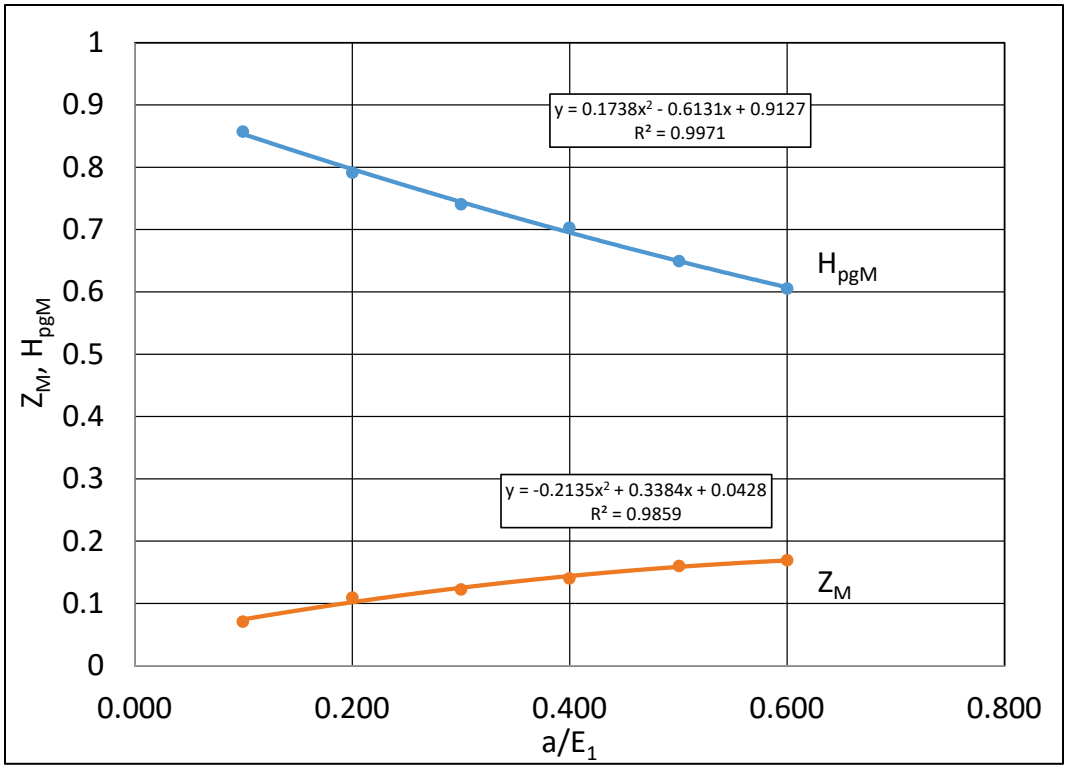

Figure 33. Pressure distribution developed from Kim (2007) data with a 5 cm gate opening.

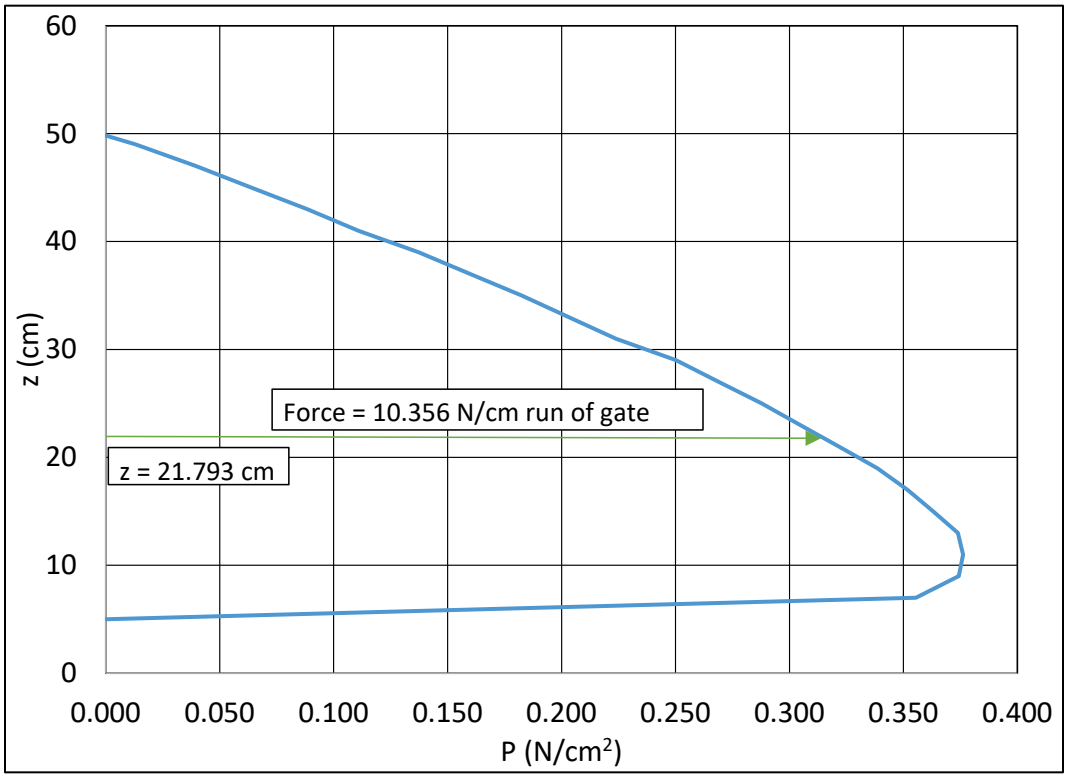

A simplified method for approximating the area under the pressure distribution curve was investigated because integration of the curve shown in Figure 33 was somewhat cumbersome. The area under the curve was approximated using simplified geometric shapes. Figure 34 shows the horizontal pressure distribution curve from Figure 33 (in blue) approximated using a triangle, a rectangle, and another triangle (in green). The total area from these three shapes gives an approximated hydrodynamic force of 10.306 N/cm run of gate, acting at 21.336 cm. The difference in resultant horizontal force values and their resultant location values between the blue curve and the green simplified shapes are 0.55% and 2%, respectively.

Figure 34. Pressure distribution from Kim (2007) data with a 5 cm gate opening approximated using two triangles and a rectangle.

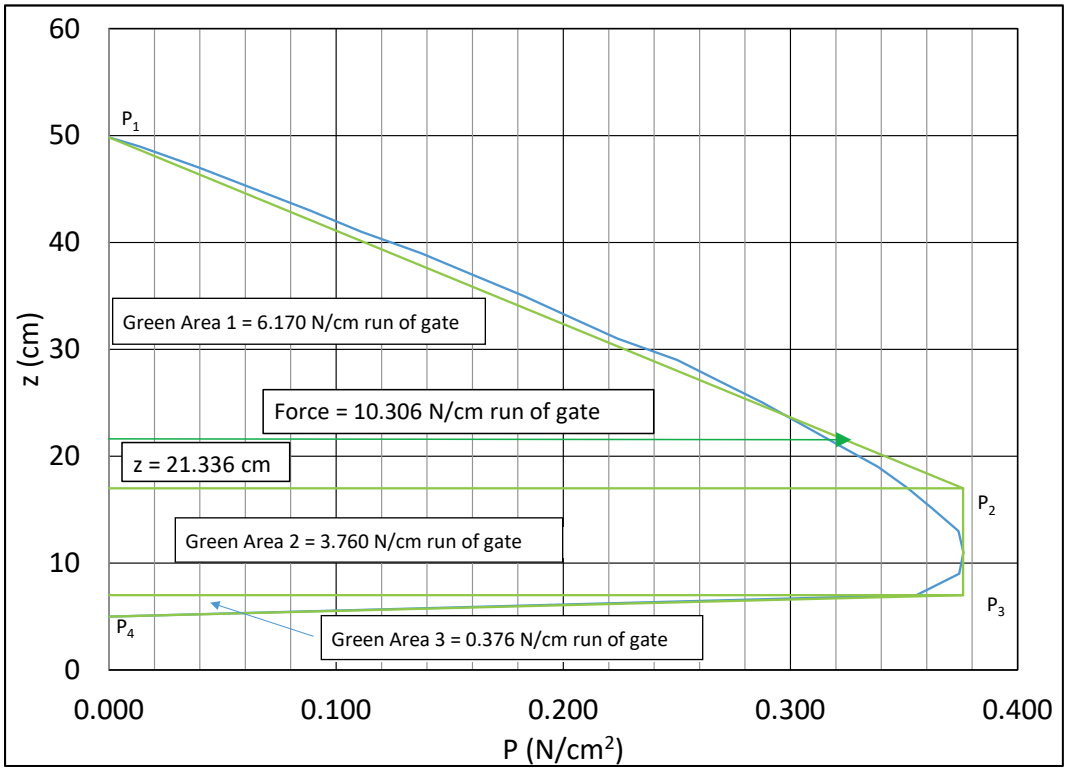

In Figure 34, the pressure terms P_1, P_2, P_3, and P_4 are shown acting on the vertical-lift gate. The location of the lateral equivalent force (h_{Lat}) can be determined using the one-third/one-sixth method developed by Ebeling et al. (2018) and also presented in Section 2.3.2.4 of this report. Table 7 shows the values used in this analysis.

Table 7. The simplified three shapes, pseudo-static hydrodynamic pressure diagram components, and lever arm used to determine location, h_{Lat}, of the resultant hydrodynamic force acting on a sluice gate with a 5 cm gate opening.

Pressure Component (N/cm²)	Lever Arm (z) (cm)
$P_1 = 0$	$h_1 = 49.82$
$P_2 = 0.376$	$h_2 = 17.00$
$P_3 = 0.376$	$h_3 = 7.00$
$P_4 = 0$	$h_4 = 5.00$

Equation (102) was developed by applying this method for the lateral forces and summing moments about point 4:

$$h_{Lat} = \frac{(h_1 - h_2)\left(\frac{P_1}{3} + \frac{P_2}{6}\right)h_1 + (h_1 - h_2)\left(\frac{P_1}{6} + \frac{P_2}{3}\right)h_2}{F_{Lat}} \quad (102)$$

$$\frac{+(h_2 - h_3)\left(\frac{P_2}{3} + \frac{P_3}{6}\right)h_2 + (h_2 - h_3)\left(\frac{P_2}{6} + \frac{P_3}{3}\right)(h_3)}{F_{Lat}}$$

$$\frac{(h_3 - h_2)\left(\frac{P_3}{3} + \frac{P_4}{6}\right)(h_3) + (h_3 - h_4)\left(\frac{P_3}{6} + \frac{P_4}{3}\right)(h_4)}{F_{Lat}}.$$

Using the values in Table 7 and Equation (102), h_{Lat} is calculated to be equal to 21.336 cm. This z value for the resultant force is in exact agreement with the z value computed using Autodesk AutoCAD and reported in Figure 34. In summary, the resultant unit force from the pressure distribution shown in Figure 34 for the simplified three shapes is 10.306 N/cm run of gate, acting at z = 21.336 cm. This resultant force value is 0.5% below the 10.356 N/cm acting at z = 21.793 cm for the curve in Figure 33, whose area was determined by numerical integration. This level of accuracy in the simplified three shape, pseudo-static hydrodynamic pressure diagram approximation is considered acceptable by the authors of this technical report. The procedure that has been outlined in this subsection may be used to establish a pseudo-static hydrodynamic pressure distribution for tailwater below the top of the gate opening.

The vertical locations of P_2 and P_3 need to be related to a parameter that can be used by personnel adopting the simplified shape approach to determine the hydrodynamic force on a spillway gate. The procedure described in Kim (2007) provided the dimensionless depth, Z_M, for a/E_1 values between 0.1 and 0.6, as reproduced by the authors of this report in Figure 32. With an a/E_1 value of 0.1, the bottom equation in Kim (2007, Figure 8) is

used to compute a Z_m value of 0.079. From Equation (100), with $Z = Z_M$ = 0.079, a = 5 cm gate opening, and E_1 = 50 cm, the z_M location of the maximum pressure is 8.55 cm above the datum. The z locations of P_2 and P_3 in Figure 34 are z_2 = 17 cm and z_3 = 7 cm, respectively, above the datum. These values were selected because they provided an area approximation using the simple shapes that was very similar to the area determined from integrating the blue curve in Figure 34. If we use z_M to normalize z_2 and z_3, the result is z_2/z_M = 1.99 and z_3/z_M = 0.82. This result is with a/E_1 = 0.1. Figure 35 can be used to determine values of z_2 and z_3 for values of a/E_1 up to 0.6.

Figure 35. Ratio of z_2 and z_3 locations to z_M for a/E_1 from 0.1 to 0.6.

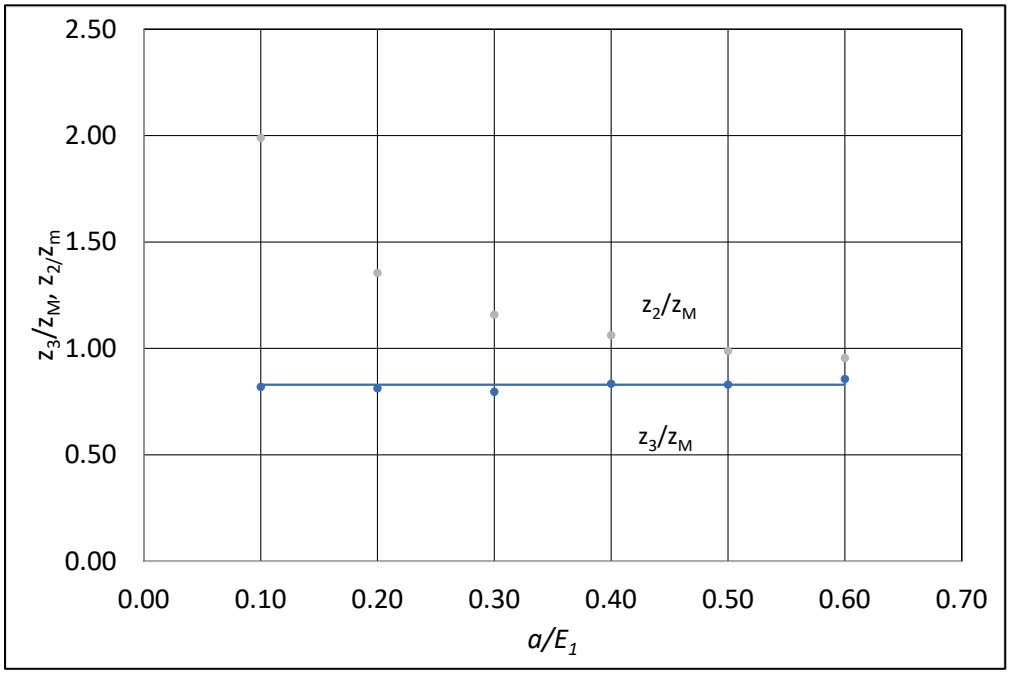

It was reasonable to believe these ratios of z_2/z_M and z_3/z_M would change as a/E_1 changed. To further investigate this supposition, these ratios were computed for a/E_1 = 0.1, 0.2, 0.3, 0.4, 0.5, and 0.6. Figure 35 shows the ratios that were computed (z_3/z_M in gray, and z_3/z_M in blue). There is much more variation in the location of z_2 with a/E_1 values less than 0.3. The ratios of z_3/z_M were very similar. A horizontal line was drawn at a z_3/z_M ratio of 0.83 to show the minor variations throughout the range of a/E_1.

The procedure to determine the z locations for P_2 and P_3 in Figure 34 was developed for use if a mathematical tool to integrate the curve representing the hydrodynamic pressure distribution was not available. The discretization of the curve was found to slightly influence the results when

computing the area approximation using the simplified shapes. For example, the value of H_{pg}/H_{pgM} changes significantly with Z less than 0.2, as shown in Kim (2007, Figures 7 and 8). The discretization of Z values between a and E_1 should be finer between Z = 0 and Z = 0.2, less fine between Z = 0.2 and Z = 0.5, and could be coarse between 0.5 and 1.

As an example, the z values in Table 6 were discretized at 2 cm intervals, which resulted in only five values of Z less than 0.2. To observe the difference in the shape of the pressure distribution curve with an interval of 0.5 cm between z = 5 cm and z = 14 cm and an interval of 5 cm between z = 14 cm and z = 50 cm, Figure 36 was constructed. The hydrodynamic force from the orange curve with the finer resolution was 10.509 N/cm run of gate, compared to a force of 10.356 N/cm run of gate with the blue curve. This indicates the resolution of the curve makes a difference, although it is considered minimal, and use of the simplified shapes to determine the hydrodynamic force provides satisfactory results.

An example problem using this procedure to determine the resultant hydrodynamic force and its location for a spillway gate with a tailwater less than the gate opening is shown in Appendix B for the MLD spillway vertical-lift gate.

Figure 36. Comparison of hydrodynamic force determined from coarse and fine resolution curves.

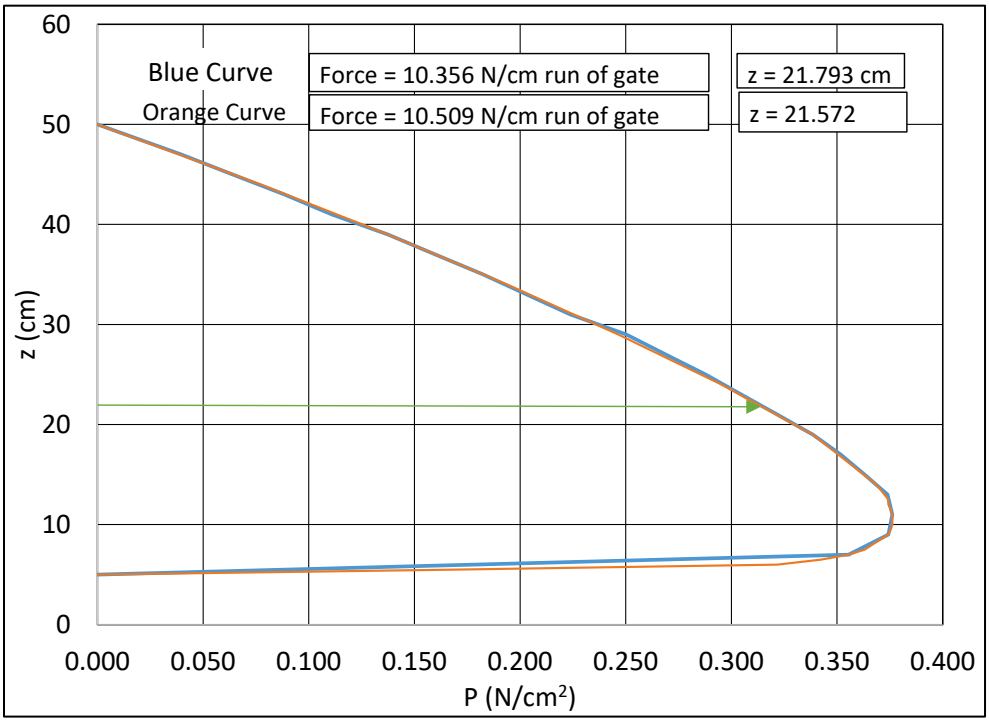

2.3.3.3 Location for Resultant Hydrodynamic Force with Tailwater above the Gate Opening

The magnitude of the resultant hydrodynamic force was determined using the conservation of momentum procedures described in Section 2.3.3.1. The location of this resultant hydrodynamic force acting on the surface of the gate needs to be addressed for projects similar to MPLD, where the tailwater is almost always higher than the gate opening. The procedure in Section 2.3.3.2 was modified to account for tailwater higher than the gate opening. This is considered a simplified approach, and a more sophisticated approach would be required to compute the hydrodynamic pressure distribution. This would require a CFD model that accounts for nonhydrostatic flows and some technique to include turbulence, such as a Detached Eddy Simulation model.

The first step in this modified procedure is to develop the hydrodynamic pressure distribution (Section 2.3.3.2) for the gate with the tailwater lower than the gate opening. To help illustrate this procedure, an example using the MPLD spillway gate with a 1 ft gate opening will be used. Figure 37 shows the hydrodynamic pressure distribution for the spillway gate with a 1 ft gate opening, which was developed from the procedures in Section 2.3.3.2 for a tailwater lower than the gate opening.

The pressures on the surface of the gate are assumed to act normal to the curved surface of the gate and are considered the same as those determined with no tailwater (Figure 37). Figure 38 shows the hydrodynamic pressure distribution estimated with a TW El of 395 and a 1 ft gate opening. The pressures above z = 16 ft are the same as those shown in Figure 37. The TW El of 395 minus the spillway crest el of 379 gives the z value of 16 ft. The pressures acting on the surface of the gate between the TW El and the bottom of the gate were simply estimated by subtracting the hydrostatic pressure due to the TW El from the pressure at the same value of z determined using the procedures presented Section 2.3.3.2. Table 8 shows the hydrodynamic pressures determined for no tailwater and for a TW El of 395, which are plotted in Figure 38.

Figure 37. Hydrodynamic pressure distribution developed for the MPLD spillway gate open 1 ft and no tailwater effects.

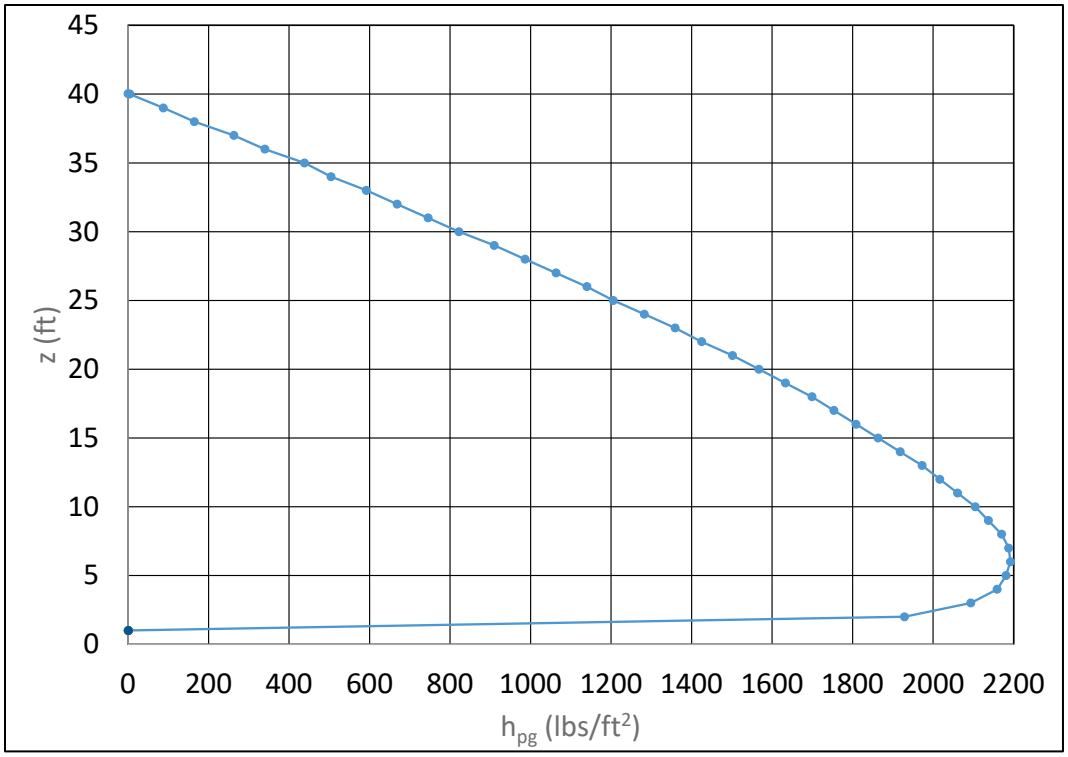

Figure 38. Hydrodynamic pressure distribution developed for the MPLD spillway gate open 1 ft for no tailwater effects and a tailwater elevation (TW El) of 395.

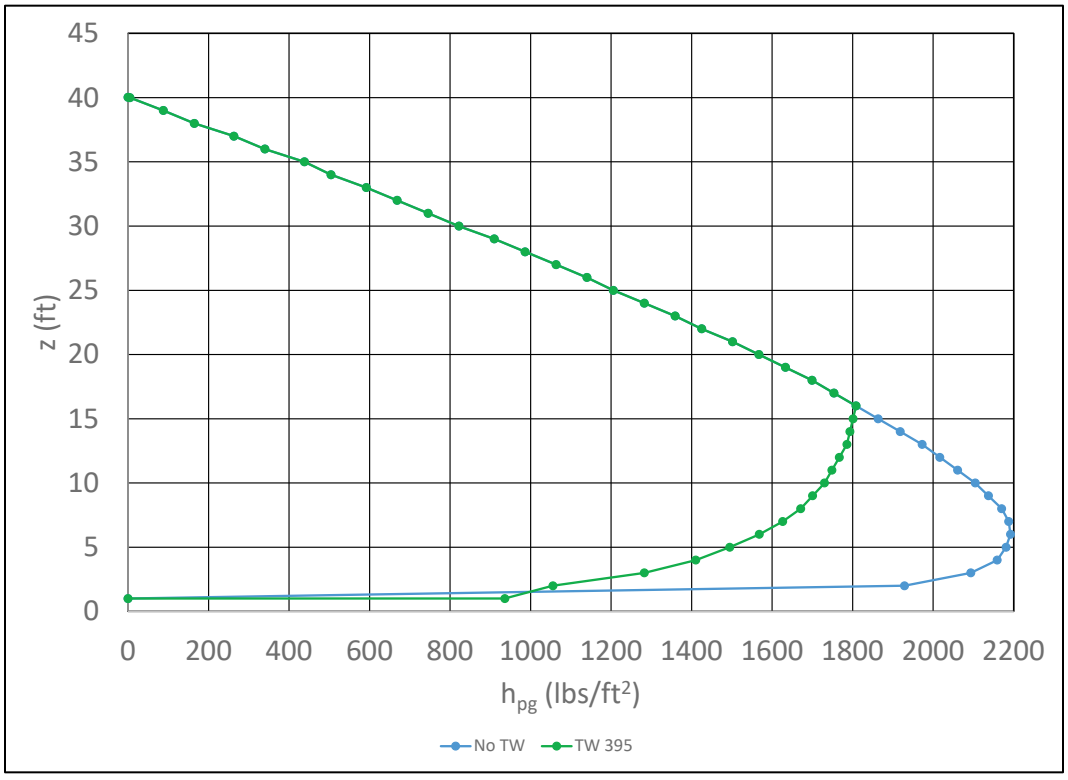

Table 8. Hydrodynamic pressure distribution with no tailwater effects and a TW El of 395 for the MPLD spillway gate with 1 ft gate opening.

Z (ft)	h_{pg} (lb/ft^2), No TW	z (ft)	h_{pg} (lb/ft^2), TW 395
1	0	1	936
2	1,929	2	1055
3	2,094	3	1282
4	2,159	4	1410
5	2,181	5	1495
6	2,192	6	1,568
7	2,188	7	1,626
8	2,170	8	1,671
9	2,137	9	1,701
10	2,104	10	1,730
11	2,061	11	1,749
12	2,017	12	1,767
13	1,973	13	1,786
14	1,918	14	1,793
15	1,863	15	1,801
16	1,809	16	1,809
17	1,754	17	1,754
18	1,699	18	1,699
19	1,633	19	1,633
20	1,567	20	1,567
21	1,502	21	1,502
22	1,425	22	1,425
23	1,359	23	1,359
24	1,282	24	1,282
25	1,206	25	1,206
26	1,140	26	1,140
27	1,063	27	1,063
28	986	28	986
29	910	29	910
30	822	30	822
31	745	31	745
32	669	32	669
33	592	33	592

Table 8 (cont.). Hydrodynamic pressure distribution with no tailwater effects and a TW El of 395 for the MPLD spillway gate with 1 ft gate opening.

Z (ft)	h_{pg} (lb/ft²) No TW	z (ft)	h_{pg} (lb/ft²) TW 395
34	504	34	504
35	438	35	438
36	340	36	340
37	263	37	263
38	164	38	164
39	88	39	88
40	4	40	4

As shown in Table 8, z values of 16 ft and greater are equivalent to those values with no tailwater effect. The hydrodynamic pressure distribution for z values less than 16 ft was reduced by the hydrostatic pressure due to tailwater. For example, at z = 10 ft, the hydrodynamic pressure is 2,104 lb/ft² with no tailwater. To determine the hydrodynamic pressure with a TW El of 395, subtract 62.4 lb/ft³ × (16 ft – 10 ft) from 2,104 to get 1,730 lb/ft². The centroid for the area underneath the curve for the plot with the TW El of 395 is then determined and is considered the location of the resultant hydrodynamic force acting on the gate.

This procedure is not considered valid when values of z close to the gate opening give negative computed values for the hydrodynamic pressure. This occurs because the hydrostatic pressure due to tailwater is larger than the hydrodynamic pressure using the procedures in Section 2.3.3.2. The authors chose to plot the hydrodynamic pressures and adjust those with low z values to give a reasonable value for the hydrodynamic pressure. As mentioned, the magnitude of the hydrodynamic force is determined by the procedures given in Section 2.3.3.2. Appendix A provides a complete description of how to determine the location of the resultant hydrodynamic force with tailwater effects for the MPLD project.

2.3.4 Combined Hydrostatic and Wave Loads for STGs

Wave loads are project specific and are considered for projects that experience significant wind and fetch. Section 2.3.3.2 shows the development of wave loading using the Goda (2010) recommendations. The authors of this report suggest that this procedure replace the guidance provided in the SPM (Coastal Engineering Research Center 1984b). These loads will be added to the hydrostatic load, and when determining wave-loading effects,

the load category will reflect the coincident water-surface elevation and wind conditions that produce the maximum effects. The gate may be overtopped with the maximum wave height, and the Goda procedure accounts for this condition. The computational results for the MPLD STGs demonstrate that wind-induced wave forces can account for 15% of the combined hydrostatic plus wave load when the gates are closed.

2.3.5 Combined Hydrodynamic and Wave Loads for STGs

The highest hydrodynamic loads will occur when the gates are at small openings, the tailwater is low, and the upper pool is constant. The higher the gate is raised, the higher the tailwater becomes, and the lower the differential head across the gate is. With the upper pool constant, a higher gate opening will result in more freeboard on the gate and a lower likelihood that wave overtopping will occur. Adapting the Goda (2010) wave pressure distribution procedure to an STG accommodates this condition. The computational results for the MPLD STG demonstrate that the wind-induced wave force can account for 20% of the magnitude of the combined hydrodynamic plus wave loads for a 1 ft gate opening.

2.3.6 Summary of Hydraulic Loads for STGs

The hydraulic loads on the spillway consist primarily of the hydrostatic, wave, and hydrodynamic loads. The loads should be combined as appropriate to give the maximum expected for the tainter gate. The wind to wave force conversion indicated the wave forces made a significant contribution to the combined loads. The authors of this report recommend that wind-induced wave forces be determined using the Goda (2010) design procedure discussed in Section 2.3.2.3 and the wind speed estimation discussed in Section 2.3.2.7.

The tailwater is the primary variable for changes in the hydraulic load. The maximum hydrostatic load occurs with no tailwater effect, and the hydrodynamic load reduces as the tailwater rises above the spillway crest el. The example project presented in Appendix A had significant tailwater impacts, as is typical of many USACE inland navigation projects.

2.4 Probabilistic Characterization of the Hydrostatic and Hydrodynamic Loads for the STG

2.4.1 Probabilistic Characterization of the Hydrostatic Load

The LRFD procedures need estimates of the dispersion of the hydrostatic load to conduct the analysis. Statistics are needed to estimate the dispersion in the hydrostatic loads. The example problem in Appendix A for the MPLD provides a method for developing these statistics. For a project operated similarly to this one, the mean upper pool el is considered to be the normal navigation pool el.

Fluctuations above and below the normal upper pool el occur when gate changes are made, and gate operations and responses to maintain the upper pool do not occur instantaneously. As discussed previously, the maximum hydrostatic load results when the tainter gate is closed, which normally means low discharge conditions through the spillway. Adjusting gates adjacent to a closed gate causes the upper pool to fluctuate above and below the normal pool. This fluctuation is considered when developing the dispersion of the hydrostatic loads. Historical hydraulic data provides the best estimate for the magnitude of the fluctuation; however, a record of gate operations is also needed to determine which gates were closed when the upper pool was recorded.

For the MPLD project, an estimate of 2 ft above and 2 ft below the normal upper pool el was used to develop the statistics for the hydrostatic load. This estimate was selected to demonstrate a procedure, and if actual historical data were available for a project, a better estimate could be made. The standard deviation, σ, can be determined by subtracting the minimum from the maximum and then dividing the difference by 6 (i.e., [maximum – minimum]/6). The standard deviation for the MPLD project was determined to be 0.667 ft. The values for the dispersion in the hydraulic load calculated using this technique are shown in Table 9 and again in Table A-16.

Table 9. Hydrostatic gate force per foot of gate run for the upper pool els +6σ and −6σ around the mean upper pool for the MPLD STG.

Upper Pool El	Statistic	H_s (lb/ft)
415	−6σ	40,435
415.666	−5σ	41,943
416.333	−4σ	43,489
417	−3σ	45,053
417.666	−2σ	46,646
418.333	−σ	48,269
419	Mean	49,920
419.667	+σ	51,599
420.334	+2σ	53,305
421	+3σ	55,037
421.667	+4σ	56,801
422.334	+5σ	58,591
423	+6σ	60,403

Figure 39 shows a schematic of a project with the hydrostatic pressure distribution at the upper pool +6σ, the mean upper pool, and the upper pool −6σ. Figure 40 shows a plot of the hydrostatic pressures computed for the MPLD STG for the upper pool +6σ, the mean upper pool, and the upper pool −6σ. The hydrostatic force per foot for the width of the gate computed from Equation (12) ranged from 60,403 lb/ft for the upper pool +6σ to 40,435 lb/ft for the upper pool −6σ, as shown in Table 9.

Figure 39. Hydrostatic pressure distribution for upper pool els +6σ and −6σ around the mean upper pool.

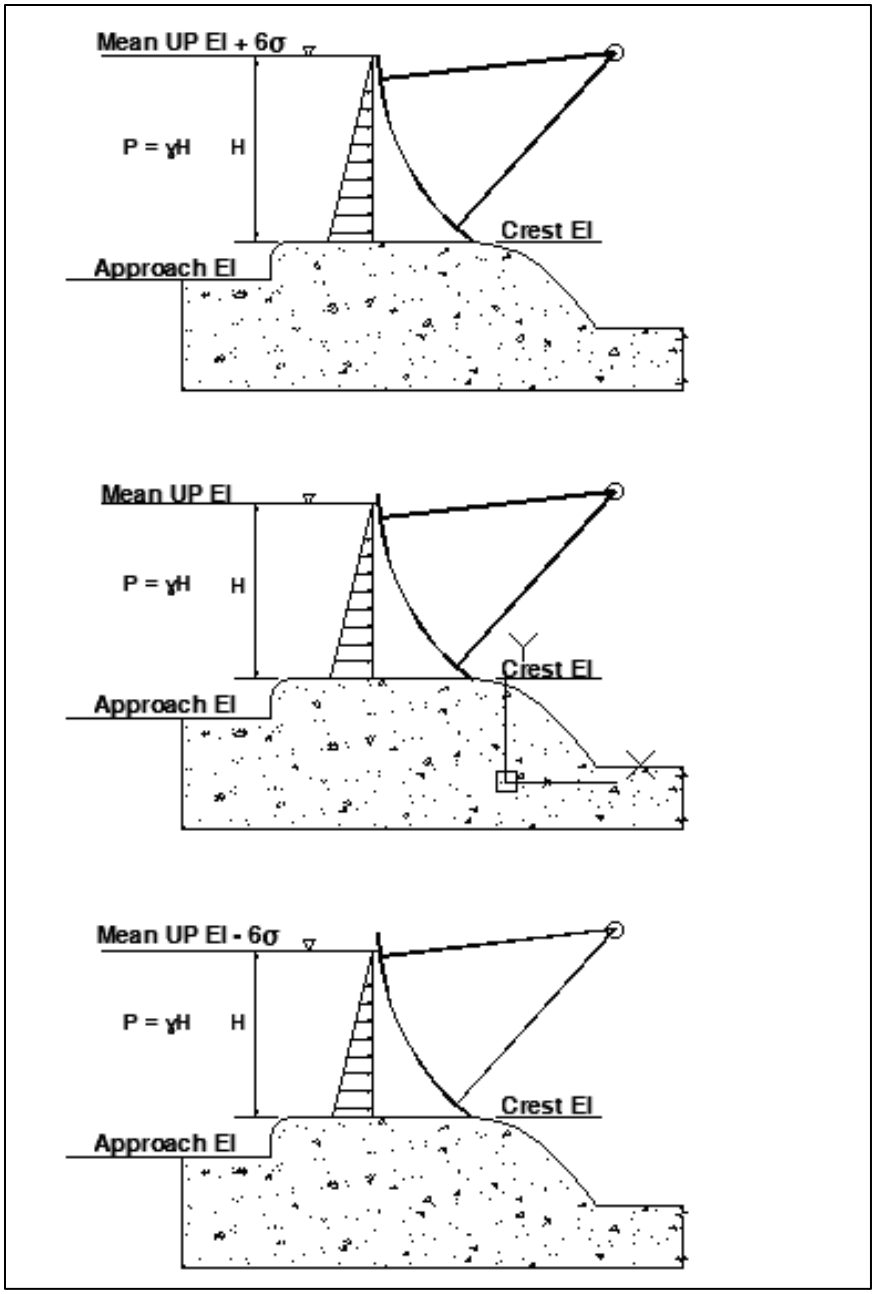

Figure 40. Hydrostatic pressures computed for the MPLD spillway gate for upper pool els +6σ and −6σ around the normal upper pool and the mean upper pool.

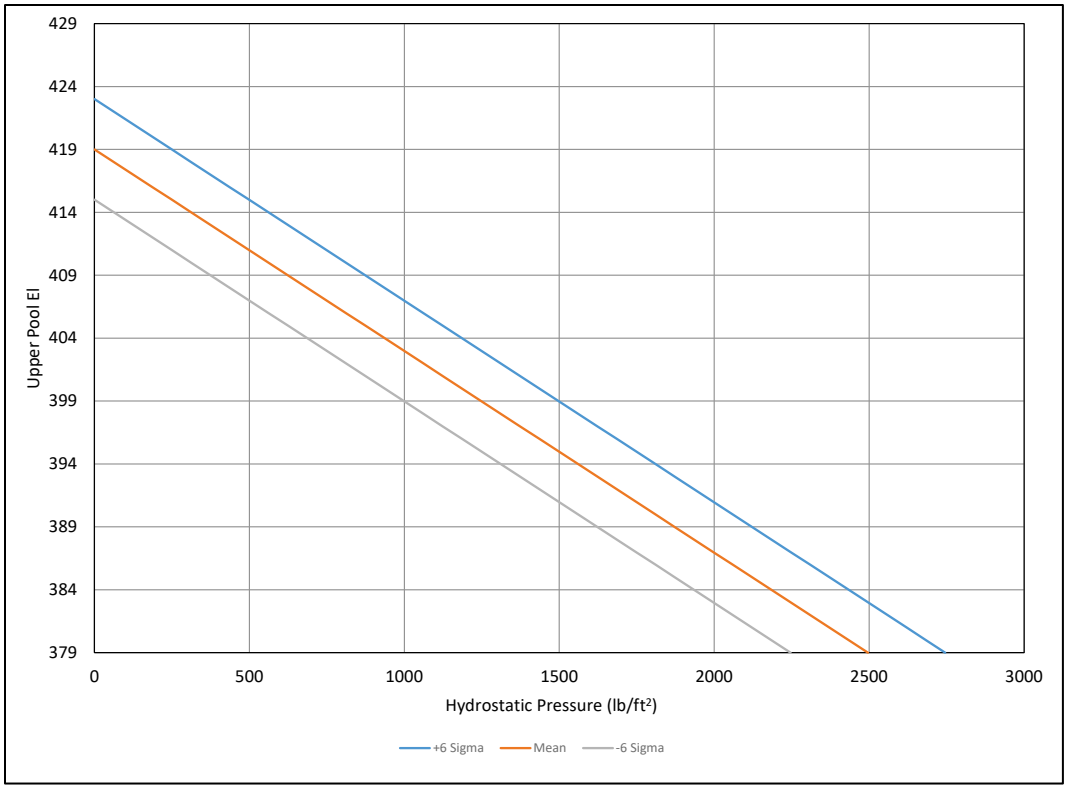

2.4.2 Probabilistic Characterization of the Hydrodynamic Load

The statistics for the hydrodynamic load are determined for conditions with and without a tailwater greater than the spillway gate opening. The procedure shown in Section 2.3.3.1, based on the conservation of momentum for conditions where the tailwater is higher than the gate opening and the upper pool is constant, can be used to compute the hydrodynamic force. Appendix A, Section A.5.2, describes a method developed by Mr. Barry White and Dr. Robert Ebeling of the ITL to determine the statistics for these computed hydrodynamic forces for the MPLD project for a constant upper pool with varying gate openings and tailwater. This procedure could be adopted for similarly operated navigation projects that have historical data for the tailwater and gate openings.

The procedure described in Section 2.3.3.2 for projects with tailwaters less than the gate opening can be used to determine the statistics for the hydrodynamic forces. A method similar to that used for the hydrostatic force can be used to determine the standard deviation for the upper pool used for varying values of z associated with +6σ and −6σ above and below the mean upper pool. Appendix B provides an example procedure for

determining the statistics for the hydrodynamic loads for the MLD vertical-lift gate.

2.5 Other Loadings for STGs

Other loadings on an STG are discussed in the sections that follow.

2.5.1 Barge Impact

Barge impacts are considered an extreme loading event; however, they have occurred at a few USACE projects. Barge impact is considered an accidental event that is not practical to design for and currently is not specifically considered in design (EM 1110-2-2702, HQUSACE 2000, rescinded).

There are many factors that need to be accounted for in a barge impact. One of the primary variables is the mass of the barge. A standard jumbo barge on the inland waterway system is 195 ft long (l) by 35 ft wide (w), and the draft (d) is generally taken as 9 ft. So if this is converted to weight (W_B) using fresh water at a unit weight (γ) of 62.4 lb/ft^3, the estimated weight is

$$W_B = l * w * d * \gamma = 3{,}832{,}920 \text{ lb.} \quad (103)$$

This is equivalent to 1916.5 tons. This is a huge mass, so even a small impact velocity results in a very large impact force.

Another important consideration is the angle of the impact. A head-on impact is worse than a glancing impact. The geometry of the dam also affects the impact force. The gate bay width, pier shape, pier length, and pier width all contribute to the resulting force. The hydraulic conditions, which primarily consist of the approach current speed, have a significant role in determining the impact force.

Considering these factors, the worst case barge impact force would result from a fully loaded barge train approaching the spillway gate at or above the current velocity and impacting the gate normal to the axis of the gate with no interference from the piers.

2.5.2 Debris Impact

Debris can impact the tainter gate both upstream and downstream from the gate. The debris on the upstream side of the gate is included in the ice-impact load described in Section 2.5.3. On the downstream side of the gate, design guidance suggests that the end frames and girders be positioned to minimize debris accumulation. Navigation projects are particularly susceptible to swirling debris on the downstream side, and damage has occurred to some of the bracing members. For this case, deflector plates were developed to protect the framing from impact damage due to debris. In addition, if debris becomes lodged between the side of the gate and the adjacent pier, this can result in gate binding during lifting. If debris starts to accumulate, it can cause additional weight on the gate.

2.5.3 Ice Impact

The existing USACE guidance states,

> The ice-impact load is specified to account for impact of debris (timber, ice, and other foreign objects) or lateral loading due to thermal expansion of ice sheets. Additionally, this load provides the overall structure with a margin of safety against collapse under barge impact. (HQUSACE 2000, 3-15).

Current practice is to treat the ice load (I) as a uniformly distributed load of 73 kN/m (5.0 kips/ft) acting in the downstream direction that is applied along the width of the gate at the upper pool el. In the design example for the MPLD project, an ice impact load of 10 kips/ft was used with the normal upper pool el, and 5 kips/ft was used when the upper pool el was 2 ft above normal. The guidance also indicates that when designing the skin plate, the ice impact is frequently set to zero with the intent of allowing local damage to the skin plate for very infrequent loading events. EM 1110-2-1603 (HQUSACE 1990) suggests EM 1110-2-1612 (the most recent version of which is HQUSACE 2002) should be used for guidance on ice forces.

2.5.4 Operational Loadings

Operational loads due to operating machinery occur during gate lifting and lowering. Operating machinery loads should be quantified in consultation with the machinery designer. The location and layout of the operating

machinery is generally project specific, and often there are many alternatives. The final selection is usually based on a cost analysis of the hoist system, tainter gate design, gate anchorage, and pier layout.

2.5.4.1 Trunnion and Bearing Friction

In early tainter gate designs, trunnion friction was not totally accounted for, and operational problems and gate failures occurred. Since then, studies have been performed and additional information concerning friction magnitude and structural detailing to accommodate these magnitudes has been gained.

During gate operations, friction loads occur around the surface of the trunnion pin, between the bushing and the pin, and at the end of the hub between the hub bushing and side plate. Current practice is to use a conservative value for the coefficient of friction to account for wear and possible inadequate maintenance, but to ensure that detailed criteria are specified regarding the proper maintenance techniques, these guidelines are provided in USACE manuals.

2.5.4.2 Side Seal Friction

EM 1110-2-2702 (HQUSACE 2000, rescinded) provides guidance on the side seal friction load. An equation is presented for normal tainter gate configurations that provides an estimation for side seal friction loads.

2.5.4.3 Gate Binding

Gate binding may occur if the gate rotates and becomes immovable between the piers during gate movement. This is due to the frictional forces present during the gate movement and is more prevalent for gates that are supported on only one side. Precautions include side bumpers or rollers that bear on side seal plates. ETL 1110-2-584 (HQUSACE 2014) indicates a 3D finite element may be needed to determine the normal forces that occur during gate binding.

2.5.5 Flow-Induced Vibration (Design or Operational Counter Measures)

The hydrodynamic loading due to flow-induced vibrations may need to be determined through modeling. An effort should be made to minimize these effects through proper seal designs and possible gate operations. Modeling may help determine the gate operations that are acceptable.

For HSS, structural vibrations can be caused by fluctuating loads due to (1) extraneous flow pulsations and (2) self-sustained flow pulsations. Naudascher (1982) described the basic mechanisms of excitation as extraneous excitation, instability excitation, and movement excitation. Extraneous excitation results from a pulsation in flow or pressure that is not part of the vibrating system (e.g., the submerged roller that exists downstream from a partially open sluice gate). Instability excitation is caused by a flow instability that, in most cases, is part of the vibrating system (e.g., the alternating shear layer reattachment underneath a gate lip). Movement excitation is due to exciting forces caused from the movement of a structure or a body within the vibrating system.

2.6 Summary and Conclusions

This chapter investigated the hydraulic loads on the STG. The maximum hydrostatic load occurred with the upper pool el at the top of the gate with the gate closed. The dispersion of the hydrostatic load was determined by estimating the fluctuation of the upper pool about the mean upper pool el. The standard deviation, σ, was then computed, and the dispersion in the hydrostatic load was based on the loads determined between upper pool els from +6σ to −6σ about the mean pool el.

The wave loading was determined by modifying procedures developed by Goda (2010) for coastal structures. The wave load for an inland structure is based on the wind speed and direction at the structure. This is referred to as a wind-induced wave load. A comparison of wave heights and wave periods computed from guidance in the SPM (Coastal Engineering Research Center 1984b) and the procedures in Goda (2010) was made, and the authors recommended the Goda (2010) method. These procedures are shown in Section 2.3.2 and in Appendix A.

The hydrodynamic loads for the STG were developed for conditions with and without tailwater above the spillway gate opening. For conditions with the tailwater below the gate opening, a procedure to determine the hydrodynamic pressure distribution on the gate based on experimental work by Roth and Hager (1999) and numerical modeling by Kim (2007) was adopted. Using this procedure, the hydrodynamic force was determined by integrating the hydrodynamic pressure distribution, and the location of the resultant force was through the centroid of this distribution.

For conditions with the tailwater above the gate opening, the hydrodynamic force was estimated using the conservation of momentum principle presented in Roberson and Crowe (1985) for a rectangular sluice gate. Using this method, the velocity downstream of the gate was assumed to be uniform from the spillway crest el (i.e., gate seat el) to the TW El. This provides the hydrodynamic force, although the location of the resultant force is not known. To determine the location of the resultant force, the method described previously, using Roth and Hager (1999) and Kim (2007), was modified in an attempt to develop the hydrodynamic pressure distribution. This distribution could then be used to find the centroid.

The statistics for the hydrostatic and hydrodynamic loads were based on the fluctuation of the upper pool about the mean upper pool el. The methodology is presented in Section 2.4 and in Appendix A.

More details and a discussion of nonhydraulic loads will be presented in subsequent reports associated with this research.

3 Loadings Applied to Vertical-Lift Gates

Vertical-lift gates are used for project features other than the spillway; however, this chapter describes the characteristic loads associated with spillway vertical-lift gates and summarizes the dispersion in these applied loads and distributions of pressure.

3.1 Existing Guidance for Vertical-Lift Gate Design

This report initially focuses on the vertical-lift gates used for inland navigation projects. The main purposes of inland navigation projects are to provide water depths sufficient for safe travel upstream and downstream from the project and a method or structure that allows the vessel to transit through the project. Control of the water levels is accomplished by spillway gates. The four spillway gate designs used for most USACE projects are the tainter (most common), vertical-lift, roller, and rolling. The loadings for the STGs were evaluated and are provided in Chapter 2 and Appendix A.

The vertical-lift gate is rectangular in shape and consists of a structural frame with a flat skin plate that is typically attached on the upstream face. The gate moves vertically within slots on a sliding bearing, which generally consists of a sliding surface (i.e., slide gate), a wheel gate, or a tractor gate. The hoisting system is usually a track-mounted gantry crane that is moved from gate to gate for opening and closing operations. The principal hydraulic design features of the vertical-lift gate are the shape of the bottom lip, the shape of the gate slots, and the efficiency of the gate to pass flow (i.e., hydraulic capacity).

3.1.1 ETL 1110-2-584, *Design of Hydraulic Steel Structures*

ETL 1110-2-584 (HQUSACE 2014, Appendix E) provides guidance for the design of vertical-lift gates. Although the tainter gate is the most common spillway gate, the vertical-lift gate has some advantage in that the spillway crest requires a shorter length of spillway pier, which provides some economic savings. The vertical-lift gate is usually raised using a gantry crane or fixed hoists located on the deck of the spillway dam or on some other type of operating platform. The gate is generally held in position by a dogging device located in the gate slot, but it may be on the gate itself.

A single-section vertical-lift gate can be used to control discharge if the gate position can be readily changed. Multiple-section gates can have two

or more sections in the same slot, either between the sections or between the bottom section and the sill, that control the flow. This type of gate often has latching mechanisms that allow the sections to be attached so that it can then function as a single-section gate. Figure 41 shows the structural components of a vertical-lift gate with multiple sections. The double-section gate is another type of vertical-lift gate that was used in the past. In this type of gate, each section is located in separate slots, and the flow discharge occurs either over the top section or beneath the bottom section. This gate was probably originally designed for ice and debris passage, and operating issues have made this type of gate undesirable. ETL 1110-2-584 (HQUSACE 2014) lists other issues with the double-section gate; these include difficulty removing the gate from the slot, increased sealing complications, and the need for a longer pier to accommodate both sections.

Figure 41. Structural components of spillway vertical-lift gate. (Image adapted from Engineer Transmittal Letter [ETL] 1110-2-584, HQUSACE 2014.)

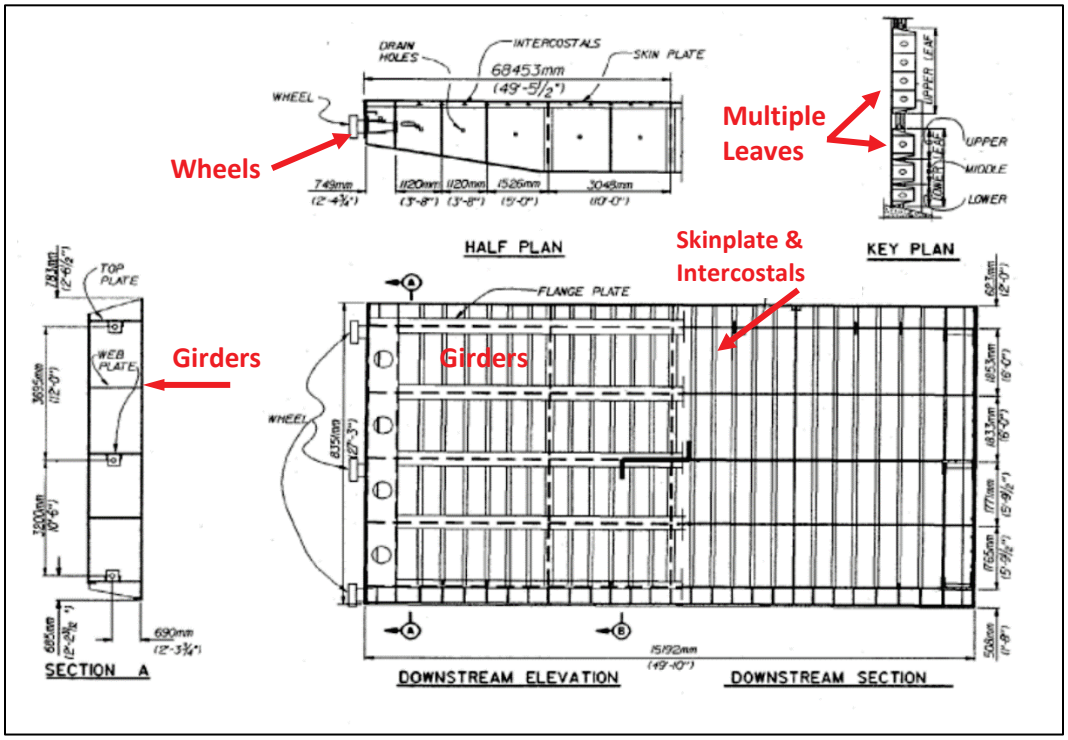

The end supports for the vertical lift are described according to the method by which the load is transferred from the gate to the gate guides or slots. The gate guides receive the main reaction component from the horizontal load. A brief description of the end supports follows.

- Fixed wheel. Wheels are either cantilevered from the body of the gate or supported at each end by the web of a vertical girder(s) attached to the gate frame. These wheels revolve on fixed axles. The wheels may also be mounted by pairs in trucks that carry the wheel loads through center pins to end girders attached to the gate frame.
- Tractor (Caterpillar). This end support uses a rotating band of small rollers mounted either directly on the vertical end girder or on members attached to the vertical end girder. A chain and roller is also in this category of tractor end supports.

ETL 1110-2-584 (HQUSACE 2014) provides guidance for designing new HSS and conducting major rehabilitation of existing HSS using LRFD. The design philosophy for HSS is to achieve the objectives of constructability, safety, and serviceability for the specified limit states while considering inspections and economics. This ETL states, "The structural system of an HSS shall be proportioned and detailed to ensure the development of significant and visible inelastic deformations at the strength and extreme event limit states before failure" (2-1). Limit states applicable to HSS are strength, serviceability, fatigue, and fracture. The design life of HSS is assumed to be 100 yr.

ETL 1110-2-584 (HQUSACE 2014, Appendix E, Sections E.3 and E.4) provides design information for spillway vertical-lift gates and describes the load conditions. Some of the load conditions apply to both the navigation lift gate and the spillway crest gate. Loads that are applicable to spillway crest vertical-lift gates include self-weight, gravity, hydrostatic and hydrodynamic, operating, environmental, impact, and earthquake. Table 10 shows the load factors for spillway crest vertical-lift gates. The load factor is designated with the Greek symbol γ.

Table 10. Load factors for spillway crest vertical-lift gates. (Table adapted from ETL 1110-2-584, HQUSACE 2014, Table E-2.)

Load Cases			Loads/Load Factors							
Limit State	Description	Case	γD	γG	γH_s	γH_d	γQ	γEV	γIM	γEQ
Strength 1	Gate closed	1	1.2	1.6	1.4	1.4(I)	0	1.6(I)	1.6(I)	0
Strength 2	Gate open	2	1.2	1.6	0	1.0(I)	0	1.3(I)	0	0
Extreme	Gate closed	3	1.2	1.2	1.4	0	0	0	0	1.0

Notes: (I) Select one at a time; γ = load factor; D = self-weight (dead load); G = gravity load, which includes weight of the gate (D), mud weight (M), and ice weight (I); H_s = hydrostatic load; H_d = wave load; Q = machinery load; EV = wind load; IM = ice-impact load; EQ = earthquake load.

ETL 1110-2-584 (HQUSACE 2014, Sections 3.2.3.1, 3.2.3.2, C3.2.3.1 and C3.2.3.2) describes the hydrostatic and hydrodynamic loads to be considered. It states that loads caused by the hydrostatic head differential across the HSS with due consideration from any tailwater effects should be considered (Section 3.2.3.2). It also states, "While considered a hydrostatic load, the hydraulic head can be a function of hydrodynamic conditions, particularly by the tailwater under flowing conditions. A Hydraulic Engineer should be consulted to quantify tailwater effects" (3-2).

ETL 1110-2-584 (HQUSACE 2014) further states, "Hydrostatic loads consist of hydrostatic pressure on the gate considering both upper and lower pools" (D-7). Three levels of hydrostatic loads are considered, as described in the ETL. The ETL also states, "The primary hydrodynamic load considered in design is the wave load (WA)" (D-8), and it directs readers to see Section 2.2.3.2 of that text for determining wave loads. Readers were also directed to see Section 3.2.3.2 of that ETL for a discussion of how flow-induced vibration shall be limited.

EM 1110-2-2702 (HQUSACE 2000, Chapter 3, Section 3-4, rescinded) described the three levels of hydrostatic loads that are considered. The three levels of hydrostatic loads considered in the design are the same as those for the STG and are provided in Chapter 2 of this report.

For single-section gates, flow only passes under the gate, and no consideration is given to flow over the gate. For multiple-section gates, water can pass over the top of the sections of the gate because the sections can be split to allow flow at various sections. For double-section gates, flow can also occur over the top of the section. The head produced by flow over the top of the gate needs to be known so the hydrostatic load can be determined. Also, operation of the bottom section needs to consider uplift on the bottom of the gate. The net uplift is determined from the combined effects of downpull forces. EM 1110-2-1602 (*Hydraulic Design of Reservoir Outlet Works*; HQUSACE 1980) and accompanying references may be used to determine these loads acting on the outlet works gate. Another reference is the USACE HDC Sheets 320-2 to 320-2/3 (WES 1980). HDC sheets were developed from data for vertical-lift gates located in outlet works projects.

3.1.2 EM 110-2-1603, *Hydraulic Design of Spillways*

EM 1110-2-1603 (HQUSACE 1990) states the following:

> The hydraulic design of crest gates involves the determination of the hydrostatic and hydrodynamic forces acting on the gate and crest in the immediate vicinity of the gate; the design and evaluation of gate seals, seats, and slots with respect to flow-induced vibrations and cavitation-related problems; the determination of the rate of flow from partially open gates; and the evaluation of gate seat locations, the trunnion elevation, and other hydraulics-related structural features. (6-1)

EM 1110-2-1603 (HQUSACE 1990, Appendix C, Plate 6-4) shows suggested design guidance for developing the discharge coefficient for a vertical-lift spillway gate with no tailwater effect. The hydraulic downpull or uplift loads on the gate are primarily influenced by the flow under the gate, especially high-velocity flow. Flow past the gate slot and the conditions immediately downstream from the gate when tailwater is present for open channel flow or pressurized flow in a conduit also contribute to the hydraulic loads on the gate.

3.1.3 EM 1110-2-1605, *Hydraulic Design of Navigation Dams*

EM 1110-2-1605 (HQUSACE 1987, Chapter 5, Section 5-15) states, "Reference is made to EM 1110-2-2701 and EM 1110-2-1603 for design of vertical-lift gates" (5-39). There is no guidance for the design of vertical-lift gates in this manual, although there is some information on spillway pier details.

3.1.4 Spillway Vertical-Lift Gate Operation—Navigation Dam

Navigation dam spillways with vertical-lift gates are usually older projects that have been in operation for several decades. Due to the cumbersome hoisting equipment, many of these projects operate with the gates completely open or completely closed. The gates in the middle of the spillway are generally the first to be lifted to pass the desired discharge. As the discharge increases, the gates adjacent to the middle gates are then usually lifted.

3.1.5 Vertical-Lift Gate Load Cases

EM 1110-2-2702 (2000, rescinded) states that all loads that HSS will be subjected to shall be considered in the design. These loads include gravity (e.g., weight, ice, mud), hydrostatic, hydrodynamic, operational and machinery, floating and thermal ice, debris, vessel impacts, and environmental (typically wind and temperature). Frequency of loading is considered in the design for the three load categories and specified in terms of frequency of occurrence. Section 2.1.5 of this report contains load information for the usual, unusual, and extreme categories; it was taken directly from ETL 1110-2-584 (HQUSACE 2014). Load combinations and cyclic and noncyclic loads are also presented in Chapter 2 of this report.

3.2 Hydraulic Data Collection and Statistical Data

The reliability analysis for the spillway vertical-lift gate requires that the mean and standard deviation of the loads be determined. Hydraulic data are needed to develop these values. The discharge, upper pool el, gate setting, and TW El are needed to determine hydraulic loads. Historical data are necessary to develop the samples and statistical data required for the analysis.

3.2.1 Upper Pool El

A navigation project is operated to maintain the desired upper pool by lifting the gates as the discharge increases. The nominal loads needed for the statistical analysis will generally occur with a near-constant upper pool el. The mean and standard deviation for the upper pool need to be determined. The design example chosen for this report was MLD on the Columbia River. Appendix B contains the methodology used to determine the hydraulic data and the statistical data reduction.

3.2.2 Tailwater

The tailwater was a primary variable affecting the load on the tainter gate for most navigation projects, especially low head projects. As mentioned previously, the older USACE projects with vertical-lift gates mostly operate with the gate fully open or completely closed. The tailwater effect would reduce the hydrostatic load across a closed gate. The McNary project described in Appendix B has no tailwater effect.

3.2.3 Flow Regimes for Vertical-Lift Gates

The vertical-lift gate is used to control the discharge to maintain desired upper pool levels. Empirical relationships have been developed to account for factors that affect the quantity of flow under the gate. The very basic weir equation described Chapter 2 and Equations (1) and (2) are also applicable to the vertical-lift gate.

3.2.3.1 Free Controlled Flow

For this flow regime, the gates are controlling the flow, and there is no tailwater effect on the discharge. The equation for free controlled flow was developed beginning with the equation for free uncontrolled flow, shown here and in Equation (5):

$$Q = C_d L\sqrt{2g}H^{3/2},$$

where

C_d = the discharge coefficient for free uncontrolled flow, and
L = the weir length or gate width.

For low-head orifices, King (1954) recommended modifying Equation (5) to the following:

$$Q_G = C_{dl}\sqrt{2g}L\left(H_2^{3/2} - H_1^{3/2}\right), \quad (104)$$

where

Q_G = the gate controlled discharge,
C_{dl} = the discharge coefficient,
L = the gate width,
H_1 = the head on the gate lip, and
H_2 = the head on the gate seat.

Figure 42 shows a schematic of the parameters in Equation (104). The figure is from EM 1110-2-1603 (HQUSACE 1990, Appendix C, plate 6-4) and is also provided in HDC sheet 312 (WES 1980). An investigation by WES (1963) showed that relating the gate controlled discharge to the free uncontrolled discharge (discharge with the same head but no gate) provided

better correlation between the two discharge coefficients. This was accomplished by dividing Equation (104) by Equation (5) to give the following:

$$\frac{Q_G}{Q} = \frac{C_{dl}}{C_d}\left(\frac{H_2^{3/2} - H_1^{3/2}}{H^{3/2}}\right). \tag{105}$$

Figure 42. Schematic for parameters used in Equation (104). (Image reproduced from HQUSACE 1990, plate 6-4. Public domain.)

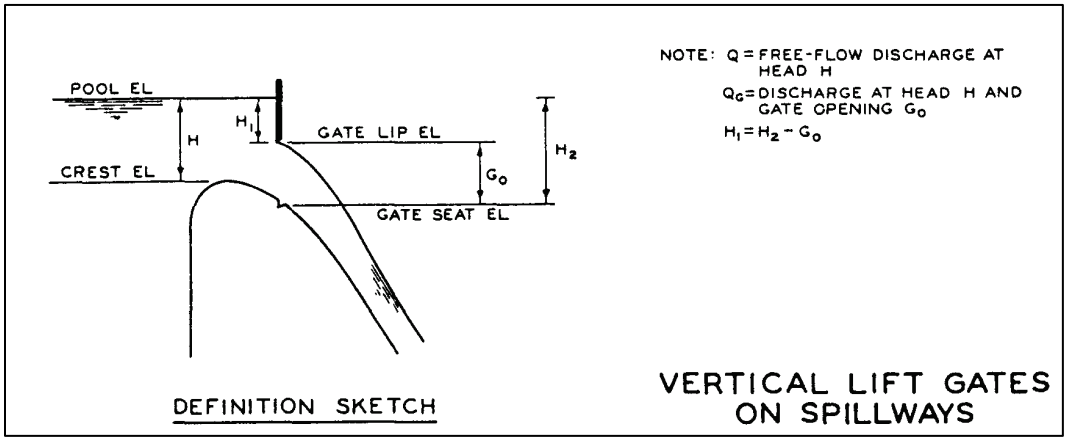

This relationship is shown in Figure 43, and the line drawn through the data points represents C_{dl}/C_d equal to unity. To determine Q_G from Equation (105), Q must be computed from Equation (5) or selected from an existing rating curve. USACE projects should already have a spillway discharge rating curve where Q_G can be found.

Figure 43. Discharge coefficients for vertical-lift gates on a spillway. (Image reproduced from HQUSACE 1990, plate 6-4. Public domain.)

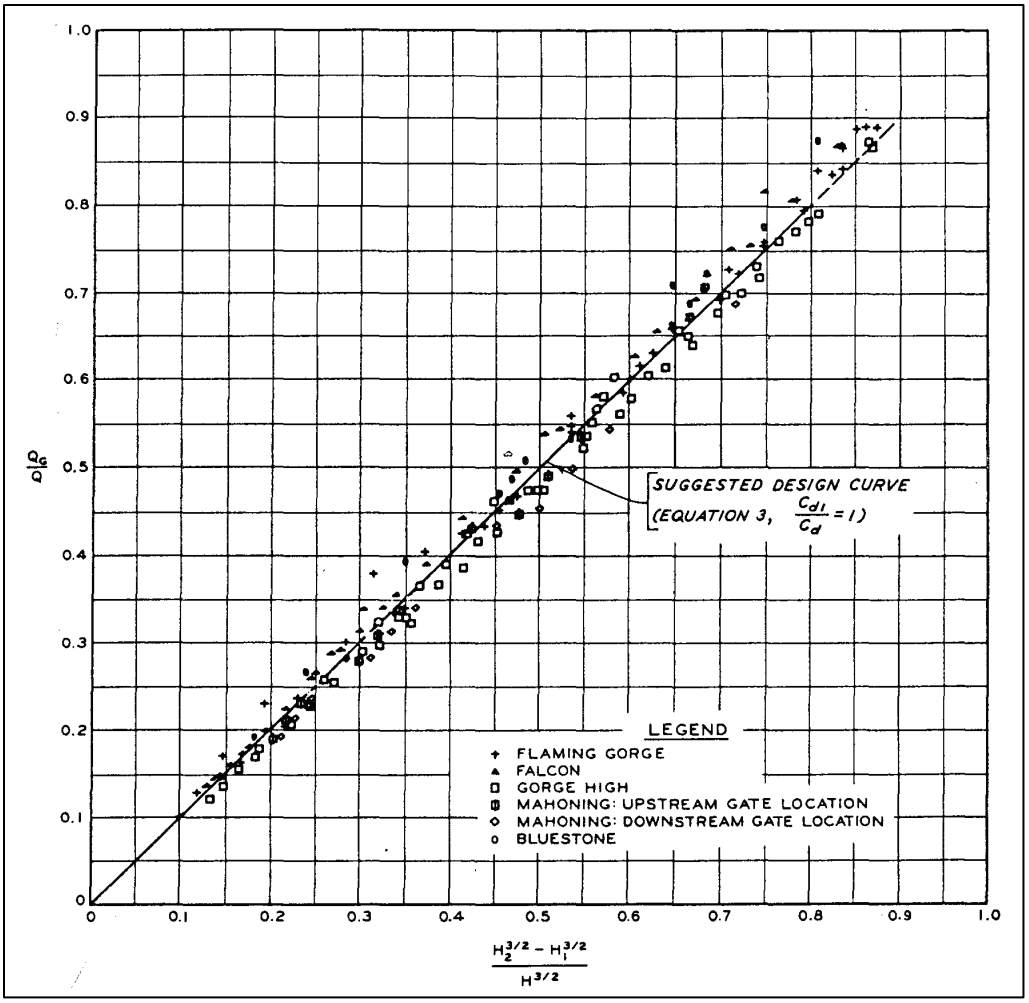

3.2.3.2 Submerged Controlled Flow

For this flow regime, the gates are partially open, and the discharge (and upper pool el) is controlled by the gate opening and submergence effect. The discharge equations are the same as those shown in Chapter 2 for the STG.

3.3 Hydraulic Loading for Vertical-Lift Gates

Hydraulic loads consist of all loads due to water. These include hydrostatic (i.e., weight of water), hydrodynamic (i.e., load due to flowing water), and wave action. These are the predominant hydraulic loads, in terms of magnitude and frequency, experienced by HSS. Vibrations caused by flowing water, constricted flow, and water hammer are also considered hydraulic loads.

3.3.1 Hydrostatic Load for Vertical-Lift Gates

The hydrostatic load is due to the hydraulic head across the vertical-lift gate. The load on the gate results from the hydrostatic pressure acting on the gate. If tailwater is present, it will affect the hydrostatic load. The maximum hydrostatic load occurs when the gate is closed and there is no tailwater effect on the gate. This condition generally happens during minimum discharges. Changes in head near the gate are caused primarily by wind waves and tailwater effect.

The hydrostatic pressure on a closed gate is expressed as γH, where γ is the unit weight of water, and H is the total head on the gate. Figure 44 is an illustration of the hydrostatic pressure distribution on the vertical-lift gate. When the gate is closed, H represents the difference between the upper pool el and the spillway crest el when the tailwater is lower than the crest el. A conventional equation found in many textbooks that is used to compute the hydrostatic pressure (p) is Equation (10), which is repeated here. As stated, γ is the unit weight of water, and y is the vertical distance from the water surface to the location of the hydrostatic pressure of interest (Figure 15). The maximum hydrostatic pressure (Equation 11, repeated here) on the gate would be at the bottom of the gate, which is the spillway crest el:

$$p = \gamma y,$$

$$p_{max} = \gamma H.$$

The hydrostatic pressure is multiplied by the area the pressure is acting on to obtain the hydrostatic force, H_s, shown in Figure 15. H_s is the resultant force computed from the triangular pressure distribution acting on the gate area. In most cases, a unit gate width is used to compute the gate area, resulting in Equation (12), shown again here, which is the hydrostatic force per unit width of the gate. The location of the resultant force is $H/3$ above the spillway crest when H is the head on the gate (Figure 15) for the STG:

$$H_s = \frac{1}{2}\gamma H^2.$$

Figure 44. Hydrostatic pressure distribution for vertical-lift gate.

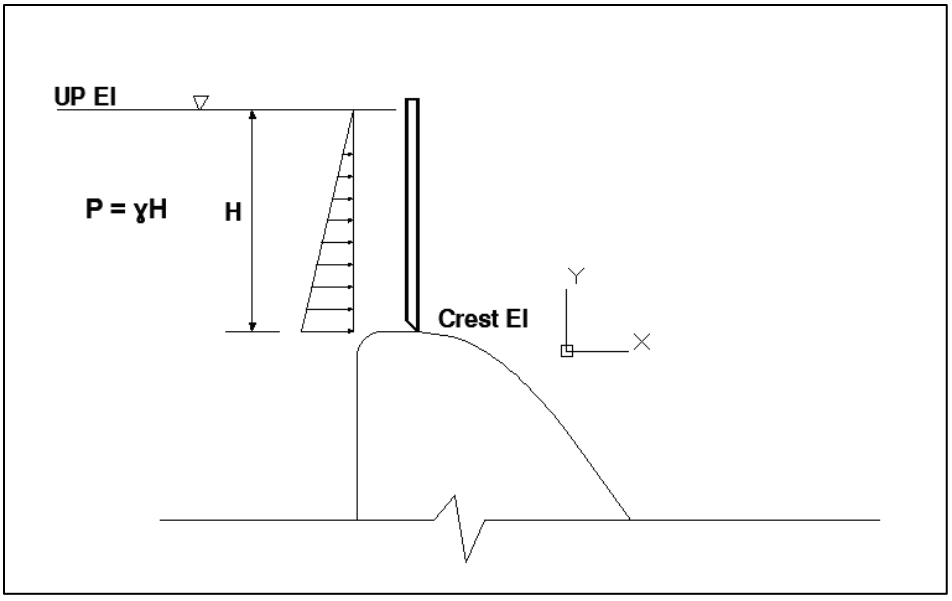

3.3.2 Wave Load for Vertical-Lift Gates

Wave loads are project specific and are considered for projects that experience significant wind and fetch. The same procedures used for the STG can be applied to the spillway vertical-lift gate. These procedures are described in Chapter 2. The Goda (2010) procedures are the recommended guidance for wind-induced wave loadings for inland navigation projects. The Goda wave pressure distribution procedure for vertical-lift spillway gates is shown in Figure 45.

Figure 45. Goda's (2010) wave pressure distribution adapted for a vertical-lift spillway gate.

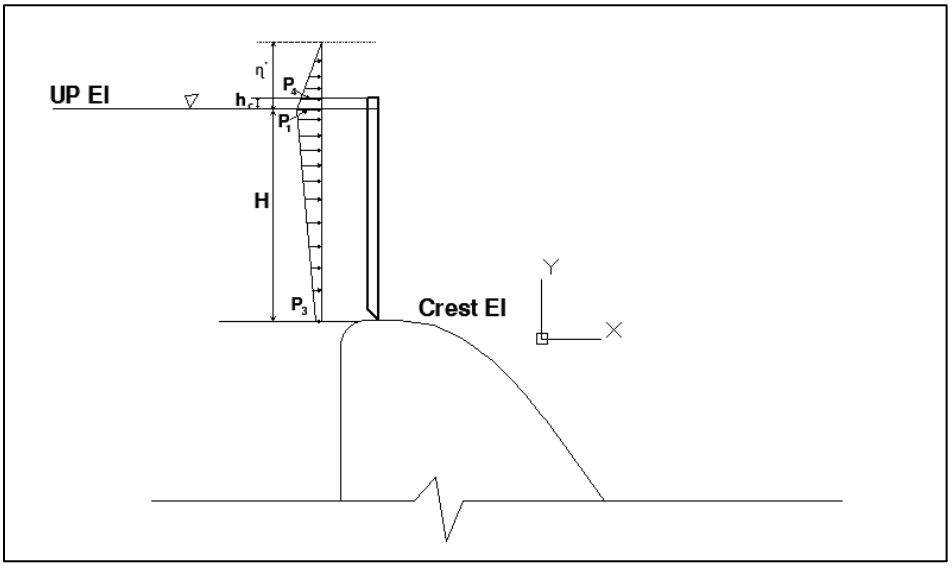

Appendix B contains an example procedure for computing the wave pressure on the vertical-lift gate using the Goda (2010) procedure.

3.3.3 Hydrodynamic Load for Vertical-Lift Gates

The magnitude of the hydrodynamic loads caused by flowing water are also a function of the usual, unusual, and extreme load category. The deviations from the mean hydrodynamic load can also result from many factors. Wind, waves, ice, debris, vessel impact, approach flow asymmetry, gate setting, and tailwater effects can cause deviations. The effects of gate settings and tailwater on the hydrodynamic loads are the main factors that contribute to deviations about the mean load.

The hydrodynamic load results from the force due to water flowing under the gate. The pressure distribution near the upper part of the gate is primarily hydrostatic because the velocity is slow in this location. The velocity starts to increase with depth, and near the bottom of the gate, the velocity can be fast. In this area, there is a deviation from the hydrostatic pressure distribution.

3.3.3.1 Hydrodynamic Load for a Vertical-Lift Gate with Tailwater

This variable pressure on the gate makes it difficult to determine the force on the gate by integrating the pressure over the gate surface. The momentum equation applied to a control volume upstream and downstream from the gate can be used to estimate the force on the gate. This is a simplified method because the flow across the control volume is assumed to be uniform and steady. The equations shown in Section 2.3.3 to estimate the hydrodynamic force on the STG with a tailwater effect are applicable to the vertical-lift spillway gate. The equations, which were originally presented as Equations (82) through (94), are presented again here for the reader's benefit.

The momentum equation from Roberson and Crowe (1985) is modified as

$$\frac{\gamma H^2 b}{2} - \frac{\gamma h^2 b}{2} + F_{GW} - F_{visc} = V_1 \rho(-V_1 H b) + V_2 \rho(V_2 h b).$$

Considering the viscous force (F_{visc}) is negligible and $V_1 H b = V_2 h b = Q$,

$$F_{GW} = \rho Q(-V_1) + \rho Q(V_2) - \frac{1}{2}\gamma b(H^2 - h^2).$$

F_{GW} is the force of the gate acting on the water in the control section. To obtain the force on the gate (F_G), F_{GW} is solved, and the sign on F_{GW} is changed:

$$F_G = \rho Q(V_1 - V_2) + \frac{1}{2}\gamma b(H^2 - h^2),$$

where

Q = the discharge per gate in ft^3/sec,
V_1 = the approach velocity in ft/sec,
V_2 = the velocity downstream of the gate in ft/sec,
ρ = the mass density = 1.936 slugs/ft^3,
γ = the unit weight of water = 62.4 lb/ft^3, and
b = the gate width in feet,

with

H = upper pool el – spillway crest el, and

h = TW El – spillway crest el.

The solution to Equation (84) requires that Q, V_1, and V_2 be known. Figure 46 contains a schematic of some of the terms used in Equation (82). Using flow through a single gate for the discharge, Q, the approach velocity, V_1, can be determined from

$$V_1 = \frac{Q}{A_1}.$$

A_1 is the area upstream from the gate, and when using flow through a single gate, it can be computed from the terms shown in Figure 46 as UP EL – approach el, P, times the gate width, b, or

$$A_1 = P * b.$$

If no tailwater is present, Equation (105) can be used to determine the discharge under the gate. If tailwater is present and affects the discharge through the gate, V_2 is determined using the submerged controlled flow equation, first presented as Equations (89) through (91) and shown again here:

$$Q = C_{gs} b h \sqrt{2g\Delta H},$$

where

$$h = \text{TW El} - \text{spillway crest el},$$

and the differential head, ΔH, is

$$\Delta H = H - h.$$

Most projects have used Equation (89) to develop the spillway rating curves that are used to set the desired gate opening. The coefficient, C_{gs}, in Equation (89) is obtained from EM 1110-2-1605 (HQUSACE 1987, Figure 5-12). The data were collected for an STG but are considered applicable for the vertical-lift gate. Figure 47 is a reconstruction of the figure from HQUSACE (1987) and is for B = 20 ft. This was the value for B used in the example problem in Appendix A. Figure 47 was interpolated from B = 18 ft and B = 31 ft, which are shown in Figure 5-12 in EM 1110-2-1605.

To use Figure 47, h/G_0 and B are needed: h is determined from Equation (90), and G_0 is the gate opening (G_0), as illustrated in Figure 46. B is given as

$$B = \text{spillway crest el} - \text{stilling basin floor el.}$$

C_{gs} is then chosen from Figure 5-12 of EM 1110-2-1605 (HQUSACE 1987). The discharge in Equation (89) can now be computed because b, h, ΔH, *and* C_{gs} are all known. The value of discharge determined from Equation (89) is generally used to develop the project spillway rating curve.

Typically, a spillway rating curve is used to determine what gate opening to set for a given discharge and TW El. If the discharge rating curve is available, the discharge, Q, is known, and one can take advantage of this information to determine V_2 in Equation (93), which is repeated here.

If V_2 is assumed to be the representative velocity downstream from the gate between the tailwater and the spillway crest, it can be computed from

$$V_2 = \frac{Q}{A_2},$$

where A_2 for a project with tailwater is

$$A_2 = b * h,$$

and Q has either been computed using Equation (89) or determined from the spillway rating curve. If there is no spillway rating curve and no tailwater, Equation (105) can used to compute the discharge under the gate, and A_2 is

$$A_2 = b * G_0. \tag{106}$$

All the parameters in Equation (84) have now been determined, so the hydrodynamic force on the gate, F_g, can be computed.

Figure 46. Schematic for terms used in Equation (84) for a vertical-lift gate with tailwater.

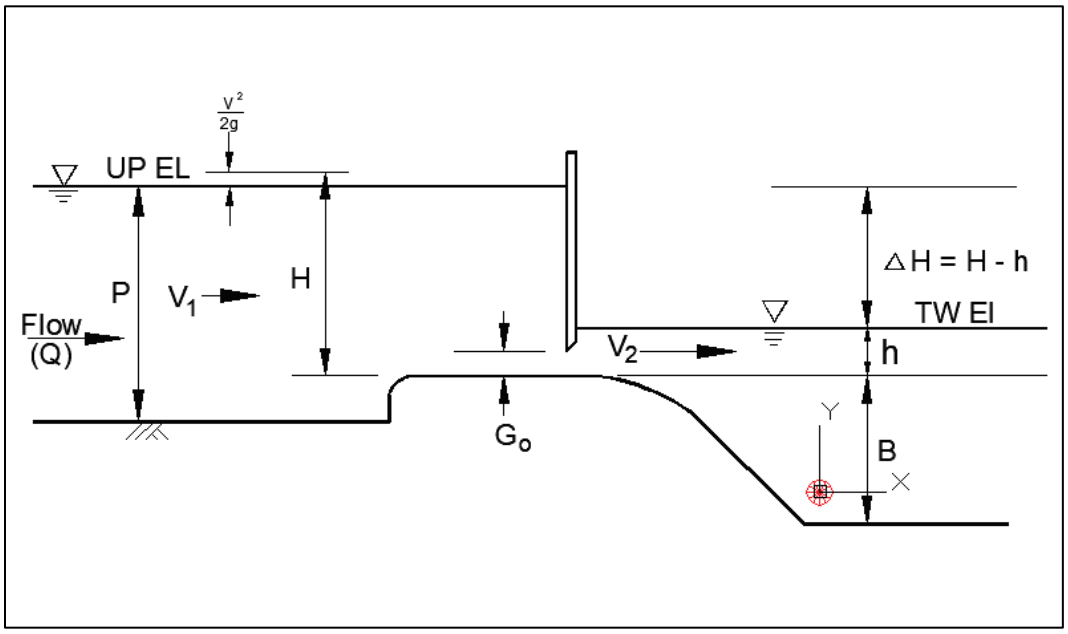

Figure 47. Discharge coefficients (C_{gs}) for a submerged controlled flow vertical-lift gate. (Image adapted from EM 1110-2-1605, HQUSACE 1987.)

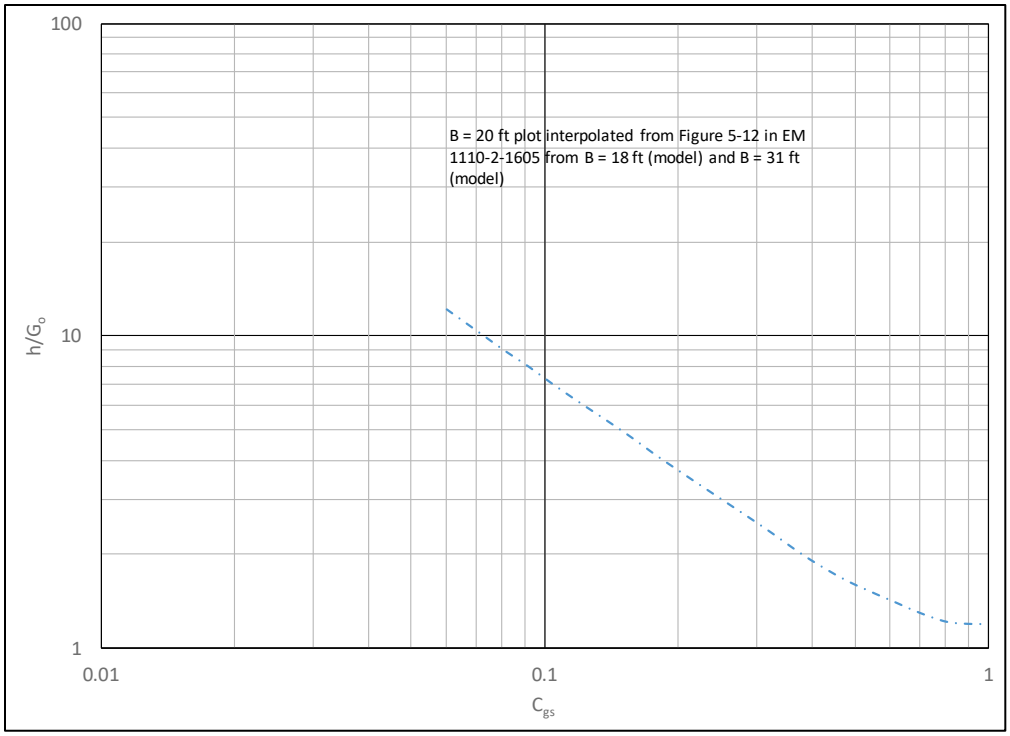

3.3.3.2 *Hydrodynamic Load for a Vertical-Lift Gate with No Tailwater*

Figure 48 shows a schematic of this pressure distribution with no tailwater effects. Figure 49 shows a schematic of the terms used to compute V_1 and V_2 in Equation (84) for a vertical-lift gate with no tailwater.

Figure 48. Schematic of pressure distribution on a vertical-lift gate with the gate open and no tailwater.

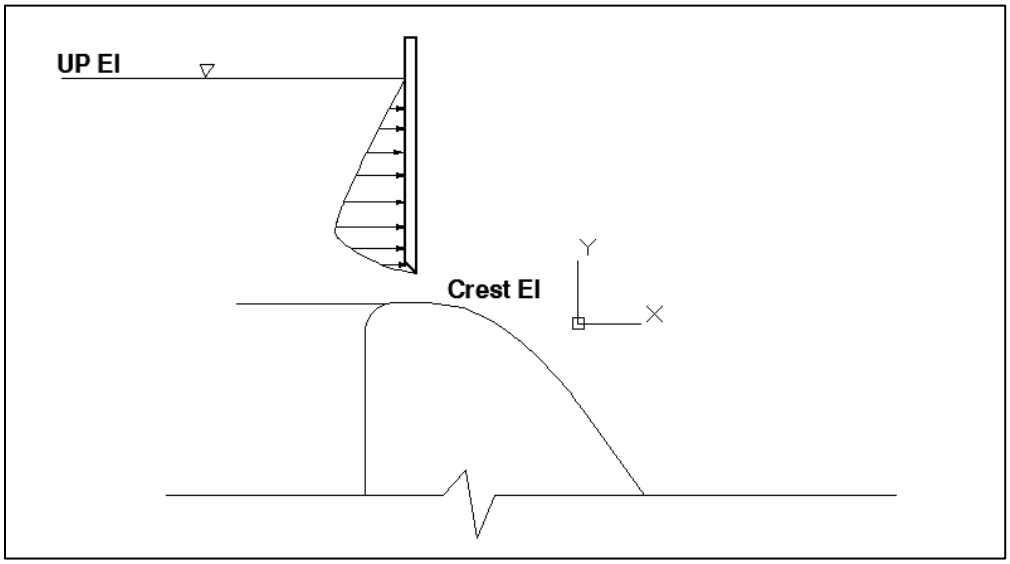

Figure 49. Schematic for terms used in Equation (105) for a vertical-lift gate with no tailwater.

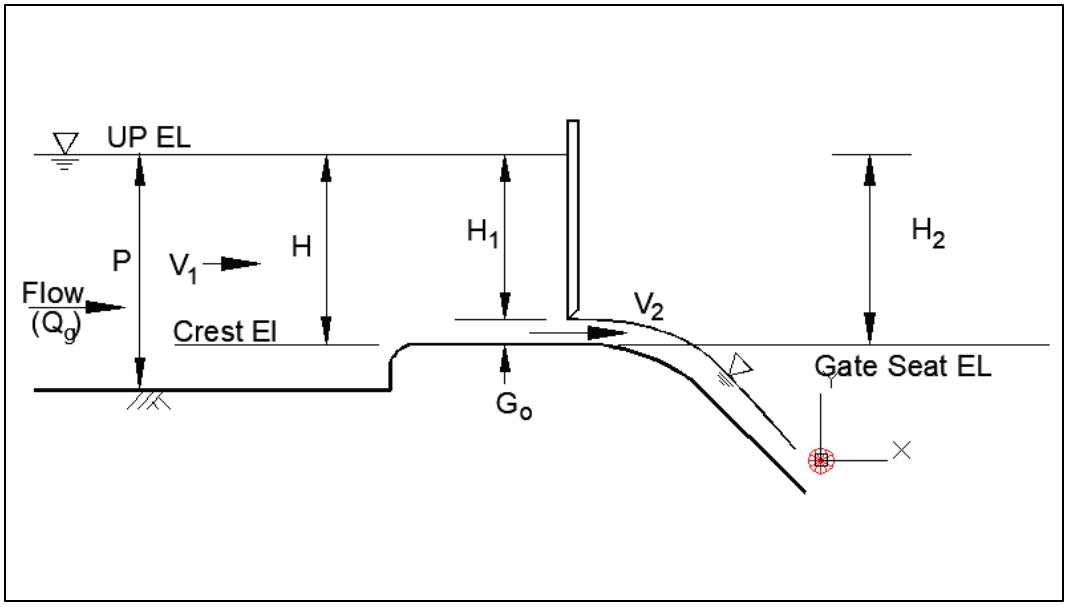

Appendix B illustrates how to determine the hydrodynamic load on the spillway vertical-lift gate with no tailwater. Appendix B also shows the hydrodynamic loads computed for the spillway vertical-lift gate using the conservation of momentum principles described in the preceding sections at the MLD project.

Another procedure that can be used to determine the hydrodynamic force on the spillway vertical-lift gate was investigated. This procedure is described in detail in Section 2.3.3.2. This procedure was based on the results of a numerical investigation by Kim (2007) and an experimental investigation by Roth and Hager (1999). The advantage of this procedure is the hydrodynamic pressure distribution acting on the gate can be determined and then integrated to give the hydrodynamic force on the gate. This procedure also allows the location of the resultant force to be determined. Appendix B contains an example problem using the McNary vertical-lift gate project data. A comparison of the hydrodynamic force using both methods is also provided.

3.3.3.3 Flow-Induced Vibration

The hydrodynamics of the flow under a gate may cause instabilities, such as flow separations and reattachments, and consequently, undesirable pressure fluctuations. These conditions may lead to vertical oscillations and vibrations and are highly dependent on the bottom shape of the

vertical-lift gate. Guidance for the hydrodynamic load analysis on a vertical-lift gate is provided in HDC 320-2 to 320 2/3 (WES 1980).

3.3.4 Combined Hydrostatic and Wave Loads for Vertical-Lift Gates

Wave loads are project specific and are considered for projects that experience significant wind and fetch. The development of wave loading for the STG that was shown in Section 2.3.2.3 and used the Goda (2010) recommendations is considered applicable for the vertical-lift gate. These loads will be added to the hydrostatic load, and when determining wave loading effects, the load category will reflect the coincident water-surface elevation and wind conditions that produce the maximum effects. The gate may be overtopped with the maximum wave height, and the Goda procedure accounts for this condition. Appendix B contains an example of the combined hydrostatic and wave loads.

3.3.5 Combined Hydrodynamic and Wave Loads for Vertical-Lift Gates

The highest hydrodynamic loads will occur when the gates are at small openings, the tailwater is low, and the upper pool is at its highest. The higher the gate is raised, the higher the tailwater becomes, and the differential head across the gate is less if the tailwater is higher than the spillway crest. With no tailwater present, the higher the gate is raised with the upper pool remaining the same or changing slightly, the lower the hydrodynamic load will be. With the upper pool constant, a higher gate opening will result in more freeboard on the gate, and wave overtopping is less likely to occur. Adapting the Goda (2010) wave pressure distribution procedure to a spillway vertical-lift gate accommodates this condition. Appendix B contains an example of a combined hydrodynamic and wave load.

3.3.6 Summary of Hydraulic Loads for Vertical-Lift Gates

The hydraulic loads on the spillway consist primarily of the hydrostatic, wave, and hydrodynamic loads. The loads should be combined as appropriate to give the maximum expected for the vertical-lift gate. The wind to wave force conversion indicated the wave forces made a significant contribution to the combined loads. The authors of this report recommend that wind-induced wave forces be determined using the Goda (2010) design procedure discussed in Section 2.3.2.3 and the wind speed estimation discussed in Section 2.3.2.7.

The tailwater is the primary variable for changes in the hydraulic load. The maximum hydrostatic load occurs with no tailwater effect, and the hydrodynamic load reduces as the tailwater rises above the spillway crest el. The example project presented in Appendix E had no tailwater effects.

3.4 Probabilistic Characterization of the Hydrostatic and Hydrodynamic Loads for the Vertical-Lift Gate

3.4.1 Probabilistic Characterization of the Hydrostatic Load for the Vertical-Lift Gate

The LRFD procedures require the dispersion of the hydrostatic load to perform the analysis. An appropriate range for the upper pool at most navigation projects is considered plus 6σ and minus 6σ about the mean upper pool. The range in the hydrostatic load can then be determined for this range of upper pool els. Appendix B of this report provides an example of the hydrostatic loads computed for the McNary vertical-lift project data with the range of upper pool els between +6σ and –6σ.

3.4.2 Probabilistic Characterization of the Hydrodynamic Load for the Vertical-Lift Gate

The LRFD procedures also require the dispersion of the hydrodynamic load to perform the analysis. To determine the dispersion in the hydrodynamic load, the pressure distribution on the gate is computed using the procedure described in Section 2.3.3.2. The hydrodynamic load on the gate is the largest with small gate openings, so for typical projects, the 1 ft gate opening is used to demonstrate the dispersion in the hydrodynamic load. The change in the load is due to the fluctuation of the upper pool between +6σ and –6σ about the mean upper pool el. Appendix B provides an example of how to determine the hydrodynamic load for the MLD spillway vertical-lift gate with a 1 ft gate opening.

3.5 Other Loadings for Vertical-Lift Gates

Other loadings on a vertical-lift gate are discussed in this report. Section 2.5.1 contains information on barge impacts, Section 2.5.2 contains information on debris impacts, and Section 2.5.3 provides information on ice impacts. Additional guidance on operational loads can also be found in ETL 110-2-584 (HQUSACE 2014, Sections 3.2 and 3.3).

3.6 Summary and Conclusions

The hydraulic loads acting on the spillway vertical-lift gate are similar to those acting on the STG, although the mechanical loads are different due to the hoisting mechanisms.

The hydrostatic load is the maximum and would occur with the upper pool at the top of a closed gate. The fluctuation of the upper pool about the mean upper pool el determines the statistics for the hydrostatic load. The wind-induced wave load was determined using the procedures described by Goda (2010).

The hydrodynamic loads were determined using the Roth and Hager (1999) and Kim (2007) procedures, which were described in detail in Chapter 2, for a project with the tailwater lower than the gate opening. Appendix B provides examples of the load development for the MLD spillway vertical-lift gate.

Nonhydraulic loads acting on the vertical-lift gate will be discussed in subsequent reports associated with this research.

4 Loadings Applied to Roller Gates

This chapter describes the characteristic loads associated with spillway roller gates.

4.1 Existing Guidance for Roller Gate Design

This chapter focuses on the roller gates used for inland navigation projects. The roller gate is used on older, low head navigation dams. They are shaped like a hollow tube with gears at each end that roll up a toothed track mounted on the spillway pier. Figure 50 shows a drawing of the side view of the roller gate at the RCBLD project. Figure 51 is a picture of a roller gate at an Upper Mississippi River project.

Figure 50. Roller gate at the R. C. Byrd Locks and Dam (RCBLD) project. (Image reproduced from USACE-LRH files.)

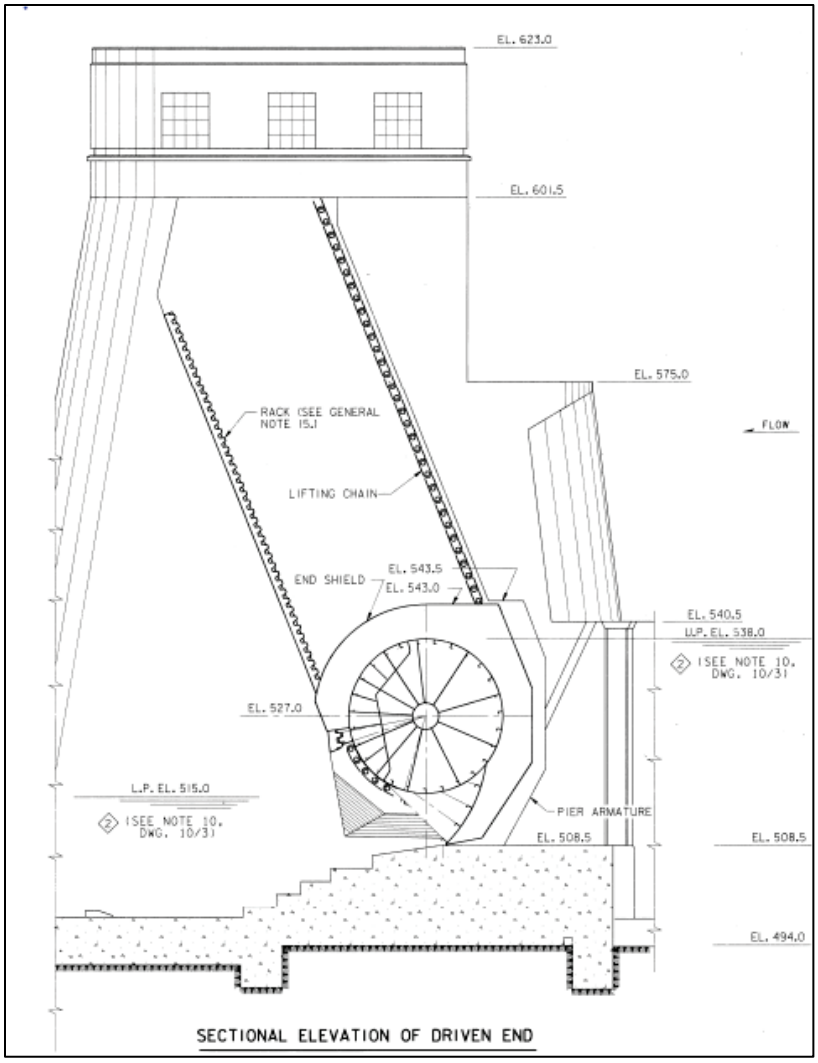

Figure 51. Roller gate at the Upper Mississippi River project. (Image reproduced from USACE, Rock Island District [USACE-MVR], files.)

4.1.1 ETL 1110-2-584, *Design of Hydraulic Steel Structures*

ETL 1110-2-584 (HQUSACE 2014) provides guidance for designing new HSS and conducting major rehabilitation of existing HSS using LRFD. The design philosophy for HSS is to achieve the objectives of constructability, safety, and serviceability for the specified limit states while considering inspectability and economy. This ETL states, "The structural system of an HSS shall be proportioned and detailed to ensure the development of significant and visible inelastic deformations at the strength and extreme event limit states before failure" (HQUSACE 2014, 2-1). The limit states applicable to HSS are strength, serviceability, fatigue, and fracture. The design life of HSS is assumed to be 100 yr.

ETL 1110-2-584 (HQUSACE 2014) does not provide detailed design guidance for the roller gate. Details of a roller gate designed to replace the existing gates at the RCBLD (formerly Gallipolis Locks and Dam) were obtained from USACE-LRH to assist in the development of LRFD for the

roller gate. The new gate had the same basic dimensions as the one being replaced. The new gate was welded, so some of the framing was altered slightly to accommodate the welded connections. The weight of the new gate was essentially the same, so the overall weight and operational characteristics were not affected. An existing structural model (ANSYS 4.3) was used to analyze the structural components of the gate. Additional analyses were also done analytically to compare with the ANSYS 4.3 structural model results to help determine allowable stress.

Chapter 2 provided a review of existing guidance for the STG, and this guidance is also applicable to the spillway roller gate. Refer to Chapter 2 for guidance on the hydrostatic and hydrodynamic loads for the spillway roller gate.

4.1.2 EM 1110-2-1605, *Hydraulic Design of Navigation Dams*

This EM describes the roller gate as "a long metal cylinder with 'ring gears' at each end that mesh with inclined metal racks supported by the piers. The cylinder is braced internally to act as a beam to transmit the hydraulic load into the piers" (HQUSACE 1987, 5-35). The damming height can be increased by adding an apron that rotates into contact with the sill when the gate is lowered. The gate is raised and lowered using a chain wrapped around one end of the tube with a hoist mounted in the pier. This design and manner of operation results in a limited amount of frictional contact at the sealing points. Because the weight of the gate is divided between the chain and the pier, the roller gate has lower power requirements than other spillway gates. There have been roller gates constructed for a head of 30 ft and lengths of up to 150 ft, depending on the foundation strength.

4.1.3 Roller Gate Load Cases

EM 1110-2-2702 (HQUSACE 2000, rescinded) states that all loads that HSS will be subjected to shall be considered in the design. These loads include gravity (i.e., weight, ice, mud), hydrostatic, hydrodynamic, operational and machinery, floating and thermal ice, debris, vessel impacts, and environmental (typically wind and temperature). Frequency of loading is considered in the design for the three load categories (i.e., usual, unusual, and extreme) that were described in Section 2.1.5 of this report and were specified in terms of frequency of occurrence. The information on usual, unusual, and extreme loads was taken directly from ETL 1110-2-584

(HQUSACE 2014). Load combinations and cyclic and noncyclic loads are also presented in Chapter 2 of this report.

In the design of the replacement roller gates for the RCBLD project, the USACE-LRH considered four load cases:

I Gate completely down and supported by chain (full head)
II Gate completely down and supported by sill (full head)
III Gate rotated 40°
IV Gate rotated 185°

For load cases III and IV, the weight of the gate is increased by 10% to account for debris in the roller gate.

4.2 Hydraulic Data Collection and Statistical Data Reduction for Mean Loading and Dispersion for Spillway Roller Gates

The reliability analysis for the roller gate requires that the mean and standard deviation of the loads be determined. Hydraulic data are needed to develop these values. The discharge, upper pool el, gate setting, and TW El are needed to determine hydraulic loads. Historical data are necessary to develop the samples and statistical data required for the analysis.

4.2.1 Upper Pool El

A navigation project is operated to maintain the desired upper pool by lifting the gates as the discharge increases. The nominal loads needed for the statistical analysis will generally occur with a near constant upper pool el. The mean and standard deviation for the upper pool needs to be determined. The design example chosen for the spillway roller gate was the RCBLD on the Ohio River. Appendix C contains the methodology used to determine the hydraulic data and the statistical data reduction.

4.2.2 Tailwater

The tailwater is a primary variable affecting the load on the tainter gate for most navigation projects, especially low head projects. This is also the case for the spillway roller gate. The tailwater influences the discharge through the gate, which will affect the hydrodynamic loads. The R. C. Byrd project has tailwater effects, and Appendix C describes the procedures used to determine the hydrodynamic loads.

4.2.3 Flow Regimes for Spillway Roller Gates

4.2.3.1 Free Controlled Flow

The discharge equations for the free controlled flow regime for the spillway roller gate are the same as those for the tainter gate and are described in Chapter 2.

4.2.3.2 Submerged Controlled Flow

For this flow regime, the gates are partially open, and the discharge (and upper pool el) is controlled by the gate opening and submergence effect. The discharge equation (Equation 9, repeated here) is similar to the one shown in Chapter 2 for the STG.

$$Q = C_{gs} L h \sqrt{2g\Delta H},$$

where

C_{gs} = the discharge coefficient for submerged controlled flow, and
ΔH = the difference in the total head upstream and the TW El.

Figure 13 shows a plot of h/G_o versus C_{gs} that was obtained from EM 1110-2-1605 (HQUSACE 1987). The spillway rating curve provided by the USACE-LRH for the R. C. Byrd roller gate was used to obtain discharge coefficients to compare to those in Figure 13. Figure 52 shows this data compared to the curve constructed from Figure 13 data with B = 20 ft (the blue curve in Figure 52). The blue curve was used for the STG analysis in the submerged controlled flow regime. The orange dots in Figure 52 represent the points obtained from the R. C. Byrd spillway rating curve.

Figure 52. Comparison of discharge coefficients for the RCBLD spillway roller gate and those in EM 1110-2-1605 (HQUSACE 1987) for submerged controlled flow.

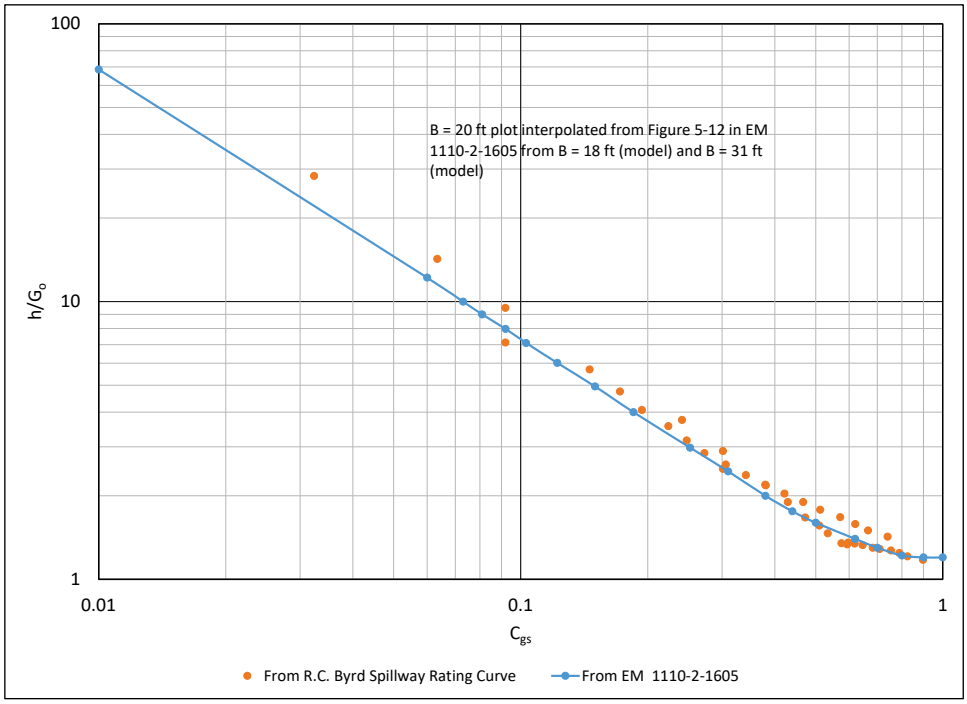

4.3 Hydraulic Loading for Spillway Roller Gates

Hydraulic loads consist of all loads due to water. These include hydrostatic (i.e., weight of water), hydrodynamic (i.e., load due to flowing water), and wave action. These are the predominant hydraulic loads, in terms of magnitude and frequency, experienced by HSS. Vibrations caused by flowing water, constricted flow, and water hammer are also considered hydraulic loads.

4.3.1 Hydrostatic Load for Spillway Roller Gates

The hydrostatic load is due to the hydraulic head across the roller gate. The load on the gate results from the hydrostatic pressure acting on the gate. If tailwater is present, it will affect the hydrostatic load. The maximum hydrostatic load occurs when the gate is closed and there is no tailwater effect on the gate. This condition generally happens during minimum discharges. Changes in head near the gate are caused primarily by wind waves and tailwater effect.

A conventional equation found in many fluid mechanics and hydraulics textbooks and used to compute the hydrostatic pressure (p) was shown as Equation (10) and is repeated here. As stated previously, γ is the unit

weight of water, and y is the vertical distance from the water surface to the location of the hydrostatic pressure of interest (Figure 14):

$$p = \gamma y.$$

The horizontal hydrostatic pressure on a closed gate is typically expressed as γH, where γ is the unit weight of water, and H is the total head on the gate. Figure 53 shows an illustration of the hydrostatic pressure distribution on the roller gate. When the gate is closed, H represents the difference between the upper pool el and the spillway crest el when the tailwater is lower than the crest el:

$$p_{max} = \gamma H.$$

The hydrostatic pressure is multiplied by the area the pressure is acting on to obtain the force. The maximum hydrostatic pressure would occur if the upper pool el was the same as the top of a closed gate. Typically, this would not occur because, with a higher than normal upper pool, the gates would be raised. The resultant hydrostatic force per foot of width for the roller gate is shown in Equation (12), repeated here, and is located $H/3$ above the spillway (Figure 15):

$$H_s = \frac{1}{2}\gamma H^2.$$

Figure 53. Hydrostatic pressure distribution for the roller gate.

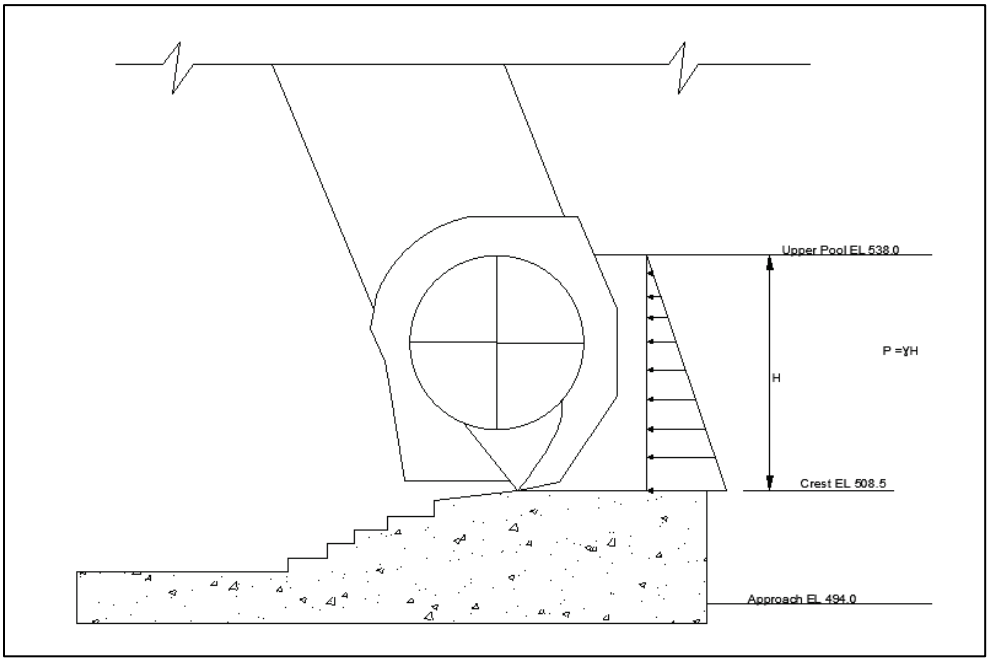

4.3.2 Wave Load for Spillway Roller Gates

Wave loads are project specific and are considered for projects that experience significant wind and fetch. The same procedures used for the STG can be applied to the roller gate. These procedures are described in Chapter 2. The Goda (2010) procedures are the recommended guidance for wind-induced wave loadings for inland navigation projects. Figure 54 shows the Goda wave pressure distribution procedure for the roller gate.

Figure 54. Wave pressure distribution adapted from Goda (2010) for a spillway roller gate.

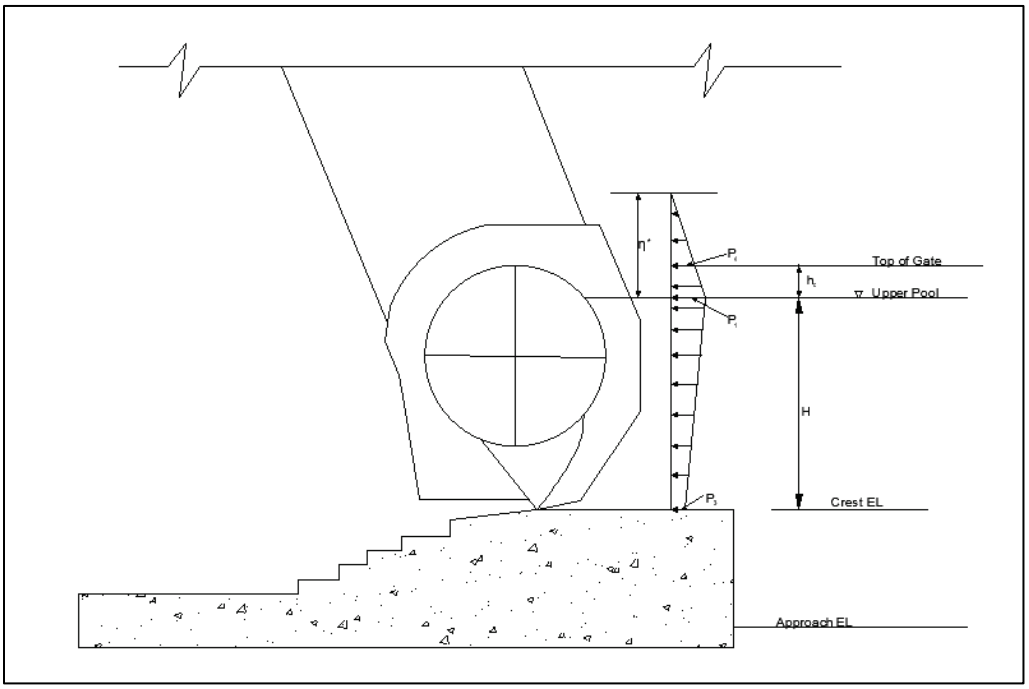

Appendix C contains an example procedure for computing the wave pressure on the roller gate using the Goda (2010) procedure.

4.3.3 Hydrodynamic Load for Spillway Roller Gates

The magnitudes of the hydrodynamic loads caused by flowing water are also a function of the usual, unusual, and extreme load categories. The deviations from the mean hydrodynamic load can also result from many factors. Wind, waves, ice, debris, vessel impact, approach flow asymmetry, gate setting, and tailwater effects can cause deviations. The effects of gate settings and tailwater on the hydrodynamic loads are the main factors that contribute to deviations about the mean load.

The hydrodynamic load results from the force due to water flowing under the gate. The pressure distribution near the upper part of the gate is primarily hydrostatic because the velocity is slow in this location. The velocity starts to increase with depth, and near the bottom of the gate, the velocity can be fast. In this area, there is a deviation from the hydrostatic pressure distribution. Figure 55 shows a schematic of this pressure distribution.

Figure 55. Schematic of hydrodynamic pressure distribution on an open roller gate.

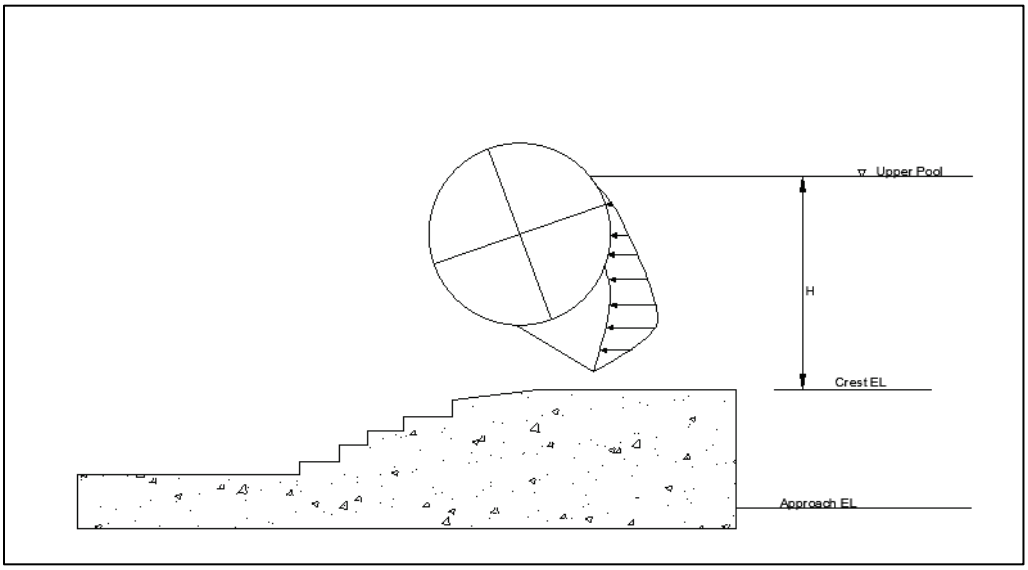

This variable pressure on the gate makes it difficult to determine the force on the gate by integrating the pressure over the gate surface. A procedure using the momentum equation applied to a control volume upstream and downstream from the gate was used to estimate the force on the gate. This is a simplified method because the flow across the control volume is assumed to be uniform and steady. The equations shown in Chapter 2, Section 2.3.3, to estimate the hydrodynamic force on the STG with a tailwater effect are applicable to spillway roller gates. If no tailwater is present, Equation (105) can be used to determine the discharge under the gate. If tailwater is present and affects the discharge through the gate, V_2 is determined using the submerged controlled flow equation (Equations 89–91, repeated here):

$$Q = C_{gs} b h \sqrt{2g\Delta H},$$

where

$$h = \text{TW El} - \text{spillway crest el},$$

and the differential head, ΔH, is

$$\Delta H = H - h.$$

Most projects have used Equation (87) to develop the spillway rating curves that are used to set the desired gate opening. The coefficient, C_{gs}, in Equation (87) can be obtained from Figure 5-12 in EM 1110-2-1605 (HQUSACE 1987, 5-16) if the rating curve is not available. The data were collected for an STG but are considered applicable for the roller gate. As discussed previously, Figure 52 was reconstructed for clarity for B = 20 ft. This was the value for B used in the example problem in Appendix A. The orange dots were the data obtained from the roller gate at R. C. Byrd and are similar to those shown in Figure 5-12 in EM 1110-2-1605 (HQUSACE 1987, 5-16). To use Figure 52, h/G_0 and B are needed; h is determined from Equation (88), and G_0 is the gate opening (G_0). B is given as

$$B = \text{spillway crest el} - \text{stilling basin floor el.}$$

C_{gs} is then chosen from Figure 52, and the discharge in Equation (89) can now be computed because b, h, ΔH, and C_{gs} are all known. The value of discharge determined from Equation (89) is generally used to develop the project spillway rating curve.

Typically, a spillway rating curve is used to determine what gate opening to set for a given discharge and TW El. If the discharge rating curve is available, the discharge, Q, is known, and one can take advantage of this information to determine V_2 in Equation (93), which is repeated here.

If V_2 is assumed to be the representative velocity downstream from the gate between the tailwater and the spillway crest, it can be computed from

$$V_2 = \frac{Q}{A_2},$$

where A_2 for a project with tailwater is

$$A_2 = b * h.$$

For a project with tailwater, Q can be computed using Equation (87) or determined from the spillway rating curve. If there is no spillway rating

curve and no tailwater, Equation (105) can be used to compute the discharge under the gate, and A_2 is

$$A_2 = b * G_0.$$

All the parameters in Equation (84) have now been determined, so the hydrodynamic force on the gate, F_g, can be computed. These parameters are shown in Figure 56.

Figure 56. Schematic for terms used in Equation (84) for a roller gate with tailwater.

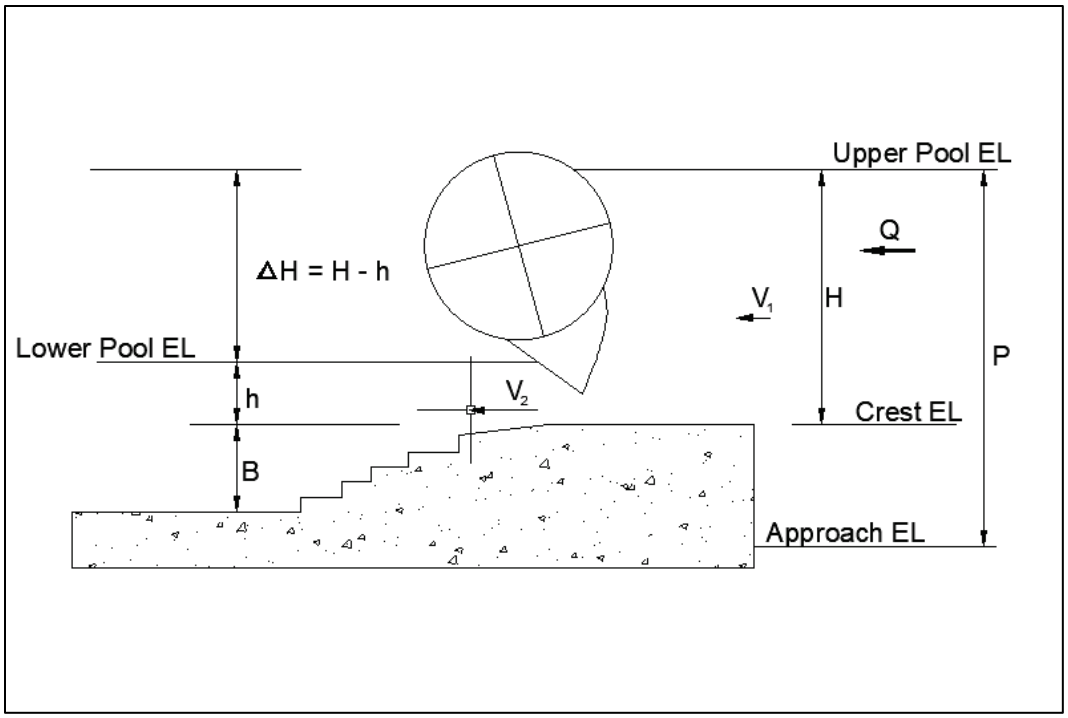

Appendix C shows the hydrodynamic loads computed for the roller gate at the RCBLD project.

4.3.4 Combined Hydrostatic and Wave Loads for Spillway Roller Gates

Wave loads are project specific and are considered for projects that experience significant wind and fetch. The development of wave loading for the STG shown in Section 2.3.2.3 and using the Goda (2010) recommendations is considered applicable for the roller gate. These loads will be added to the hydrostatic load, and "when determining wave-loading effects, the load category will reflect the coincident water-surface elevation and wind conditions that produce the maximum effects" (HQUSACE 2014, 3-5). The gate may be overtopped with the maximum wave height, and the Goda

procedure accounts for this condition. Appendix C shows an example of the combined hydrostatic and wave loads.

4.3.5 Combined Hydrodynamic and Wave Loads for Spillway Roller Gates

The highest hydrodynamic loads will occur when the gates are at small openings, the tailwater is low, and the upper pool is at its highest. The higher the gate is raised, the higher the tailwater becomes, and the differential head across the gate is less if the tailwater is higher than the spillway crest. With no tailwater present, the higher the gate is raised with the upper pool remaining the same or changing slightly, the lower the hydrodynamic load will be. With the upper pool constant, a higher gate opening will result in more freeboard on the gate, and wave overtopping is less likely to occur. Adapting the Goda (2010) wave pressure distribution procedure to a spillway roller gate accommodates this condition. Appendix C shows an example of a combined hydrodynamic and wave load.

4.3.6 Summary of Hydraulic Loads for Spillway Roller Gates

The hydraulic loads on the spillway consist primarily of the hydrostatic, wave, and hydrodynamic loads. The loads should be combined as appropriate to give the maximum expected for the roller gate. The wind-to-wave force conversion indicated the wave forces made a significant contribution to the combined loads. The authors of this report recommend that wind-induced wave forces be determined using the Goda (2010) design procedure discussed in Section 2.3.2.3 and the wind speed estimation discussed in Section 2.3.2.7.

Tailwater is the primary variable for changes in the hydraulic load. The maximum hydrostatic load occurs with no tailwater effect, and the hydrodynamic load reduces as the tailwater rises above the spillway crest el.

4.4 Probabilistic Characterization of the Hydrostatic and Hydrodynamic Loads for the Roller Gate

The dispersion of the hydrostatic load for the roller gate needs to be determined to conduct the LRFD analysis. Statistics are needed to estimate the dispersion in the hydrostatic loads. Appendix A contains an example problem for the MPLD and provides a method for developing these statistics for a project operated similarly to this one, in which the mean upper pool el is considered to be the normal navigation pool el. Because the normal

upper pool for the roller gate is at the top of the gate, this upper pool el would be the maximum for the hydrostatic load. Therefore, the fluctuation of the upper pool el occurs from the normal upper pool to an el lower, which is nominally taken as 1 ft. Appendix C provides a design example and methodology for the hydrostatic load dispersion for the R. C. Byrd spillway roller gate.

The dispersion of the hydrodynamic load for the roller gate also needs to be determined to conduct the LRFD analysis. The example problem in Appendix A for the MPLD provides a method for developing these statistics for a project operated similarly to this one, in which the mean upper pool el is considered to be the normal navigation pool el. Appendix C provides a design example and methodology for the hydrodynamic load dispersion for the roller gate.

5 Loadings Applied to Sector Gates

This chapter describes the characteristic loads associated with sector gates and summarizes the dispersion in these applied loads and the distribution of pressures.

5.1 Existing Design Guidance for Sector Gates

The sector gate has been used for lock gates at projects where the lift is usually very low. A lift of 10 ft or less is considered to be a very low lift lock. They are typically used for locks in coastal areas and are sometimes used for inland protection from storm surges. As mentioned in EM 1110-2-1604 (HQUSACE 2006), USACE has used the sector gate lock exclusively for very low lifts since 1950.

5.1.1 ETL 1110-2-584, *Design of Hydraulic Steel Structures*

Sector gates consist of two leaves that join in the center of the lock and rotate into recesses in the lock wall when in the fully open position. Each leaf is shaped like a sector of a cylinder and rotates about a vertical axis. Sector gates in very low lift locks can also be used to fill and empty the lock and are often referred to as an *end filling and emptying system*. This eliminates the need for a separate filling and emptying system. A unique advantage of sector gates is that they can be operated with small differential heads or with flow through the lock. Figure 57 shows a plan view of a sector gate lock, and Figure 58 shows an overhead view of a sector gate used as a lock gate.

Figure 57. Plan view of a sector gate lock. (Image reproduced from HQUSACE 2006, 3-8. Public domain.)

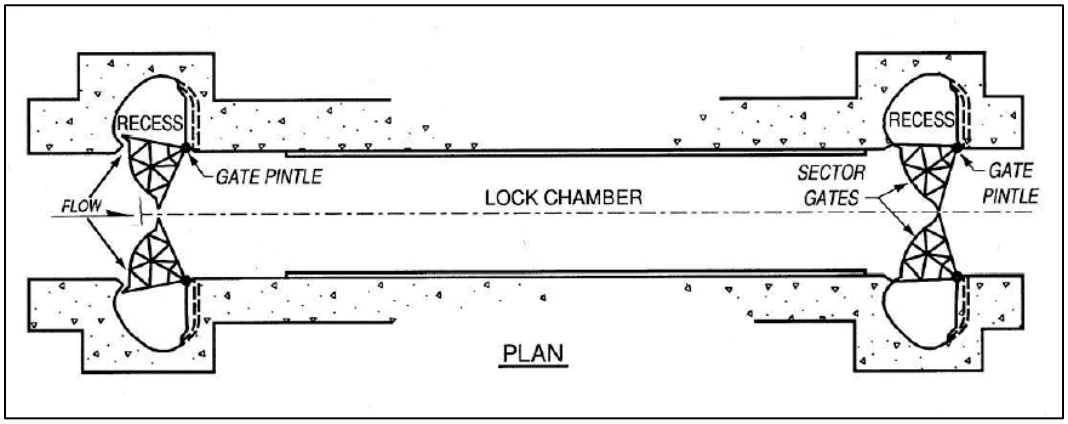

Figure 58. Sector gate used as a lock gate. (Image reproduced from HQUSACE 2014, B-7. Public domain.)

EM 1110-2-2702 (HQUSACE 2000, Chapter 3, Section 3-4, rescinded) described the three levels of hydrostatic loads that are considered in designs: the maximum hydrostatic load, H_1, which is defined as the maximum net hydrostatic load that will ever occur; the design hydrostatic load, H_2, which is the maximum net hydrostatic load for conditions up to a 10 yr flood event; and the normal hydrostatic load, H_3, which is the net load from the upper and lower pool levels that exist up to 50% of the time during the year.

When applied to the sector gate used as a lock gate, these hydrostatic loads depend on the upstream and downstream water-surface elevations. Because these low lift locks are typically located near coastal areas in navigation canals, these upstream and downstream water levels can reverse during storm events. The maximum net hydrostatic head (H_1) would occur if the upstream water level was at the top of the gate and the lower water level was a minimum el. This minimum el could be affected by low tide.

5.1.2 EM 1110-2-1604, *Hydraulic Design of Navigation Locks*

EM 1110-2-1604 (HQUSACE 2006, Section 4-13) provides references concerning the hydraulic loading on the sector gate. The forces required to open and close the sector gate for both normal and reverse head are affected by the gate lip shape. Figure 59 contains a plan schematic of the typical structural members of a sector gate.

Figure 59. Plan view of the typical structural members of a sector gate. (Image reproduced from HQUSACE 2006, B-5. Public domain.)

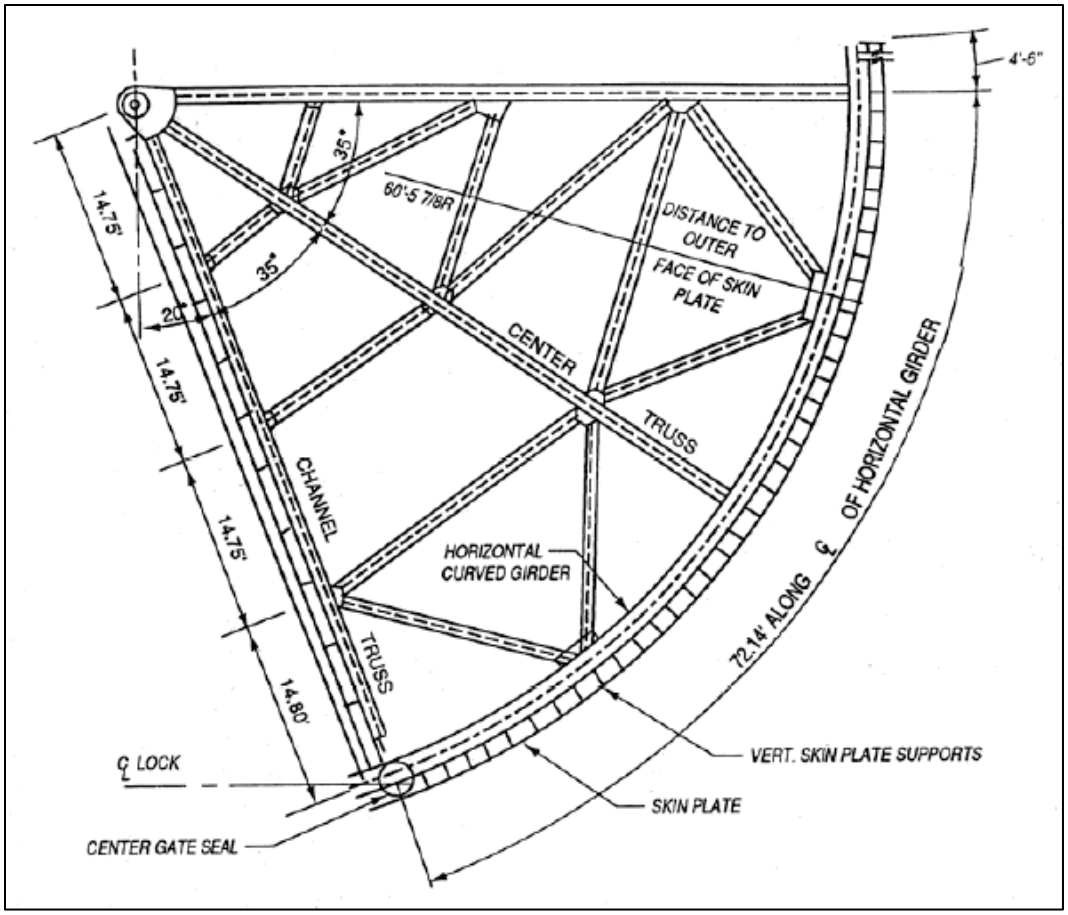

ETL 1110-2-584 (HQUSACE 2014, Sections 3.4.2 and 3.4) describes the applicable loads the design requirements for HSS. EM 1110-2-2702 (HQUSACE 2000, rescinded) states that all loads that HSS will be subjected to shall be considered in the design. These loads include gravity (i.e., weight, ice, mud), hydrostatic, hydrodynamic, operational and machinery, floating and thermal ice, debris, vessel impacts, and environmental (typically wind and temperature).

5.1.3 EM 1110-2-2703, *Lock Gates and Operating Equipment*

EM 1110-2-2703 (HQUSACE 1994, Chapter 4) provides guidance on the design and operation of sector gates. The basic sector gate leaf frame consists of three horizontal trusses and three vertical trusses, each with similar structural members. The top and middle horizontal frames are designed based on the water load and a vessel impact load. The vessel impact load is 125 kips being applied at any point on the horizontal beam and

at any panel point on the canal side of the truss. The bottom horizontal frame is designed for water load only.

The normal operating forces on sector gates are primarily caused by friction on the trunnion and hinge pin, forces on the seal bracket, bottom friction, and hydraulic loads. Torque curves are provided in EM 1110-2-2703 (HQUSACE 1994, Plate B-81) and were reproduced from Oswalt (1970). Bastian (1971; MP H-71-4) is referenced for establishing reasonable values of hinge and pintle friction.

5.1.4 EM 1110-2-2610, *Mechanical and Electrical Design for Lock and Dam Operating Equipment*

EM 1110-2-2610 (HQUSACE 2013, Chapter 5) contains design guidance for sector gate operating machinery. "The design of a sector gate ensures that the hydrostatic forces across the skin plate do not directly counteract the operating machinery" (5-1) and, therefore, are better suited for operation with differential heads. The first sector gate designs experienced operational difficulty. Prototype tests indicated that the "hydrodynamic forces on the vertical steel member near the nose of the gate created much greater loads than anticipated during design" (5-5). Appendix D contains sample calculations for determining closing loads with a reverse head.

5.2 Hydraulic Data Collection for Sector Gates

The reliability analysis for the sector gate requires that the mean and standard deviation of the loads be determined, and hydraulic data are needed to develop these values. The primary hydraulic forces on the sector gate used as a lock gate are the hydrostatic, hydrodynamic, and wind-induced wave forces. These forces depend on the navigation canal water levels. Historical data for these levels are needed to develop the statistics required for the analysis.

Sector gates are often used in areas where both coastal and riverine environments are experienced by the gates. The higher water levels occur during flood events in the riverine environment. The higher water levels in the coastal environment occur during storm events, with the highest levels usually associated with hurricanes. Both of these conditions need to be evaluated to determine the maximum head differential. The nominal loads needed for the statistical analysis will generally occur with average water levels. The mean and standard deviation for these water levels need to be

determined. Calcasieu Lock, on the GIWW located near Lake Charles, Louisiana, was selected as an example of a sector gate design. Appendix D contains the methodology used to determine the hydraulic data and the statistical data reduction.

5.3 Hydraulic Loading for Sector Gates

Hydraulic loads consist of all loads due to water. These include hydrostatic (i.e., weight of water), hydrodynamic (i.e., load due to flowing water), and wave action. These are the primary hydraulic loads, in terms of magnitude and frequency, experienced by the HSS. Vibrations caused by flowing water, constricted flow, and water hammer are also considered hydraulic loads.

5.3.1 Hydrostatic Load for Sector Gates

The hydrostatic load is due to the hydraulic head across the sector gate. The load on the gate results from the hydrostatic pressure acting on the gate. The maximum hydrostatic load probably occurs when the sector gate is in the closed position, the lock is dewatered for maintenance, and bulkheads are not used (Figure 60*a*). If bulkheads are used to dewater the lock, the maximum hydrostatic load would result from the maximum difference between the water level on either side of the gate (Figure 60*b*). During a storm condition, the water surface is most likely at the top of the gate or even overtopping the gate, and the head across the gate would be minimal. A sector gate located in an area subject to storm surge could have a reverse head condition (Figure 60*c*).

The mean hydrostatic pressure on the sector gate is expressed as γH, where γ is the unit weight of water, and H is the average total head on the gate. Chapter 2 provided a detailed description of the hydrostatic pressure and hydrostatic force associated with a gate.

Figure 60. Hydrostatic pressure distribution for a sector gate.

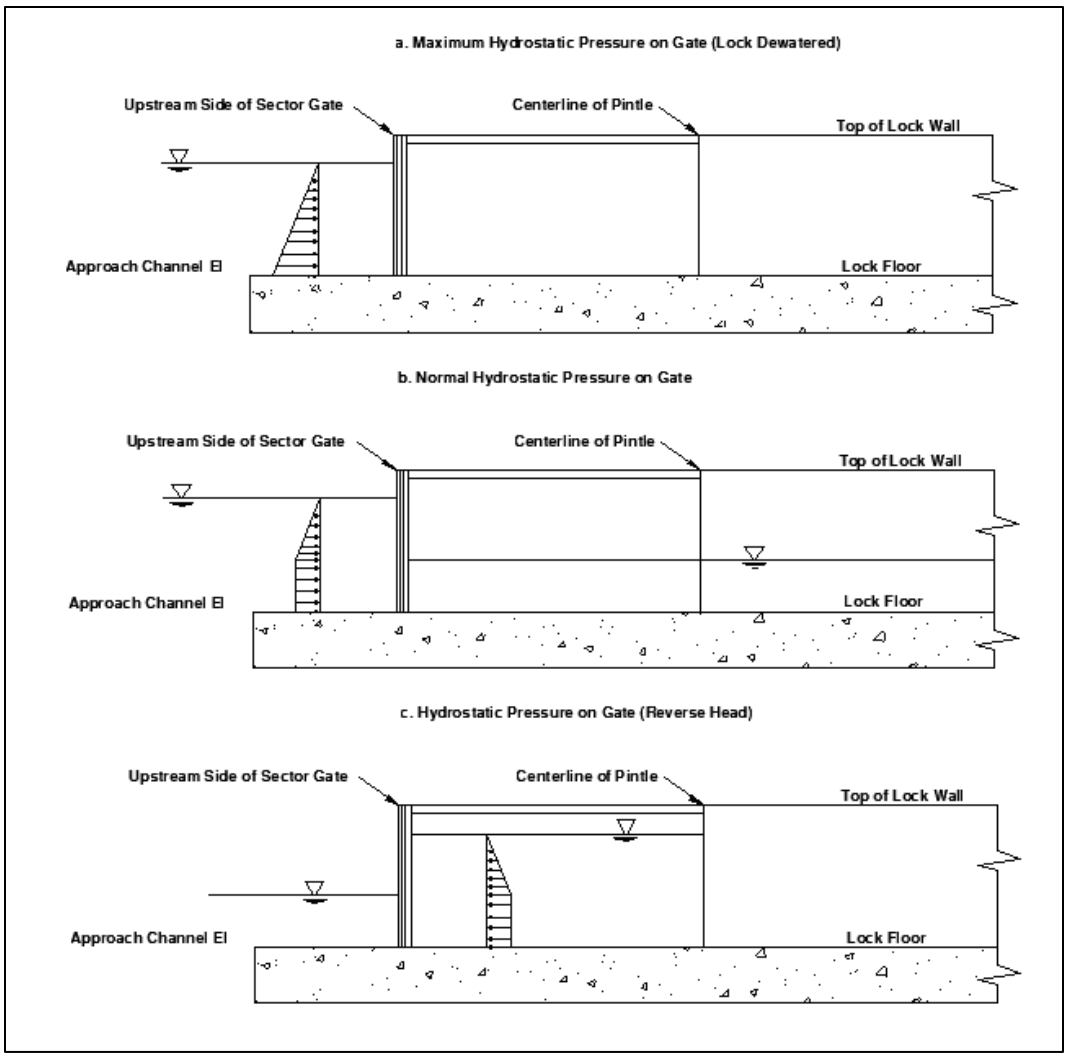

5.3.2 Wave Load for Sector Gates

Wave loads are project specific and are considered for projects that experience significant wind and fetch. The wave load for the sector gate in the closed position is similar to that discussed for the other HSS. Chapter 2 contains a detailed description of the procedures used to develop the wind-induced wave load. Appendix D provides a design example problem for determining wind-induced wave loads for the east sector gate of the Calcasieu Lock on the GIWW.

5.3.3 Hydrodynamic and Hydrostatic Load for Sector Gates

The normal operating forces on sector gates are primarily caused by friction on the trunnion and hinge pin, forces on the seal bracket, bottom

friction, and hydraulic loads (HQUSACE 1994). These hydraulic loads on the gate include the gate drag during opening or closing and also hydrostatic loads that occur due to slow operation and the head differential. The drag is caused primarily by the projected width of the miter beam, skin plate, and seal bracket. Because operation of the sector gate is fairly slow, there are hydrostatic pressure influences on the gate during opening and closing. According to Bastian (1971), the hydrostatic loads on both the vertical I-beams next to the leaf nose and the vertical seal bracket are a high percentage of the total forces developed on the sector gate.

EM 1110-2-2703 (HQUSACE 1994) states that loads due to reverse head conditions will usually establish the size of the operating machinery to be used; however, normal heads should be checked. A reverse head occurs when the water level on the frame side of the sector gate is higher than that on the skin plate side of the gate and is typically due to drainage basin discharge, tide conditions, and the direction and force of the wind.

Under reverse head conditions, the loads due to flowing water tend to close the gate. Oswalt (1970) showed that these loads increased with gate openings up to 5–7 ft and then tended to slowly decrease as the gate opening increased. EM 1110-2-2703 (HQUSACE 1994) indicated that a gate opening of 6 ft can be used to predict peak torque for various lower pool and reverse head conditions and that "the major loads on the gate are caused by structural members in the immediate vicinity of the skin plate at the miter noses of the gate leaves and by the side seal bracket that blocks side flow at the recess edge of the skin plate" (5-5).

Oswalt (1970) and Oswalt and Murphy (1971) can be used as guides to determine the operating loads for a sector gate if the design of the gate is similar to those they tested. EM 1110-2-2703 (HQUSACE 1994) recommends that if a gate design is different from those studied, then model studies should be performed to help develop the design loads. Figure 61 presents the effects of head on the closing pintle torque for 5 and 7 ft gate openings, as presented in Oswalt and Murphy (1971). The pintle torque shown in Figure 61 was measured in a 1:20-scale model (magnitudes have been converted to prototype values in figure) that minimized forces due to friction, so these values are considered to be hydraulic load only. The tests were performed with a steady-state flow at a fixed gate opening. Gate openings are usually reported as distance from the tip of the gate leaf perpendicular to the longitudinal centerline of the gate bay multiplied by 2.

For example, a 10 ft gate opening would mean the tip of each gate leaf is 5 ft from the longitudinal centerline of the gate bay.

Figure 61. Head versus pintle torque for Type A1 sector gate design with a 12 ft deep lower pool and gate openings (G_O) of 5 and 7 ft. (Image adapted from Oswalt and Murphy 1971.)

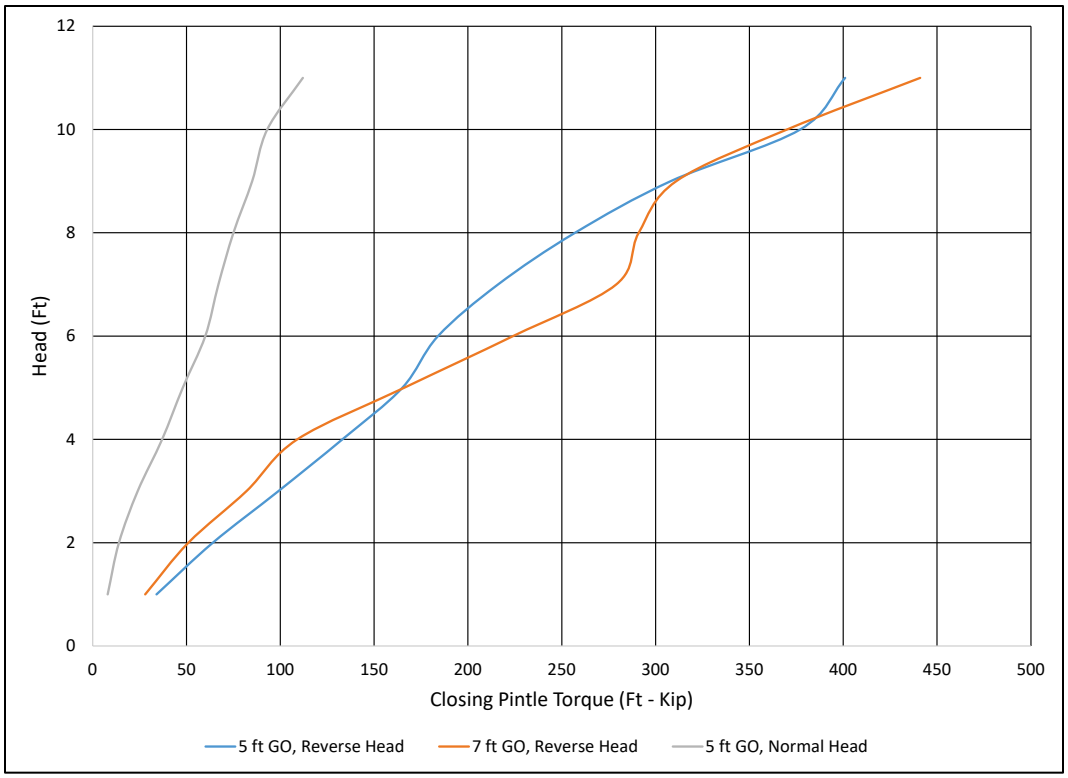

EM 1110-2-2703 (HQUSACE 1994, Appendix B, plate B-82, sheets 1–3) presents a design example for determining the total pintle torque on a sector gate. The example uses results from Oswalt and Murphy (1971) with a 5 ft reverse head and a 16 ft lower pool depth to determine the hydraulic load and offers guidance on how to determine the total frictional load.

5.3.4 Probabilistic Characterization of the Hydrostatic and Hydrodynamic Loads for the Sector Gate

The statistics for the hydraulic loads on the sector gates need to be determined for the LRFD analysis.

5.3.4.1 Probabilistic Characterization of the Hydrostatic Load for the Sector Gate

The dispersion of the hydrostatic load is a result of the changes in the water levels on the upstream and downstream sides of the gate. The maximum hydrostatic load occurs with the maximum head on the gate. For the

sector gate, this will most likely occur if the lock is undergoing maintenance and bulkheads are not used (Figure 60*a*). The computation of the fluctuations in hydrostatic load on the gate require the selection of an appropriate range of upper and lower water-level combinations. Appendix D provides a design example of the statistics developed for the Calcasieu Lock sector gate, which can be used in the LRFD analysis.

5.3.4.2 Probabilistic Characterization of the Hydrodynamic Load for the Sector Gate

The dispersion of the hydrodynamic load on the sector gate is also due to the changes in the water levels, which give different values of head and the gate operating rate. The gate operating rate is usually reported as the time required for the gate to move from the open to the closed position. The example loads shown in Figure 61 were obtained with the sector gate in stationary positions. EM 1110-2-2703 (HQUSACE 1994, plate B-82, sheets 1–3) can be used to determine the hydrodynamic dispersion of the total pintle torque on a sector gate for the selected range of upper and lower water levels. The choice of the range of pool els and gate operating speeds need to be selected by the designer performing the LRFD analysis.

5.3.5 Summary of Hydraulic Loads for the Sector Gate

The hydraulic loads on the sector gate consist of hydrostatic, wave, and hydrodynamic loads and certain temporary loads. The loads should be combined as appropriate to give the maximum expected load. The wind-to-wave force conversion can, in some cases, make a significant contribution to the combined loads. The authors of this report recommend that wind-induced wave forces be determined using the Goda (2010) design procedure that was discussed in previous chapters. A procedure that uses either existing computer programs or a new code to compute the hydrodynamic loads needs to be developed to improve the design process.

6 Loadings Applied to Lock Miter Gates

This chapter focuses on hydraulic loads applied to lock miter gates. Miter gates are used by USACE for many navigation locks with moderate to high lifts. Miter gates have two sides; each side is typically referred to as a *leaf*, so the entire gate is a double-leaf miter gate. This type of gate is favored because it can be opened and closed faster and has lower maintenance costs than other types of lock gates. A disadvantage is that it cannot operate in an emergency condition when flow is uncontrolled into the chamber. The major hydraulic loads are hydrostatic, hydrodynamic, and those due to wind-generated waves. These structures also require seals to prevent excessive leakage along the bottom.

6.1 Existing Guidance for Miter Gates

The two sides of the miter gate form a three-hinged arch angled upstream. The arch shape is beneficial for spanning large distances between the lock walls. When the gate is in the closed position under head, each side or leaf bears on a lock wall and at the center on the other leaf. The angle of the leaf in the closed position is usually 1:3. Figure 62 shows a view of the upstream miter gate looking downstream of the new McAlpine Lock during construction.

Figure 62. View of the upper miter gate during construction of the new McAlpine Lock.

6.1.1 ETL 1110-2-584, *Design of Hydraulic Steel Structures*

Miter gates are framed either vertically or horizontally. Vertically framed gates have been used when the height-to-width ratio of the leaf is less than 0.5. The gate resists the water pressure using a series of vertical girders attached to a skin plate. The girders span from the sill at the bottom to a horizontal girder at the top. The skin plate of a horizontally framed gate is supported by horizontal members that are either straight girders acting as beams or circular arches. Each horizontal member is supported by the vertical quoin post near the lock wall side and at the miter post on the other end. The hydrostatic load is transmitted through the girders to the quoin blocks and into the lock walls.

When they are in the open position, the miter gates are located in recesses in the lock walls. These recesses generally extend lower than the bottom of the gate to help prevent operating problems due to drift and sediment accumulations. Locks that experience icing conditions sometimes have larger recesses for easier ice removal, and air bubbler systems are recommended to clear ice from the gate recess. Table 11 provides the load factors for miter gates. ETL 1110-2-584 (HQUSACE 2014, Chapter 3 and Appendix C) describes the design requirements for gates using LRFD. Loads that apply to miter gate design include self-weight, gravity, hydrostatic and hydrodynamic, operating, barge and other impact, ice, and earthquake loads.

Table 11. Load factors for miter gates. (Table adapted from ETL 1110-2-584, HQUSACE 2014, C-3.)

Load Cases			Loads/Load Factors							
			D	*G*	H_s	H_d	*Q*	EV	IM	EQ
Limit State	Description	Case	γD	γG	γHs	γHd	γQ	γEV	γIM	γEQ
Strength I	Gate closed	1a	0	0	1.4	0	0	0	0	0
Strength I	Gate closed	1b	0	0	1.4	1.0	0	0	0	0
Strength II	Gate open	2	1.2	1.6	0	1.0(1)	1.2(1)	0	0	0
Extreme I	Gate closed	3	0	0	1.4	0	0	0	1.0(1)	1.0(1)
Fatigue I	Finite life	4a	0	0	1.0	1.0	0	0	0	0
Fatigue II	Infinite life	4b	0	0	1.0	1.0	0	0	0	0

Notes: (1) Select one at a time; γ = load factor; *D* = self-weight (dead load); *G* = gravity load, which includes weight of the gate (IM) mud weight (*M*), and ice weight (*I*); H_s = hydrostatic load; H_d = wave load; *Q* = machinery load; EV = wind load; IM = ice-impact load; EQ = earthquake load

6.1.2 EM 1110-2-1604, *Hydraulic Design of Navigation Locks*

According to EM 1110-2-1604 (HQUSACE 2006, Figure 4-1), the lower miter gate swing requires about 60 ft for a 110 ft clear width lock (see also

EM 110-2-2703, HQUSACE 1994). Design practice is to provide about 10 ft of space for obstructions and clearance at the upper sill and clearance at the lower leaf while the leaf is approaching the fully recessed position. Figure 63 shows some of the components of a miter gate.

Figure 63. Upstream elevation and sectional view of a miter gate. (Image reproduced from EM 1110-2-1604, HQUSACE 2006, B-3. Public domain.)

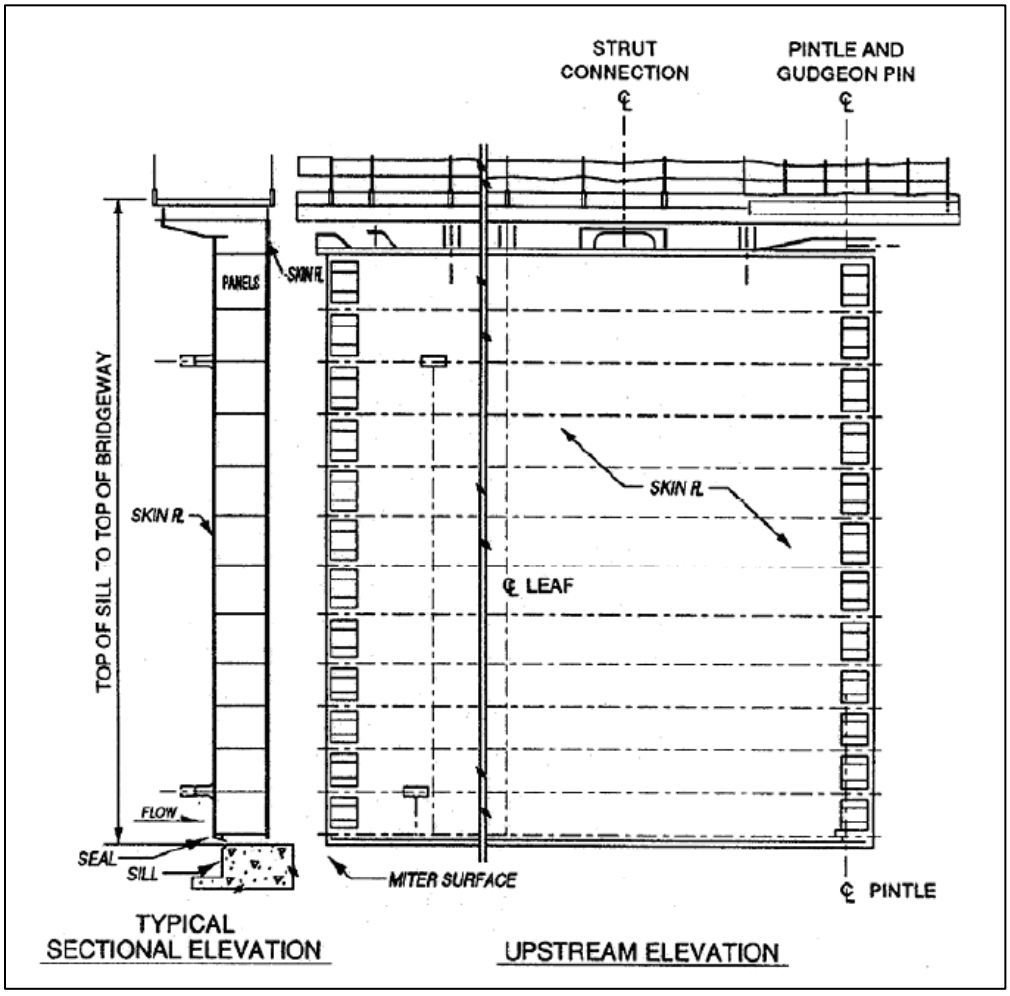

6.1.3 EM 1110-2-2703, *Lock Gates and Operating Equipment*

EM 1110-2-2703 (HQUSACE 1994) states that vertically framed miter gates are not recommended for new construction. The slight increase in cost is offset by the greater rigidity of the horizontally framed design. The quoin end of a miter gate leaf is held vertical by the pintle and gudgeon pin, which can leave the miter end free to twist out of vertical alignment. The deadweight of the leaf along with ice or mud can also contribute to the gate twisting. To help prevent this twisting, keep the leaf in vertical alignment while stationery, and to eliminate excessive deflection during

operation, diagonals are used on the downstream face of the horizontally framed miter gate leaf.

The primary structural elements of a single gate leaf consist of a series of horizontal girders, connected vertically by a skin plate, two end diaphragms, and a number of intermediate diaphragms. The horizontal girders act as a series of three-hinged arches that transmit the water pressures to the lock walls through the quoin hinges.

EM 1110-2-2703 (HQUSACE 1994, Section 2-1) provides guidance on the stress analysis of a horizontally framed miter gate. Figure 64 shows a schematic of the parameters used in the analysis of the horizontally framed miter gate in a mitered position. The horizontal girder in the figure is half of the three-hinged arch and is acted upon by water pressure due to the differential head. The differential head varies in magnitude with the depth of the girder below the water surface and the panel width it supports.

Figure 64. Schematic of a horizontally framed miter gate in the mitered position and the symbols used to describe the reactions.

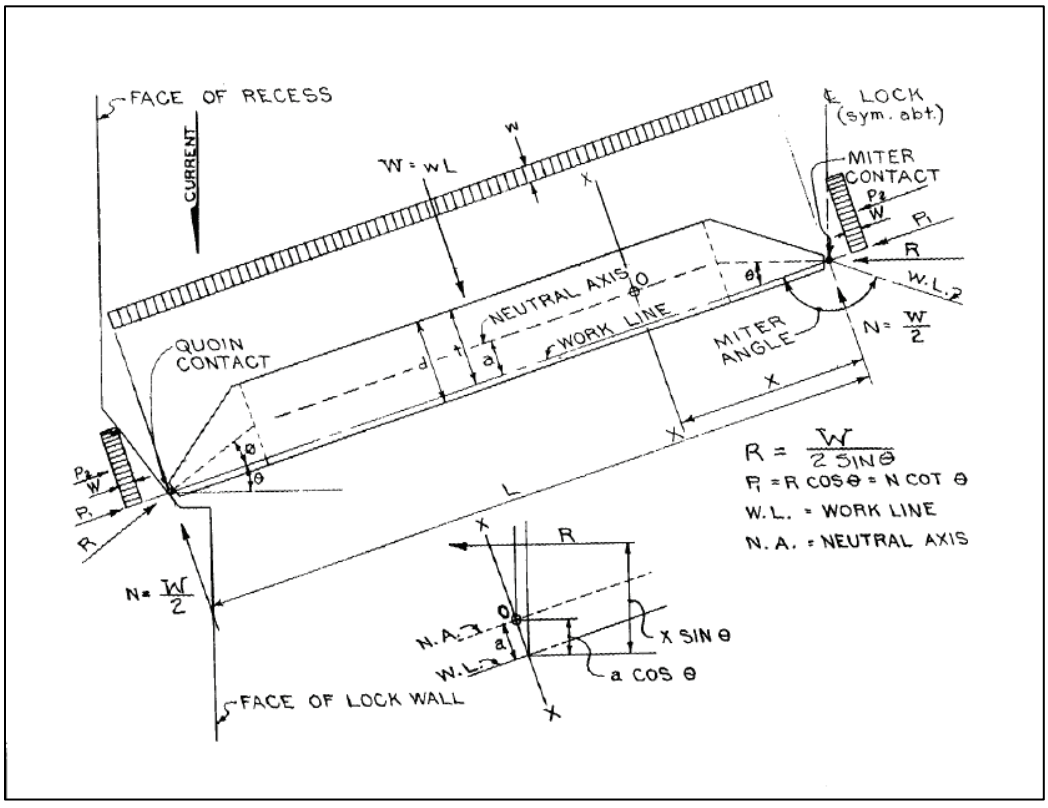

Note: *R* is the reaction of the girder at the wall quoin and miter blocks, *N* is the component of *R* perpendicular to work line of leaf, and P_1 is the component of *R* parallel to work line leaf. P_2 is the corresponding water force on the end of each girder, determined from the water pressure on the surface extending from the contact point to the upstream side of the skin plate, and *W* is the total corresponding water force on each girder, determined by the pressure and the length of the leaf, adjusted by the effective width of the damming surface.

In Figure 64, the three-hinged arch formed by the two leaves is symmetrical about the center line of the lock. Therefore, the miter-end reaction, *R*, is perpendicular to the lock center line. If *R* is extended to intersect the resultant water load, *W*, and from this point of intersection, a line is drawn to the point of contact at the quoin end, this line is the working line that connects the quoin and the miter contact points. The angle θ is the complement of one-half of the miter angle. *R*, *N*, and P_1, are related to the total water force, *W*, as shown here and in Figure 64:

$$R = \frac{W}{2\sin\theta}, \tag{107}$$

$$N = \frac{W}{2}, \tag{108}$$

$$P_1 = R\cos\theta = N\cot\theta. \tag{109}$$

EM 1110-2-2703 (HQUSACE 1994) also provides guidance for loads on the operating machinery. It states that operating loads on the miter gate machinery should be derived by hydraulic similarity from test data obtained from model studies. The model study available for design is included in Technical Report 2-651 (WES 1964). Normal operating hydraulic loads on miter gates are primarily caused by submergence, the speed of the gate, and the clearance under the gate.

6.1.4 EM 1110-2-2602, *Planning and Design of Navigation Locks*

EM 1110-2-2602 (HQUSACE 1995b) states that miter gates can be designed for operating times of 1 to 2 min. The sills for horizontally framed miter gates are used to provide a sealing arrangement and to form the damming surface below the gate. The horizontally framed miter gate sills are not required to resist any part of the gate thrust because the entire thrust load is transferred to the lock walls. Vertically framed miter gate sills differ in design based on the method of load application from the gate. A portion of the vertically framed gate load is taken by the sill.

6.1.5 EM 1110-2-2610, *Mechanical and Electrical Design for Lock and Dam Operating Equipment*

EM 1110-2-2610 (HQUSACE 2013) provides guidance on the design of miter gate operating machinery. It states that "the forces to be overcome by the gate-operating machinery are friction, wind loads, surges, hydraulic drag forces, and head differential created by the gate leaves moving

through the water" (4-14). The friction and wind loads can only be estimated and are generally small compared to the hydraulic loads. The manual indicates that the evaluation of operating forces caused by hydraulic drag and head differential could be made through tests on existing lock gates, although experience has shown that it is difficult to make accurate load measurements in the field. In addition, it is not practical to vary field operating conditions with regard to gate speed and gate submergence.

Operating loads on the miter gate machinery should be derived by hydraulic similarity from test data obtained from model studies. EM 1110-2-2610 (HQUSACE 2013) cites the model study by WES (1964). Lejeune (1974) demonstrated an analytical means to calculate gate operating forces. Appendix C of this manual includes an example design for computing pintle torque for various lock designs and operating conditions.

6.2 Hydraulic Data Collection and Statistical Data Reduction for Mean Loading and Dispersion for the Miter Gate

The reliability analysis for the miter gate requires that the mean and standard deviation of the loads be determined. Hydraulic data are needed to develop these values. The hydraulic data required for the miter gate are the upper and lower pool els. The wind conditions would also need to be evaluated to determine the wind-induced wave loads. The miter gate is exposed to other wave loads due to overfill, overempty, and propeller wash. Historical data are necessary for developing the samples and statistical data required for the analysis.

6.2.1 Upper Pool El

To determine the hydraulic loads, the upper pool el is needed. Most miter gates operate under conditions in which the maximum head differential between the upper and lower pools probably occurs during normal operations. When above-normal pools occur, the lift is usually less than a normal lift. Therefore, the nominal loads needed for the statistical analysis will generally occur with a near-normal upper pool el. The maximum head differential is needed to develop the hydrostatic load. The upper pool el also effects the hydrodynamic (i.e., water resistance) load during gate operations. The mean and standard deviation for the upper pool needs to be determined.

In higher lift locks, the lower miter gate is often much larger than the upper miter gate. The Barkley Lock on the Cumberland River, which has a normal lift of 57 ft, was chosen as a design example for a miter gate. Appendix E contains the methodology used to determine the hydraulic data and the statistical data reduction.

6.2.2 Tailwater or Lower Pool El

The TW El is also needed to develop the hydraulic loads based on the maximum head differential and the hydrodynamic loads for the lower miter gate.

6.3 Hydraulic Loading for the Lock Miter Gate

Hydraulic loads consist of all loads due to water. These include hydrostatic (i.e., weight of water), hydrodynamic (i.e., load due to flowing water), and wave action (i.e., load due to wind, lock filling and emptying operations, and propeller wash). Vibrations caused by flowing water, constricted flow, and water hammer are also considered hydraulic loads.

6.3.1 Hydrostatic Load for the Miter Gate

The maximum hydrostatic load for the upper miter gate occurs when the lower pool is below the upper miter sill or when the lock is dewatered and the upper gate is used as the damming surface. The hydrostatic pressure is the difference in the upper pool and the bottom el of the upper miter gate, which is probably close to the upper sill el. For a project where the lower pool is higher than the upper lock sill, the hydrostatic load on the upper miter gate is due to the hydraulic head across the miter gate. The load is due to the hydrostatic pressure caused by the difference in water level on each side of the miter gate; this is also the case for the lower miter gate.

The same method for developing the hydrostatic load for the other HSS is applicable to the miter gate. Chapter 2 provides a detailed explanation of the hydrostatic load. The maximum hydrostatic pressure on the structure is expressed as γH (Equation 10, repeated here), where γ is the unit weight of water, and H is the head on the miter gate:

$$p = \gamma H.$$

To obtain the force, the hydrostatic pressure is multiplied by the area the pressure is acting on. The hydrostatic force per unit width of miter gate is given by Equation (12), which is repeated here:

$$H_s = \frac{1}{2}\gamma H^2.$$

The location of the resultant hydrostatic force, H_s, is H/3 above the bottom of the hydrostatic pressure distribution. Figure 65 shows a schematic of the hydrostatic pressure distribution along a section that is normal to the skin plate of the upper lock gate in the mitered position with the lower pool below the upper sill el.

Figure 65. Section view of the hydrostatic pressure distribution normal to the skin plate of the upper gate in the mitered position.

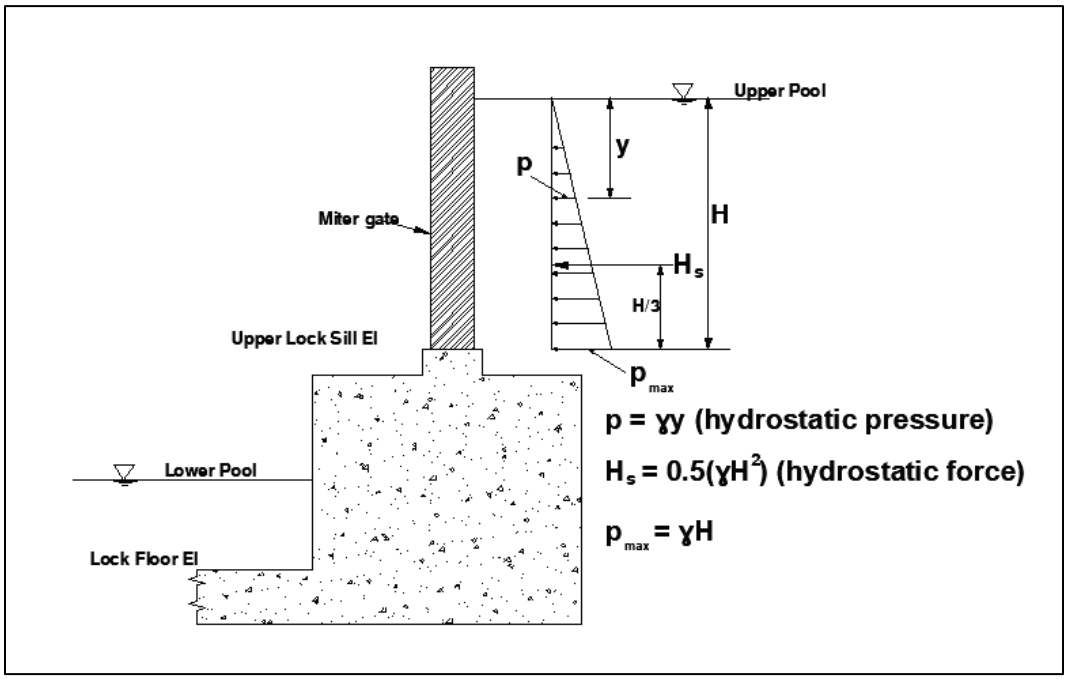

Figure 66 shows a schematic of the hydrostatic pressure distribution along a section that is normal to the skin plate of the lower lock gate in the mitered position. The location of H_s is determined by locating the centroid of the hatched area.

Figure 66. Section view of the hydrostatic pressure distribution normal to the skin plate of the lower gate in the mitered position.

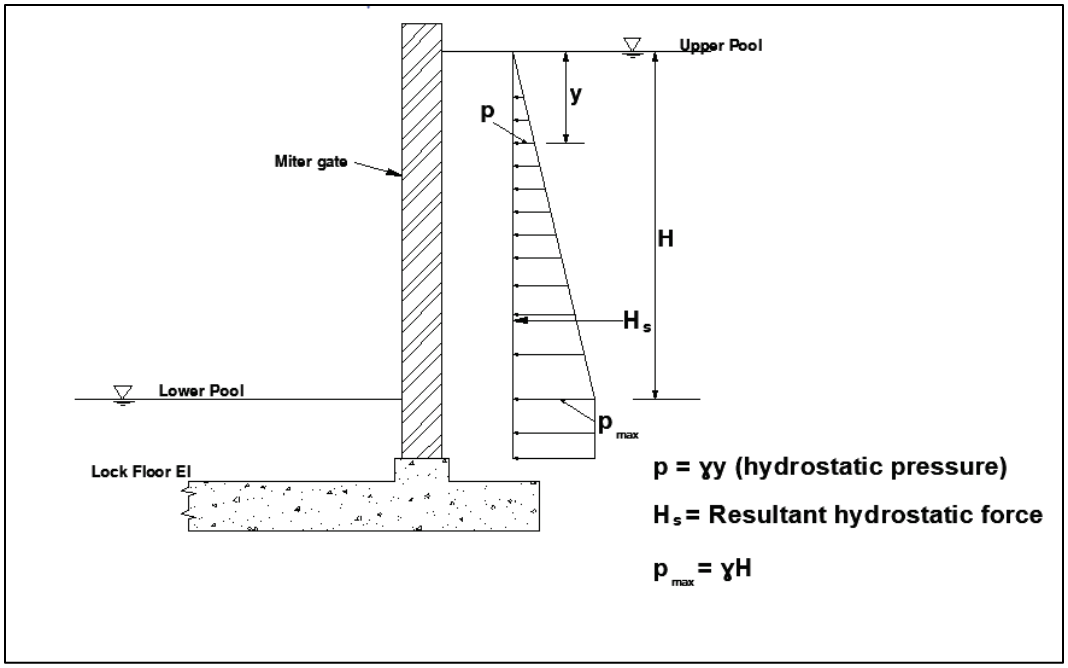

6.3.2 Wind-Induced Wave Load for the Miter Gate

Wind-induced wave loads are project specific and are considered for projects that experience significant wind and fetch. The same procedures used for the other HSS can be applied to the miter gate. These procedures are described in Chapter 2. The Goda (2010) procedures are the recommended guidance for wind-induced wave loadings for inland navigation projects. The Goda wave pressure distribution procedure for the miter gate is the same as that for the vertical-lift spillway gate shown in Figure 45. Appendix E contains an example procedure for computing the wave pressure on the miter gate using the Goda procedure.

6.3.3 Temporary Hydraulic Wave Load for Miter Gates

Davis (1989) stated that temporary loads caused by ship waves, tides, propeller wash, seiches, surges, or a combination of these can increase the maximum direct static load on the miter gates. A reverse head almost always occurs as a result of temporary conditions. He also stated that, "If the temporary load produces a reverse head on the gate of a duration greater than 30 seconds, its full value should be considered for design purposes" (59). Davis suggested that a temporary load of 1.25 ft for durations exceeding 30 sec should be used as a minimum value for the design of miter gate operating machinery. He also suggested that a minimum value of 2.5 ft

should be used for temporary loads for direct or reverse heads in the structural design of the miter gate. He indicated that the most serious temporary loading condition usually occurs as a result of reverse heads that are produced by overfilling and overemptying of the lock. Near the end of a lock filling operation, the momentum of the flow moving in the culverts causes the lock water surface to momentarily rise higher than the upper pool. The height of the rise above the upper pool is the overfill. At the maximum rise, the flow in the culvert reverses, and the lock water surface falls and then rises again above the upper pool. The second rise is lower than the first, and this pendulation of flow continues until damped by the friction in the culverts. The same condition occurs during lock emptying, with the lock water level falling below the lower pool. For initial filling and emptying system design, EM 1110-2-1604 (HQUSACE 2006) recommends a value of 1 ft for overfill.

6.3.4 Combined Hydrostatic, Wind-Induced Wave Loads, and Temporary Loads for Miter Gates

Wind-induced wave loads and temporary loads are project specific and are considered for projects that experience conditions described in Sections 6.3.2 and 6.3.3. The hydrostatic and wind-induced wave loading can be developed using procedures similar to those used for the other HSS provided in previous chapters. The temporary loads are determined based on project-specific conditions.

6.3.5 Hydrodynamic Loads for Miter Gates

The hydrodynamic loads on lock miter gates are generally included in descriptions of the lock gate operating forces and the hydraulic resistance of the gate during opening or closing. WES (1964) is referenced several times in the existing USACE guidance documents concerning operating machinery requirements and operating forces. In this laboratory study, the operating forces on a set of miter gates were measured for different linkage configurations. The effects of chamber length, the bottom clearance of gates, the presence of barges in the lock chamber, and the nonsynchronous operation of the gate leaves were also studied. The laboratory miter gates were constructed to minimize frictional resistance.

An observation of the torque measurements revealed that the maximum hydraulic resistance to operation of the miter gates occurred as the leaves entered the mitered position. This supports the supposition that the

primary cause of loads on the operating machinery is the head differential across the gate leaf. If the hydraulic drag were the dominant influence, then the peak load would be expected to occur when the angular movement of the gate was at its highest. WES (1964) summarized some of their laboratory results pertinent to hydrodynamic loads as follows:

- "Peak hydraulic resistance to operation of the miter gate was observed as the leaves entered and left the mitered (closed) position with the maximum resistance occurring as the leaves entered the mitered position.
- "An increase in submergence of the gate leaves [depth from water surface to bottom of gate] or speed of operation resulted in increased hydraulic resistance.
- "Hydraulic resistance increased as the bottom clearance of the gate leaves decreased" (vii).

Lejeune (1974) listed three resistant forces encountered by the miter gate during opening and closing. These were mechanical resistant forces, hydrodynamic resistant forces, and resistant forces due to mud, debris, ice, wind, waves, and other forces that might impede the gate (these are project specific). He indicated that the hydrodynamic-resistant forces were of primary importance and categorized them as forces due to the difference in water level on each side of the gate during operation and the force that the water opposes to the rotary motion of the gate. Lejeune presented a method for computing the hydrodynamic forces of a miter gate during operation.

The current method used by USACE to determine the operating forces on a miter gate could possibly be updated based on the advances made in CFD modeling.

6.3.6 Probabilistic Characterization of the Hydrostatic and Hydrodynamic Loads for the Miter Gate

The statistics for the hydraulic loads on the miter gates need to be determined for the LRFD analysis.

6.3.6.1 Probabilistic Characterization of the Hydrostatic Load

The dispersion of the hydrostatic load is a result of the changes in the upper and lower pool els. The maximum hydrostatic load occurs with the

maximum head on the gate. For a navigation project, when the upper pool is above normal, so is the lower pool, and the combination of maximum upper pool and minimum lower pool is very unlikely to occur. The computation of the fluctuations in hydrostatic load on the gate are the result of the selection of an appropriate range of upper and lower pool combinations. Appendix E of this report provides a design example of the statistics developed for the Barkley Lock lower miter gate, which can be used in the LRFD analysis.

6.3.6.2 Probabilistic Characterization of the Hydrodynamic Load

The dispersion of the hydrodynamic load on the miter gate is due to the changes in the lower pool els, which give different values for submergence and the gate opening rate. The gate opening rate is usually reported as the time required for the gate to move from the mitered to the recessed position. USACE-LRN personnel computed example loads on the gate operating machinery when the gate was being designed. These example loads can be found in Design Memorandum No. 9 (USACE-LRN 1958, Table I-13). This example is for one submergence and one gate opening rate. The choice of the range of pool els and gate operating speeds would need to be selected by the designer performing the LRFD analysis.

6.3.7 Summary of Hydraulic Loads for Miter Gates

The hydraulic loads on the miter gate consist of hydrostatic, wave, and hydrodynamic loads and certain temporary loads. The loads should be combined as appropriate to give the maximum expected load. The wind-to-wave force conversion can, in some cases, make a significant contribution to the combined loads. The authors of this report recommend that wind-induced wave forces be determined using the Goda (2010) design procedure that was discussed in previous chapters. A procedure using either existing computer programs or a new code to compute the hydrodynamic loads needs to be developed to improve the design process.

7 Loadings Applied to Submergible Tainter Gates for Locks

This chapter describes the characteristic loads associated with submergible tainter gates used as the upper lock gate and summarizes the dispersion in these applied loads and the distribution of pressures.

7.1 Existing Design Guidance for Submergible Tainter Gates for Locks

The submergible tainter gate has been used as a spillway gate and a lock gate, usually at the upstream end of the lock chamber. The submergible tainter gate used as a spillway gate has the advantage of being able to conveniently flush ice and debris downstream. Operational problems and excessive vibrations resulted in very limited use of the gate in a submerged condition. This chapter presents the loads used for a submergible tainter used as the upper lock gate.

7.1.1 ETL 1110-2-584, *Design of Hydraulic Steel Structures*

The submergible tainter gate that is used for lock gate applications is raised to close the chamber in preparation for lock filling and lowered to allow the vessel in the chamber to travel upstream. The end frames of the gate are recessed in the lock walls and do not obstruct the usable lock width. This type of gate might be less expensive than a conventional miter gate and may allow a reduction in the length of the approach channel because the miter gate requires upstream recesses. There are primarily two potential issues with this type of gate. The first is skewing of the gate during opening and closing, and the second is that it is susceptible to more damage if hit by vessels using the lock. These issues can be minimized with proper design and operational practices.

Figure 67 shows a cross-section view of a submergible tainter gate used as an upper lock gate, and Figure 68 shows a typical end frame and lock recess. The configuration and design of the submergible tainter gate used as an upper lock gate is similar to those for a tainter gate used as a spillway gate, as described in Appendix D of ETL 1110-2-584. Because navigation locks are typically wider than spillway gate bays, the main horizontal structural members will be trusses or plate girders. Also because of lock clearance requirements, the trunnions, struts, and lifting devices must be

located in recesses in the lock walls. Guidance for the STG is also provided in Chapter 2 of this report.

Figure 67. Cross section of a submergible tainter gate used as an upper lock gate. (Image reproduced from HQUSACE 2014, D-48. Public domain.)

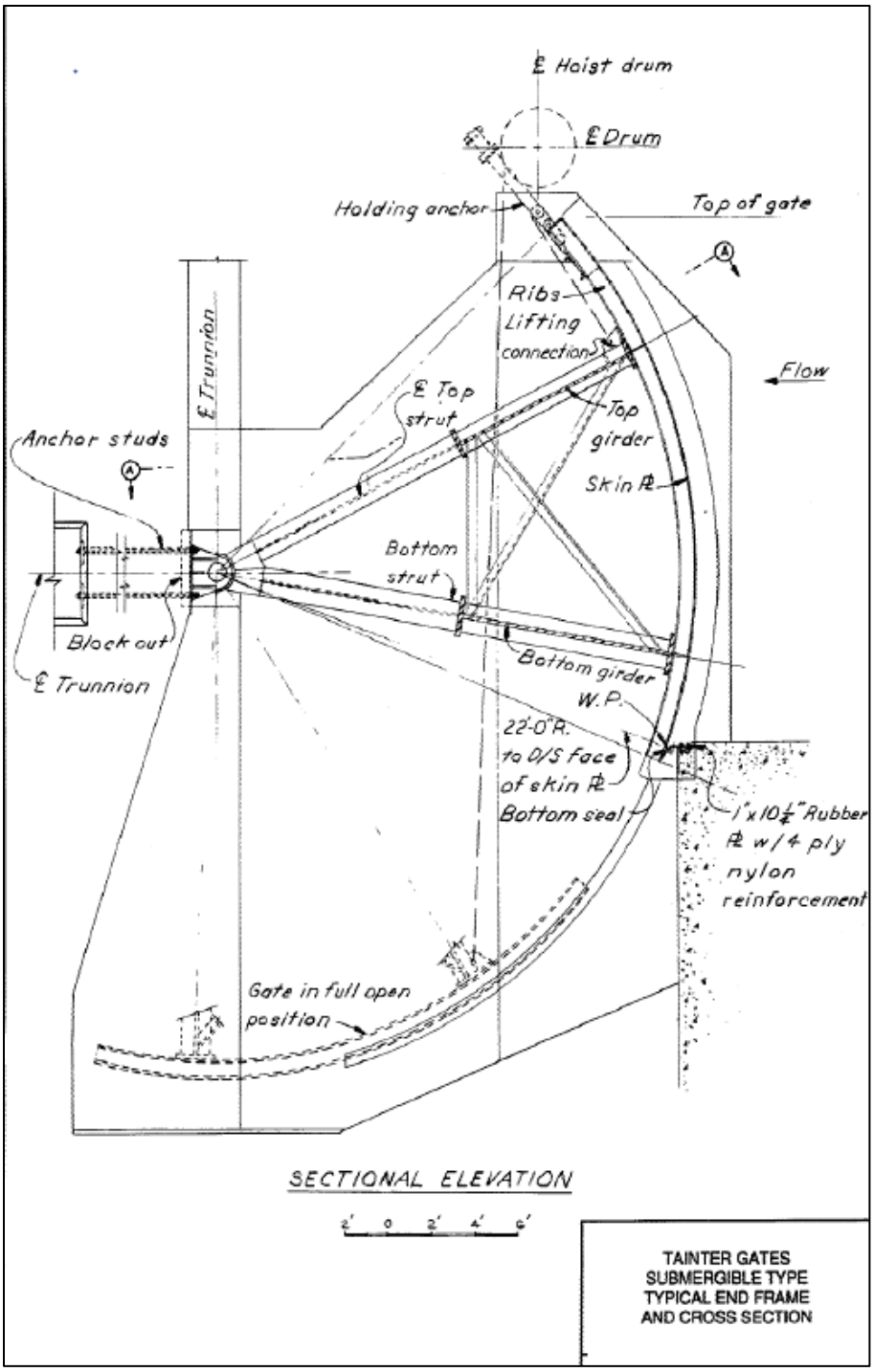

Figure 68. End frame and lock recess for a submergible tainter gate. (Image reproduced from HQUSACE 2014, D-49. Public domain.)

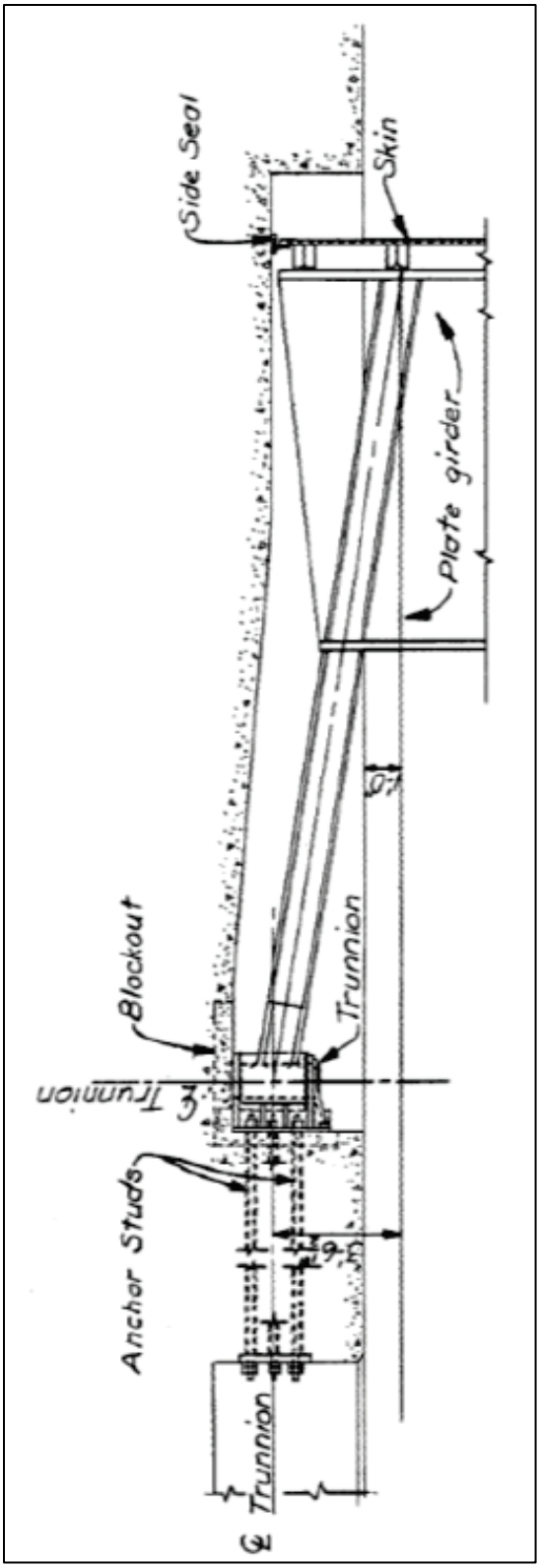

EM 1110-2-2702 (HQUSACE 2000, Chapter 3, Section 3-4, rescinded) describes the three levels of hydrostatic loads that are considered in the design: the maximum hydrostatic load, H_1, which is defined as the maximum net hydrostatic load that will ever occur; the design hydrostatic load, H_2, which is defined as the maximum net hydrostatic load for conditions up to a 10 yr flood event; and the normal hydrostatic load, H_3, which is defined as the net load from the upper and lower pool levels that exist up to 50% of the time during the year.

Hydrostatic loads applied to submergible tainter gates used as upper lock gates depend on the upper pool el. The maximum possible net hydrostatic head (H_1) occurs if the upper pool el is at the top of the gate. H_1 would then be calculated by subtracting the lock sill el from the top of gate el when in the closed position.

7.1.2 EM 1110-2-1604, *Hydraulic Design of Navigation Locks*

EM 1110-2-1604 (HQUSACE 2006, Chapter 4, Section 4-2) gives the typical dimensions for locks using the submergible tainter gate as the upper lock gate. These locks are usually 86 ft wide, with a usable length of 675 ft. Section 7-12 of the EM describes types of closure systems and lists the submergible tainter gate as an alternative for emergency closure. If used in this manner, the gate would be located in an emergency sill upstream from the upper lock gates. Section B-3 of the EM states that there are fewer operating and maintenance problems with submergible tainter gates than with submergible vertical-lift gates.

7.1.3 Submergible Tainter Operations—Navigation Locks

Most of the navigation locks that use a submergible tainter gate as the upper lock gate are located on the Snake River in the USACE-NWW. Ice Harbor Lock, Little Goose Lock, and Lower Granite Lock are the three main locks in this category. For a downbound tow, the submergible tainter gate is lowered into its recess at the upper sill when the lock chamber water surface el is the same as the upper pool el. Once the tow is safely moored in the chamber, the submergible gate is fully raised from the recess in the upper sill. The lock can then be emptied. Once empty, the lower lock gates are opened, and the tow can continue downstream.

For an upbound tow, the lower lock gates are open, and the lock water surface el is the same as the lower pool el when the chamber is entered. The

upper submergible tainter is in the raised position. The lock is then filled, and when the tow is ready to continue upstream, the submergible tainter gate is lowered into its recess. The submergible tainter gate experiences a differential head once the lock water surface el reaches the upper lock sill el during lock filling. This differential head begins to decrease as the lock continues to fill and becomes zero when the lock water surface el reaches the upper pool el.

7.1.4 Submergible Tainter Gate Load Cases

ETL 1110-2-584 (HQUSACE 2014, Sections 3.4 and 3.4.2) describes the applicable loads and the design requirements for the submergible tainter gate. EM 1110-2-2702 (HQUSACE 2000, rescinded) states that all loads that HSS will be subjected to must be considered in the design. These loads include gravity (i.e., weight, ice, mud), hydrostatic, hydrodynamic, operational and machinery, floating and thermal ice, debris, vessel impacts, and environmental (typically wind and temperature).

7.2 Hydraulic Data Collection for Submergible Tainter Gates

The reliability analysis for the submergible tainter gate requires that the mean and standard deviation of the loads be determined, and hydraulic data are needed to develop these values. Because the submergible tainter gate used as an upper lock gate is only used as a closure gate, the hydrostatic and wind-induced wave forces are the primary hydraulic forces. These forces depend on the upper pool el. Historical data for the upper pool are necessary for developing the statistics required for the analysis.

Navigation projects are operated to maintain the upper pool els needed for navigation and other project functions. This is accomplished by operating the spillway gates to discharge the quantity of flow needed to achieve the desired upper pool el. The nominal loads needed for the statistical analysis generally occur with a near-constant upper pool el. The mean and standard deviation for the upper pool need to be determined. The Ice Harbor Lock and Dam Project, located on the Snake River, was chosen as the design example for the submergible tainter gate used as an upper lock. Appendix F contains the methodology used to determine the hydraulic data and the statistical data reduction.

7.3 Hydraulic Loading for Submergible Tainter Gates

Hydraulic loads consist of all loads due to water. These include hydrostatic (i.e., weight of water), hydrodynamic (i.e., load due to flowing water), and wave action. These are the primary hydraulic loads, in terms of magnitude and frequency, experienced by HSS. Vibrations caused by flowing water, constricted flow, and water hammer are also considered hydraulic loads.

7.3.1 Hydrostatic Load for Submergible Tainter Gates

The hydrostatic load is due to the hydraulic head across the submergible tainter gate. The load on the gate results from the hydrostatic pressure acting on the gate. The maximum hydrostatic load occurs when the submergible tainter gate is in the raised position, the upper pool el is at the top of the gate, and the lock water surface el is below the upper lock sill el. This is not a normal operating condition because the upper pool el is usually a few feet below the top of the gate.

The mean hydrostatic pressure on the raised submergible tainter gate is expressed as γH, where γ is the unit weight of water, and H is the total head on the gate. Figure 69 is an illustration of the hydrostatic pressure distribution on the submergible tainter. When the gate is raised, H represents the difference between the upper pool el and the upper lock sill el when the lock water surface el is lower than the upper gate sill el. To obtain the force, the hydrostatic pressure is multiplied by the area the pressure is acting on. Appendix F provides a design example problem for determining the hydrostatic loads for the submergible tainter gate at Ice Harbor Lock. Chapter 2 provides a detailed description of the hydrostatic pressure and hydrostatic force associated with a gate.

Figure 69. Hydrostatic pressure distribution for a submergible tainter gate.

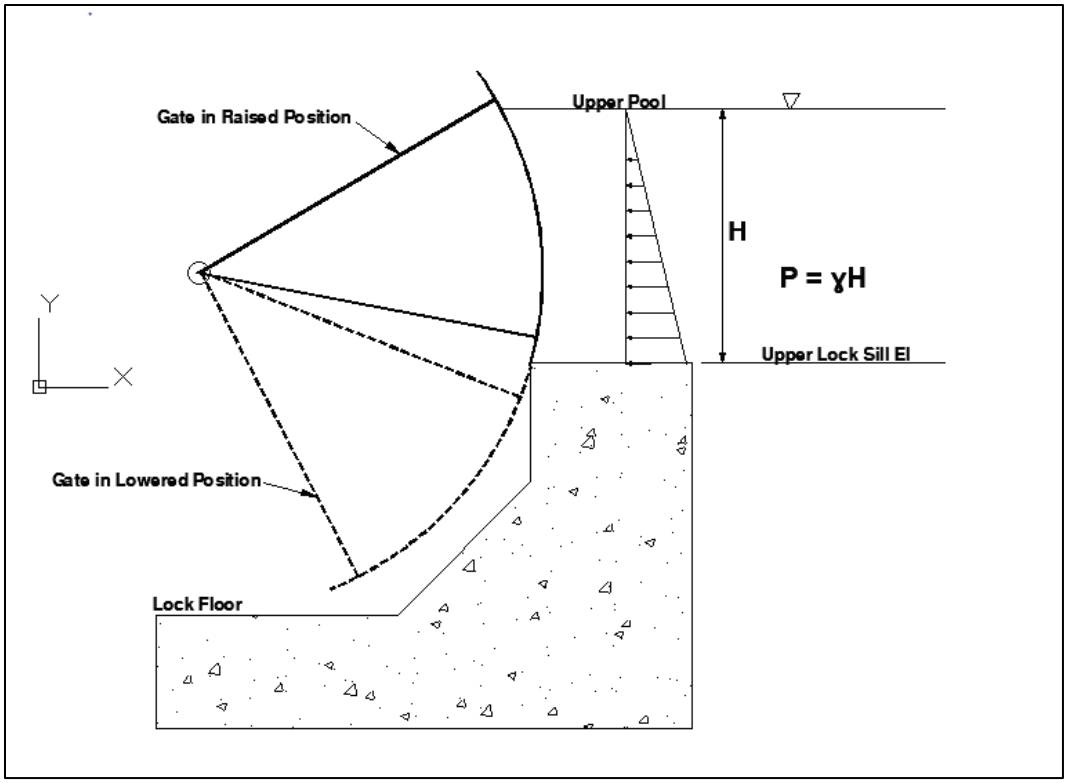

7.3.2 Wave Load for Submergible Tainter Gates

Wave loads are project specific and are considered for projects that experience significant wind and fetch. For the submergible tainter in the raised position, the wave load is similar to that discussed for the other HSS. Refer to Chapter 2 for a detailed description of the procedures used to develop the wind-induced wave load. Appendix F provides a design example problem for determining wind-induced wave loads for the submergible tainter gate at Ice Harbor Lock.

7.4 Probabilistic Characterization of the Hydrostatic Load for the Submergible Tainter Gate

The submergible tainter gate experiences fluctuations in the hydrostatic load due to changes in the upper pool el. The statistics for the upper pool are determined from the historical data available at the project. Appendix F provides an example of how these statistics were used to determine the dispersion of the hydrostatic force for the Ice Harbor Lock submergible tainter gate.

8 Loadings Applied to Bulkheads

Some loads applied to bulkheads are very similar to those applied to vertical-lift gates in a closed position. They are typically used to dewater other HSS that cannot be inspected or maintained during normal operations. The major load is due to the hydrostatic pressure, and the wave load should also be included. Some bulkheads are placed in flowing water when there are problems with another gate. These are referred to as *emergency bulkheads*, and the loads associated with these bulkheads are more complex due to the rapidly changing dynamics of the flow. Hydrostatic and hydrodynamic loads need to be considered. Maynord and Stockstill (2012) described issues and provided project data for bulkheads used for emergency closure of uncontrolled flow at locks and dams.

8.1 Existing Guidance for Bulkheads

Bulkheads are steel gates that primarily consist of a single fabricated section that is lowered into slots on the sides of an opening. The term bulkhead is commonly used when referring to closure structures or stoplogs. In this report, a bulkhead will be considered a steel structure with some type of horizontal truss system. A one-piece bulkhead is used for narrow openings, such as spillway crests or outlet works intakes. Stackable bulkheads are used for larger openings, such as lock approaches or spanning spillway bays. Another name for a bulkhead is a poiree dam. Some of the older projects use this type of structure for wide openings with shallow depths, such as the lower lock approach. Removable frames attached to a concrete base are installed at intervals across the opening. Beams or panels are then placed between the frames to provide the damming surface. Loadings for the spillway vertical-lift gate have been evaluated and are provided in Chapter 3 and Appendix B.

8.1.1 ETL 1110-2-584, *Design of Hydraulic Steel Structures*

ETL 1110-2-584 (HQUSACE 2014, Appendix G) provides guidance for the design of bulkheads. Their designs are typically similar to those for lift gates. For tall bulkheads, the beam spacing and skin plate thickness can be adjusted along the height to help reduce costs and provide a more uniform loading on the beams. To help distribute the load between girders or to transfer the load from a damaged girder, vertical diaphragms are often used. Figure 70 contains an example picture of a bulkhead.

Stackable bulkheads are designed as simple spans that usually have horizontal trusses instead of beams. The individual units are shallow and have tapered ends to fit in slots. They can be designed independently because the water load varies with depth, and there should be no horizontal load transfer between units. The gravity loads on the stackable units are transferred vertically to the concrete sill so the bearing surfaces need to be matched up.

The bulkhead skin plate is usually on the water side. This configuration allows the skin plate to provide continuous vertical bracing along the compression chord of the truss. There are some instances where the skin plate is placed on the dewatered side to minimize the dewatered area and increase the working space. A lifting beam is often required to position the bulkhead and connect the crane to the bulkhead.

Figure 70. Structural components of a one-piece bulkhead. (Image reproduced from ETL 1110-2-584, HQUSACE 2014, B-8. Public domain.)

The hydrostatic loads discussed in ETL 1110-2-584 (HQUSACE 2014, Section 3.2.3.1) for the spillway gates are applicable to the bulkhead. They are also discussed in Chapters 2 and 3 of this report.

8.1.2 EM 110-2-1603, *Hydraulic Design of Spillways*

Much of the guidance on vertical-lift gates provided in EM 1110-2-1603 (HQUSACE 1990, Chapter 6, Section 6-3) is applicable to bulkheads. The bulkhead slot design in the EM discusses the gate bottom shape for vertical-lift gates, which may be useful when designing emergency bulkheads.

8.1.3 EM 1110-2-1605, *Hydraulic Design of Navigation Dams*

EM 1110-2-1605 (HQUSACE 1987, Chapter 5, Section 5-13) contains helpful information on bulkheads. It also directs readers to Section 5-16 for a discussion of supplemental closure facilities and to EM 1110-2-2701 (HQUSACE 1997) and EM 1110-2-1603 (HQUSACE 1990) for the design of vertical-lift gates.

Chapter 7, Section 7-4, of this EM discusses the use of bulkheads to help pass ice and debris through a project. Section 7-10 discusses the use of bulkheads for emergency closures (HQUSACE 1987, 7-14).

8.1.4 EM 1110-2-2702, *Design of Spillway Tainter Gates* (Rescinded)

EM 1110-2-2702 (HQUSACE 2000, Appendix C, Section C-2) provides guidance on bulkheads used as temporary closure structures. Navigation dam spillways with vertical-lift gates are usually older projects that have been in operation for several decades. Due to the cumbersome hoisting equipment, many of these projects operate with the gates completely open or completely closed. The gates in the middle of the spillway are generally the first to be lifted to pass the desired discharge. As the discharge increases, the gates adjacent to the middle gates are then usually lifted.

8.1.5 EM 1110-2-2607, *Planning and Design of Navigation Dams*

EM 1110-2-2607 (HQUSACE 1995a) indicates that USACE projects primarily use stacked bulkheads and vertical-lift gates for emergency closures. The preferred design for these structures has end rollers and an open truss with the skin plate on the upstream side. Appendix C of this EM provides information concerning barge collisions and the potentially catastrophic consequences of this type of accident. The manual states, “Past experience and model testing by WES have shown that bulkheads cannot be lowered safely one at a time in flowing water. Therefore, the stacked bulkhead system was developed so that the flowing water never goes over the top of the bulkheads” (HQUSACE 1995a, 6-4).

8.1.6 Bulkhead Load Cases

EM 1110-2-2702 (HQUSACE 2000, rescinded) states that all loads that HSS will be subjected to must be considered in the design. These loads include gravity (i.e., weight, ice, mud), hydrostatic, hydrodynamic, operational and machinery, floating and thermal ice, debris, vessel impacts, and environmental (typically wind and temperature). Frequency of loading is considered in the design for the three load categories that are described in Section 2.1.5 and are specified in terms of frequency of occurrence. The load information for the usual, unusual, and extreme categories was taken directly from ETL 1110-2-584 (HQUSACE 2014). Load combinations and cyclic and noncyclic loads are also presented in Chapter 2 of this report.

8.2 Hydraulic Data Collection and Statistical Data Reduction for Mean Loading and Dispersion for Bulkheads

The reliability analysis for the bulkhead requires that the mean and standard deviation of the loads be determined. Hydraulic data are needed to develop these values and depend on the intended use of the bulkhead. For a bulkhead placed in static water, the upper and lower pool els are required. The wind conditions also need to be evaluated to determine the wave loads. The upper and lower pool elevations and some data to help estimate discharge over and under a bulkhead unit are necessary for a bulkhead used in an emergency closure. Historical data are necessary for developing the samples and statistical data required for the analysis.

8.2.1 Upper Pool El

For bulkheads used to dewater the upstream side of the HSS, the upper pool el is needed. Because the project conditions when the bulkhead is in place would most likely be similar to those experienced during normal operations, the upper pool el used to design the spillway or lock gates could be used. The nominal loads needed for the statistical analysis generally occur with a near-normal upper pool el. The mean and standard deviation for the upper pool need to be determined. The BLD on the Cumberland River was chosen as the design example for the bulkhead. Appendix G contains the methodology used to determine the hydraulic data and the statistical data reduction. The procedures for developing the hydrostatic and wave forces are similar to those for the vertical-lift gate.

8.2.2 Tailwater

Tailwater is a primary variable affecting the load on the tainter and vertical-lift gates for most navigation projects, especially low head projects. The TW El is important when the bulkheads are used on the downstream side of the HSS to be dewatered. As mentioned with the upper pool el, the TW El used to design the spillway or lock gates could be used with the bulkheads. Figure 71 shows a dewatering bulkhead used in the lower lock approach where the TW El is the hydrostatic condition.

Figure 71. Dewatering bulkhead in lower lock approach. (Image reproduced from ETL 1110-2-584, HQUSACE 2014, B-8. Public domain.)

8.2.3 Flow Regimes for Bulkheads

Because the dewatering bulkhead is not designed to control flow, there is no concern for the flow regime. However, when the bulkhead is used in an emergency situation, flow will be present. However, this flow regime is not characterized like those for the spillway gates. The flow conditions that occur are rapidly changing and can be extremely unstable as the bulkhead nears the closed position. This may also occur if a bulkhead experiences simultaneous flow over and under the section being positioned. The speed at which the unit is lowered combined with the distribution of flow over and under the unit can cause excessive uplift forces followed by significant downward forces. Figure 72 shows a plot of the vertical hydraulic force measured in a physical model study of the Barkley Spillway bulkheads, taken from Hite and Pickering (1983), as the bulkhead and lifting

mechanism were at selected positions above the crest (bulkhead seat). The plot shows that, when the lifting mechanism and bulkhead unit were between 5 and 10 ft above the crest, large fluctuating forces occurred. Hite and Pickering showed that these fluctuating forces still occurred during lowering (i.e., dynamic) tests, but they were considerably reduced. The forces shown in Figure 72 were measured with a relatively high tailwater (h/H =0.7), which appeared to increase the instability of the flow. Further discussion of the hydrodynamic forces associated with flow conditions that exist with emergency bulkheads will follow in Section 8.3.3.

Figure 72. Vertical hydraulic forces from a model study of the Barkley Bulkhead. (Image reproduced from Hite and Pickering 1983, Plate 13. Public domain.)

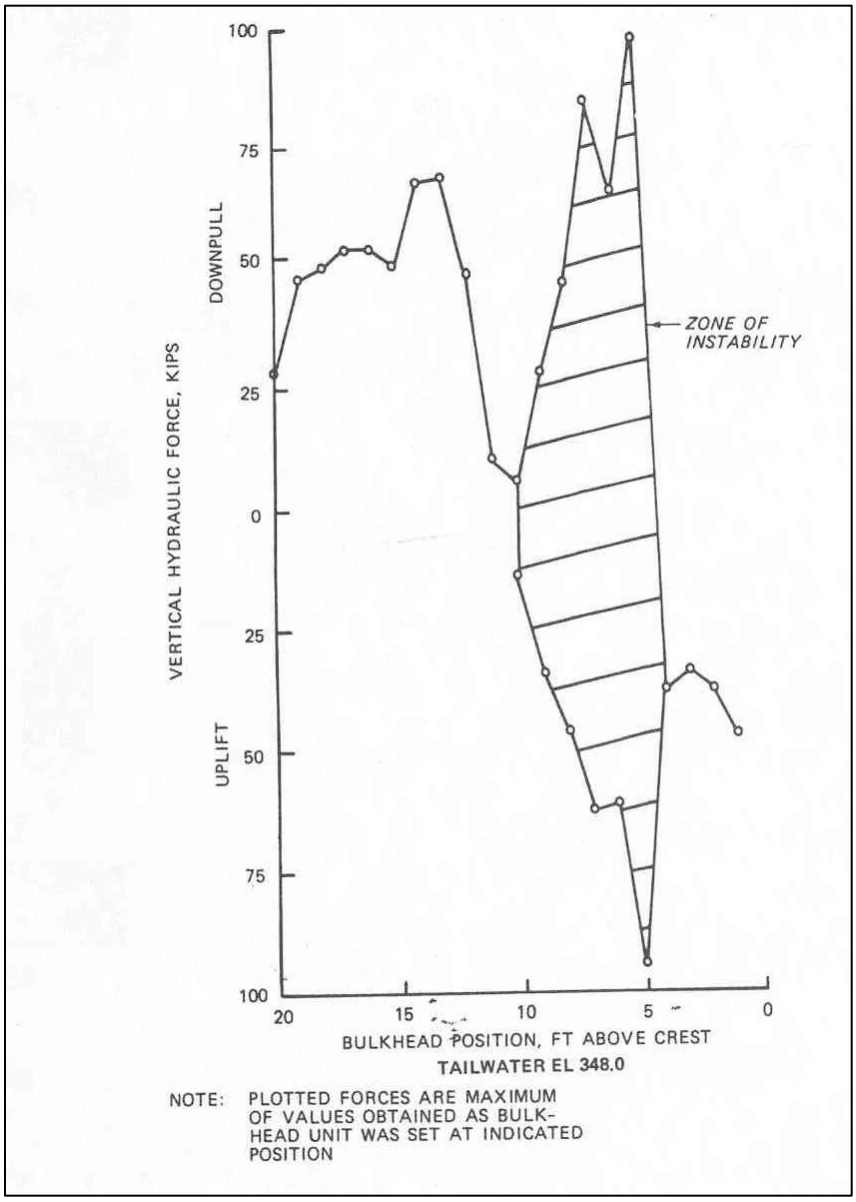

8.3 Hydraulic Loading for Bulkheads

Hydraulic loads consist of all loads due to water. These include hydrostatic (i.e., weight of water), hydrodynamic (i.e., load due to flowing water), and wave action. These are the predominant hydraulic loads, in terms of magnitude and frequency, experienced by HSS. Vibrations caused by flowing water, constricted flow, and water hammer are also considered hydraulic loads.

8.3.1 Hydrostatic Load for Bulkheads

The hydrostatic load is due to the hydraulic head across the bulkhead. The load on the bulkhead results from the hydrostatic pressure. A conventional equation found in many fluid mechanics and hydraulics textbooks and used to compute the hydrostatic pressure (p) was first included as Equation (10) and is repeated here. As stated previously, γ is the unit weight of water, and y is the vertical distance from the water surface to the location of the hydrostatic pressure of interest (Figure 15):

$$p = \gamma y.$$

The same method for developing the hydrostatic load for the vertical-lift gate in Chapter 3 is applicable to the dewatering bulkhead. The hydrostatic pressure on the seated bulkhead is expressed as γH, where γ is the unit weight of water, and H is the difference between the water level on the damming surface of the bulkhead and the bulkhead seat. Figure 73 shows an illustration of the hydrostatic pressure distribution on a bulkhead used to dewater a spillway bay. When the bulkhead is in place, H represents the difference between the upper pool el and the spillway crest el. Equation (11), which is repeated here, can be used to calculate the maximum hydrostatic pressure:

$$p_{max} = \gamma H.$$

For the bulkhead used for dewatering, the maximum hydrostatic load occurs when the bulkhead is seated and the water level on the damming surface of the bulkhead is at the maximum level. To obtain the force, the hydrostatic pressure is multiplied by the area the pressure is acting on. The resultant hydrostatic force per foot of width for the roller gate was first shown in Equation (12) and is repeated here; it is located at $H/3$ above the spillway crest (Figure 15):

$$H_s = \frac{1}{2}\gamma H^2.$$

Figure 73. Hydrostatic pressure distribution for a bulkhead.

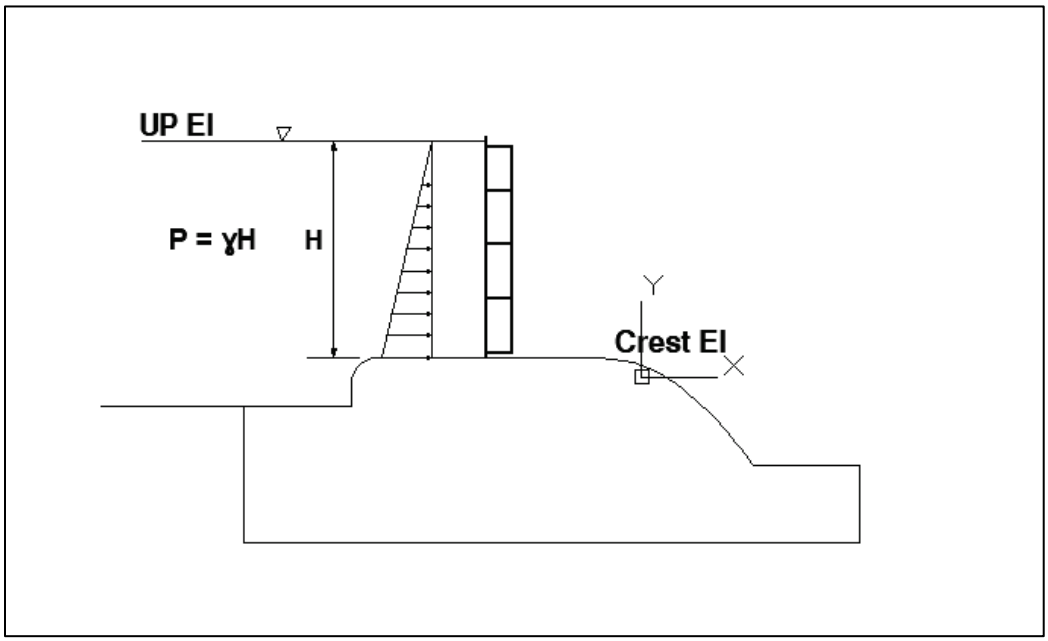

8.3.2 Wave Load for Bulkheads

Wave loads are project specific and are considered for projects that experience significant wind and fetch. The same procedures used for the STG can be applied to the bulkhead. These procedures are described in Chapter 2. The Goda (2010) procedures are the recommended guidance for wind-induced wave loadings for inland navigation projects. The Goda (2010) wave pressure distribution procedure for the bulkhead is the same as that for the vertical-lift spillway gate shown in Figure 45. Appendix G shows an example procedure for computing the wave pressure on the bulkhead gate using the Goda procedure.

8.3.3 Hydrodynamic Load for Bulkheads

The hydrodynamic load on the bulkhead results from the force due to water flowing over and under the gate. When flow only occurs under the bulkhead, the hydrodynamic forces are similar to those of the vertical-lift gate. The procedures shown in Chapter 3 can be used to determine these forces. When flow occurs both over and under the bulkhead, the net hydrodynamic forces become much more difficult to determine analytically. Figure 74 shows a schematic of the flow near a submerged bulkhead. As the bulkhead is lowered, the flow splits between the flow over and under

the bulkhead, causing flow control shifts with fluctuating pressures that can result in the load changes seen in Figure 72. Figure 75 shows a schematic of the estimated pressure distribution on a bulkhead with flow over and under it.

Figure 74. Schematic of flow around a submerged bulkhead.

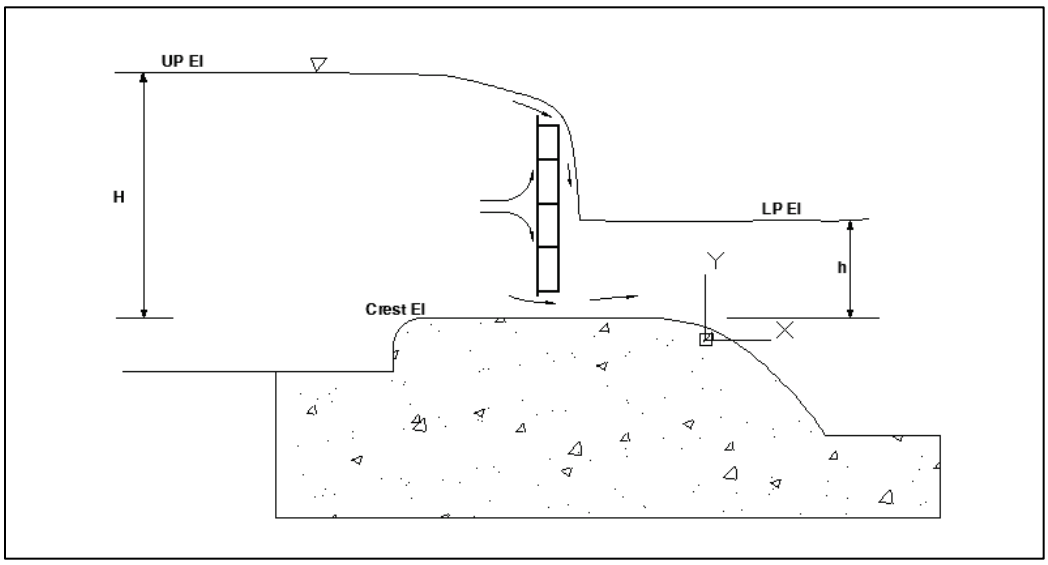

Figure 75. Schematic of pressure distribution on a bulkhead with flow over and under the bulkhead.

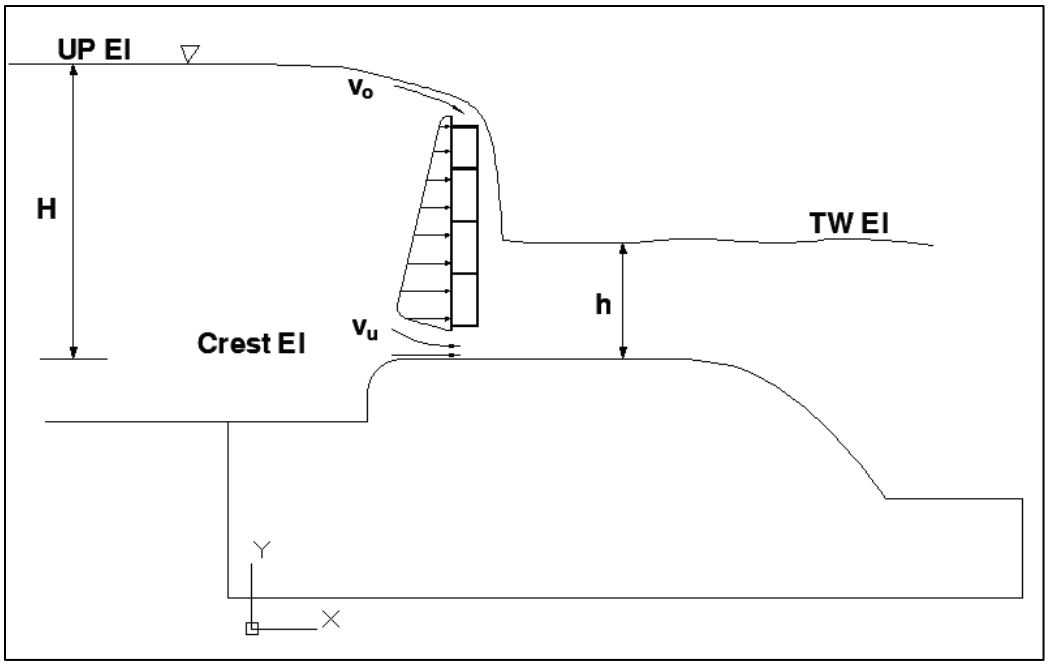

Eschler (1958) conducted a generalized study of the placement of bulkhead sections in a spillway bay using a 1:51-scale model. The bulkhead was

2.8 m high by 2.8 m deep and 23 m wide and was constructed as an open truss with a skin plate on the upstream side. Figure 76 shows the vertical hydraulic forces measured for the largest flows tested with a single bulkhead set at designated locations above the bulkhead sill. The initial depth of flow was assumed to be 10 m. The data are considered the average load values even though the loads are time varying. The submerged weight of the gate was removed from the load value, so the loads shown are the vertical hydraulic forces. The highest vertical force was 88 tons and occurred when the bottom section was between 5 and 8 m above the sill. When the bottom section was less than 2 m, the load became an uplift force, which caused difficulty in seating the bulkhead.

Melsheimer and Murphy (1961) performed laboratory tests using a 1:25-scale model of the lifting mechanism and bulkheads for the New Cumberland Locks and Dam spillway. Vertical hydraulic forces were measured for several combinations of lifting mechanisms, bulkhead arrangements, and head. Figure 76 shows the results from a lowering test with the lifting mechanism and one bulkhead compared to the Eschler (1958) data. The head on the gate sill was 9.14 m. The maximum range of forces was reported when they were not constant. This occurred when the bottom of the bulkhead was between 0.61 and 4.27 m above the gate sill.

Figure 76. Comparison of Eschler (1958) and Melsheimer and Murphy (1961) results for deployment of an individual closure gate.

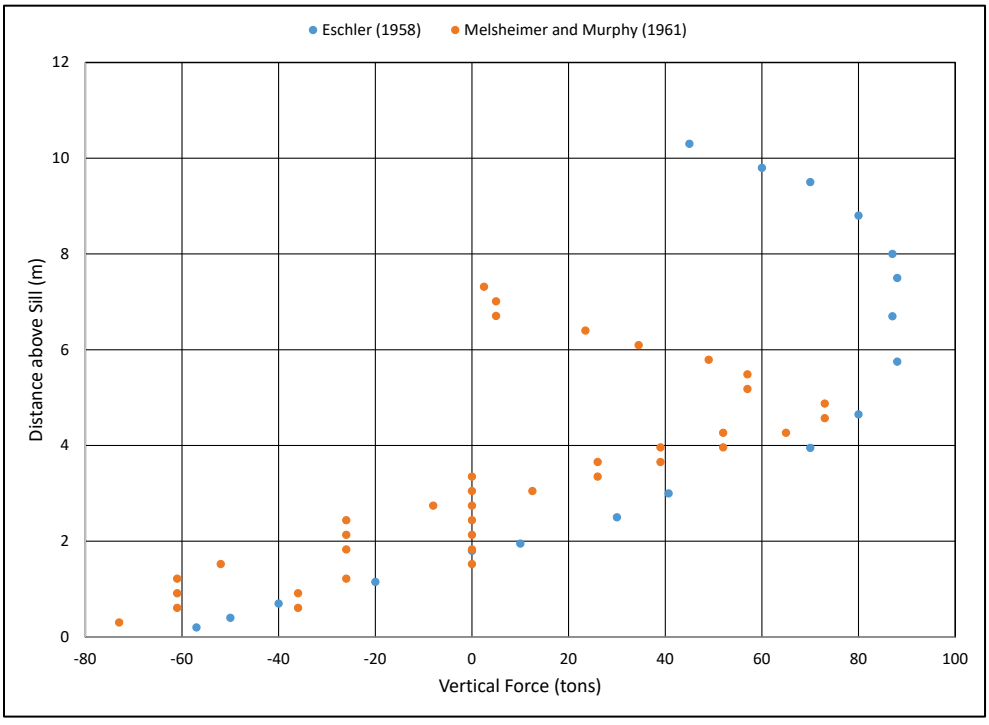

Hite and Pickering (1983) measured hydraulic loads for a bulkhead with an accompanying lifting mechanism. This bulkhead unit was 3.66 m high by 0.85 m deep and 17.68 m wide. The data shown in Figure 72 were measured in this study and showed the impact of high tailwater (h/H = 0.7). These data are also plotted in Figure 77 for a comparison of data measured with no tailwater effect. The zone of instability indicated in Figure 72 is represented by the large variation in data (i.e., the orange dots) with a tailwater of 348 when the distance from the bottom of the bulkhead to the sill was between 1.5 and 3 m. The vertical hydraulic forces measured with no tailwater effect (i.e., the blue dots) showed a more stable trend. Based on the data obtained from Hite and Pickering (1983), USACE-LRN decided that if an emergency occurred while the tailwater was high, the other gates could help control the upper pool until the tailwater was low enough to safely use the emergency bulkheads.

Figure 77. Hite and Pickering (1983) results adapted for deployment of an individual closure gate.

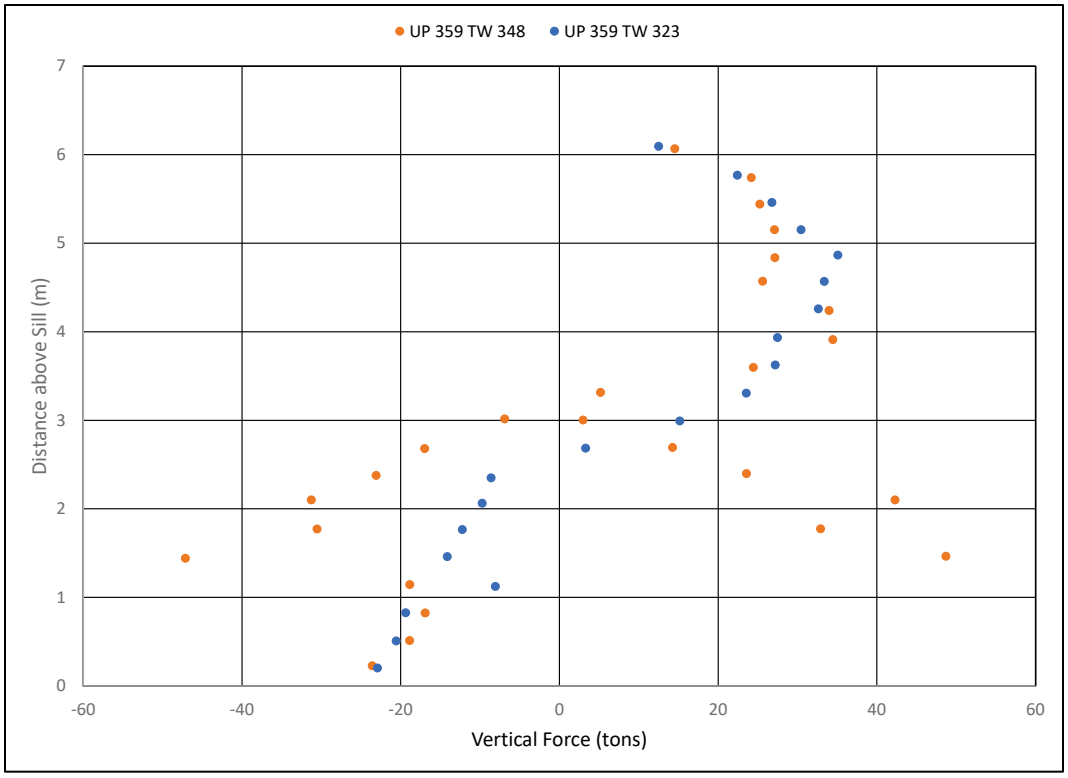

As shown by the data in Figure 76 and Figure 77, the fluctuating flows that occur when flow over and under the bulkhead occurs make the estimation of the hydraulic forces very difficult, especially when the bottom of the bulkhead approaches the sill.

Historically, the preferred techniques for determining these hydraulic forces has been to measure them either in place at the project during a dynamic test or to use a scaled physical model in the laboratory. Maynord and Stockstill (2012) summarized several studies performed both in the field and laboratory to measure hydraulic forces. These studies revealed that the bottom shape of the bulkhead has a significant influence on the hydraulic forces and the tendency for vibration issues. The authors of this report recommend determining the hydraulic forces for bulkheads used for emergency closure by conducting prototype tests. A combination of load cells, strain gages, and dynamic pressure cells could be installed in strategic locations on the bulkhead to help evaluate the hydraulic forces (especially the hydrodynamic forces) as the bulkhead is lowered under flowing water. Load measurements at the four corners of the bulkhead and enough pressure measurements to obtain a good estimate of the pressure distribution on the face of the bulkhead are desirable. A technical team consisting of structural, hydraulic, sensor, and operations personnel is recommended for planning and executing a prototype testing program.

8.3.4 Combined Hydrostatic and Wave Load for Bulkheads

Wave loads are project specific and are considered for projects that experience significant wind and fetch. The procedures for developing hydrostatic and wave loading for the bulkhead are similar to those used for both the tainter gate and vertical-lift gates, which were provided in previous chapters. These procedures can be used for the bulkhead.

8.3.5 Combined Hydrodynamic and Wave Load for Bulkheads

A bulkhead used for dewatering or static closure will not experience any hydrodynamic loads. A bulkhead used for emergency closure will have flow over the top of the bulkhead for a brief period of time. The wind-induced wave load requires time to establish a significant wave. This time is very likely to be longer than required to place the bulkhead in flowing water, so the combined hydrodynamic and wave load is not considered significant.

8.3.6 Summary of Hydraulic Loads for Bulkheads

The hydraulic loads on bulkheads used for dewatering and closures consist primarily of the hydrostatic and wave loads. The loads should be combined as appropriate to give the maximum expected for the bulkhead. The wind-

to-wave force conversion in some cases can make a significant contribution to the combined loads. The authors of this report recommend that wind-induced wave forces be determined using the Goda (2010) design procedure discussed in previous chapters.

8.4 Probabilistic Characterization of the Hydrostatic and Hydrodynamic Loads for Bulkheads

8.4.1 Probabilistic Characterization of the Hydrostatic Load for the Bulkhead

The dispersion of the hydrostatic load needs to be determined to perform the analysis for the LRFD. An appropriate range for the upper pool at most navigation projects is considered plus 6 standard deviations (σ) and minus 6σ about the mean upper pool. A bulkhead designed for a navigation project and used during static conditions needs to function during normal pool conditions. The standard deviation for the range of the normal pool is more appropriate for evaluating the dispersion of the hydrostatic load for the bulkhead than the maximum and minimum upper pool els. The top el of the bulkhead is considered a good choice for the maximum allowable upper pool el before the bulkhead is removed from service. The historical minimum upper pool el is considered appropriate for use as the minimum el. Appendix G provides the design example for the dispersion of the hydrostatic load for the Barkley spillway bulkhead used in a static condition.

8.4.2 Probabilistic Characterization of the Hydrodynamic Load for Bulkheads

Developing the dispersion of the hydrodynamic load for the bulkhead can require data obtained from the laboratory, field, and numerical computations. At present, the hydraulic loads on a bulkhead used in a dynamic condition are estimated from these sources of data. Measuring hydraulic loads in the laboratory or in the field is challenging. An experienced team of personnel familiar with test design, data collection, and data processing and analysis is needed. Computing hydraulic loads using numerical methods or models is also quite challenging and has not been attempted by many researchers. The mesh resolution needed to model the small structural members results in a mesh with millions of cells, which can cause prohibitively long computation periods.

8.5 Summary and Conclusions

A spillway bulkhead that is used for dewatering and closures is primarily subjected to hydrostatic and wave loads. The service gate is used to close off the flow before the bulkhead is deployed. These loads are computed similarly to those for the spillway tainter and vertical-lift gates.

The hydraulic forces associated with a bulkhead used in an emergency (i.e., flowing water) condition can rapidly vary in both magnitude and direction. Previous experience with this type of bulkhead operation in both laboratory and field studies indicates that when the bulkhead has simultaneous flow over and under the bulkhead, the flow can oscillate, causing the bulkhead to become unstable. The instability can result in damage to the hoisting mechanisms and possibly the bulkhead itself if it comes in contact with the dam or becomes wedged in the bulkhead slots. Section 8.4.2 provides recommendations on current methods to collect hydraulic data that could be used to estimate the hydrodynamic loads and the dispersion of the loads.

9 Loadings Applied to Rolling Gates

Some loads applied to rolling gates are very similar to those for bulkheads used as closure structures. The rolling gate is typically used as flood closure structure for levees or floodwalls. The major hydraulic loads are due to the hydrostatic pressure and wave load.

9.1 Existing Guidance for Rolling Gates

Rolling gates have wheels that require a track embedded in the sill across the opening to be closed, and the gate must be stored when not in use. The gate is supported by the wheels and can be operated in a variety of ways. A cable and winch system is often used. The cable could also be connected directly to a vehicle that is then used to pull the gate from the stored area. If this type of structure is used on a project where floods occur rapidly, the gate needs to be designed to open and close from the protected side.

9.1.1 ETL 1110-2-584, *Design of Hydraulic Steel Structures*

ETL 1110-2-584 (HQUSACE 2014, Appendix F) provides information concerning the design of closure gates. Section F.2 of the ETL states that the design must consider operation, function, maintenance, aesthetics, safety, security, construction, and economics. Section F.3.4 of the ETL describes the advantages and disadvantages of the rolling gate and its different designs.

Figure 78 shows a rolling gate that is stabilized with two lines of wheels. The wheels support and stabilize the gate against overturning and are usually V-grooved castings that roll on tracks made of inverted angles with embedded anchorages. The depth of the bottom girder is usually set by the required transverse spacing between the supporting wheels, rather than by the hydrostatic load. A bottom girder that is 30 to 36 in. wide is generally required to accommodate the spacing between the two lines of wheels and provide stability for the gate during closing and opening operations. The bottom girder width also depends on the gate height and exposure to wind.

Figure 78. Rolling gate with two lines of wheels. (Image reproduced from HQUSACE 2014, F-12. Public domain.)

There are rolling gates with a single line of wheels. They are typically composed of a trussed steel frame covered with a skin plate or bridge planks. The gates are supported by a single line of wheels and are stabilized laterally by an extended top girder that is supported by trolleys that are attached to the top of the floodwall. The extended top girder makes this design practical for smaller openings (i.e., those of 30 ft or less). The girder depths are set by the hydrostatic load.

Rolling gates can also have an L-frame design. These are constructed of a series of L-shaped structural steel frames that are interconnected by horizontal and diagonal members. The gates are supported at the bottom by two lines of wheels. Figure 79 contains an example of this type of design. Hooks attached to the heel of each of the L-frames engage anchorages embedded in the concrete-sill structure to stabilize the gate against the hydrostatic load.

Figure 79. Rolling gate with L-frame design. (Image reproduced from HQUSACE 2014, F-12. Public domain.)

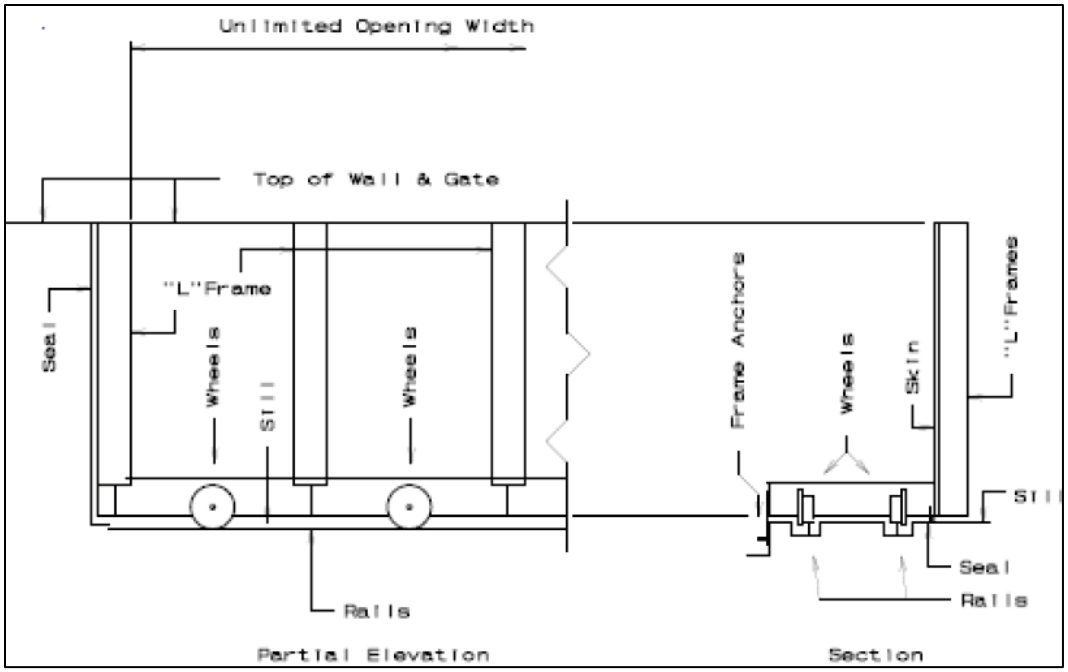

9.1.2 Rolling Gate Load Cases

EM 1110-2-2702 (HQUSACE 2000, rescinded) states that all loads that HSS will be subjected to must be considered in the design. These loads include self-weight, gravity (ice and mud determined on site-specific basis), hydrostatic, hydrodynamic (design engineer decides if these are applicable), operational and machinery, impact (design engineer decides if these are applicable), and environmental (typically wind and temperature). ETL 1110-2-584 (HQUSACE 2014, Appendix F) contains the design loads for closure structures.

9.2 Hydraulic Data Collection and Statistical Data Reduction for Mean Loading and Dispersion for Rolling Gates

The reliability analysis for the rolling gate requires that the mean and standard deviation of the loads be determined. Hydraulic data are needed to develop these values. The water level on the flood side of the gate is required for a rolling gate placed in a levee or floodwall. The wind conditions also need to be evaluated to determine the wave loads. Historical data are necessary to develop the samples and statistical data required for the analysis.

9.2.1 Flood-Side Water Level

The water level on the flood side of the rolling gate is available in the hydraulic analysis performed to design the levee or floodwall. The top of the rolling gate is almost always the same as the top of the levee or floodwall.

9.2.2 Wave Load

The wave load results from wind conditions and possibly from vessels navigating the channel. The probability of vessels navigating during a flood event is very small and may not be included in the design process.

9.3 Hydraulic Loading for Rolling Gates

Hydraulic loads consist of all loads due to water. These include hydrostatic (i.e., weight of water), hydrodynamic (i.e., load due to flowing water), and wave action. These are the predominant hydraulic loads, in terms of magnitude and frequency, experienced by HSS. Vibrations caused by flowing water, constricted flow, and water hammer are also considered hydraulic loads.

9.3.1 Hydrostatic Load for the Rolling Gate

The hydrostatic load is due to the hydraulic head across the rolling gate. The load on the bulkhead results from the hydrostatic pressure. ETL 1110-2-584 (HQUSACE 2014) states that the hydrostatic load may be conservatively taken as water to the top of the gate with no tailwater.

The same method for developing the hydrostatic load for the bulkhead in Chapter 8 is applicable to the rolling gate with no tailwater. A conventional equation that is found in many fluid mechanics and hydraulics textbooks and is used to compute the hydrostatic pressure (p) was first included as Equation (10) in this report and is repeated here. As stated previously, γ is the unit weight of water, and y is the vertical distance from the water surface to the location of the hydrostatic pressure of interest (Figure 15):

$$p = \gamma y.$$

The mean hydrostatic pressure on the seated roller gate is expressed as γH, where γ is the unit weight of water, and H is the difference between the water level at the top of the rolling gate and the gate sill (generally the same as the bottom of the gate). Figure 80 contains a schematic of the

hydrostatic pressure distribution on a rolling gate with no tailwater. To obtain the force, the hydrostatic pressure is multiplied by the area the pressure is acting on. The maximum hydrostatic pressure would occur if the upper pool el was the same as the top of the rolling gate, and it can be computed using this equation (which was first included as Equation 11 in this report):

$$p_{max} = \gamma H.$$

The hydrostatic force per foot of width for the rolling gate is as follows:

$$H_s = \frac{1}{2}\gamma H^2.$$

Figure 80. Hydrostatic pressure distribution on the rolling gate.

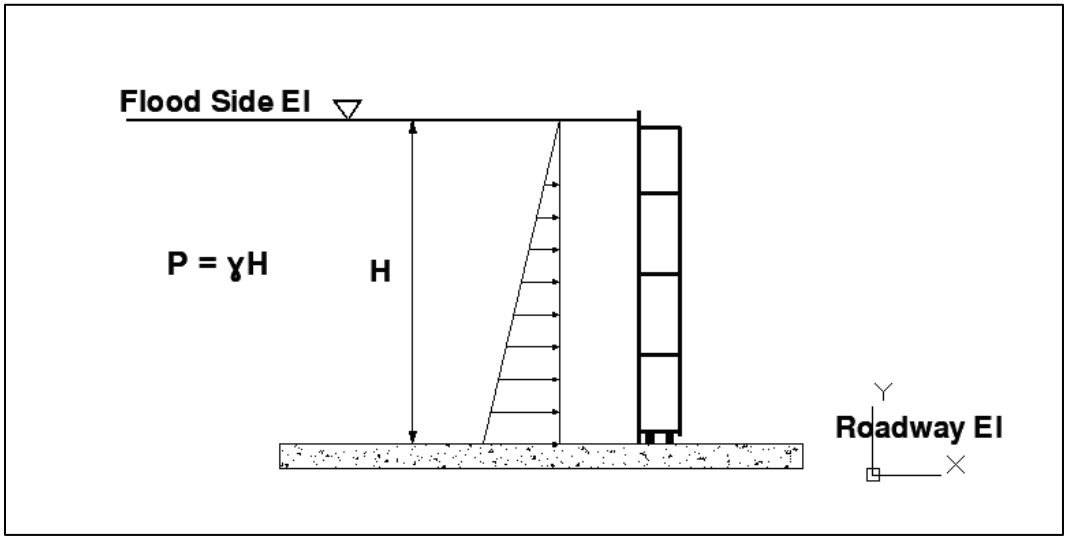

9.3.2 Wave Load for Rolling Gates

ETL 1110-2-584 (HQUSACE 2014) indicates that waves or other hydrodynamic wave loads are project specific and are considered for projects that experience significant wind and fetch. The same procedures used for the previous HSS (Chapters 2–8) can be applied to the rolling gate. The Goda (2010) procedures are the recommended guidance for wind-induced wave loadings for inland navigation projects. The Goda wave pressure distribution procedure for the rolling gate is the same as that for the vertical-lift spillway gate shown in Figure 45. An example procedure to compute the wave pressure on the rolling gate using the Goda procedure is shown in Appendix H.

9.3.3 Combined Hydrostatic and Wave Load for Rolling Gates

Wave loads are project specific and are considered for projects that experience significant wind and fetch. The procedures for developing hydrostatic and wave loading for the rolling gate are similar to those used for both vertical-lift gates and the bulkhead, which were provided in previous chapters.

9.3.4 Probabilistic Characterization of the Hydrostatic Load for the Rolling Gate

The dispersion of the hydrostatic load for the rolling gate needs to be determined to conduct the LRFD analysis. Statistics are needed to estimate the dispersion in the hydrostatic loads. Appendix H provides a design example for developing the statistics for the hydrostatic load.

9.3.5 Summary of Hydraulic Loads for Rolling Gates

The hydraulic loads on rolling gates used as flood closure structures consist primarily of the hydrostatic and wave loads. The loads should be combined as appropriate to give the maximum expected for the rolling gate. Depending on the wind speed and fetch, the wind-to-wave force conversion, in some cases, can make a significant contribution to the combined loads. The authors of this report recommend that wind-induced wave forces be determined using the Goda (2010) design procedure discussed in previous chapters.

10 Loadings Applied to Needle Dam / Girder Beams (ND/GB)

Loads applied to ND/GB are very similar to bulkheads used as dewatering structures. The ND/GB discussed in this chapter are those used to dewater a lock so components that cannot be inspected or maintained during normal operations can be observed and evaluated. The major hydraulic loads are caused by the hydrostatic pressure and the wave load. These structures also require seals to prevent excessive leakage along the bottom and sides.

10.1 Existing Guidance for ND/GB

ND/GB are generally steel or possibly aluminum structures that are used for dewatering a lock. They can be used both in the upper and lower approaches to the lock. They are placed vertically, adjacent to one another, and are braced on top by large girders that span the lock walls along the top of the needles. They are secured on the bottom by an offset in the approach floor, as shown for the upper and lower ends of the lock in Figure 81 and Figure 82. They require seals to minimize leakage.

Figure 81 and Figure 82 contain examples of ND/GB for the Chickamauga Lock project on the Tennessee River in the USACE-LRN. Appendix I provides a design example for determining the hydraulic loads for this project. Figure 83 shows a view of the ND/GB closure structure at the upper end of Chickamauga Lock, looking upstream. The box girder can be seen bracing the individual steel needle.

Figure 81. Side view of the ND/GB for the upper end of the lock.
(Image reproduced from USACE, Nashville District [USACE-LRN], files.)

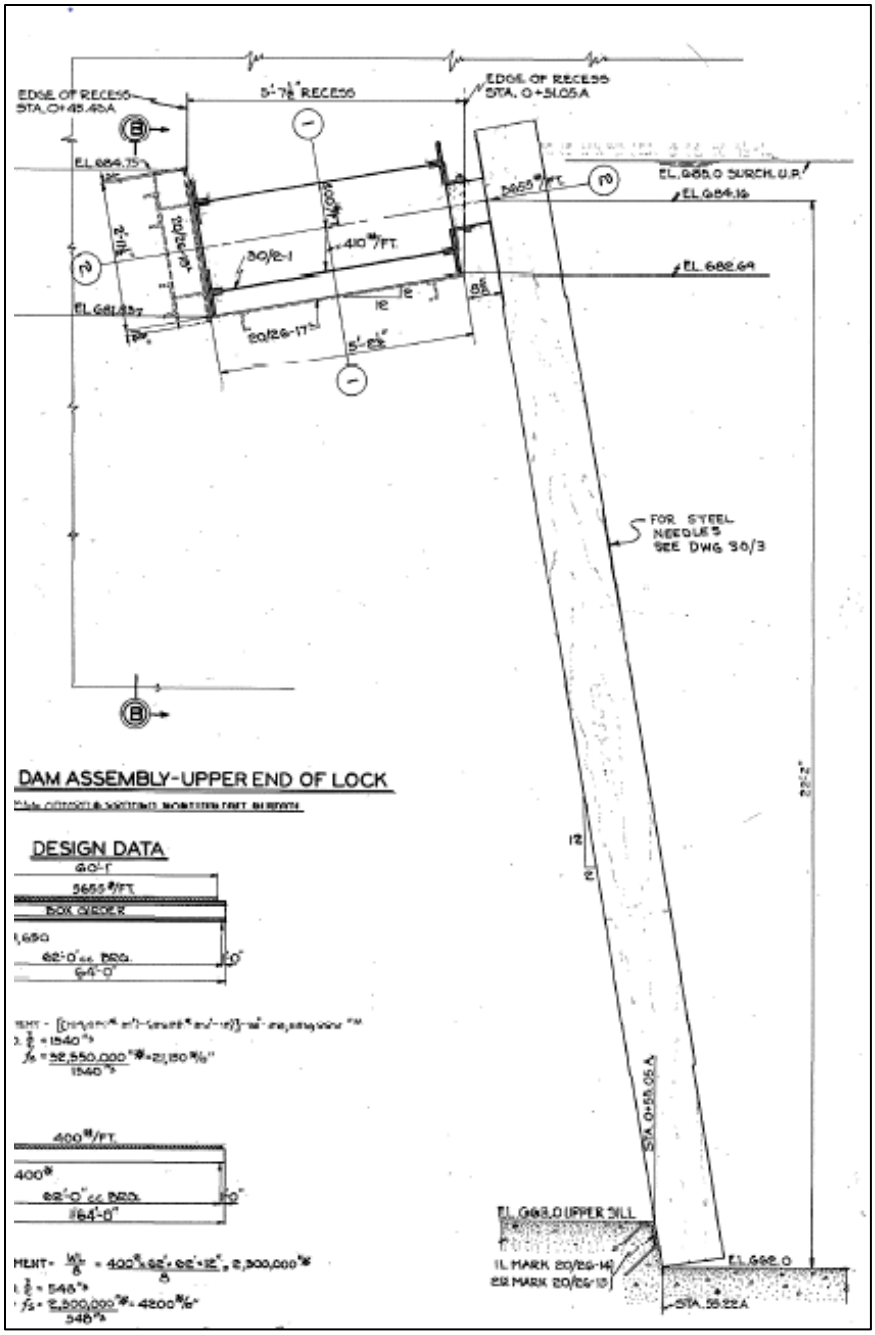

Figure 82. Side view of the ND/GB for the lower end of the lock.
(Image reproduced from USACE-LRN files.)

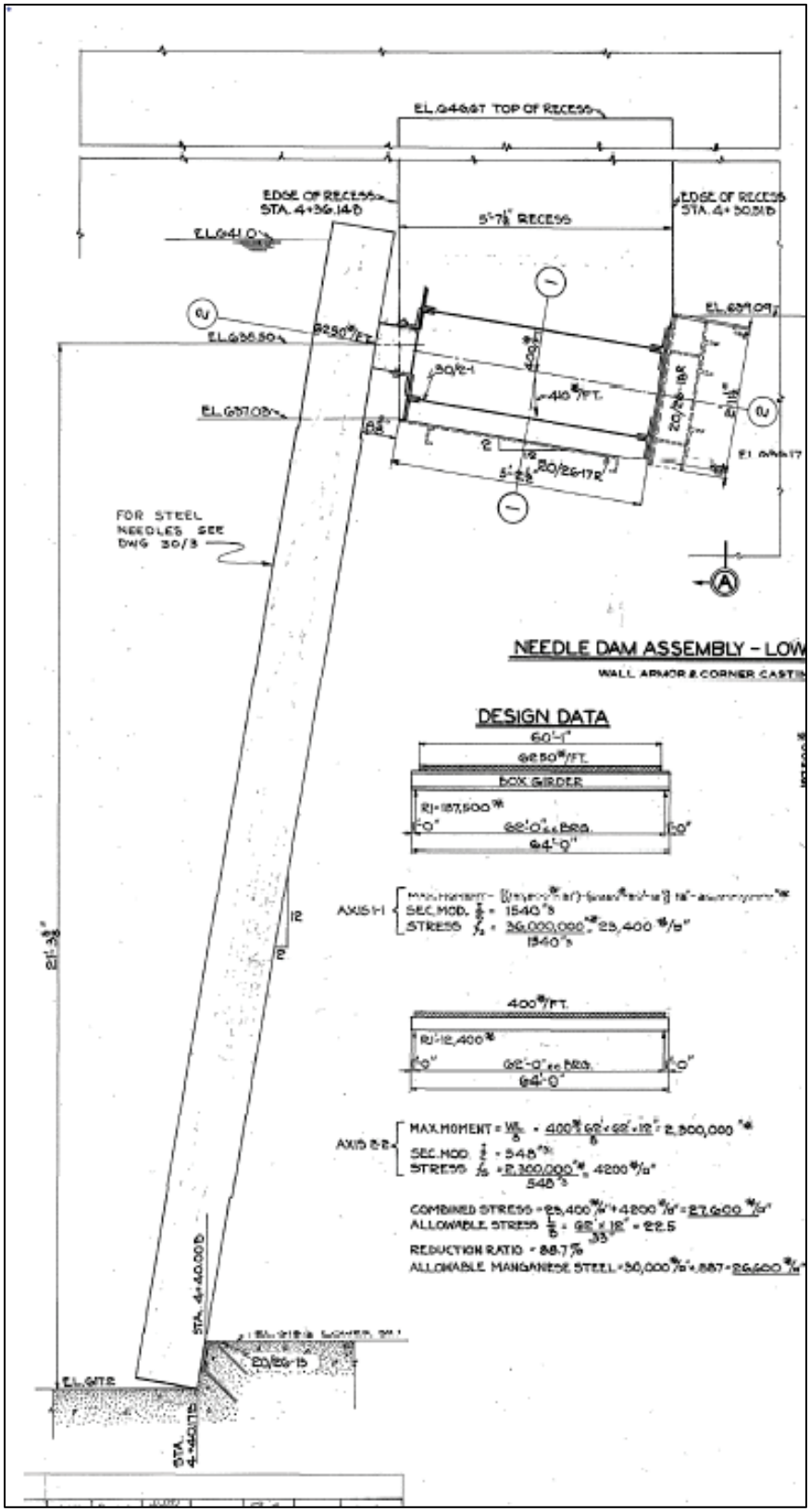

Figure 83. Looking upstream at the ND/GB closure structure for the upper end of the Chickamauga Lock.

10.1.1 ETL 1110-2-584, *Design of Hydraulic Steel Structures*

ETL 1110-2-584 (HQUSACE 2014) does not mention the ND/GB specifically; however, Appendix F of the ETL describes the design of closure structures, and much of this information is applicable to the ND/GB. Advantages of the ND/GB include their simple and economical fabrication methods, low initial costs, adaptability to wide openings, and that they can be fabricated in sections to simplify handling and storage. The design loads for closure structures are provided in Section F.4.1 of the ETL.

10.1.2 ND/GB Load Cases

EM 1110-2-2702 (HQUSACE 2000, rescinded) states that all loads that HSS will be subjected to must be considered in the design. These loads include gravity (i.e., weight, ice, mud), hydrostatic, hydrodynamic, operational and machinery, floating and thermal ice, debris, vessel impacts, and environmental (typically wind and temperature).

10.2 Hydraulic Data Collection and Statistical Data Reduction for Mean Loading and Dispersion for the ND/GB

The reliability analysis for the ND/GB requires that the mean and standard deviation of the loads be determined. Hydraulic data are needed to develop these values. The upper and lower pool els are the primary information required for the ND/GB placed in static water. The wind conditions also need to be evaluated to determine the wave loads. Historical data are necessary for developing the samples and statistical data required for the analysis.

10.2.1 Upper Pool El

For ND/GB used on the upstream side of the lock to be dewatered, the upper pool el is needed. Because the ND/GB are in place when conditions are most likely similar to those during normal operations, the upper pool el used to design the spillway or lock gates can be used. The nominal loads needed for the statistical analysis will generally occur with a near-normal upper pool el. The mean and standard deviation for the upper pool needs to be determined. Chickamauga Lock and Dam on the Tennessee River was chosen as the design example for an ND/GB. Appendix G contains the methodology used to determine the hydraulic data and the statistical data reduction. These procedures for developing the hydrostatic and wave forces are similar to those used for the bulkhead closure structure described in Chapter 8 and Appendix G.

10.2.2 Tailwater Elevation (TW El)

The TW El is important when ND/GB are used on the downstream side of the lock to be dewatered. The TW El used to design the spillway or lock gates is also appropriate for ND/GB. TW El is the hydrostatic condition.

10.3 Hydraulic Loading for ND/GB

Hydraulic loads consist of all loads due to water. These include hydrostatic (i.e., weight of water), hydrodynamic (i.e., load due to flowing water), and wave action. These are the predominant hydraulic loads, in terms of magnitude and frequency, experienced by HSS. Vibrations caused by flowing water, constricted flow, and water hammer are also considered hydraulic loads.

10.3.1 Hydrostatic Load for the ND/GB

The hydrostatic load is due to the hydraulic head across the ND/GB. The load is due to the hydrostatic pressure caused by the difference in water level on each side of the ND/GB. The maximum hydrostatic load occurs when the ND/GB are seated and the water level on the damming surface is at the maximum level.

The same method for developing the hydrostatic load for the other HSS is applicable to the dewatering ND/GB. Chapter 2 provided a detailed explanation of the hydrostatic load. The maximum hydrostatic pressure on the structure is expressed as γH (Equation 11), where γ is the unit weight of water, and H is the difference between the water level at the top of the damming surface and the bottom of the needle dam. Figure 84 shows an illustration of the hydrostatic pressure distribution on an ND/GB used to dewater a lock. The hydrostatic pressure (p) can be computed using Equation (10), which is repeated here:

$$p = \gamma y.$$

To obtain the force, the hydrostatic pressure is multiplied by the area the pressure is acting on. The maximum hydrostatic force occurs if the upper pool or TW El is the same as the top of the ND/GB. The location of the resultant hydrostatic force, H_s, is $H/3$ above the upper approach floor:

$$H_s = \frac{1}{2}\gamma H^2.$$

Figure 84. Hydrostatic pressure distribution and the location of the resultant hydrostatic force for the ND/GB at the upper end of the lock.

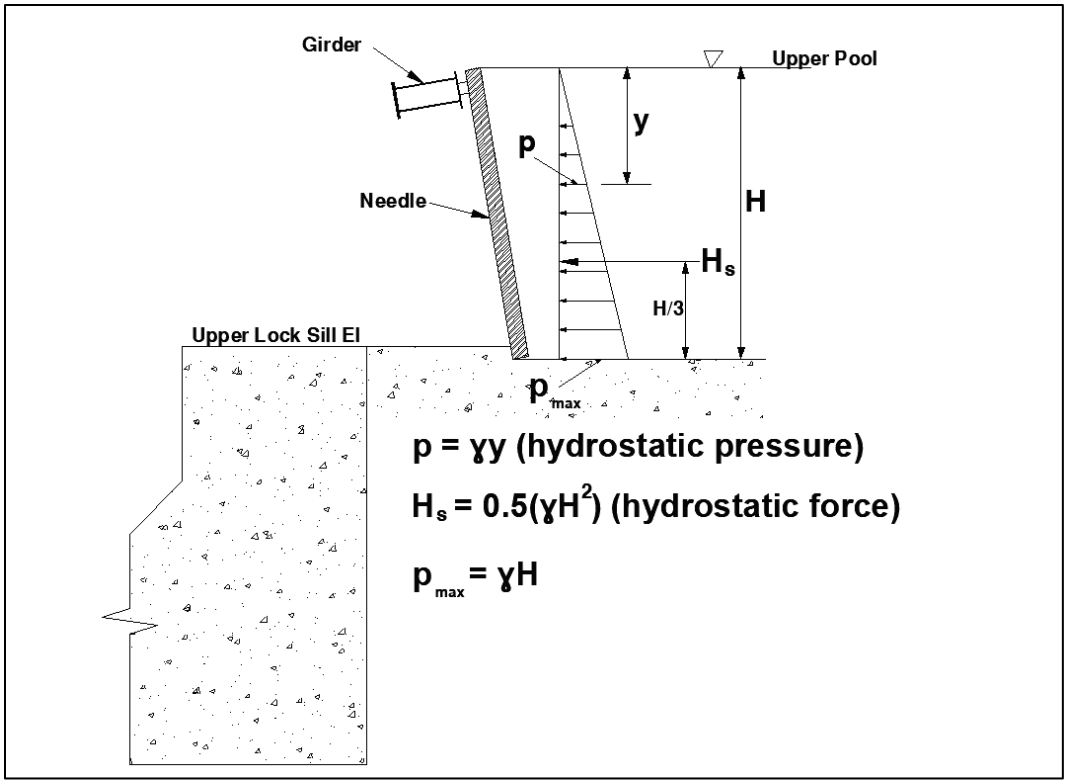

10.3.2 Wave Load for ND/GB

Wave loads are project specific and are considered for projects that experience significant wind and fetch. The same procedures used for the other HSS can be applied to the ND/GB. These procedures are described in Chapter 2. The Goda (2010) procedures are the recommended guidance for wind-induced wave loadings for inland navigation projects. The Goda wave pressure distribution procedure for the ND/GB is the same as that for the vertical-lift spillway gate shown in Figure 45. Appendix I contains an example procedure to compute the wave pressure on the ND/GB using the Goda procedure.

10.3.3 Probabilistic Characterization of the Hydrostatic Load for the ND/GB

The dispersion of the hydrostatic load needs to be determined for the LRFD analysis. The fluctuation of the hydrostatic load results from changes in the upper pool if the ND/GB is used on the upstream side of the lock and from changes in the lower pool if the ND/GB is used on the downstream side of the lock. Appendix I contains an example of

developing the statistics needed to determine the dispersion of the hydrostatic load for the ND/GB for the Chickamauga Lock.

10.3.4 Combined Hydrostatic and Wave Load for ND/GB

Wave loads are project specific and are considered for projects that experience significant wind and fetch. The hydrostatic and wave loading can be developed for the ND/GB using the procedures described in previous chapters for the other HSS.

10.3.5 Summary of Hydraulic Loads for ND/GB

The hydraulic loads on the ND/GB used for dewatering consist primarily of the hydrostatic and wave loads. The loads should be combined as appropriate to give the maximum load expected. The wind-to-wave force conversion, in some cases, can make a significant contribution to the combined loads. The authors of this report recommend that wind-induced wave forces be determined using the Goda (2010) design procedure discussed in previous chapters.

11 Loadings Applied to Reverse Tainter Valves

This chapter discusses hydraulic loads as they apply to reverse tainter valves used to fill and empty a navigation lock. Reverse tainter valves are used for many navigation locks and are the most common type used on major locks constructed by USACE. Davis (1989) reported "with only two exceptions, all of the locks built in the United States since 1940 have had reverse tainter valves" (145–146).

The conventional tainter gate typically used for spillways has the trunnions located downstream from the skin plate. The trunnions for the reverse tainter valve are located upstream from the skin plate, with the convex surface of the skin plate facing downstream. The valve seals against the downstream side of the valve well. Figure 85 shows a side view of a reverse tainter valve used in the *Watts Bar Lock Valve Model Study* (Bislip-Morales and Hite 2013). This reverse orientation prevents air from being drawn into the culvert during valve operations. Air pockets in the culvert are highly undesirable because they can cause violent expulsions from the valve well, the bulkhead slots, or possibly through the ports and into the chamber. This can be unsafe for small vessels in the lock chamber.

EM 1110-2-1604 (HQUSACE 2006) states that there are three structurally different types of reverse tainter valves: horizontally framed, vertically framed, and double skin plate. All three can be constructed to provide the desired rigidity. Experiences from operating lock valves at many projects over several years have shown the double skin plate and vertically framed valves are less prone to load variations and critical hydraulic loads during the opening cycle.

The double skin plate valve has been used successfully at USACE navigation locks with higher lifts (i.e., 60 ft or higher). In more recent years (starting in the 1980s), there has been concern that the internal structural members cannot be easily inspected, and some districts have chosen to replace some of the double skin plate valves with vertically framed reverse tainter valves. The long-term performance of these vertically framed replacement valves has yet to be determined.

Figure 85. Side view of a reverse tainter valve (flow is left to right). (Image reproduced from Bislip-Morales and Hite 2013, 7. Public domain.)

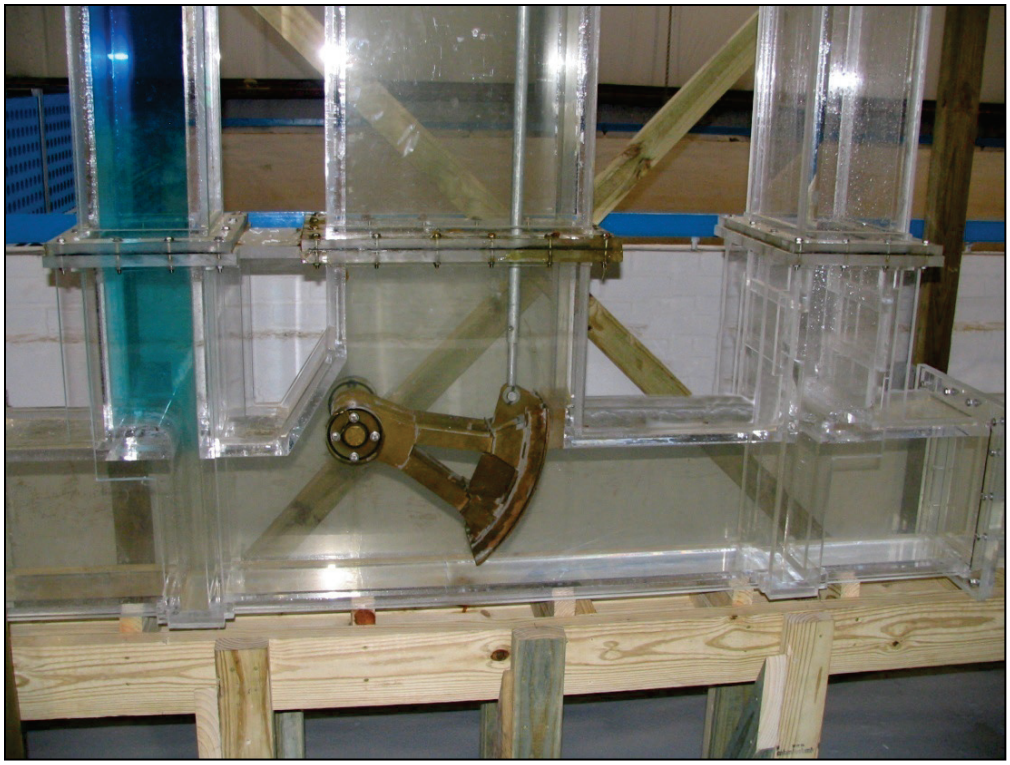

11.1 Existing Guidance for Reverse Tainter Valves

Numerous studies have been conducted to develop designs and evaluate the hydraulic performance of the reverse tainter valves. Stockstill et al. (2011) thoroughly examined hydraulic design considerations and provided applicable references. Stockstill et al. (2015) reported on a navigation project that experienced operating issues after the original double skin plate valves were replaced with vertically framed reverse tainter valves. Some structural design guidance can be found in USACE EMs and will be discussed in the sections that follow.

11.1.1 ETL 1110-2-584, *Design of Hydraulic Steel Structures*

ETL 1110-2-584 (HQUSACE 2014) provides general design guidance and philosophy for HSS but does not specifically cover the structural design of reverse tainter valves.

11.1.2 EM 1110-2-1610, *Hydraulic Design of Lock Culvert Valves*

EM 1110-2-1610 (HQUSACE 1975) describes hydraulic loads due to flowing water. The hydraulic loads are the summation of forces on the valve

members due to flowing water considered as a single force. A downpull load acts to rotate the valve to the closed position, and an uplift load acts to rotate the valve to the open position.

11.1.2.1 Horizontally Framed Valve

This valve design consists of a skin plate attached to a series of horizontal beams. The loads are transmitted to the trunnion arms through vertical members (usually girders) near the sides of the valve. Figure 86 shows a model of a horizontally framed valve used during a model study of Lock 19 on the Mississippi River.

Figure 86. Photo of a scale model of a horizontally framed reverse tainter valve, which reproduced the structural members shown in the section view. (Image reproduced from EM 1110-2-1610, HQUSACE 1975, 3-9. Public domain.)

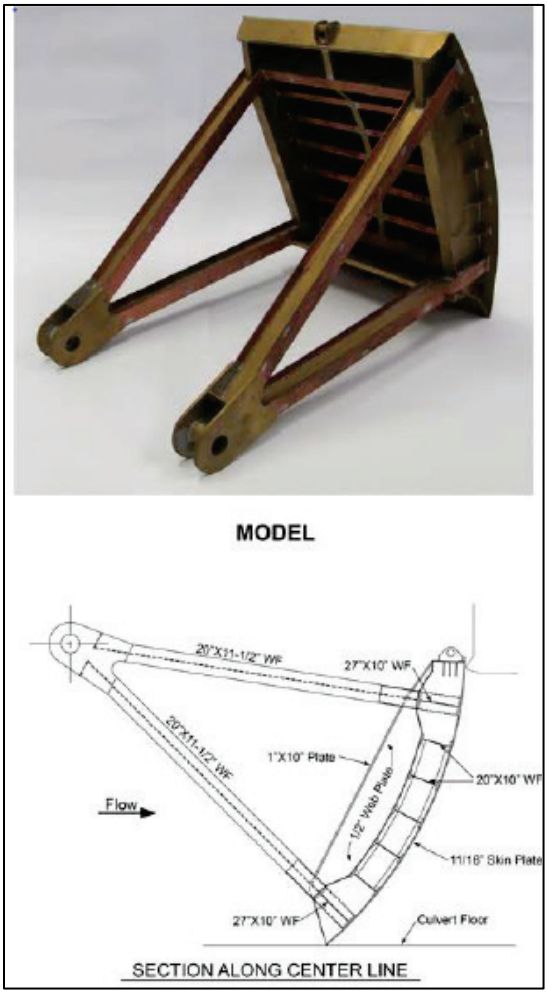

These valves were used in earlier low-lift (i.e., less than 25 or 30 ft) locks and worked adequately. The lift at Lock 19 on the Mississippi River was greater than 35 ft, and problems were encountered when operating the valves. When the valve was between two-thirds and full open, fluctuating loads began to occur and caused load reversals on the operating machinery. This was not acceptable, and changes to the design were necessary to resume normal operations. Due to these observations, this type of valve has not been used in the modern era.

11.1.2.2 Double Skin Plate Reverse Tainter Valve

The double skin plate valve evolved to improve the hydraulic conditions during valve operations. A smooth upstream surface, rather than exposed beams and structural members, resulted in more streamlined flow around the valve. In most cases, the valve is filled with water for greater stability. The semicircular shapes at the top and bottom of the valve can result in flow oscillations (i.e., control shifts) and cause the entire valve to vibrate. Figure 87 shows a model of a double skin plate valve.

The long-term performance of the valves has varied among USACE projects. The valves at the Barkley Lock were field tested (Neilson 1975) and found to be performing as designed and did not experience vibrations. The double skin plate reverse tainter valves used at John Day and the Dalles Locks were found to have cracks in the steel wrapper plate, and the structural performance has been considered unreliable by USACE-NWP. Figure 88 shows a double skin plate valve removed from operation at the Dalles project due to cracking in the steel wrapper plate. The USACE-NWP has been investigating the structural design of these valves for the last few years and has proposed field tests to measure pressure, strain, and accelerations at selected locations to identify performance issues.

Figure 87. Photo of a scale model of a double skin plate reverse tainter valve, which reproduced the structural members shown in the section view. (Image reproduced from EM 1110-2-1610, HQUSACE 1975, 3-9. Public domain.)

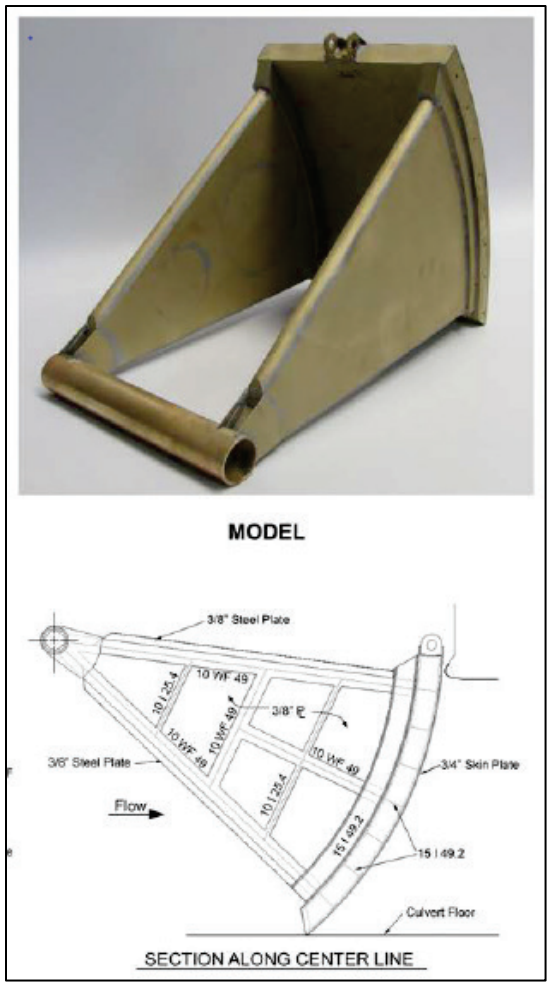

Figure 88. Double skin plate tainter valve at the Dalles Lock removed for repair.

11.1.2.3 Vertically Framed Reverse Tainter Valve

The vertically framed reverse tainter valve is constructed from a series of parallel curved T-beam ribs attached to a skin plate. Two horizontal girders are usually used at the top and bottom of the valve and are attached to the T-beam vertical ribs. The trunnion arms on each side of the valve are attached to these horizontal girders. The horizontal girders transmit the water load to the trunnion arms. The spaces between the T-beam ribs provide an open area for water to flow along the skin plate to minimize the hydrodynamic forces on the valve. Figure 89 shows a photo of a model of a vertically framed valve and the structural members reproduced in the model.

The vertically framed valve has been used on most of the locks constructed since 1970. This type of valve has generally performed well, although there have been cases that required frequent maintenance. At Holt Lock, the lifting mechanisms vibrate during lock operations. A structural design similar to that used for the Holt Lock valve was also used at the Bankhead Lock, and it performs well. The Bankhead valve is 34% heavier than the Holt valve. Slight modifications to the bottom of the Holt valve resulted in

much worse performance, indicating that slight changes to the valve shape can cause significant changes to the hydrodynamic loads.

Figure 89. Photo of a scale model of a vertically framed reverse tainter valve, which reproduced structural members shown in the section view. (Image reproduced from EM 1110-2-1610, HQUSACE 1975, 3-9. Public domain.)

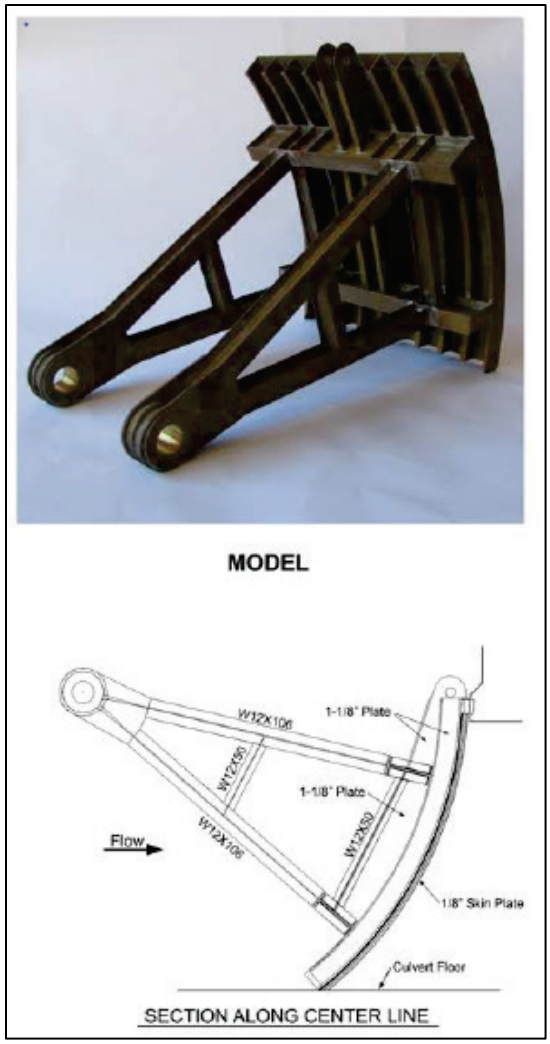

11.1.2.4 Performance Comments

EM 1110-2-1610 (HQUSACE 1975) states that "the two features that most affect loads on the valve hoist due to flowing water are the depth of the lower girder and the extension of the lower lip of the skin plate below the lower girder" (3-6). This was the case for all three types of valves. The peak downpull and load variations were reduced when the depth of the lower girder was decreased. The range of valve positions where downpull occurs

was also reduced, along with an increase in the range of valve positions where uplift occurs. Similar results of reduction in downpull and the range of valve positions where downpull occurs were also observed with an increase in the extension of the lower lip below the lower girder.

11.1.3 EM 1110-2-1604, *Hydraulic Design of Navigation Locks*

This manual indicates that the normal tainter valve has not been precluded from lock design when used as an emptying valve. The manual provides guidance on valve sizing and siting (i.e., location).

11.1.4 EM 1110-2-2602, *Planning and Design of Navigation Locks*

EM 1110-2-2602 (HQUSACE 1995b) states that, currently, all medium- to high-lift major locks under construction use the reverse tainter valve.

11.1.5 EM 1110-2-2610, *Mechanical and Electrical Design for Lock and Dam Operating Equipment*

EM-1110-2-2610 (HQUSACE 2013) states that the valve hoist load should be designed for all of the following:

- The gate connection load due to flowing water under the valve
- The buoyant (submerged) weight of the valve
- The weight of the operating equipment linkages or wire rope
- The side seal friction
- The trunnion bushing friction under maximum normal flowing water load
- Bushing friction at other points in the drive
- The head differential across the top seal of the valve

This EM suggests that the reverse tainter valve is recommended for the majority of modern locks due to improved hydraulic characteristics, ease of fabrication, and lower installation and maintenance costs. It states, “For new locks, model studies should be conducted to determine the best valve configuration that will complement the hydraulic characteristics of the filling and emptying system. See EM 1110-2-1610 and ERDC TR 11-4 for further discussion” (HQUSACE 2013, 6-9).

11.2 Hydraulic Data Collection and Statistical Data Reduction for Mean Loading and Dispersion for the Reverse Tainter Valve

The reliability analysis for the reverse tainter valve requires that the mean and standard deviation of the loads be determined. Hydraulic data are needed to develop these values. To determine the hydrostatic load, the hydrodynamic load during valve operation and the upper and lower pool els are required. Historical data are necessary for developing the samples and statistical data required for the analysis.

11.2.1 Forebay El

For the reverse tainter valve, the forebay el contributes to both the hydrostatic and hydrodynamic loads. The nominal loads needed for the statistical analysis generally occur with a near-normal forebay el. The mean and standard deviation for the forebay need to be determined. The Dalles Lock and Dam on the Columbia River was the design example chosen for the reverse tainter valve. Appendix J contains the methodology used to determine the hydraulic data and the statistical data reduction. Appendix J also provides the procedures for developing the hydrostatic and hydrodynamic loads for the Dalles reverse tainter valve.

11.2.2 TW El

The TW El is also needed to determine the hydraulic forces. The net head on the valve is needed for the hydrostatic load. The maximum net head occurs when the tailwater is minimal and the forebay el is normal or above normal.

11.3 Hydraulic Loading for Reverse Tainter Valves

Hydraulic loads consist of all loads due to water. For the reverse tainter valve, these include hydrostatic (i.e., weight of water) and hydrodynamic (i.e., load due to flowing water). Vibrations caused by flowing water, constricted flow, and water hammer are also considered hydraulic loads. The reverse tainter valve used on high-lift locks is susceptible to vibration.

11.3.1 Hydrostatic Load for the Reverse Tainter Valve

The hydrostatic load on the reverse tainter valve is due to the head difference between the forebay and the TW Els. The maximum hydrostatic load occurs when this difference is at its highest. Because the reverse

tainter valve is used during lock operations, there can be times when the forebay elevation is too high for navigation. During a flow event that causes navigation to cease, the difference in the forebay el and the TW El is generally less than the difference between the normal forebay and the normal TW Els.

Chapter 2 provides a detailed explanation of the hydrostatic load for the STG. Figure 90 shows a schematic of the hydrostatic pressure on the reverse tainter structure, which is expressed as $\gamma \Delta H$, where γ is the unit weight of water, and ΔH is the difference between the forebay and TW Els. The hydrostatic pressure is multiplied by the area the pressure is acting on to obtain the force per foot of gate width:

$$H_s = \gamma \Delta H B. \tag{110}$$

The resultant hydrostatic force, H_s, is $B/2$ above the culvert floor.

Figure 90. Hydrostatic pressure distribution and the location of the resultant hydrostatic force for a reverse tainter valve in a lock.

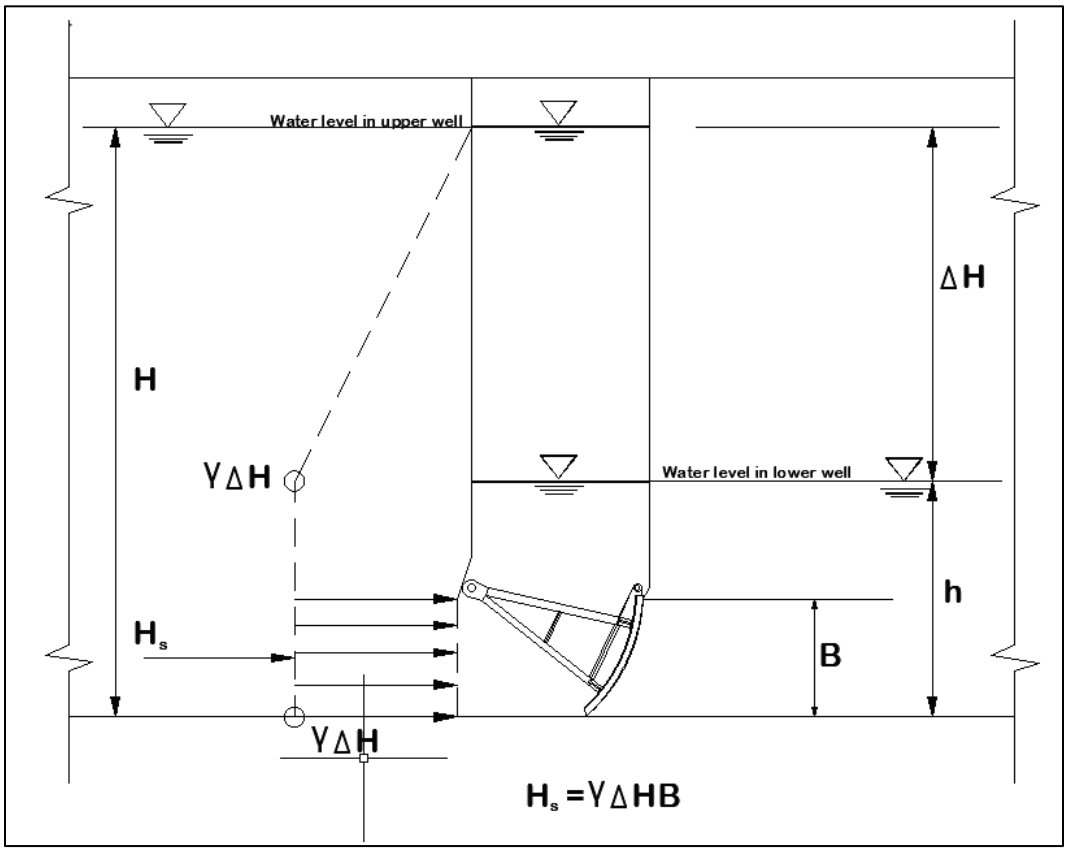

11.3.2 Hydrodynamic Load for Reverse Tainter Valves

Hydrodynamic loads for reverse tainter valves are associated with the hoist loads required to raise the valve. Many studies have been performed to measure hoist loads in physical models and in the prototype. EM 1110-2-1610 (HQUSACE 1975) presents typical hoist loads on reverse tainter valves. The total hoist load is the sum of the forces on the valve strut with flowing water and the stem load in the dry. The hydraulic forces are the sum of hydrostatic and hydrodynamic forces due to local accelerations as flow passes the valve. When hoist-load values are greater than the load due to the valve's dry hoist load, hydraulic forces are acting to close the valve and are generally referred to as downpull forces. When hoist-load values are less than the load due to the valve's dry hoist load, hydraulic forces are acting to open the valve and are generally referred to as uplift forces. Figure 91 illustrates these conditions.

Figure 91. Illustration of flow conditions around a reverse tainter valve that cause downpull and uplift forces. (Image reproduced from HQUSACE 1975, 3-13. Public domain.)

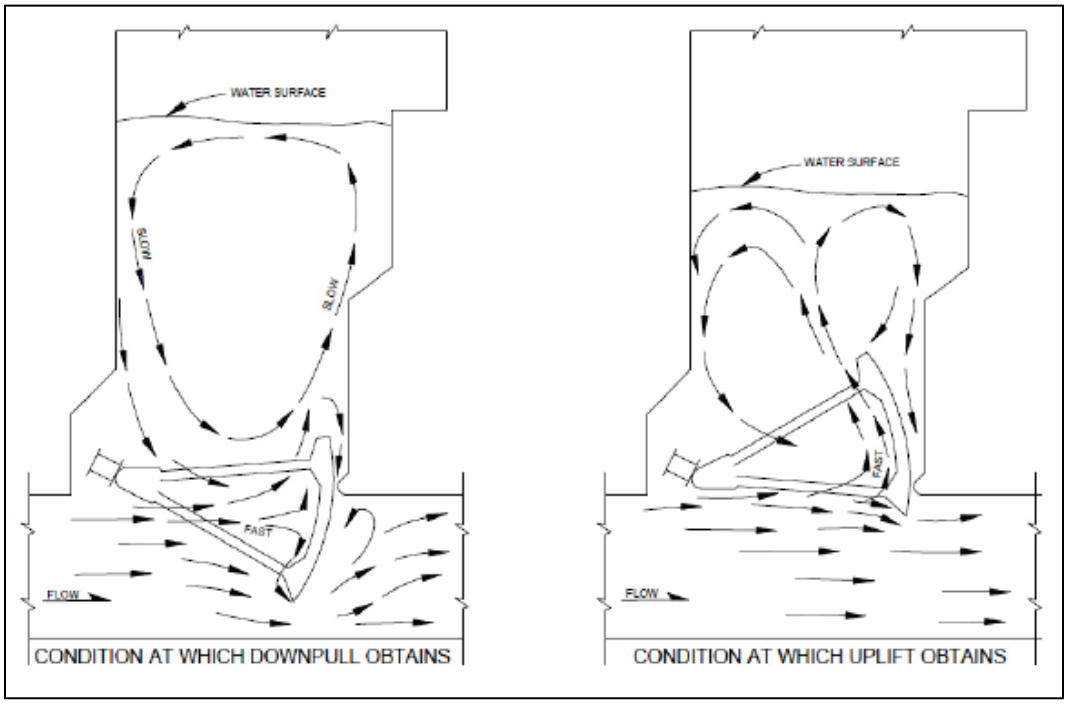

Figure 92 contains an example of hoist-load data from model studies. This information is intended as guidance when developing hoist loads for a new lock valve. According to Stockstill et al. (2011), to help predict valve performance, research that uses both numerical and physical models is recommended. Recently, USACE-NWP has tried to instrument a lock valve at the Dalles project to better understand the hydrodynamic forces associated

with the interaction of the valve structural members and the moving water. The authors of this report recommend that a prototype investigation be undertaken that instruments the valve sufficiently so that the loads, pressures, and vibration data required to validate a numerical code can be obtained. This would require a team of hydraulic, structural, instrumentation, electrical, mechanical, and operation specialists.

Figure 92. Total hoist loads from EM 1110-2-1610 used as design guidance. (Image reproduced from HQUSACE 1975, 3-14. Public domain.)

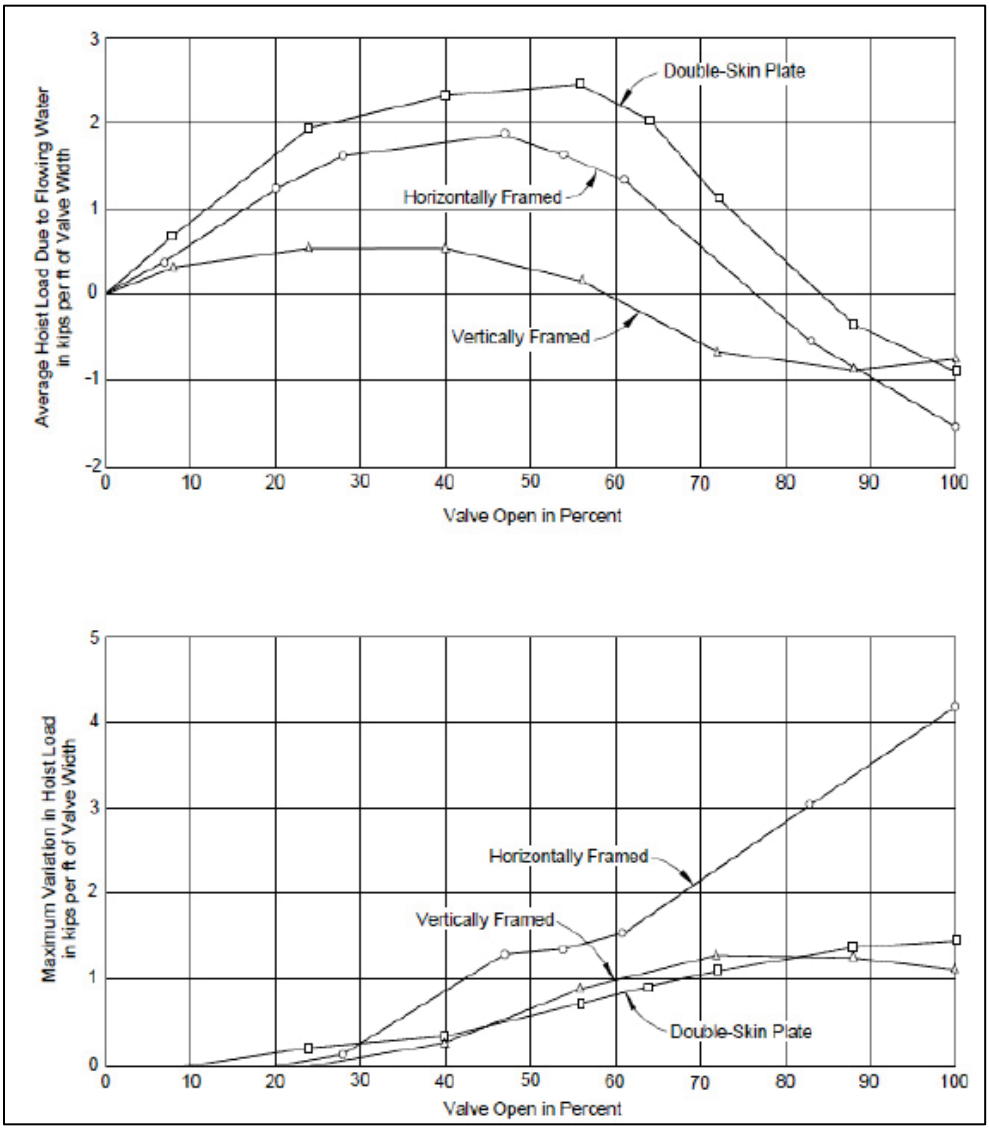

11.3.3 Probabilistic Characterization of the Hydrostatic and Hydrodynamic Loads for the Reverse Tainter Valve

The statistics for the hydraulic loads on the reverse tainter valves need to be determined for the LRFD analysis.

11.3.3.1 Probabilistic Characterization of the Hydrostatic Loads for the Reverse Tainter Valve

The dispersion of the hydrostatic load is a result of the changes in the upper and lower pool els inside the lock. The maximum hydrostatic load occurs with the maximum head on the reverse tainter valve. The fluctuations in hydrostatic load on the valve can be computed after determining the standard deviation of the head and selecting the range of this standard deviation about the main head. Appendix J in this report provides a design example of the statistics developed for the Dalles Lock reverse tainter valve using a range from $+3\sigma$ to -3σ about the mean head, which can be used in the LRFD analysis.

11.3.3.2 Probabilistic Characterization of the Hydrodynamic Load for the Reverse Tainter Valve

The dispersion of the hydrodynamic loads on the reverse tainter valve are difficult to determine, especially for high-lift projects, due to the interaction of rapidly varying turbulent flow and the structural components of the valves. As stated previously, the authors of this report recommend that field studies and numerical studies be performed to help develop more confidence in the hydrodynamic forces on the reverse tainter valve. USACE-NWP has made progress toward this effort. They have instrumented the valve at the Dalles Lock and have used a CFD model to help decide what type of modification can be made to the top seal and seat to minimize vibration issues.

11.3.4 Summary of Hydraulic Loads for Reverse Tainter Valves

The hydraulic loads on the reverse tainter valve consist primarily of hydrostatic and hydrodynamic loads. The hydrostatic loads are straightforward, and a good estimate of these loads can be determined from the project's hydraulic data. The current methods for determining the hydrodynamic loads are based on hoist load data in EM 1110-2-1610 (HQUSACE 1975) and include extraneous forces mostly due to friction. Nevertheless, the hydrodynamic load will have a greater effect on the performance of the reverse tainter valve.

12 Summary, Conclusions, and Recommendations

12.1 Report Summary

This report provides basic guidance on methods for determining the hydraulic loads that are needed to conduct an LRFD analysis for USACE HSS. The reports that are included in the research effort provide a description of the reliability analysis as it relates to LRFD of HSS and the procedures used to develop the necessary limit states and load factors for the analysis. A structural finite element model will be used to evaluate the resistance of the structural components from applied loads.

Many of the 10 HSS selected for this research effort have similar procedures for estimating hydraulic loads; some of them, however, are unique and will require more research to develop the confidence needed to compute some of the loads. This research will need to incorporate a combination of numerical modeling and field experiments and, possibly, laboratory experiments.

Much of the existing USACE guidance for LRFD methods does not provide sufficient information to complete this type of analysis, and this report provides additional guidance and information on how to estimate some of the hydraulic loads. The authors cite existing guidance in each individual chapter for specific gate types. Ten appendixes are included to show examples of how some of the loads can be computed.

12.2 Conclusions and Recommendations

The following list contains a brief description of the conclusions and recommendations that were formed from this portion of the research.

- Hydrostatic loads are generally straightforward calculations with a high degree of confidence in their load values. Similar methods can be used to determine these loads for closed spillway gates, closed lock gates, bulkheads, and closure structures.
- A new procedure to estimate wind-induced wave loads for inland hydraulic structures was suggested. The procedure is based on developing the 100 yr return period wind speed and following Goda's (2010) guidelines to compute the accompanying wave load. The 30 yr record

of wind speed should be used, if possible, to develop the 100 yr return period wind speed. Most of the wind data used in this research were from airports near the inland project of interest. This technique was considered to have a moderate to high confidence level.

- The hydrodynamic loads were more difficult to estimate. A conservation of momentum equation was used to estimate the hydrodynamic force for a spillway gate with a tailwater influence. The confidence level from this technique was considered moderate. A procedure from numerical research by Kim (2007) and laboratory experiments by Roth and Hager (1999) was adopted to compute the hydrodynamic force for a spillway gate without a tailwater influence. The confidence level from this technique was considered high.
- USACE guidance for computing hydrodynamic loads for lock gates needs additional research. Much of the existing guidance for estimating machinery and operating loads was developed from model studies performed many years ago, although years of operational experience have demonstrated that these methods seem adequate. The additional research may allow less conservatism in estimating these loads.
- Of the 10 HSS that were evaluated, it was most difficult to compute the hydrodynamic loads for the reverse tainter valve. USACE-NWP has performed both numerical and field experiments to increase confidence in estimates of the hydraulic loads for the design of the replacement valves being considered for both John Day and the Dalles Locks.

References

AISC (American Institute of Steel Construction). 1980. *Manual of Steel Construction*. 8th ed. New York: American Institute of Steel Construction.

Bastian, D. F. 1971. *Calcasieu Saltwater Barrier Prototype Sector Gate Tests*. MP-H-71-4. Vicksburg, MS: US Army Engineer Waterways Experiment Station. https://hdl.handle.net/11681/10745.

Bishop, C. T., M. A. Donelan, and K. K. Kahama. 1992. "Shore Protection Manual's Wave Prediction Reviewed." *Coastal Engineering* 17 (1–2): 25–48. https://doi.org/10.1016/0378-3839(92)90012-J.

Bislip-Morales, C. B., and J. E. Hite, Jr. 2013. *Watts Bar Lock Valve Model Study*. ERDC/CHL-TR-13-12. Vicksburg, MS: US Army Engineer Research and Development Center, Coastal and Hydraulics Laboratory. http://hdl.handle.net/11681/7329.

Coastal Engineering Research Center. 1984a. *Shore Protection Manual*. Vol. 1. Vicksburg, MS: US Army Engineer Waterways Experiment Station. https://luk.staff.ugm.ac.id/USACE/USACE-ShoreProtectionManual1.pdf.

Coastal Engineering Research Center. 1984b. *Shore Protection Manual*. Vol. 2. Vicksburg, MS: US Army Engineer Waterways Experiment Station. https://luk.staff.ugm.ac.id/USACE/USACE-ShoreProtectionManual2.pdf.

Cox, R. G. 1972. *Pertinent Data on Spillway Tainter Gates for Corps of Engineers Projects*. MP-H-72-7. Vicksburg, MS: US Army Engineer Waterways Experiment Station. https://hdl.handle.net/11681/10729.

Davis, J. P. 1989. *Hydraulic Design of Navigation Locks*. MP-HL-89-5. Vicksburg, MS: US Army Engineer Waterways Experiment Station. https://apps.dtic.mil/sti/pdfs/ADA213174.pdf.

Donelan, M. A. 1980. "Similarity Theory Applied to the Forecasting of Wave Heights, Periods, and Directions." In *Proceedings of the Canadian Coastal Conference,* 22–24 April, Burlington, Ontario, Canada, 47–61. Ontario, Canada: Associate Committee for Research on Shoreline Erosion and Sedimentation.

Ebeling, R. M., M. T. Fong, and B. C. White. 2016. *Analysis of a Floodplain I-Wall Embedded in Horizontally Stratified Soil Layers during Flood Events Using Corps_I-Wall Software*. Version 1.0. ERDC/ITL TR-16-3. Vicksburg, MS: US Army Engineer Research and Development Center, Information Technology Laboratory. http://hdl.handle.net/11681/20242.

Ebeling, R. M., and B. C. White. 2019. *Load Factors for Earth Retaining, Reinforced Concrete Hydraulic Structures Based on a Reliability (β) Derived from the Probability of Unsatisfactory Performance (PUP): Phase 1 Study*. ERDC/ITL TR-19-5. Vicksburg, MS: US Army Engineer Research and Development Center, Information Technology Laboratory. https://hdl.handle.net/11681/33227.

Ebeling, R. M., and B. C. White. 2021. *Load and Resistance Factors for Earth Retaining, Reinforced Concrete Hydraulic Structures Based on a Reliability Index (β) Derived from the Probability of Unsatisfactory Performance: Phase 2 Study*. ERDC/ITL TR-21-1. Vicksburg, MS: US Army Engineer Research and Development Center, Information Technology Laboratory. https://hdl.handle.net/11681/39881.

Ebeling, R. M., B. C. White, and M. T. Fong. 2018. *Analysis of a River Bank, Levee, or Floodplain I-Wall Embedded in Stratified Soil Layers during Flood Events Using Corps_I-Wall (CI-Wall) Version 2*. ERDC/ITL TR-18-2. Vicksburg, MS: US Army Engineer Research and Development Center, Information Technology Laboratory. https://hdl.handle.net/11681/31502.

Ebeling, R. M., B. C. White, J. E. Hite, J. R. Tallent, L. M. Williams, B. C. McCoy, A. Hill, C. Dell, J. Bruhl, and K. McMullen. 2023. *Load and Resistance Factors from Reliability Analysis Probability of Unsatisfactory Performance (PUP) of Flood Mitigation, Batter Pile-Founded T-Walls Given a Target Reliability Index (β)*. ERDC TR-23-9. Vicksburg, MS: US Army Engineer Research and Development Center. http://dx.doi.org/10.21079/11681/47245.

Eschler, H. 1958. *Investigations as Regards the Lowering of Weir Stop Logs in Flowing Water*. Translation No. 58-2. Vicksburg, MS: US Army Engineer Waterways Experiment Station.

Freedman, D., and P. Diaconis. 1981. "On the Histogram as a Density Estimator: L_2 Theory." *Zeitschrift für Wahrscheinlichkeitstheorie und Verwandte Gebiete* 57: 453–476. https://doi.org/10.1007/BF01025868.

Goda, Y. 1974. "New Wave Pressure Formulae for Composite Breakwater." In *Proceedings of the 14th International Conference on Coastal Engineering*, 24–28 June, Copenhagen, Denmark, 1,702–1,720. New York: ASCE. https://doi.org/10.1061/9780872621138.103.

Goda, Y. 2010. *Random Seas and Design of Maritime Structures*. 3rd ed. Hackensack, NJ: World Scientific. https://doi.org/10.1142/7425.

Grace, J. L. 1964. *Spillway for Typical Low-Head Navigation Dam, Arkansas River, Arkansas: Hydraulic Model Investigation*. Technical Report 2-655. Vicksburg, MS: US Army Engineer Waterways Experiment Station. https://erdc-library.erdc.dren.mil/jspui/bitstream/11681/13120/1/TR-HL-74-13.pdf.

Gringorten, I. I. 1963. "A Plotting Rule for Extreme Probability Paper." *Journal of Geophysical Research* 68 (3): 813–814. https://doi.org/10.1029/JZ068i003p00813.

Hite, J. E., Jr., and G. A. Pickering. 1983. *Barkley Dam Spillway Tainter Gate and Emergency Bulkheads, Cumberland River, Kentucky: Hydraulic Model Investigation*. Technical Report HL-83-12. Vicksburg, MS:US Army Engineer Waterways Experiment Station. https://erdc-library.erdc.dren.mil/jspui/bitstream/11681/13705/1/TR-HL-83-12.pdf.

HQUSACE (Headquarters, US Army Corps of Engineers). 1975. *Hydraulic Design of Lock Culvert Valves*. EM 1110-2-1610. Washington, DC: Department of the Army. https://www.publications.usace.army.mil/Portals/76/Users/182/86/2486/EM_1110-2-1610.pdf.

HQUSACE (Headquarters, US Army Corps of Engineers). 1980. *Hydraulic Design of Reservoir Outlet Works*. EM 1110-2-1602. Washington, DC: Department of the Army. https://www.publications.usace.army.mil/Portals/76/Publications/EngineerManuals/EM_1110-2-1602.pdf.

HQUSACE (Headquarters, US Army Corps of Engineers). 1987. *Hydraulic Design of Navigation Dams*. EM 1110-2-1605. Washington, DC: Department of the Army. https://www.publications.usace.army.mil/Portals/76/Publications/EngineerManuals/EM_1110-2-1605.pdf?ver=CKI0VCTAeRKnUDUmbbb4Pw%3d%3d.

HQUSACE (Headquarters, US Army Corps of Engineers). 1990. *Hydraulic Design of Spillways*. EM 1110-2-1603. Washington, DC: Department of the Army. https://www.publications.usace.army.mil/Portals/76/Publications/EngineerManuals/EM_1110-2-1603.pdf?ver=9IVt6Fb0elyNQuII674sGQ%3d%3d.

HQUSACE (Headquarters, US Army Corps of Engineers). 1994. *Lock Gates and Operating Equipment*. EM 1110-2-2703. Washington, DC: Department of the Army. https://apps.dtic.mil/sti/tr/pdf/ADA402894.pdf.

HQUSACE (Headquarters, US Army Corps of Engineers). 1995a. *Planning and Design of Navigation Dams*. EM 1110—2-2607. Washington, DC: Department of the Army. https://www.publications.usace.army.mil/Portals/76/Publications/EngineerManuals/EM_1110-2-2607.pdf.

HQUSACE (Headquarters, US Army Corps of Engineers). 1995b. *Planning and Design of Navigation Locks*. EM 1110-2-2602. Washington, DC: Department of the Army. https://www.publications.usace.army.mil/Portals/76/Publications/EngineerManuals/EM_1110-2-2602.pdf?ver=NMVvdtjpQ9RfOueoXUqLXA%3d%3d.

HQUSACE (Headquarters, US Army Corps of Engineers). 1997. *Vertical Lift Gates*. EM 1110-2-2701. Washington, DC: Department of the Army. https://planning.erdc.dren.mil/toolbox/library/EMs/em1110.2.2701.pdf.

HQUSACE (Headquarters, US Army Corps of Engineers). 2000. *Design of Spillway Tainter Gates*. EM 1110-2-2702 (rescinded). Washington, DC: Department of the Army. https://apps.dtic.mil/sti/pdfs/ADA402900.pdf.

HQUSACE (Headquarters, US Army Corps of Engineers). 2001. *Inspection, Evaluation, and Repair of Hydraulic Steel Structures*. EM 1110-2-6054. Washington, DC: Department of the Army. https://www.publications.usace.army.mil/portals/76/publications/engineermanuals/em_1110-2-6054.pdf.

HQUSACE (Headquarters, US Army Corps of Engineers). 2002. *Engineering and Design: Ice Engineering*. EM 1110-2-1612. Washington, DC: Department of the Army. https://www.publications.usace.army.mil/Portals/76/Publications/EngineerManuals/EM_1110-2-1612.pdf.

HQUSACE (Headquarters, US Army Corps of Engineers). 2006. *Hydraulic Design of Navigation Locks*. EM 1110-2-1604. Washington, DC: Department of the Army. https://www.publications.usace.army.mil/LinkClick.aspx?fileticket=xNjjSmfehoc%3d&tabid=16439&portalid=76&mid=43544.

HQUSACE (Headquarters, US Army Corps of Engineers). 2013. *Mechanical and Electrical Design for Lock and Dam Operating Equipment*. EM 1110-2-2610. Washington, DC: Department of the Army. https://www.publications.usace.army.mil/LinkClick.aspx?fileticket=F9mXQfvmyPE%3d&tabid=16439&portalid=76&mid=43544.

HQUSACE (Headquarters, US Army Corps of Engineers). 2014. *Design of Hydraulic Steel Structures*. ETL 1110-2-584. Washington, DC: Department of the Army. https://www.publications.usace.army.mil/portals/76/publications/engineertechnicalletters/etl_1110-2-584.pdf.

Iowa State University. n.d. "Iowa Environmental Mesonet." Accessed between 2019 and 2022. https://mesonet.agron.iastate.edu/request/download.phtml?network=MS_ASOS.

Kim, D. G. 2007. "*Numerical Analysis of Free Flow Past a Sluice Gate.*" *KSCE Journal of Civil Engineering* 11 (2): 127–132. https://doi.org/10.1007/BF02823856.

King, H. W. 1954. *Handbook of Hydraulics*. 3rd ed. New York: McGraw-Hill.

Maynord, S. T., and R. L. Stockstill. 2012. *Emergency Closure of Uncontrolled Flow at Locks and Dams*. ERDC/CHL TR-12-8. Vicksburg, MS: US Army Engineer Research and Development Center, Coastal and Hydraulics Laboratory. http://hdl.handle.net/11681/7524.

Melsheimer, E. S., and T. E. Murphy. 1961. *Spillway for New Cumberland Locks and Dam (Final Design) Ohio River, West Virginia*. Technical Report 2-5855. Vicksburg, MS: US Army Engineer Waterways Experiment Station.

Naudascher, E. 1982. *Flow Induced Forces and Vibrations. Notes for Short Course at Alden Research Laboratory*. Worcester, MA: Worcester Polytechnic Institute.

NCDC (National Climate Data Center). n.d. "Climate Data Online: Dataset Discovery." *NOAA, National Centers for Environmental Education*. Accessed June 2019. https://www.ncdc.noaa.gov/cdo-web/datasets.

Neilson, F. M. 1975. *Barkley Lock Prototype Tests, Cumberland River, Kentucky*. Technical Report H-75-11. Vicksburg, MS: US Army Engineer Waterways Experiment Station. http://hdl.handle.net/11681/13586.

Oswalt, N. R. 1970. *Operating Forces on Sector Gates under Reverse Heads*. Technical Report H-70-2. Vicksburg, MS: US Army Engineer Waterways Experiment Station. http://hdl.handle.net/11681/13504.

Oswalt, N. R., and T. E. Murphy. 1971. *Operating Forces on Sector Gates under Reverse Heads, Appendix A: Results of Supplemental Tests*. Technical Report H-70-2. Vicksburg, MS: US Army Engineer Waterways Experiment Station. http://hdl.handle.net/11681/13498.

Rattanapitikon, W., and T. Shibayama. 2000. "Verification and Modification of Breaker Height Formulas." *Coastal Engineering Journal* 42 (4): 389–406. https://doi.org/10.1142/S0578563400000195.

Roberson, J. A., and C. C. Crowe. 1985. *Engineering Fluid Mechanics*. 3rd ed. Boston, MA: Houghton Mifflin Company.

Roth, A., and W. H. Hager. 1999. "Underflow of Standard Sluice Gate." *Experiments in Fluids* 27 (4): 339–350. http://dx.doi.org/10.1007/s003480050358.

Smith, J. M. 1991. *Wind-Wave Generation on Restricted Fetches*. MP CERC-91-2. Vicksburg, MS: US Army Engineer Waterways Experiment Station. http://hdl.handle.net/11681/13018.

Stockstill, R. L., E. A. Hammack, and J. E. Hite, Jr. 2011. *Lock Culvert Valves: Hydraulic Design Considerations*. ERDC/CHL TR-11-4. Vicksburg, MS: US Army Engineer Research and Development Center, Coastal and Hydraulics Laboratory. http://hdl.handle.net/11681/7720.

Stockstill, R. L., E. A. Hammack, D. S. Smith, C. B. Bislip-Morales, K. K. Green, and J. M. Vaughan. 2015. *Hydraulic Evaluation of Culvert Valves at Eisenhower and Snell Locks, St. Lawrence Seaway*. ERDC/CHL TR-15-7. Vicksburg, MS: US Army Engineer Research and Development Center, Coastal and Hydraulics Laboratory. http://hdl.handle.net/11681/7328.

USACE (US Army Corps of Engineers). n.d. "Access to Water Resources Data." Accessed February 14, 2020. http://water.usace.army.mil/a2w/f?p=100:1:0.

USACE (US Army Corps of Engineers). n.d. "Water Levels of Rivers and Lakes." *RiverGages.com*. Accessed February 14, 2020. https://rivergages.mvr.usace.army.mil/WaterControl/new/layout.cfm.

USACE-LRN (US Army Corps of Engineers, Nashville District). 1958. *Barkley Dam Project, Cumberland River, Kentucky and Tennessee*. Design Memorandum No. 9, Lock–Analysis of Design. Nashville, TN: US Army Corps of Engineers Nashville District.

USACE-MVN (US Army Corps of Engineers, New Orleans District). 2011. *Lake Pontchartrain and Vicinity Hurricane Protection Project LPV 18.2–Williams Blvd. Floodgate, Jefferson Parish, LA*. US Army Corps of Engineers New Orleans District.

USACE-MVP (US Army Corps of Engineers, St. Paul District). 2014. *Oxbow-Hickson-Bakke (OHB) Levee Wind-Wave Analysis: Final Draft*. St. Paul, MN: US Army Corps of Engineers St. Paul District.

USACE-MVS (US Army Corps of Engineers, St. Louis District). 1971. *Locks and Dam No. 26 (Replacement) Mississippi River–Alton, Illinois*. Design Memorandum No. 1, Hydrology. St. Louis, MO: US Army Corps of Engineers St. Louis District.

USACE-NWP (US Army Corps of Engineers, Portland District). 2020. *John Day and the Dalles Navigation Lock Tainter Valve*. Design Documentation Report No. 38 (95 Percent DDR). Portland, OR: US Army Corps of Engineers Portland District.

USGS (US Geological Survey). "National Water Information System: Mapper." *USGS*. Accessed February 14, 2020. https://maps.waterdata.usgs.gov/mapper/index.html.

WES (US Army Engineer Waterways Experiment Station). 1961. *Culvert Tainter Valves, New Lock 19, Mississippi River, Hydraulic Model Investigation*. Technical Report No. 2-537. Vicksburg, MS: US Army Engineer Waterways Experiment Station.

WES (US Army Engineer Waterways Experiment Station). 1963. *Discharge Rating Curves for Vertical Lift Gates on Spillway Crests*. MP No. 2-606. Vicksburg, MS: US Army Engineer Waterways Experiment Station. http://hdl.handle.net/11681/21147.

WES (US Army Engineer Waterways Experiment Station). 1964. *Operating Forces on Miter-Type Lock Gates*. Technical Report No. 2-651. Vicksburg, MS: US Army Engineer Waterways Experiment Station. http://hdl.handle.net/11681/4728.

WES (US Army Engineers Waterways Experiment Station). 1980. *Hydraulic Design Criteria*. Vol. 1. Vicksburg, MS: US Army Engineer Waterways Experiment Station. https://apps.dtic.mil/sti/tr/pdf/ADA092237.pdf.

Appendix A: Example Hydraulic Load Computations for the Melvin Price Locks and Dam (MPLD) Spillway Tainter Gate (STG)

In this appendix, the procedures discussed in Chapter 2 of the main report are presented using data from an existing US Army Corps of Engineer (USACE) Navigation project. The data needed to quantify the hydraulic loads for the spillway tainter gate (STG) and example computations are described.

A.1 The 30 yr Record of Hydrologic Data of the Tailwater for MPLD

The Melvin Price Locks and Dam (MPLD) project on the Mississippi River was chosen to illustrate how to determine the hydraulic loads on the STG. Design Memorandum 1, *Hydrology* (USACE-MVS 1971), was used for flow and stage frequencies. The report contains data on discharge, tailwater elevation (TW El), and upper pool frequency. The spillway rating curve for the project was furnished by USACE, St. Louis District (USACE-MVS). The pertinent data for the project are provided here and are shown schematically in Figure A-1.

- Spillway crest elevation (el) = 379
- Normal upper pool el = 419
- Approach el = 370
- Stilling basin floor el = 359
- Spillway gate width = 110 ft
- Spillway gate top el when gate is closed = 421
- Trunnion el = 422

Figure A-1. Melvin Price Locks and Dam (MPLD) spillway and basin elevations.

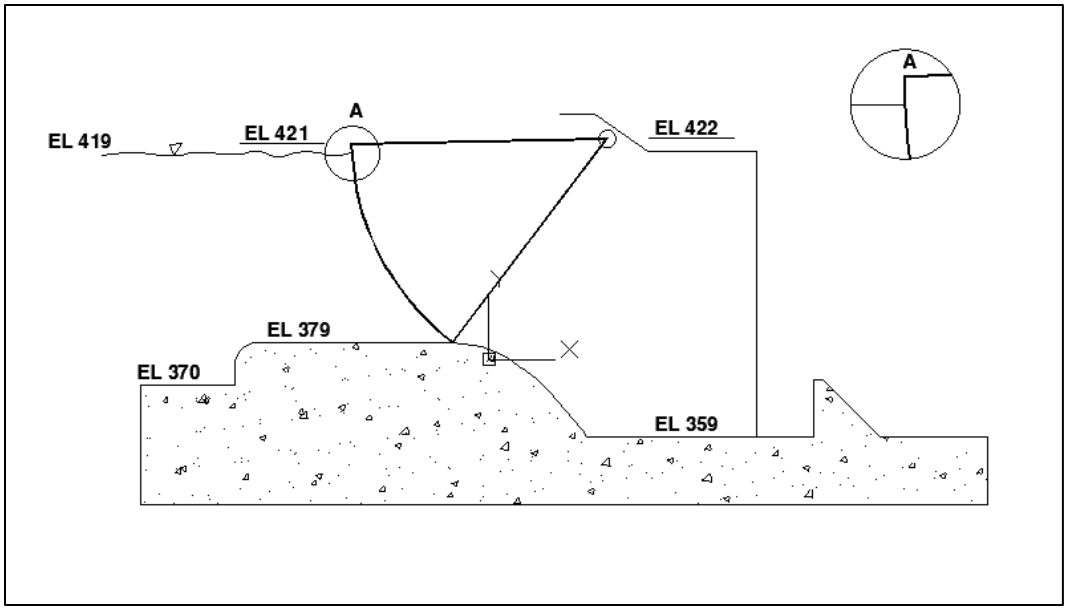

Tailwater is the primary variable affecting the load on a tainter gate for most inland navigation projects, especially low-head projects. The tailwater reduces the head across the gate once it begins to submerge the downstream side of the gate. At the MPLD project on the Mississippi River, a hydrograph that contained the average, maximum, and minimum tailwater stages during the period 1939 to 1969 (i.e., for 31 years) was found in the Hydrology Design Memorandum (Design Memorandum No. 1, USACE-MVS 1971) for the project.

The average tailwater stage was investigated first. The average stage hydrograph represented a 31 yr daily average of the tailwater. For example, the average stage was recorded on 1 January for 31 yr, and an average of these 31 values was designated the average tailwater stage for 1 January. This was repeated for every day of the year (Figure A-2). The average TW El over this 31 yr period was determined to be 402.69. (Elevations were referenced to National Geodetic Vertical Datum of 1929 [NGVD29].)

The maximum and minimum values shown represent the maximum and minimum TW Els recorded on each day of the year during the observation period. For example, the value shown for 1 January represents the maximum tailwater observed on that day over the 31 yr observation period. Likewise, the minimum value shown on 1 January represents the minimum value observed on that day over the 31 yr observation period.

Figure A-2. Average, maximum, and minimum tailwater hydrographs used in the design of MPLD.

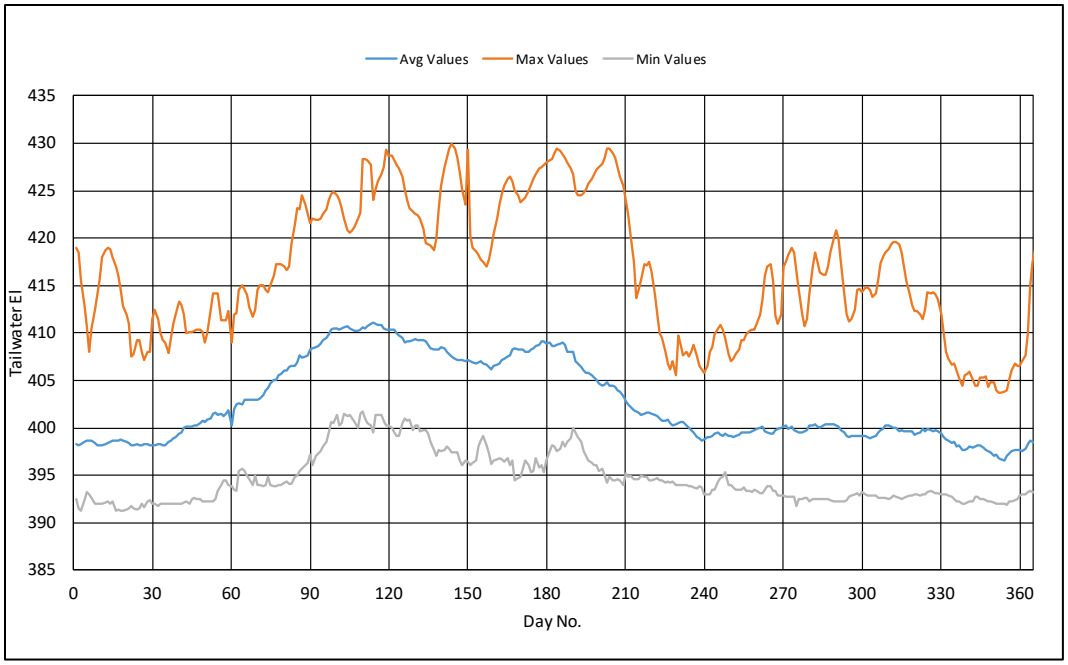

Statistics for the TW El were determined for subsequent analysis in the Load and Resistance Factor Design (LRFD) procedures. From the average discharge data, a histogram was created for use in developing the probability density function (PDF). The histogram shown in Figure A-3 represents the number of occurrences of tailwater in a selected range. There are 29 bins, each with a bin width of 0.5 ft. The area of each bin was computed, and the total area was determined by summing the individual bin areas. These areas were normalized by dividing each individual area by the total area to give the PDF shown in Figure A-4. A cumulative distribution function (CDF) was developed by cumulatively summing the normalized areas of the PDF, as shown in Figure A-5. The information provided in these figures will be used in the subsequent analysis of the hydraulic loads.

Figure A-3. Histogram of average daily tailwater elevation (TW El) from 1939 through 1969.

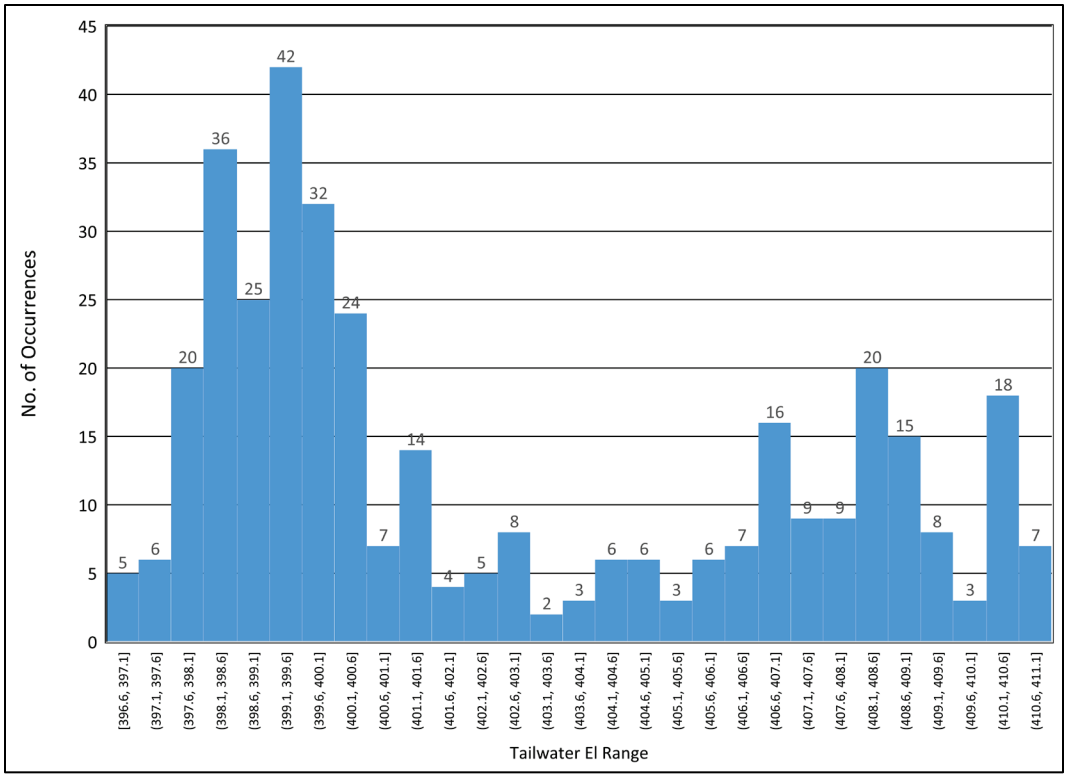

Figure A-4. Probability density function (PDF) from histogram of average daily tailwater.

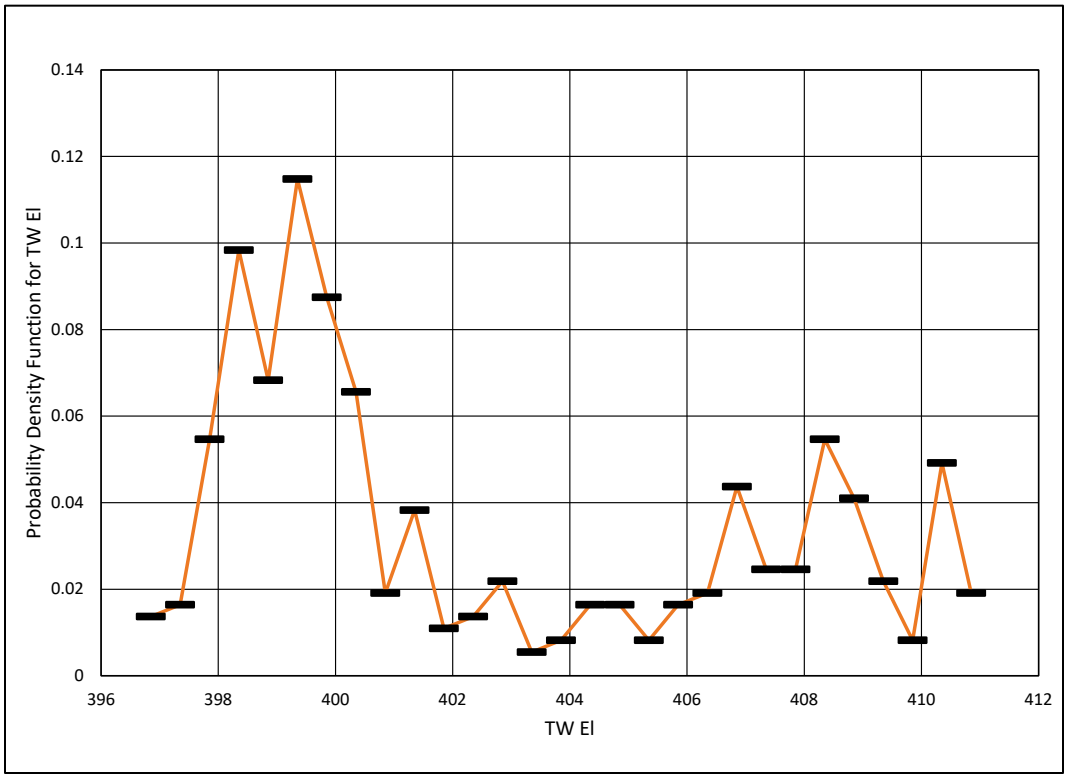

Figure A-5. Cumulative distribution function (CDF).

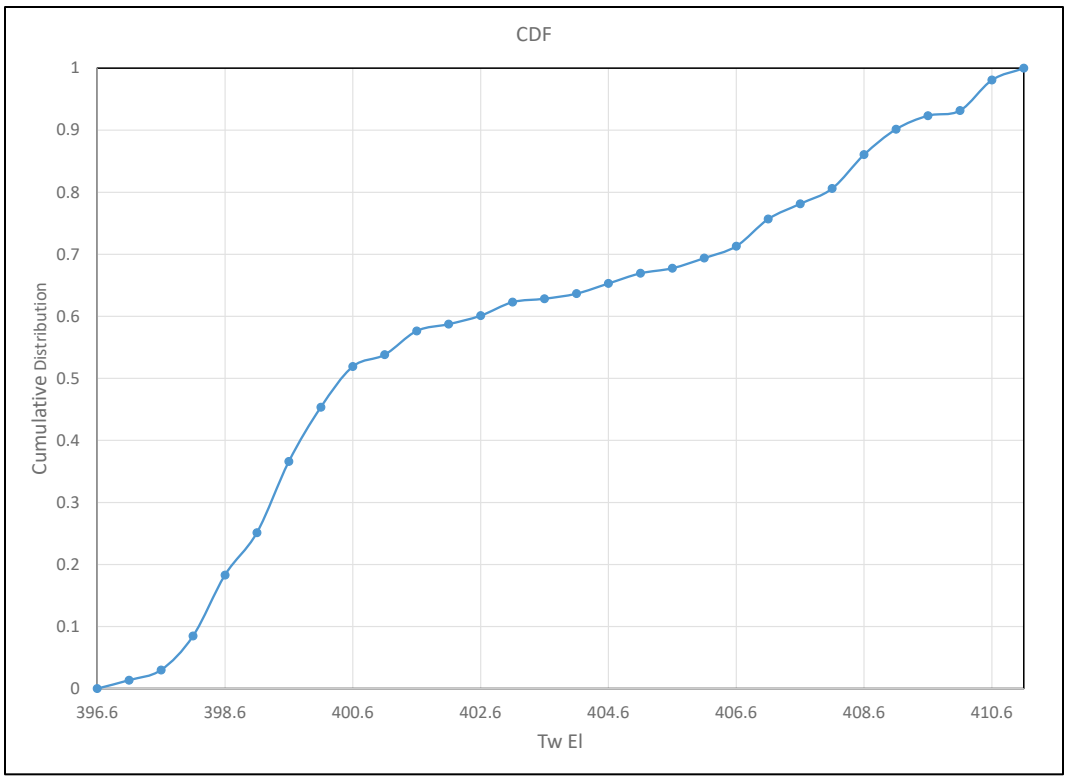

The standard deviation, σ, can be developed when given only maximum and minimum values by taking the difference in the maximum and minimum values and dividing this value by six. (See Ebeling and White 2019, Appendix C, for a further discussion.) This procedure assumes the data are normally distributed and that the maximum to minimum range covers 99.7% of the values. This was done for the maximum and minimum values shown in Figure A-2, and Figure A-6 shows the standard deviation for the TW El for each day over the 31 yr period. Figure A-6 shows that the mean standard deviation was 3.64. Figure A-7 was constructed to try to determine if a relationship was apparent between the differential head (ΔH = upper pool el – TW). The computed standard deviation for the tailwater was plotted versus ΔH. The plot suggested there was no strong correlation between these two variables. Additional research is necessary to develop better correlation characterization of the variables. As this research progresses, data will be obtained from other projects and hopefully provide more insight.

Figure A-6. Standard deviation determined from (maximum – minimum)/6.

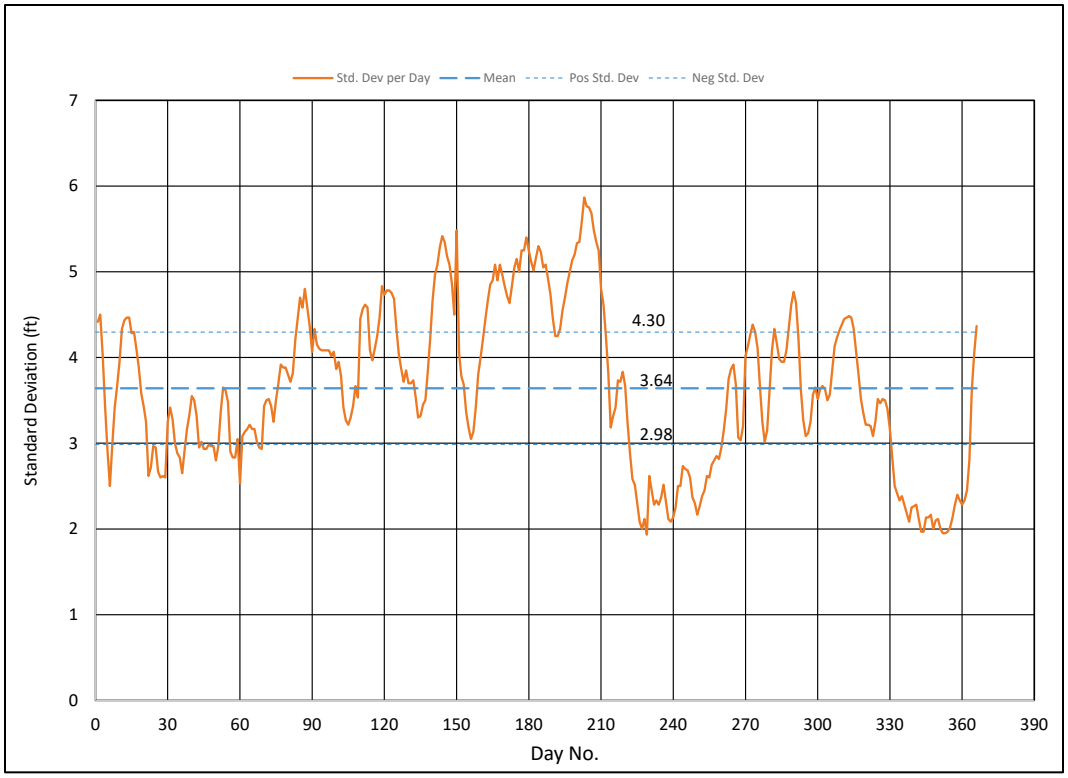

Figure A-7. Standard deviation for the TW El (σTW El) versus Δ*H*.

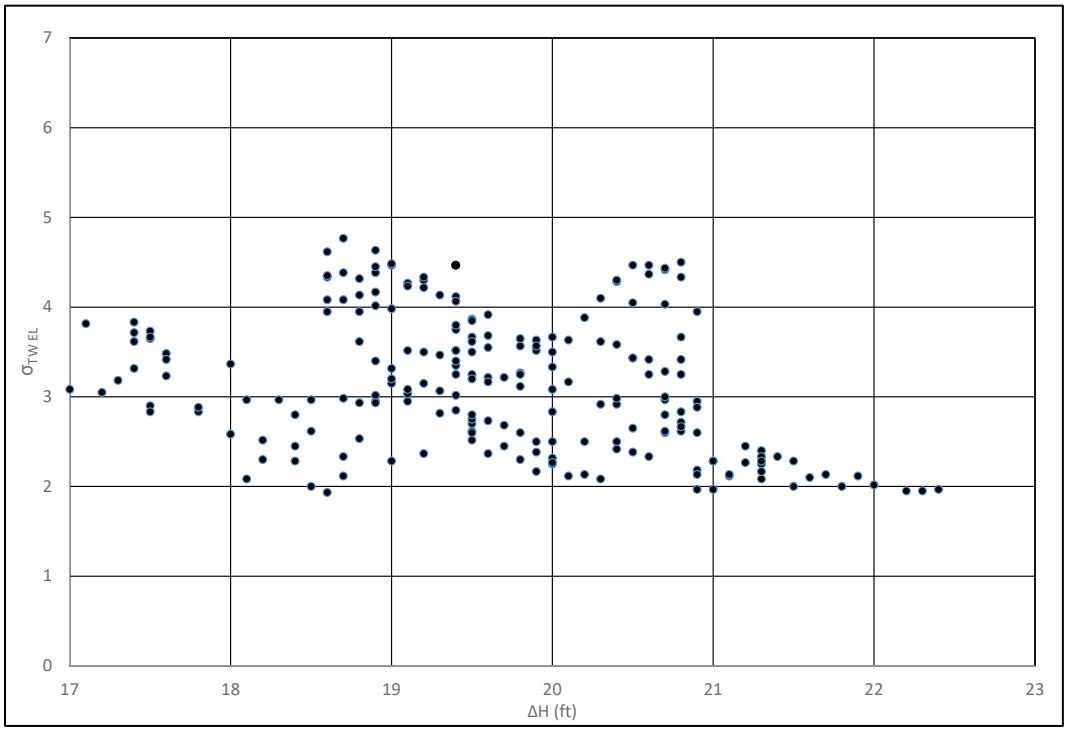

A.2 Hydrostatic Load for MPLD without Tailwater Effect

Equation (10), which is repeated here, is a conventional equation found in many fluid mechanics and hydraulics textbooks and is used to compute hydrostatic pressure (p). As stated previously, γ is the unit weight of water, and y is the vertical distance from the water surface to the location of the hydrostatic pressure of interest (Figure 14):

$$p = \gamma y.$$

The horizontal hydrostatic pressure on a closed gate is typically expressed as γH, where γ is the unit weight of water, and H is the total head on the gate. When the gate is closed, H represents the difference between the upper pool el and the spillway crest el when the tailwater is lower than the crest el. The maximum hydrostatic pressure can be computed using the equation that follows, which also appeared as Equation (11) of this text:

$$p_{max} = \gamma H.$$

The resultant hydrostatic force per foot of width for the tainter gate can be found using Equation (12), which is repeated here; it is located $H/3$ above the spillway crest (Figure 14):

$$H_s = \frac{1}{2}\gamma H^2,$$

where

γ = the unit weight of water = 62.4 lb/ft^3,
H = the head on the gate = 419 – 379 = 40 ft, and
Hydrostatic load = 0.5 [62.4 lb/ft^3 * (40 ft)^2] = 49,920 lb/ft.

The maximum hydrostatic load would be experienced if the upper pool were at the top of the tainter gate with the gate in the closed position and no tailwater effect. H would then be 42 ft, and the hydrostatic load would be 55,037 lb/ft. This load condition represents H_1 (i.e., the maximum net hydrostatic load that will ever occur), which is one of the three hydrostatic loads that are to be considered. The location of the horizontal resultant force is $H/3$ above the spillway crest when H is the head on the gate (Figure 14).

A.3 Wave Load Based on Wave Height and Period for MPLD

The dispersion due to wave load about the mean hydrostatic and hydrodynamic loads needs to be determined. The wave load is considered a primary load that contributes to load fluctuations. Previous practice for wave load was to use the guidance in the *Shore Protection Manual* (SPM; Coastal Engineering Research Center 1984b). In this investigation, updated methods (discussed in Section 2.3.2) are used to determine the wave loads. The wind speed, direction, and fetch must be determined to develop a wave load.

A.3.1 Wind Speed and Fetch

The wind speed and wind direction data were obtained from meteorological data collected at the St. Louis Regional (SLR) airport and the Saint Charles County (SCC) airport. The SLR airport is located approximately 6 mi east of the project, and the SCC airport is about 15 mi west of the project. Figure A-8 shows the data collection sites in relation to the project.

Figure A-8. Satellite imagery showing the wind speed and direction data collection sites for MPLD. (Map data: Google Earth 2014.)

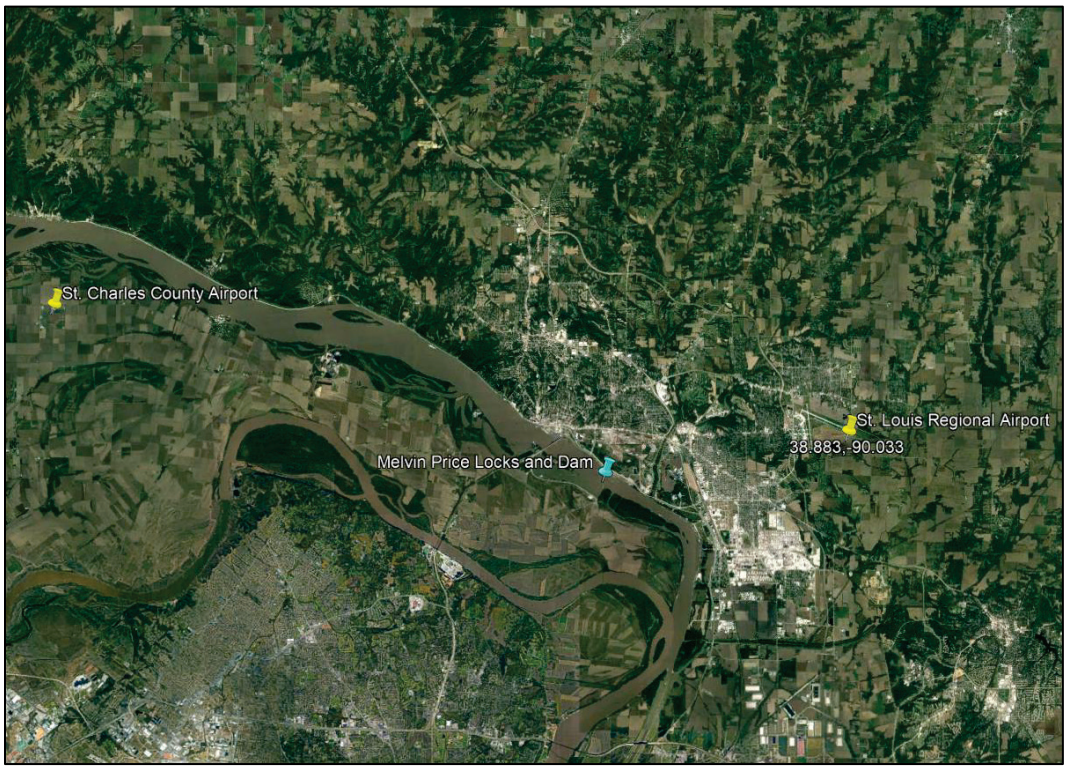

The SLR airport dataset was fairly complete for the years 1983 to 2005. Data were obtained from the National Climate Data Center (NCDC; n.d.).

The station designation was 724394 99999, the latitude was 38.883, and the longitude was –90.033. Column descriptions of the pertinent data used for this example are shown here:

- 01–06 USAF = Air Force catalog station number
- 08–12 WBAN = NCDC Weather Bureau Army Navy (WBAN) number
- 14–25 YR–MODAHRMN = year–month, day, hour, minute in Greenwich Mean Time
- 27–29 DIR = wind direction (DIR) in compass degrees, 990 = variable, reported as "***" when air is calm (speed [SPD] will then be 000)
- 31–37 SPD & GUS = wind speed and gust (GUS) in miles per hour

Table A-1 shows a sample of the wind speed and wind direction data from the meteorological dataset. The data in columns 14–37, as described previously, are shown in the Table A-1.

Table A-1. Sample of wind speed and direction data for station number 724395 99999, latitude 38.883, longitude –90.033, elevation 166.

YR–MODAHRMM	DIR (deg)	SPD (mph)	GUS (mph)
198310111400	160	9	***
198310111600	170	11	22
198310111700	160	17	23
198310111800	180	17	***
198310112000	170	14	23
198310112100	160	11	23
198310112200	140	10	***

*** Data not available. DIR is direction, SPD is speed, and GUS is gust.

Observations of several storm events indicated that high wind speeds lasting several hours were possible near the MPLD project. For example, Figure A-9 shows the wind speeds from a storm event that occurred in January 2005. The primary wind direction for this event was 300° (north = 0° proceeding clockwise).

Figure A-9. Wind speed from the St. Louis Regional (SLR) airport data for a storm event.

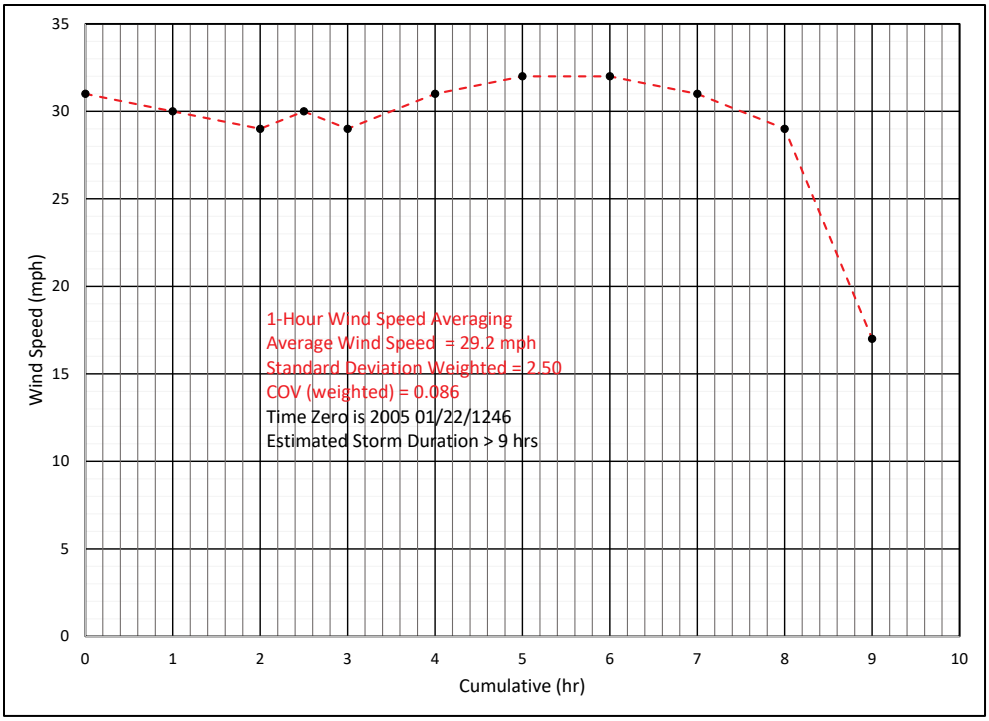

The mean wind speed was 29.2 mph, with several hourly periods above 30 mph. Figure A-10 shows the fetch determined for the MPLD project. The inland electronic charts were used to locate the spillway and river channel shown in Figure A-10. The wind direction that impacts the project perpendicular to the spillway axis is 304°. The fetch is 7.72 mi.

Figure A-10. Fetch and wind direction determined for the MPLD project.

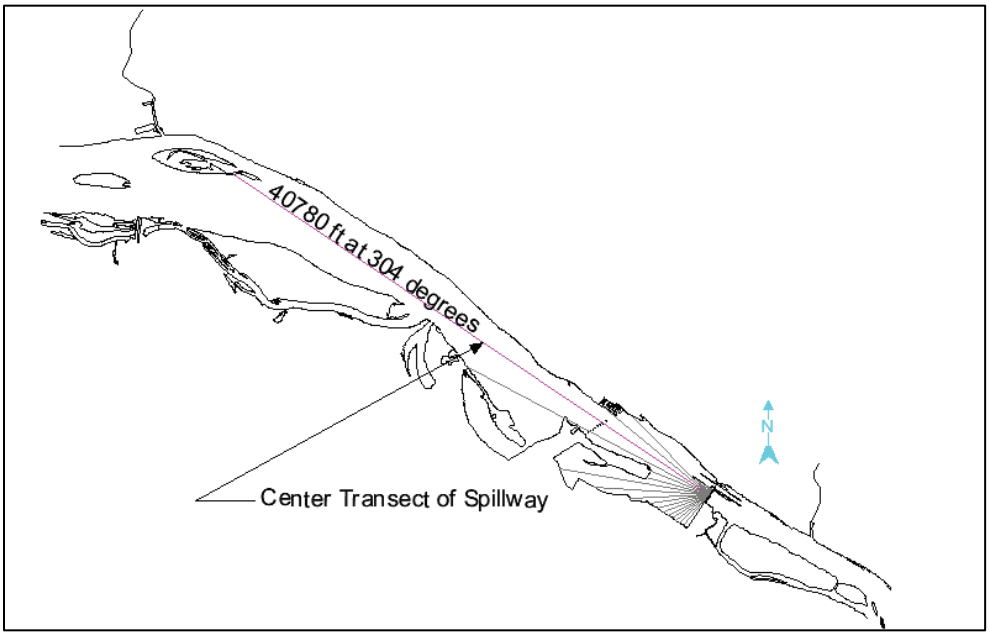

A.3.2 Wind Speed Analyses

A method to determine the appropriate wind speeds to use for estimating wave heights and subsequent wave force distributions was needed for the LRFD process. The wave heights are based on wind speed and fetch. The maximum wind speed that occurred during storm events was reviewed for the SLR and SCC airport datasets. The statistics computed and shown in Figure A-9 gave equal weight to each wind speed observation (a 1 hr average). Because the data were not always reported at similar time intervals, the computed statistics determined using equal weights were not considered truly representative of the data. A procedure that used a weighting factor based on time increments was employed to determine the statistics. This procedure is described here. The notation for wind speed is U.

In this analysis, t = time and Δt is the time interval width in minutes. The first time interval width, Δt_1, is then calculated as

$$t_N - t_1 = \text{the total time for the event for } N \text{ data points,} \tag{A.1}$$

$$\Delta t_1 = \frac{t_2 - t_1}{2}. \tag{A.2}$$

The midpoints, defined as all data points except the first and last, are designated Δt_i and calculated as

$$\Delta t_i = \frac{\{(t_{i+1} - t_i) + (t_i - t_{i-1})\}}{2}. \tag{A.3}$$

The last time interval width is Δt_n, where

$$\Delta t_n = \frac{(t_N - t_{N-1})}{2}. \tag{A.4}$$

A weighted time factor is then determined by dividing each time factor width by the total time,

$$W_i = \frac{\Delta t_i}{t_N - t_1}. \tag{A.5}$$

A weighted time factor is determined for each value of Δt, which includes W_1, all the values for W_i, and W_n. The sum of all these individual weighed time factors is equal to 1. This weighting factor is then multiplied by the

actual wind speed (U) to give a factored wind value. The sum of all these factored wind values is the mean wind speed:

$$\mu_U = \sum_{i=1}^{n} U_i * W_i. \tag{A.6}$$

Similarly, a variance (or standard deviation squared) is computed by

$$\mathrm{var}_U = \sum_{i=1}^{n} W_i * (U_i - \mu_U)^2. \tag{A.7}$$

The standard deviation is the square root of the variance,

$$\mathrm{stddev}_U = \sqrt{\mathrm{var}_U}, \tag{A.8}$$

and the coefficient of variation is the standard deviation divided by the mean:

$$\mathrm{cov} = \frac{\mathrm{stddev}_U}{\mu_U}. \tag{A.9}$$

Figure A-11 is a plot of the same storm event shown in Figure A-9 but using this weighting procedure. There are slightly higher values for the mean, standard deviation, and coefficient of variation using this weighting procedure than when using the nonweighted result tabulated in Figure A-9. Continuing the analysis of wind speed, a method to determine the appropriate wind speed value to be used for computing wave heights must be established.

Figure A-11. Wind speed data using the weighting procedure for the storm event from the SLR airport.

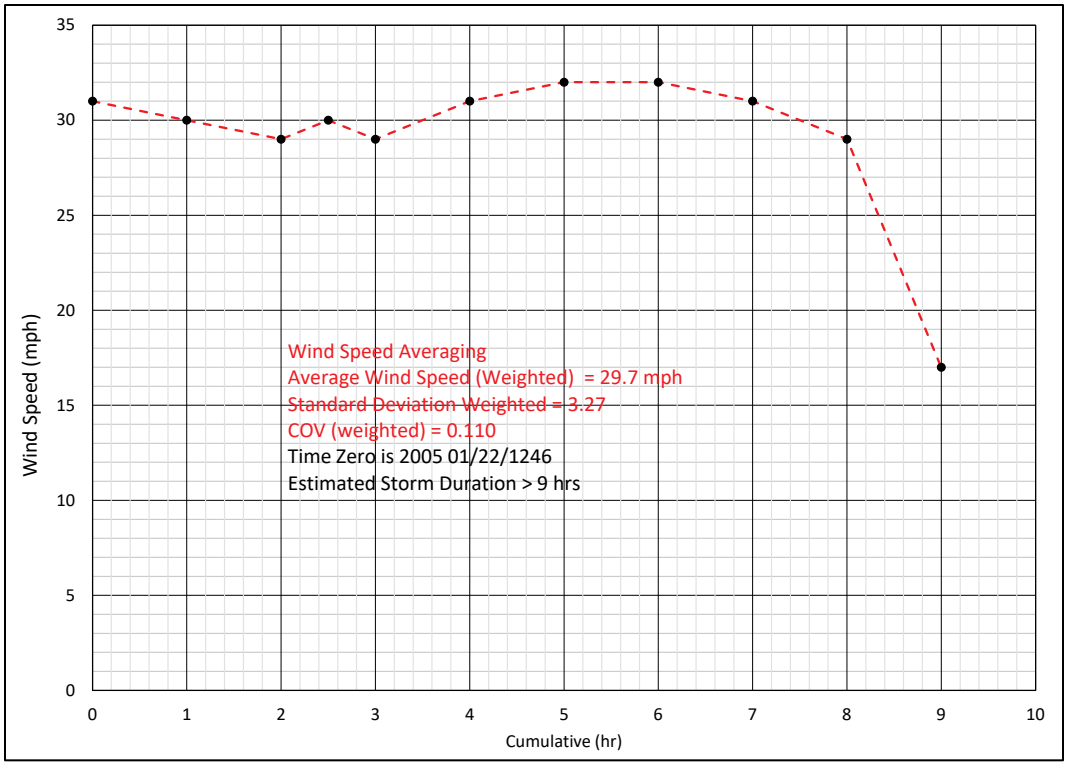

A.3.3 Extreme Value Estimation based on US Army Corps of Engineers, St. Paul District (USACE-MVP), Project Using Maximum Yearly Values of Wind Speed for MPLD

The first method investigated followed a procedure used by USACE-MVP (2014) in the *Oxbow-Hickson-Bakke (OHB) Levee Wind-Wave Analysis*. This study was performed to determine the levee heights required for the flood protection project. Initially, the maximum annual wind speed data were determined for the period of record. The data from the SLR airport were obtained for the period 1983 to 2005. The SCC airport data were obtained for the period 1998 to 2019. As mentioned previously, the SLR airport is located approximately 6 mi east of the project, and the SCC airport is about 15 mi west of the project.

The type 1 Gumbel distribution was used for a generalized extreme value (GEV) analysis. This analysis is typically used to evaluate extreme, low probability meteorological and hydrological events. The probability of nonexceedance and wind speed are plotted, and a linear regression can be used to estimate values for extreme return periods.

Figure A-12 shows the results from extreme value estimation using the peak annual values for the SLR airport data. Table A-2 shows the peak annual values of wind speed for wind directions between 280° and 320° toward the project. The 100 yr recurrence interval wind speed from this analysis was 49.6 mph.

Figure A-12. Extreme wind speed estimation for the SLR airport based on peak annual values of wind speed.

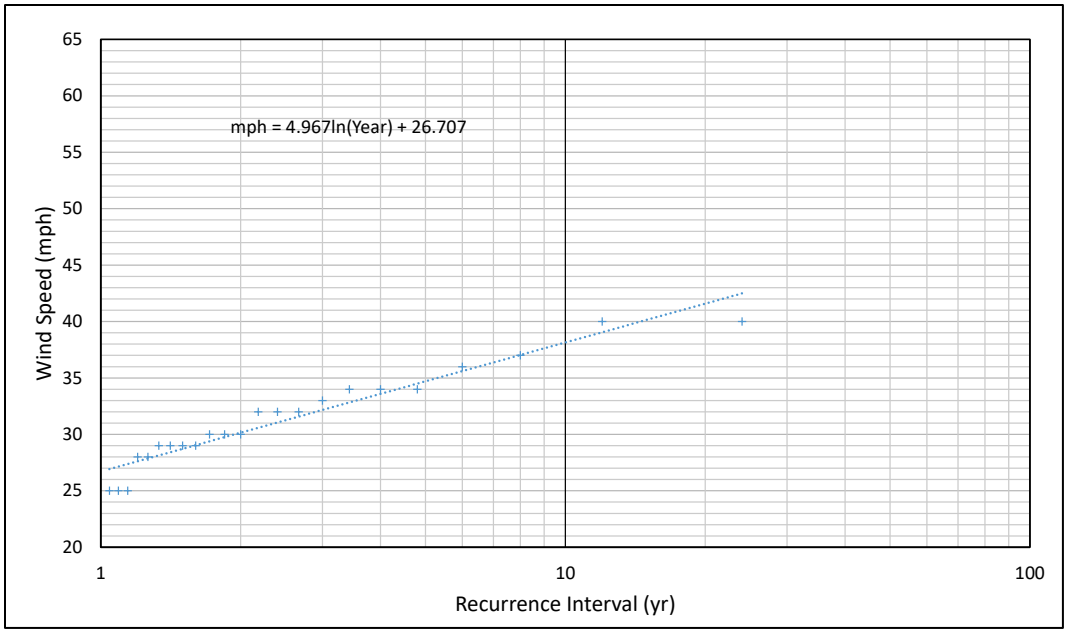

Table A-3 and Figure A-13 show the results using the peak annual wind speed values for the SCC airport. The 100 yr recurrence interval wind speed for the SCC airport was 62.8 mph. Using the magnitude of the 100 yr recurrence interval for wind speed was considered a suitable frequency for wave height calculations. However, the wind speed magnitudes determined from the extreme value estimation did not compare favorably to the wind speeds observed from the airport data. Also, the duration of the wind is important and will be discussed in later sections.

Table A-2. Peak annual wind speed values at the SLR airport for the 1983 to 2005 observation period.

Year	Peak Annual Wind Speed (mph)
1983	25
1984	36
1985	32
1986	30
1987	29
1988	33
1989	30
1990	30
1991	40
1992	34
1993	29
1994	34
1995	40
1996	34
1997	29
1998	29
1999	28
2000	25
2001	25
2002	37
2003	28
2004	32
2005	32

Table A-3. Peak annual wind speed values at the Saint Charles County (SCC) airport for the 1998 to 2019 observation period.

Year	Peak Annual Wind Speed (mph)
1998	34.5
1999	33.4
2000	34.5
2001	33.4
2002	38.0
2003	31.0
2004	35.7
2005	35.7
2006	38.0

Table A-3 (cont.). Peak annual wind speed values at the Saint Charles County (SCC) airport for the 1998 to 2019 observation period.

Year	Peak Annual Wind Speed (mph)
2007	40.2
2008	38.0
2009	40.2
2010	33.4
2011	43.7
2012	39.1
2013	42.6
2014	39.1
2015	33.4
2016	51.9
2017	52.9
2018	33.4
2019	36.8

Figure A-13. Extreme wind speed estimation for the Saint Charles County (SCC) airport based on maximum yearly values of wind speed.

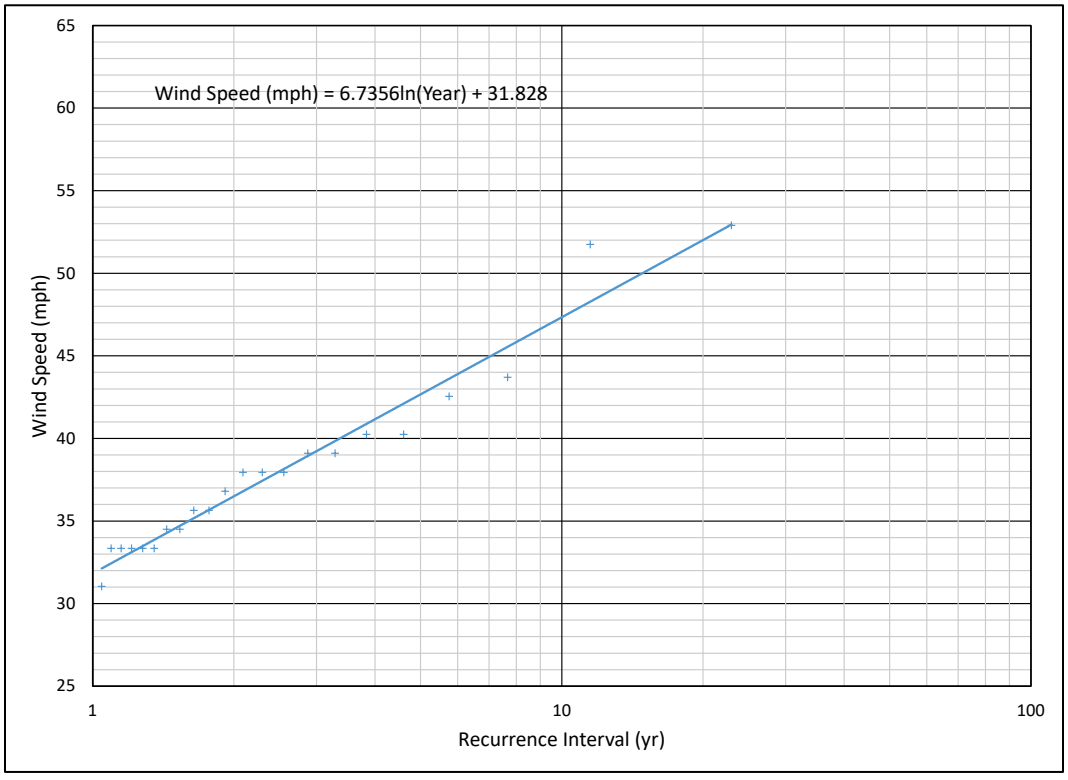

A.3.4 Wind Frequency Based on Gumbel Type 1 Distribution with Gringorten's Method Using Maximum Yearly Values of Wind Speed for MPLD

The type 1 Gumbel distribution can be used with Gringorten's (1963) plotting position formula to create another method for evaluating wind speed. Chapter 2 contained a description of this procedure. Figure A-14 shows a plot of the return period versus wind speed determined using this procedure for the data from the SLR airport. The wind speed for the 100 yr return period was 45 mph. Figure A-15 shows the wind frequency determined using this procedure with the SCC airport data. The wind speed for the 100 yr return period was 51 mph.

Figure A-14. Wind frequency from Gumbel type 1 distribution with Gringorten's method for the SLR airport using the peak annual values.

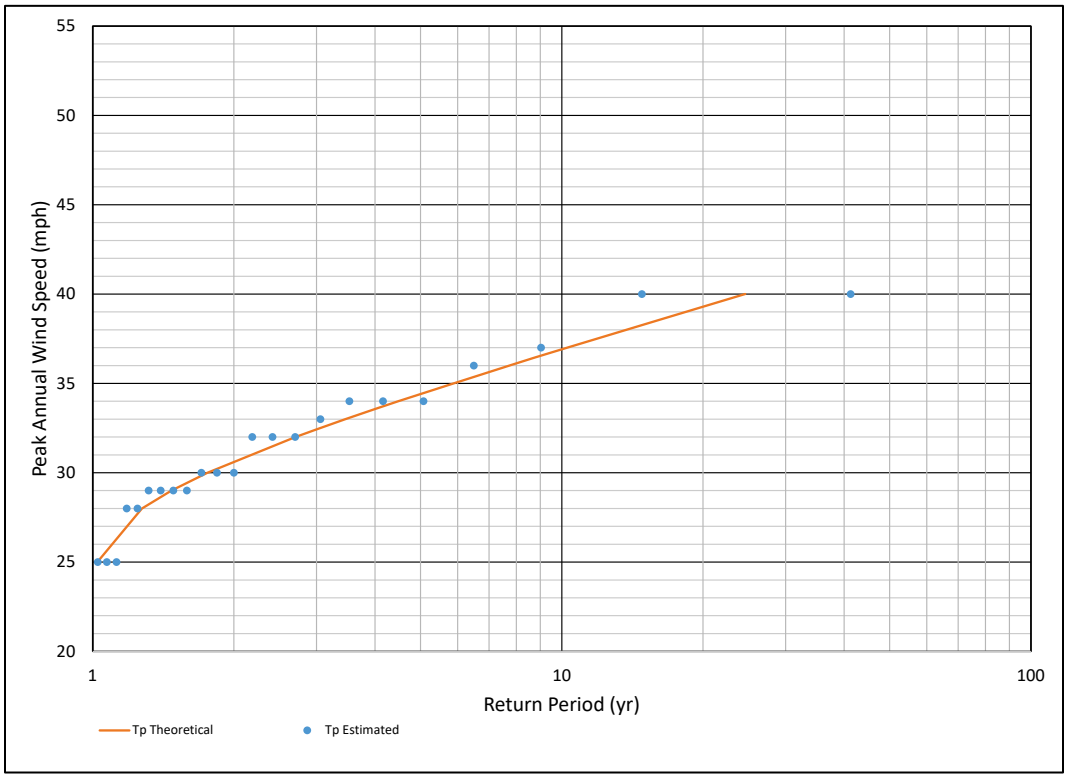

Figure A-15. Wind frequency from Gumbel type 1 distribution with Gringorten's method for the SCC airport using the peak annual values.

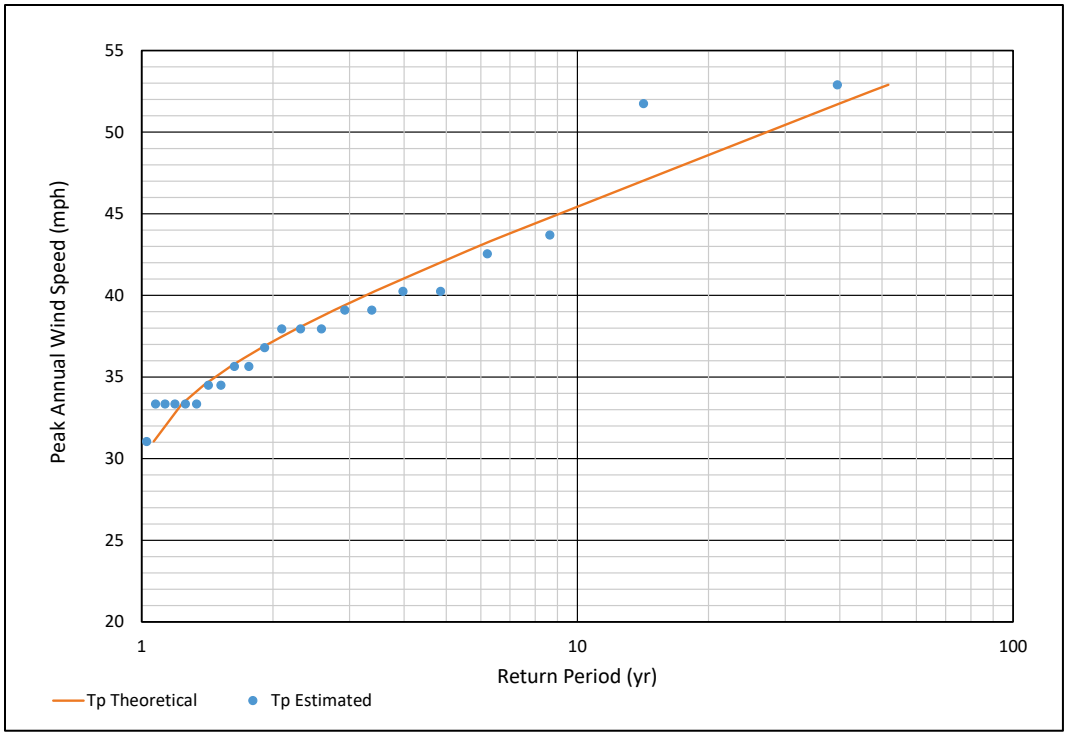

A.3.5 Extreme Value Estimation Based on the USACE-MVP Project Using Maximum 2 hr Average Yearly Value of Wind Speed for MPLD

As the maximum storm event per year was being investigated, it became obvious that using a maximum single value of wind speed would skew the values toward a higher speed than was realistic for wave height estimation. A minimum wind duration is needed to produce the significant wave height and period, as discussed for Goda's (2010) procedure in Section 2.3.2.3 of Chapter 2 of the main report. Based on the t_{min} values computed from Equation (50), which is repeated here, the minimum duration required to produce the significant wave height and wave period for wind speeds between 35 and 40 mph with a 7.72 mi fetch was about 1 hr and 40 min:

$$t_{min} = 1.0F^{0.73}U_{10}^{-0.46},$$

where t_{min} is in hours, U_{10} is the wind velocity 10 m above the water surface in meters per second, and F is in kilometers.

Table A-4 gives the t_{min} values calculated using Equation (50) for wind speeds of 30, 40, and 50 mph.

Table A-4. Minimum wind duration times to obtain significant wave height.

U_{10} (mph)	t_{min} (hr)
30	1.79
40	1.62
50	1.51

Table A-4 indicates t_{min} should probably be between 1.6 and 1.8 hr; therefore, the maximum 2 hr average wind speed during the highest storm event was considered a more reasonable value for the statistical analysis than the maximum yearly value. Figure A-16 shows an example of the data from Figure A-9 that were used to determine the maximum 2 hr average wind speed at the SLR airport for the year 2005.

Figure A-16. Wind speed data for the SLR airport used to determine the maximum 2 hr average for a maximum storm event in 2005.

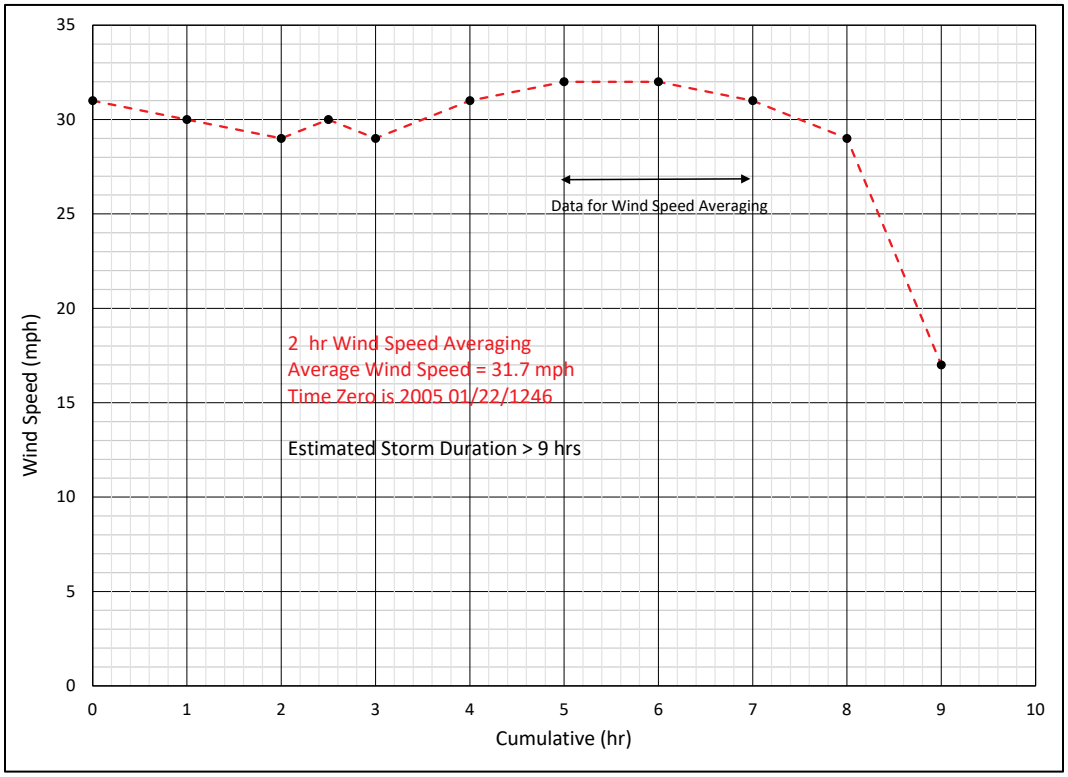

Table A-5, Table A-6, Figure A-17, and Figure A-18 show the results of the extreme value estimation using the maximum 2 hr average wind speed for the SLR airport and the SCC airport, respectively. Using the equation shown in Figure A-17, the 100 yr recurrence interval wind speed from this analysis for the SLR airport data was 39.7 mph. The 100 yr recurrence interval wind speed from the equation shown in Figure A-18 for the SCC

airport data was 40.8 mph. These results were in close agreement and were considered better estimates of wind speed for the 100 yr recurrence interval.

The wind speed values using the extreme value estimation procedure for the 100 yr recurrence interval were considered too high based on the wind speed data collected at the SLR and SCC airports. The wind frequency based on the Gumbel type 1 distribution with Gringorten's plotting position formula was considered more representative of actual storm event possibilities. Therefore, the extreme value estimation was not used in the data analyses of both airports or in any other further statistical analysis.

Table A-5. Maximum 2 hr average annual wind speed values at the SLR airport for the 1983 to 2005 observation period.

Year	Max 2 hr Avg. Annual Wind Speed (mph)
1983	22.8
1984	29.8
1985	29.7
1986	27.3
1987	29.0
1988	31.0
1989	29.3
1990	28.0
1991	26.5
1992	24.7
1993	29.0
1994	27.3
1995	33.7
1996	25.0
1997	25.0
1998	28.3
1999	27.0
2000	23.0
2001	23.7
2002	23.0
2003	25.3
2004	27.7
2005	31.7

Figure A-17. Extreme wind speed estimation for the SLR airport based on maximum 2 hr average annual values of wind speed.

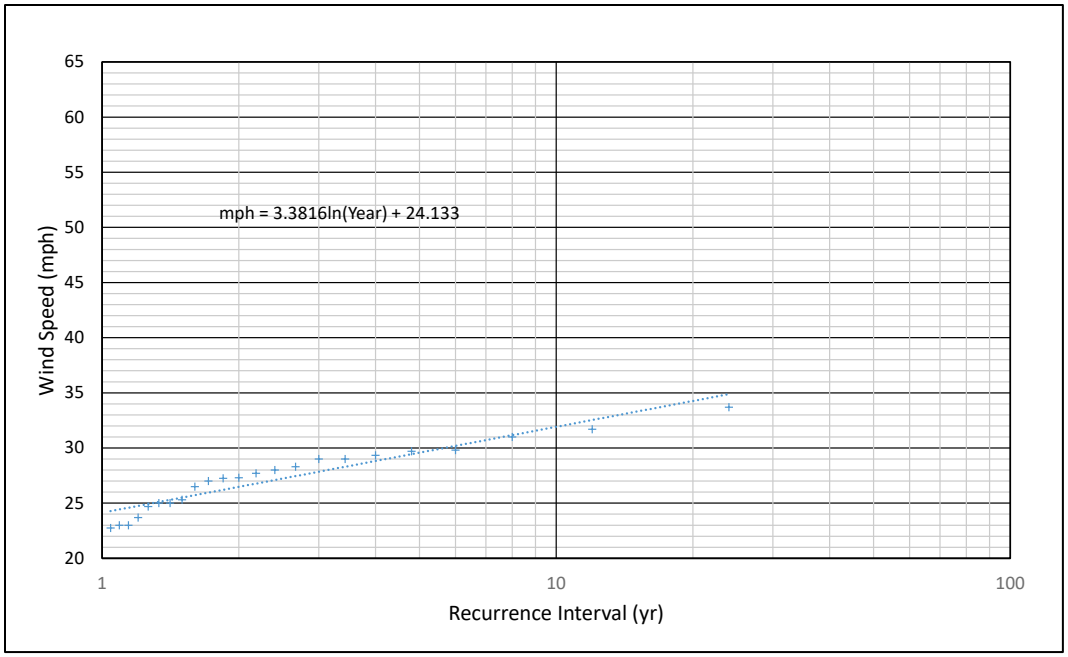

Figure A-18. Extreme wind speed estimation for the SCC airport based on maximum 2 hr average annual values of wind speed.

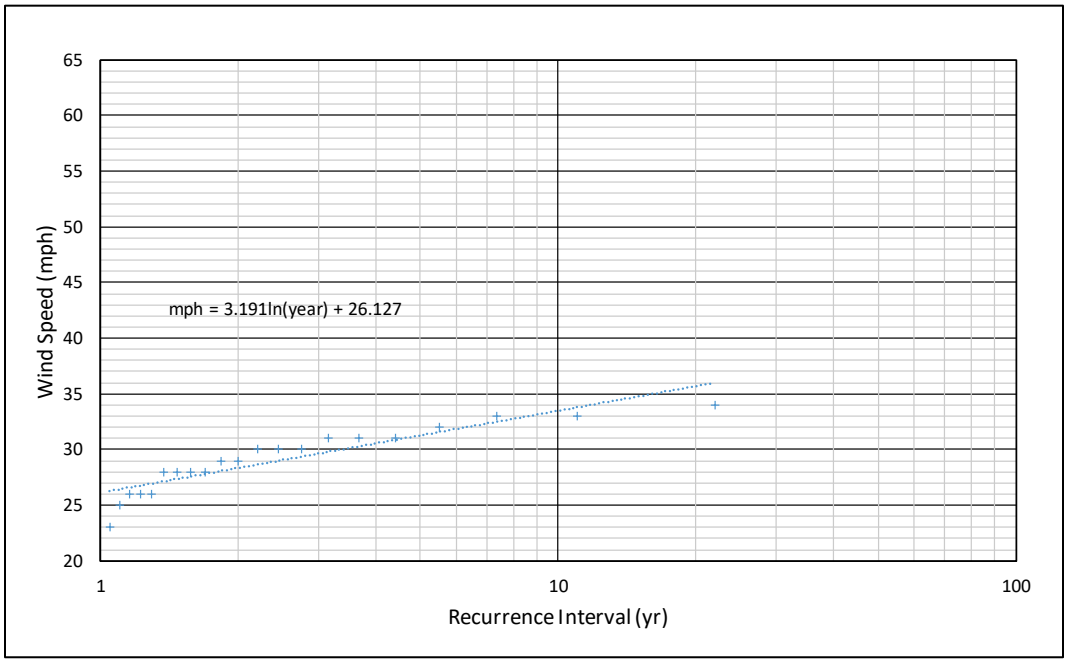

Table A-6. Maximum 2 hr average annual wind speed values at the SCC airport for the 1999 to 2019 observation period.

Year	Max 2 hr Avg. Annual Wind Speed (mph)
1999	31.0
2000	31.0
2001	33.0
2002	32.0
2003	26.0
2004	30.0
2005	29.0
2006	31.0
2007	28.0
2008	34.0
2009	30.0
2010	25.0
2011	29.0
2012	33.0
2013	23.0
2014	28.0
2015	26.0
2016	33.0
2017	28.0
2018	26.0
2019	28.0

A.3.6 Wind Frequency Based on Gumbel Type 1 Distribution with Gringorten's Method Using Maximum 2 hr Average Yearly Values of Wind Speed for MPLD

Figure A-19 shows a plot of the return period versus wind speed determined using the wind frequency based on the Gumbel type 1 distribution with Gringorten's plotting position formula for the maximum 2 hr average yearly value for the data from the SLR airport. Extrapolating the orange curve, the wind speed for the 100 yr return period was 36.8 mph. Figure A-20 shows the wind frequency determined using this procedure with the SCC airport data. The wind speed for the 100 yr return period was 38.3 mph. These results were also in good agreement.

Figure A-19. Wind frequency from Gumbel type 1 distribution with Gringorten's method for the SLR airport using the maximum yearly 2 hr average wind speed values.

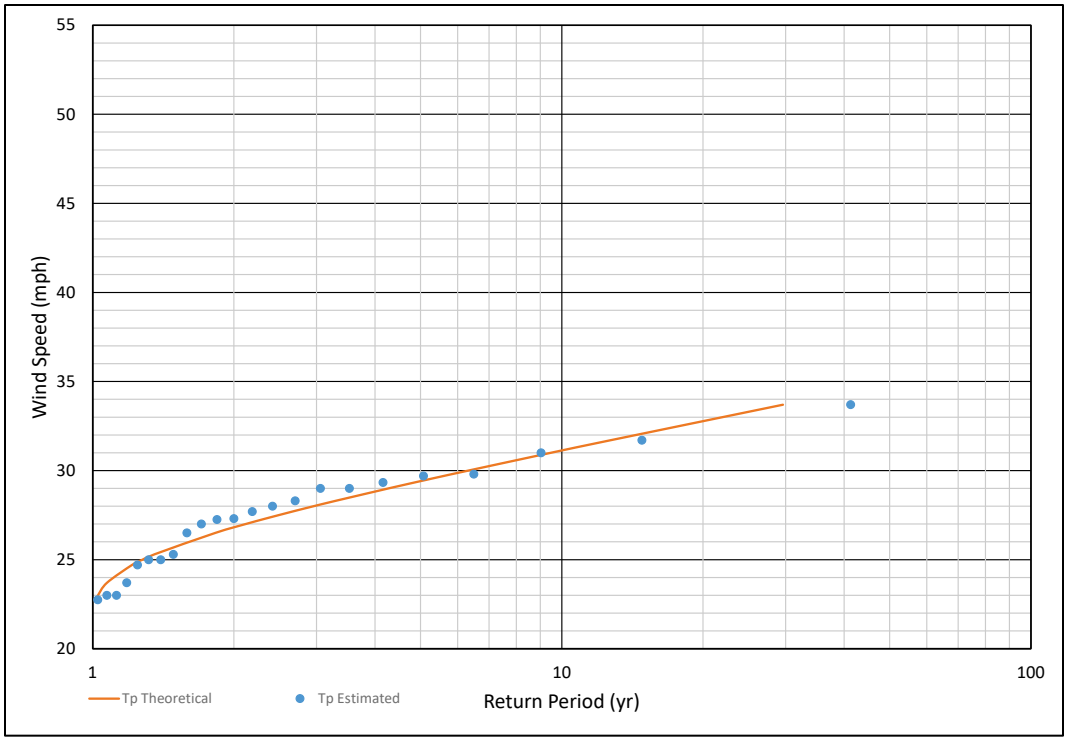

Figure A-20. Wind frequency from Gumbel type 1 distribution with Gringorten's method for the SCC airport using the maximum yearly 2 hr average wind speed values.

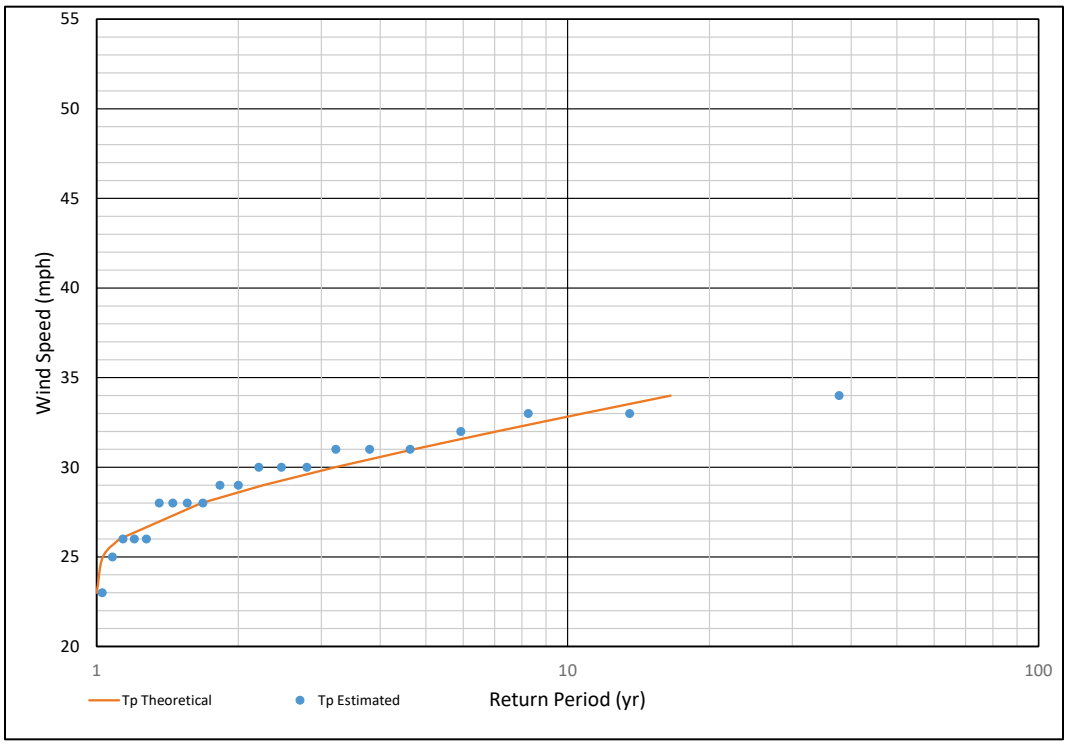

Observations of the data from both airports showed that the results from the wind frequency determined from the Gumbel type 1 distribution using Gringorten's plotting position were in good agreement. These results from both airports were then combined to give a larger sample size for further analyses. Table A-7 lists the maximum 2 hr average annual values of wind speed for both airports. Figure A-21 shows a plot of the return period versus wind speed determined using the wind frequency based on the Gumbel type 1 distribution with Gringorten plotting position formula for the maximum 2 hr average annual value for the data from both the SLR and SCC airports. Extrapolating from the orange curve, the wind speed for the 100 yr return period was 37.9 mph.

Table A-7. Maximum 2 hr average annual wind speed values at the SLR and SCC airports for the 1983 to 2019 observation period.

Year	Max 2 hr Avg. Annual Wind Speed (mph)
1983	22.8
1984	29.8
1985	29.7
1986	27.3
1987	29.0
1988	31.0
1989	29.3
1990	28.0
1991	26.5
1992	24.7
1993	29.0
1994	27.3
1995	33.7
1996	25.0
1997	25.0
1998	28.3
1999	31.0
2000	31.0
2001	30.0
2002	32.0
2003	26.0
2004	30.0
2005	31.7

Table A-7 (cont.). Maximum 2 hr average annual wind speed values at the SLR and SCC airports for the 1983 to 2019 observation period.

Year	Max 2 hr Avg. Annual Wind Speed (mph)
2006	31.0
2007	28.0
2008	34.0
2009	30.0
2010	25.0
2011	29.0
2012	33.0
2013	23.0
2014	28.0
2015	26.0
2016	33.0
2017	28.0
2018	26.0
2019	28.0

Figure A-21. Wind frequency from Gumbel type 1 distribution with Gringorten's method for the combined SLR and SCC airports using the maximum yearly 2 hr average wind speed values.

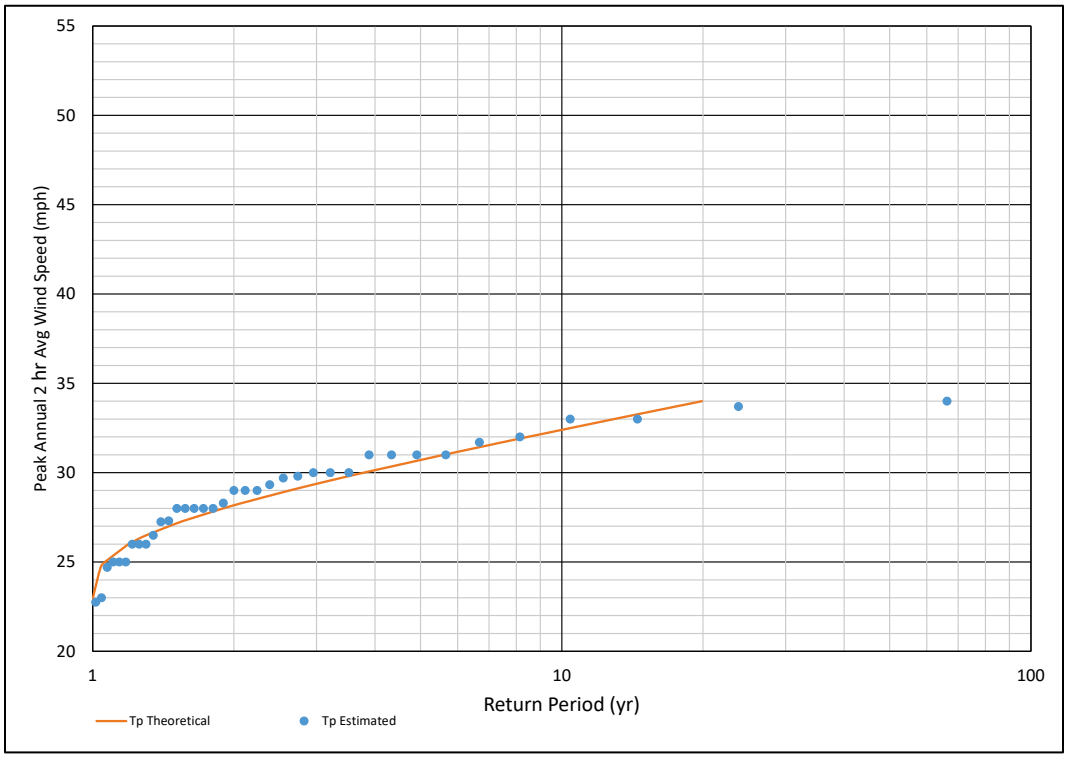

To further investigate the statistics for the wind speed, a formula for determining the standard error was used for the data presented in Figure A-19 through Figure A-21. The standard error or standard deviation is defined as follows:

$$\text{std} = \sqrt{\frac{\sum[U_i - U_{new}]^2}{n-1}}, \tag{A.10}$$

where

U_i = the wind speed (U) value for the T_p estimated point,
U_{new} = the new value determined from a log-linear interpolation (further explanation follows), and
n = the number of samples.

The T_p estimated points are the blue points shown in Figure A-19 through Figure A-21. Each T_p estimated point has a T_p theoretical point with the same value of wind speed associated with it. For clarity, these points are not shown in these figures, but they will be discussed and are shown in Figure A-22.

In the standard error equation, the wind speed, U_{new}, value of the orange curve in Figure A-19 through Figure A-21 is determined by a log-linear interpolation of the line segment between the T_p theoretical points (orange points in Figure A-22). The first step is to record the value of the T_p estimated point (blue point). Next, record the closest value of T_p theoretical that is smaller than the selected T_p estimated point and the closest T_p theoretical value larger than the selected T_p estimated point. Now there are values of T_p theoretical (orange points) on each side of the T_p estimated point (blue point). The T_p theoretical points can be thought of as being backward and forward of the T_p estimated point. Now the wind speed value for each of the T_p theoretical points is recorded. These two points (backward and forward T_p theoretical values and their associated wind speed values) are then used in the log-linear interpolation. To simplify the notation for the following discussion, let T_p theoretical backwards = $T_{p\,back}$ and T_p theoretical forward = $T_{p\,for}$. The wind speed values are designated U_{back} and U_{for}.

The linear interpolation will take the form of

$$U_{new} = mx + b. \tag{A.11}$$

The slope of the orange line segment between the two T_p theoretical points, $T_{p\,back}$ and $T_{p\,for}$, is m:

$$m = \frac{U_{for} - U_{back}}{\log 10(T_{p\,for}) - \log 10(T_{p\,back})}, \quad \text{(A.12)}$$

$$x = \log 10\left(T_p \text{ estimated}\right) - \log 10\left(T_{p\,back}\right), \quad \text{(A.13)}$$

where $b = U_{back}$.

U_{new} can now be determined, and then Equation (A.10) can be used to compute the standard error.

The standard error is also referred to as the standard deviation about the fit curve. The standard deviation (σ) is a way of describing how well the sample points align with a curve fitted to the data. In the case of the Gumbel type 1 distribution curve (T_p theoretical), this standard deviation provides an estimate of the changes in the wind speed from the fitted curve or a way to bound the values of wind speed.

Figure A-22 shows the fitted curve bounded by plus and minus 1 and 2 standard deviations (σ) for the SLR airport wind data (n = 23). The standard deviation was determined to be 0.589 mph. The use of the 100 yr return period plus 2 standard deviations gives a wind speed of 38.0 mph. Based on the storm event data, the extreme event analysis, and the Gumbel type 1 distribution analysis for the 100 yr return period increased by 2 standard deviations and the discussions that follow, a wind speed between 38.0 and 40.0 mph seems very reasonable for developing the design wave height and period.

The wind data for the SCC airport was analyzed in the same manner as the SLR airport data (n = 21). The standard error was computed and used to gain confidence in the wind speed selection. The standard deviation determined for the data was 0.844 mph. The wind speed for the 100 yr return period plus 2 standard deviations was 40.0 mph (Figure A-23).

Figure A-22. Wind frequency curves based on peak yearly 2 hr average wind speed for the SLR airport data bounded by plus and minus 1 and 2 standard deviations.

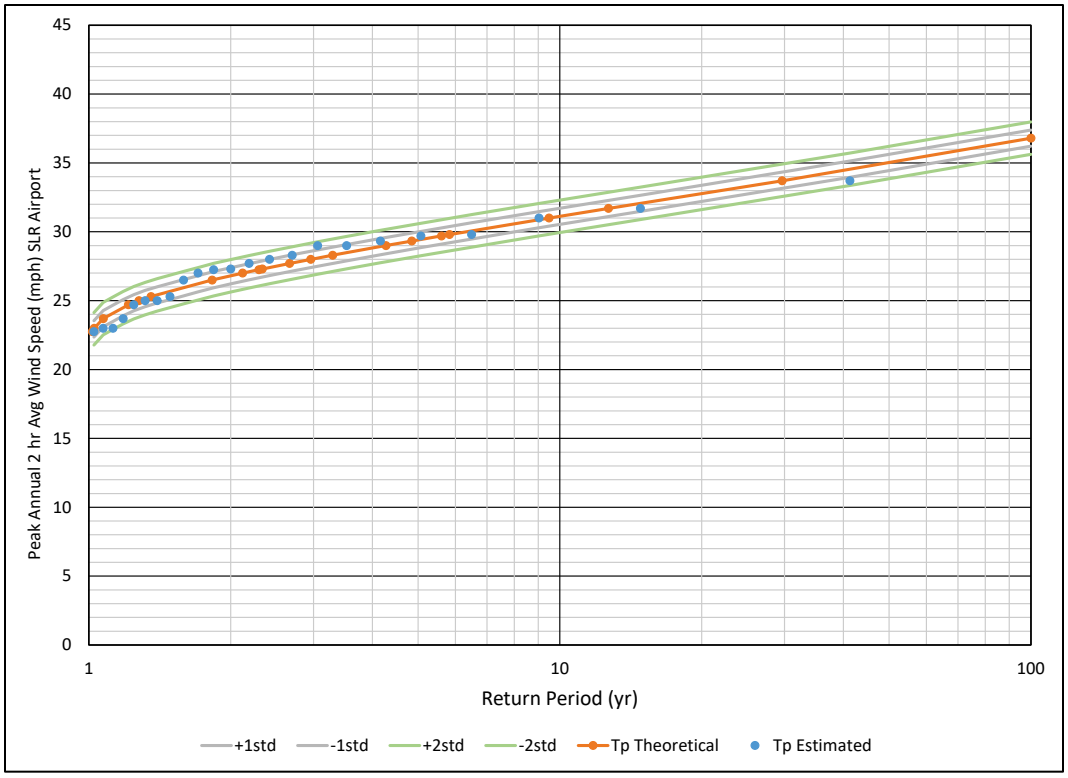

Figure A-23. Wind frequency curves based on peak yearly 2 hr average wind speed for the SCC airport data bounded by plus and minus 1 and 2 standard deviations.

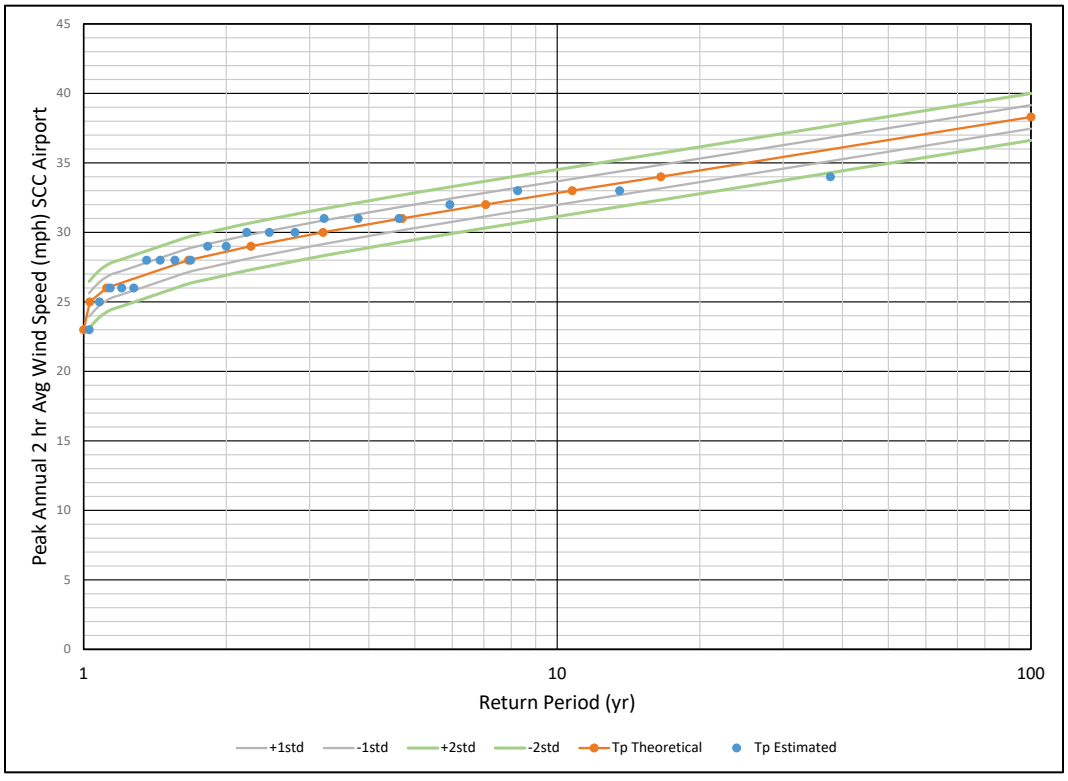

The wind data for both the SCC and SLR airports were also analyzed in the same manner as previously described (n = 37). The standard error was computed and used to gain confidence in the wind speed selection. The mean value for the 100 yr return period was 37.9 mph. The standard deviation determined for this data was 0.780 mph. The wind speed for the mean 100 yr return period plus and minus 3 standard deviations is shown in Figure A-24. Results from the wind speed analyses are shown graphically in Figure A-22 through Figure A-24 and are also summarized in Table A-8.

Figure A-24. Wind frequency curves based on peak yearly 2 hr average wind speed for the SLR and SCC airport data bounded by plus and minus 1, 2, and 3 standard deviations.

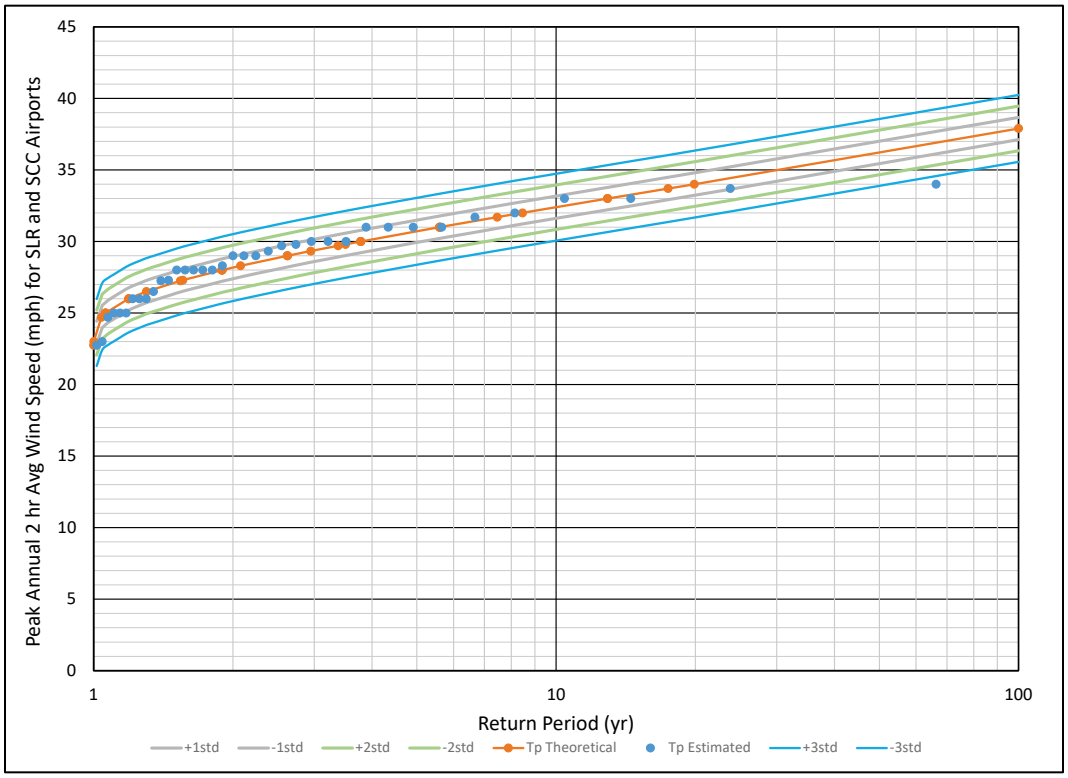

Table A-8. Results from wind speed analyses for MPLD.

Airport	Statistic	100 yr Wind Speed (mph)
SLR	+2σ	38.0
SLR	+1σ	37.4
SLR	Mean	36.8
SLR	−1σ	36.2
SLR	−2σ	35.6
SCC	+2σ	40.0
SCC	+1σ	39.1
SCC	Mean	38.3
SCC	−1σ	37.5
SCC	−2σ	36.6
SLR and SCC	+3σ	40.2
SLR and SCC	+2σ	39.5
SLR and SCC	+1σ	38.7
SLR and SCC	Mean	37.9
SLR and SCC	−1σ	37.1
SLR and SCC	−2σ	36.3
SLR and SCC	−3σ	35.6

In summary, the data from both airports combined are considered the most appropriate to use for the wave height and wave period analysis. It covers a period from 1983 to 2019, and the data from each individual airport support the results determined from using both airports. All three analyses show a small variation in the wind speed for the 100 yr return period. The type 1 Gumbel distribution with Gringorten's plotting position formula was the method chosen to process the wind speed data and develop the 100 yr return period wind speed and is recommended for the LRFD process for hydraulic steel structures (HSS).

A.3.7 Wave Height and Period from Smith (1991) and Ebeling et al. (2023)

Smith (1991) developed guidance to determine significant wave height and peak period based on wind speed and fetch. As part of this research project, Dr. Tallent updated Smith's NARFET Fortran computer program to a more recent computer language (Python). Table A-9 shows the input data and results from the use of the NARFET program for the MPLD project. The program input requires the radial lengths of the fetch and the angle increments for resolution of the wind direction. Figure A-10 shows the radial lengths (a total of 29) determined for an angle increment of 6°. The

significant wave height and period for a wind speed of 30 mph, wind direction of 300°, and a duration of 8 hr were 1.06 m (3.48 ft) and 3.63 sec, respectively. Table A-9 shows the results for 40 and 50 mph wind speeds for comparison. Based on observations of the wind data, it was considered highly unlikely that a sustained 50 mph wind would occur at the project. The wave heights and wave periods for the minimum and maximum wind speeds of 35.6 and 40.0 mph from Table A-8 for a 2 hr duration are also shown in Table A-9. The corresponding wave heights using these wind speeds were 1.24 and 1.38 m.

Table A-9. Example wave height and wave period computed using the NARFET model.

Wind Speed (mph)	Wind Direction (deg)	Wind Duration (hr)	Angle Increment (deg)	Wave Height (m)	Wave Period (sec)
30	300	8	6	1.06	3.63
40	300	8	6	1.38	4.07
50	300	8	6	1.69	4.45
35.6	300	2	6	1.24	3.89

Figure A-25 shows the wave heights computed for the mean 100 yr return period curve and plus 1, 2, and 3 standard deviations for both airports using the NARFET model.

Figure A-25. Wave height versus wind speed from Smith's NARFET model.

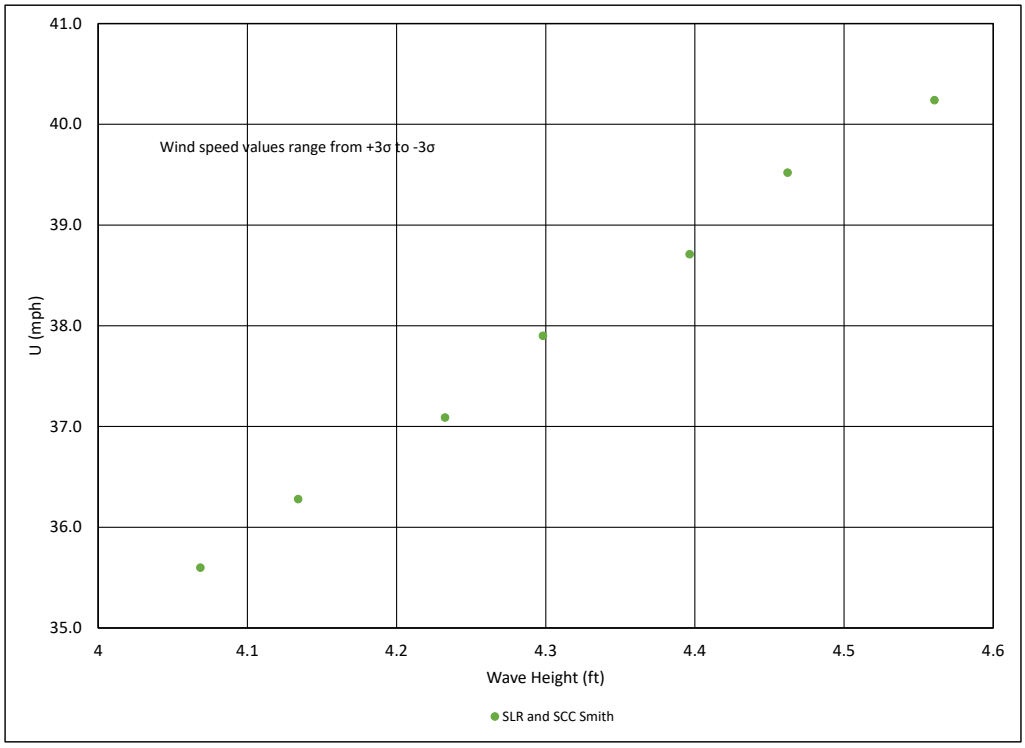

A.3.8 Wave Load from Goda

Goda (2010) also recommended formulations for determining significant wave height and period based on wind speed and fetch. His designation for wind speed was U_{10}, and it represents the wind speed 10 m above the sea surface. These formulations are shown in Section 2.3.2.3 as Equations (45) and (46). Goda proposed using Equation (48) to determine the minimum duration (t_{min}) needed to achieve the significant wave height and significant wave period. Table A-10 lists the significant wave height and period and T_{min} computed from these equations for wind speeds of 30, 40, 50, and 36.2 mph. The wind speeds of 30 and 50 mph are shown for comparison, and the wind speeds of 35.6 and 40 mph are the minimum and maximum from Table A-3 determined from the statistical analysis of the 100 yr return period wind speed.

Table A-10. Significant wave height and wave period using Goda's formulations.

Wind Speed (mph)	Minimum Duration, t_{min} (hr)	Significant Wave Height (m)	Significant Wave Period (sec)
30	1.79	1.16	3.61
50	1.51	1.76	4.25
35.6	1.69	1.34	3.82
40.0	1.62	1.47	3.96

Figure A-26 shows a plot of wind speed (U) versus wave height determined from Goda's (2010) recommended formulations from the statistical analysis of the wind speed data for the combined airports.

The wave pressure distribution and subsequent wave force for the STG can now be determined from the significant wave height and wave period. The complete description of this procedure is shown in Chapter 2, Section 2.3.2.3. Based on the parameters listed in Table A-11 and on the Goda formulations in Section 2.3.2.3, an example solution was reached. Table A-11 lists the parameters used in the example wave force calculation (imperial and metric units included).

Figure A-26. Wave height versus wind speed using Goda's (2010) procedure.

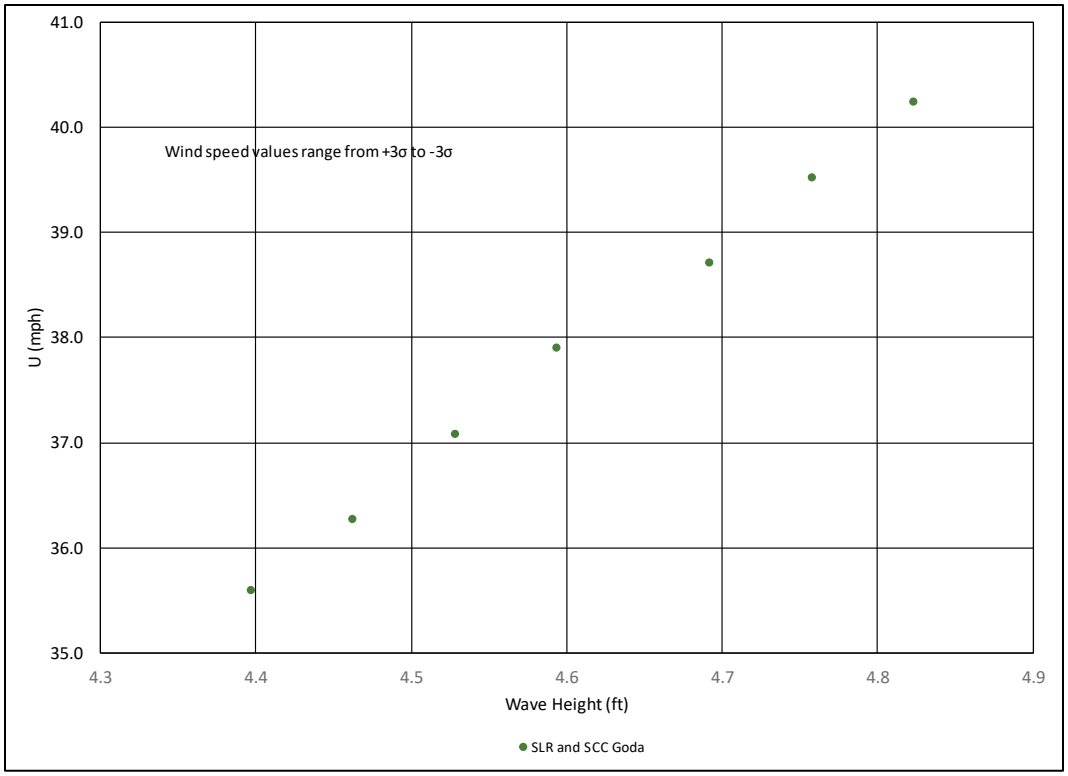

Table A-11. Parameters used in example wave force calculation (imperial and metric units included).

Parameter	Value (Imperial Units)	Value (Metric Units)	Description
h_c	2.0 ft	0.61 m	Gate height above upper pool el
d (originally d_{SWL}, also H in Figure A-29)	40 ft	12.19 m	Difference between upper pool el and spillway crest el
h (originally h_{SWL})	49 ft	14.93 m	Difference between upper pool el and approach channel invert el
tan θ	0	0	Bottom slope toward gate
β_D	0 deg	0 deg	Design incident wave angle
$H_{1/3}$	3.48 ft	1.06 m	Significant wave height for example problem
$T_{1/3}$	3.63 sec	3.63 sec	Significant wave period for example problem
L_D	67.5 ft	20.57 m	Design wave length for example problem
ρ	62.4 lb/ft^3	1,000 kg/m^3	Density of freshwater
g	32.2 ft/sec^2	9.81 m/sec^2	Acceleration due to gravity
h'	40 ft	12.19 m	For the spillway tainter gate: $h' = H = d_{SWL}$

The design wave height (H_D) is the minimum of $\alpha_h H_{1/3}$ and H_b, where α_h ranges from 1.6 to 2.0. For the design of nearshore vertical structures, Goda (2010) suggests using a value of 1.8 for α_h:

$$H_d = H_{Max} = \min\{\alpha_h * H_{1/3}, H_b\},$$

$$H_b = 0.17 * L_D \left\{1 - \exp\left[-1.5\frac{\pi h_b}{L_D}\left(1 + 15 * \tan^{\frac{4}{3}}\theta\right)\right]\right\},$$

where

$$h_b = h + 5 * H_{1/3} * \tan\theta.$$

Therefore,

$$\alpha_h H_{1/3} = 1.8 * 1.06 \text{ m} = 1.91 \text{ m (6.26 ft)},$$

$$h_b = 14.93 \text{ m} + 5 * 1.06 \text{ m} * \tan(0) = 14.93 \text{ m (49 ft)},$$

$$H_b = 0.17 * 20.57 \text{ m}\left\{1 - \exp\left[-1.5\frac{\pi 14.93 \text{ m}}{20.57 \text{ m}}\left(1 + 15 * \tan^{\frac{4}{3}}(0)\right)\right]\right\} = 3.38 \text{ m (11.10 ft)},$$

so

$$H_d = H_{Max} = \min\{1.91 \text{ m}, 3.38 \text{ m}\} = 1.91 \text{ m (6.26 ft)}.$$

Next, calculate the coefficients of wave pressure (α_1, α_2, and α_3) given in the equations that follow:

$$\alpha_1 = 0.6 + \frac{1}{2}\left[\frac{\frac{4\pi h}{L_D}}{\sinh\left(\frac{4\pi h}{L_D}\right)}\right]^2,$$

$$\alpha_2 = \min\left[\frac{h_b - d}{3h_b}\left(\frac{H_D}{d}\right)^2, \frac{2d}{H_D}\right],$$

$$\alpha_3 = 1 - \frac{h'}{h}\left[1 - \frac{1}{\cosh\left(\frac{2\pi h}{L_D}\right)}\right].$$

The h and d values in the preceding equations are respectively equivalent to the h_{SWL} and d_{SWL} from Table A-11. Substituting these values gives

$$\alpha_1 = 0.6 + \frac{1}{2}\left[\frac{\frac{4\pi 14.93\text{ m}}{20.57\text{ m}}}{\sinh\left(\frac{4\pi 14.93\text{ m}}{20.57\text{ m}}\right)}\right]^2 = 0.60 \text{ (from Equation 56)},$$

$$\alpha_2 = \min\left[\frac{14.93\text{ m} - 12.19\text{ m}}{3(14.93\text{ m})}\left(\frac{1.91\text{ m}}{12.19\text{ m}}\right)^2, \frac{2(12.19)\text{ m}}{1.91\text{ m}}\right] = \min[0.0015\text{ m}, 12.77\text{ m}]$$
$$= 0.0015 \text{ (from Equation 57)},$$

and because $h' = d_{SWL} = H$,

$$\alpha_3 = 1 - \frac{12.19\text{ m}}{14.93\text{ m}}\left[1 - \frac{1}{\cosh\left(\frac{2\pi 14.93\text{ m}}{20.57\text{ m}}\right)}\right] = 0.201 \text{ (from Equation 56)}.$$

The lateral pressure components P_1 and P_3 (from Equations 52 and 54) are evaluated here:

$$P_1 = 0.5\ (1\ + \cos\beta_D)\ (\alpha_1 + \alpha_2 * cos^2\beta_D)\ \rho * g * H_D,$$

$$P_3 = \alpha_3 P_1.$$

The solutions to P_1 and P_3 are

$$P_1 = 0.5(1 + \cos(0))(0.60 + 0.001555 * \cos^2(0)) * 1{,}000\text{ kg/m}^3 * 9.81\text{ m/sec}^2$$
$$* 1.98\text{ m} = 11{,}259\text{ N/m}^2 = 11.259\text{ kN/m}^2 = 235.1\text{ (lb/ft}^2),$$

$$P_3 = 0.201 * 11.259\text{ kN/m}^2 = 2.2631\text{ kN/m}^2\ (47.26\text{ lb/ft}^2).$$

As in Section 2.3.2.3 and Figure 16 (shown again as Figure A-27), the total lateral force per linear width (F_{Lat}) on the face of the tainter gate is

$$F_{Lat} = 0.5(P_1 + P_3)H + 0.5(P_1 + P_4)h_c',$$

where

$$P_4 = P_1\left(1 - \frac{h_c}{\eta^*}\right), \text{if } \eta^* > h_c,$$

or

$$P_4 = 0, \text{ if } \eta^* \leq h_c,$$

$$\eta^* = 0.75(1 + \cos(\beta_D))H_D,$$

$$h_C' = \min\{\eta^*, h_C\}.$$

Therefore, the solution for Equation (67), which shows the resultant force, F_{Lat}, is given as

$$h_c = 0.61 \text{ m (2 ft) (from Table A-5)},$$

$$\eta^* = 0.75(1 + \cos(0))1.908 \text{ m} = 2.862 \text{ m (9.39 ft)}.$$

Because $\eta^* > h_c$,

$$P_4 = 11.259 \text{ kN/m}^2 (1 - 0.61 \text{ m}/2.862 \text{ m}) = 8.858 \text{ kN/m}^2 (184.96 \text{ lb/ft}^2),$$

$$h_C' = \min\{2.862 \text{ m}, 0.61 \text{ m}\} = 0.61 \text{ m (2 ft)},$$

$$F_{Lat} = 0.5\left(11.259 \frac{\text{kN}}{\text{m}^2} + 2.263 \frac{\text{kN}}{\text{m}^2}\right) * 12.19 \text{ m} + 0.5(11.259 \frac{\text{kN}}{\text{m}^2} + 8.858 \frac{\text{kN}}{\text{m}^2}) * 0.61 \text{ m} = 88.55 \text{ kN/m (6,067 lb/ft)}.$$

The preceding analysis indicates the total lateral wave force per linear width of the STG for a sustained 30 mph wind is 6,067 lb/ft. The same analysis done for a 40 mph sustained wind showed the total lateral wave force to be 8,087 lb/ft.

In Figure A-28, the pressure terms P_1, P_3, and P_4 are shown acting on the tainter gate. The location of the lateral equivalent force (h_{Lat}) can be determined using the one-third/one-sixth method developed by Ebeling et al. (2018) and also presented in Chapter 2, Section 2.3.2.4, of this report. By applying this method for the lateral forces and summing moments about point 3, Equation (A-14) was developed:

$$h_{Lat} = \frac{(h_4 - h_1)\left(\frac{P_4}{3} + \frac{P_1}{6}\right)h_4 + (h_4 - h_1)\left(\frac{P_4}{6} + \frac{P_1}{3}\right)h_1 + (h_1 - h_3)\left(\frac{P_1}{3} + \frac{P_3}{6}\right)h_1}{F_{Lat}}, \quad \text{(A.14)}$$

$$h_{Lat} = \frac{0.61\text{m}\left(\frac{8.86\frac{\text{kN}}{\text{m}^2}}{3} + \frac{11.26\frac{\text{kN}}{\text{m}^2}}{6}\right)12.8 \text{ m} + 0.61 \text{ m}\left(\frac{8.86\frac{\text{kN}}{\text{m}^2}}{6} + \frac{11.26\frac{\text{kN}}{\text{m}^2}}{3}\right)12.19 \text{ m}}{88.55\frac{\text{kN}}{\text{m}}}$$

$$\frac{+12.19 \text{ m}\left(\frac{11.26\frac{\text{kN}}{\text{m}^2}}{3} + \frac{2.26\frac{\text{kN}}{\text{m}^2}}{6}\right)12.19 \text{ m}}{88.55\frac{\text{kN}}{\text{m}}}$$

$$h_{Lat} = 7.80 \text{ m}.$$

Figure A-27. Goda wave pressure distribution adapted for the spillway tainter gate (STG).

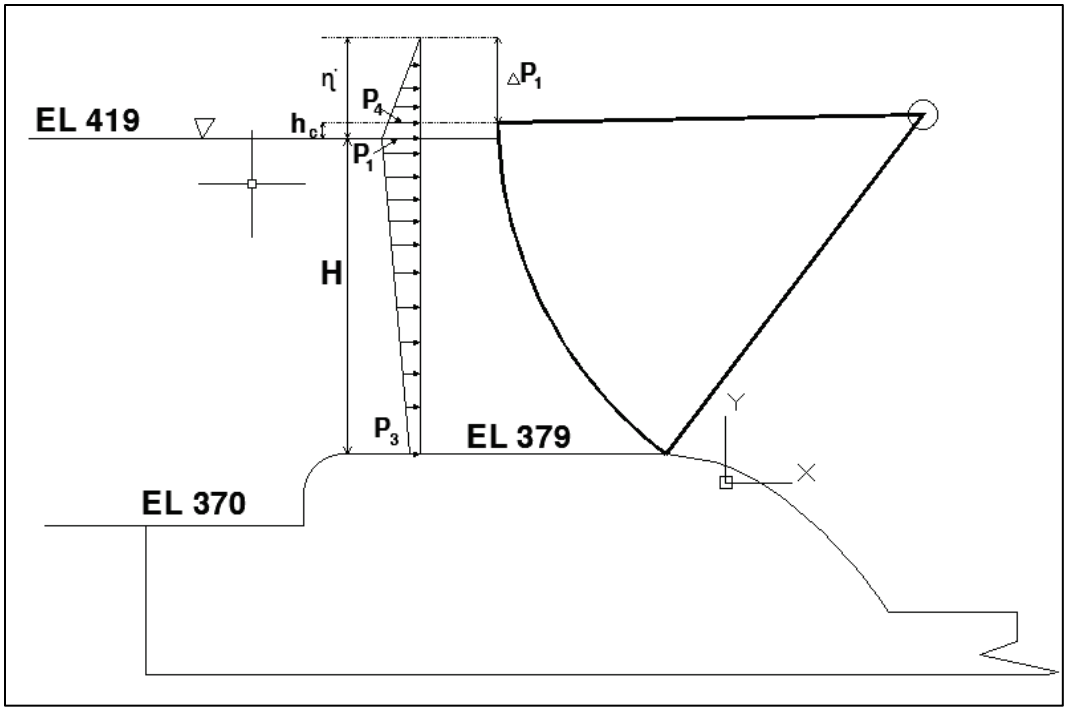

Figure A-28. Definition of wave pressure moment arm terms on an STG.

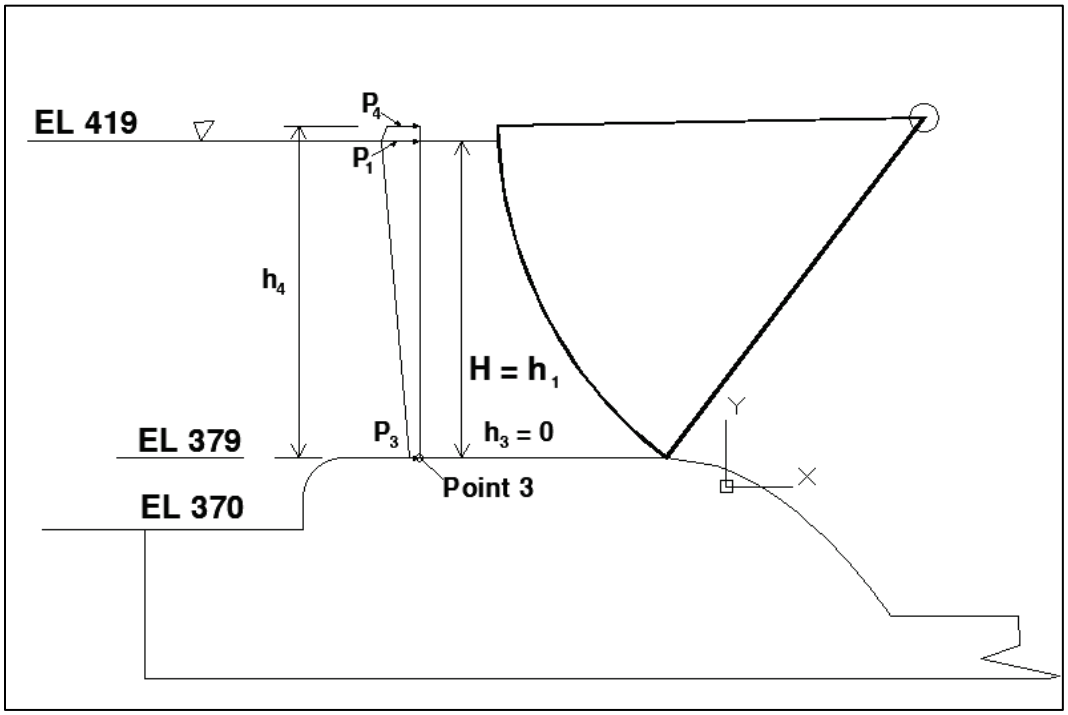

Table A-12 shows the wave heights and wave periods used for computing the wave forces and pressure distributions determined from the wind speed analysis for both airports. The wave forces and pressure

distributions computed from Goda's (2010) procedure for the data in Table A-12 are shown in Table A-13. The definition of Goda's parameters shown in Table A-11 and Table A-13 are illustrated in Figure 16 and again in Figure A-27.

Table A-12. Goda's (2010) procedure for wave height, period, and wavelength for combined airport data.

Statistic	Wind Speed (mph)	Wave ht, $H_{1/3}$ (m)	Wave Period, $T_{1/3}$ (sec)	Wave Length, $L_{1/3}$ (m)	Wave ht, $H_{1/3}$ (ft)
+3σ	40.24	1.47	3.98	24.62	4.82
+2σ	39.52	1.45	3.95	24.30	4.76
+1σ	38.71	1.43	3.92	23.98	4.69
100 yr	37.90	1.40	3.89	23.65	4.59
−1σ	37.09	1.38	3.87	23.33	4.53
−2σ	36.28	1.36	3.84	23.00	4.46
−3σ	35.60	1.34	3.81	22.67	4.40

Table A-13. Wave force and pressure distribution computations using Goda's (2010) procedure for data in Table A-12.

Airport Data	Statistic						
	+3σ	+2σ	+1σ	100 yr	−1σ	−2σ	−3σ
Wind Speed (mph)	40.24	39.52	38.71	37.90	37.09	36.28	35.60
η^* (m)	3.969	3.915	3.861	3.78	3.726	3.672	3.618
P_1 (N/m^2)	15,650	15,435	15,220	14,898	14,683	14,468	14,254
P_3 (N/m^2)	3,448	3,368	3,291	3,193	3,129	3,057	2,995
P_4 (N/m^2)	13,245	13,030	12,815	12,494	12,279	12,065	11,850
F_{Lat} (kN/m)	125.21	123.29	121.38	118.62	116.79	114.91	113
h_{Lat} (m)	7.76	7.76	7.76	7.77	7.77	7.77	7.77
h_{Lat} (ft)	25.4	25.4	25.5	25.5	25.5	25.5	25.5
P_1 (lb/ft^2)	327	322	318	311	307	302	298
P_3 (lb/ft^2)	72	70	69	67	65	64	63
P_4 (lb/ft^2)	277	272	268	261	256	252	247
F_{Lat} (lb/ft)	8,580	8,448.0	8,317.2	8,128.1	8,002.7	7,873.8	7,749

A.4 Hydrodynamic Loads for MPLD

A.4.1 Average Hydrodynamic Load on STGs Based on Average Tailwater Elevation (TW El)

To develop the hydraulic loads on the STG, upper and lower pool els, discharge, and gate opening must be known. The normal operating procedure is to raise the gates high enough to pass the discharge required to maintain

the upper pool at a near constant of el 419. If the discharge keeps increasing, the gates are eventually raised completely out of the flow, and open river conditions exist. At this point, there are no hydrostatic or hydrodynamic loads on the tainter gate.

An example of how to determine the pertinent hydraulic data to compute the hydrodynamic load is presented. The discharge versus frequency curve indicates that for 50% of the time, the discharge is at or above 72,000 cfs. Therefore, 72,000 cfs could be considered the average discharge. The project has nine gates, so each gate passes about 8,000 cfs. The spillway rating curve provides the discharge per gate for gate openings between 0.1 and 10 ft for TW Els between 395 and 414.5. As mentioned, the upper pool remains constant at el 419. The average tailwater can be determined from the historical data, and once this is known, the spillway rating curve can be used to find the gate opening for this discharge and tailwater combination. Section A.1 describes the process of developing the average tailwater from the historical data.

The average hydrodynamic load on the STG can be determined next based on the average TW El. The normal upper pool el is 419, and the average TW El determined from the statistical analysis is 402.69. This gives a net head on the gate of 16.31 ft. The average discharge at MPLD is assumed to be 72,000 cfs. This was determined from a plot of discharge versus percent of time the discharge was at or above in Design Memorandum 9 (USACE-LRN 1958, Plate 10). The project has nine gates, so this is equivalent to a discharge of 8,000 cfs per gate. From the spillway rating curve (Figure 28) with a discharge of 8,000 cfs per gate and a TW El of 402.69, the gate opening would be 2.9 ft.

The momentum equation from Roberson and Crowe (1985) was given as

$$\frac{\gamma H^2 b}{2} - \frac{\gamma h^2 b}{2} + F_{GW} - F_{visc} = V_1 \rho(-V_1 H b) + V_2 \rho(V_2 h b).$$

Considering the viscous force (F_{visc}) is negligible and $V_1 H b = V_2 h b = Q$,

$$F_{GW} = \rho Q(-V_1) + \rho Q(V_2) - \frac{1}{2}\gamma b(H^2 - h^2).$$

F_{GW} is the force of the gate acting on the water in the control section. To obtain the force on the gate (F_G), F_{GW} is solved, and the sign on F_{GW} is changed. Equation (82) is repeated here:

$$F_G = \rho Q(V_1 - V_2) + \frac{1}{2}\gamma b(H^2 - h^2),$$

where

V_1 = the approach velocity,
V_2 = the velocity downstream of the gate,
p = 1.936 slugs/ft^3,
γ = 62.4 lb/ft^3,
b = the gate width (ft),
H = upper pool El – crest El, and
h = TW El – crest el.

Figure A-29 shows a schematic with some of the terms used in Equation (82) and described in the discussion that follows. The approach velocity, V_1, can be determined from Equation (85), which is repeated here:

$$V_1 = \frac{Q}{A_1}.$$

In Equation (86), which is repeated here, A_1 is the area upstream from the gate and is the upper pool el – the approach el (P in Figure A-29) or 419 – 370 = 49 ft multiplied by the width of the gate, b (110 ft), which gives 5,390 ft^2:

$$A_1 = P * b.$$

V_1 is equal to 8,000 ft^3/sec divided by 5,390 ft^2, or 1.48 ft/sec. V_2 is

$$V_2 = \frac{Q}{A_2},$$

where A_2 is

$$A_2 = b * h.$$

This gives (8,000 ft^3/sec) / (110 ft × 23.69 ft) = 3.07 ft/sec.

If the value for discharge, Q, is not available from a spillway rating curve, it can be computed from the equation that follows. In this example, the differential head, ΔH, is 40 ft – 23.69 ft = 16.31 ft, and h = TW El – crest El, which is 402.69 – 379 = 23.69 ft. C_{gs} in Equation (87), which is repeated

here, is obtained from Figure 5-12 in Engineer Manual (EM) 1110-2-1605 (HQUSACE 1987):

$$Q = C_{gs} b h \sqrt{2g\Delta H},$$

where

$$h = \text{TW El} - \text{spillway crest el},$$

and the differential head, ΔH, is

$$\Delta H = H - h.$$

Figure A-29. Schematic of parameters used for MPLD in Equation (82).

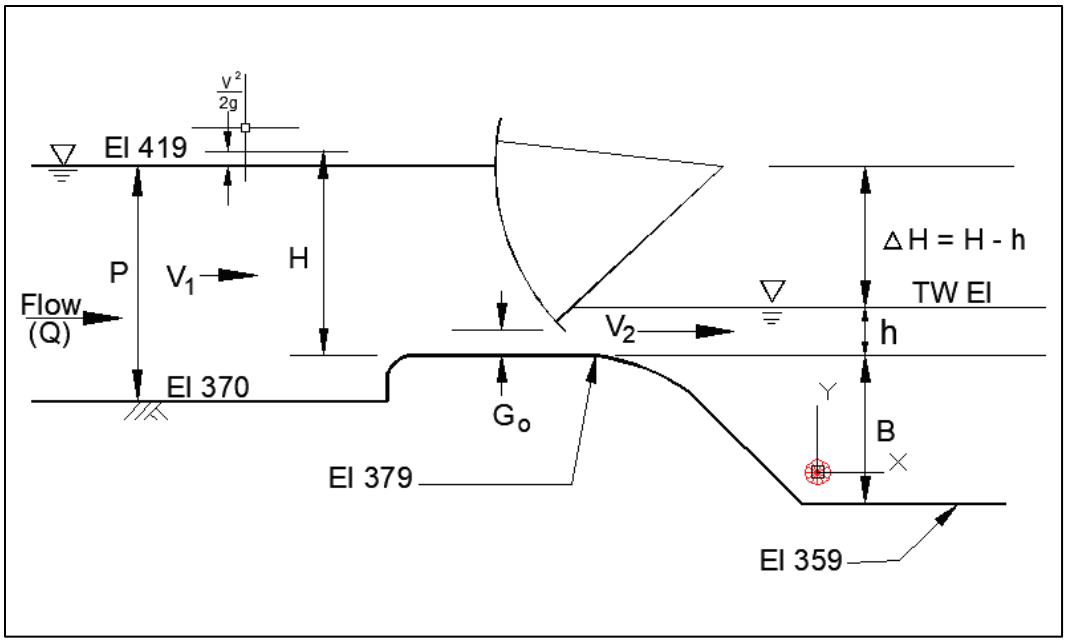

Everything is now known, and F_G in Equation (82) can be computed. The mean hydrodynamic load for a TW El of 402.69 was determined to be 32,187 lb per foot of gate width.

A.4.2 Hydrodynamic Loads for Different Gate Operations

At MPLD, the gates are operated to maintain a near constant navigation pool el of 419. For example, when the TW El is 395, and the discharge per gate is 8,000 ft^3/sec, the gates are open 2.4 ft (as determined from Figure 28). When the TW El is 414 with this discharge, the gates are open 5.2 ft. The hydrodynamic loads for different gate settings were determined from

the spillway rating curve (Figure 28) and the procedure described previously. Figure A-30 shows the hydrodynamic load per foot of gate width for gate openings between 1 and 10 ft and TW Els of 395, 405 and 414.5. These represented a high, low, and median TW El. The two points shown at the upper-right side of the plot that are labeled 400.8 and 404.1 represent the lowest TW El for the 9 and 10 ft gate openings that could be read from Figure 28. The plots show that the tailwater dominates the hydrodynamic load because there is not much change in the magnitude of the hydrodynamic force when the gate opening varies. This is because the second term on the right-hand side of Equation (82) is much larger than the first term on the right-hand side of the equation. As the tailwater increases, the difference between the approach velocity, V_1, and the velocity downstream from the gate, V_2, becomes less, and the first term on the right-hand side of Equation (82) becomes even smaller.

Figure A-30. Hydrodynamic force on STGs for varying gate openings and tailwater (upper pool el 419).

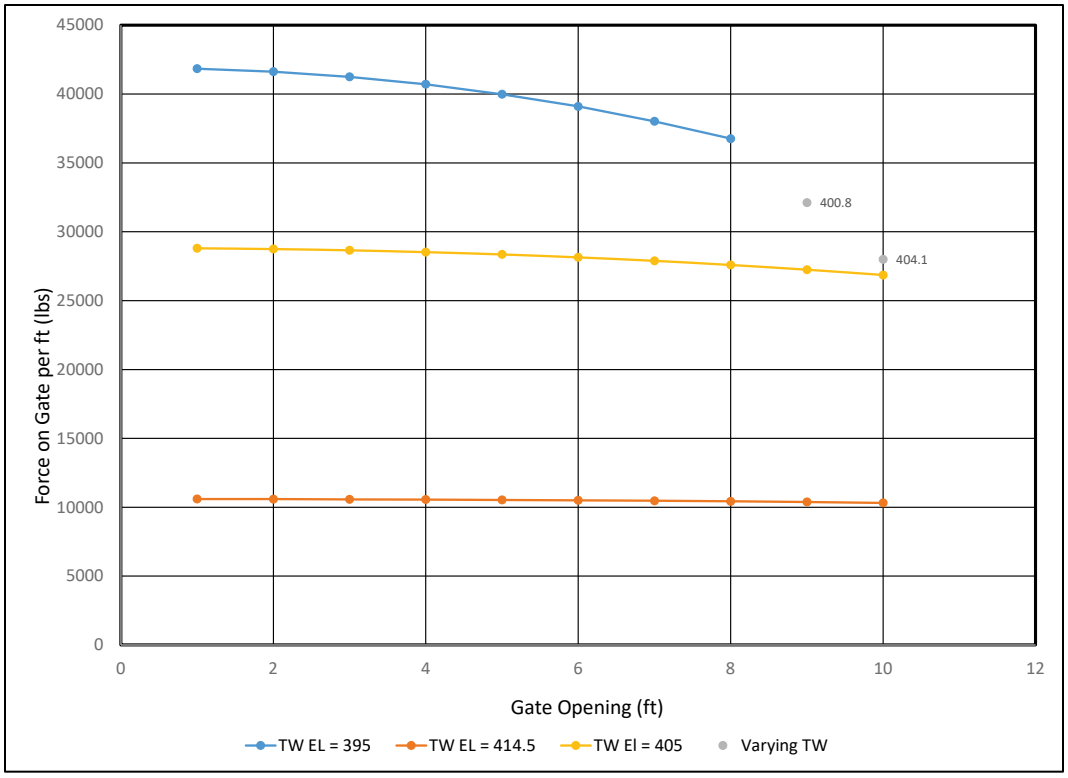

Table A-14 provides the values used to produce the plot shown in Figure A-30. The procedure to develop the values in Table A-14 consisted of choosing three TW Els that represented minimum, maximum, and medium (i.e., 395, 414.5 and 405) and selecting the discharge from Figure 28

associated with this tailwater and the desired gate opening. The gate openings were from 1 to 10 ft in 1 ft increments.

Table A-14. Hydrodynamic loads for varying tailwater and gate openings from 1–10 ft.

Gate Opening (G_o) (ft)	TW El	Q (cfs)	V_1 (ft/sec)	h (ft)	ΔH (ft)	h/G_o	V_2 (ft/sec)	F_g (lb)	F_g (lb/ft)
1	395	3,650	0.68	16	24	16.0	2.07	4,602,738	41,843
1	414.5	1,650	0.31	35.5	4.5	35.5	0.42	1,165,650	10,597
1	405	2,750	0.51	26	14	26.0	0.96	3,168,765	28,807
2	395	6,700	1.25	16	24	8	3.81	4,579,353	41,630
2	414.5	2,900	0.54	35.5	4.5	17.75	0.74	1,164,873	10,590
2	405	5,200	0.96	26	14	13.0	1.82	3,162,576	28,751
3	395	10,050	1.86	16	24	5.33	5.71	4,537,784	41,253
3	414.5	4,400	0.82	35.5	4.5	11.33	1.13	1,163,378	10,576
3	405	7,650	1.42	26	14	8.67	2.67	3,152,573	28,660
4	395	13,450	2.50	16	24	4.00	7.64	4,478,592	40,714
4	414.5	5,800	1.08	35.5	4.5	8.88	1.49	1,161,427	10,558
4	405	10,250	1.90	26	14	6.59	3.58	3,137,786	28,525
5	395	17,000	3.15	16	24	3.20	9.66	4,398,512	39,986
5	414.5	7,250	1.35	35.5	4.5	7.10	1.86	1,158,842	10,535
5	405	12,750	2.37	26	14	5.20	4.46	3,119,515	28,358
6	395	20,500	3.80	16	24	2.67	11.65	4,301,280	39,103
6	414.5	8,700	1.61	35.5	4.5	5.92	2.23	1,155,683	10,506
6	405	15,400	2.86	26	14	4.33	5.38	3,095,813	28,144
7	395	24,100	4.47	16	24	2.29	13.69	4,182,334	38,021
7	414.5	10,250	1.90	35.5	4.5	5.07	2.62	1,151,671	10,470
7	405	18,000	3.34	26	24	3.71	6.29	3,068,220	27,893
8	395	27,700	5.14	16	24	2.00	15.74	4,044,187	36,765
8	414.5	11,600	2.15	35.5	4.5	4.44	2.97	1,147,642	10,433
8	405	20,700	3.84	26	14	3.25	7.24	3,035,020	27,591
9	400.8	27,000	5.01	21.8	18.2	2.42	11.26	3,533,471	32,122
9	414.5	13,200	2.45	35.5	4.5	3.94	3.38	1,142,222	10,384
9	405	23,400	4.34	26	14	2.89	8.18	2,997,187	27,247
10	404.1	27,000	5.01	25.1	14.9	2.51	9.78	3,079,679	27,997
10	414.5	14,700	2.73	35.5	4.5	3.55	3.76	1,134,569	10,314
10	405	26,100	4.84	26	14	2.60	9.13	2,954,721	26,861

Table A-15 gives the area downstream from the gate (A_2) for the three TW Els. For example, with a TW El of 395 and a 1 ft gate opening, the discharge per gate is 3,650 cfs. Knowing the discharge, V_1 and V_2 can be

computed, and knowing the upper pool el and TW El, the values for *h* and *H* can be determined.

Table A-15. Exit area used for calculations in Table D-14.

TW El	A_2 (ft²)
395	1,760
414.5	3,905
405	2,860

A.5 Probabilistic Characterization of the Hydrostatic and Hydrodynamic Loads for the MPLD STG

A.5.1 Statistical Analysis of Hydrostatic Loads for MPLD

In this analysis, the hydrostatic load is considered without tailwater effects because it is higher than those with tailwater effects. For this project, the mean upper pool el is considered to be the normal navigation pool el of 419. Realizing that gate operations and responses to maintain the upper pool do not occur instantaneously, fluctuations above and below the normal upper pool el probably occur when gate changes are made. As discussed previously, the maximum hydrostatic load results when the tainter gate is closed, which normally means low discharge conditions through the spillway and no tailwater effect. Closing adjacent gates would cause the upper pool to fluctuate above and below normal pool. This fluctuation is considered when developing the dispersion of the hydrostatic loads. Historical hydraulic data provides the best estimate for the magnitude of the fluctuation; however, a record of gate operations is also needed to determine which gates were closed when the upper pool was recorded.

For the MPLD project, an estimate of 2 ft above and 2 ft below the normal upper pool el was used to develop the statistics for the hydrostatic load. This estimate was selected to demonstrate a procedure, and if actual historical data were available for a project, a better estimate could be made. An accepted method to determine the standard deviation, σ, is to use a value from this equation: (maximum – minimum)/6, assuming a normal distribution and that the minimum to maximum range covers 99.7% of the values. The standard deviation for the MPLD project was determined to be 0.667 ft, and the values for the dispersion in the hydrostatic load using this technique are shown in Table A-16. Figure 39 shows the hydrostatic pressure distribution for the upper pool +6σ, the mean upper pool, and the upper pool –6σ. Figure 40 shows a plot of the hydrostatic pressures

computed for MPLD for the upper pool +6σ, the mean upper pool, and the upper pool −6σ. The hydrostatic force per foot width of the gate computed from Equation (12) ranged from 60,403 lb/ft for the upper pool +6σ to 40,435 lb/ft for the upper pool −6σ (Table A-16).

Table A-16. Hydrostatic gate force per foot of gate run for the upper pool els +6σ and −6σ around the mean upper pool for the Melvin Price STG.

Upper Pool El	Statistic	H_s (lb/ft)
415	−6σ	40,435
415.666	−5σ	41,943
416.333	−4σ	43,489
417	−3σ	45,053
417.666	−2σ	46,646
418.333	−σ	48,269
419	Mean	49,920
419.667	+σ	51,599
420.334	+2σ	53,305
421	+3σ	55,037
421.667	+4σ	56,801
422.334	+5σ	58,591
423	+6σ	60,403

A.5.2 Statistical Analysis of Hydrodynamic Loads for MPLD with Tailwater Higher than the Gate Opening

A statistical analysis was performed for the hydrodynamic loads to develop the load dispersion for the LRFD process. The procedure described here is applicable to projects where the tailwater is higher than the gate opening and therefore effects the hydrodynamic force on the STG. The computation of the hydrodynamic force, F_G, using Equation (82) requires input values for the upper pool el, TW El, discharge per gate, gate opening, spillway crest El, and gate width. For normal operating conditions, the upper pool is maintained at el 419. The (downstream) TW El varies depending on the river discharge. In the subsequent statistical analysis of the F_G value discussed in this subsection, TW El is considered the primary independent variable. The tailwater statistics discussed in Section A.1 were developed from a 31 yr record collected between 1939 and 1969. These data were part of the design memorandums for the MPLD.

These statistics were used in the hydraulic loading analysis for the projects' STGs. Leap year was included, along with a minimum and maximum range summary for each day's data. The resulting project-specific data curves are shown in Section A.1. Figure A-2 shows the maximum daily values, the minimum daily values, and the average daily values. To perform a formal, standard statistical, data-driven uncertainty/dispersion mathematical assessment, additional information regarding the daily distribution of the tailwater data is needed. The reduced-data form of presentation in Figure A-2 did not allow recovery of the distribution data for that period. Therefore, because the LRFD method includes statistical analysis of the loading conditions, the authors had to look at less rigorous statistical methods, which will discussed in the paragraphs that follow.

The project spillway rating curve (Figure 28) was used in this analysis of the hydrodynamic loads. This curve was prepared by USACE-MVS and is used to determine the gate settings needed to maintain the upper pool el near constant (el 419) for a given tailwater and discharge. The curves were developed for a tailwater range from el 395 to el 414.5. It was assumed that once the TW El exceeded 414.5, the spillway gates were no longer used to control the flow. The authors of this report observed that the average tailwater curve for the 31 yr record lies within this gate operational range between 395 and 414.5. This is the range where the spillway rating curves are applicable. The tailwater data points that lie outside of this range are not applicable because the hydrodynamic force computed using Equation (82) is intended for gated flow conditions. Equation (82) requires the discharge per gate (Q) value, and the value for Q is obtained from Figure 28.

Based on the limitation of tailwater data as discussed in the previous paragraph, the authors of this report believe that the daily average TW Els from Figure A-2 are a good representation for the project and are suitable for developing the statistics needed for the LRFD process.

Figure A-31 shows the authors' constructed TW El PDF from the curve in Figure A-2 for the average tailwater data, in histogram form, computed from the 366 daily average values. The number of bins was determined using the Freedman-Diaconis rule, which uses the interquartile range to determine bin widths (Freedman and Diaconis 1981).

Figure A-31. TW El PDF histogram.

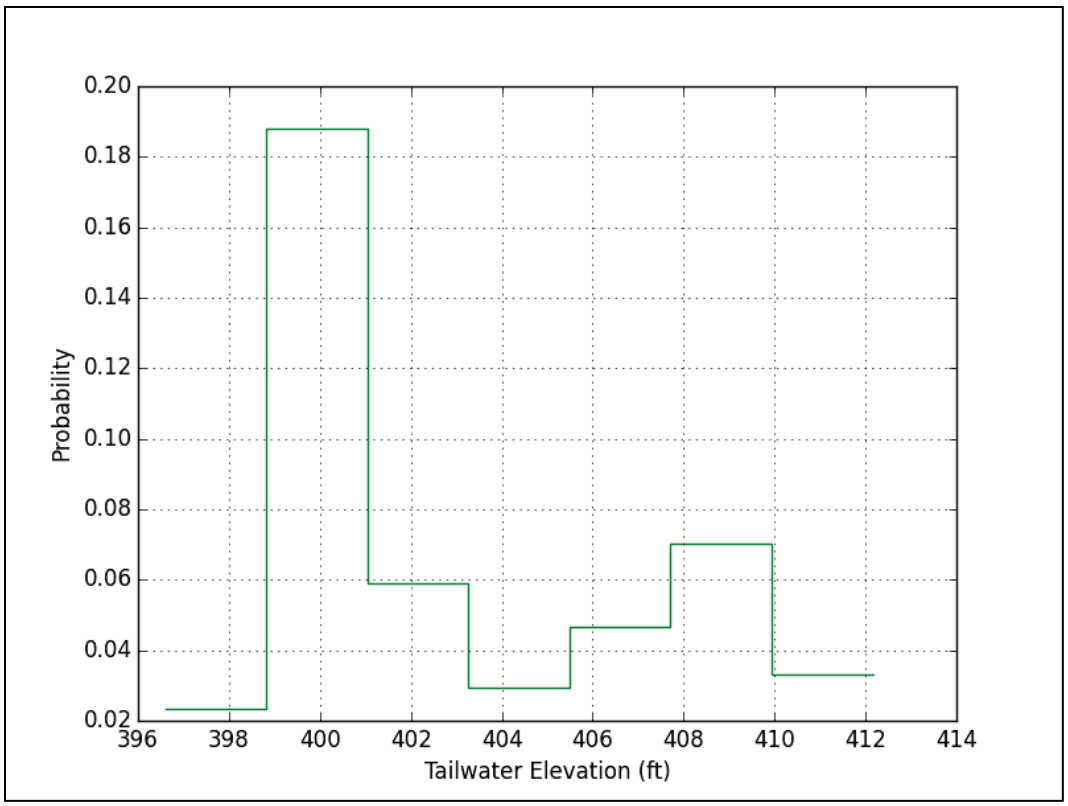

Figure A-32 through Figure A-41 show the results of converting the TW Els to PDF distributions of hydrodynamic forces for gate openings, G_o, between 1 and 10 ft. The hydrodynamic forces were computed for the gate with openings from 1 to 10 ft, using 1 ft intervals. The hydrodynamic forces were computed using the discharge from the equations shown in Figure A-42 and applying Equation (82). Figure A-42 was constructed using the relationships between tailwater, gate opening, and discharge presented in Figure 28 and by developing a fit curve (and equation) for each gate opening between 1 and 10 ft. The displayed values are given per foot of gate. The MPLD STG is 110 ft wide, so the full force acting on the gate is the hydrodynamic force per foot of gate multiplied by 110 ft. Additional development of Figure A-42 is provided in a later paragraph.

Figure A-32. PDF for hydrodynamic force per foot of gate for 1 ft gate opening.

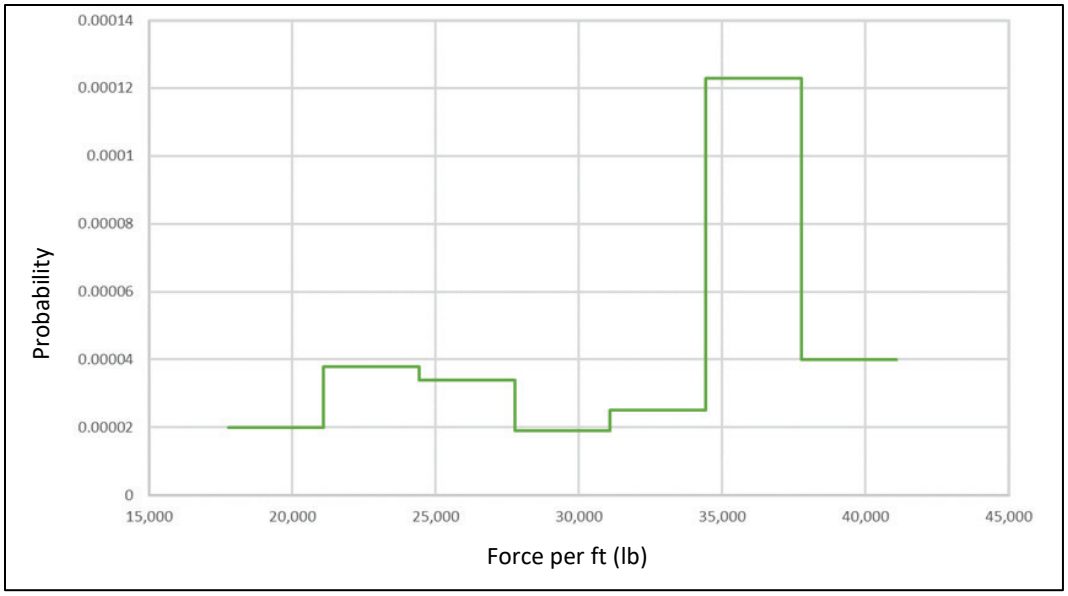

Figure A-33. PDF for hydrodynamic force per foot of gate for 2 ft gate opening.

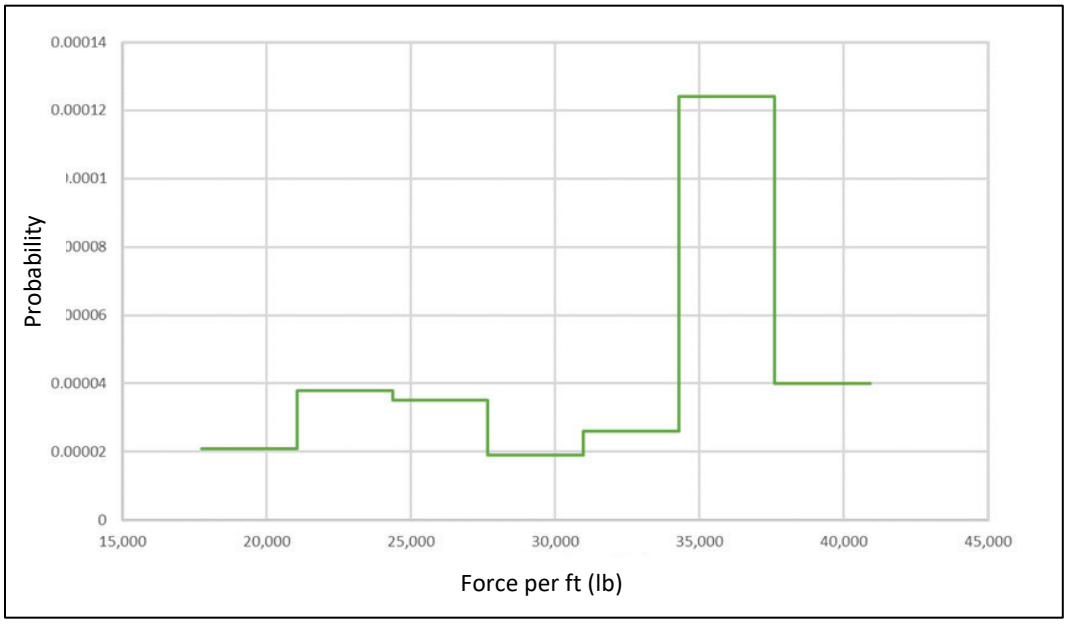

Figure A-34. PDF for hydrodynamic force per foot of gate for 3 ft gate opening.

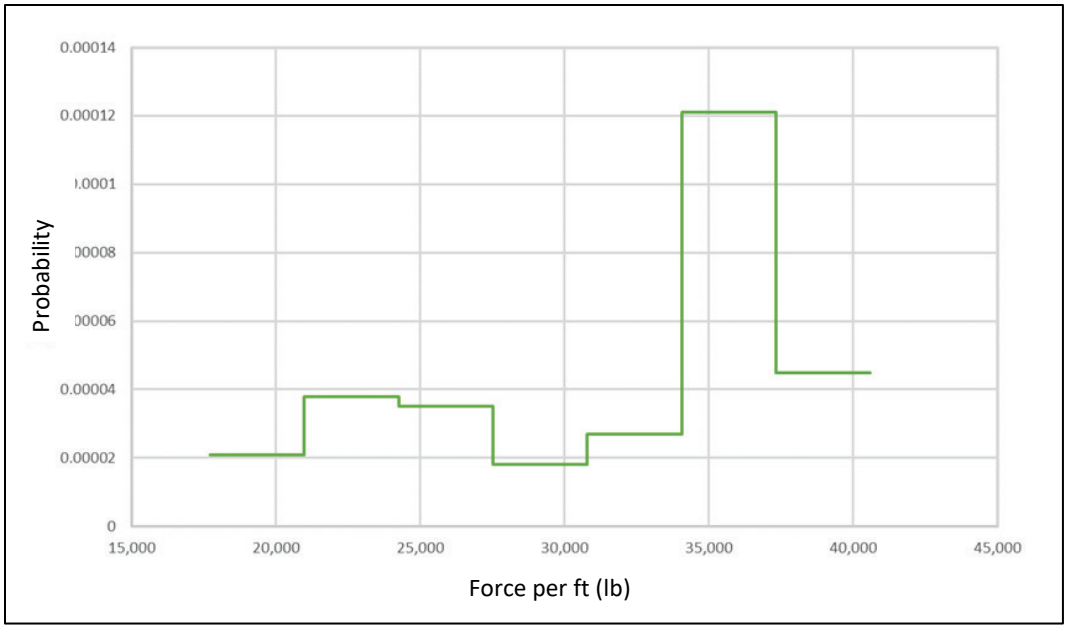

Figure A-35. PDF for hydrodynamic force per foot of gate for 4 ft gate opening.

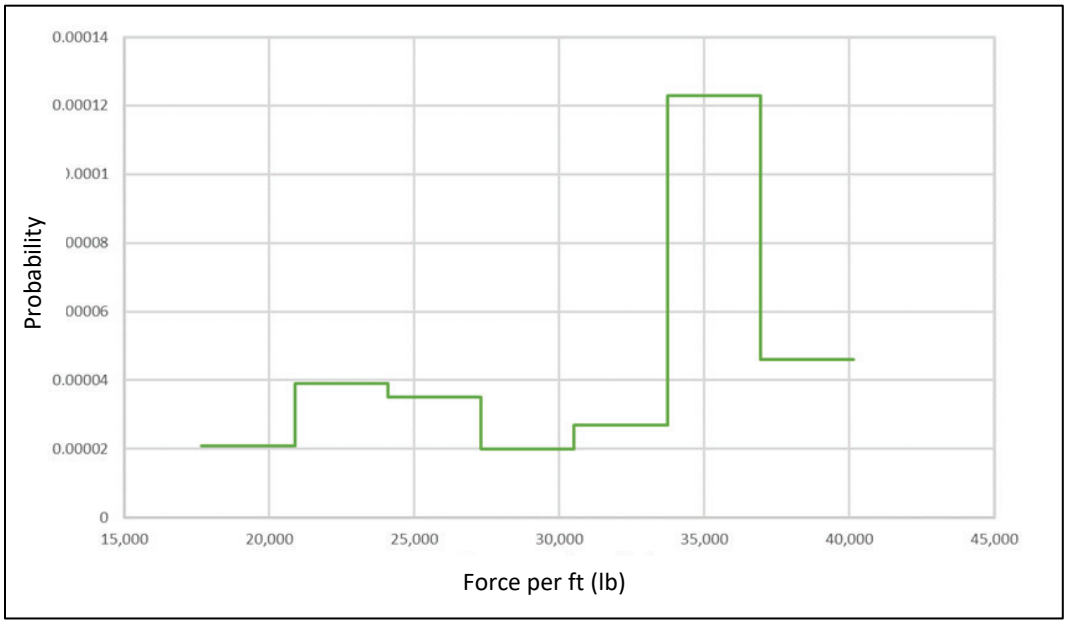

Figure A-36. PDF for hydrodynamic force per foot of gate for 5 ft gate opening.

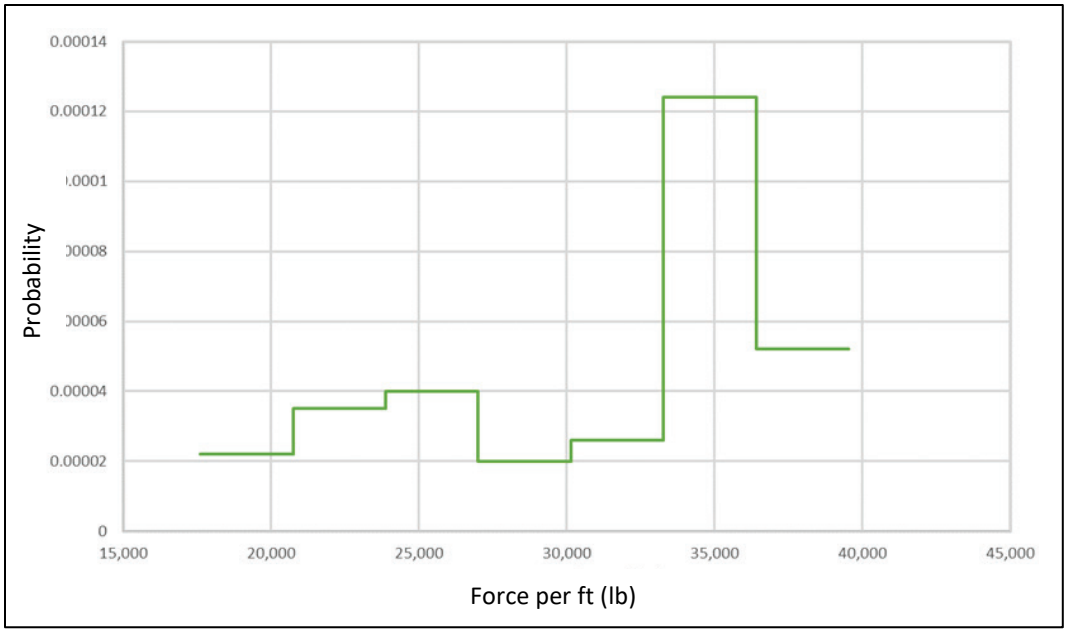

Figure A-37. PDF for hydrodynamic force per foot of gate for 6 ft gate opening.

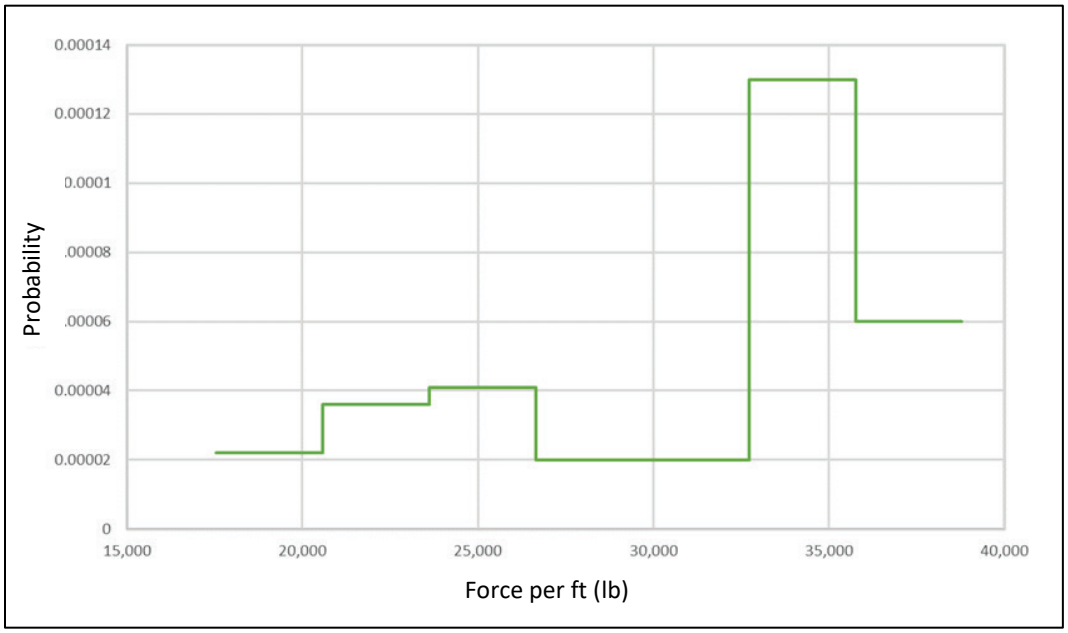

Figure A-38. PDF for hydrodynamic force per foot of gate for 7 ft gate opening.

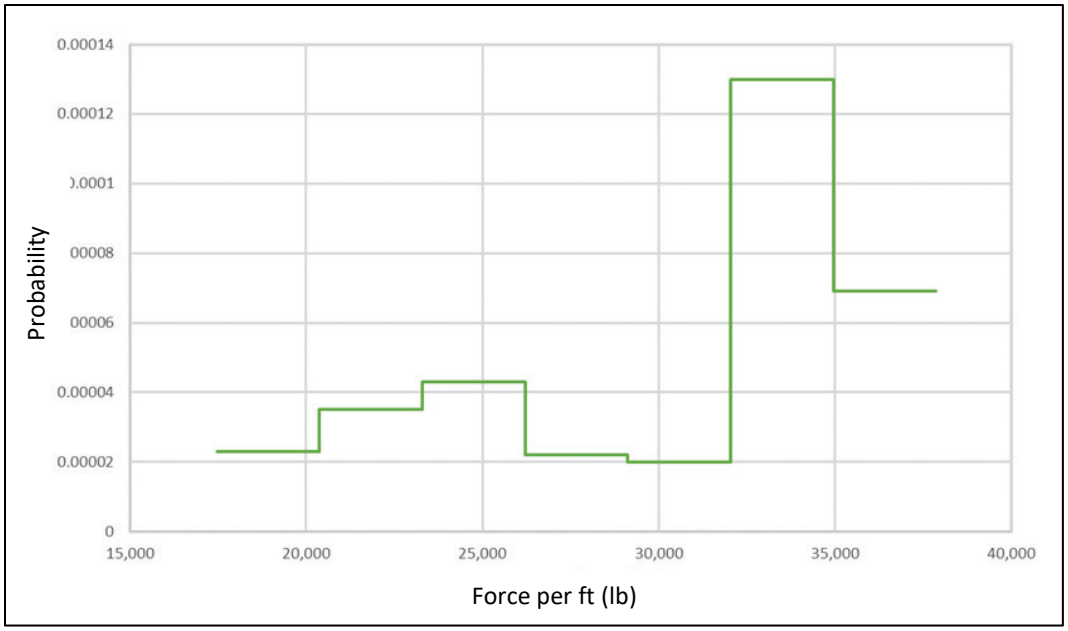

Figure A-39. PDF for hydrodynamic force per foot of gate for 8 ft gate opening.

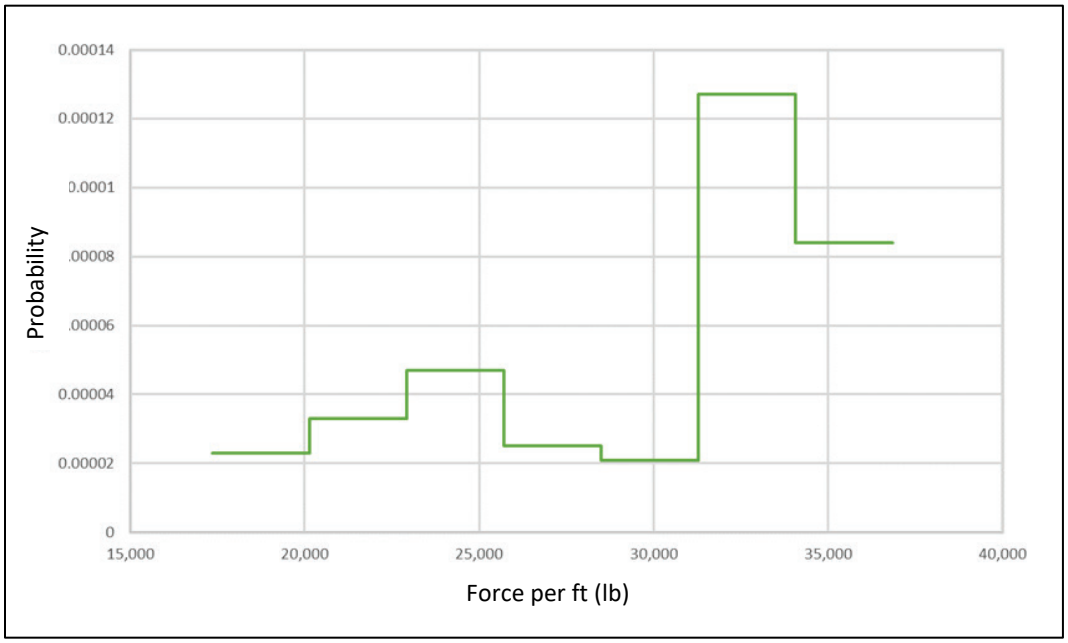

Figure A-40. PDF for hydrodynamic force per foot of gate for 9 ft gate opening.

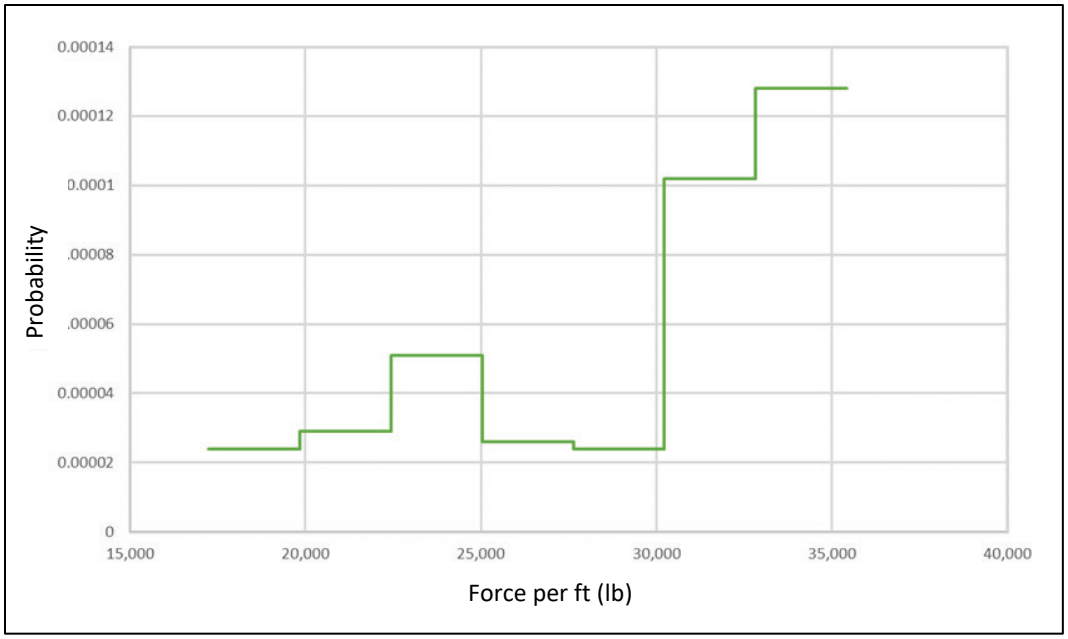

Figure A-41. PDF for hydrodynamic force per foot of gate for 10 ft gate opening.

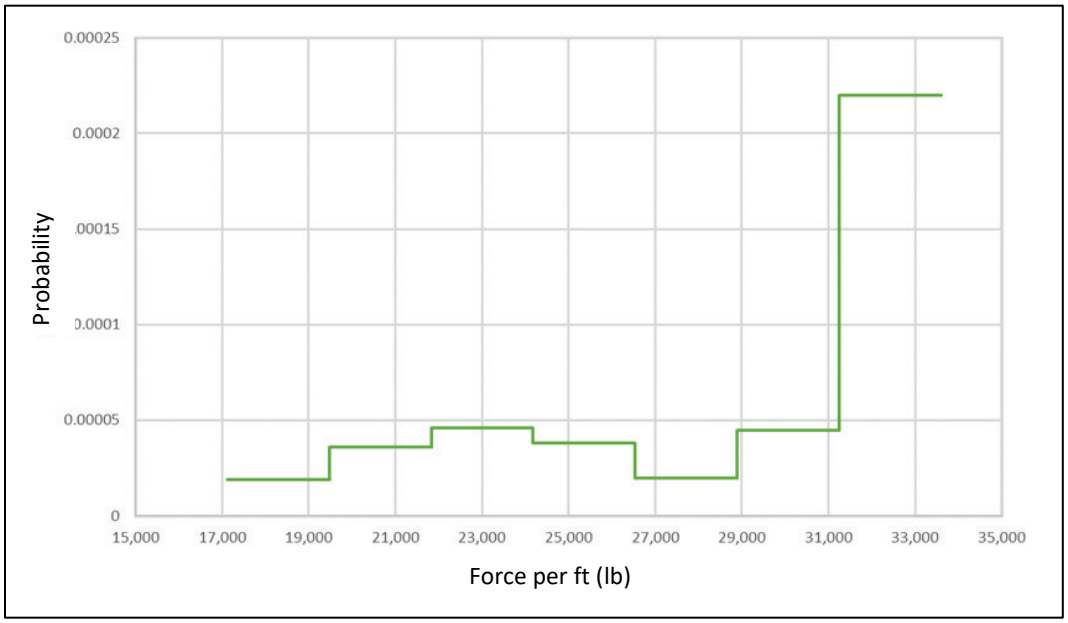

The shape of the PDF distributions for F_G in Figure A-32 through Figure A-41 as a function of gate opening do not follow the trend of a normal Gaussian PDF shape. Additionally, these 10 PDFs possesses a distinct chimney at the high end of the F_G distribution. The shape of these 10 PDFs reflect the shape of the Figure A-31 tailwater PDF. Observe in Figure A-31 that a chimney is observed at the lower values of the tailwater distribution range. By Equation (82) and general hydraulic principles, the largest

computed hydrodynamic force will be associated with the lowest TW El (for a constant upstream pool el of 419). In summary, the low TW El chimney in Figure A-31 translated through Equation (82) into the high hydrodynamic force chimney in each of the 10 F_G PDF distributions. These chimneys reflect the highest probability for the F_G value among its range in values for each specific gate opening. Further observe in these 10 figures that these peak probability F_G values decrease in magnitude with increasing gate opening.

Figure A-42 reports the fitted equations through the spillway discharge data obtained from Figure 28. Using the Excel (equation) curve fit software feature, coefficients of a second order polynomial equation were determined by the software; it provides the best fit through the discharge versus TW El data for each gate opening. The x-value in these equations is the TW El in feet, and the y-value is the discharge per gate opening in cubic feet per second for a 110 ft wide gate. These equation fits were quite good; the lowest R^2 value (0.99982) was computed for the 3 ft gate opening curve. An R^2 value rating of 1.0 means that the curve has been perfectly described by the equation. These equations facilitated the computations using Equation (82) for F_G, resulting in the F_G PDFs of Figure A-32 through Figure A-41.

Figure A-42. Fitted spillway rating curves for the gate openings from 1 to 10 ft.

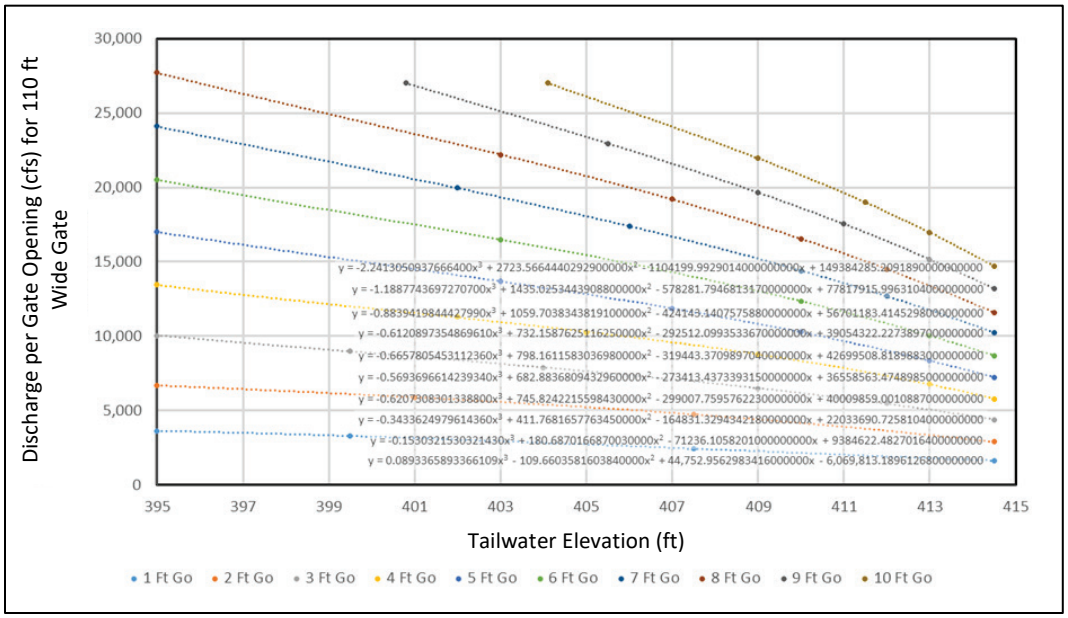

Figure A-43 shows the maximum hydrodynamic forces (per foot of gate) that are exerted on the gates from the average tailwater histogram. Notice

that the forces calculated are inverted from the TW Els in Figure A-31. Higher tailwaters result in lower hydrodynamic forces acting on the gate.

Figure A-43. Maximum hydrodynamic force (per foot of gate) occurring on the gate for gate openings from 1 to 10 ft.

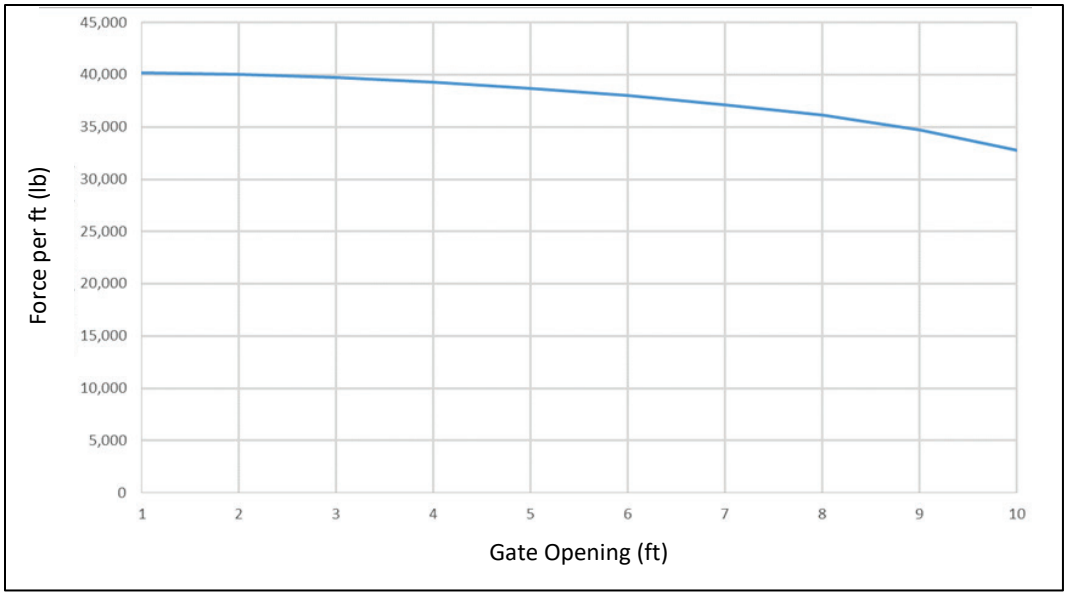

The F_G histogram PDFs from Figure A-32 through Figure A-41 are based on a limited sample of 366 data points and are therefore quite coarse. However, these histograms provide insights that can inform the production of simpler statistical models that provide conservative estimations of tailwater distributions. Given the coarseness of the tailwater distribution data, more conservative estimates are considered beneficial to the LRFD process because they avoid underestimation of hydrodynamic forces.

The minimum and maximum, average (mean), and median TW El values listed in Table A-17 summarize the statistical aggregation of the 366 data points shown in Figure A-2 from the average daily values of TW El. These four values can form the basis of a simple distribution for the range of gate openings that conservatively characterizes tailwater probabilities. The mean is the arithmetic average of a set of numbers, or a distribution. The median is described as the numeric value separating the higher half of a sample, a population, or a probability distribution from the lower half. The minimum TW El value was chosen as the minimum of the 366 minimum sample data values. The maximum TW El value was chosen as the maximum of the 366 maximum sample data values. The mean TW El was chosen as the average of the 366 mean sample data values. The median TW El value was chosen as the median of the 366 mean sample data values. This

selection was performed by sorting the 366 mean sample data values in ascending order and then selecting the central value (at index 183) as the median value. This guarantees that nearly half of the values lie above the median, and half lie below. The most important observation is that the median TW El is less than the average TW El by 2.7 ft in a range of 14.5 ft. (In Figure A-2, the maximum average value is 411.1, and the minimum average value is 396.6.) This is an indicator that the distribution is skewed toward lower TW El. This is shown to be true with the histogram shaped PDF of Figure A-31.

Table A-17. Tailwater statistics from average daily values

Maximum TW El	Median TW El	Average TW El	Minimum TW El
411.1	400.4	402.7	396.6

Note: Upper pool el = 419, gate width = 110 ft, gates are out of the water for tailwater el of 414.5 and above, and el 395.0 to 414.5 is the range where gate control is required. This is the range over which the spillway rating curves are applicable.

Figure A-44 shows the trend of F_G forces computed from the Table A-17 values with respect to gate openings. For the mean computed force, all 366 TW Els were used to compute forces, and then the forces were averaged for each individual gate opening. The range in F_G values versus gate openings in this figure are defined by the maximum tailwater, shown as a dashed blue curve, and the minimum tailwater, shown as a dashed red curve. Again, observe that the minimum tailwater results in the largest F_G values. The definition of the median value states that half of the 366 data points are between the minimum tailwater (maximum force) curve and the median curve, and the other half are between the maximum tailwater (minimum force) curve and the median curve. The median F_G curve is the dashed orange curve in Figure A-44. The final two curves in this figure are the curve for the force computed from the average TW El (dotted gray) and the average force computed from all of the sample TW Els (dotted yellow). These two curves differ because of the nonlinear relationship of TW El to F_G in Equation (82). These two curves do not lie on the median TW El force curve, providing more evidence that the probability density of the sample values is skewed. A conservative estimator could be formed by selecting a distribution that has symmetry of probability density about an arbitrary mean value and assigning the mean value to be the hydrodynamic force computed from the median average tailwater value. A normal Gaussian distribution meets this criteria. The standard deviation must be found to complete this distribution description.

Figure A-44. Maximum total hydrodynamic force for the median and mean TW Els and the minimum and maximum TW Els for each of the 1–10 ft gate openings and a gate width of 110 ft.

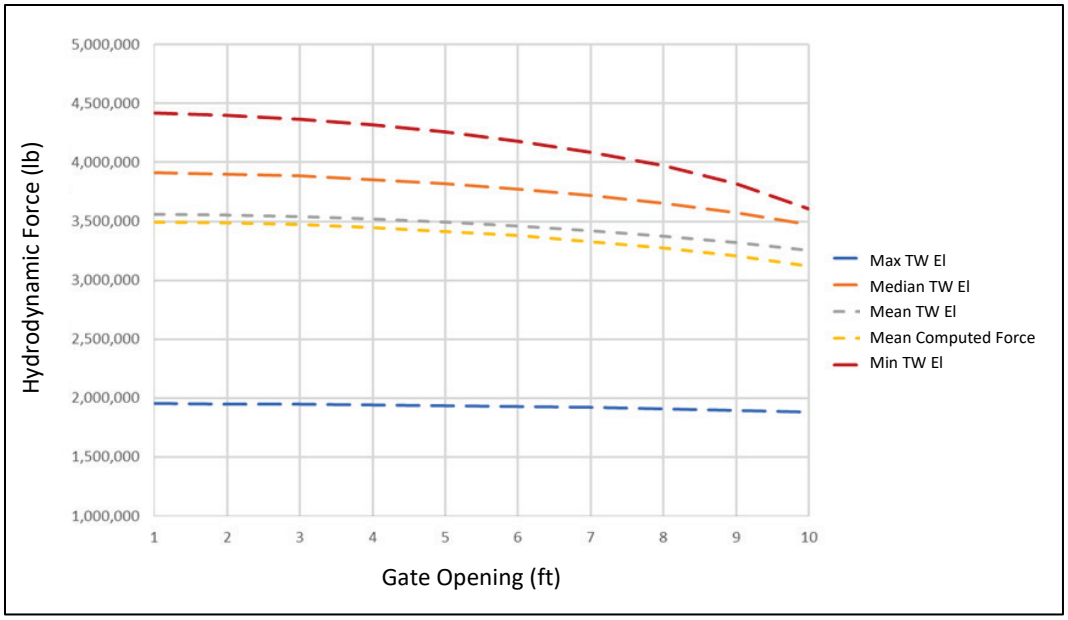

Based on the minimum TW El, the maximum total hydrodynamic force value is the dashed red line of data shown in Figure A-44 for each of the 10 gate openings. If the minimum value for TW El is accurate (which the authors believe is true), then this red line of total gate force values represents the maximum force values that can be developed on a 110 ft wide gate for a gate opening from 1 to 10 ft. This detail is important to keep in mind for the subsequent discussion. In Figure A-44, the dashed red line of maximum hydrodynamic forces corresponds to the blue line of maximum hydrodynamic forces per foot of gate in Figure A-43. The values in Figure A-43 were multiplied by the gate width of 110 ft to give the values in Figure A-44.

In LRFD analysis, the dispersion in the distribution of loading data must be defined. When a complete set of data does not exist, as is the case for TW El, an approach to developing a value for the standard deviation, σ, needs to be devised. The technique adopted for this analysis was based on the sparse data approach that was described by Ebeling and White (2019, Appendix C). The sparse-data-based approach states that for distributions where the minimum and maximum values are known but the standard deviation is not available, the 6-sigma method can be used to develop the standard deviation. This method assumes that the precisely defined sample range of data contains 99.74% (−3σ to +3σ) of the true population of

TW Els, which may have outlier events with extremely small probabilities. This leads to

$$\sigma = \frac{\text{Max} - \text{Min}}{6}. \quad \text{(A.15)}$$

This equation is applied to the minimum and maximum forces computed for the minimum and maximum TW El in order to characterize the dispersion in the distribution for hydrodynamic force. Note that if the range in data cannot be precisely defined, the value for the denominator is changed from a value of six. This detail is discussed in Ebeling and White (2019, Appendix C).

Table A-18 shows the maximum and minimum hydrodynamic forces and the computed approximation for the value of standard deviation using this 6-sigma method for each of the gate openings. Figure A-45 shows the results of applying a symmetric distribution centered about the median tailwater forces using the 6-sigma-based standard deviation. The area between the brown lines indicates where samples will be chosen with plus or minus 1 standard deviation of probability, the range between the solid green lines within plus or minus 2 standard deviations of probability, and the range between the solid blue lines within plus or minus 3 standard deviations of probability.

Table A-18. Results of computations using the 6-sigma method; total hydrodynamic force values on the 110 ft wide gate given minimum and maximum forces for each of the 10 gate openings.

Gate Opening (ft)	Max Tailwater Force (lb)	Min Tailwater Force (lb)	(Max Force – Min Force)/6 (lb)
1.0	1,954,051.7	4,420,070.3	411,003.1
2.0	1,951,961.5	4,401,033.6	408,178.7
3.0	1,948,468.6	4,368,296.6	403,304.7
4.0	1,943,315.0	4,321,299.2	396,330.7
5.0	1,937,359.7	4,257,620.8	386,710.2
6.0	1,929,581.2	4,180,140.5	375,093.2
7.0	1,920,438.8	4,085,029.6	360,765.1
8.0	1,909,655.5	3,975,980.5	344,387.5
9.0	1,897,436.1	3,819,906.0	320,411.6
10.0	1,882,974.0	3,603,896.8	286,820.5

Figure A-45. Median hydrodynamic force for each of the 1–10 ft gate openings and standard deviation ranges for –σ to +σ (*orange*), −2σ to + 2σ (*green*), and −3σ to +3σ (*blue*).

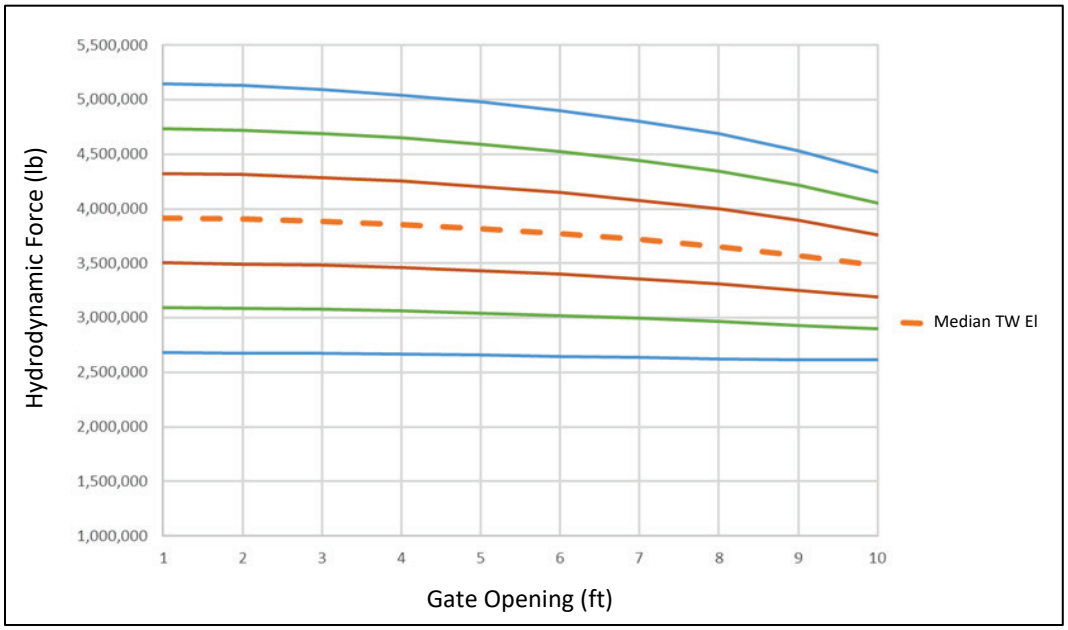

Figure A-46 shows the ranges with respect to the computed forces from the extreme (minimum and maximum) tailwater data events from the collected data along with the curves from Figure A-45. Using the 6-sigma standard deviations for a normal distribution centered at the median value does not fit the actual spread of the data very well. Creating Monte Carlo samples with this distribution underpredicts high tailwater events and overpredicts low tailwater events.

Underprediction of high tailwater events is shown by the fact that the maximum tailwater force lies outside the −3 sigma prediction range in Figure A-46. This gives that force a very low probability, which means that most high tailwater samples will be chosen with a tailwater value that does not approach the maximum. Because these values give lower forces, it is a conservative result for our purposes.

Overprediction of low tailwater events is shown by the fact that the minimum tailwater force is near the +1 sigma prediction range for the gate openings in Figure A-46. This means that the hydrodynamic force that occurs with minimum tailwater force has a fairly high probability and, worse, that even lower TW El outside the range of collected data has a less than +2 sigma probability. This means that high forces are grossly overpredicted by this distribution, leading to overly conservative results in terms of force.

Figure A-46. Comparison of σ ranges to collected data range from TW El.

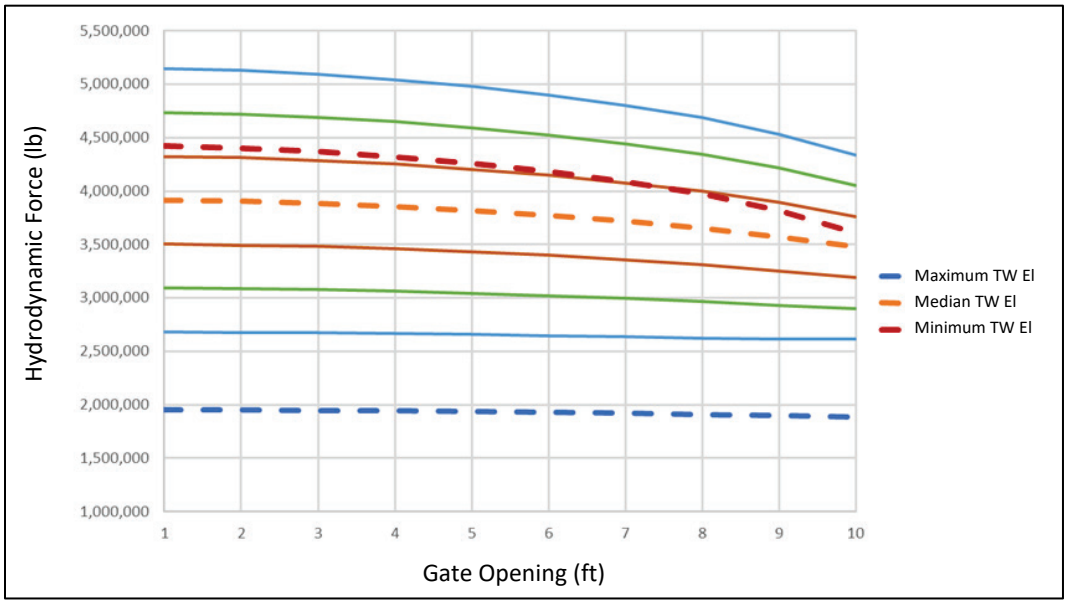

The issue of overprediction and underprediction of F_G values arises because of the probability density of collected points. Half of the collected TW El forces are between the median TW El forces and either of the extreme TW El forces. The probability density between the median and minimum TW El forces is greater than the probability density between the median and maximum TW El forces because the force value range is smaller for the median to minimum TW El.

The observations made in the previous paragraph suggest a method to encapsulate the greatest density of sample points while not exceeding the bounds of the data. A reduced 6-sigma method can be created by assuming symmetry in the range of the data points about the median collected point. This symmetry is enforced by finding the smallest value change between the extreme values and the median value. In our case, the force differential between the minimum and median TW El force is smaller than the force differential between the maximum and median TW El force. The force range is therefore adjusted to two times the minimum force range differential, Δ. If we assume that this range covers 99.74% of the data samples, we can estimate the standard deviation to be equal to $\Delta/6$. This represents an extension of the 6-sigma method through range manipulation, making the new range symmetric about the median sample values.

Table A-19 and Figure A-47 show the results of using the reduced 6-sigma method. This value is much more conservative with respect to lower values

of hydrodynamic force, but it is less likely to generate forces outside of the minimum and maximum force range.

Table A-19. Summary of results of computations using the reduced 6-sigma method, total hydrodynamic force values on a 110 ft wide gate given a range in minimum and maximum forces at 10 gate openings.

Gate Opening (ft)	Max Tailwater Force (lb)	Median Tailwater Force (lb)	Min Tailwater Force (lb)	Estimated σ using reduced 6-sigma method (Δ/6) (lb)
1.0	1,954,051.7	3,914,690.5	4,420,070.3	168,459.9
2.0	1,951,961.5	3,902,872.3	4,401,033.6	166,053.8
3.0	1,948,468.6	3,883,825.5	4,368,296.6	161,490.4
4.0	1,943,315.0	3,855,655.7	4,321,299.2	155,214.5
5.0	1,937,359.7	3,818,593.8	4,257,620.8	146,342.3
6.0	1,929,581.2	3,772,788.1	4,180,140.5	135,784.1
7.0	1,920,438.8	3,717,019.6	4,085,029.6	122,670.0
8.0	1,909,655.5	3,652,996.1	3,975,980.5	107,661.5
9.0	1,897,436.1	3,573,075.2	3,819,906.0	82,276.9
10.0	1,882,974.0	3,476,336.4	3,603,896.8	42,520.2

Figure A-47. Median hydrodynamic force for each of the 1–10 ft gate openings and reduced 6-sigma standard deviation ranges for −σ to +σ (*orange*), −2σ to +2σ (*green*), and −3σ to +3σ (*blue*).

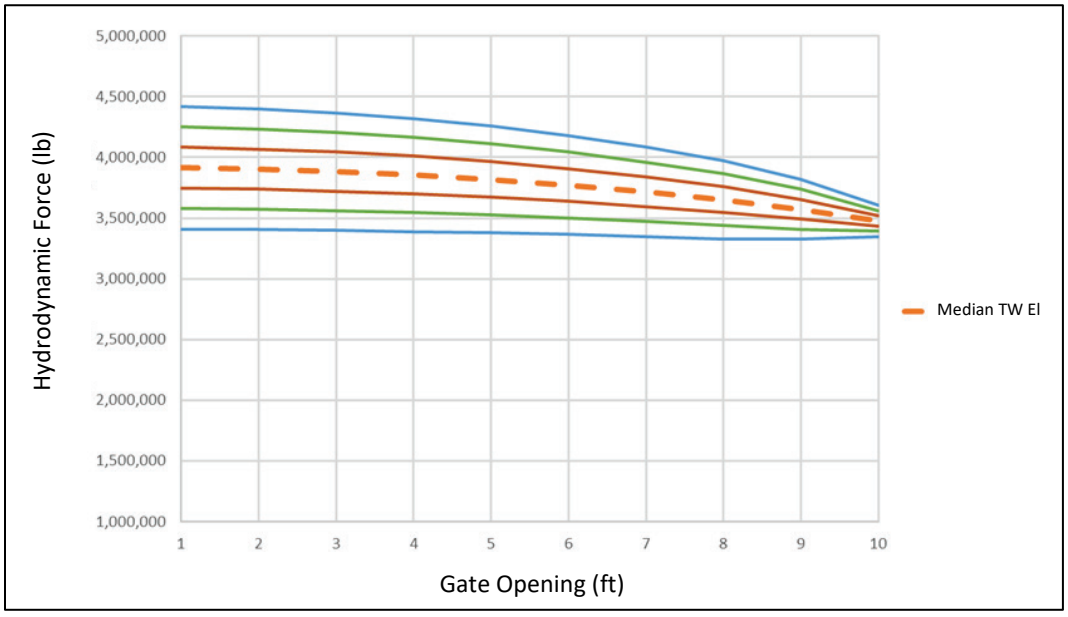

Figure A-48 shows the reduced 6-sigma ranges with respect to the extreme data values. Because the minimum TW El force curve (i.e., the red dashed line) directly aligns with the +3σ curve (i.e., the solid blue line), it is less

likely that values with hydrodynamic force that exceeds our collected data will be generated in a Monte Carlo simulation. The possibility of lower forces being drawn by the distribution has also been significantly reduced, but because the major concern is higher forces, this is a conservative change. A greater portion of the collected data is covered by the normal distribution centered at the median without exceeding the range of the collected data.

Figure A-48. Comparison of reduced 6-sigma standard deviation ranges to collected data range from TW El.

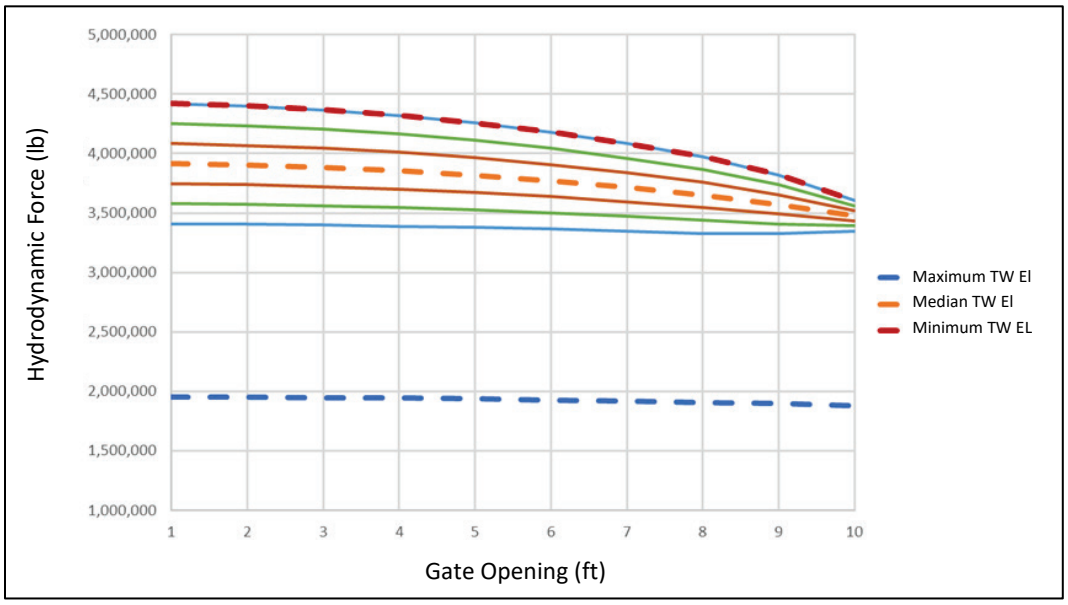

Table A-20 gives the values of the force ranges computed using the reduced 6-sigma method for each of the 10 gate openings. These values match the forces shown in Figure A-47 and Figure A-48.

Table A-20. Ranges in total hydrodynamic forces about the median hydrodynamic force value on a 110 ft wide gate using the reduced 6-sigma method for the 10 gate openings.

Gate Opening (ft)	Hydrodynamic Gate Force, F_G, Tabulated Relative to the Force Computed for the Median Tailwater Average						
	−3σ (lb)	−2σ (lb)	−σ (lb)	Median (lb)	+σ (lb)	+2σ (lb)	+3σ (lb)
1	3,409,310.8	3,577,770.7	3,746,230.6	3,914,690.5	4,083,150.4	4,251,610.3	4,420,070.2
2	3,404,710.9	3,570,764.7	3,736,818.5	3,902,872.3	4,068,926.1	4,234,979.9	4,401,033.7
3	3,399,354.3	3,560,844.7	3,722,335.1	3,883,825.5	4,045,315.9	4,206,806.3	4,368,296.7
4	3,390,012.2	3,545,226.7	3,700,441.2	3,855,655.7	4,010,870.2	4,166,084.7	4,321,299.2
5	3,379,566.9	3,525,909.2	3,672,251.5	3,818,593.8	3,964,936.1	4,111,278.4	4,257,620.7
6	3,365,435.8	3,501,219.9	3,637,004.0	3,772,788.1	3,908,572.2	4,044,356.3	4,180,140.4
7	3,349,009.6	3,471,679.6	3,594,349.6	3,717,019.6	3,839,689.6	3,962,359.6	4,085,029.6
8	3,330,011.6	3,437,673.1	3,545,334.6	3,652,996.1	3,760,657.6	3,868,319.1	3,975,980.6
9	3,326,244.5	3,408,521.4	3,490,798.3	3,573,075.2	3,655,352.1	3,737,629.0	3,819,905.9
10	3,348,775.8	3,391,296.0	3,433,816.2	3,476,336.4	3,518,856.6	3,561,376.8	3,603,897.0

Figure A-49 shows a comparison of the computed normal force PDF distribution with respect to the force computed from tailwater histogram distribution for a gate opening of 1 ft (Figure A-32). This plot shows how the gray line normal Gaussian distribution is conservative for the computation of hydrodynamic forces as reflected in its dispersion relative to the green line and step PDF distribution and, yet, captures the peak probabilities of occurrence. The orange dashed line is fixed at the point of force computed from the median tailwater and a 1 ft gate opening. For a symmetrical, normal Gaussian distribution, mean, median, and mode values are the same. The authors of this report recognize that in LRFD development, it is far more important to not overestimate maximum hydrodynamic forces in the developmental process than it is to overestimate the minimum hydrodynamic forces. Maximum forces typically dominate an engineering design process.

The development of the statistics for the hydrodynamic loads for the STG at the MPLD demonstrated the need to obtain quality historical stage data. Each USACE District probably collects stage data in some form. The ideal dataset would contain recordings of the stage information every hour or less since the construction of the project. The Water Management personnel in each district are able to find available historical stage information. NOAA, the National Weather Service, and the USGS also collect environmental data and may have data that could be useful in a statistical analysis. Both USACE and the USGS currently maintain websites that contain stage data (USACE, “Water Levels,” n.d., “Access to Water Resources,” n.d.; USGS, n.d.).

A 30 yr stage record is considered sufficient for developing the required statistics. The preceding analysis showed that a daily distribution of tailwater (rather than one average value) was needed to perform a rigorous statistical procedure for the dispersion of the hydrodynamic forces. When the river is controlled by the spillway gates, the tailwater should not fluctuate drastically. A brief search of stage data on inland waterway systems was performed to determine how many tailwater readings per day were needed to provide an adequate distribution. Periods when rapid rises occurred were observed to quantify stage changes in a 24 hr period.

Figure A-49. Comparison of PDFs for a narrow normal distribution for the hydrodynamic force distribution per foot of gate to a broader step PDF distribution from average tailwater data for a gate opening of 1 ft.

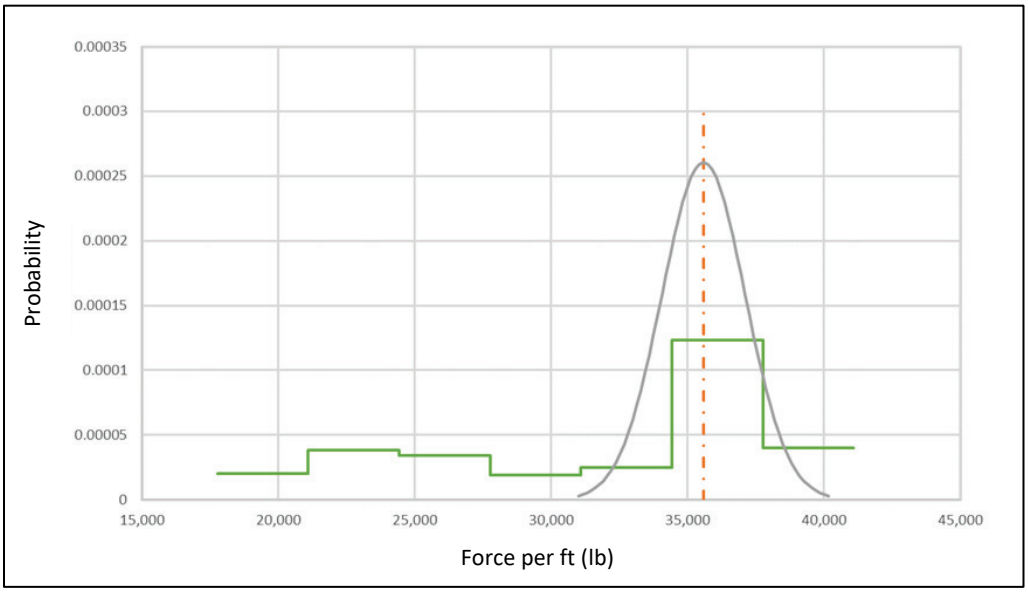

Figure A-50 through Figure A-52 show results of stage changes on the Mississippi, Arkansas, and Ohio Rivers at different periods over recent years. Figure A-50*A* shows the stage upstream from Lock and Dam 5a on the Mississippi River, and Figure A-50*B* shows the stage downstream between 16 March and 1 April in 2011. On 25 March, the stage downstream from the project rose around 2 ft (Figure A-50*B*). Figure A-51*A* shows the stage upstream from James W. Trimble Lock and Dam on the Arkansas River, and Figure A-51*B* shows the stage downstream between 21 May and 26 May in 2019. On 22 May, the stage downstream from the project rose between 5 and 6 ft (Figure A-51*B*). Figure A-52*A* shows the stage upstream from McAlpine Locks and Dam on the Ohio River, and Figure A-52*B* shows the stage downstream between 16 and 26 February in 2011. On 25 February, the stage downstream from the project rose around 10 ft (Figure

A-52*B*). The 10 ft rise on the Ohio River in a 24 hr period is likely representative of the maximum rise on an inland waterway river. If four samples of the TW El were available for this 10 ft rise, it would give an adequate distribution of the tailwater stage for this day. This cursory investigation suggests that four daily readings of tailwater are good enough for a rigorous statistical analysis of the dispersion of the hydrodynamic forces.

Figure A-50. (*A*) Stages upstream and (*B*) stages downstream from Lock and Dam 5a on the Mississippi River between 16 March and 1 April 2011.

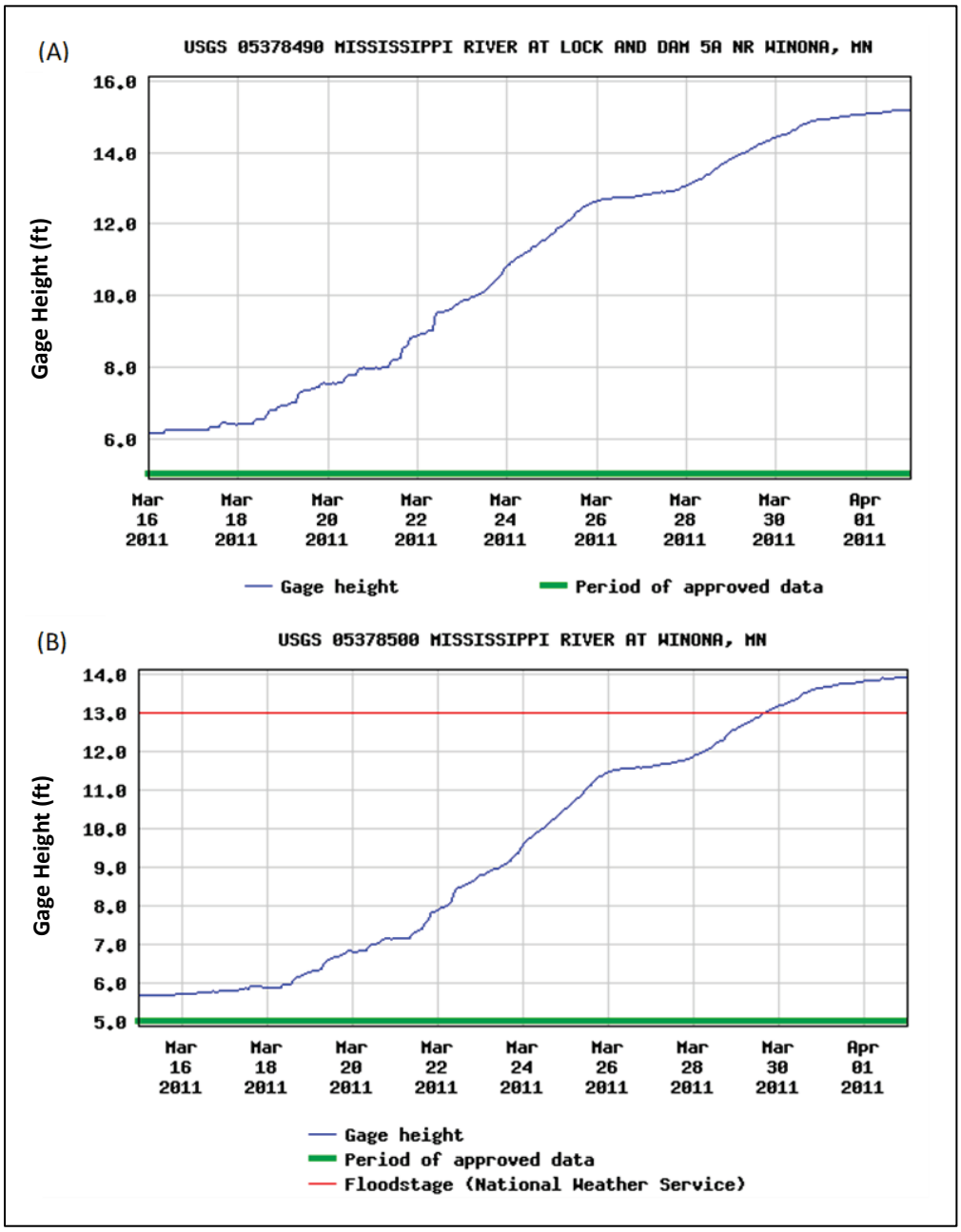

Figure A-51. (*A*) Stages upstream and (*B*) stages downstream from James W. Trimble Lock and Dam on the Arkansas River between 21 and 27 May 2019.

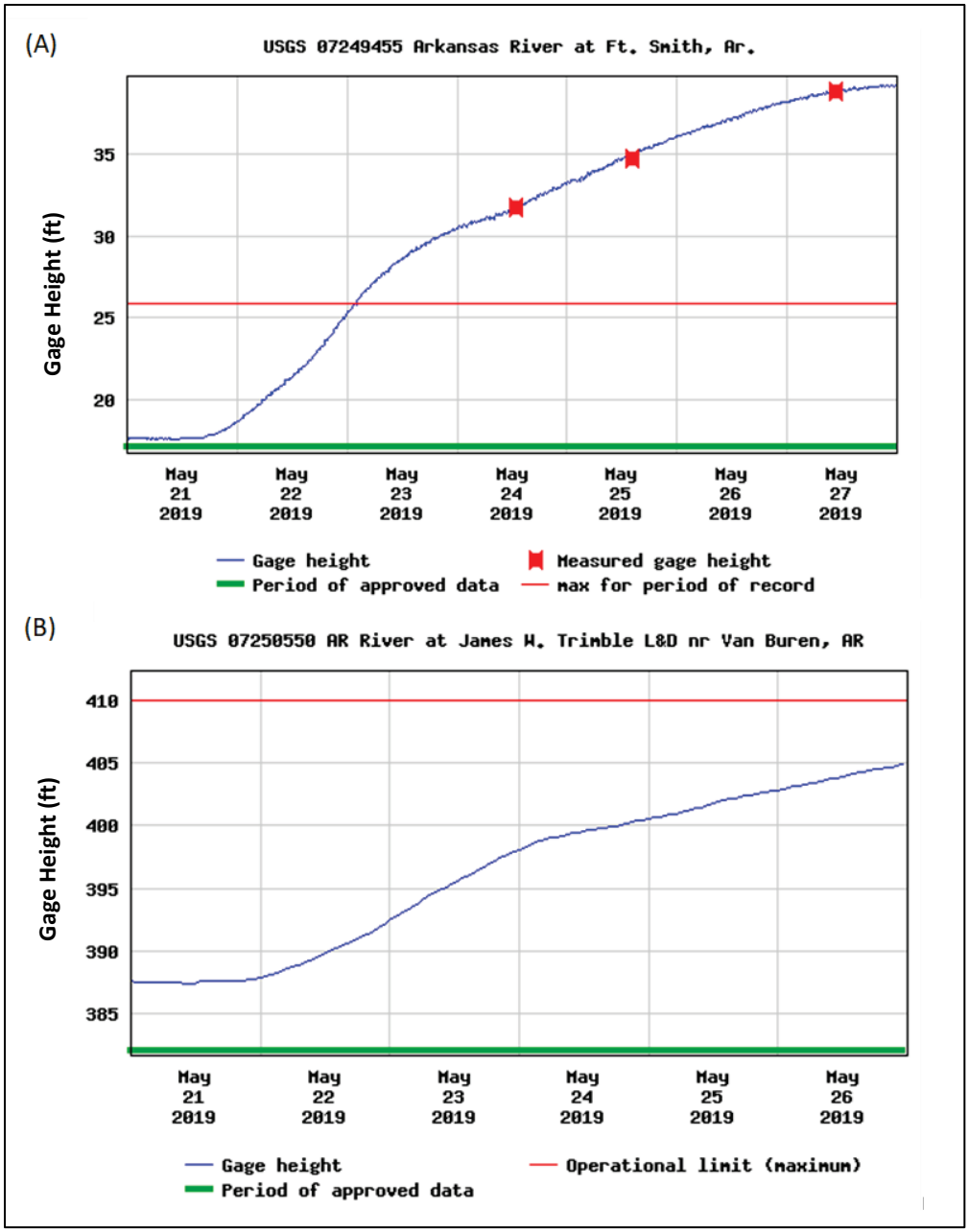

Figure A-52. (*A*) Stages upstream and (*B*) stages downstream from McAlpine Lock and Dam on the Ohio River between 16 and 26 February 2011.

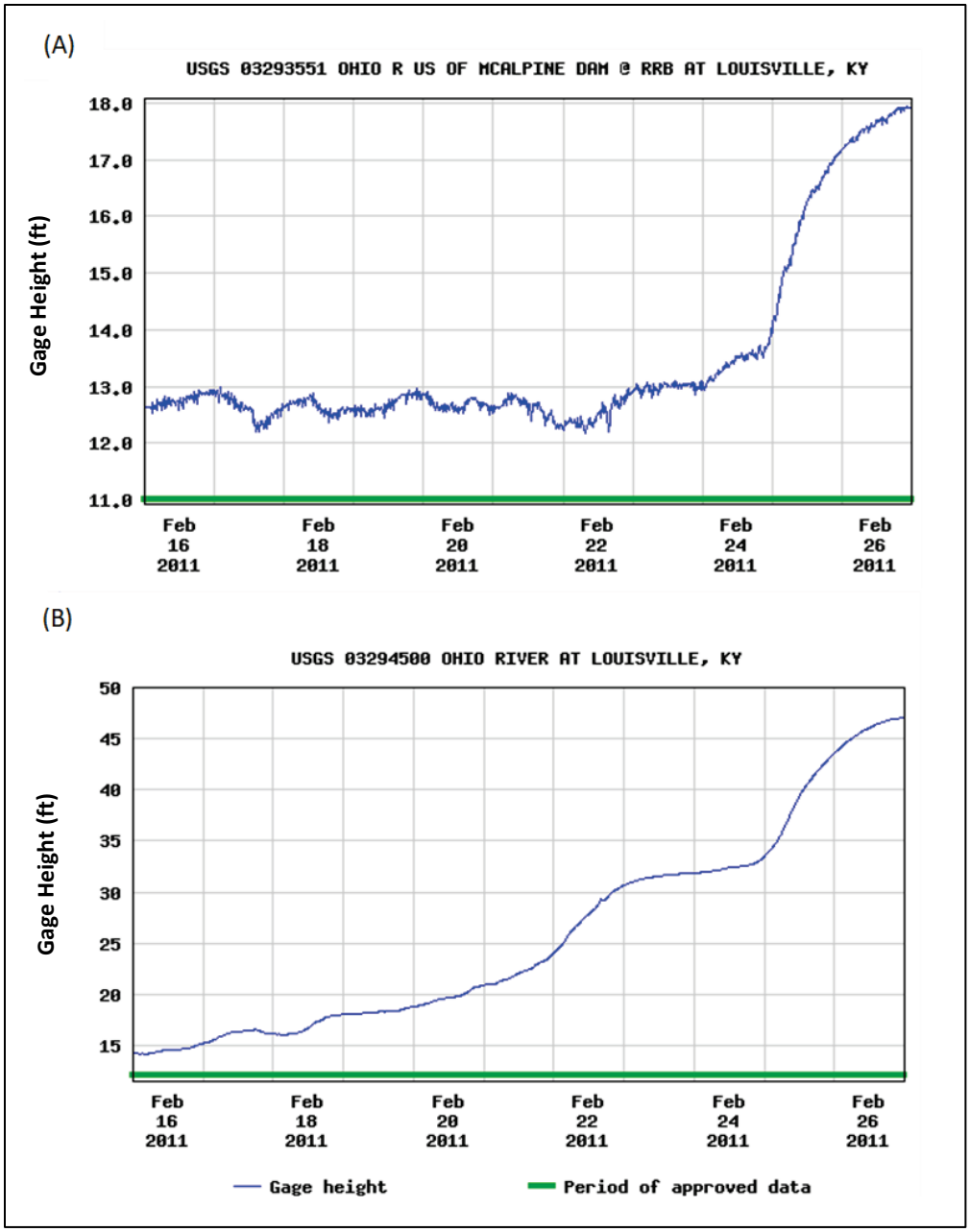

A.5.3 Statistical Analysis of Hydrodynamic Loads for MPLD with Tailwater Lower than the Gate Opening

The analysis of the dispersion of the MPLD STG with the tailwater lower than the gate opening was not performed because this condition does not occur at this project. Appendix B contains the procedures used to demonstrate this analysis for the McNary Lock and Dam (MLD) spillway vertical-lift gate.

Appendix B: Example Hydraulic Load Computations for the McNary Lock and Dam (MLD) Vertical-Lift Gate

In this appendix, the procedures discussed in Chapter 3 of the main report are presented using data from an existing USACE Navigation project. The data needed to quantify the hydraulic loads for the spillway vertical-lift gate and example computations are described.

B.1 A 30 yr Record of Hydrologic Data for MLD for Forebay Statistics

The MLD project on the Columbia River was chosen to illustrate how to determine the hydraulic loads on the spillway vertical-lift gate. USACE, Walla Walla District (USACE-NWW), provided a 30 yr record of hydraulic data from October 1989 to May 2020. The data included forebay el, TW El, discharge, and gate settings for the spillway. The pertinent project-specific data for the analysis are listed here:

- Spillway crest el = 291
- Normal upper pool el operating range = 335–340
- Estimated approach el = 234–252, avg = 246
- Total no. of gates = 22
- Spillway gate width = 50 ft
- Spillway gate height = 51 ft
- Spillway gate top el when gate is closed = 342

Figure B-1 shows a cross-section view of the McNary spillway and vertical-lift gate, and Figure B-2 shows a section of the spillway looking upstream.

Figure B-1. McNary Lock and Dam (MLD) spillway vertical-lift gate. (Image reproduced from US Army Corps of Engineers, Walla Walla District [USACE-NWW], files.)

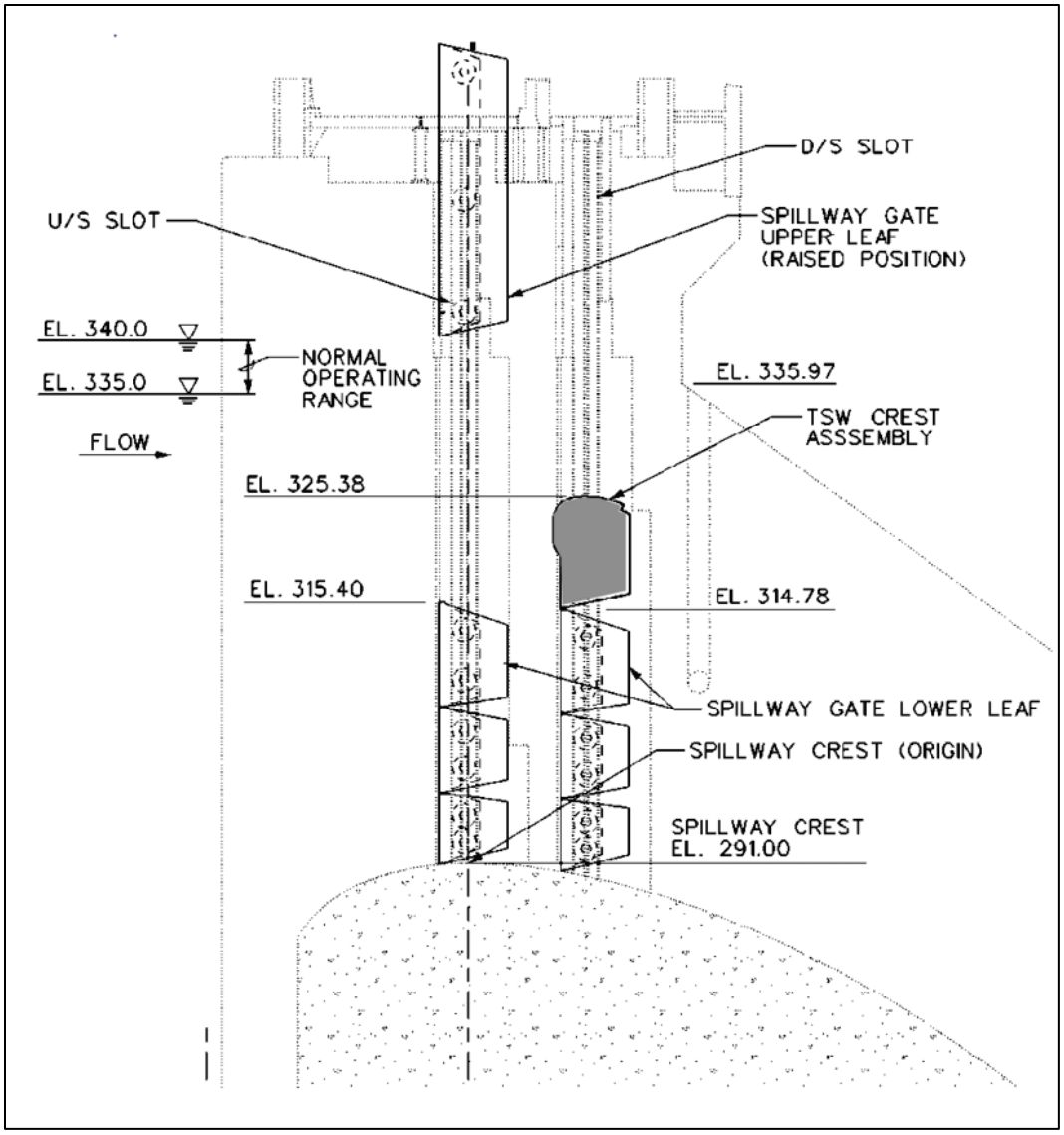

Figure B-2. Looking upstream at McNary spillway vertical-lift gates.

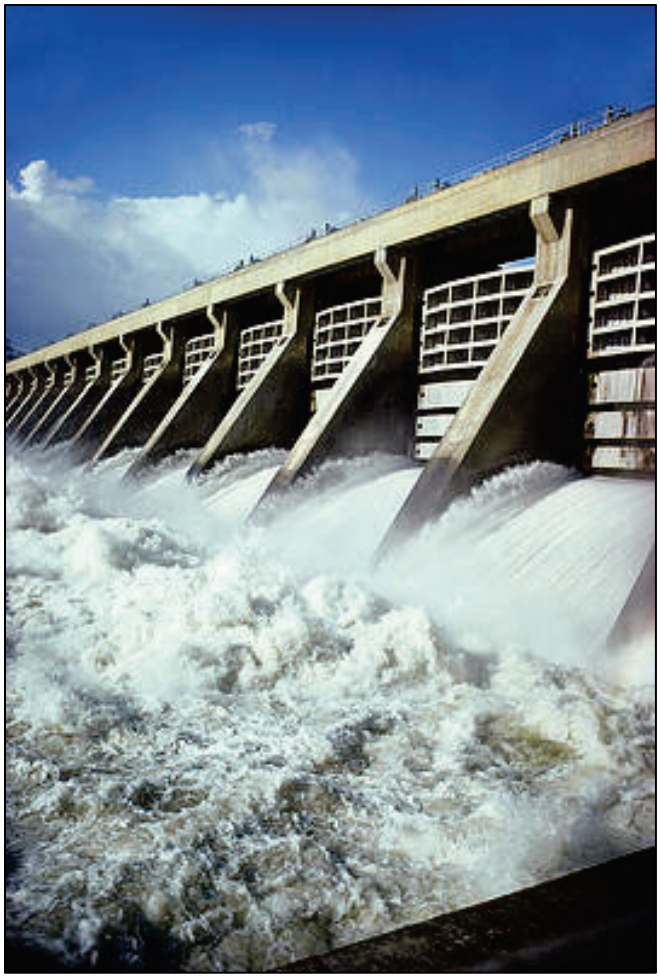

The upper pool el, also referred to as the forebay el, is the primary variable affecting the load on the vertical-lift gate for most inland navigation projects that do not have tailwater effects. Figure B-3 shows a histogram of the forebay el over the 30 yr period. The mean forebay el was 338.79, the maximum el was 340.5, and the minimum el was 334.99. The standard deviation was 0.57 ft. The histogram shown in Figure B-3 represents the number of occurrences of forebay in the selected range.

There are 23 bins in the histogram, each with a bin width of 0.25 ft. The area of each bin was computed, and the total area was determined by summing the individual bin areas. These areas were normalized by dividing each individual area by the total area to give the PDF shown in Figure B-4. A CDF was developed by cumulatively summing the normalized areas of the PDF in (Figure B-5).

Figure B-3. Histogram of forebay el for MLD from 1989 through 2020.

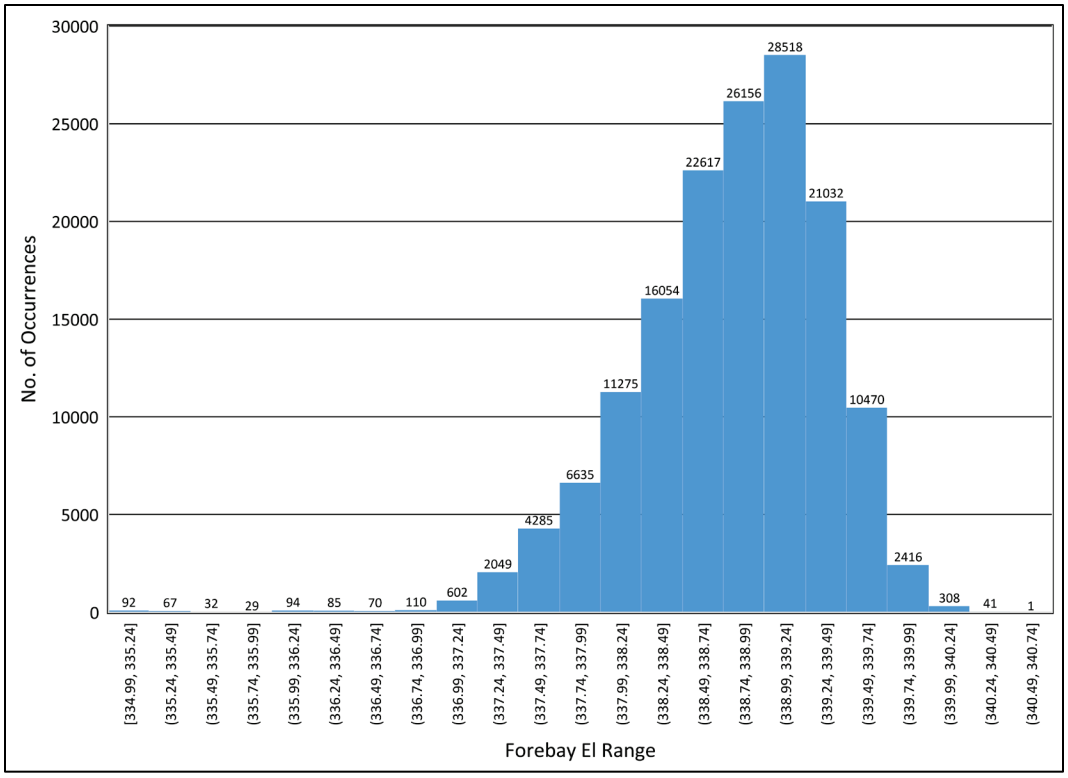

Figure B-4. PDF from histogram of forebay el for MLD.

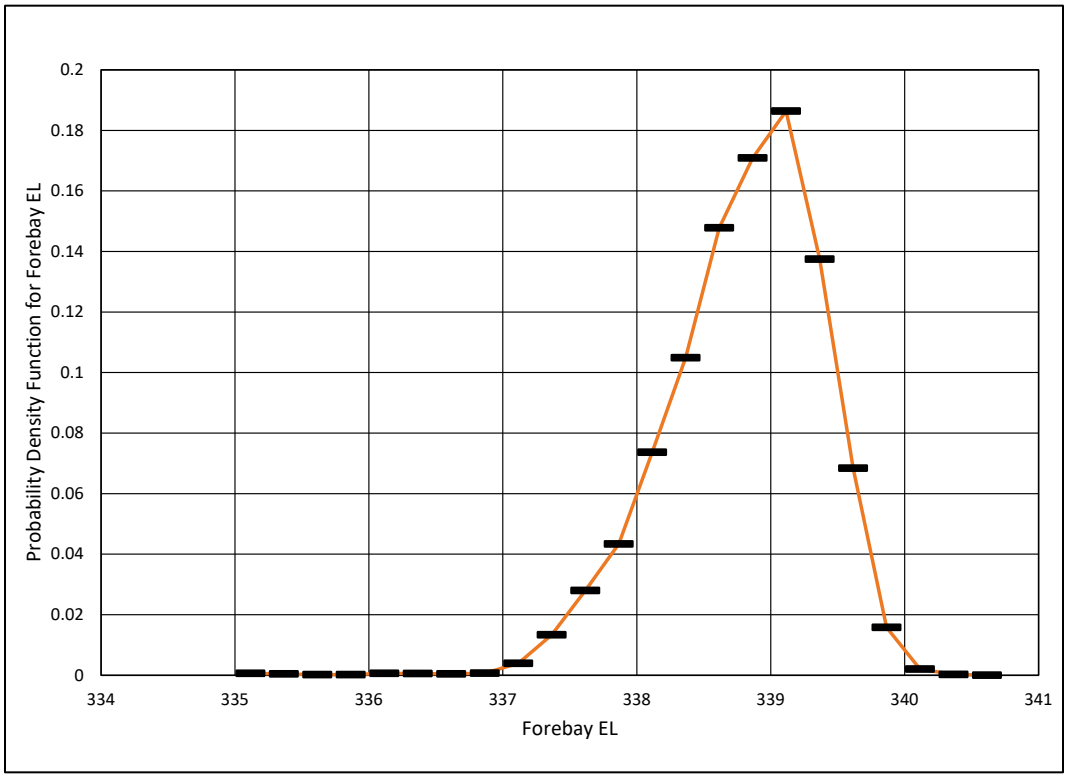

Figure B-5. CDF of forebay el for MLD.

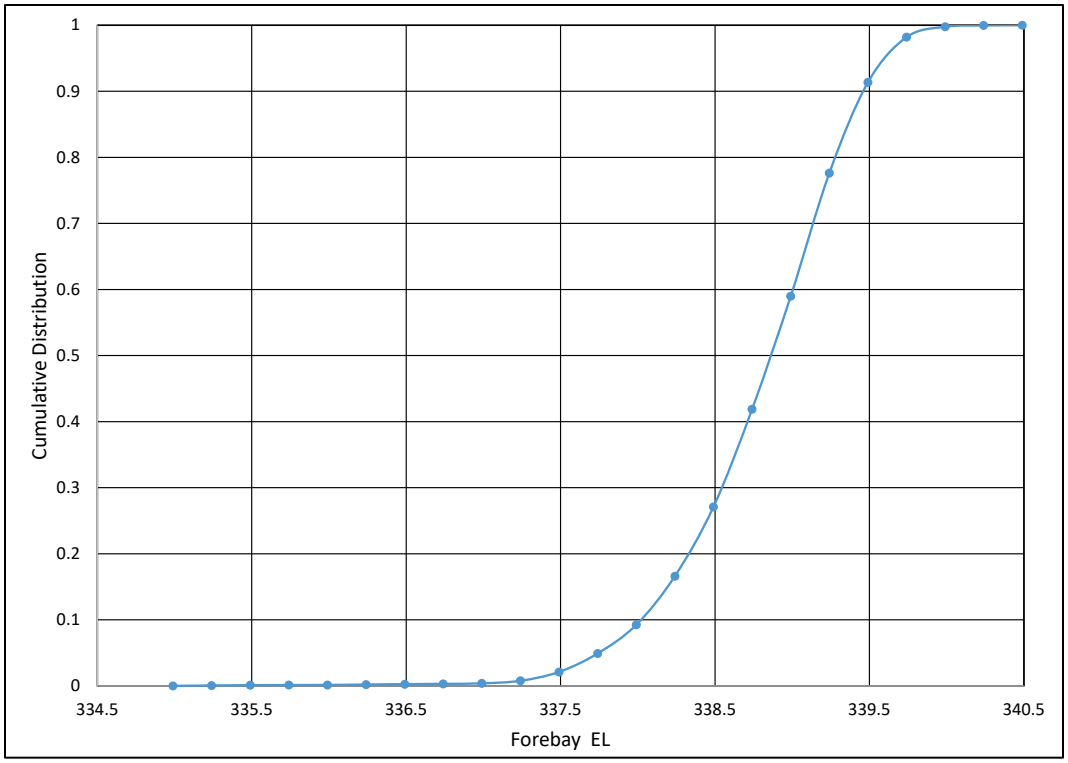

B.2 Hydrostatic Load for MLD without Tailwater Effect

Equation (10), which is repeated here, is a conventional equation found in many fluid mechanics and hydraulics textbooks and is used to compute the hydrostatic pressure (p). As previously stated, γ is the unit weight of water, and y is the vertical distance from the water surface to the location of the hydrostatic pressure of interest (Figure 15):

$$p = \gamma y.$$

The horizontal hydrostatic pressure on a closed gate is expressed as γH, where γ is the unit weight of water, and H is the total head on the gate. When the gate is closed, H represents the difference between the upper pool el and the spillway crest el when the tailwater is lower than the crest el. Equation (11), which is repeated here, can be used to compute the maximum hydrostatic pressure:

$$p_{max} = \gamma H.$$

The hydrostatic pressure acting along the vertical imaginary plane in Figure 15 is integrated over depth to obtain the resultant horizontal

hydrostatic force, H_s. H_s is the resultant force computed from the triangular pressure distribution acting on the gate area. In most cases, a unit gate width is used to compute the gate area, resulting in Equation (12), which is repeated here and is the hydrostatic force per unit width of the gate. The location of the horizontal resultant force is $H/3$ above the spillway crest when H is the head on the gate (Figure 15):

$$H_s = \frac{1}{2}\gamma H^2,$$

where

γ = the unit weight of water = 62.4 lb/ft^3,
H = the average head on the gate = 338.79 – 291 = 47.79 ft, and
Mean hydrostatic load = 0.5 [62.4 lb/ft^3 * (47.79 ft)^2] = 71,257 lb/ft.

The maximum hydrostatic load is experienced if the upper pool is at the top of the tainter gate with the gate in the closed position and no tailwater effect. H would then be 51.0 ft, and the hydrostatic load would be 81,151 lb/ft. This load condition represents H_1 (i.e., the maximum net hydrostatic load that will ever occur), which is one of the three hydrostatic loads that are to be considered.

B.3 Wave Load Based on Wave Height and Period for MLD

The dispersion due to wave load about the mean hydrostatic and hydrodynamic loads needs to be determined. The wave load is a primary load that contributes to load fluctuations. The procedures and methods used to determine wave load for the STG, which were presented in Chapter 2 and Appendix A, were used for the vertical-lift gate. The supporting data and computations used to determine the load for the McNary project are presented in the sections that follow. As mentioned, developing a wave load requires determining the wind speed, wind direction, and fetch.

B.3.1 Wind Speed and Fetch for MLD

The wind speed and wind direction data were obtained from meteorological data collected over a 20 yr period between 1999 and 2020 at the Hermiston Municipal (HM) airport in Oregon. The HM airport is located approximately 8 mi south of the project. Figure B-6 shows the data collection site in relation to the project.

Figure B-6. Satellite imagery of the wind speed and direction data collection site for MLD. (Map data: Google Earth 2013.)

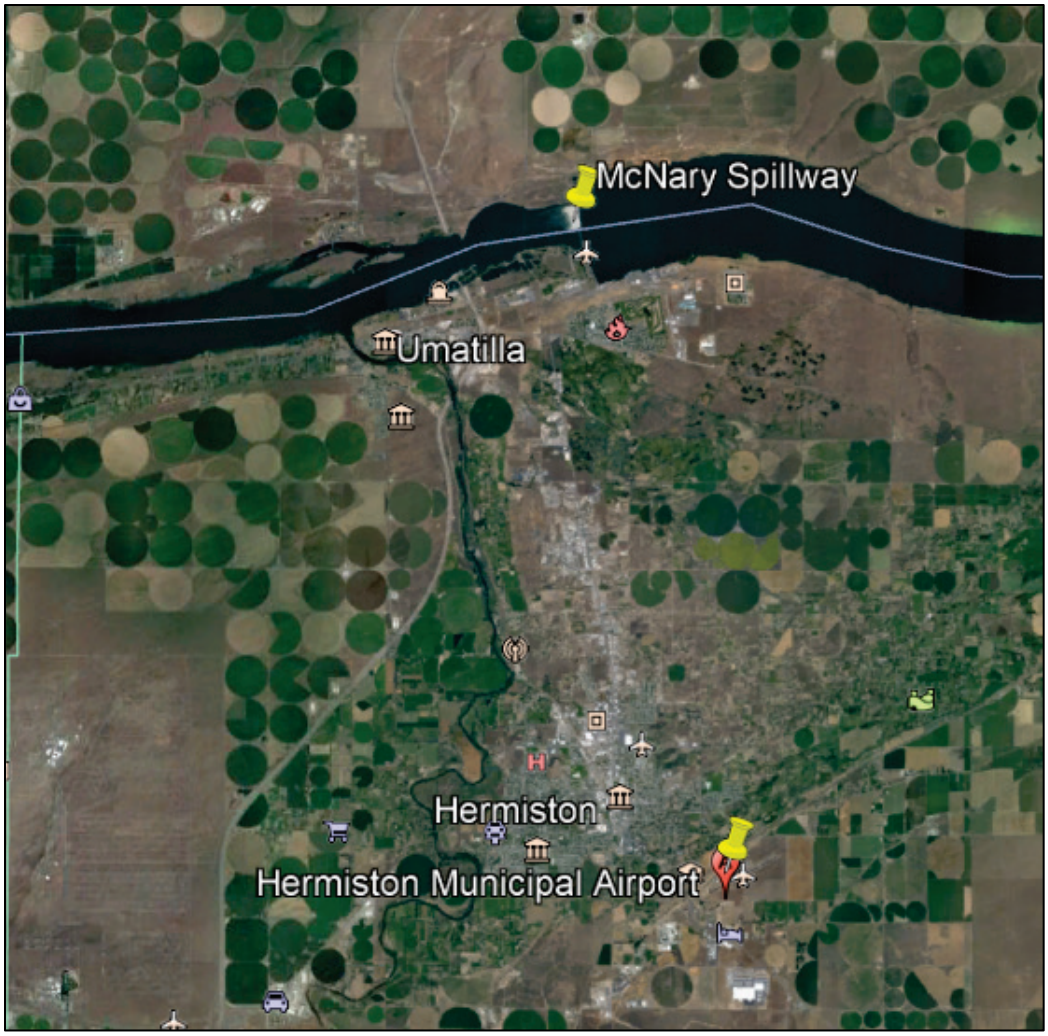

The dataset was fairly complete for the period from 1999 to May 2020, with wind speeds and directions reported hourly. The latitude of the airport is 45.8258, and the longitude is –119.261. The data were obtained from Iowa State University (n.d.).

Figure B-7 shows the fetch determined for the MLD project. The wind direction that impacts the project perpendicular to the spillway axis is 82°. The fetch is approximately 3 mi.

Figure B-7. Fetch and wind direction determined for the McNary project.

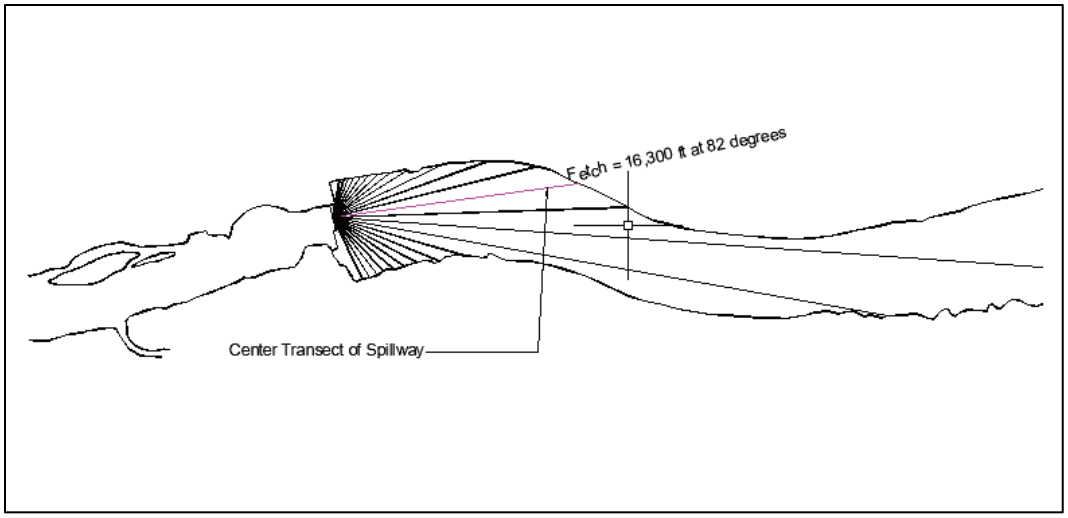

B.3.2 Wind Speed Analyses for MLD

The methods for determining the appropriate wind speed for the analyses of the wave load developed for the STG were also used for the spillway vertical-lift gate. Based on the fetch length and wind speed, Equation (50) can be used to determine the time required for full wave growth. Using an estimated wind speed between 30 and 40 mph and a fetch length of 3 mi, the minimum time to reach full wave growth was just under 1 hr. The wind speed data were then used to determine the maximum 1 hr average wind speed with a wind direction between 60° and 100° per year. Table B-1 shows the wind speed values used in the analyses.

Table B-1. Maximum yearly 1 hr average wind speed for wind directions between 60° and 100° at the HM airport for the 1999 to 2020 observation period.

Year	Max 1 hr Avg Wind Speed (mph)
1999	16.1
2000	15.0
2001	23.0
2002	18.4
2003	14.8
2004	16.7
2005	17.3
2006	20.0
2007	11.9
2008	16.1
2009	20.1

Table B-1 (cont.). Maximum yearly 1 hr average wind speed for wind directions between 60° and 100° at the HM airport for the 1999 to 2020 observation period.

Year	Max 1 hr Avg Wind Speed (mph)
2010	17.3
2011	15.5
2012	32.2
2013	17.3
2014	16.1
2015	23.0
2016	17.3
2017	21.9
2018	17.3
2019	20.1
2020	18.4

B.3.3 Extreme Value Estimation Using Maximum 1 hr Average Yearly Values of Wind Speed for MLD

The type 1 Gumbel distribution was used for a GEV analysis. This analysis is typically used to evaluate extreme, low probability meteorological and hydrological events. The probability of nonexceedance and wind speed are plotted, and a linear regression can be used to estimate values for extreme return periods.

Figure B-8 shows the results from extreme value estimation using the maximum 1 hr average annual values for the HM airport data. The 100 yr recurrence interval wind speed from this analysis was 35.7 mph. The magnitude of the 100 yr recurrence interval for wind speed was considered a suitable frequency for wave height calculations.

Figure B-8. Extreme wind speed estimation for Hermiston Municipal (HM) airport based on maximum 1 hr average annual values of wind speed.

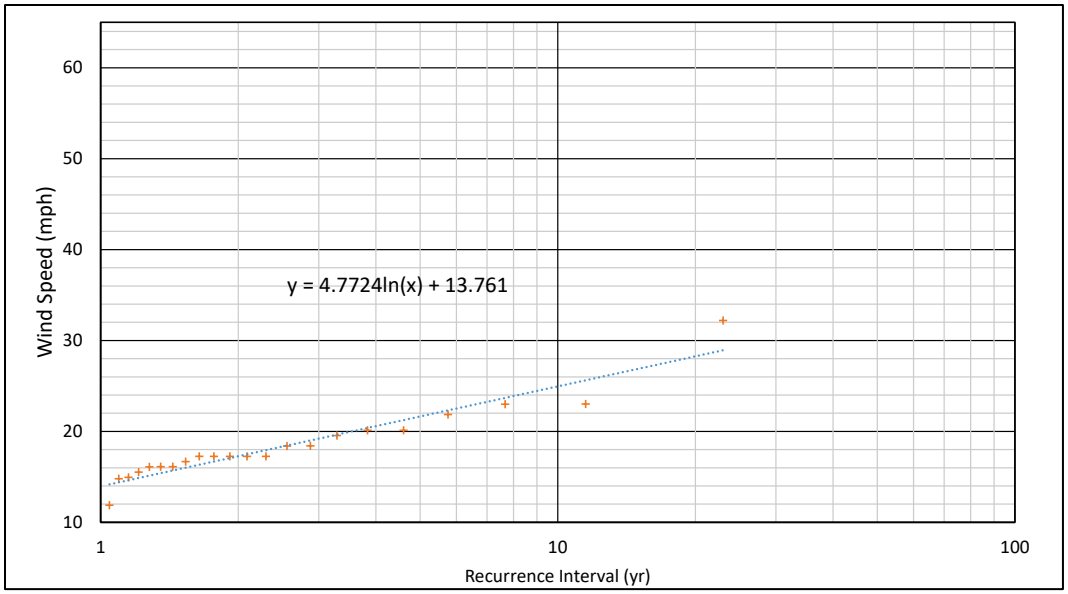

B.3.4 Wind Frequency Based on Gumbel Type 1 Distribution with Gringorten's Method Using Maximum Yearly Values of Wind Speed for MLD

The type 1 Gumbel distribution can be used with Gringorten's (1963) plotting position formula to create another method for evaluating wind speed. A description of this procedure is given in Chapter 2. Figure B-9 shows a plot of the return period versus wind speed determined using this procedure for the data from the HM airport. The wind speed for the 100 yr return period was 31.3 mph. Table B-2 contains the results from the wind speed analysis for MLD.

Table B-2. Results from the wind speed analysis for MLD.

Statistic	100 yr Wind Speed (mph)
+3σ	35.9
+2σ	34.7
+1σ	33.4
Mean	32.2
−1σ	31.0
−2σ	29.7
−3σ	28.5

Figure B-9. Wind frequency from Gumbel type 1 distribution with Gringorten's method for the HM airport using the maximum 1 hr average annual wind speed.

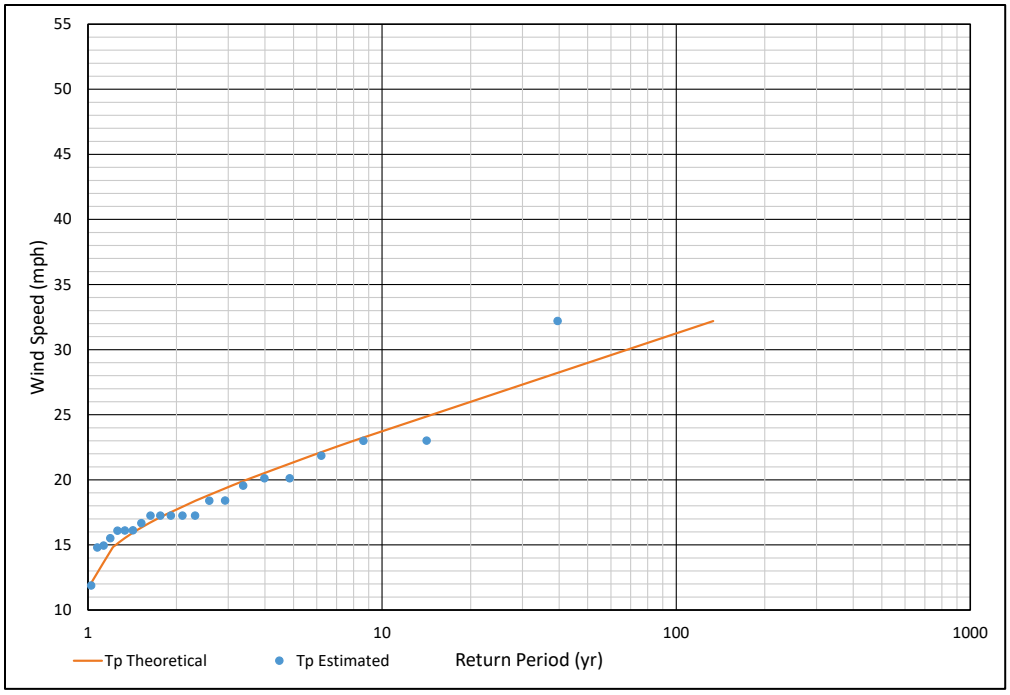

To further investigate the statistics for the wind speed, a formula to determine the standard error (Appendix A) was used for the data presented in Figure B-9. The standard error or standard deviation is defined as

$$\text{std} = \sqrt{\frac{\sum[U_i - U_{new}]^2}{n - 1}},$$

where

U_i = the wind speed (U) value for the T_p estimated point,
U_{new} = the new value determined from a log-linear interpolation (further explanation below), and
n = the number of samples.

The T_p estimated points are the blue points shown in Figure B-9. Each T_p estimated point has a T_p theoretical point with the same value of wind speed associated with it. These points are not shown in Figure B-9, but they will be discussed and are shown in Figure B-10. The interpolation procedure is explained in Appendix A.

The standard error is also referred to as the standard deviation about the fit curve. The standard deviation (σ) provides a way of describing how well

the sample points align with a curve fitted to the data. In the case of the Gumbel type 1 distribution curve (T_p theoretical), this standard deviation provides an estimate of the changes in the wind speed from the fitted curve or a way to bound the values of wind speed.

Figure B-10 shows the fitted curve bounded by plus and minus 1, 2, and 3 standard deviations (σ) for the HM airport wind data (n = 22). The standard deviation was determined to be 1.238 mph. The mean 100 yr return period wind speed was 32.2 mph. The use of the 100 yr return period plus 3 standard deviations gives a wind speed of 35.9 mph.

Figure B-10. Wind frequency curves based on peak yearly 1 hr average wind speed for the HM airport data.

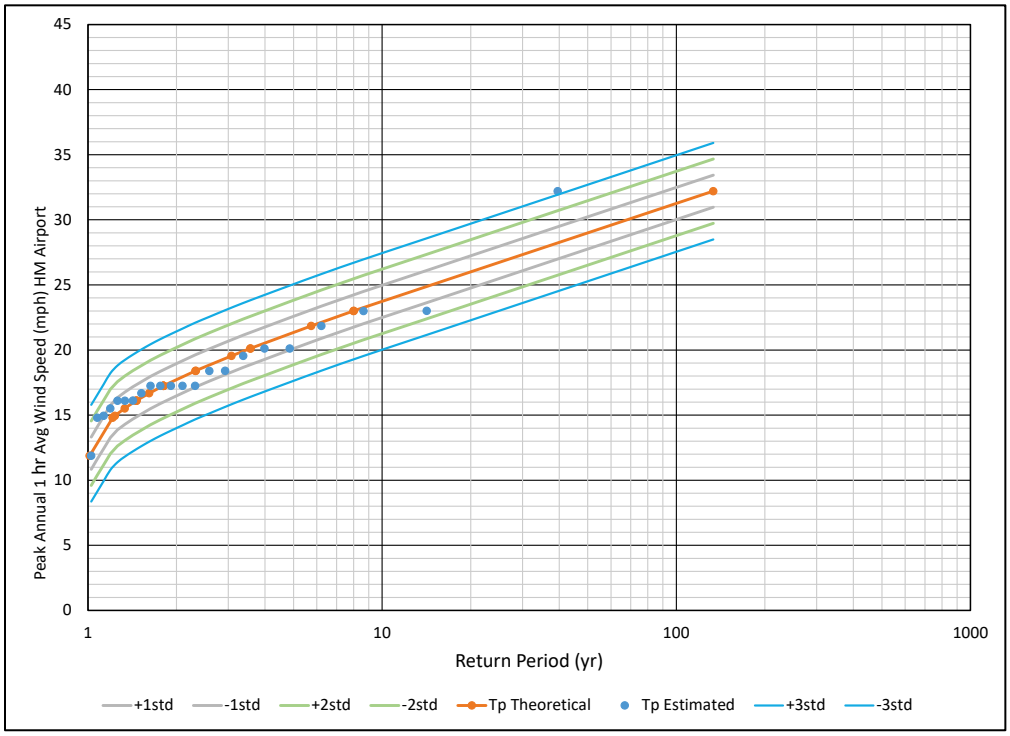

B.3.5 Wave Height and Period from NARFET Model

Table B-3 shows the input data and results from the use of the NARFET program for the MLD project. The program input requires the radial lengths of the fetch and the angle increments for resolution of the wind direction (Figure B-7). Figure B-7 shows the radial lengths (a total of 25) determined for an angle increment of 6°. Figure B-11 shows the significant wave height and period for the wind speeds determined between −3σ and +3σ for the 100 yr return period. The wind direction was between 60° and 100° for a duration of 1 hr.

Table B-3. Wave height, period, and wavelength computed using the NARFET model for the McNary project.

Wind Speed (mph)	Wind Direction (deg)	Wind Duration (hr)	Angle Increment (deg)	Wave Height (m)	Wave Period (sec)	Wave Length (m)
35.91	60–100	1	6	1.23	3.86	23.3
34.68	60–100	1	6	1.19	3.81	22.6
33.44	60–100	1	6	1.15	3.75	22.0
32.2	60–100	1	6	1.11	3.70	21.3
30.96	60–100	1	6	1.03	3.56	19.8
29.72	60–100	1	6	1.00	3.50	19.2
28.49	60–100	1	2	0.96	3.45	18.5

Figure B-11. Wind speed versus wave height from Smith's NARFET model for MLD.

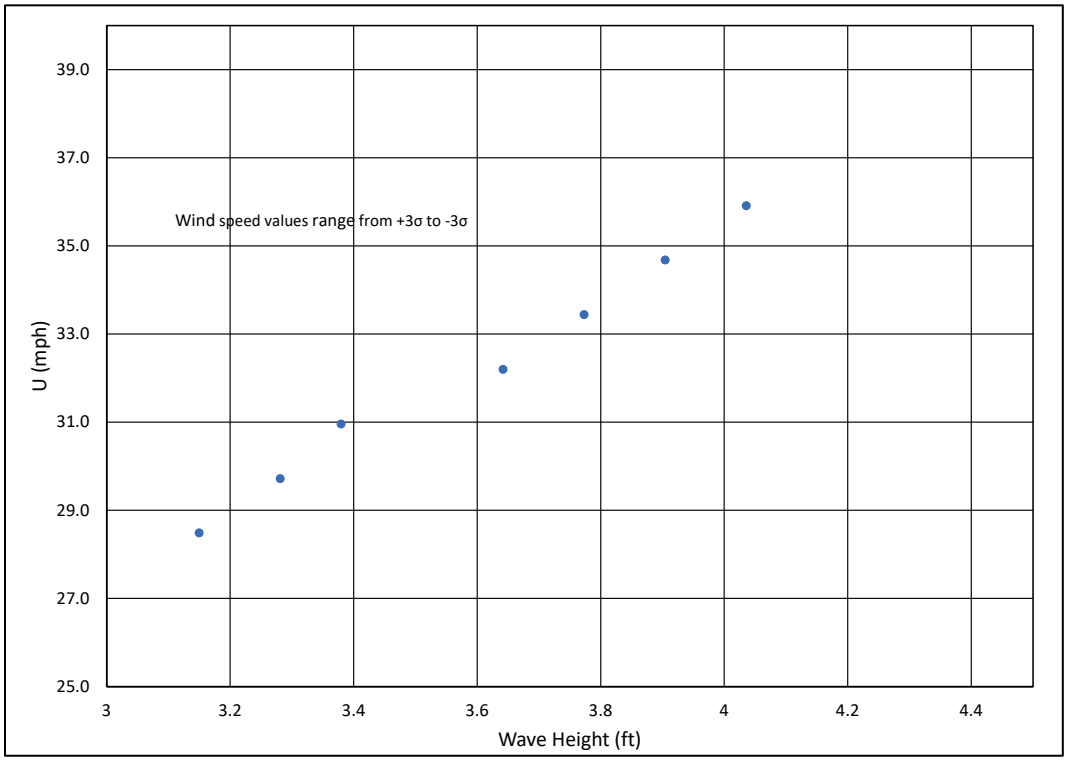

B.3.6 Wave Load from Goda for MLD

Goda (2010) also recommended formulations for determining significant wave height and period based on wind speed and fetch. Chapter 2 provides the background and supporting equations for his formulations. This methodology is considered applicable to the spillway vertical-lift gate. A plot of wind speed (U) versus wave height determined from Goda's recommended formulations from the statistical analysis of the wind speed data for the HM airport is listed in Table B-4 and shown graphically in Figure B-12.

Table B-4. Significant wave height, period, and wavelength from Goda's (2010) formulations for the McNary project.

Wind Speed (mph)	Minimum Duration, t_{min} (hr)	Significant Wave Height (m)	Significant Wave Period (sec)	Significant Wave Length (m)
35.91	0.86	0.887	2.944	13.54
34.68	0.87	0.863	2.914	13.26
33.44	0.88	0.838	2.881	12.96
32.20	0.90	0.814	2.848	12.67
30.96	0.91	0.789	2.813	12.36
29.72	0.92	0.763	2.779	12.05
28.49	0.93	0.738	2.742	11.74

Figure B-12. Wind speed versus significant wave height from Goda's (2010) procedure for the McNary project.

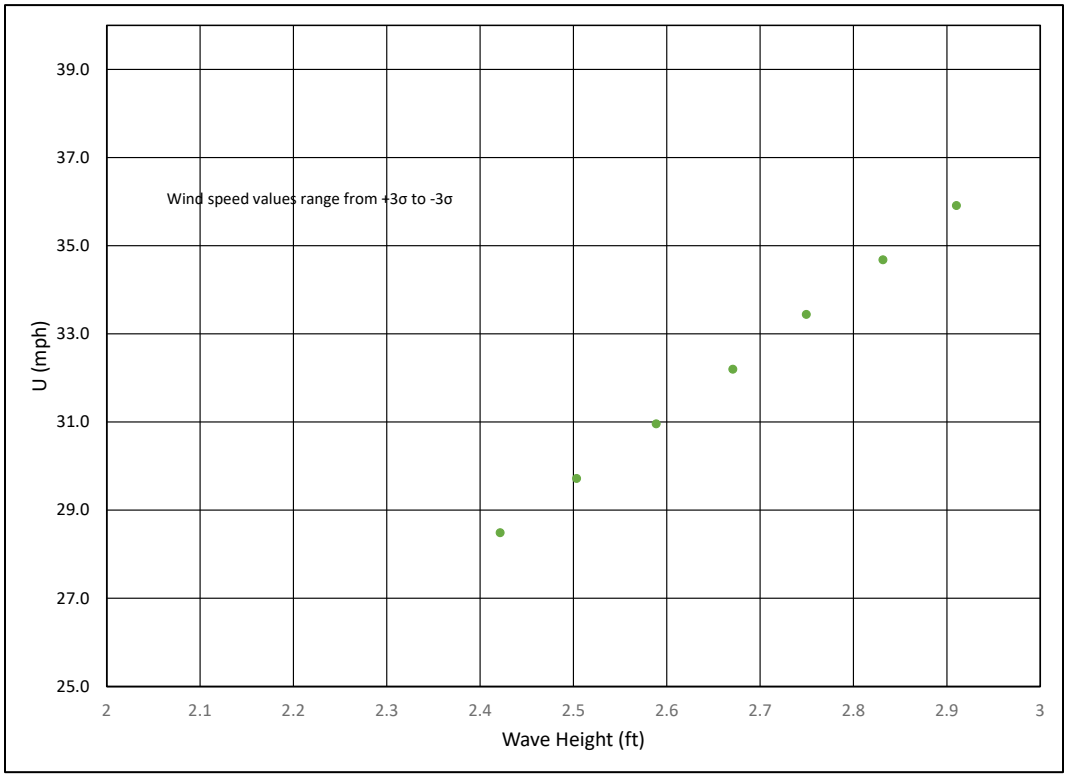

The wave pressure distribution and subsequent wave force for the spillway vertical-lift gate can now be determined from the significant wave height and wave period. Chapter 2 and Section 2.3.2.3 contain the complete description of this procedure. Based on the parameters listed in Table B-4 and the Goda formulations in Section 2.3.2.3, an example solution was reached. Table B-5 lists the parameters used in the example wave force calculation (imperial and metric units included).

Table B-5. Parameters used in example wave force calculation (imperial and metric units included) for McNary project for a wind speed of 33.7 mph.

Parameter	Value (Imperial Units)	Value (Metric Units)	Description
h_c	3.20 ft	0.98 m	Gate height above upper pool el
d (originally d_{SWL}, also H in Figure A-29)	47.8 ft	14.57 m	Difference between upper pool el and spillway crest el
h (originally h_{SWL})	92.8 ft	28.28 m	Difference between upper pool el and approach channel invert el
tan θ	0	0	Bottom slope toward gate
β_D	0 deg	0 deg	Design incident wave angle
$H_{1/3}$	2.79 ft	0.85 m	Significant wave height for example problem
$T_{1/3}$	2.85 sec	2.85 sec	Significant wave period for example problem
L_D	41.6 ft	12.68 m	Design wave length for example problem
ρ	62.4 lb/ft^3	1,000 Kg/m^3	Density of freshwater
g	32.2 ft/sec^2	9.81 m/sec^2	Acceleration due to gravity
h'	47.8 ft	12.19 m	For the vertical-lift gate: $h' = H = d_{SWL}$

The design wave height (H_D) is the minimum of $\alpha_h H_{1/3}$ and H_b, where α_h ranges from 1.6 to 2.0. For the design of nearshore vertical structures, Goda (2010) suggests using a value of 1.8 for α_h:

$$H_d = H_{Max} = \min\{\alpha_h * H_{1/3}, H_b\},$$

$$H_b = 0.17 * L_D \left\{1 - \exp\left[-1.5\frac{\pi h_b}{L_D}\left(1 + 15 * \tan^{\frac{4}{3}}\theta\right)\right]\right\},$$

where

$$h_b = h + 5 * H_{1/3} * \tan\theta.$$

Therefore,

$$\alpha_h H_{1/3} = 1.8 * 0.85 \text{ m} = 1.53 \text{ m (5.02 ft)},$$

$$h_b = 28.28 \text{ m} + 5 * 0.85 \text{ m} * \tan(0) = 28.28 \text{ m (92.8 ft)},$$

$$H_b = 0.17 * 12.68 \text{ m}\left\{1 - \exp\left[-1.5\frac{\pi 28.28 \text{ m}}{12.68 \text{ m}}\left(1 + 15 * \tan^{\frac{4}{3}}(0)\right)\right]\right\}$$
$$= 2.16 \text{ m (7.07 ft)}.$$

So,

$$H_d = H_{Max} = \min\{1.53 \text{ m}, 2.16 \text{ m}\} = 1.53 \text{ m (5.02 ft)}.$$

Next, we calculate the coefficients of wave pressure (α_1, α_2, and α_3) given in the equations that follow:

$$\alpha_1 = 0.6 + \frac{1}{2}\left[\frac{\frac{4\pi h}{L_D}}{\sinh\left(\frac{4\pi h}{L_D}\right)}\right]^2,$$

$$\alpha_2 = \min\left[\frac{h_b - d}{3h_b}\left(\frac{H_D}{d}\right)^2, \frac{2d}{H_D}\right],$$

$$\alpha_3 = 1 - \frac{h'}{h}\left[1 - \frac{1}{\cosh\left(\frac{2\pi h}{L_D}\right)}\right].$$

The h and d values in the preceding equations are respectively equivalent to the h_{SWL} and d_{SWL} of Table B-4. Substituting the values gives

$$\alpha_1 = 0.60,$$

$$\alpha_2 = \min\left[\frac{28.28 \text{ m} - 14.57 \text{ m}}{3(28.28 \text{ m})}\left(\frac{1.53 \text{ m}}{14.57 \text{ m}}\right)^2, \frac{2(14.57) \text{ m}}{1.53 \text{ m}}\right] = \min[0.0018 \text{ m}, 19.05 \text{ m}]$$
$$= 0.0018 \text{ (from Equation 57)},$$

and because $h' = d_{SWL} = H$,

$$\alpha_3 = 0.485 \text{ (from Equation 58)}.$$

The lateral pressure components P_1 and P_3 (from Equations 52 and 54) are evaluated here:

$$P_1 = 0.5\,(1 + \cos\beta_D)\,(\alpha_1 + \alpha_2 * \cos^2\beta_D)\,\rho * g * H_D,$$

$$P_3 = \alpha_3 P_1.$$

The solutions to P_1 and P_3 are

$$P_1 = 9{,}032 \text{ N/m}^2 = 9.032 \text{ kN/m}^2 = 188.61 \text{ (lb/ft}^2\text{)},$$

$$P_3 = 4{,}379 \text{ N/m}^2 = 4.379 \text{ kN/m}^2 \text{ (91.43 lb/ft}^2\text{)}.$$

As shown in Section 2.3.2.3 and Figure B-13, the total lateral force per linear width (F_{Lat}) on the face of the vertical-lift gate is

$$F_{Lat} = 0.5(P_1 + P_3)H + 0.5(P_1 + P_4)h_c',$$

where

$$P_4 = P_1\left(1 - \frac{h_c}{\eta^*}\right), \text{if } \eta^* > h_c,$$

or

$$P_4 = 0, \text{ if } \eta^* \leq h_c,$$

$$\eta^* = 0.75(1 + \cos(\beta_D))H_D,$$

$$h_C' = \min\{\eta^*, h_C\}.$$

Therefore, the solution for the resultant force, F_{Lat}, from Figure B-12 is given as

$$h_c = 0.98 \text{ m } (3.20 \text{ ft}) \text{ (from Table B-5)},$$

$$\eta^* = 2.295 \text{ m } (7.53 \text{ ft}).$$

Because $\eta^* > h_c$,

$$P_4 = 6.395 \text{ kN/m}^2 \ (133.53 \text{ lb/ft}^2),$$

$$h_C' = \min\{2.295 \text{ m}, 0.98 \text{ m}\} = 0.98 \text{ m } (3.20 \text{ ft}),$$

$$F_{Lat} = 104.66 \text{ kN/m } (7{,}172 \text{ lb/ft}).$$

The preceding analysis indicates the total lateral wave force per linear width of the spillway vertical-lift gate for a sustained 33.7 mph wind is 7,172 lb/ft. The same analysis done for a 28.7 mph sustained wind showed the total lateral wave force to be 6,136 lb/ft.

In Figure B-13 and Figure B-14, the pressure terms P_1, P_3, and P_4 are shown acting on the vertical-lift gate. The location of the lateral equivalent force (h_{Lat}) can be determined using the one-third/one-sixth method

developed by Ebeling et al. (2018) and also presented in Chapter 2, Section 2.3.2.4, of this report. By applying this method for the lateral forces and summing moments about point 3, Equation (A-14) was developed:

$$h_{Lat} = \frac{(h_4 - h_1)\left(\frac{P_4}{3} + \frac{P_1}{6}\right)h_4 + (h_4 - h_1)\left(\frac{P_4}{6} + \frac{P_1}{3}\right)h_1 + (h_1 - h_3)\left(\frac{P_1}{3} + \frac{P_3}{6}\right)h_1}{F_{Lat}},$$

$$h_{Lat} = \frac{0.97\text{ m}\left(\frac{5.176\frac{\text{kN}}{\text{m}^2}}{3} + \frac{9.032\frac{\text{kN}}{\text{m}^2}}{6}\right)15.24\text{ m} + 0.97\text{ m}\left(\frac{5.176\frac{\text{kN}}{\text{m}^2}}{6} + \frac{9.032\frac{\text{kN}}{\text{m}^2}}{3}\right)14.57\text{ m}}{104.662\frac{kN}{m}}$$

$$+ \frac{14.57\text{ m}\left(\frac{9.032\frac{\text{kN}}{\text{m}^2}}{3} + \frac{4.379\frac{\text{kN}}{\text{m}^2}}{6}\right)14.57\text{ m}}{104.662\frac{\text{kN}}{\text{m}}}$$

$$h_{Lat} = 8.566\text{ m}.$$

Figure B-13. Goda wave pressure distribution adapted for vertical-lift gates.

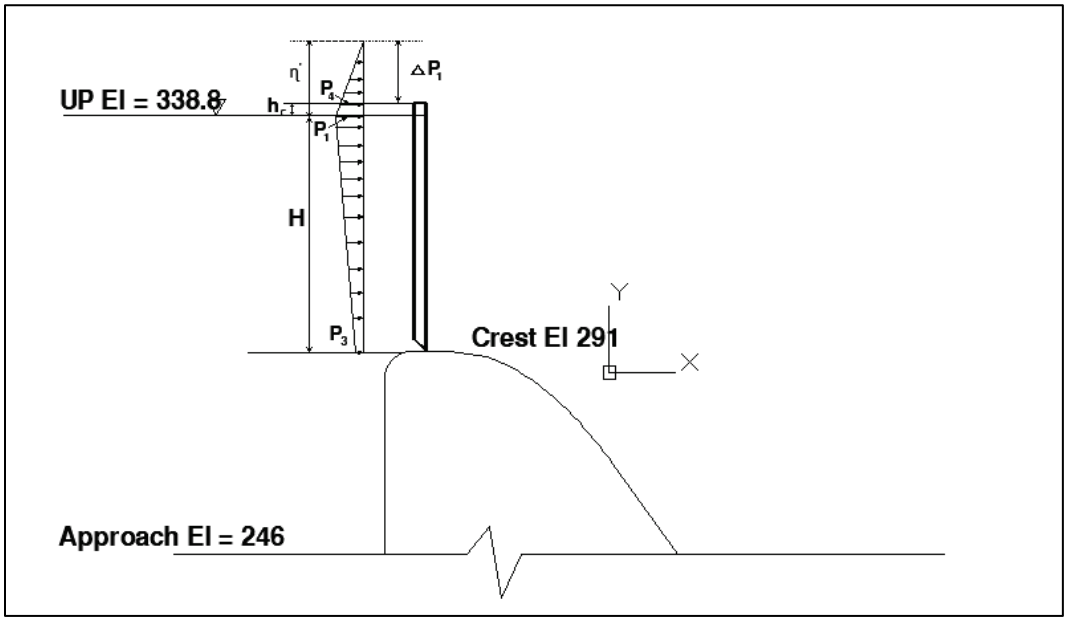

Figure B-14. Definition of wave pressure moment arm terms on a vertical-lift gate.

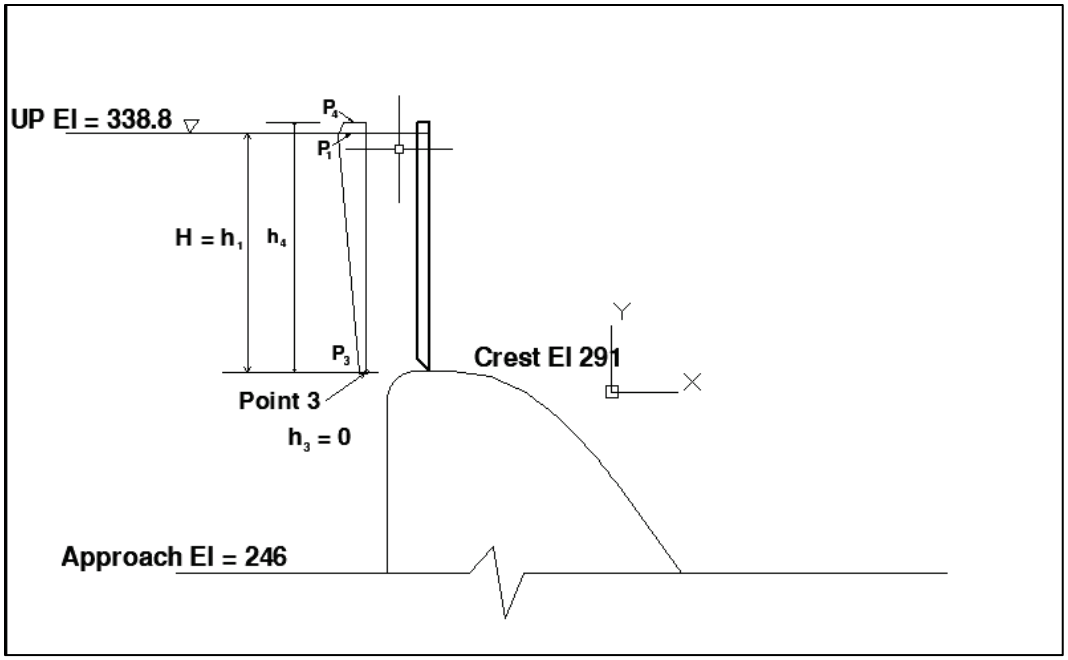

The wave forces and pressure distributions computed from Goda's (2010) procedure for the data in Table B-4 are shown in Table B-6. The definition of Goda's parameters found in Table B-5 and used in the preceding equations are illustrated in Figure B-13 and Figure B-14.

Table B-6. Wave force and pressure distribution computations using Goda's (2010) procedure for the McNary project.

McNary Data	Statistic						
	+3σ	+2σ	+1σ	Mean	−1σ	−2σ	−3σ
Wind speed (mph)	35.91	34.68	33.44	32.20	30.96	29.72	28.49
η^* (m)	2.395	2.330	2.263	2.198	2.130	2.060	1.993
P_1 (N/m²)	9,428	9,171	8,904	8,648	8,381	8,103	7,836
P_3 (N/m²)	4,571	4,446	4,317	4,192	4,063	3,928	3,799
P_4 (N/m²)	5,570	5,314	5,047	4,792	4,525	4,248	3,982
F_{Lat} (kN/m)	109.33	106.30	103.15	100.12	96.98	93.70	90.56
h_{Lat} (m)	8.571	8.568	8.565	8.561	8.557	8.553	8.549
h_{Lat} (ft)	28.12	28.11	28.10	28.09	28.08	28.06	28.05
P_1 (lb/ft²)	197	191	186	181	175	169	164
P_3 (lb/ft²)	95	93	90	88	85	82	79
P_4 (lb/ft²)	116	111	105	100	94	89	83
F_{Lat} (lb/ft)	7,491	7,284	7,068	6,861	6,645	6,421	6,205

B.4 Hydrodynamic Loads for MLD Spillway Vertical-Lift Gate

B.4.1 Average Hydrodynamic Load on Spillway Vertical-Lift Gates Using the Conservation of Momentum Procedure

An example of determining the pertinent hydraulic data to compute the hydrodynamic load for the vertical-lift gate at the McNary project will be discussed. The project data received from USACE-NWW were used to develop a relationship between gate opening and discharge. Spillway bay 10 was considered representative of the 22 gates and was selected for the analysis.

The 30 yr record of data included gate opening, discharge, and forebay el. Figure B-15 shows a plot of discharge versus gate opening using data for three different time periods with frequent gate operations. These time periods were March to July 2010, April to August 2012, and March to August 2014. The forebay el has a slight effect on the discharge versus gate opening, but when observed over a long enough time, this effect appeared to be minor. The mean forebay el for the entire 30 yr period was 338.8. As shown in Figure B-15, the mean for the three time periods selected was very close to 338.8. Because the data were essentially linear, an equation was developed and was considered applicable between gate openings between 1 and 15 ft. The relationship was not linear below a 1 ft gate opening.

The discharge computed from this equation can be used to determine the information needed to compute force on the gate from Equation (84). Because there was no tailwater effect at this project, h in Equation (84) was the gate opening. The average hydrodynamic load on the spillway vertical-lift gate was determined using Equation (82). Figure B-16 shows the plot of the hydrodynamic force on the gate per unit width versus the gate opening, and Table B-7 provides the values used in Figure B-16.

Figure B-15. Discharge versus gate opening for McNary spillway bay 10.

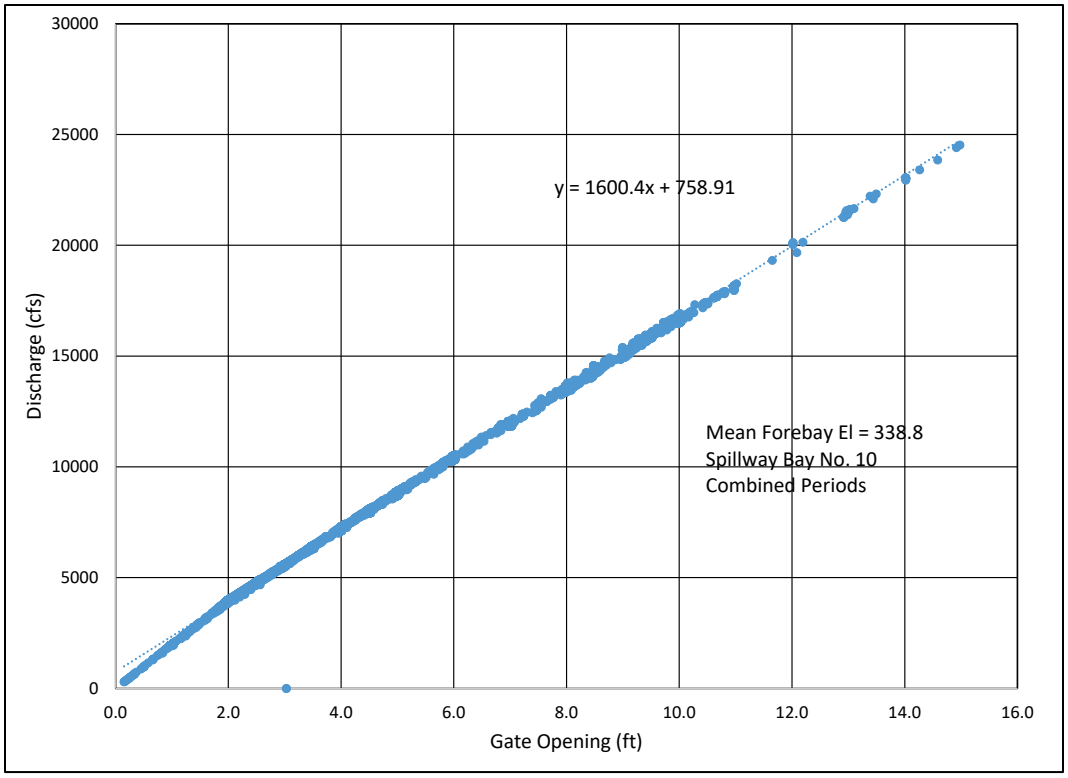

Figure B-16. Hydrodynamic force on gate versus gate opening for McNary spillway bay 10.

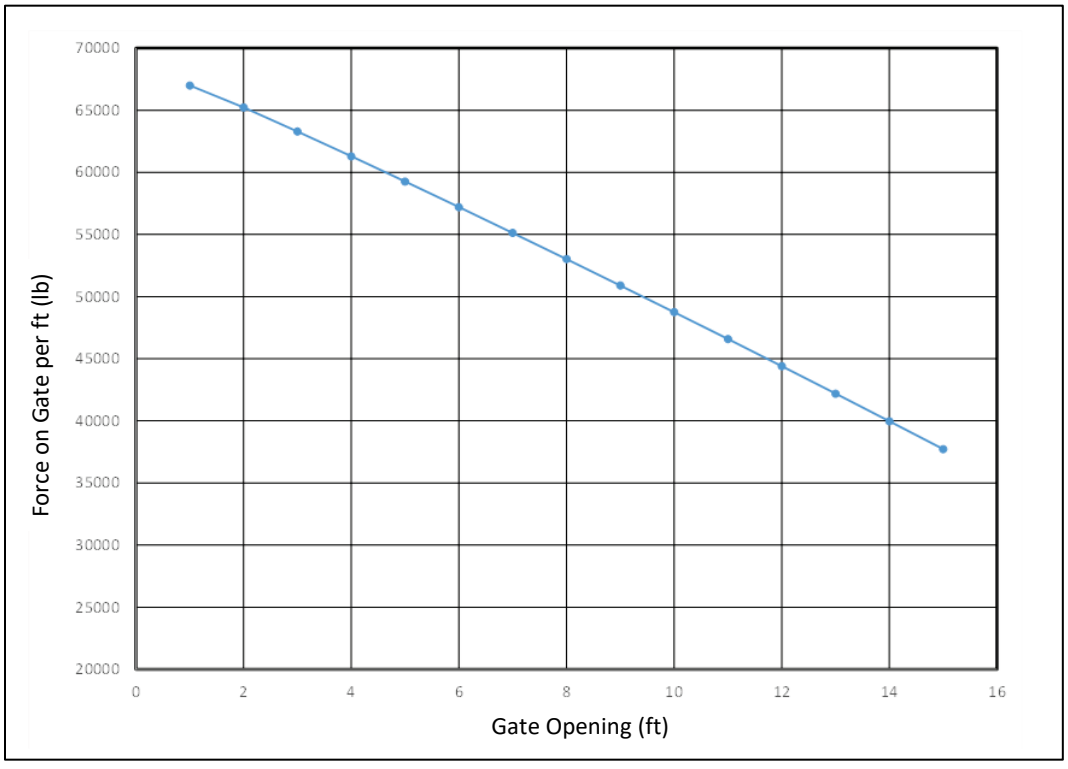

Table B-7. Hydrodynamic loads for gate openings from 1–15 ft using the conservation of momentum procedure.

Gate Opening (G_o) (ft)	Q (cfs)	V_1 (ft/sec)	h (ft)	ΔH (ft)	V_2 (ft/sec)	F_g (lb)	F_g (lb/ft)
1	2,359	0.51	1	46.8	47.2	3,349,584	66,992
2	3,960	0.85	2	45.8	39.6	3,261,101	65,222
3	5,560	1.20	3	44.8	37.1	3,164,202	63,284
4	7,160	1.54	4	43.8	35.8	3,064,462	61,289
5	8,761	1.89	5	42.8	35.0	2,962,996	59,260
6	10,361	2.23	6	41.8	34.5	2,860,175	57,204
7	11,962	2.58	7	40.8	34.2	2,756,160	55,123
8	13,562	2.92	8	39.8	33.9	2,651,029	53,021
9	15,163	3.27	9	38.8	33.7	2,544,827	50,897
10	16,763	3.61	10	37.8	33.5	2,437,580	48,753
11	18,363	3.96	11	36.8	33.4	2,329,306	46,856
12	19,964	4.30	12	35.8	33.3	2,220,015	44,400
13	21,564	4.65	13	34.8	33.2	2,109,715	42,194
14	23,165	4.99	14	33.8	33.1	1,998,414	39,968
15	24,765	5.34	15	32.8	33.0	1,886,111	37,722

B.4.2 Hydrodynamic Load on Spillway Vertical-Lift Gates Using Kim's (2007) Procedure

Another example of determining the hydrodynamic load for the vertical-lift gate at the McNary project is presented here using the Kim (2007) procedure described in Chapter 2, Section 2.3.2.3, for a spillway gate with tailwater less than the gate opening. This procedure uses a pseudo or static hydrodynamic pressure distribution on the gate to develop the magnitude and location of the resultant hydrodynamic force.

This example is presented for a 1 ft gate opening because this is the largest hydrodynamic force for a typical navigation project. Table B-8 provides the parameters needed for the analysis using the Kim (2007) procedure. The pressures for h_{pg} in Table B-8 and in Table B-10 through Table B-12 are shown in both feet of water and pounds per square foot.

Table B-8. Parameters used to compute hydrodynamic pressures from the Kim (2007) procedure for the MLD spillway vertical-lift gate with a 1 ft gate opening.

Z (ft)	Z	H_{pg}/H_{pgM}	H_{pg}	h_{pg} (ft)	h_{pg} (lb/ft^2)
1	0	0	0	0	0
2	0.021	0.865	0.7785	36.44	2,274
4	0.064	0.975	0.8775	41.07	2,563
6	0.107	0.995	0.8955	41.91	2,615
8	0.150	0.99	0.891	41.70	2,602
10	0.192	0.985	0.8865	41.49	2,589
12	0.235	0.965	0.8685	40.65	2,537
14	0.278	0.925	0.8325	38.96	2,431
16	0.320	0.892	0.8028	37.57	2,345
18	0.363	0.845	0.7605	35.59	2,221
20	0.406	0.805	0.7245	33.91	2,116
22	0.449	0.76	0.684	32.01	1,998
24	0.491	0.712	0.6408	29.99	1,872
26	0.534	0.655	0.5895	27.59	1,722
28	0.577	0.6	0.54	25.27	1,577
30	0.620	0.545	0.4905	22.96	1,433
32	0.662	0.49	0.441	20.64	1,288
34	0.705	0.43	0.387	18.11	1,130
36	0.748	0.37	0.333	15.59	973
38	0.791	0.313	0.2817	13.18	823
40	0.833	0.255	0.2295	10.74	670
42	0.876	0.19	0.171	8.00	499
44	0.919	0.125	0.1125	5.27	329
46	0.961	0.06	0.054	2.53	158
47.8	1.000	0	0	0	0

Note: a/E_1 = 0.029, H_{pgM} = 0.900, $E_1 - a$ = 46.8 ft

The value for H_{pgM} was obtained from the equation shown in Kim (2007, Figure 8) with a/E_1 = 0.029. The procedure for determining these parameters is described in Chapter 2, Section 2.3.2.3.

Figure B-17 shows a plot of the hydrodynamic pressure distribution on the gate with a 1 ft gate opening. The area under the pressure distribution curve, which is the resultant hydrodynamic force, was determined to be 77,377 lb/ft acting at a location 18.2461 ft above the crest el of 291.

Figure B-17. Hydrodynamic pressure distribution determined using Kim's (2007) procedure for the MLD spillway vertical-lift gate with 1 ft gate opening and normal upper pool el.

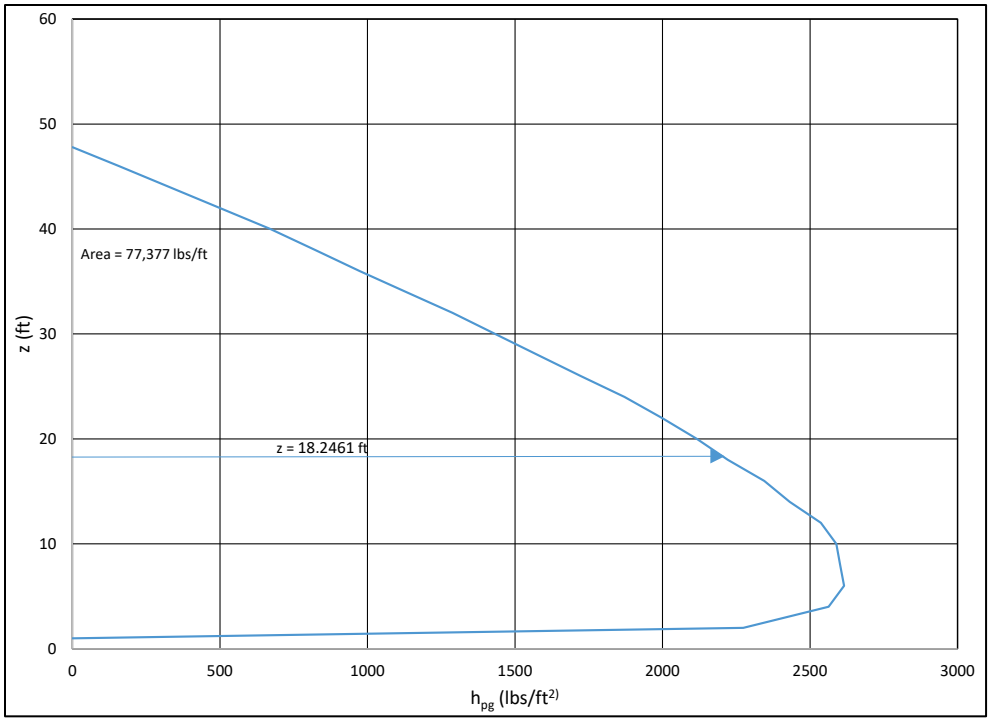

The conservation of momentum procedure resulted in a hydrodynamic force per foot of gate width of 66,992 lb/ft, compared to a value of 77,337 lb/ft using the Kim (2007) procedure. The Kim (2007) procedure is recommended when the tailwater is below the gate opening because it also allows the location of the resultant force to be determined.

B.5 Probabilistic Characterization of the Hydrostatic and Hydrodynamic Loads for the MLD Spillway Vertical-Lift Gate

B.5.1 Statistical Analysis of Hydrostatic Loads for the McNary Vertical-Lift Gate

As mentioned in Chapter 3, Section 3.4.1, an appropriate range for the upper pool at most navigation projects is considered to be +6σ and −6σ about the mean upper pool. The hydrostatic load on the vertical-lift gate depends on the upper pool el. The mean upper pool el at MLD was 338.79, with a standard deviation of 0.57 ft. The range of the upper pool el using +6σ and −6σ is 342.21 to 335.37. Table B-9 lists the values for the resultant hydrostatic force for the range of the upper pool els from +6σ to −6σ. Figure B-18 shows a plot of the resultant hydrostatic forces computed using this range of upper pool els and Equation (12).

Table B-9. Hydrostatic gate force per foot of gate run for the upper pool els +6σ and −6σ around the mean upper pool for the McNary vertical-lift gate.

Upper Pool El	Statistic	H_s (lb/ft)
335.37	−6σ	61,423
335.94	−5σ	63,012
336.51	−4σ	64,620
337.08	−3σ	66,249
337.65	−2σ	67,898
338.22	−σ	69,568
338.79	Mean	71,257
339.36	+σ	72,967
339.93	+2σ	74,697
340.5	+3σ	76,448
341.07	+4σ	78,219
341.64	+5σ	80,010
342.21	+6σ	81,821

Figure B-18. Resultant hydrostatic force per foot of gate width for range of upper pool els for the MLD spillway vertical-lift gate.

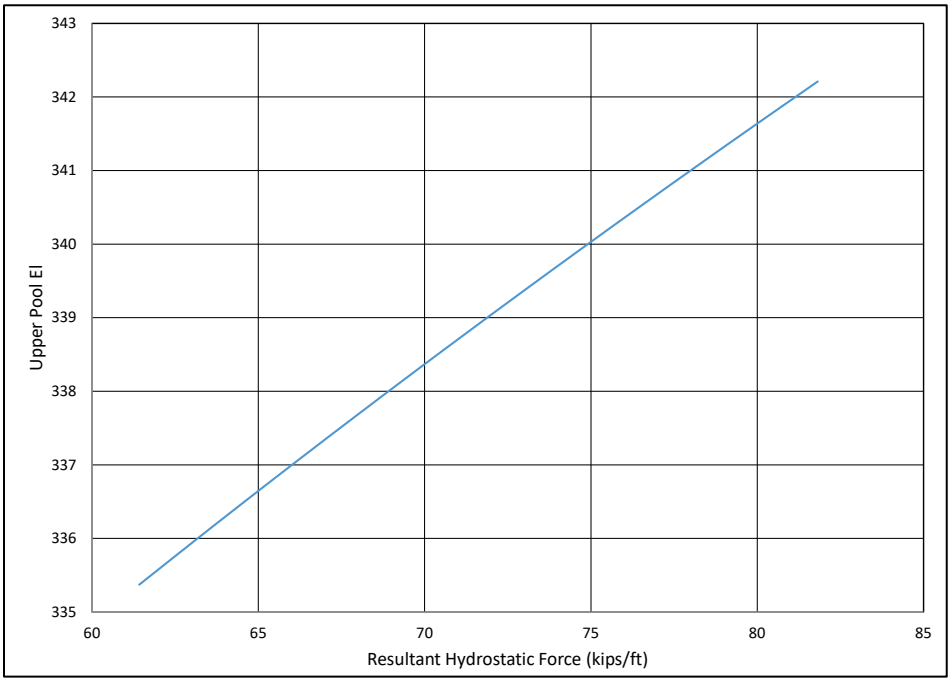

B.5.2 Statistical Analysis of Hydrodynamic Loads for the McNary Vertical-Lift Gate

As mentioned in Chapter 3, Section 3.4.1, an appropriate range for the upper pool at most navigation projects is +6σ and −6σ about the mean upper

pool. If the hydrodynamic force is computed for this range of upper pool els for the 1 ft gate opening, a range of these forces can be developed. Kim's (2007) procedure was used to compute the pressures (h_{pg}) for an upper pool el of 342.21 (i.e., +6σ) and a 1 ft gate opening (Table B-10) and the parameters determined for this analysis.

Table B-10. Parameters used to compute hydrodynamic pressures using the Kim (2007) procedure for the MLD spillway vertical-lift gate with a 1 ft gate opening and an upper pool el of 342.21.

z (ft)	Z	H_{pg}/H_{pgM}	H_{pg}	h_{pg} (ft)	h_{pg} (lb/ft²)
1	0	0	0	0	0
2	0.020	0.863	0.7767	39.00	2,433
4	0.060	0.967	0.8703	43.70	2,727
6	0.100	0.998	0.8982	45.10	2,814
8	0.139	1	0.9	45.19	2,820
10	0.179	0.992	0.8928	44.83	2,797
12	0.219	0.967	0.8703	43.70	2,727
14	0.259	0.939	0.8451	42.43	2,648
16	0.299	0.909	0.8181	41.08	2,563
18	0.339	0.872	0.7848	39.40	2,459
20	0.378	0.832	0.7488	37.60	2,346
22	0.418	0.791	0.7119	35.74	2,230
24	0.458	0.75	0.675	33.89	2,115
26	0.498	0.702	0.6318	31.72	1,979
28	0.538	0.65	0.585	29.37	1,833
30	0.578	0.599	0.5391	27.07	1,689
32	0.617	0.549	0.4941	24.81	1,548
34	0.657	0.498	0.4482	22.50	1,404
36	0.697	0.442	0.3978	19.97	1,246
38	0.737	0.386	0.3474	17.44	1,088
40	0.777	0.331	0.2979	14.96	933
42	0.817	0.275	0.2475	12.43	775
44	0.856	0.22	0.198	9.94	620
46	0.896	0.159	0.1431	7.19	448
48	0.936	0.098	0.0882	4.43	276
50	0.976	0.037	0.0333	1.67	104
51.21	1.000	0	0	0.00	0

Note: $a/E_1 = 0.0195$, $H_{pgM} = 0.900$, $E_1 - a = 50.21$ ft

Kim's (2007) procedure was also used to compute the pressures (h_{pg}) for an upper pool el of 335.37 (i.e., −6σ) and a 1 ft gate opening (Table B-11) and the parameters determined for this analysis.

Table B-11. Parameters used to compute hydrodynamic pressures using the Kim (2007) procedure for the MLD spillway vertical-lift gate with a 1 ft gate opening and an upper pool el of 335.37.

z (ft)	Z	H_{pg}/H_{pgM}	H_{pg}	h_{pg} (ft)	h_{pg} (lb/ft^2)
1	0	0	0	0	0
2	0.023	0.875	0.786625	34.12	2,129
4	0.069	0.978	0.879222	38.13	2,379
6	0.115	1	0.899	38.99	2,433
8	0.161	1	0.899	38.99	2,433
10	0.208	0.974	0.875626	37.98	2,370
12	0.254	0.942	0.846858	36.73	2,292
14	0.300	0.908	0.816292	35.40	2,209
16	0.346	0.865	0.777635	33.73	2,105
18	0.392	0.818	0.735382	31.89	1,990
20	0.438	0.771	0.693129	30.06	1,876
22	0.484	0.72	0.64728	28.07	1,752
24	0.530	0.661	0.594239	25.77	1,608
26	0.576	0.601	0.540299	23.43	1,462
28	0.623	0.541	0.486359	21.09	1,316
30	0.669	0.48	0.43152	18.72	1,168
32	0.715	0.417	0.374883	16.26	1,015
34	0.761	0.353	0.317347	13.76	859
36	0.807	0.289	0.259811	11.27	703
38	0.853	0.225	0.202275	8.77	547
40	0.899	0.154	0.138446	6.00	375
42	0.945	0.084	0.075516	3.28	204
44	0.991	0.014	0.012586	0.55	34
44.37	1.000	0	0	0.00	0

Note: a/E_1 = 0.023, H_{pgM} = 0.899, $E_1 - a$ = 43.37 ft

Kim's (2007) procedure was also used to compute the pressures (h_{pg}) for an upper pool el of 338.79 (i.e., the mean) and a 1 ft gate opening (Table B-12) and the parameters determined for this analysis.

Table B-12. Parameters used to compute hydrodynamic pressures using the Kim (2007) procedure for the MLD spillway vertical-lift gate with a 1 ft gate opening and an upper pool el of 338.79.

z (ft)	Z	H_{pg}/H_{pgM}	H_{pg}	h_{pg} (ft)	h_{pg} (lb/ft^2)
1	0	0.000	0	0	0
2	0.021	0.865	0.7785	36.43	2,273
4	0.064	0.975	0.8775	41.06	2,562
6	0.107	0.995	0.8955	41.90	2,615
8	0.150	0.990	0.891	41.69	2,601
10	0.192	0.985	0.8865	41.48	2,588
12	0.235	0.965	0.8685	40.64	2,536
14	0.278	0.925	0.8325	38.95	2,431
16	0.321	0.892	0.8028	37.56	2,344
18	0.363	0.845	0.7605	35.58	2,220
20	0.406	0.805	0.7245	33.90	2,115
22	0.449	0.760	0.684	32.00	1,997
24	0.492	0.712	0.6408	29.98	1,871
26	0.534	0.655	0.5895	27.58	1,721
28	0.577	0.600	0.54	25.27	1,577
30	0.620	0.545	0.4905	22.95	1,432
32	0.663	0.490	0.441	20.63	1,288
34	0.705	0.430	0.387	18.11	1,130
36	0.748	0.370	0.333	15.58	972
38	0.791	0.313	0.2817	13.18	822
40	0.834	0.255	0.2295	10.74	670
42	0.876	0.190	0.171	8.00	499
44	0.919	0.125	0.1125	5.26	328
46	0.962	0.060	0.054	2.53	158
47.80	1.000	0.000	0	0.00	0

Note: $a/E_1 = 0.021$, $H_{pgM} = 0.900$, $E_1 - a = 46.79$ ft

Figure B-19 shows a plot of the hydrodynamic pressure distribution determined for the mean and the +6σ and −6σ upper pool els listed in Table B-10 through Table B-12.

The hydrodynamic force is equal to the area under the pressure distribution curve, and the location of the horizontal resultant force acts at the centroid of the area and is noted as z in Figure B-19. This procedure indicates the hydrodynamic forces for the mean, +6σ, and −6σ upper pool els are 76,377 lb/ft, 87,986 lb/ft, and 65,426 lb/ft, respectively. The location

of the horizontal resultant forces for the mean, +6σ, and −6σ upper pool els are 18.2461 ft, 19.4681 ft, and 16.9876 ft above the spillway crest.

Figure B-19. Magnitude and location of resultant hydrodynamic force for +6σ, mean, and −6σ upper pool els for the McNary vertical-lift gate with a 1 ft gate opening.

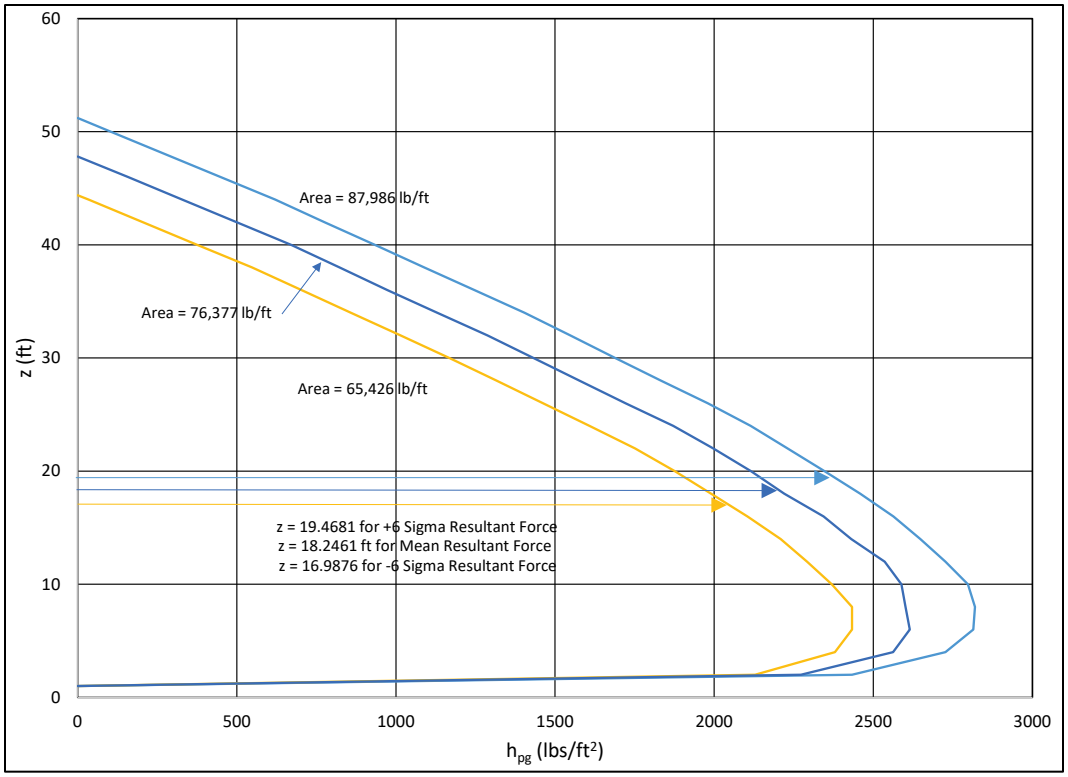

B.6 Summary of Hydraulic Loads for MLD

The hydraulic loads on the spillway consist primarily of the hydrostatic, wave, and hydrodynamic loads. Table B-13 lists the example hydraulic loads determined for the McNary project for a mean upper pool.

Table B-13. Example hydraulic loads for the McNary spillway vertical-lift gate.

Estimated Hydraulic Load	Value (kips/ft)
Hydrostatic (no tailwater effect)	Max = 81.15 (71.26 with mean forebay el)
Hydrodynamic	COM = 66.99, Kim (2007) = 76.4*
Wave**	7.49
Hydrostatic + Wave	78.75
Hydrodynamic + Wave	74.48

* Based on a mean forebay el of 338.8, discharge of 2,360 cfs, and 1.0 ft gate opening.

** Based on a mean forebay el and 35.91 mph wind speed at 81° (100 yr wind event + 3σ). P_1/P_3 = 2.06.

Some of the loads should be combined to give the maximum loads expected for the gate. Table B-13 shows these combined loads. The wave force results in the table indicate that wind-induced wave forces are significant and need to be included in spillway vertical-lift gate design force computations.

Appendix C: Example Hydraulic Load Computations for R. C. Byrd Locks and Dam (RCBLD) Spillway Roller Gate

In this appendix, the procedures discussed in Chapter 4 of the main report are presented using data from an existing USACE Navigation project. The data needed to quantify the hydraulic loads for the spillway roller gate and example computations are described.

C.1 Record for Hydrologic Data for RCBLD

The R. C. Byrd Locks and Dam (RCBLD) project on the Ohio River was chosen to illustrate how to determine the hydraulic loads on a spillway roller gate. USACE, Huntington District (USACE-LRH), provided a 27 yr record of hydraulic data from April 1993 through August 2020. The data included forebay el, TW El, and spillway discharge rating curves. The normal upper pool is el 538, and the normal lower pool is el 515. The project-specific data for the analysis are listed here:

- Spillway crest el = 508.5
- Normal upper pool el = 538.0
- Estimated approach el = 494
- Total no. of gates = 8
- Spillway gate width = 125.5 ft
- Spillway gate height = 29.5 ft
- Spillway gate top el when gate is closed = 538.0

A section view of the R. C. Byrd spillway and roller gate was shown in Figure 50 and is repeated here as Figure C-1.

Figure C-1. R. C. Byrd Lock and Dam (RCBLD) spillway section view. (Image reproduced from USACE, Huntington District [USACE-LRH] files.)

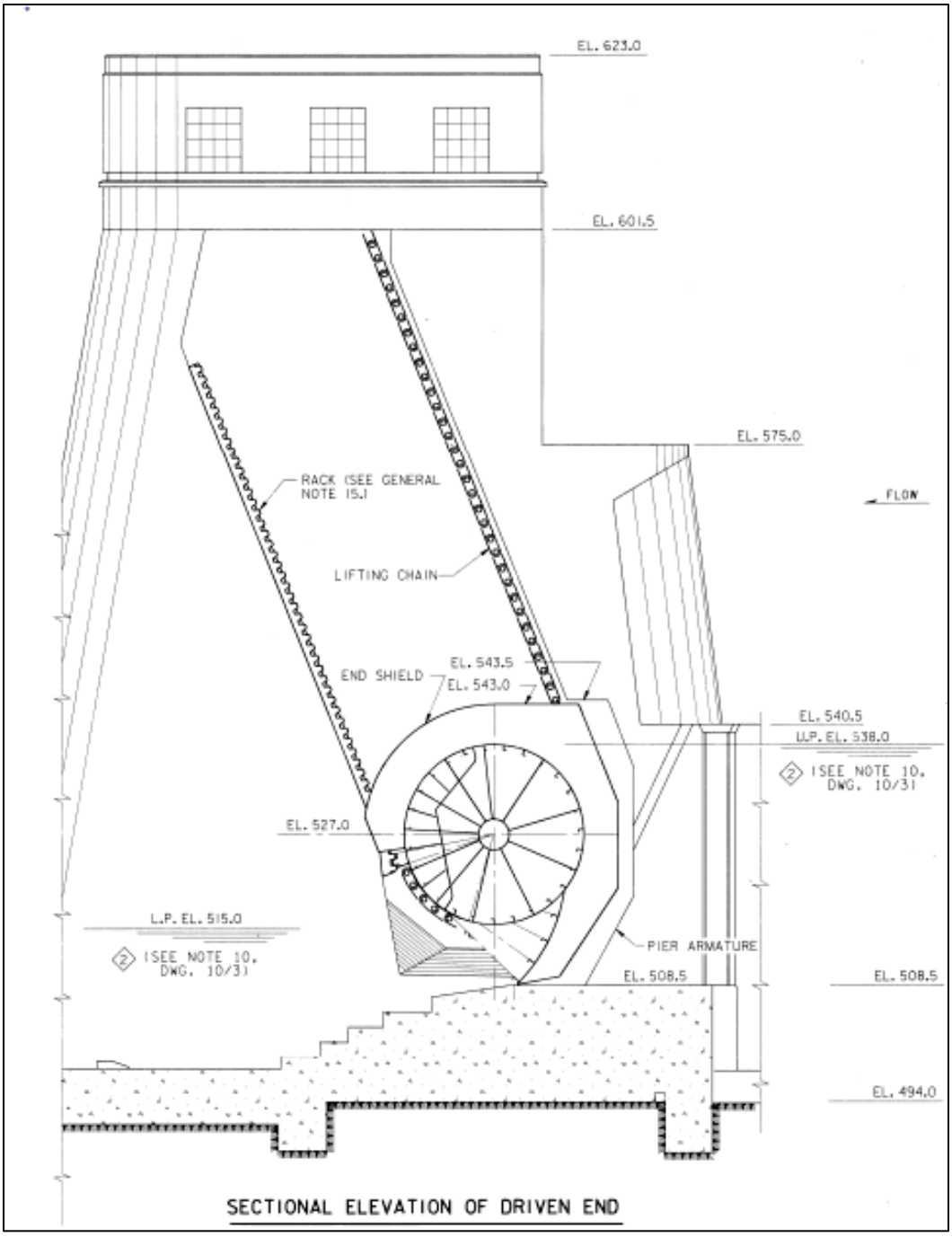

C.1.1 Upper Pool El Statistics for RCBLD

The upper pool el, also referred to as the *upper pool stage*, is one of the primary variables that affects the load on the spillway roller gate for most inland navigation projects. Figure C-2 shows a histogram of the upper pool stage el from 1999 to 2020. To convert upper stage readings to upper pool

el, el 526 is added to the upper stage reading. The mean upper pool el was 538.88, the maximum el was 556.9, and the minimum el was 526.0. The standard deviation was 1.72 ft. The histogram shown in Figure C-2 represents the number of occurrences of upper stage in the selected range.

The histogram contains 62 bins, each with a bin width of 0.50 ft. The area of each bin was computed, and the total area was determined by summing the individual bin areas. These areas were normalized by dividing each individual area by the total area to give the PDF shown in Figure C-3. A CDF, shown in Figure C-4, was developed by cumulatively summing the normalized areas of the PDF.

Figure C-2. Histogram of upper pool el from 1999 through 2020.

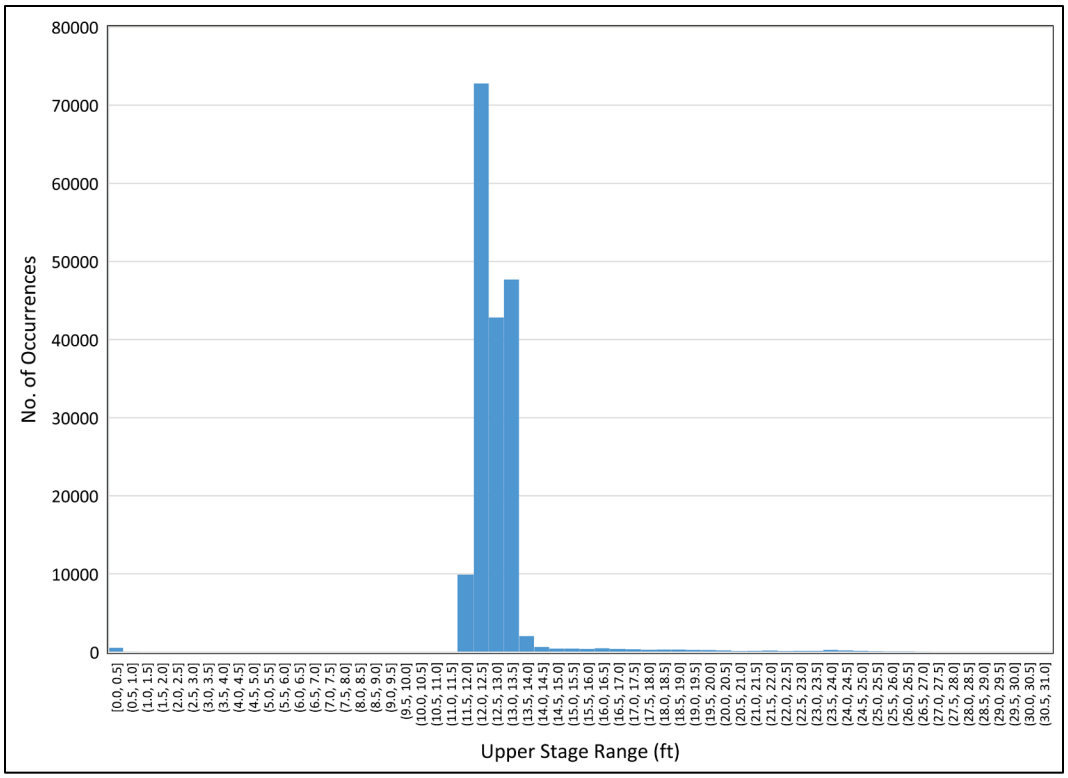

Figure C-3. PDF from histogram of upper pool el.

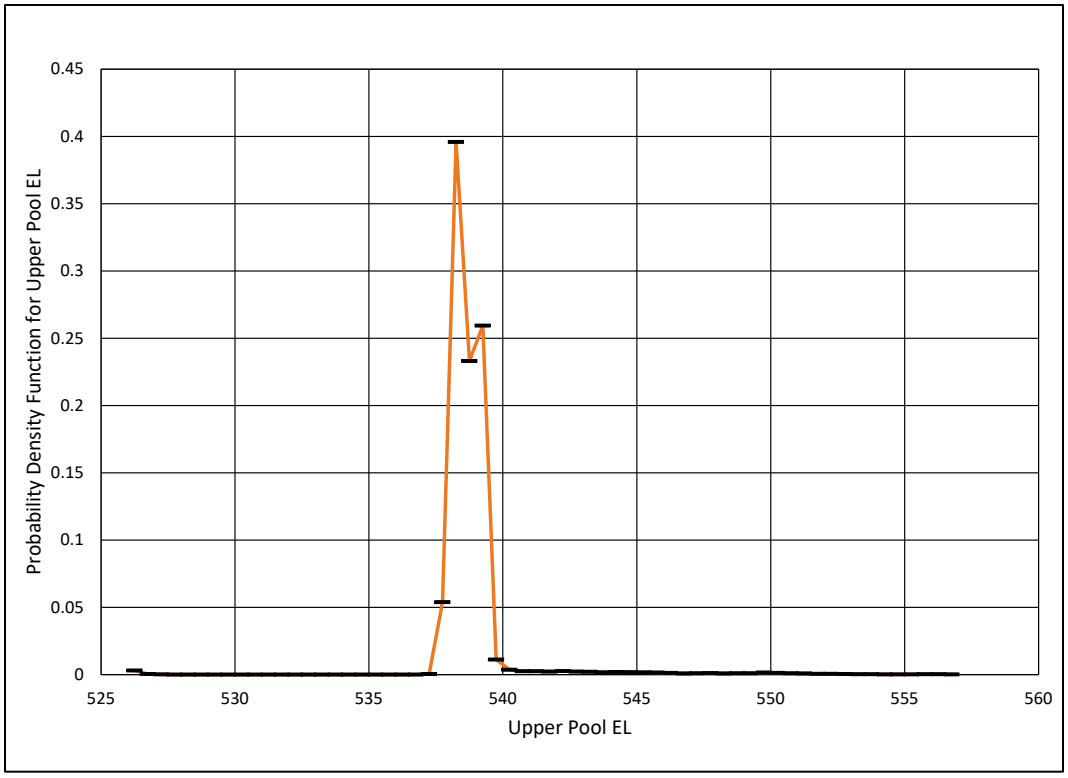

Figure C-4. CDF for upper pool el.

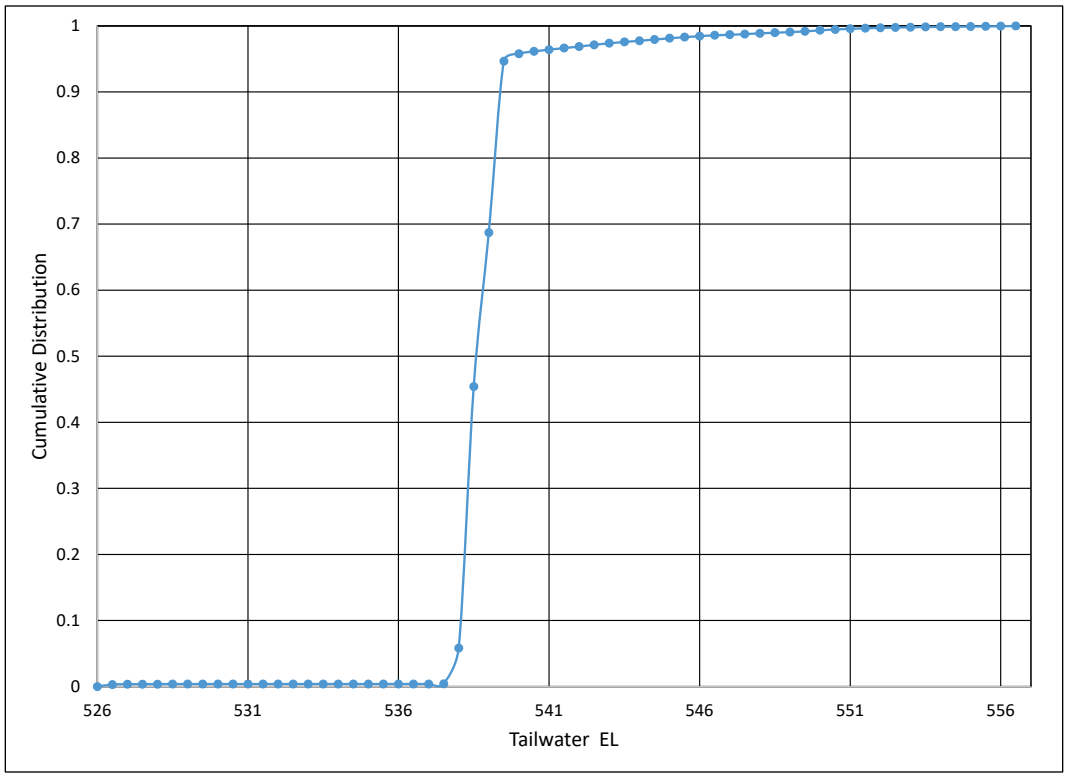

C.1.2 Tailwater Statistics for RCBLD

Similar statistics were computed for the TW Els at RCBLD. Figure C-5 shows a histogram of the lower stage from 1993 to 2020. To convert the lower stage reading to lower pool el, add el 503 to the lower stage reading. The mean TW El was 522.43, the maximum el was 558.01, and the minimum el was 502.68. The standard deviation was 7.31 ft.

The histogram contains 56 bins, each with a bin width of 1.0 ft. The area of each bin was computed, and the total area was determined by summing the individual bin areas. These areas were normalized by dividing each individual area by the total area to give the PDF shown in Figure C-6. A CDF, shown in Figure C-7, was developed by cumulatively summing the normalized areas of the PDF.

Figure C-5. Histogram of TW El between 1993 and 2020.

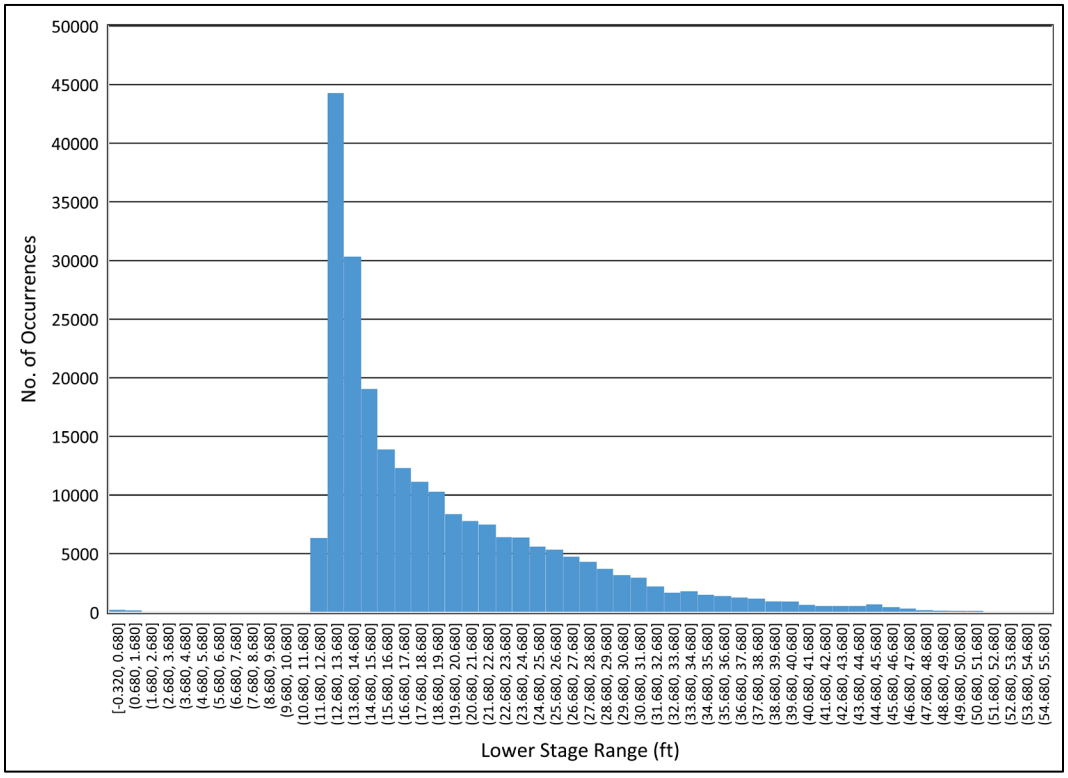

Figure C-6. PDF from histogram of TW El.

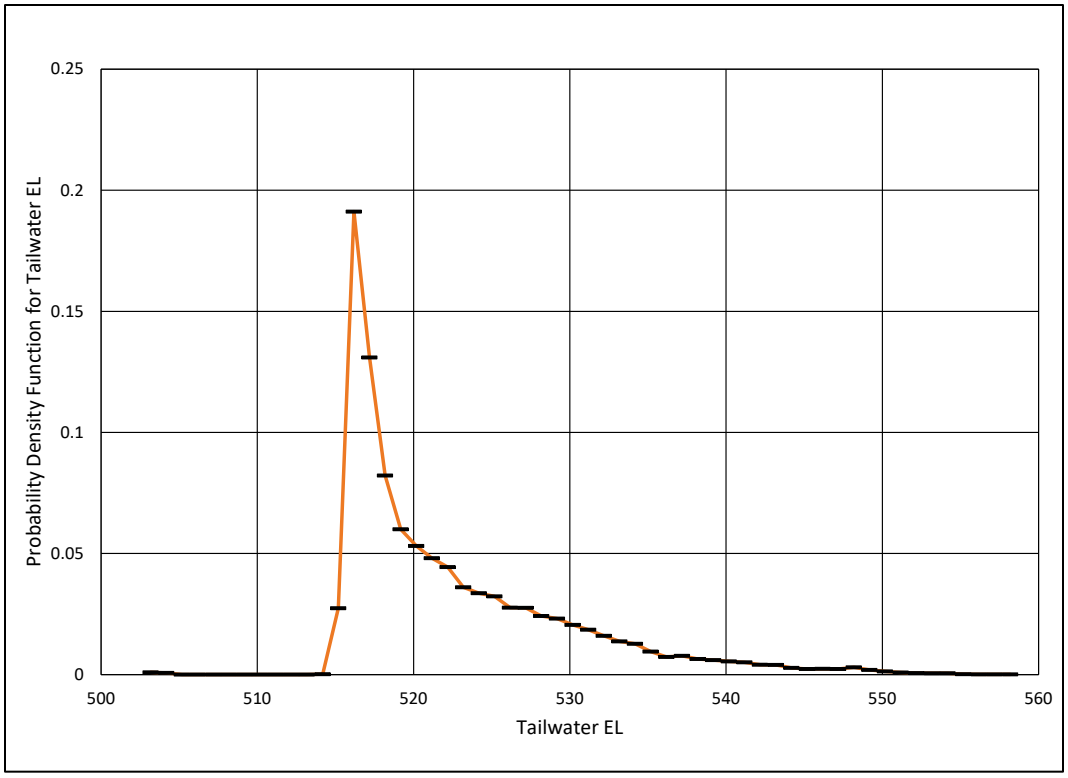

Figure C-7. CDF for TW El.

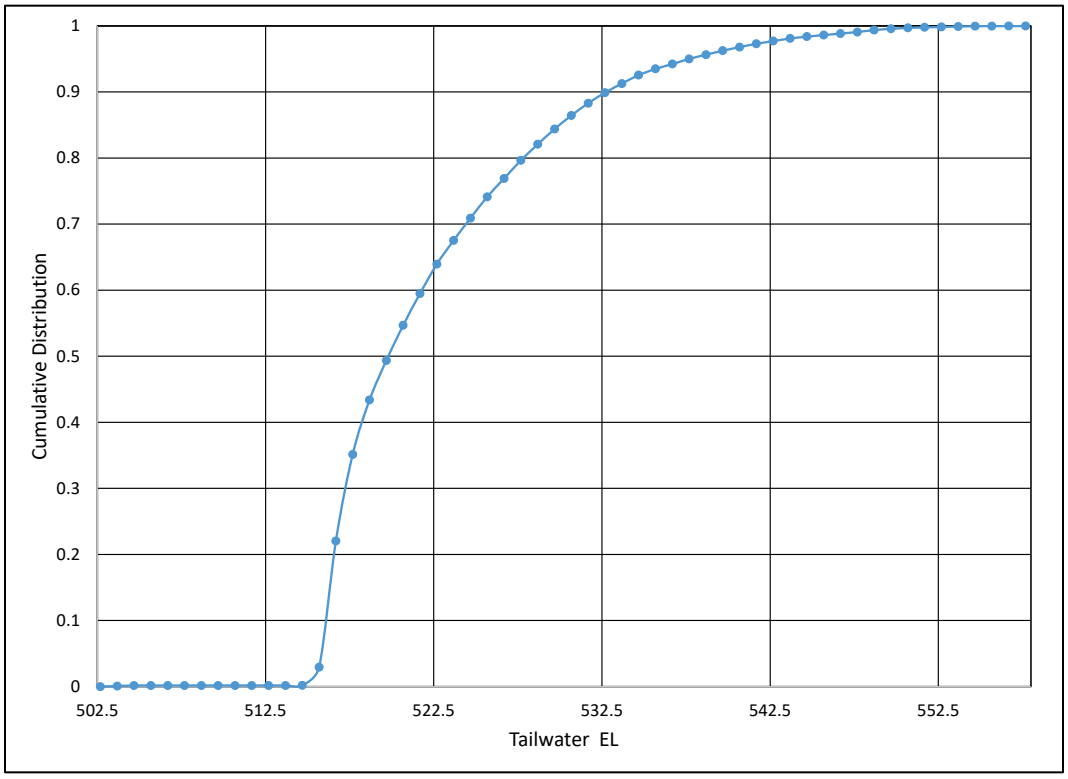

C.2 Hydrostatic Load for RCBLD without Tailwater Effect for RCBLD

Equation (10), which is repeated here, is a conventional equation found in many fluid mechanics and hydraulics textbooks and is used to compute the hydrostatic pressure (p). As stated previously, γ is the unit weight of water, and y is the vertical distance from the water surface to the location of the hydrostatic pressure of interest (Figure 15):

$$p = \gamma y.$$

The horizontal hydrostatic pressure on a closed gate is expressed as γH, where γ is the unit weight of water, and H is the total head on the gate. When the gate is closed, H represents the difference between the upper pool el and the spillway crest el when the tailwater is lower than the crest el (Figure 53). Equation (11), repeated here, can be used to calculate the maximum hydrostatic pressure:

$$p_{max} = \gamma H.$$

The hydrostatic force per foot of width for the roller gate is

$$H_s = \frac{1}{2}\gamma H^2,$$

where

γ = the unit weight of water = 62.4 lb/ft^3,
H = the head on the gate = 538 – 508.5 = 29.5 ft, and
Max hydrostatic load = 0.5 [62.4 lb/ft^3 * (29.5 ft)^2]= 27,152 lb/ft.

The maximum hydrostatic load would be experienced if the upper pool were at the top of the roller gate. Because the roller gate was designed with the top of the gate at the normal upper pool el, the maximum hydrostatic load occurs with the normal upper pool. This load condition represents H_1 (i.e., the maximum net hydrostatic load that will ever occur), which is one of the three hydrostatic loads that are to be considered.

C.3 Wave Load Based on Wave Height and Period for RCBLD

The dispersion due to wave load about the mean hydrostatic and hydrodynamic loads needs to be determined. The wave load is considered a primary load that contributes to load fluctuations. The procedures and methods used to determine wave load for the STG, which were presented in Chapter 2 and Appendix A, were used for the R. C. Byrd roller gate. The supporting data and computations to determine the load for the project are presented in the sections that follow. The wind speed, wind direction, and fetch must be determined to develop a wave load.

C.3.1 Wind Speed and Fetch for RCBLD

The wind speed and wind direction data were obtained from meteorological data collected between 2005 and 2020 at the Point Pleasant Airport (PPA) near Point Pleasant, West Virginia. The wind data were sparse for this location. The PPA is located approximately 17 mi north of the project. Figure C-8 shows the data collection site in relation to the project.

Figure C-8. Satellite imagery of the wind speed and direction data collection site in relation to R. C. Byrd Spillway. (Map data: Google Earth 2016.)

The dataset was fairly complete for the years 2015 to August 2020 and included wind speeds and directions reported multiple times per hour. Between 2005 and 2015, the wind speed and direction were usually reported on an hourly basis. The latitude of the airport is 38.9146, and the longitude is –82.0986. The data were obtained from Iowa State University (n.d.).

Figure C-9 shows the fetch determined for the RCBLD project. The wind direction that impacts the project perpendicular to the spillway axis is 0°. The fetch is approximately 0.65 mi.

Figure C-9. Satellite imagery showing the fetch and wind direction determined for the RCBLD project. (Map data: Google Earth 2015.)

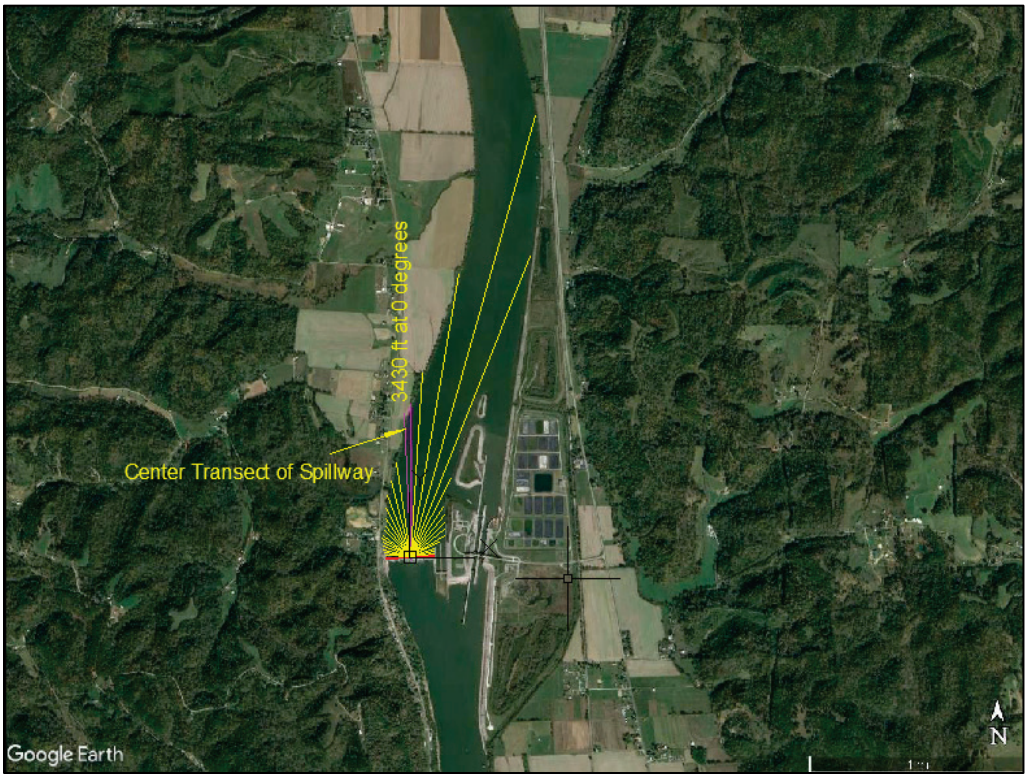

C.3.2 Wind Speed Analyses for RCBLD

The methods used to determine the appropriate wind speed for the analyses of the wave load developed for the STG were also used for the roller gate. Based on the fetch length and wind speed, Equation (50), which is repeated here, can be used to determine the time required for full wave growth:

$$t_{min} = 1.0F^{0.73}U_{10}^{-0.46}.$$

Using an estimated wind speed of 20 mph and a fetch length of 0.65 mi, the minimum time to reach full wave growth was around 20 min, so a t_{min} value of 0.3 hr was used in the analysis. Equation (50) requires the use of metric units. The wind speed data was then processed to determine the maximum 20 min average wind speed with a wind direction between 340° and 20° per year. Table C-1 shows the wind speed values used in the analyses. A wind direction of 0° did not appear to be a dominant direction. Much higher winds were observed in other directions.

Table C-1. Maximum yearly 0.3 hr average wind speed for a wind directions between 340° and 20° at the Point Pleasant Airport (PPA) for the 2005 to 2020 observation period.

Year	Max 0.3hr Avg Wind Speed (mph)
2005	5.8
2006	9.2
2007	8.1
2008	6.9
2009	10.0
2010	9.2
2011	8.1
2012	8.1
2013	9.2
2014	15.0
2015	10.0
2016	5.8
2017	9.8
2018	9.8
2019	4.6
2020	9.8

C.3.3 Extreme Value Estimation Using Maximum 0.3 hr Average Yearly Values of Wind Speed for RCBLD

The type 1 Gumbel distribution was used for a GEV analysis. Figure C-10 shows the results from extreme value estimation using the maximum 0.3 hr average annual values for the PPA data. The 100 yr recurrence interval wind speed from this analysis was 18.8. Using the magnitude of the 100 yr recurrence interval for wind speed was considered a suitable frequency for wave height calculations.

Figure C-10. Extreme wind speed estimation for Point Pleasant Airport (PPA) based on max 0.3 hr average annual values of wind speed.

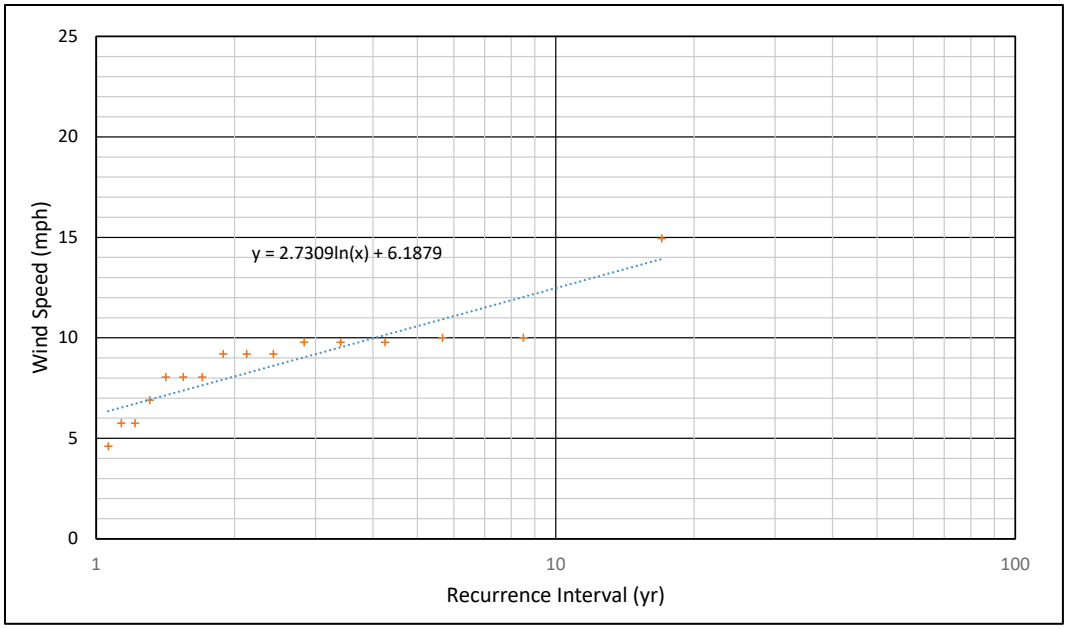

C.3.4 Wind Frequency Based on Gumbel Type 1 Distribution with Gringorten's Method Using Maximum Yearly 0.3 hr Average Values of Wind Speed

The type 1 Gumbel distribution can be used with Gringorten's (1963) plotting position formula to create another method for evaluating wind speed. Chapter 2 contained a description of this procedure. Figure C-11 shows a plot of the return period versus wind speed determined using this procedure for the data from the PPA. The wind speed for the 100 yr return period was 16.2 mph.

To further investigate the statistics for the wind speed, a formula to determine the standard error (Appendix A) was used for the data presented in Figure C-11.

Figure C-11. Wind frequency from Gumbel type 1 distribution with Gringorten's method for the PPA using the maximum 0.3 hr average annual wind speed.

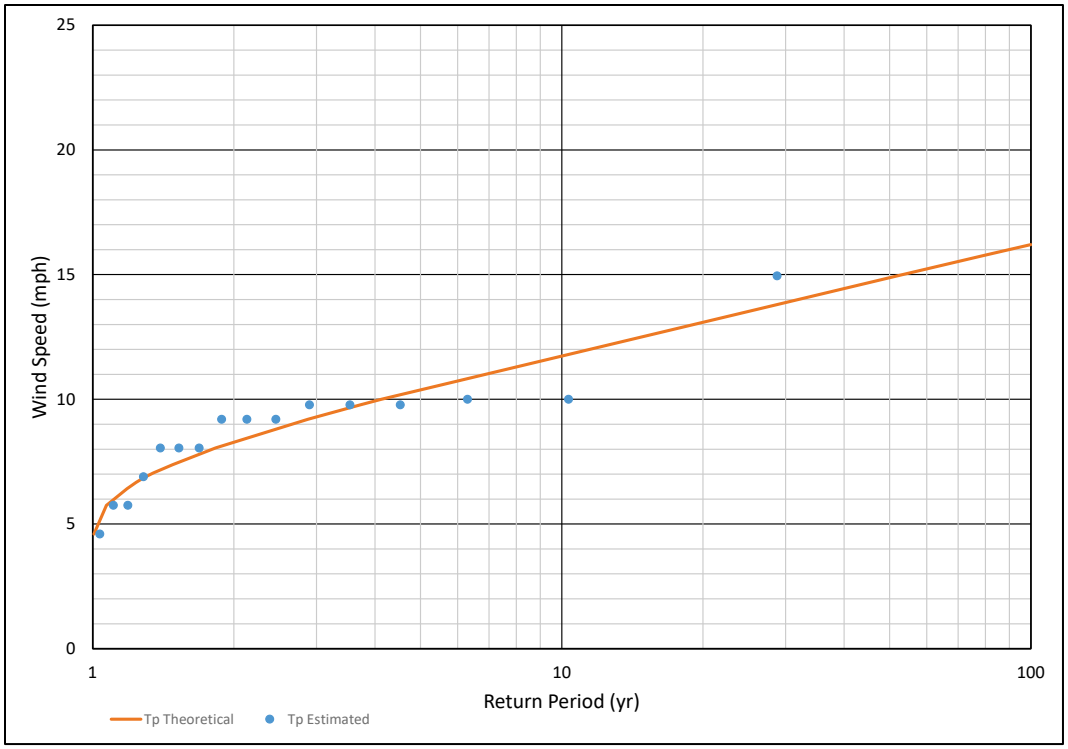

Figure C-12 shows the fitted curve bounded by plus and minus 1, 2, and 3 standard deviations (σ) for the PPA wind data (n = 16). Table C-2 shows the values for these statistics. The mean 100 yr return period wind speed was 16.2 mph. The standard deviation was determined to be 0.801 mph. The use of the 100 yr return period plus 3 standard deviations gave a wind speed of 18.6 mph.

Table C-2. Results from the wind speed analysis for the R. C. Byrd roller gate.

Statistic	100 yr Wind Speed (mph)
+3σ	18.6
+2σ	17.8
+1σ	17.0
Mean	16.2
−1σ	15.4
−2σ	14.6
−3σ	13.8

Figure C-12. Wind frequency curves based on peak yearly 0.3 hr average wind speed for the PPA data.

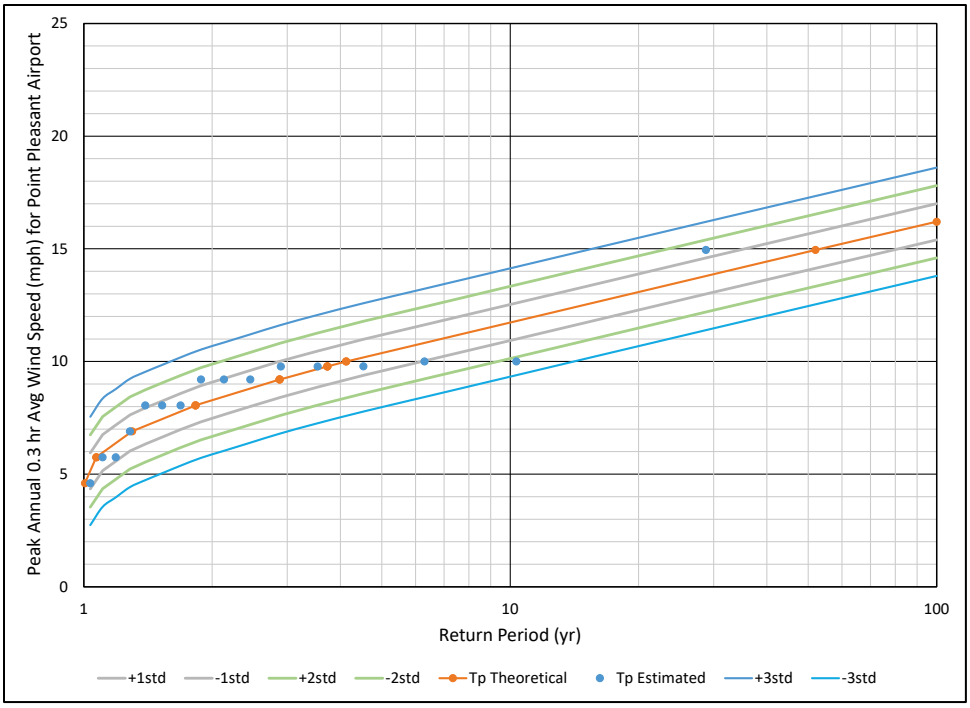

C.3.5 Wave Height and Period from NARFET Model for RCBLD

Table C-3 shows the input data and results from the use of the NARFET program for the R. C. Byrd roller gate. The program input requires the radial lengths of the fetch and the angle increments for resolution of the wind direction (Figure C-9). The radial lengths (a total of 29) determined for an angle increment of 6° are shown in Figure C-9. The significant wave height, period, and wavelength for the wind speeds determined between −3σ and +3σ for the 100 yr return period shown in Figure C-12 are listed in Table C-3. The wind direction was between 340° and 20° for a duration of 0.3 hr. Figure C-13 shows the wave heights computed from NARFET.

Table C-3. Wave height, wave period, and wavelength computed using the NARFET model for the R. C. Byrd roller gate.

Wind Speed (mph)	Wave Height (m)	Wave Period (sec)	Wavelength (m)
18.6	0.25	1.72	4.6
17.8	0.24	1.66	4.3
17.0	0.23	1.63	4.2
16.2	0.21	1.58	3.9
15.4	0.20	1.55	3.7
14.6	0.19	1.49	3.5
13.8	0.17	1.43	3.2

Figure C-13. Wave height versus wind speed from Smith's NARFET model for the R. C. Byrd roller gate.

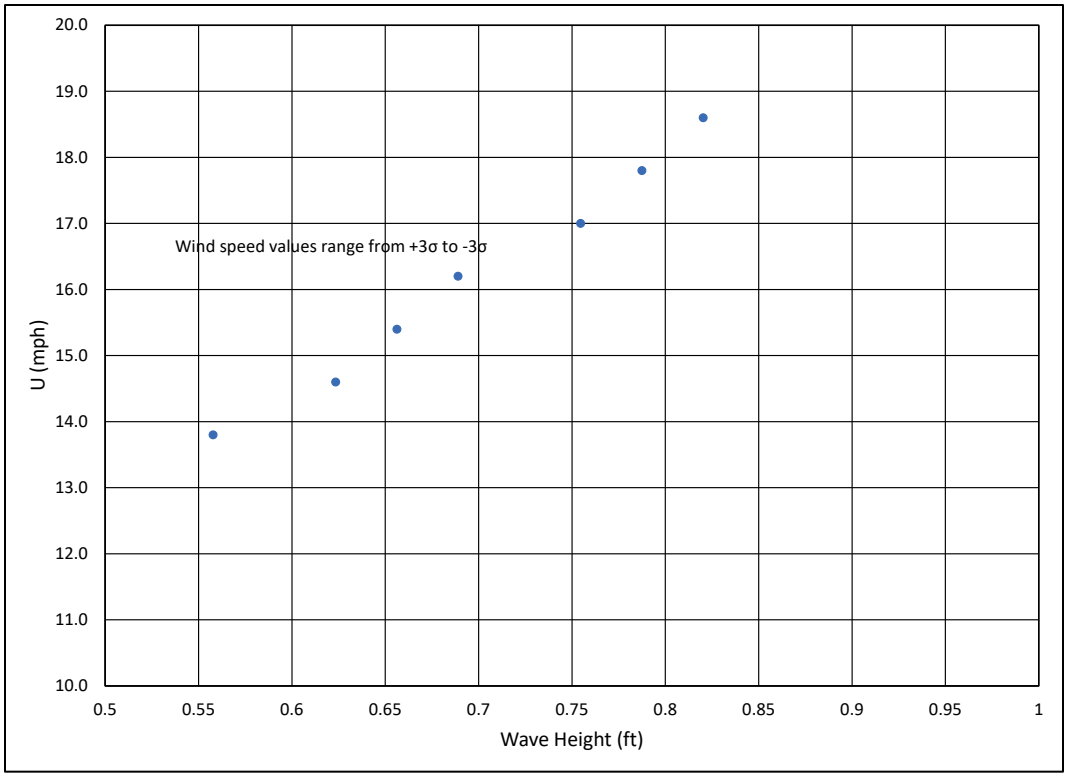

C.3.6 Wave Load from Goda for RCBLD

Goda (2010) also recommended formulations for determining significant wave height, period, and wavelength based on wind speed and fetch. The background and supporting equations for his formulations were provided in Chapter 2. This methodology is considered applicable to the spillway roller gate.

Figure C-14 contains a plot of wind speed (U) versus wave height determined using Goda's recommended formulations for the statistical analysis of the wind speed data for the PPA.

Figure C-14. Wave height versus wind speed from Goda's (2010) procedure for the R. C. Byrd roller gate.

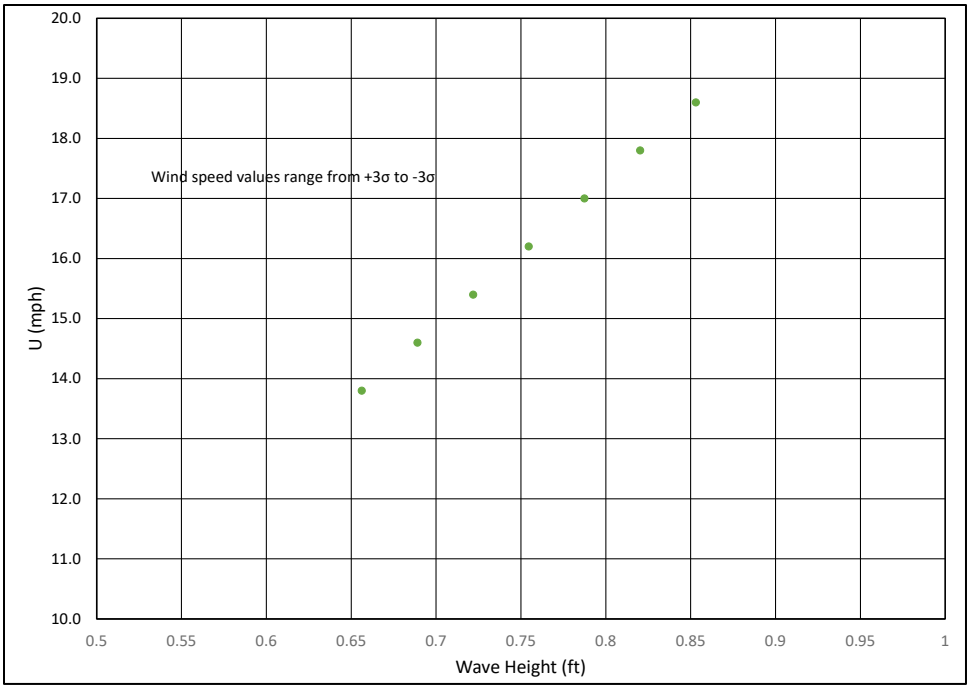

The wave pressure distribution and subsequent wave force for the roller gate were determined from the significant wave height and wave period. Section 2.3.2.3 contains a complete description of this procedure. Based on the parameters listed in Table C-4 and the Goda formulations in Section 2.3.2.3, an example solution was reached. Table C-5 lists the parameters used in the example wave force calculation (imperial and metric units included). The example uses an upper pool el of 538, a top of roller gate of 539, and the mean 100 yr return period wind speed of 16.2 mph. This example assumed the gate height was 30.5 ft to demonstrate the wave pressure distribution. While the gate was actually 29.5 ft high, any wave pressure would occur with the gates partially open.

Table C-4. Significant wave height, wave period, and wavelength from Goda's formulations for the R. C. Byrd roller gate.

Wind Speed (mph)	Wave Height (m)	Wave Period (sec)	Wavelength (m)
18.6	0.26	1.52	3.62
17.8	0.25	1.50	3.52
17.0	0.24	1.48	3.43
16.2	0.23	1.46	3.33
15.4	0.22	1.44	3.23
14.6	0.21	1.42	3.13
13.8	0.20	1.39	3.03

Table C-5. Parameters used in example wave force calculation (imperial and metric units included) for the R. C. Byrd project for a wind speed of 16.2 mph.

Parameter	Value (Imperial Units)	Value (Metric Units)	Description
h_c	1.00 ft	0.305 m	Roller gate height above upper pool el
d (originally d_{SWL})	29.5 ft	8.99 m	Difference between upper pool el and spillway crest el
h (originally h_{SWL})	44.0 ft	13.41 m	Difference between upper pool el and approach channel invert el
tan θ	0	0	Bottom slope toward bulkhead
β_D	0 deg	0 deg	Design incident wave angle
$H_{1/3}$	0.75 ft	0.230 m	Significant wave height for example problem
$T_{1/3}$	1.46 sec	1.46 sec	Significant wave period for example problem
L_D	10.93 ft	3.33 m	Design wave length for example problem
ρ	62.4 lb/ft^3	1,000 kg/m^3	Density of freshwater
g	32.2 ft/sec^2	9.81 m/sec^2	Acceleration due to gravity
h'	29.5 ft	8.99 m	For the roller gate: $h' = H = d_{SWL}$

The design wave height (H_D) is the minimum of $\alpha_h H_{1/3}$ and H_b, where α_h ranges from 1.6 to 2.0. For the design of nearshore vertical structures, Goda (2010) suggested using a value of 1.8 for α_h:

$$H_d = H_{Max} = \min\{\alpha_h \times H_{1/3}, H_b\},$$

$$H_b = 0.17 \times L_D \left\{1 - \exp\left[-1.5\frac{\pi h_b}{L_D}\left(1 + 15 \times \tan^{\frac{4}{3}}\theta\right)\right]\right\},$$

where

$$h_b = h + 5 \times H_{1/3} \times \tan\theta.$$

Therefore,

$$\alpha_h H_{1/3} = 1.8 \times 0.23 \text{ m} = 0.414 \text{ m (1.36 ft)},$$

$$h_b = 13.41 \text{ m} + 5 \times 0.814 \text{ m} \times \tan(0) = 13.41 \text{ m (44.0 ft)},$$

$$H_b = 0.17 \times 3.33 \text{ m}\left\{1 - \exp\left[-1.5\frac{\pi 13.41 \text{ m}}{3.33 \text{ m}}\left(1 + 15 \times \tan^{\frac{4}{3}}(0)\right)\right]\right\}$$
$$= 0.566 \text{ m (1.86 ft)}.$$

So,

$$H_d = H_{Max} = \min\{0.414 \text{ m}, 0.566 \text{ m}\} = 0.414 \text{ m (1.36 ft)}.$$

Next, we calculated the coefficients of wave pressure (α_1, α_2, and α_3) given in the equations that follow:

$$\alpha_1 = 0.6 + \frac{1}{2}\left[\frac{\frac{4\pi h}{L_D}}{\sinh\left(\frac{4\pi h}{L_D}\right)}\right]^2,$$

$$\alpha_2 = \min\left[\frac{h_b - d}{3h_b}\left(\frac{H_D}{d}\right)^2, \frac{2d}{H_D}\right],$$

$$\alpha_3 = 1 - \frac{h'}{h}\left[1 - \frac{1}{\cosh\left(\frac{2\pi h}{L_D}\right)}\right].$$

The h and d values in the preceding equations are, respectively, equivalent to the h_{SWL} and d_{SWL} of Table C-5. Substituting those values gives

$$\alpha_1 = 0.60 \text{ (from Equation 56)},$$

$$\alpha_2 = \min\left[\frac{13.41 \text{ m} - 8.99 \text{ m}}{3(13.41 \text{ m})}\left(\frac{0.414 \text{ m}}{8.99 \text{ m}}\right)^2, \frac{2(8.99) \text{ m}}{0.414 \text{ m}}\right] = \min[0.0002 \text{ m}, 43.43 \text{ m}]$$
$$= 0.0002 \text{ (from Equation 57)},$$

and because $h' = d_{SWL} = H$,

$$\alpha_3 = 0.330 \text{ (from Equation 58)}.$$

The lateral pressure components P_1 and P_3 (from Equations 52 and 54) are evaluated here:

$$P_1 = 0.5\,(1 + \cos\beta_D)\,(\alpha_1 + \alpha_2 \times \cos^2\beta_D)\,\rho * g * H_D,$$

$$P_3 = \alpha_3 P_1.$$

The solutions to P_1 and P_3 are

$$P_1 = 2{,}438 \text{ N/m}^2 = 2.438 \text{ kN/m}^2 = 50.90 \text{ (lb/ft}^2\text{)},$$

$$P_3 = 803 \text{ N/m}^2 = 0.803 \text{ kN/m}^2 \text{ (16.76 lb/ft}^2\text{)}.$$

As shown in Section 2.3.2.3, the total lateral force per linear width (F_{Lat}) on the face of the vertical-lift gate is

$$F_{Lat} = 0.5(P_1 + P_3)\mathrm{H} + 0.5(P_1 + P_4)h_c',$$

where

$$P_4 = P_1\left(1 - \frac{h_c}{\eta^*}\right), \text{if } \eta^* > h_c,$$

or

$$P_4 = 0, \text{ if } \eta^* < h_c,$$

$$\eta^* = 0.75(1 + \cos(\beta_D))H_D,$$

$$h_C' = \min\{\eta^*, h_C\}.$$

Therefore, the solution of the resultant force, F_{Lat}, is given as

$$h_c = 0.305 \text{ m } (1.00 \text{ ft}) \text{ (from Table C-5)},$$

$$\eta^* = 0.621 \text{ m } (2.04 \text{ ft}).$$

Because $\eta^* > h_c$,

$$P_4 = 1{,}240 \text{ N/m}^2,\ 1.240 \text{ kN/m}^2\ (25.89 \text{ lb/ft}^2),$$

$$h_C' = \min\{0.621 \text{ m}, 0.305 \text{ m}\} = 0.305 \text{ m } (1.00 \text{ ft}),$$

$$F_{Lat} = 15.13 \text{ kN/m } (1{,}037 \text{ lb/ft}).$$

The analysis indicated the total lateral wave force per linear width of the roller gate for a sustained 16.2 mph wind was 1,037 lb/ft.

In Figure A-27 and Figure A-28, the pressure terms P_1, P_3, and P_4 are shown acting on the tainter gate, which would be similar to the roller gate. The location of the lateral equivalent force (h_{Lat}) can be determined using the one-third/one-sixth method developed by Ebeling et al. (2018) and also presented in Chapter 2, Section 2.3.2.4, of this report. By applying

this method for the lateral forces and summing moments about point 3, Equation (A.14), repeated here, was developed:

$$h_{Lat} = \frac{(h_4 - h_1)\left(\frac{P_4}{3} + \frac{P_1}{6}\right)h_4 + (h_4 - h_1)\left(\frac{P_4}{6} + \frac{P_1}{3}\right)h_1 + (h_1 - h_3)\left(\frac{P_1}{3} + \frac{P_3}{6}\right)h_1}{F_{Lat}},$$

$$h_{Lat} = \frac{0.31\text{ m}\left(\frac{1.24\frac{\text{kN}}{\text{m}^2}}{3} + \frac{2.438\frac{\text{kN}}{\text{m}^2}}{6}\right)9.3\text{ m} + 0.31\text{ m}\left(\frac{1.24\frac{\text{kN}}{\text{m}^2}}{6} + \frac{2.438\frac{\text{kN}}{\text{m}^2}}{3}\right)8.99\text{ m}}{104.662\frac{\text{kN}}{\text{m}}}$$

$$\frac{+ 8.99\text{ m}\left(\frac{2.438\frac{\text{kN}}{\text{m}^2}}{3} + \frac{0.803\frac{\text{kN}}{\text{m}^2}}{6}\right)8.99\text{ m}}{104.662\frac{\text{kN}}{\text{m}}}$$

$$h_{Lat} = 5.40\text{ m}.$$

Table C-4 shows the wave heights and wave periods used to compute the wave forces and pressure distributions determined from the wind speed analysis at the R. C. Byrd project. Table C-6 shows the wave forces and pressure distributions computed from Goda's procedure for the data in Table C-4.

Table C-6. Wave force and pressure distribution computations using Goda's (2010) procedure for data in Table C-4.

	Statistic						
R. C. Byrd Data	+3σ	+2σ	+1σ	Mean	−1σ	−2σ	−3σ
Wind Speed (mph)	18.6	17.8	17.0	16.2	15.4	14.6	13.8
η^* (m)	0.702	0.675	0.648	0.621	0.594	0.567	0.540
η^* (ft)	2.30	2.21	2.13	2.04	1.95	1.86	1.77
P_1 (N/m^2)	2,756	2,650	2,544	2,438	2,332	2,226	2,120
P_3 (N/m^2)	908	873	838	803	769	734	699
P_4 (N/m^2)	1,559	1,453	1,347	1,240	1,134	1,028	922
F_{Lat} (kN/m)	17.13	16.46	15.80	15.13	14.46	13.80	13.13
h_{Lat} (m)	5.41	5.40	5.40	5.40	5.40	5.40	5.39
h_{Lat} (ft)	5.93	5.92	5.92	5.92	5.92	5.92	5.92
P_1 (lb/ft^2)	58	55	53	51	49	46	44
P_3 (lb/ft^2)	19	18	18	17	16	15	15
P_4 (lb/ft^2)	33	30	28	26	24	21	19
F_{Lat} (lb/ft)	1,174	1,128	1,082	1,037	991	945	900

The definitions of Goda's parameters found in Table C-5 and used in the preceding equations are illustrated in Figure 54 for the spillway roller gate and also shown for the STG in Figure 16 and Figure A-27.

C.4 Hydrodynamic Loads for RCBLD

To develop the hydraulic loads on the spillway roller gate, upper and lower pool els, discharge, and gate opening must be known. The normal operating procedure is to raise the gates high enough to pass the discharge required to maintain the upper pool at a near constant of el 538. If the discharge keeps increasing, the gates are eventually raised completely out of the flow, and open river conditions exist. At this point, there are no hydrostatic or hydrodynamic loads on the roller gate.

An example of determining the pertinent hydraulic data to compute the hydrodynamic load is discussed in Appendix A and is similar for the roller gate. Portions of the discussion will be repeated here for reader clarity.

The momentum equation from Roberson and Crowe (1985) is given as

$$\frac{\gamma H^2 b}{2} - \frac{\gamma h^2 b}{2} + F_{GW} - F_{visc} = V_1 \rho(-V_1 H b) + V_2 \rho(V_2 h b).$$

Considering the viscous force (F_{visc}) is negligible and $V_1 H b = V_2 h b = Q$,

$$F_{GW} = \rho Q(-V_1) + \rho Q(V_2) - \frac{1}{2}\gamma b(H^2 - h^2).$$

F_{GW} is the force of the gate acting on the water in the control section. To obtain the force on the gate (F_G), F_{GW} is solved, and the sign on F_{GW} is changed, as follows:

$$F_G = \rho Q(V_1 - V_2) + \frac{1}{2}\gamma b(H^2 - h^2),$$

where

V_1 = the approach velocity,
V_2 = the velocity downstream of gate,
ρ = 1.936 slugs/ft^3,
γ = 62.4 lb/ft^3,
b = the gate width (ft),
H = upper pool el – crest el, and

H = TW El – crest el.

Figure C-15 shows a schematic with some of the terms used in Equation (84) and described in the discussion that follows. The approach velocity, V_1, can be determined from

$$V_1 = \frac{Q}{A_1}.$$

Figure C-15. Schematic for terms used in Equation (82) for a roller gate with tailwater.

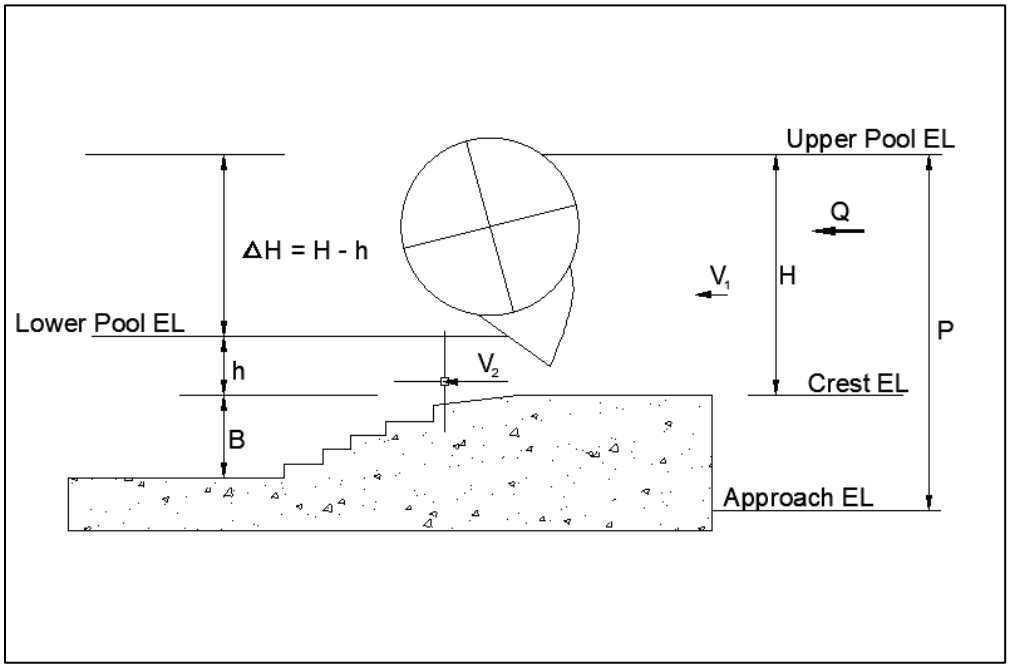

A_1 is the area upstream from the gate and is the upper pool el – the approach el (P in Figure C-15) or 538 – 494 = 44 ft multiplied by the width of the gate, b (i.e., 125.5ft), which gives 5,522 ft^2:

$$A_1 = P * b.$$

For this example problem, the discharge, Q, is equal to 4,600 cfs for a single gate, the gate opening is equal to 1 ft, and the TW El is 514.2 (considered the minimum for this gate opening). The gate opening is the vertical distance from the bottom point on the roller gate to the spillway crest. Therefore, V_1 is equal to 4,600 ft^3/sec divided by 5,522 ft^2, or 0.83 ft/sec. V_2 is

$$V_2 = \frac{Q}{A_2},$$

where A_2 is

$$A_2 = b * h,$$

and this gives (4,600 ft^3/sec) / (125.5 ft * 5.70 ft) = 6.43 ft/sec.

If the value for discharge is not available from a spillway rating curve, it can be computed using Equation (87). Figure C-16 shows the spillway rating curves. In this example, the differential head, ΔH, is 29.5 ft – 5.7 ft = 23.3 ft, and H = TW EL – crest el, which is 514.2 – 508.5 = 5.70 ft.

The hydrodynamic load on the spillway roller gate can now be computed because all the parameters in Equation (82) are known. The normal upper pool el was 538, and the range of the TW El was determined from the spillway rating curves provided by USACE-LRH, which were then used to develop Figure C-16. The top curve represents a gate opening of 20 ft, and the bottom curve represents a gate opening of 1 ft. These curves were digitized and used to determine the discharge and gate opening relationships used in the computation of the hydrodynamic forces. Figure C-17 shows the hydrodynamic forces on the spillway roller gate per linear foot and was computed using the preceding procedure. The bottom (i.e., blue) curve represents the higher end of the TW El, and the upper (i.e., orange) curve represents the forces with the minimum tailwater for that particular gate opening. The largest force computed occurred with the normal upper pool el of 538, a TW El of 514.2, a gate opening of 1 ft, and a discharge per gate of 4,600 cfs and was 25,741 lb/ft.

Figure C-16. Spillway rating curves for the R. C. Byrd roller gate, redrawn from original curves provided by USACE-LRH.

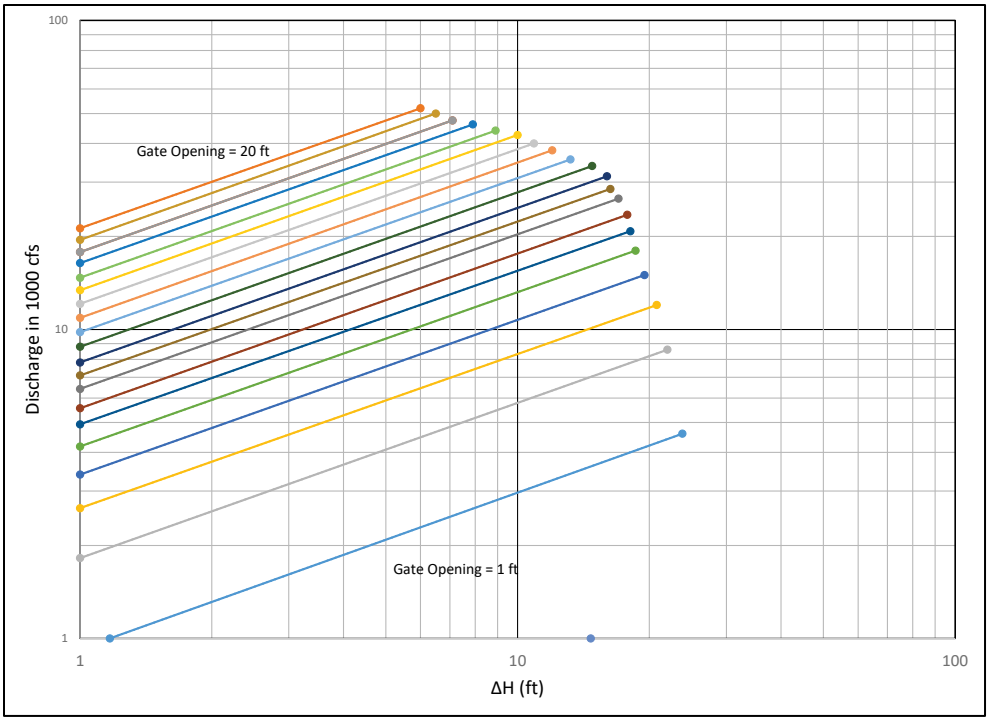

Figure C-17. Hydrodynamic force per foot of gate for the R. C. Byrd roller gate.

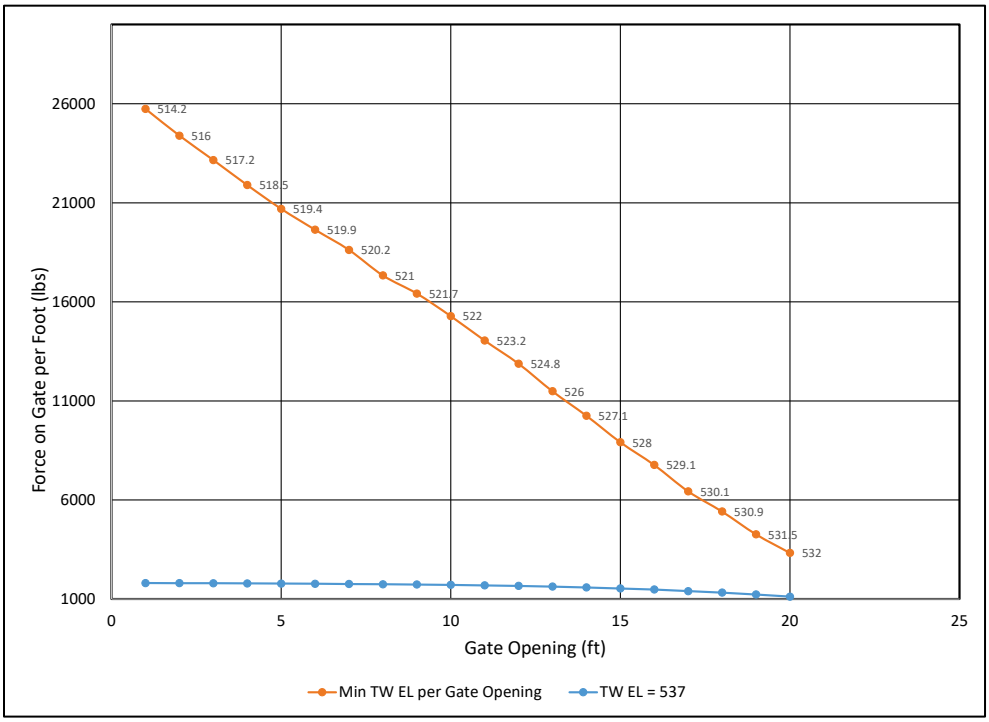

C.5 Probabilistic Characterization of the Hydrostatic and Hydrodynamic Loads for the R. C. Byrd Spillway Roller Gate

C.5.1 Probabilistic Characterization

The dispersion of the hydrostatic load for the R. C. Byrd spillway roller gate needs to be determined to conduct the LRFD analysis. Statistics are needed to estimate the dispersion in the hydrostatic loads. The example problem in Appendix A for the MPLD provides a method for developing these statistics for a project operated similarly to this one, where the mean upper pool el is considered to be the normal navigation pool el. Because the normal upper pool el at RCBLD is the same as the top el of the roller gate (i.e., el 538), the maximum hydrostatic load occurs under this condition. The fluctuation or dispersion of this load would probably be minimal because the project is designed to maintain a normal upper pool. For this example problem, to determine the dispersion of the hydrostatic load, the fluctuation of the upper pool was taken between el 538 (normal upper pool) and upper pool historical data between 1999 and 2020 that were below el 538. These data contained several erroneous readings, probably from faulty gage readings, and the decision was made to disregard all upper pool el readings below 536.8. The mean upper pool el for this dataset was 537.918, and the standard deviation, σ, was 0.097 ft. Figure C-18 shows the hydrostatic pressure distribution for the mean upper pool el for this dataset and plus and minus 6σ. The mean hydrostatic force was 27,001 lb/ft run of gate. The hydrostatic force with an upper pool el of +6σ (538.5) was 28,080 lb/ft run of gate, and the hydrostatic force with an upper pool el of −6σ (537.336) was 25,940 lb/ft (Table C-7).

Table C-7. Hydrostatic force statistics for the R. C. Byrd spillway roller gate for a range of upper pool els from −6σ (537.336) to +6σ (538.5) about the mean of 537.918.

Hydrostatic Force		Hydrostatic Force	
−6σ (lb/ft)	25,940	+σ (lb/ft)	27,180
−5σ (lb/ft)	26,120	+2σ(lb/ft)	27,360
−4σ (lb/ft)	26,290	+3σ (lb/ft)	27,540
−3σ (lb/ft)	26,470	+4σ(lb/ft)	27,720
−2σ (lb/ft)	26,650	+5 (lb/ft)	27,900
−σ (lb/ft)	26,820	+6σ (lb/ft)	28,080
Mean (lb/ft)	27,000	—	—

Figure C-18. Hydrostatic pressure distribution for the RCBLD roller gate with an upper el of 537.918 (mean), 538.5 (+6σ), and 537.336 (−6σ).

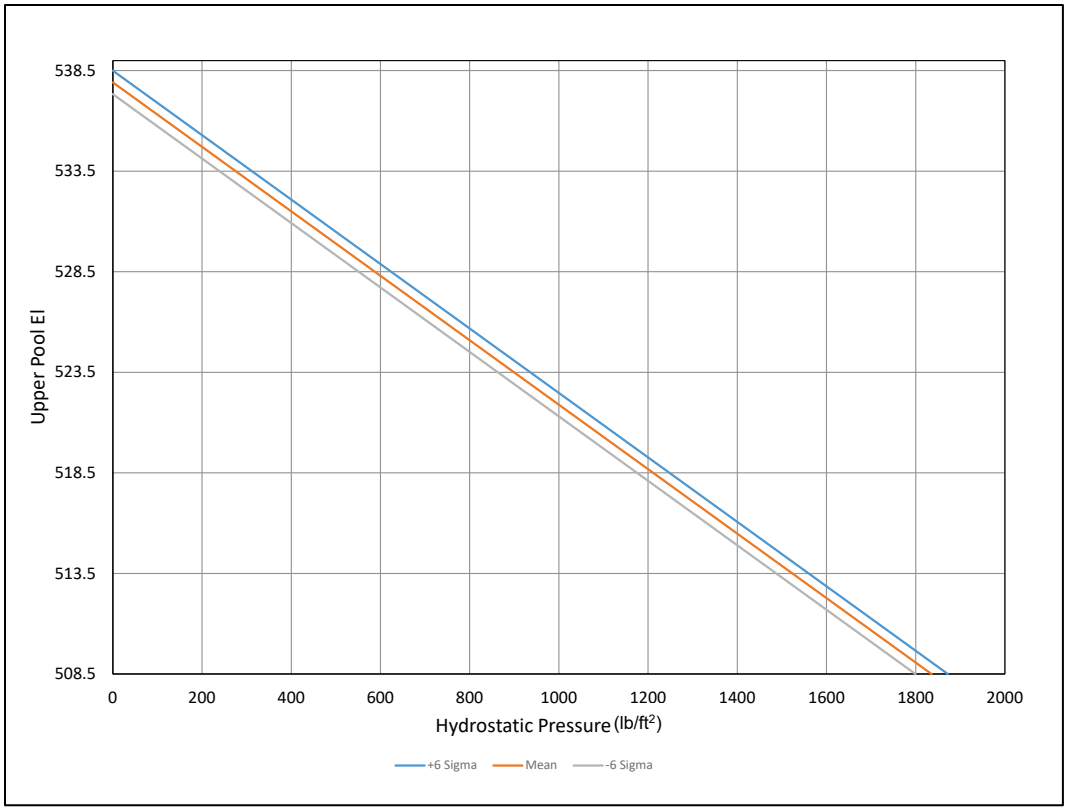

C.5.2 Probabilistic Characterization

The dispersion of the hydrodynamic load for the roller gate also needs to be determined to conduct the LRFD analysis. The procedure chosen to compute the hydrodynamic load produces the highest load for small gate openings and low tailwater. In this analysis, the range of hydrodynamic loads were computed based on the minimum and maximum tailwater that occurs at the project with a 1 ft gate opening. Figure C-18 shows these values. The minimum TW El with a 1 ft gate opening was 514.2, and the maximum was 537.0. The mean TW El was 522.43. The standard deviation, from (max – min)/6, is 3.8 ft. Table C-8 provides the range of hydrodynamic loads associated with +3σ and −3σ TW El and the normal upper pool el of 538.0.

Table C-8. Hydrodynamic force statistics for the R. C. Byrd spillway roller gate with 1 ft gate opening, normal upper pool el of 538, and TW El range from −3σ (511.3) to +3σ (533.83).

−3σ (lb/ft)	−2σ (lb/ft)	−σ (lb/ft)	Mean (lb/ft)	+σ (lb/ft)	+2σ (lb/ft)	+3σ (lb/ft)
25,900	25,570	23,800	21,020	17,300	12,670	7,130

These hydrodynamic forces were computed from the procedure described in Section C.4.

C.6 Summary of Hydraulic Loads for RCBLD

The hydraulic loads on the spillway roller gate consist primarily of the hydrostatic, wave, and hydrodynamic loads. Table C-9 lists the example hydraulic loads determined for the RCBLD project for a normal upper pool.

Table C-9. Example hydraulic loads for the RCBLD spillway roller gate.

Max Estimated Hydraulic Load	Value (kips/ft)
Hydrostatic (no tailwater effect)	27.15
Hydrodynamic*	25.74
Wave**	0.117
Hydrostatic + Wave	27.27
Hydrodynamic + Wave	25.86

* Based on an upper pool el of 538, discharge of 4,600 cfs through the gate, and 1.0 ft gate opening.

** Based on an upper pool el of 538 and 18.6 mph wind speed at 0° (100 yr wind event + 3σ). $P_1/P_3 = 3.04$.

Appendix D: Example Hydraulic Load Computations for Calcasieu Lock East Sector Gate

In this appendix, the procedures discussed in Chapter 5 of the main report are presented using data from an existing USACE Navigation project. The data needed to quantify the hydraulic loads for the sector gate and example computations are described. The example project for the sector gate was the Calcasieu Lock sector gate located in the USACE, New Orleans District (USACE-MVN), about 10 mi south of Lake Charles, Louisiana. The example is for the east sector gate. The lock is 75 ft wide by 1,206 ft long, is nominally 13 ft deep, and is part of the Gulf Intracoastal Waterway (GIWW) system. The lock maintains navigation and serves to prevent saltwater intrusion from the Calcasieu River into the Mermentau River basin. Replacement sector gates are currently being designed by USACE-MVN.

D.1 Hydrologic Data for Calcasieu River East Sector Gate

The hydrologic data for the Calcasieu Lock were obtained from the River Gages website (USACE, n.d., "Water Levels"). The period of record was from 2004 to 2022, and the stage readings on the east and west side of the lock were reported at 8:00 am daily, although there were significant gaps in the data. The data were considered adequate to use in the example problem presented in this appendix. The pertinent project-specific data for the analysis are listed here. Gage zero is 0 ft Mean Low Gulf (MLG). MLG is a reference datum often used in coastal waterways such as the GIWW and the Calcasieu River and Pass navigation channel. Caution must be exercised when using elevation data because there are several datums that have been used historically to identify water levels and structure elevations. Refer to local USACE district offices to obtain datum conversions:

- Top of sector gate el = 18.8 (MLG, gate assumed to be 30 ft high)
- Normal east stage el = 2.32 (MLG)
- Normal west stage el = 2.39 (MLG)
- Total sector gates width = 75 ft
- Gate sill el = –11.2 (MLG)

Figure D-1 shows an aerial view of the Calcasieu Lock project.

Figure D-1. Satellite imagery of Calcasieu Lock on the Gulf Intracoastal Waterway (GIWW). (Map data: Landsat/Copernicus, n.d.)

The head on the sector gate is one of the variables needed to determine the hydraulic load. The head was determined by taking the difference in the stage readings on the east and west side of the lock at the same time on the same day. Because some of the data were missing, the time period of record was from 2004 to 2020. Figure D-2 shows a histogram of the head on the east sector gate for this period. The mean head was −0.09 ft, the maximum head was 4.36 ft, and the minimum head was −4.78 ft. The standard deviation was 0.839 ft. A negative value of head indicates that the west side stage is higher than the east side stage, which is referred to as a reverse head.

There are 32 bins, each with a bin width of 0.24 ft. The area of each bin was computed, and the total area was determined by summing the individual bin areas. These areas were normalized by dividing each individual area by the total area to give the PDF shown in Figure D-3. A CDF was developed by cumulatively summing the normalized areas of the PDF, as shown in Figure D-4.

Figure D-2. Histogram of head on the Calcasieu Lock east sector gate, 2004 through 2020.

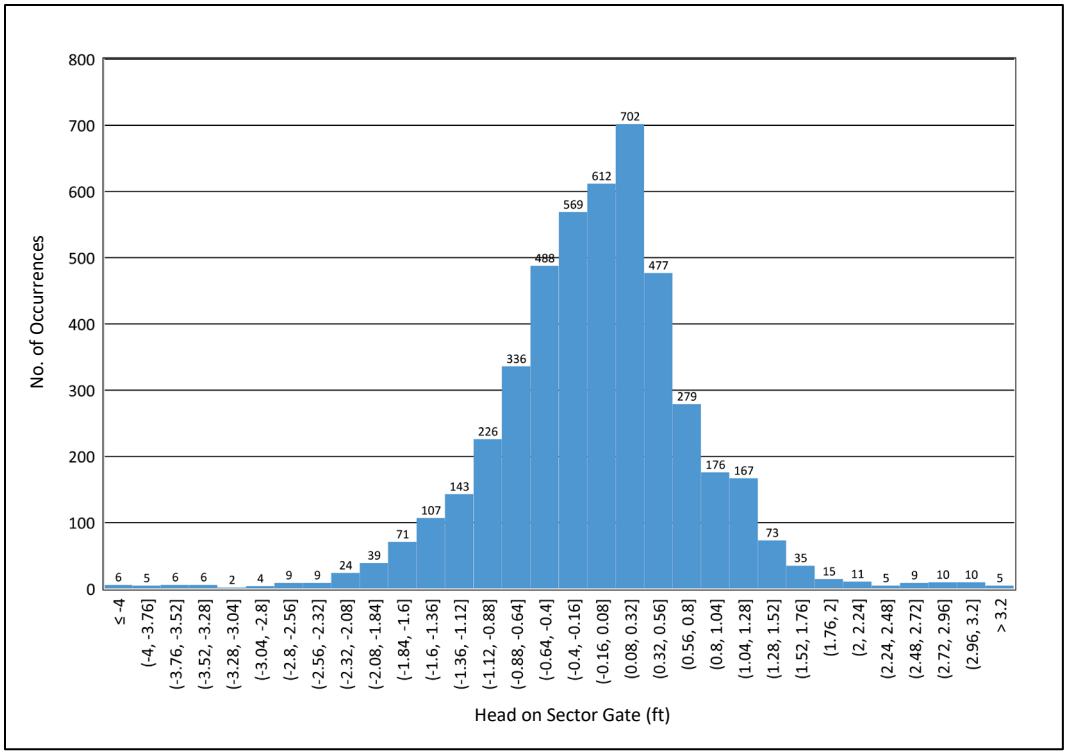

Figure D-3. PDF from histogram of head on sector gate.

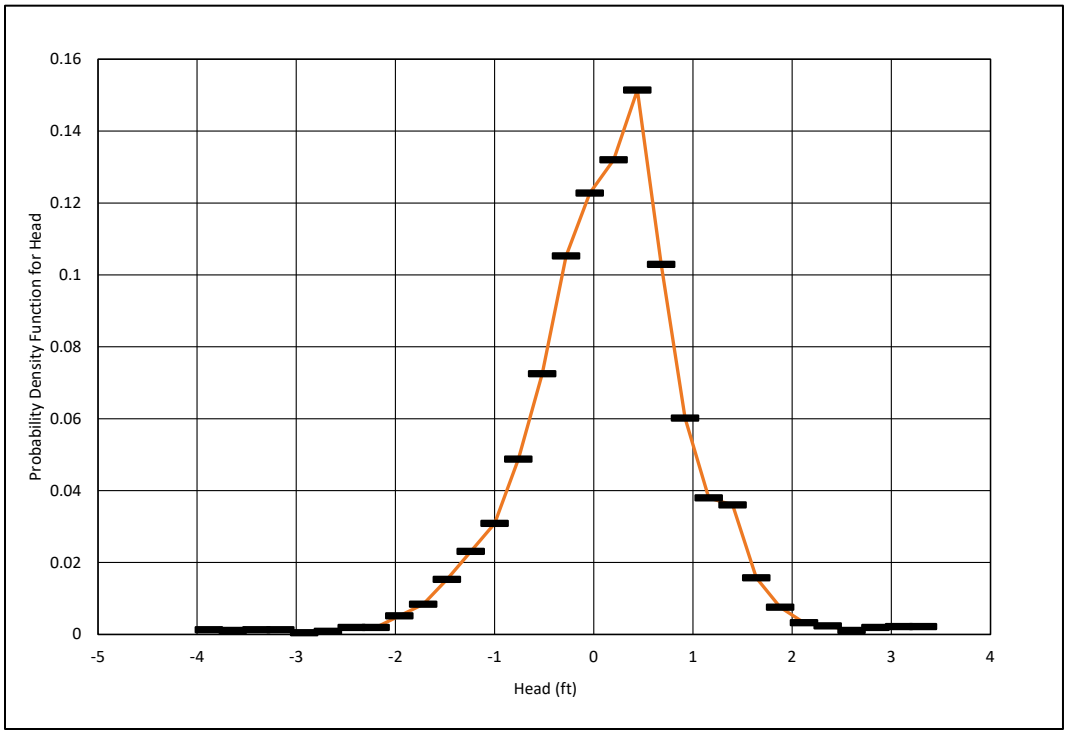

Figure D-4. CDF for head on east sector gate.

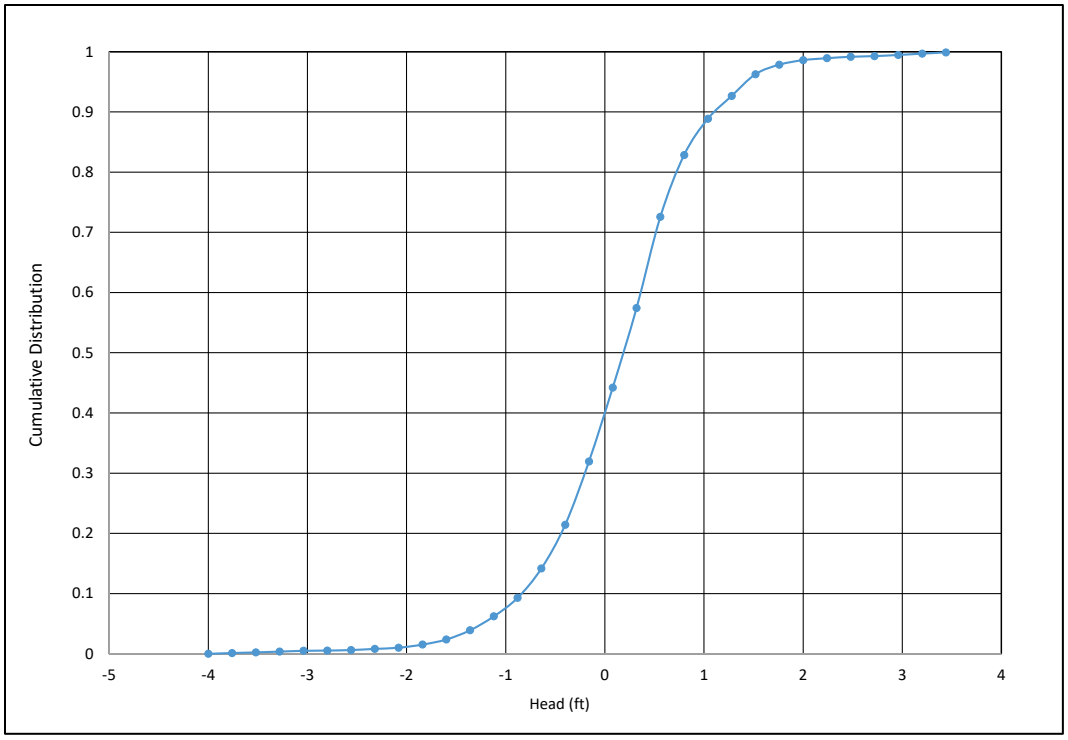

D.2 Hydrostatic Load for Calcasieu Lock East Sector Gate with Maximum Head on the Sector Gate

Equation (10), which is repeated here, is a conventional equation found in many fluid mechanics and hydraulics textbooks and is used to compute the hydrostatic pressure (p). As mentioned previously, γ is the unit weight of water, and y is the vertical distance from the water surface to the location of the hydrostatic pressure of interest. In this example for the maximum hydrostatic pressure, the vertical distance is taken from the top of the sector gate to the gate sill el, which is 30 ft. This condition results if the lock is dewatered and an extreme condition causes the east side stage to be at the top of the gate. A more typical condition would be if the east side stage were at the mean el (2.32 ft MLG) and the lock was dewatered. This would result in a head of 13.52 ft. Equation (10) is as follows:

$$p = \gamma y.$$

The horizontal hydrostatic pressure on a closed gate is expressed as γH where γ is the unit weight of water, and H is the total head on the gate. When the gate is closed, H represents the difference between the east and

west side stages. Equation (11), which is repeated here, can be used to calculate the maximum hydrostatic pressure:

$$p_{max} = \gamma H.$$

Hydrostatic pressure acting along the vertical imaginary plane is integrated over depth to obtain the resultant horizontal hydrostatic force, H_s. H_s is the resultant force computed from the triangular pressure distribution acting on the gate area. In most cases, a unit gate width is used to compute the gate area, resulting in Equation (12), which is the hydrostatic force per unit width of the gate. The location of the horizontal resultant force is $H/3$ above the gate sill when H is the head on the gate. In Equation (12),

$$H_s = \frac{1}{2}\gamma H^2,$$

where

γ = the unit weight of water = 62.4 lb/ft^3,
H = the maximum head on the gate with the lock dewatered = 30.0 ft.
Max hydrostatic load = 0.5 [62.4 lb/ft^3 * (30 ft)^2] = 28,080 lb/ft,
H = the typical head on the gate with the lock dewatered = 13.52 ft, and
Typical hydrostatic load = 0.5 [62.4 lb/ft^3 * (13.52 ft)^2] = 5,703 lb/ft.

This maximum load condition represents H_1 (i.e., the maximum net hydrostatic load that will ever occur), which is one of the three hydrostatic loads that are to be considered.

D.3 Wave Load Based on Wave Height and Period for the Calcasieu Lock East Sector Gate

The dispersion due to wave load about the mean hydrostatic load needs to be determined. The wave load is considered a primary load that contributes to load fluctuations. The procedures and methods used to determine wave load for the STG presented in Chapter 2 and Appendix A were used for the sector gate. The supporting data and computations used to determine the load for the Calcasieu Lock sector gate will be presented in the

sections that follow. As mentioned, developing a wave load requires determining the wind speed, wind direction, and fetch.

D.3.1 Wind Speed and Fetch for the Calcasieu Lock East Sector Gate

The wind speed and wind direction data were obtained from meteorological data collected over a 31 yr period between 1990 and 2021 at the Lake Charles (LCH) airport in Louisiana. The LCH airport is located approximately 4.75 mi northeast of the Calcasieu Lock. Figure D-5 shows the data collection site in relation to the project.

Figure D-5. Satellite imagery of the wind speed and direction data collection site. (Map data: Landsat/Copernicus, n.d.)

The dataset was fairly complete for the years 1990 to December 2009, with wind speeds and directions reported hourly. From January 2010 to December 2021, the wind speed and direction were often reported multiple times per hour. The latitude of the airport is 30.1255, and the longitude is −90.2277. The data were obtained from Iowa State University (n.d.).

Figure D-6 shows the fetch determined for the Calcasieu Lock east sector gate. The wind direction that impacts the project perpendicular to the sector gate is 130°. The fetch is approximately 1.47 mi.

Figure D-6. Satellite imagery of fetch and wind direction determined for the Calcasieu Lock east sector gate. (Map data: Landsat/Copernicus, n.d.)

D.3.2 Wind Speed Analyses for the Calcasieu Lock East Sector Gate

The methods for determining the appropriate wind speed for the analyses of the wave load developed for the sector gate were also used for the previous HSS described in Chapters 2 through 4 and in Appendix A through Appendix C. Based on the fetch length and wind speed, Equation (50) can be used to determine the time required for full wave growth. Using an estimated wind speed between 30 and 40 mph and a fetch length of 1.45 mi, the minimum time to reach full wave growth was about 0.5 hr. The wind speed data were then used to determine the maximum 0.5 hr average wind speed with a wind direction between 110° and 150° per year. Table D-1 shows the wind speed values used in the analyses that follow.

Table D-1. Maximum yearly 0.5 hr average wind speed for wind directions between 110° and 150° at LCH for the 1990 to 2021 observation period.

Year	Max 0.5 hr Avg Wind Speed (mph)
1990	27.6
1991	27.6
1992	28.75
1993	23.58
1994	21.85
1995	26.45
1996	31.05
1997	23.0
1998	28.75
1999	24.15
2000	24.73
2001	21.85
2002	29.67
2003	21.56
2004	29.71
2005	25.3
2006	34.5
2007	24.15
2008	44.28
2009	26.45
2010	18.98
2011	23.0
2012	28.43
2013	28.75
2014	28.37
2015	29.33
2016	32.2
2017	33.35
2018	24.15
2019	30.59
2020	31.63
2021	23.77

D.3.3 Extreme Value Estimation Using Maximum 0.5 hr Average Yearly Values of Wind Speed for the Calcasieu Lock East Sector Gate

The type 1 Gumbel distribution was used for a GEV analysis. This analysis is typically used to evaluate extreme, low probability meteorological and

hydrological events. The probability of nonexceedance and wind speed are plotted, and a linear regression can be used to estimate values for extreme return periods.

Figure D-7 shows the results from extreme value estimation using the maximum 0.5 hr average annual values for the LCH airport data. The 100 yr recurrence interval wind speed from this analysis was 47.4 mph. Using the magnitude of 100 yr recurrence interval for wind speed was considered a suitable frequency for wave height calculations.

Figure D-7. Extreme wind speed estimation for the Lake Charles (LCH) airport based on maximum 0.5 hr average annual values of wind speed.

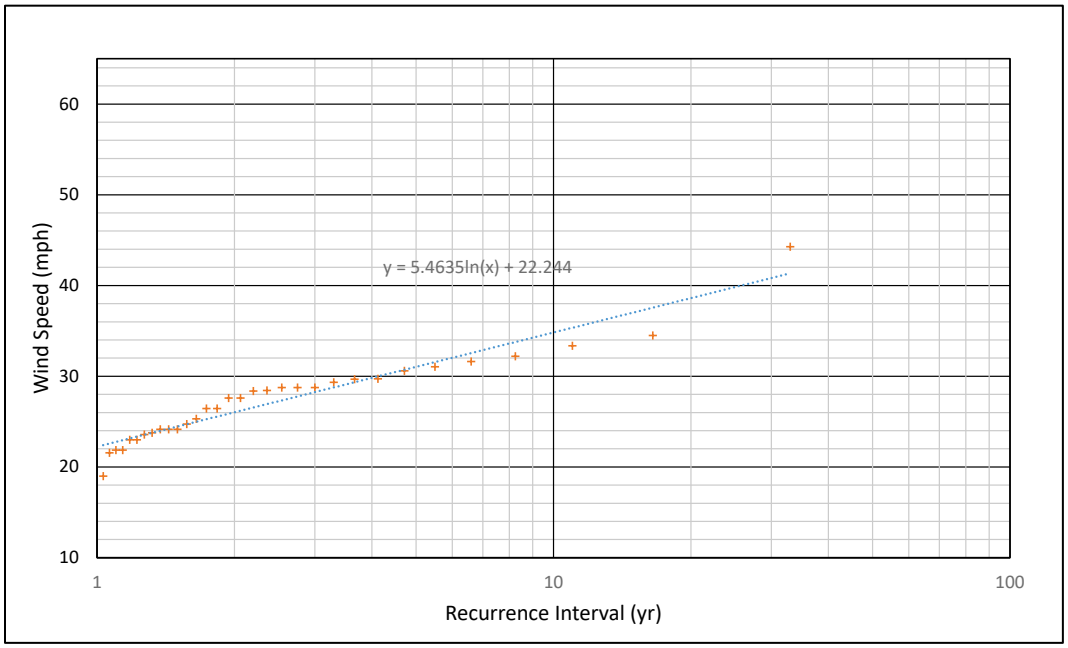

D.3.4 Wind Frequency Based on Gumbel Type 1 Distribution with Gringorten's Method Using Maximum Yearly Values of Wind Speed

The type 1 Gumbel distribution can be used with Gringorten's (1963) plotting position formula to create another method for evaluating wind speed. A description of this procedure is given in Chapter 2. A plot of the return period versus wind speed determined using this procedure is shown in Figure D-8 for the data obtained from the LCH airport. The wind speed for the 100 yr return period was 42.7 mph.

Figure D-8. Wind frequency from Gumbel type 1 distribution with Gringorten's method for the LCH airport using the maximum 0.5 hr average annual wind speed.

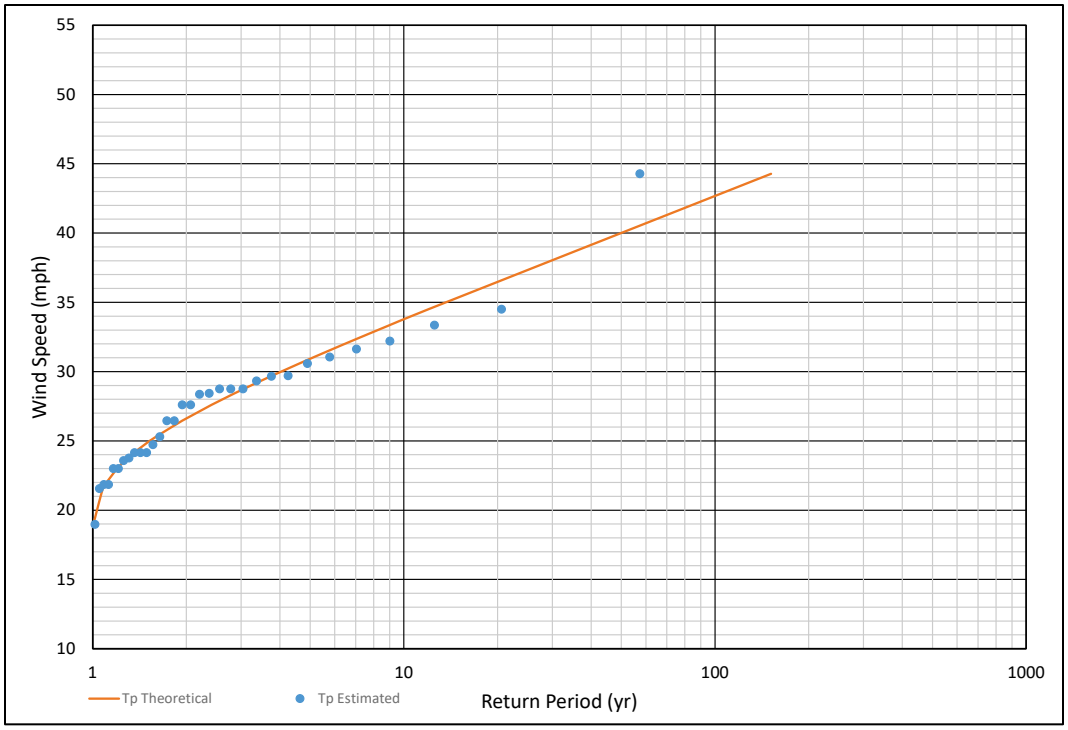

To further investigate the statistics for the wind speed, a formula to determine the standard error (discussed in Appendix A) was used for the data presented in Figure D-8. The standard error or standard deviation is defined as

$$\text{std} = \sqrt{\frac{\Sigma[U_i - U_{new}]^2}{n-1}},$$

where

U_i = the wind speed (U) value for the T_p estimated point,
U_{new} = the new value determined from a log-linear interpolation (further explanation follows), and
n = the number of samples.

The T_p estimated points are the blue points shown in Figure D-8. Each T_p estimated point has a T_p theoretical point with the same value of wind speed associated with it. These points are not shown in Figure D-8 for clarity, but they will be discussed and are shown in Figure D-9. The interpolation procedure is explained in Appendix A.

The standard error is also referred to as the standard deviation about the fit curve. The standard deviation (σ) provides a way of describing how well the sample points align with a curve fitted to the data. In the case of the Gumbel type 1 distribution curve (T_p theoretical), this standard deviation provides an estimate of the changes in the wind speed from the fitted curve or a way to bound the values of wind speed.

Table D-2 shows the results from the wind speed analysis for the Calcasieu Lock east sector gate. Figure D-9 shows the fitted curve bounded by plus and minus 1, 2, and 3 standard deviations (σ) for the LCH airport wind data (n = 32). The standard deviation was determined to be 0.994 mph. The mean 100 yr return period wind speed was 42.5 mph. The use of the 100 yr return period plus 3 standard deviations gives a wind speed of 45.5 mph.

Table D-2. Results from wind speed analysis for the Calcasieu Lock east sector gate.

Statistic	100 yr Wind Speed (mph)
+3σ	45.5
+2σ	44.5
+1σ	43.5
Mean	42.5
−1σ	41.5
−2σ	40.5
−3σ	39.5

Figure D-9. Wind frequency curves based on peak yearly 0.5 hr average wind speed for the LCH airport data.

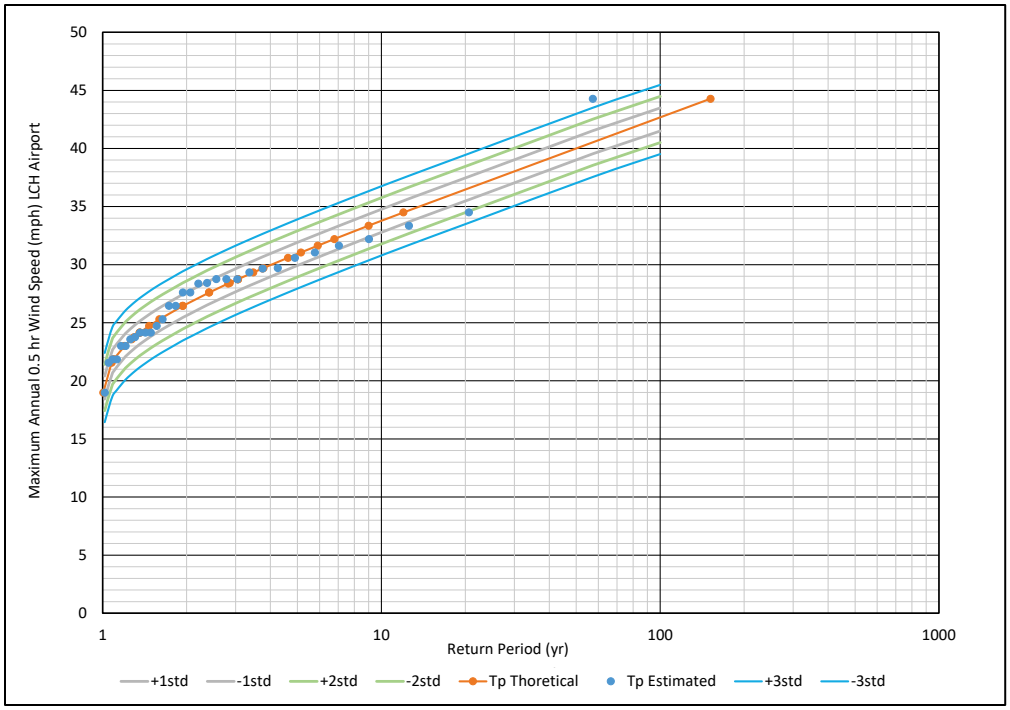

D.3.5 Wave Height and Period from the NARFET Model.

Table D-3 shows the input data and results from the use of the NARFET program for the Calcasieu Lock east sector gate. The program input requires the radial lengths of the fetch and the angle increments for resolution of the wind direction (Figure D-6). The radial lengths (a total of 22) determined for an angle increment of 6° are shown in Figure D-6. Figure D-10 shows the significant wave height and period for the wind speeds determined between −3σ and +3σ for the 100 yr return period. The wind direction was between 110° and 150° for a duration of 0.5 hr.

Table D-3. Wave height, period, and wavelength computed using the NARFET model for the Calcasieu Lock east sector gate.

Wind Speed (mph)	Wave Height (m)	Wave Period (sec)	Wave Length (m)
45.5	0.42	2.15	7.2
44.5	0.41	2.13	7.1
43.5	0.4	2.11	6.9
42.5	0.40	2.09	6.8
41.5	0.39	2.07	6.7
40.5	0.38	2.05	6.6
39.5	0.37	2.03	6.4

Note: Wind direction 110°–150°, duration 0.5 hr, angle increments 6°.

Figure D-10. Wind speed versus wave height from Smith's NARFET model for the Calcasieu Lock east sector gate.

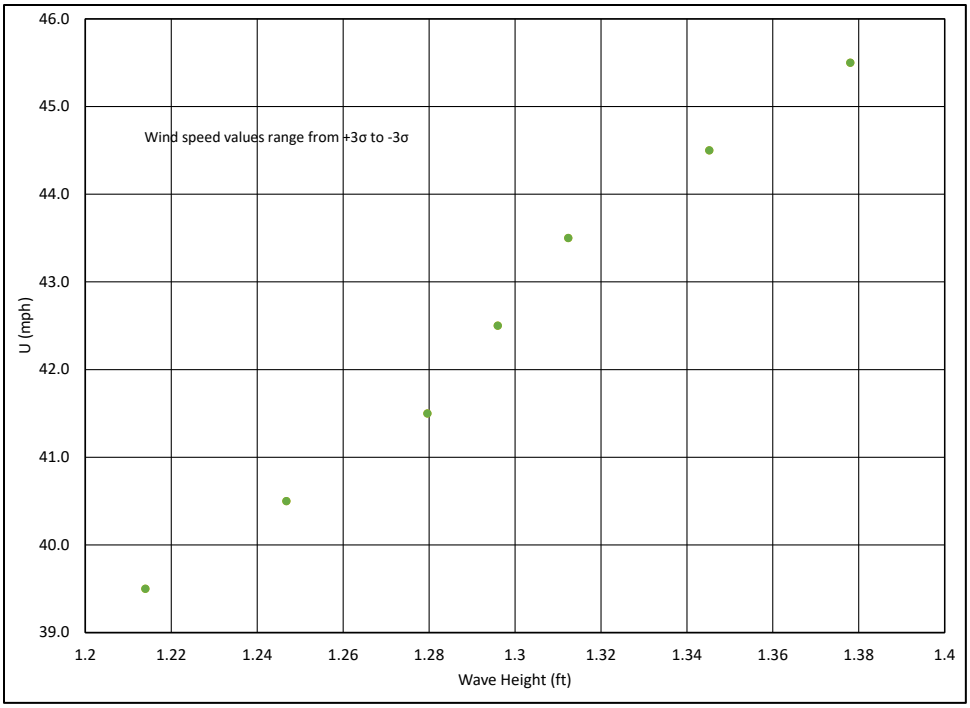

D.3.6 Wave Load from Goda for the Calcasieu Lock East Sector Gate

Goda (2010) recommended formulations for determining significant wave height and period based on wind speed and fetch. Chapter 2 provides background and supporting equations for his formulations. This methodology is applicable to the sector gate in the closed position. A plot of wind speed (U) versus wave height determined from Goda's recommended formulations from the statistical analysis of the wind speed data for the LCH airport is listed in Table D-4 and shown graphically in Figure D-11.

Table D-4. Significant wave height, period, and wavelength using Goda's (2010) formulations for the Calcasieu Lock east sector gate.

Wind Speed (mph)	Significant Wave Height (m)	Significant Wave Period (sec)	Significant Wave Length (m)
45.5	0.744	2.52	9.88
44.5	0.732	2.50	9.76
43.5	0.719	2.48	9.63
42.5	0.706	2.47	9.50
41.5	0.693	2.45	9.37
40.5	0.681	2.43	9.24
39.5	0.668	2.42	9.11

Figure D-11. Wind speed versus wave height from Goda's (2010) procedure for the Calcasieu Lock east sector gate.

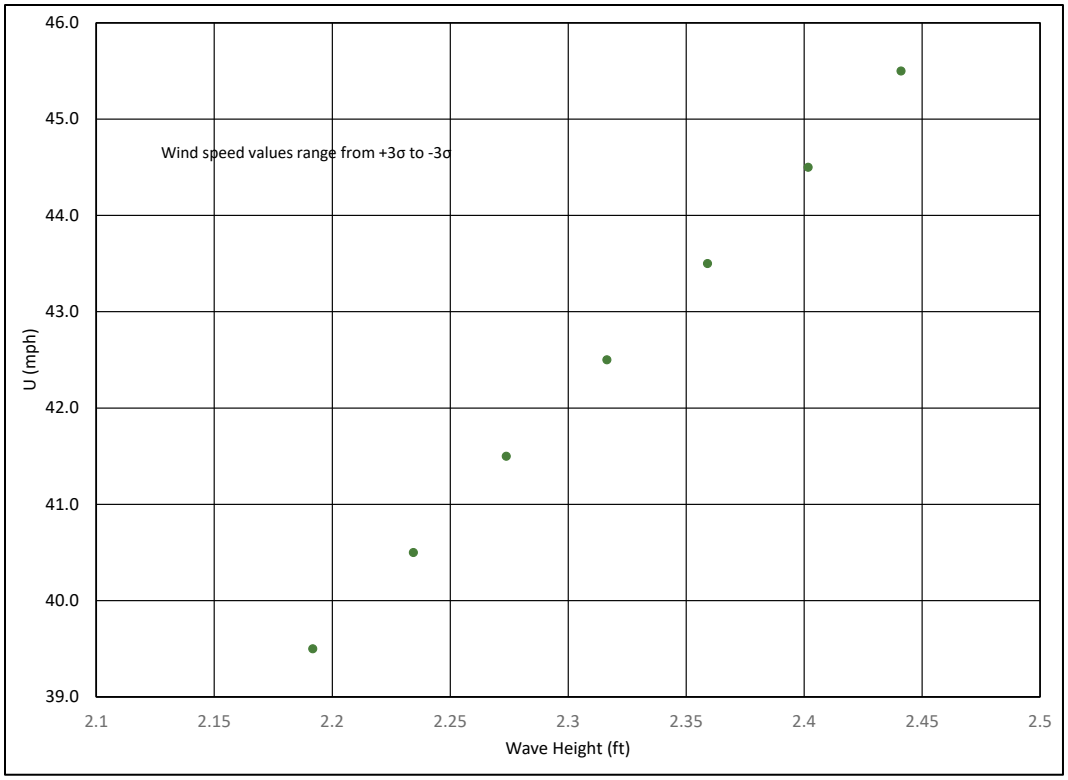

The wave pressure distribution and subsequent wave force for the sector gate can now be determined from the significant wave height and wave period. The complete description of this procedure is shown in Chapter 2, Section 2.3.2.3. Based on the parameters listed in Table D-4 and the Goda formulations in Section 2.3.2.3, an example solution was reached. Table D-5 lists the parameters used in the example wave force calculation (imperial and metric units included).

Table D-5. Parameters used in example wave force calculation (imperial and metric units included) for the Calcasieu Lock east sector gate for a wind speed of 42.5 mph.

Parameter	Value (Imperial Units)	Value (Metric Units)	Description
h_c	16.48 ft	5.02 m	Gate height above east side stage el
d (originally d_{SWL}, also H in Figure A-29)	13.52 ft	4.12 m	Difference between east side normal stage and sill el
h (originally h_{SWL})	15.52 ft	4.73 m	Difference between normal east side stage el and approach channel invert el (assumed 2 ft lower than sill)
tan θ	0	0	Bottom slope toward gate
β_D	0 deg	0 deg	Design incident wave angle
$H_{1/3}$	2.316 ft	0.706 m	Significant wave height for example problem
$T_{1/3}$	2.47 sec	2.47 sec	Significant wave period for example problem
L_D	31.2 ft	9.5 m	Design wave length for example problem
ρ	62.4 lb/ft^3	1,000 kg/m^3	Density of freshwater
g	32.2 ft/sec^2	9.81 m/sec^2	Acceleration due to gravity
h'	13.52 ft	4.12 m	For the sector gate: $h' = H = d_{SWL}$

The design wave height (H_D) is the minimum of $\alpha_h H_{1/3}$ and H_b, where α_h ranges from 1.6 to 2.0. For the design of nearshore vertical structures, Goda (2010) suggests using a value of 1.8 for α_h.

$$H_d = H_{Max} = \min\{\alpha_h * H_{1/3}, H_b\},$$

$$H_b = 0.17 * L_D \left\{1 - \exp\left[-1.5\frac{\pi h_b}{L_D}\left(1 + 15 * \tan^{\frac{4}{3}}\theta\right)\right]\right\},$$

where

$$h_b = h + 5 * H_{1/3} * \tan\theta.$$

Therefore,

$$\alpha_h H_{1/3} = 1.8 * 0.706 \text{ m} = 1.271 \text{ m (4.17 ft)},$$

$$h_b = 4.73 \text{ m} + 5 * 0.706 \text{ m} * \tan(0) = 4.73 \text{ m (15.52 ft)},$$

$$H_b = 0.17 * 9.5 \text{ m}\left\{1 - \exp\left[-1.5\frac{\pi 4.73 \text{ m}}{9.5 \text{ m}}\left(1 + 15 * \tan^{\frac{4}{3}}(0)\right)\right]\right\}$$
$$= 1.463 \text{ m (4.80 ft)}.$$

So,

$$H_d = H_{Max} = \min\{1.271 \text{ m}, 1.463 \text{ m}\} = 1.271 \text{ m (4.17 ft)}.$$

Next, we calculate the coefficients of wave pressure (α_1, α_2, and α_3) given in the equations that follow:

$$\alpha_1 = 0.6 + \frac{1}{2}\left[\frac{\frac{4\pi h}{L_D}}{\sinh\left(\frac{4\pi h}{L_D}\right)}\right]^2,$$

$$\alpha_2 = \min\left[\frac{h_b - d}{3h_b}\left(\frac{H_D}{d}\right)^2, \frac{2d}{H_D}\right],$$

$$\alpha_3 = 1 - \frac{h'}{h}\left[1 - \frac{1}{\cosh\left(\frac{2\pi h}{L_D}\right)}\right].$$

The h and d values in the preceding equations are, respectively, equivalent to the h_{SWL} and d_{SWL} of Table D-5. Substituting the values gives

$$\alpha_1 = 0.600 \text{ (from Equation 56)},$$

$$\alpha_2 = \min[0.0041 \text{ m}, 6.153 \text{ m}] = 0.0041 \text{ (from Equation 57)},$$

and because $h' = d_{SWL} = H$,

$$\alpha_3 = 0.206 \text{ (from Equation 58)}.$$

The lateral pressure components P_1 and P_3 (from Equations 52 and 54) are evaluated here:

$$P_1 = 0.5\,(1 + \cos\beta_D)\,(\alpha_1 + \alpha_2 * \cos^2\beta_D)\,\rho * g * H_D,$$

$$P_3 = \alpha_3 P_1.$$

The solutions to P_1 and P_3 are

$$P_1 = 7{,}535 \text{ N/m}^2 = 7.535 \text{ kN/m}^2 = 157.35 \text{ (lb/ft}^2\text{)},$$

$$P_3 = 1{,}550 \text{ N/m}^2 = 1.550 \text{ kN/m}^2 \text{ (32.36 lb/ft}^2\text{)}.$$

The total lateral force per linear width (F_{Lat}) on the face of the sector gate is

$$F_{Lat} = 0.5(P_1 + P_3)H + 0.5(P_1 + P_4)h_c',$$

where

$$P_4 = P_1\left(1 - \frac{h_c}{\eta^*}\right), \text{if } \eta^* > h_c,$$

or

$$P_4 = 0, \text{ if } \eta^* \leq h_c,$$

$$\eta^* = 0.75(1 + \cos(\beta_D))H_D,$$

$$h_C' = \min\{\eta^*, h_C\}.$$

Therefore, the solution for the resultant force, F_{Lat}, is given as

$$h_c = 5.02 \text{ m } (16.47 \text{ ft}) \text{ (from Table D-5)},$$

$$\eta^* = 1.906 \text{ m } (6.25 \text{ ft}).$$

Because $\eta^* < h_c$,

$$P_4 = 0 \text{ kN/m}^2 \text{ } (0 \text{ lb/ft}^2),$$

$$h_C' = \min\{1.906 \text{ m}, 0.502 \text{ m}\} = 1.906 \text{ m } (6.25 \text{ ft}),$$

$$F_{Lat} = 37.62 \text{ kN/m } (2{,}578 \text{ lb/ft}).$$

The preceding analysis indicates the total lateral wave force per linear width of the sector gate for a sustained 42.5 mph wind is 2,578 lb/ft. The same analysis done for a 39.5 mph sustained wind showed the total lateral wave force to be 2,428 lb/ft.

In Figure B-13 and Figure B-14 the pressure terms P_1, P_3, and P_4 are shown acting on the vertical-lift gate. This method is also applicable to the sector gate. In this case, because $\eta^* < h_c$, h_4 is equal to $h_1 + \eta^*$. The location of the lateral equivalent force (h_{Lat}) can be determined using the one-third/one-

sixth method developed by Ebeling et al. (2018) and presented in Chapter 2, Section 2.3.2.4, of this report. By applying this method for the lateral forces and summing moments about point 3, Equation (A.14), which is repeated here, was developed:

$$h_{Lat} = \frac{(h_4 - h_1)\left(\frac{P_4}{3} + \frac{P_1}{6}\right)h_4 + (h_4 - h_1)\left(\frac{P_4}{6} + \frac{P_1}{3}\right)h_1 + (h_1 - h_3)\left(\frac{P_1}{3} + \frac{P_3}{6}\right)h_1}{F_{Lat}},$$

$$h_{Lat} = \frac{1.906\text{ m}\left(\frac{7.535\frac{\text{kN}}{\text{m}^2}}{6}\right)6.026\text{ m} + 1.906\text{ m}\left(\frac{7.535\frac{\text{kN}}{\text{m}^2}}{3}\right)4.12\text{ m}}{37.626\frac{\text{kN}}{\text{m}}},$$

$$h_{Lat} = \frac{+ 4.12\text{ m}\left(\frac{7.535\frac{\text{kN}}{\text{m}^2}}{3} + \frac{1.55\frac{\text{kN}}{\text{m}^2}}{6}\right)4.12\text{ m}}{37.626\frac{\text{kN}}{\text{m}}},$$

$$h_{Lat} = 2.157\text{ m}.$$

The wave forces and pressure distributions computed from Goda's (2010) procedure for the data in Table D-4 are shown in Table D-6. The definition of Goda's parameters found in Table D-5 and used in the preceding equations above are illustrated in Figure B-13 and Figure B-14.

Table D-6. Wave force and pressure distribution computations using Goda's (2010) procedure for the Calcasieu Lock east sector gate.

	Statistic						
Calcasieu Lock Data	+3σ	+2σ	+1σ	Mean	−1σ	−2σ	−3σ
Wind Speed (mph)	45.5	44.5	43.5	42.5	41.5	40.5	39.5
η^* (m)	2.009	1.976	1.941	1.906	1.871	1.839	1.804
P_1 (N/m^2)	7,948	7,817	7,676	7,535	7,393	7,263	7,123
P_3 (N/m^2)	1,714	1,654	1,594	1,550	1,493	1,440	1,399
P_4 (N/m^2)	0	0	0	0	0	0	0
F_{Lat} (kN/m)	39.85	39.13	38.36	37.62	36.86	36.16	35.43
h_{Lat} (m)	2.154	2.155	2.156	2.157	2.158	2.159	2.16
h_{Lat} (ft)	7.065	7.069	7.073	7.075	7.079	7.083	7.085
P_1 (lb/ft^2)	166	163	160	157	154	152	149
P_3 (lb/ft^2)	36	35	33	32	31	30	29
P_4 l(b/ft^2)	0	0	0	0	0	0	0
F_{Lat} (lb/ft)	2,731	2,681	2,629	2,578	2,525	2,478	2,428

D.4 Hydrodynamic Loads on Sector Gates for the Calcasieu Lock East Sector Gate

An example of determining the pertinent hydraulic data to compute the hydrodynamic load for the Calcasieu Lock east sector gate is discussed subsequently. The hydrodynamic force on the sector gate is the pintle torque. For typical design cases, the closing pintle torque during a reverse head is usually considered the design case.

Typically, the peak hydrodynamic torque is obtained using Oswalt and Murphy (1971, Appendix A, plate A4 Figure A) with correction factors to account for the difference in the geometry between the sector gate in the model study and the sector being evaluated. The geometry of the model sector gate (1:20-scale) converted to prototype dimensions were gate radius 42 ft and total projected width of miter beam, skin plate rib, and seal bracket of 30.375 in.

USACE-MVN was asked to collect information about the hydrodynamic loads for the Calcasieu Lock sector gate. They indicated that EM 1110-2-2610 (HQUSACE 2013) states the following:

> For gates varying considerably from the type shown in the report, initial load estimates prior to completion of a model study can be calculated assuming a linear profile between pool-to-pool water elevations across the channel side face of the total projected width of the miter beam, skin plate rib, and seal bracket and the reverse head water elevation on the recess side of the same components. (5-6)

As such, the estimated closing force would be half the differential reverse head acting on the projected width of those components over the average submerged height of the miter beam.

The hydrodynamic load was computed by USACE-MVN assuming an average differential head across the 4 ft wide end of the gate is 2.5 ft. This was based on a water elevation of 5.0 on the recessed end and 2.5 on the miter end. The lower elevation on the miter end results from water flowing from a water elevation of 5.0 to a water elevation of 0, which gives an average water elevation of 2.5. The distance from the centerline of the hinge and

pintle to the centerline of the 4 ft wide end beam is 66.9 ft. USACE-MVN provided the equation that follows to compute the pintle torque:

$$\text{Hydrodynamic torque} = \Delta H(\gamma)(\text{area at end})(\text{lever arm}), \quad \text{(D.1)}$$

where

ΔH = the average differential head across the ends of the gate = 2.5 ft,
γ = the unit weight of water = 62.4 lb/ft^3,
Area at the end of beam = water depth × width of the end section = (2.5 ft/2 + 16 ft) × 4 ft, and
Lever arm = the distance from the centerline of the hinge and pintle to centerline of the 4 ft wide end beam = 66.9 ft.

Using a differential head of 2.5 ft across the wide ends, the hydrodynamic pintle torque is

$$[2.5 \text{ ft } (62.4 \text{ lb/ft}^3)(2.5 \text{ ft}/2 + 18.5 \text{ ft})(4\text{ft})(66.9 \text{ ft})]/1{,}000 = 824.5 \text{ ft-kip}$$

This equation gives similar results to the procedures provided in EM 1110-2-2610 (HQUSACE 2013) if the service factor of 1.5 mentioned in the manual is used.

D.5 Probabilistic Characterization of the Hydrostatic and Hydrodynamic Loads for the Calcasieu Lock East Sector Gate

Statistics for the hydraulic loads on the Calcasieu Lock east sector gate need to be determined for the LRFD analysis.

D.5.1 Probabilistic Characterization of the Hydrostatic Load on the East Sector Gate

The dispersion of the hydrostatic load on the east sector gate is due to the changes in the stages on the east and west sides of the lock. The computation of the changes in hydrostatic load on the east gate require the selection of an appropriate range of east and west stage fluctuations.

The standard deviation (σ) of the head on the east sector gate determined for the period between 2004 and 2022 was 0.839 ft. The mean stage on

the east side of the lock for this period was el 2.317. The mean stage on the west side was essentially the same as the east side, so the head with a mean east side stage of el 2.317 was zero. The hydrostatic load on the gate consists of the increasing hydrostatic pressure with depth until the west side stage is reached and then a constant hydrostatic pressure between the water surface and the sector gate sill el.

Table D-7 shows the hydrostatic loads per foot of sector gate for the range of heads between +3σ and −3σ around the mean east side stage of 2.317. The total hydrostatic load on the gate consists of the varying hydrostatic load due to the difference in the east and west stages plus the constant hydrostatic force from the water surface to the sector gate sill el. For these computations, the west side stage was considered constant at el 2.317, so a reverse head condition resulted with deviations below the mean east side stage.

Table D-7. Hydrostatic forces computed for the Calcasieu Lock east sector gate for the range of heads from +3σ to −3σ around the mean head.

−3σ (lb/ft)	−2σ (lb/ft)	−σ (lb/ft)	Mean (lb/ft)	+σ (lb/ft)	+2σ (lb/ft)	+3σ (lb/ft)
1,530*	1,152*	493*	0	730	1,503	2,321

*Reverse head condition

For example, to obtain the total hydrostatic force per foot of gate for the +3σ head condition,

$$H = +\,3\sigma \text{ head} = 3 * 0.839 = 2.517 \text{ ft},$$

$$\text{East side stage} = 2.517 + 2.317 = 4.834,$$

$$\text{West side stage} = 2.317,$$

$$h = \text{west side stage to sector gate sill} = 2.517 - (-11.2) = 13.517 \text{ ft},$$

$$H_s = (0.5(\gamma H^2)) + (\gamma H)\text{h} = (0.5(62.4 \text{ lb/ft}^3 * (2.517\text{ft})^2)) + 62.4 \text{ lb/ft}^3 * 2.517 \text{ ft} * 13.517 \text{ ft} = 2{,}321 \text{ lb/ft}.$$

H_s acts at the centroid of the pressure distribution.

D.5.2 Probabilistic Characterization of the Hydrodynamic Load on the East Sector Gate

The dispersion of the hydrodynamic load on the east sector gate based on Equation (D.1) is due to the changes in the east and west stages, which give different values of differential head. Computing the pintle torque using the procedures in Appendix C of EM 1110-2-2610 (HQUSACE 2013) or Equation (D.1) of this report is probably adequate for initial design estimates; however, the authors recommend more efforts be considered to advance these techniques. Additional laboratory, field, and numerical investigations could be performed to help predict the hydrodynamic loads on the sector gate. If the LRFD method is used to design future sector gates and no advancement in the current procedures to compute hydrodynamic loads has been made, the designer will need to select the range of conditions needed to develop the dispersion of the hydrodynamic loads.

D.6 Summary of Hydraulic Loads for the Calcasieu Lock East Sector Gate

The hydraulic loads on the sector gate consist primarily of the hydrostatic, wave, and hydrodynamic loads. Table D-8 lists example hydraulic loads determined for the Calcasieu Lock east sector gate.

Table D-8. Example hydraulic loads for the Calcasieu Lock east sector gate.

Estimated Hydraulic Load	Value
Hydrostatic (lock dewatered no bulkheads)	5.7 kips/ft
Hydrodynamic * (pintle torque)	824.5 Ft-kips
Wave**	2.578 kips/ft
Hydrostatic + Wave	8.278 kips/ft

* Based on an average differential head of 2.5 ft with a reverse head of 5 ft – from USACE-MVN.

** Based on a mean east side stage of 2.317 and 42.5 mph wind speed at 130° (Mean 100 yr wind event). $P_1/P_3 = 4.90$.

Appendix E: Example Hydraulic Load Computations for the Barkley Lock Miter Gates

In this appendix, the procedures discussed in Chapter 6 of the main report are presented using data from an existing USACE Navigation project. The data needed to quantify the hydraulic loads for the lock miter gate and example computations are described.

E.1 The 30 yr Record of Hydrologic Data for the Barkley Lock and Dam (BLD)

The Barkley Lock and Dam (BLD) project on the Cumberland River was chosen to illustrate how to determine the hydraulic loads on a lock miter gate. USACE, Nashville District (USACE-LRN), provided a 30 yr record of hydraulic data from January 1989 through August 2020. The data included forebay el, TW El, discharge, and gate settings for the spillway. The Barkley reservoir is held at el 354.0 during the flood season, is filled to el 359.0 in the spring, and is gradually lowered back to el 354.0 during the summer and fall. Drawdown of the reservoir to as low as 346.0 in advance of an anticipated flood occurs. The pertinent project-specific data for the analysis are listed here:

- Upper miter sill el = 333.0
- Lower miter sill el = 289.0
- Top girder el = 377.75
- Maximum lift (el 375.0 – el 302.0) = 73 ft
- Maximum normal lift (el 359.0 – 302.0) = 57 ft
- Lift at flood control pool (375.0 – el 333.0) = 42 ft
- Summer and fall normal upper pool el operating range = 354.0
- Range of normal operations = 346.0 to 359.0

Figure E-1 shows a view looking upstream of the Barkley Lock upper miter gate, and Figure E-2 shows a view looking upstream of the Barkley Lock lower miter gate. According to USACE-LRN's (1958) Design Memorandum 9, the miter gate is horizontally framed and was designed as a series of three hinged arches. Water loads are transmitted to the girder by the skin plate, and the arch reactions are taken into the lock walls by the quoin posts.

Figure E-1. Looking upstream at the frame side of the upper Barkley Lock miter gate.

Figure E-2. Looking upstream at the frame side of the Barkley Lock lower miter gate.

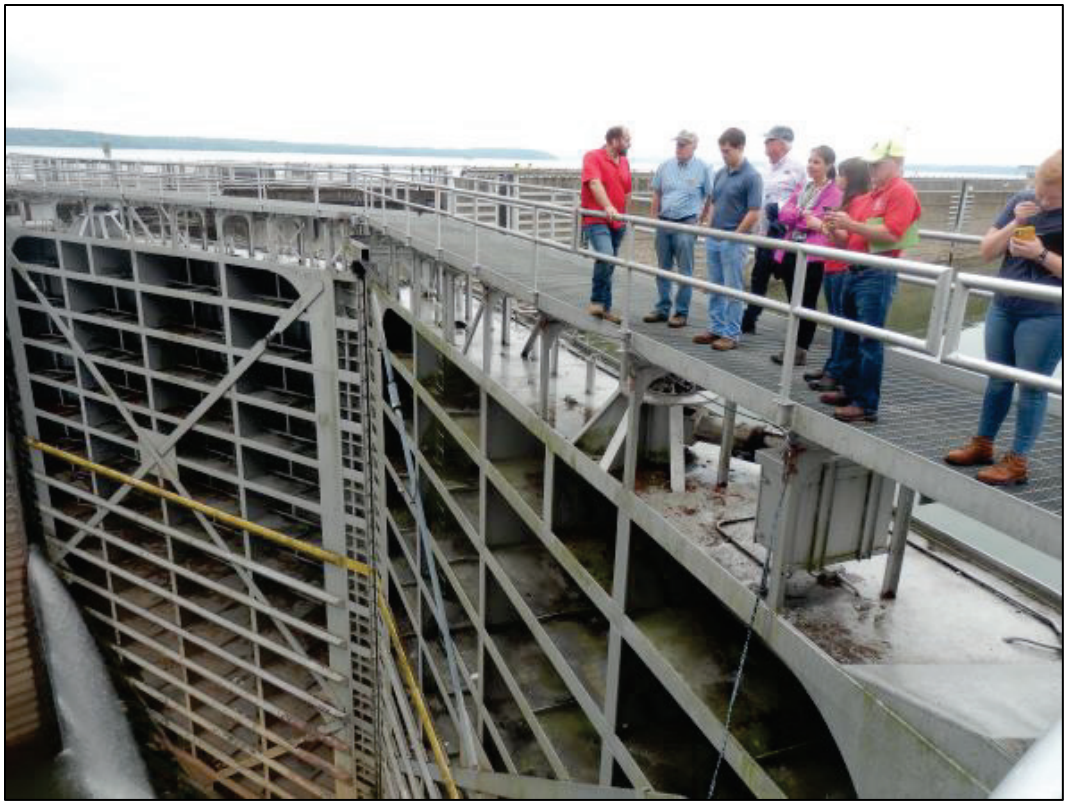

E.1.1 Forebay Statistics for the Barkley Lock Upper Miter Gate

The upper pool el, also referred to as the forebay el, is one of the primary variables that affects the load on the lock miter gate. Figure E-3 shows a histogram of the forebay el over the 31 yr period. The mean forebay el was 357.04, the maximum el was 372.5, and the minimum el was 353.26. The standard deviation was 2.21 ft. The histogram shown in Figure E-3 represents the number of occurrences of forebay in the selected range.

There are 39 bins, each with a bin width of 0.50 ft. The area of each bin was computed, and the total area was determined by summing the individual bin areas. These areas were normalized by dividing each individual area by the total area to give the PDF shown in Figure E-4. A CDF was developed by cumulatively summing the normalized areas of the PDF (Figure E-5).

Figure E-3. Histogram of forebay el from 1989 through 2020 for the upper lock gate.

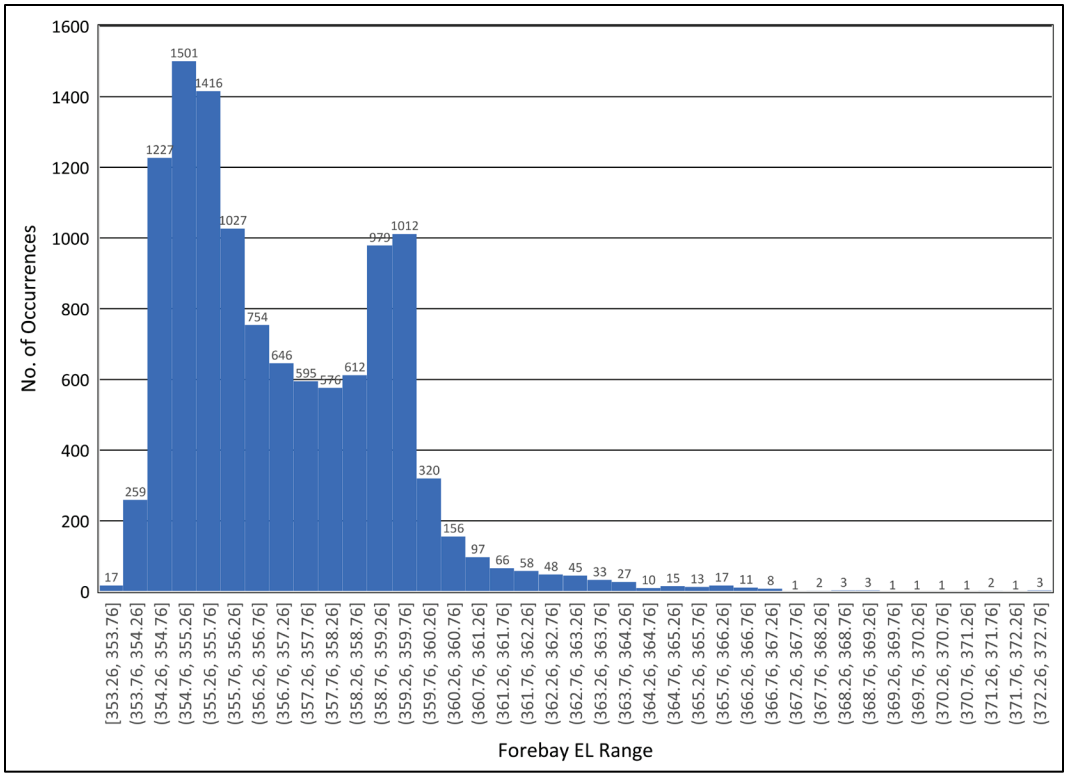

Figure E-4. PDF from histogram of forebay el for the upper lock gate.

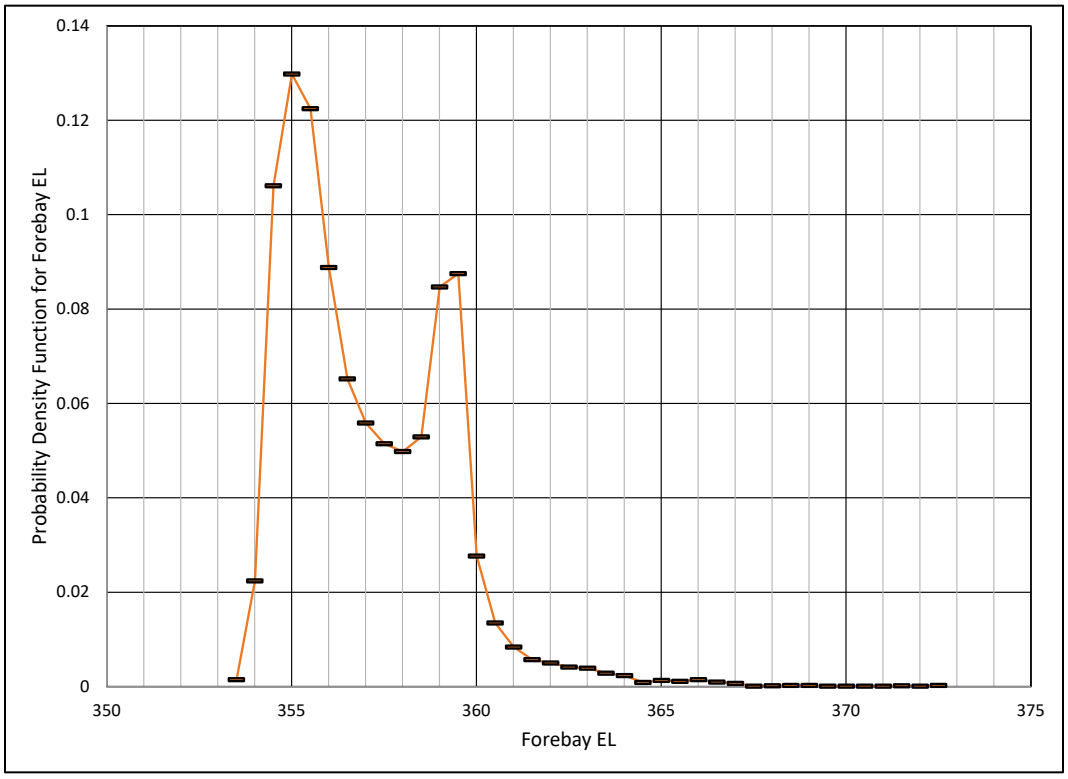

Figure E-5. CDF for forebay el for the upper lock gate.

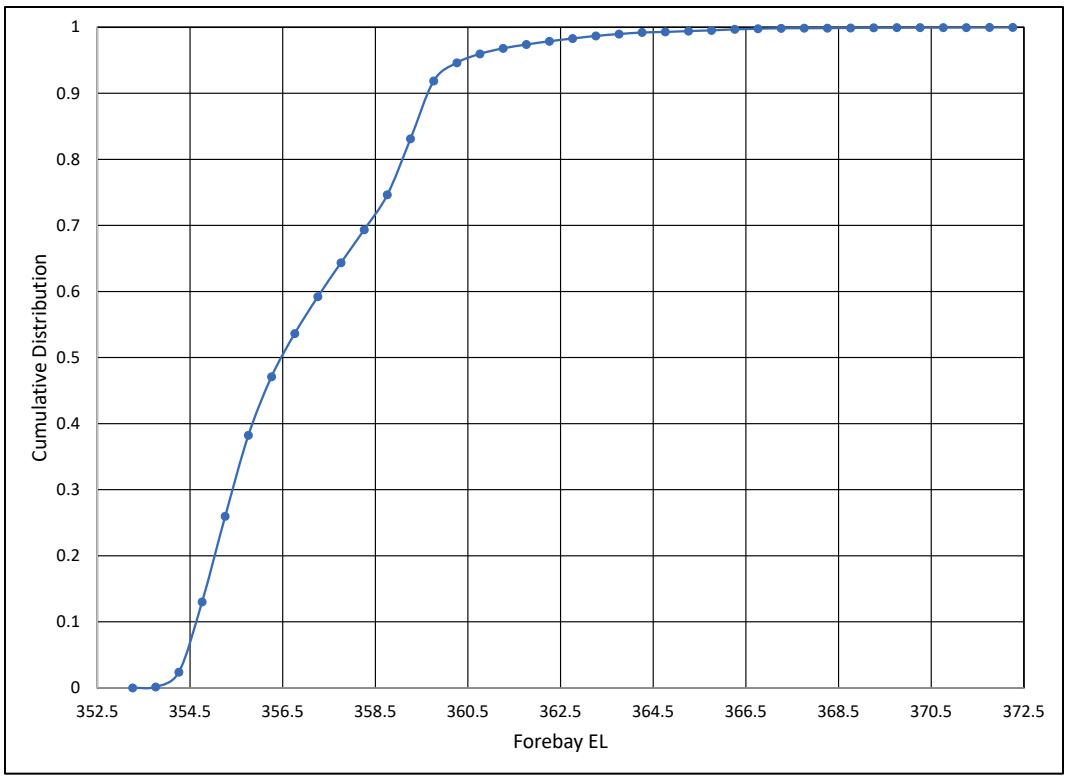

E.1.2 Tailwater Statistics for the Barkley Lock Lower Miter Gate

A histogram, PDF, and CDF were also computed for the TW El at Barkley lower miter gate. Figure E-6 shows a histogram of the TW El over the 31 yr period. The mean TW El was 314.78, the maximum el was 350.75, and the minimum el was 300.9. The standard deviation was 9.51 ft.

The histogram contains 50 bins, each with a bin width of 1.0 ft. The area of each bin was computed, and the total area was determined by summing the individual bin areas. These areas were normalized by dividing each individual area by the total area to give the PDF shown in Figure E-7. A CDF was developed by cumulatively summing the normalized areas of the PDF (Figure E-8).

Figure E-6. Histogram of TW El between 1989 and 2020 for the lower lock gate.

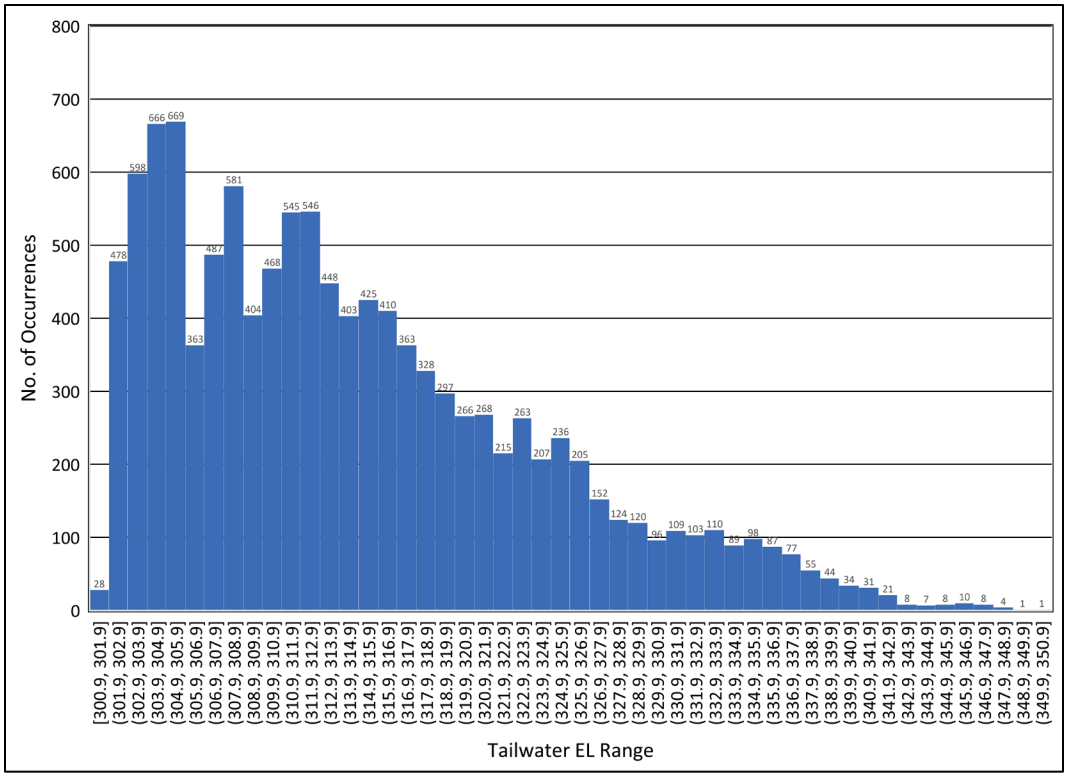

Figure E-7. PDF from the histogram of TW El for the lower lock gate.

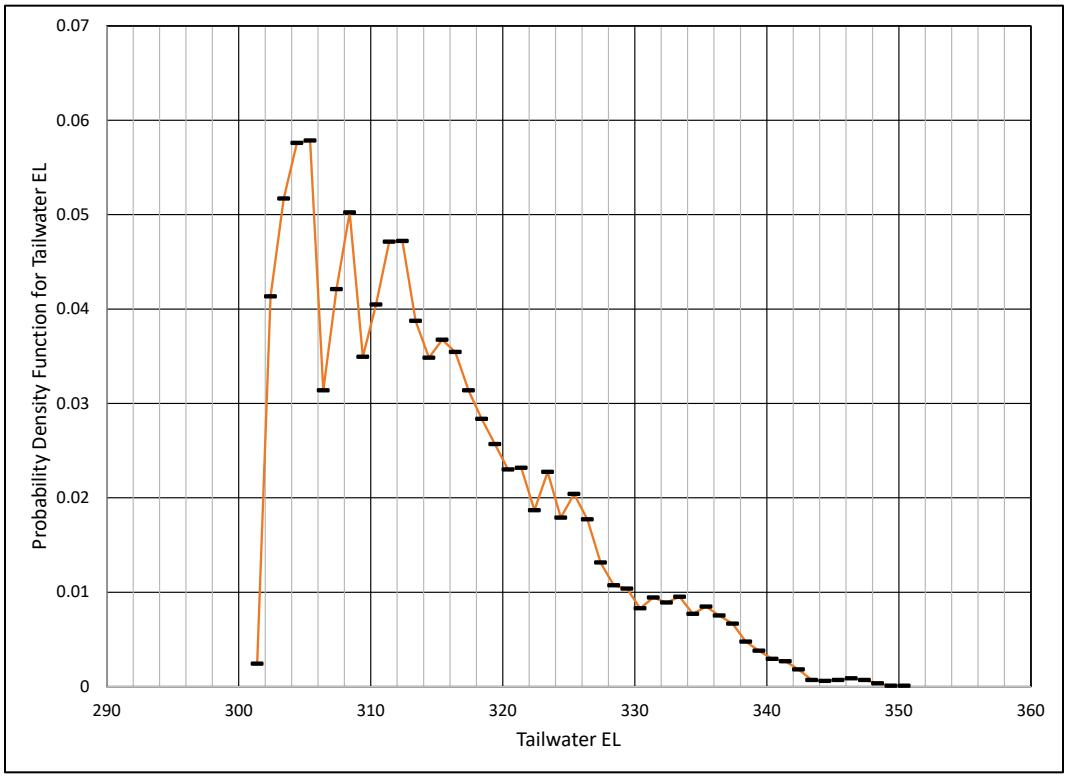

Figure E-8. CDF for TW El for the lower lock gate.

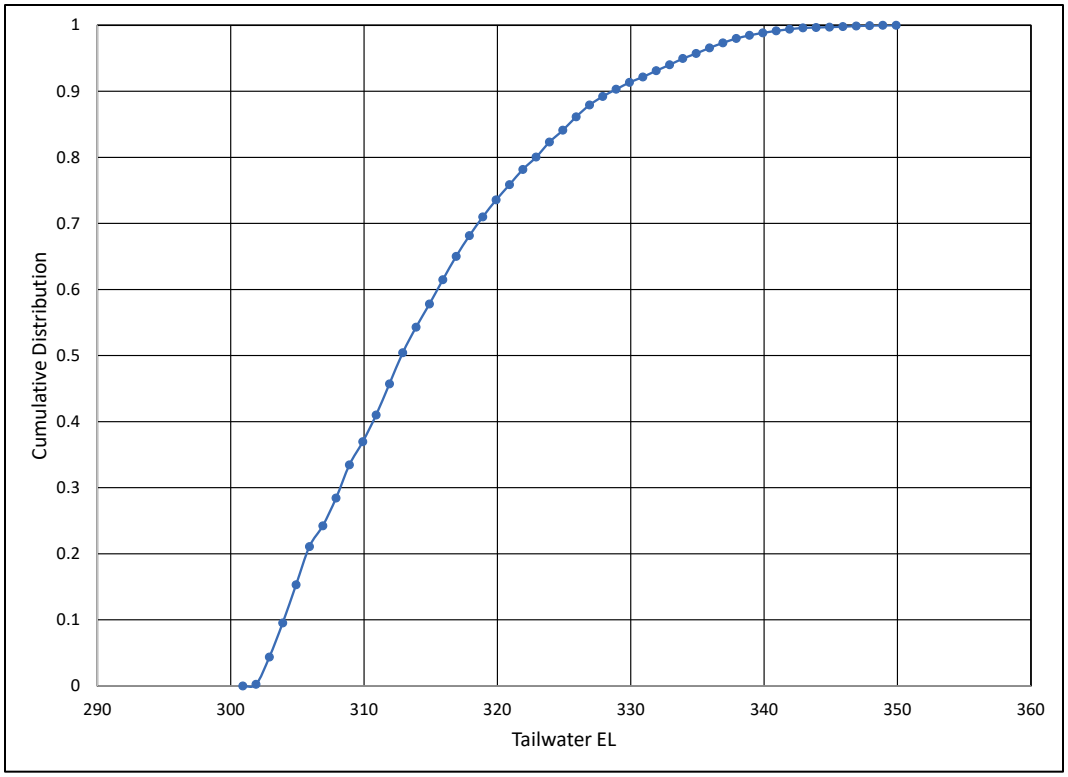

E.2 Hydrostatic Load for the Barkley Lock Gates

E.2.1 Hydrostatic Load for the Barkley Upper Lock Gate

Equation (10), which is repeated here, is a conventional equation that is found in many fluid mechanics and hydraulics textbooks and can be used to compute the hydrostatic pressure (p). As stated previously, γ is the unit weight of water, and y is the vertical distance from the water surface to the location of the hydrostatic pressure of interest (Figure 65):

$$p = \gamma y.$$

The horizontal hydrostatic pressure on the upper miter gate is expressed as γH, where γ is the unit weight of water, and H is the difference between the upper pool and the upper lock sill els. To obtain the force, the hydrostatic pressure is multiplied by the area the pressure is acting on. The hydrostatic force per unit width of miter gate is given by Equation (12), which is repeated here:

$$H_s = \frac{1}{2}\gamma H^2.$$

The resultant hydrostatic force per foot of width for the upper miter with the normal upper pool using the following parameters is

$$\gamma = \text{unit weight of water} = 62.4 \text{ lb/ft}^3,$$

$$H = \text{head on upper gate (normal)} = 359 - 333 = 26 \text{ ft},$$

$$H = \text{head on upper gate (maximum)} = 375 - 333 = 42 \text{ ft}.$$

The normal hydrostatic load (upper gate) is then

$$0.5 \, [62.4 \text{ lb/ft}^3 * (26.00 \text{ ft})^2] = 21{,}091 \text{ lb/ft},$$

and the maximum hydrostatic load (upper gate) is

$$0.5 \, [62.4 \text{ lb/ft}^3 * (42.00 \text{ ft})^2] = 55{,}037 \text{ lb/ft}.$$

The resultant hydrostatic force is located $H/3$ above the upper lock sill shown in Figure 65. The maximum hydrostatic load for the upper gate is experienced if the upper pool is at the top of the flood control pool (el 375) and the tailwater is below the upper lock sill (el 333). This load condition represents H_1 (i.e., the maximum net hydrostatic load that will ever occur for the upper gate).

E.2.2 Hydrostatic Load for the Barkley Lower Lock Gate

The resultant hydrostatic force per foot of width for the lower miter gate with the normal upper and lower pool using the following parameters is

$$H = \text{head on lower gate (normal)} = 359 - 302 = 57 \text{ ft},$$

$$H = \text{head on lower gate (maximum)} = 375 - 302 = 73 \text{ ft},$$

$$\text{Normal hydrostatic load (lower gate)} = 0.5 \, [62.4 \text{ lb/ft}^3 * (57.0 \text{ ft})^2] = 101{,}369 \text{ lb/ft},$$

$$\text{Maximum hydrostatic load (upper gate)} = 0.5 \, [62.4 \text{ lb/ft}^3 * (73.0 \text{ ft})^2] = 166{,}265 \text{ lb/ft}.$$

E.3 Wave Load Based on Wave Height and Period for the Barkley Lock Gates

The dispersion due to the wave load about the mean hydrostatic load needs to be determined. The procedures and methods used to determine wave load for the spillway vertical-lift gate that were presented in Chapter 3 and Appendix B were used for the miter gates. The supporting data and computations used to determine the load for the Barkley project are presented in the sections that follow. As mentioned previously, developing a wave load requires determining the wind speed, wind direction, and fetch.

E.3.1 Wind Speed and Fetch for the Barkley Upper Lock Gate

The wind speed and wind direction data were obtained from meteorological data collected over a 24 yr period between 1991 and 2020 at the Barkley Regional Airport (PAH) near Paducah, Kentucky. Wind data for the years 2001–2006 were not available. The PAH is located approximately 30 mi west of the project. Figure E-9 shows the data collection site in relation to the Barkley Lock project.

Figure E-9. Satellite imagery showing the wind speed and direction data collection site in relation to the Barkley Lock. (Map data: Landsat/Copernicus 2002.)

The dataset was fairly complete for the period of 2015 to August 2020, and wind speeds and directions were reported multiple times per hour.

Between 1991 and 2015, the wind speed and direction were usually reported on an hourly basis. The latitude of the airport is 37.0563, and the longitude is −88.7744. Data were obtained from Iowa State University (n.d.).

Figure E-10 shows the fetch determined for the BLD project. The wind direction that impacts the project perpendicular to the center of the upper miter gates is 154°. The fetch is approximately 0.98 mi.

Figure E-10. Fetch and wind direction determined for the Barkley upper miter gate.

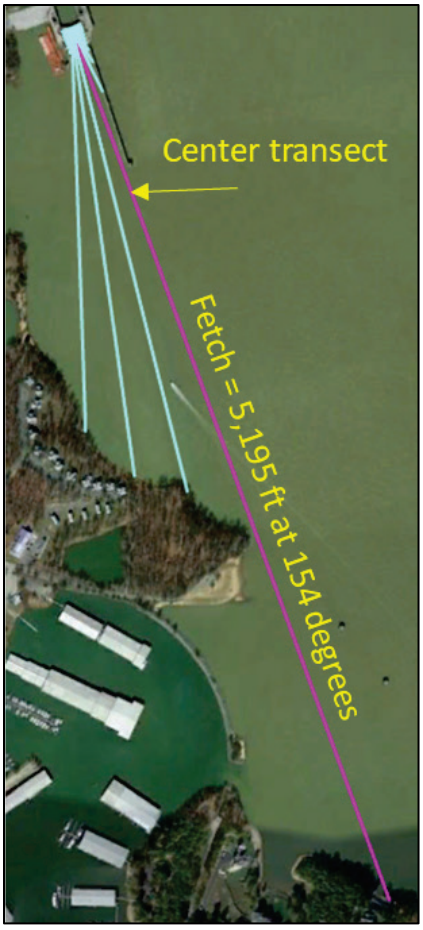

E.3.2 Wind Speed Analyses for the Barkley Lock Upper Gate

The methods used to determine the appropriate wind speed for the analyses of the wave load developed in the previous appendixes were also used for the Barkley upper lock gate. Based on the fetch length and wind speed, Equation (50), which is repeated here, can be used to determine the time required for full wave growth:

$$t_{min} = 1.0F^{0.73}U_{10}^{-0.46}.$$

Using an estimated wind speed between 30 and 40 mph and a fetch length of 0.98 mi, the minimum time to reach full wave growth was around 45 min, so a t_{min} value of 1 hr was used in the analysis. These values were considered conservative for the upper lock gate. Equation (50) requires metric units. The wind speed data were then processed to determine the maximum 1 hr average wind speed with a wind direction between 140° and 180° per year. Table E-1 shows the wind speed values used in the analyses.

Table E-1. Maximum yearly 1 hr average wind speed for wind directions between 140° and 180° at the Barkley Regional Airport (PAH) for the observation period from 1991 and 2020 and used for the Barkley Lock upper miter gate.

Year	Max 1 hr Avg Wind Speed (mph)
1991	26.5
1992	28.2
1993	31.6
1994	25.3
1995	23.9
1996	26.5
1997	23.6
1998	23.6
1999	17.3
2000	16.1
2007	20.1
2008	27.6
2009	27.0
2010	21.0
2011	19.9
2012	20.7
2013	26.8
2014	22.4
2015	26.5
2016	20.3
2017	17.4
2018	18.6
2019	21.7
2020	20.7

E.3.3 Extreme Value Estimation Using Maximum 1 hr Average Yearly Values of Wind Speed for the Barkley Lock Upper Gate.

The type 1 Gumbel distribution was used for a GEV analysis. Figure E-11 shows the results from the extreme value estimation using the maximum 1 hr average annual values for the PAH data. The 100 yr recurrence interval wind speed from this analysis was 39.5. The magnitude of the 100 yr recurrence interval for wind speed was considered a suitable frequency for wave height calculations.

Figure E-11. Extreme wind speed estimation for Barkley Regional Airport (PAH) based on maximum 1 hr average annual values of wind speed and used for the Barkley Lock upper miter gate.

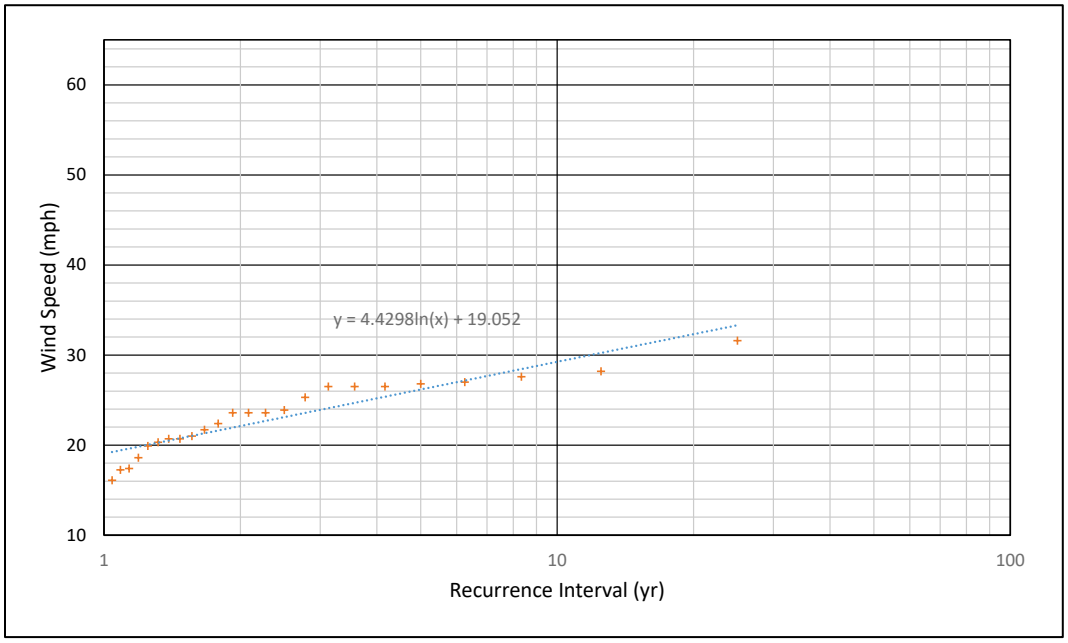

E.3.4 Wind Frequency Based on Gumbel Type 1 Distribution with Gringorten's Method Using Maximum Yearly 1 hr Average Values of Wind Speed for the Barkley Lock Upper Miter Gate.

The type 1 Gumbel distribution can be used with Gringorten's (1963) plotting position formula to create another method for evaluating wind speed. A description of this procedure is given in Chapter 2. Figure E-12 shows a plot of the return period versus wind speed determined using this procedure for the data from the PAH. The wind speed for the 100 yr return period was 36.3 mph.

Figure E-12. Wind frequency from Gumbel type 1 distribution with Gringorten's method for PAH using the maximum 1 hr average annual wind speed and used for the Barkley Lock upper miter gate.

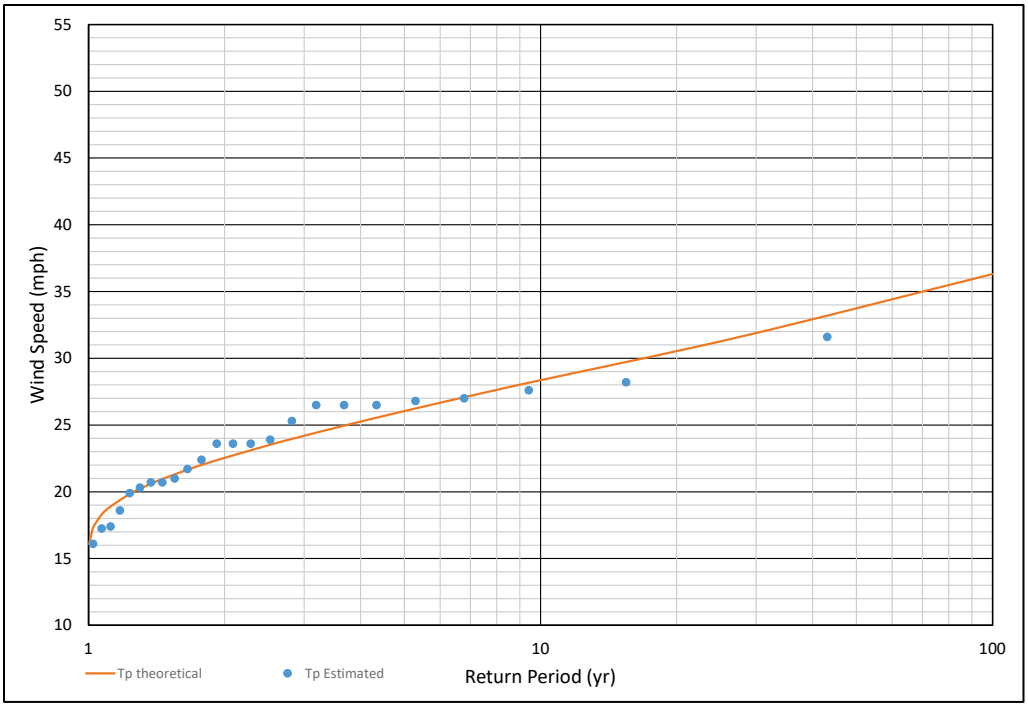

To further investigate the statistics for the wind speed, a formula to determine the standard error (discussed in Appendix A) was used for the data presented in Figure E-12.

Figure E-13 shows the fitted curve bounded by plus and minus 1, 2, and 3 standard deviations (σ) for the PAH wind data (n = 24). Table E-2 shows the values for these statistics. The mean 100 yr return period wind speed was 36.3 mph. The standard deviation was determined to be 1.004 mph. The use of the 100 yr return period plus 3 standard deviations gives a wind speed of 39.3 mph.

Table E-2. Results from wind speed analysis for the Barkley Lock upper miter gate.

Statistic	100 yr Wind Speed (mph)
+3σ	39.3
+2σ	38.3
+1σ	37.3
Mean	36.3
−1σ	35.3
−2σ	34.3
−3σ	33.3

Figure E-13. Wind frequency curves based on peak yearly 1 hr average wind speed for the PAH data and used for the Barkley Lock upper miter gate.

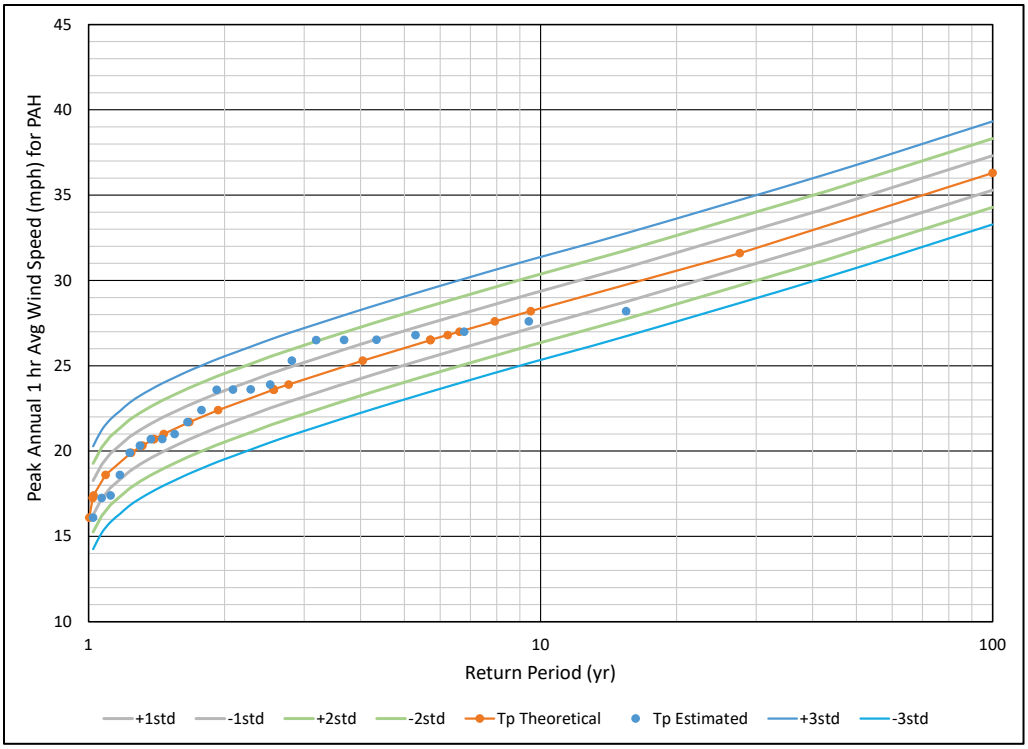

E.3.5 Wave Height and Period from the NARFET Model for the Barkley Lock Upper Miter Gate

Table E-3 shows the input data and results from the use of the NARFET program for the Barkley Lock upper miter gate. The program input requires the radial lengths of the fetch and the angle increments for resolution of the wind direction, as depicted in Figure E-10. Figure E-10 shows the radial lengths (a total of 31) determined for an angle increment of 6°. The significant wave height and period for the wind speeds determined between −3σ and +3σ for the 100 yr return period shown in Figure E-13 are listed in Table E-3. Figure E-14 shows a plot of the wind speed versus wave height. The wind direction was between 140° and 180° for a duration of 1 hr.

Table E-3. Wave height, wave period, and wavelength computed using the NARFET model for the Barkley Lock upper miter gate.

Wind Speed (mph)	Wave Height (m)	Wave Period (sec)	Wavelength (m)
39.3	0.47	2.23	7.8
38.3	0.46	2.21	7.6
37.3	0.45	2.19	7.5
36.3	0.44	2.16	7.3
35.3	0.43	2.14	7.1
34.3	0.42	2.11	7.0
33.3	0.40	2.09	6.8

Figure E-14. Wave height versus wind speed from Smith's NARFET model for the Barkley Lock upper miter gate.

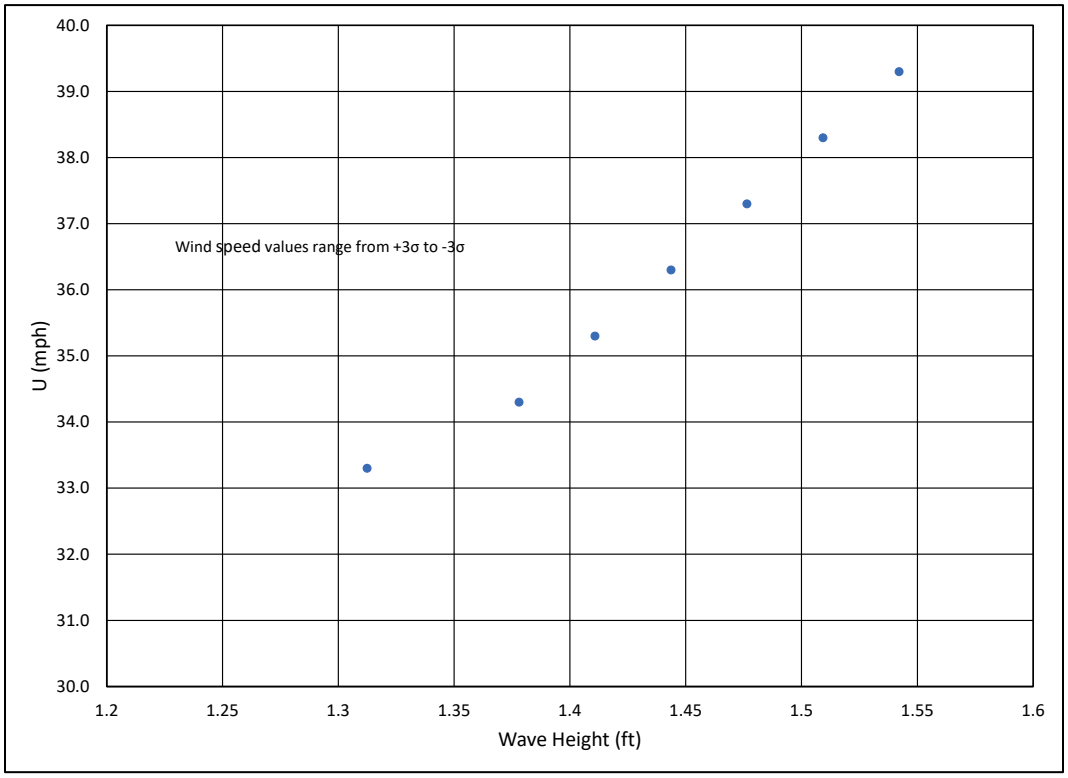

E.3.6 Wave Load from Goda for the Barkley Lock Upper Miter Gate

Goda (2010) also recommended formulations for determining significant wave height and period based on wind speed and fetch. The background and supporting equations for his formulations are provided in Chapter 2. This methodology is considered applicable to the lock upper miter gate. Table E-4 shows the results using Goda's formulations.

Table E-4. Significant wave height, wave period, and wavelength using Goda's (2010) formulations for the Barkley Lock upper miter gate.

Wind Speed (mph)	Wave Height (m)	Wave Period (sec)	Wavelength (m)
39.3	0.551	2.140	7.16
38.3	0.541	2.125	7.05
37.3	0.530	2.109	6.95
36.3	0.519	2.093	6.84
35.3	0.508	2.076	6.73
34.3	0.497	2.059	6.62
33.3	0.486	2.042	6.51

Figure E-15 shows a plot of wind speed (U) versus wave height determined from Goda's (2010) recommended formulations from the statistical analysis of the wind speed data for PAH.

Figure E-15. Wave height versus wind speed from Goda's (2010) procedure for the Barkley Lock upper miter gate.

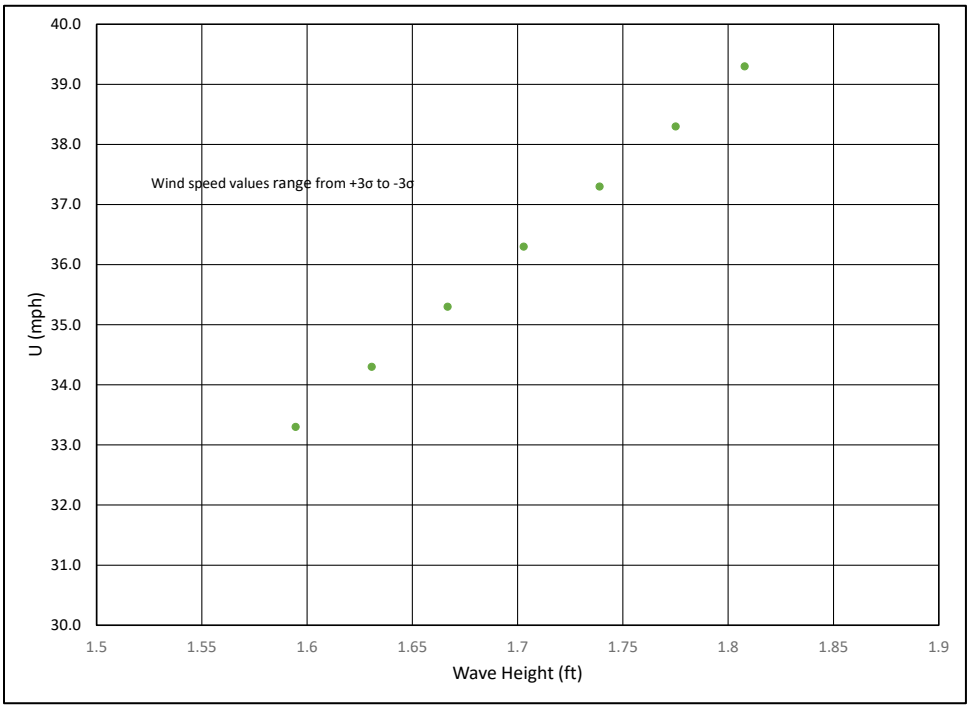

The wave pressure distribution and subsequent wave force for the upper miter gate can now be determined from the significant wave height and wave period. The complete description of this procedure is shown in Chapter 2, Section 2.3.2.3. Based on the parameters listed in Table E-5 and on the Goda formulations in Section 2.3.2.3, an example solution was reached. Table E-6 lists the parameters used in the example wave force

calculation (imperial and metric units included). The example uses the max upper pool el of 375, the upper sill el of 333, and the mean 100 yr return period wind speed of 36.3 mph.

Table E-5. Parameters used in example wave force calculation (imperial and metric units included) for the Barkley Lock upper miter gate for a wind speed of 36.3 mph.

Parameter	Value (Imperial Units)	Value (Metric Units)	Description
h_c	2.75 ft	0.84 m	Top girder height above max upper pool el
d (originally d_{SWL})	42.0 ft	12.80 m	Difference between upper pool el and upper sill el
h (originally h_{SWL})	45.0 ft	13.72 m	Difference between upper pool el and approach channel invert el (assumed)
tan θ	0	0	Bottom slope toward bulkhead
β_D	0 deg	0 deg	Design incident wave angle
$H_{1/3}$	1.70 ft	0.519 m	Significant wave height for example problem
$T_{1/3}$	2.09 sec	2.09 sec	Significant wave period for example problem
L_D	22.44 ft	6.84 m	Design wave length for example problem
ρ	62.4 lb/ft^3	1,000 kg/m^3	Density of freshwater
g	32.2 ft/sec^2	9.81 m/sec^2	Acceleration due to gravity
h'	42.0 ft	12.80 m	For the miter gate: $h' = H = d_{SWL}$

The design wave height (H_D) is the minimum of $\alpha_h H_{1/3}$ and H_b, where α_h ranges from 1.6 to 2.0. For the design of nearshore vertical structures, Goda (2010) suggests using a value of 1.8 for α_h:

$$H_d = H_{Max} = \min\{\alpha_h * H_{1/3}, H_b\},$$

$$H_b = 0.17 * L_D \left\{1 - \exp\left[-1.5 \frac{\pi h_b}{L_D}\left(1 + 15 * \tan^{\frac{4}{3}}\theta\right)\right]\right\},$$

where

$$h_b = h + 5 * H_{1/3} * \tan\theta.$$

Therefore,

$$\alpha_h H_{1/3} = 1.8 * 0.519 \text{ m} = 0.934 \text{ m (3.06 ft)},$$

$$h_b = 13.72 \text{ m} + 5 * 0.519 \text{ m} * \tan(0) = 13.72 \text{ m (45.02 ft)},$$

$$H_b = 0.17 * 6.84\text{ m}\left\{1 - \exp\left[-1.5\frac{\pi 13.72\text{ m}}{6.84\text{ m}}\left(1 + 15 * \tan^{\frac{4}{3}}(0)\right)\right]\right\}$$
$$= 1.162\text{ m (3.81 ft)},$$

so,

$$H_d = H_{Max} = \min\{0.934\text{ m},\ 1.162\text{ m}\} = 0.934\text{ m (3.06 ft)}.$$

Next, we calculate the coefficients of wave pressure (α_1, α_2, and α_3) given in the equations that follow:

$$\alpha_1 = 0.6 + \frac{1}{2}\left[\frac{\frac{4\pi h}{L_D}}{\sinh\left(\frac{4\pi h}{L_D}\right)}\right]^2,$$

$$\alpha_2 = \min\left[\frac{h_b - d}{3h_b}\left(\frac{H_D}{d}\right)^2, \frac{2d}{H_D}\right],$$

$$\alpha_3 = 1 - \frac{h'}{h}\left[1 - \frac{1}{\cosh\left(\frac{2\pi h}{L_D}\right)}\right].$$

The h and d values in the preceding equations are respectively equivalent to the h_{SWL} and d_{SWL} of Table E-5. Substituting the values gives

$a_1 = 0.60$ (from Equation 56),

$a_2 = \min[0.000119, 27.403] = 0.000119$ (from Equation 57),

and since $h' = d_{SWL} = H$,

$\alpha_3 = 0.067$ (from Equation 58).

The lateral pressure components P_1 and P_3 (from Equations 52 and 54) are evaluated here:

$$P_1 = 0.5\ (1\ + \cos\beta_D)\ (\alpha_1 + \alpha_2 * \cos^2\beta_D)\ \rho * g * H_D,$$

$$P_3 = \alpha_3 P_1.$$

The solutions to P_1 and P_3 are

$$P_1 = 5{,}500 \text{ N/m}^2 = 5.500 \text{ kN/m}^2 = 114.82 \text{ (lb/ft}^2\text{)},$$

$$P_3 = 369 \text{ N/m}^2 = 0.369 \text{ kN/m}^2 = 7.70 \text{ lb/ft}^2\text{)}.$$

As shown in Section 2.3.2.3, the total lateral force per linear width (F_{Lat}) on the face of the miter gate is

$$F_{Lat} = 0.5(P_1 + P_3)H + 0.5(P_1 + P_4)h_c',$$

where

$$P_4 = P_1\left(1 - \frac{h_c}{\eta^*}\right), \text{if } \eta^* > h_c,$$

or

$$P_4 = 0, \text{ if } \eta^* \leq h_c,$$

$$\eta^* = 0.75(1 + \cos(\beta_D))H_D,$$

$$h_C' = \min\{\eta^*, h_C\}.$$

Therefore, the solution of the resultant force, F_{Lat}, is given as

$$h_c = 0.84 \text{ m } (2.76 \text{ ft}) \text{ (from Table E-5)},$$

$$\eta^* = 1.401 \text{ m } (4.60 \text{ ft}).$$

Because $\eta^* > h_c$,

$$P_4 = 2{,}203 \text{ N/m}^2, 2.203 \text{ kN/m}^2 \text{ (46.0 lb/ft}^2\text{)},$$

$$h_C' = \min\{1.401 \text{ m}, 0.84 \text{ m}\} = 0.84 \text{ m } (2.76 \text{ ft}),$$

$$F_{Lat} = 40.79 \text{ kN/m } (2{,}795 \text{ lb/ft}).$$

The preceding analysis indicates the total lateral wave force per linear width of the miter gate for a sustained 36.3 mph wind is 2,795 lb/ft.

In Figure B-13 and Figure B-14, the pressure terms P_1, P_3, and P_4 are shown acting on the vertical-lift gates, which are similar to the upper miter

gate. The location of the lateral equivalent force (h_{Lat}) can be determined using the one-third/one-sixth method developed by Ebeling et al. (2018) and also presented in Chapter 2, Section 2.3.2.4, of this report. The distance between the top of the upper girder of the miter gate (el 377.75) and the upper sill (el 333) is h_4, and the distance from the max upper pool (el 375) and the upper sill (el 333) is h_1. By applying this method for the lateral forces and summing moments about point 3, Equation (A.14), which is repeated here, was developed:

$$h_{Lat} = \frac{(h_4 - h_1)\left(\frac{P_4}{3} + \frac{P_1}{6}\right)h_4 + (h_4 - h_1)\left(\frac{P_4}{6} + \frac{P_1}{3}\right)h_1 + (h_1 - h_3)\left(\frac{P_1}{3} + \frac{P_3}{6}\right)h_1}{F_{Lat}},$$

$$h_{Lat} = 8.653 \text{ m}.$$

Table E-4 shows the wave heights and wave periods used for computing the wave forces and pressure distributions determined from the wind speed analysis at the Barkley Lock upper miter gate. The wave forces and pressure distributions computed from Goda's (2010) procedure for the data in Table E-4 are shown in Table E-6. The definition of Goda's parameters found in Table E-5 and Table E-6 and the preceding equations are illustrated in Figure 16 and Figure A-27.

Table E-6. Wave force and pressure distribution computations using Goda's (2010) procedure for data in Table E-4 for the Barkley Lock upper miter gate.

	Statistic						
Barkley Lock Data	+3σ	+2σ	+1σ	Mean	−1σ	−2σ	−3σ
Wind Speed (mph)	39.3	38.3	37.3	36.3	35.3	34.3	33.3
η^* (m)	1.488	1.461	1.431	1.401	1.372	1.342	1.312
η^* (ft)	4.88	4.79	4.70	4.60	4.50	4.40	4.31
P_1 (N/m^2)	5,839	5,733	5,616	5,500	5,383	5,267	5,150
P_3 (N/m^2)	392	384	377	369	361	353	345
P_4 (N/m^2)	2,542	2,436	2,320	2,201	2,086	1,970	1,853
F_{Lat} (kN/m)	43.4	42.6	41.7	40.8	39.9	39.0	38.1
h_{Lat} (m)	8.66	8.66	8.66	8.65	8.65	8.65	8.64
h_{Lat} (ft)	28.4	28.4	28.4	28.4	28.4	28.4	28.3
P_1 (lb/ft^2)	101	99	97	95	93	91	89
P_3 (lb/ft^2)	8.2	8.0	7.9	7.7	7.5	7.4	7.2
P_4 (lb/ft^2)	53	51	48	46	44	41	39
F_{Lat} (lb/ft)	2,974	2,918	2,857	2,795	2,734	2,673	2,611

E.3.7 Wind Speed and Fetch for the Barkley Lower Lock Gate

The wind speed and wind-induced wave loads were also needed for the lower miter gate. The wind speed and wind direction data were obtained from meteorological data collected over a 24 yr period between 1991 and 2020 at the PAH near Paducah, Kentucky. Wind data for the years 2001 to 2006 were not available. PAH is located approximately 30 mi west of the project (Figure E-9).

The dataset was fairly complete for the years 2015 to August 2021, with wind speeds and directions reported multiple times per hour. Between 1991 and 2015, the wind speed and direction were usually reported on an hourly basis. The latitude of PAH is 37.0563, and the longitude is −88.7744. The data were obtained from Iowa State University (n.d.).

Figure E-16 shows the fetch determined for the Barkley Lock lower miter gate. The wind direction that impacts the lower lock gate perpendicular to the center of the lower miter gates is 340°. The fetch is around 0.56 mi.

Figure E-16. Fetch and wind direction determined for the Barkley lower miter gate.

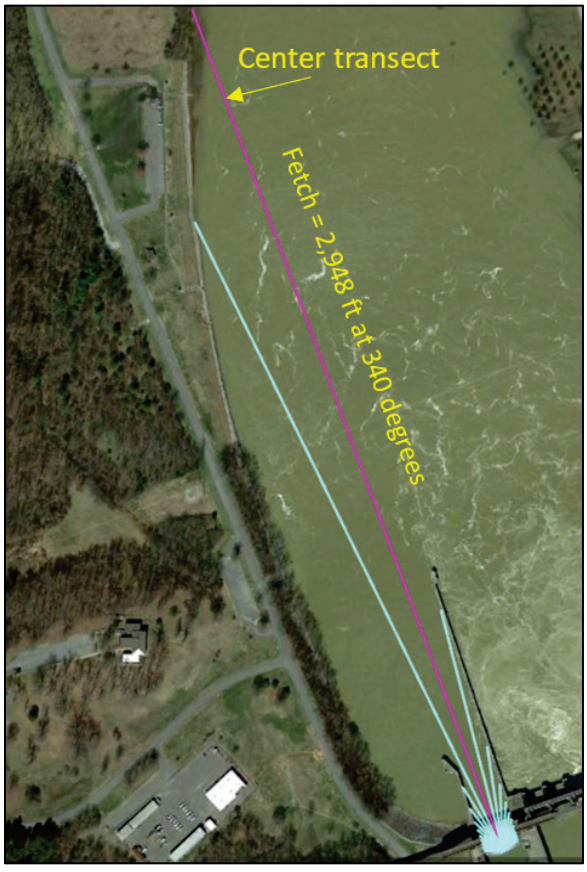

E.3.8 Wind Speed Analyses for the Barkley Lock Lower Gate

The methods used to determine the appropriate wind speed for the analyses of the wave load developed for the Barkley Lock lower miter gate were the same used for the upper lock gate, which were described in Sections E.3.1 to E.3.6. Using an estimated wind speed between 30 and 40 mph and a fetch length of 0.56 mi, the minimum time to reach full wave growth was around 15 min, so a t_{min} value of 0.25 hr was used in the analysis. The wind speed data were then processed to determine the maximum 15 min average wind speed with a wind direction between 320° and 360° per year. Table E-7 shows the wind speed values used in the analyses.

Table E-7. Maximum yearly 0.25 hr average wind speed for wind directions between 320° and 360° at PAH for the 1991 to 2020 observation period and used for the Barkley Lock lower miter gate.

Year	Max 1 hr Avg Wind Speed (mph)
1991	24.0
1992	27.6
1993	30.9
1994	24.6
1995	21.7
1996	24.2
1997	22.4
1998	25.9
1999	20.7
2000	23.4
2007	23.0
2008	21.9
2009	30.3
2010	27.0
2011	37.4
2012	33.4
2013	29.9
2014	30.7
2015	24.7
2016	34.5
2017	26.8
2018	24.5
2019	28.0
2020	26.5
2021	24.1

E.3.9 Extreme Value Estimation Using Maximum 0.25 hr Average Yearly Values of Wind Speed for the Barkley Lock Lower Gate.

The type 1 Gumbel distribution was used for a GEV analysis. Figure E-17 shows the results from the extreme value estimation using the maximum 0.25 hr average annual values for the PAH data. The 100 yr recurrence interval wind speed from this analysis was 45.3. The magnitude of the 100 yr recurrence interval for wind speed was considered a suitable frequency for wave height calculations.

Figure E-17. Extreme wind speed estimation for PAH based on maximum 0.25 hr average annual values of wind speed and used for the Barkley Lock lower miter gate.

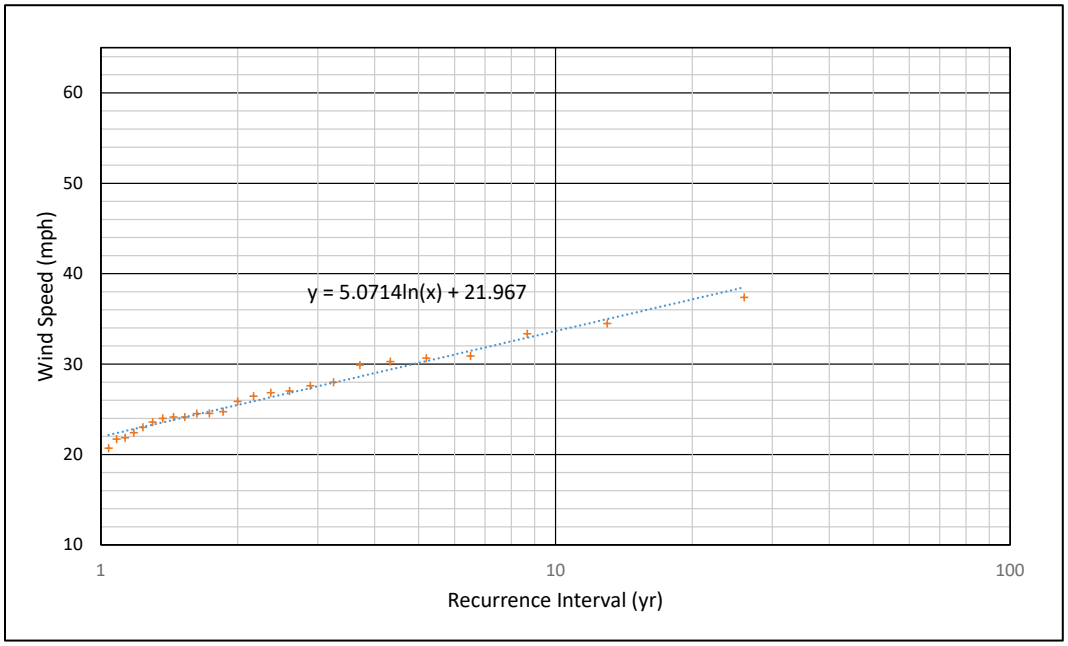

E.3.10 Wind Frequency Based on Gumbel Type 1 Distribution with Gringorten's Method Using Maximum Yearly 0.25 hr Average Values of Wind Speed for the Barkley Lock Lower Miter Gate.

The type 1 Gumbel distribution can be used with Gringorten's (1963) plotting position formula to create another method for evaluating wind speed. A description of this procedure is given in Chapter 2. A plot of the return period versus wind speed determined using this procedure is shown in Figure E-18 for the data from PAH. The wind speed for the 100 yr return period was 40.0 mph.

To further investigate the statistics for the wind speed, a formula to determine the standard error (discussed in Appendix A) was used for the data presented in Figure E-18.

Figure E-18. Wind frequency from Gumbel type 1 distribution with Gringorten's method for PAH using the maximum 0.25 hr average annual wind speed and used for the Barkley Lock lower miter gate.

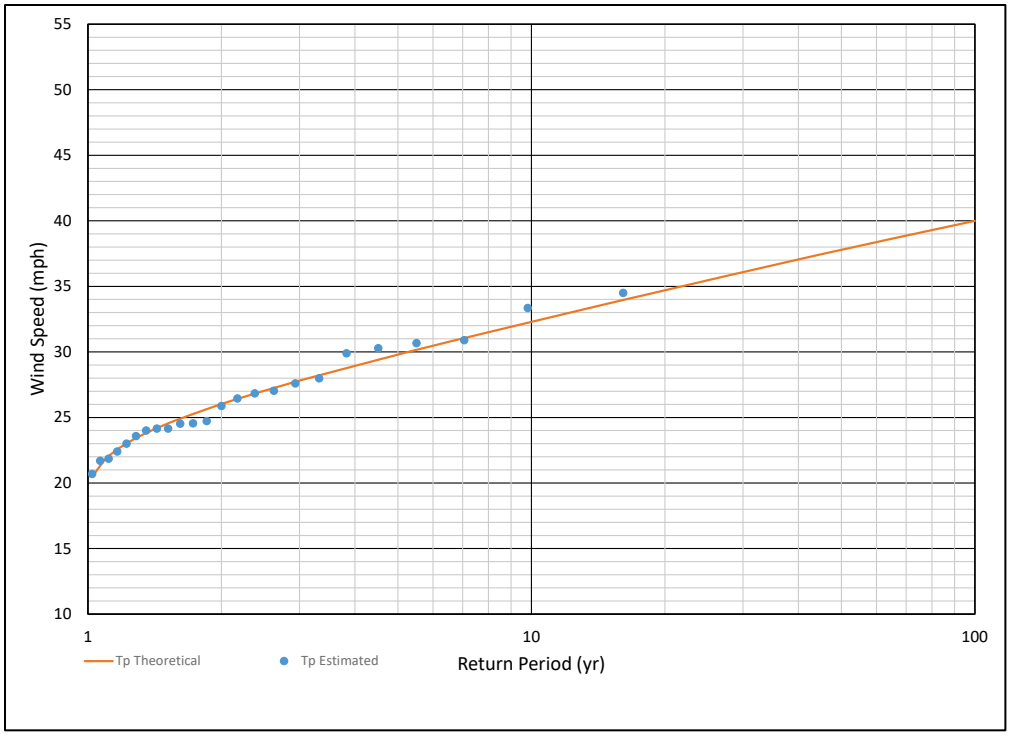

Figure E-19 shows the fitted curve bounded by plus and minus 1, 2, and 3 standard deviations (σ) for the PAH wind data (n = 25). Table E-8 shows the values for these statistics. The mean 100 yr return period wind speed was 40.0 mph. The standard deviation was determined to be 0.500 mph. The use of the 100 yr return period plus 3 standard deviations gives a wind speed of 41.5 mph.

Table E-8. Results from wind speed analysis for the Barkley Lock lower miter gate.

Statistic	100 yr Wind Speed (mph)
+3σ	41.5
+2σ	41.0
+1σ	40.5
Mean	40.0
−1σ	39.5
−2σ	39.0
−3σ	38.5

Figure E-19. Wind frequency curves based on peak yearly 0.25 hr average wind speed for the PAH data and used for the Barkley Lock lower miter gate.

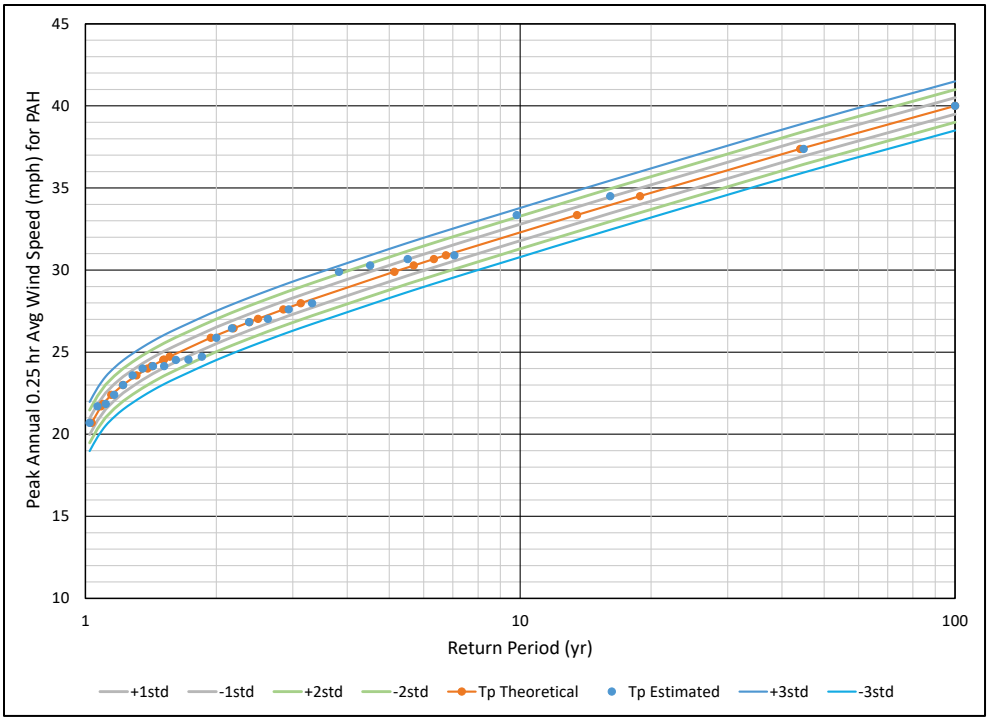

E.3.11 Wave Height and Period from the NARFET Model for the Barkley Lock Lower Miter Gate

Table E-9 shows the input data and results from using the NARFET program for the Barkley Lock lower miter gate. The program input requires the radial lengths of the fetch and the angle increments for resolution of the wind direction. Figure E-16 shows the radial lengths (a total of 31) determined for an angle increment of 6°. The significant wave height and period for the wind speeds determined between −3σ and +3σ for the 100 yr return period shown in Figure E-19 are listed in Table E-9.

Table E-9. Wave height, wave period, and wavelength computed using the NARFET model for the Barkley Lock lower miter gate.

Wind Speed (mph)	Wave Height (m)	Wave Period (sec)	Wavelength (m)
41.5	0.40	2.03	6.5
41.0	0.40	2.02	6.4
40.5	0.39	2.01	6.3
40.0	039	2.00	6.3
39.5	0.38	1.99	6.2
39.0	0.38	1.98	6.1
38.5	0.38	1.97	6.1

Figure E-20 shows a plot of the wind speed versus wave height. The wind direction was between 320° and 360° for a duration of 0.25 hr.

Figure E-20. Wave height versus wind speed from Smith's NARFET model for the Barkley Lock lower miter gate.

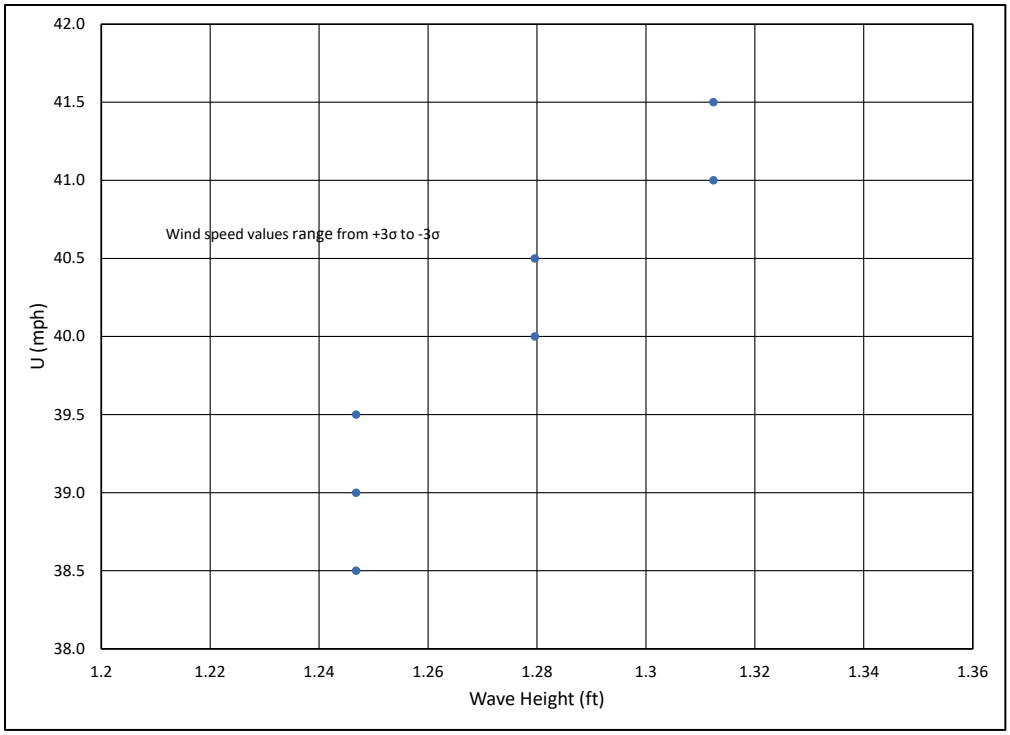

E.3.12 Wave Load from Goda for the Barkley Lock Lower Miter Gate

Goda (2010) also recommended formulations for determining significant wave height and period based on wind speed and fetch. The background and supporting equations for his formulations are provided in Chapter 2. This methodology is considered applicable to the lock lower miter gate. Table E-10 shows the results using Goda's formulations.

Table E-10. Significant wave height, wave period, and wavelength using Goda's (2010) formulations for the Barkley Lock lower miter gate.

Wind Speed (mph)	Wave Height (m)	Wave Period (sec)	Wavelength (m)
41.5	0.439	1.829	5.22
41.0	0.434	1.823	5.19
40.5	0.430	1.817	5.15
40.0	0.426	1.810	5.11
39.5	0.422	1.804	5.08
39.0	0.418	1.798	5.04
38.5	0.414	1.791	5.01

Figure E-21 shows a plot of wind speed (*U*) versus wave height determined from Goda's (2010) recommended formulations from the statistical analysis of the wind speed data for PAH and used for the lower lock miter gate.

Figure E-21. Wave height versus wind speed from Goda's (2010) procedure for Barkley Lock lower miter gate.

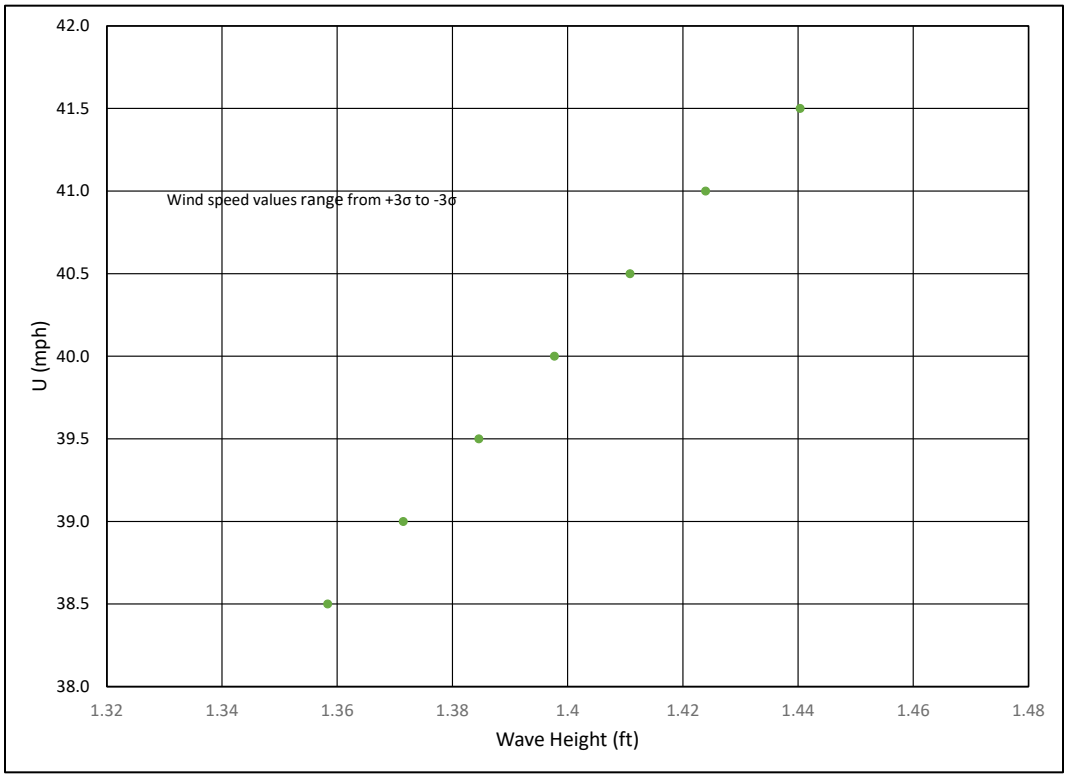

The wave pressure distribution and subsequent wave force can now be determined from the significant wave height and wave period. The complete description of this procedure is shown in Chapter 2, Section 2.3.2.3. Based on the parameters listed in Table E-10 and on the Goda formulations in Section 2.3.2.3, an example solution was reached. Table E-11 lists the parameters used in the example wave force calculation (imperial and metric units included). The example uses the max lower pool el of 350.75, the lower sill el of 289, and the mean 100 yr return period wind speed of 40.0 mph.

Table E-11. Parameters used in the example wave force calculation (imperial and metric units included) for the Barkley Lock lower miter gate for a wind speed of 36.3 mph.

Parameter	Value (Imperial Units)	Value (Metric Units)	Description
h_c	27.0 ft	8.23 m	Top girder height above max lower pool el
d (originally d_{SWL})	61.75 ft	18.82 m	Difference between max TW EL and lower sill el
h (originally h_{SWL})	64.75 ft	19.73 m	Difference between max TW EL and approach channel invert el (assumed)
tan θ	0	0	Bottom slope toward bulkhead
β_D	0 deg	0 deg	Design incident wave angle
$H_{1/3}$	1.40 ft	0.426 m	Significant wave height for example problem
$T_{1/3}$	1.81 sec	1.81 sec	Significant wave period for example problem
L_D	16.77 ft	5.11 m	Design wave length for example problem
ρ	62.4 lb/ft^3	1,000 kg/m^3	Density of freshwater
g	32.2 ft/sec^2	9.81 m/sec^2	Acceleration due to gravity
h'	61.75 ft	18.82 m	For the miter gate: $h' = H = d_{SWL}$

The design wave height (H_D) is the minimum of $\alpha_h H_{1/3}$ and H_b, where α_h ranges from 1.6 to 2.0. For the design of nearshore vertical structures, Goda (2010) suggests using a value of 1.8 for α_h:

$$H_d = H_{Max} = \min\{\alpha_h * H_{1/3}, H_b\},$$

$$H_b = 0.17 * L_D \left\{1 - \exp\left[-1.5 \frac{\pi h_b}{L_D}\left(1 + 15 * \tan^{4/3}\theta\right)\right]\right\},$$

where

$$h_b = h + 5 * H_{1/3} * \tan\theta.$$

Therefore,

$$\alpha_h H_{1/3} = 1.8 * 0.426 \text{ m} = 0.767 \text{ m (2.52 ft)},$$

$$h_b = 19.73 \text{ m} + 5 * 0.426 \text{ m} * \tan(0) = 19.73 \text{ m (64.73 ft)},$$

$$H_b = 0.17 * 5.11 \text{ m} \left\{1 - \exp\left[-1.5 \frac{\pi 19.73 \text{ m}}{5.11 \text{ m}}\left(1 + 15 * \tan^{\frac{4}{3}}(0)\right)\right]\right\} = 0.870 \text{ m (2.85 ft)},$$

so,

$$H_d = H_{Max} = \min\{0.767 \text{ m}, 0.870 \text{ m}\} = 0.767 \text{ m (2.52 ft)}.$$

Next, we calculate the coefficients of wave pressure (α_1, α_2, and α_3) given in the equations that follow:

$$\alpha_1 = 0.6 + \frac{1}{2}\left[\frac{\frac{4\pi h}{L_D}}{\sinh\left(\frac{4\pi h}{L_D}\right)}\right]^2,$$

$$\alpha_2 = \min\left[\frac{h_b - d}{3h_b}\left(\frac{H_D}{d}\right)^2, \frac{2d}{H_D}\right],$$

$$\alpha_3 = 1 - \frac{h'}{h}\left[1 - \frac{1}{\cosh\left(\frac{2\pi h}{L_D}\right)}\right].$$

The h and d values in the preceding equations are respectively equivalent to the h_{SWL} and d_{SWL} of Table E-11. Substituting the values gives

$$\alpha_1 = 0.60 \text{ (from Equation 56)},$$

$$a_2 = \min[0.0000255, 49.09] = 0.0000255 \text{ (from Equation 57)},$$

and because $h' = d_{SWL} = H$,

$$\alpha_3 = 0.046 \text{ (from Equation 58)}.$$

The lateral pressure components P_1 and P_3 (from Equations 52 and 54) are evaluated here:

$$P_1 = 0.5\,(1 + \cos\beta_D)\,(\alpha_1 + \alpha_2 * \cos^2\beta_D)\,\rho * g * H_D,$$

$$P_3 = \alpha_3 P_1.$$

The solutions to P_1 and P_3 are

$$P_1 = 4{,}514 \text{ N/m}^2 = 4.14 \text{ kN/m}^2 = 94.24 \text{ (lb/ft}^2\text{)},$$

$$P_3 = 208 \text{ N/m}^2 = 0.208 \text{ kN/m}^2 = 4.34 \text{ lb/ft}^2).$$

As shown in Section 2.3.2.3, the total lateral force per linear width (F_{Lat}) on the face of the lower miter gate is

$$F_{Lat} = 0.5(P_1 + P_3)H + 0.5(P_1 + P_4)h'_c,$$

where

$$P_4 = P_1\left(1 - \frac{h_c}{\eta^*}\right), \text{if } \eta^* > h_c,$$

or

$$P_4 = 0, \text{ if } \eta^* \leq h_c,$$

$$\eta^* = 0.75(1 + \cos(\beta_D))H_D,$$

$$h'_C = \min\{\eta^*, h_C\}.$$

Therefore, the solution of the resultant force, F_{Lat}, is given as

h_c = 8.23 m (27.00 ft) (from Table E-11),

η^* = 1.15 m (3.77 ft).

Because $\eta^* < h_c$,

P_4 = 0 N/m^2, 0 kN/m^2 (0 lb/ft^2),

h'_C = min{1.15 m, 8.23 m} = 1.15 m (3.77 ft),

F_{Lat} = 47.02 kN/m (3,222 lb/ft).

The analysis indicates the total lateral wave force per linear width of the miter gate for a sustained 40.0 mph wind is 3,222 lb/ft.

In Figure B-13 and Figure B-14, the pressure terms P_1, P_3, and P_4 are shown acting on the vertical-lift gates, which are similar to the lower miter gate. The location of the lateral equivalent force (h_{Lat}) can be determined using the one-third/one-sixth method developed by Ebeling et al. (2018) and also presented in Chapter 2, Section 2.3.2.4, of this report. The distance between the top of the girder of the lower miter gate (el 377.75) and the lower sill (el 289) is h_4, and the distance from the max lower pool (el 350.7) and the lower sill (el 289) is h_1. By applying this method for the

lateral forces and summing moments about point 3, Equation (A-14), repeated here, was developed:

$$h_{Lat} = \frac{(h_4 - h_1)\left(\frac{P_4}{3} + \frac{P_1}{6}\right)h_4 + (h_4 - h_1)\left(\frac{P_4}{6} + \frac{P_1}{3}\right)h_1 + (h_1 - h_3)\left(\frac{P_1}{3} + \frac{P_3}{6}\right)h_1}{F_{Lat}},$$

$$h_{Lat} = 20.109 \text{ m}.$$

Table E-10 shows the wave heights and wave periods used for computing the wave forces and pressure distributions determined from the wind speed analysis at the Barkley Lock lower miter gate. The wave forces and pressure distributions computed from Goda's (2010) procedure for the data in Table E-10 are shown in Table E-12.

Table E-12. Wave force and pressure distribution computations using Goda's (2010) procedure for data in Table E-4 for the Barkley Lock lower miter gate.

	Statistic						
Barkley Lock Data	+3σ	+2σ	+1σ	Mean	−1σ	−2σ	−3σ
Wind Speed (mph)	41.5	41.0	40.5	40.0	39.5	39.0	38.5
η^* (m)	1.185	1.172	1.161	1.150	1.394	1.129	1.118
η^* (ft)	3.89	3.84	3.81	3.77	3.74	3.70	3.67
P_1 (N/m^2)	4,651	4,598	4,556	4,514	4,471	4,429	4,386
P_3 (N/m^2)	215	212	210	208	206	204	202
P_4 (N/m^2)	0	0	0	0	0	0	0
F_{Lat} (kN/m)	48.54	47.96	47.49	47.02	46.56	46.1	45.63
h_{Lat} (m)	8.66	8.66	8.66	8.65	8.65	8.65	8.64
h_{Lat} (ft)	28.4	28.4	28.4	28.4	28.4	28.4	28.3
P_1 (lb/ft^2)	97.1	96.0	95.1	94.2	93.3	92.5	91.6
P_3 (lb/ft^2)	4.48	4.43	4.39	4.35	4.31	4.26	4.22
P_4 (lb/ft^2)	0	0	0	0	0	0	0
F_{Lat} (lb/ft)	3,326	3,286	3,254	3,222	3,190	3,159	3,126

E.4 Hydrodynamic Loads for the Barkley Lock Gates

The hydrodynamic loads in this appendix describe the procedures used by USACE-LRN in their original design of the Barkley miter gates. The hydrodynamic loads are considered the operating forces on the gate machinery as the miter gate is opened and closed. The arrangement of the machinery for the miter gates is similar to that of the modified Ohio River linkage (WES 1964) with the center line of the cylinder, rack, sector gear, and gate strut lying in a common horizontal plane that eliminates eccentric

connections. This linkage is essentially identical to that used at Cheatham Lock in the USACE-LRN. Operating forces were computed based on the prototype tests conducted under similar submergence at Cheatham Lock and checked against the results of the Panama Canal Lock model studies (WES 1964). Operation of the lower gate at submergences in excess of 30 ft were accomplished at reduced speeds, if necessary, to prevent exceeding the maximum working pressure equal to the relief valve setting. Upper gate machinery was identical to the lower gate design.

Design Memorandum No. 9, *Lock–Analysis of Design* (USACE-LRN 1958), provides details on how the operating forces were computed. The results from these computations are shown here for illustrative purposes. These loads were computed based on a prototype test at Cheatham Lock and model studies performed for the Panama Canal and are considered appropriate for computing operating machinery loads. They have been used in several project designs. Table E-13 shows the maximum operating forces for the Barkley Lock lower miter gate with a submergence of 35 ft. The force diagrams are provided in Design Memorandum No. 9 for 20 gate positions during the operating cycle. The total time of gate movement from the mitered position to the recessed position for the forces shown in Table E-13 was 90 sec.

Table E-13. Maximum operating forces for the Barkley Lock lower gate machinery with 35 ft submergence from USACE-LRN (1958).

Prefix	Nomenclature	Position	Max. Force (lb)
N	Force normal to gate pin	1	66,567
G	Longitudinal forces in gate from pintle pin	1	61,800
S	Strut force	1	90,800
A	Force normal to sector arm	2	44,500
T	Tension or compression in sector arm	1	85,000
P	Piston rod force	2	89,000
R	Reaction to sector gear pin	2	166,000

Note: Position is position of miter gate during operating cycle (refer to drawing Q9–22/A in design memorandum No. 9. Position 1 is closest to mitered gate.

EM 1110-2-2610 (HQUSACE 2013, plates C-62 to C-73) also shows a procedure for determining the pintle torque during gate operations for the Aliceville Lock project. This procedure demonstrates how the data in WES (1963) is adjusted to the details of the project being designed.

E.5 Probabilistic Characterization of the Hydrostatic and Hydrodynamic Loads for the Barkley Lower Lock Gate

The statistics for the hydraulic loads on the Barkley miter gates need to be determined for the LRFD analysis.

E.5.1 Probabilistic Characterization of the Hydrostatic Load for the Lower Lock Gate

The dispersion of the hydrostatic load on the lower lock gate is due to the changes in the upper and lower pool els. The maximum load occurs when the upper pool is at maximum el and the lower pool is at minimum el. For a navigation project such as BLD, when the upper pool is above normal, so is the lower pool, and the combination of maximum upper pool and minimum lower pool is very unlikely to occur. The computation of the changes in hydrostatic load on the lower gate are the result of the selection of an appropriate range of upper and lower pool fluctuations.

The head on the lower gate was determined for the 31 yr period of record for the upper and lower pool els discussed in Sections E.1.1 and E.1.2. The mean head was 42.26 ft, and the standard deviation (σ) was 9.223 ft, which corresponds to a mean upper pool el of 354.07 and a mean lower pool el of 314.78. The hydrostatic load on the gate consists of the increasing hydrostatic pressure with depth until the lower pool is reached and then a constant hydrostatic pressure between the lower pool el and the lower miter gate sill el.

Table E-14 shows the hydrostatic loads per foot of miter gate for the range of heads between +3σ and −3σ around the mean of 42.26 ft. The total hydrostatic load on the gate consists of the varying hydrostatic load due to the difference in the upper and lower pools plus the constant hydrostatic force from the lower pool el to the lower miter sill el. Figure E-22 illustrates the hydrostatic forces on the Barkley lower miter gate.

Table E-14. Hydrostatic forces computed for the Barkley lower lock gate beam for the range of heads from +3σ to −3σ around the mean head of 42.26 ft.

−3σ (lb/ft)	−2σ (lb/ft)	−σ (lb/ft)	Mean (lb/ft)	+σ (lb/ft)	+2σ (lb/ft)	+3σ (lb/ft)
27,410	51,590	81,080	115,870	165,515	212,635	265,060

Figure E-22. Hydrostatic force illustration for the Barkley lock lower gate.

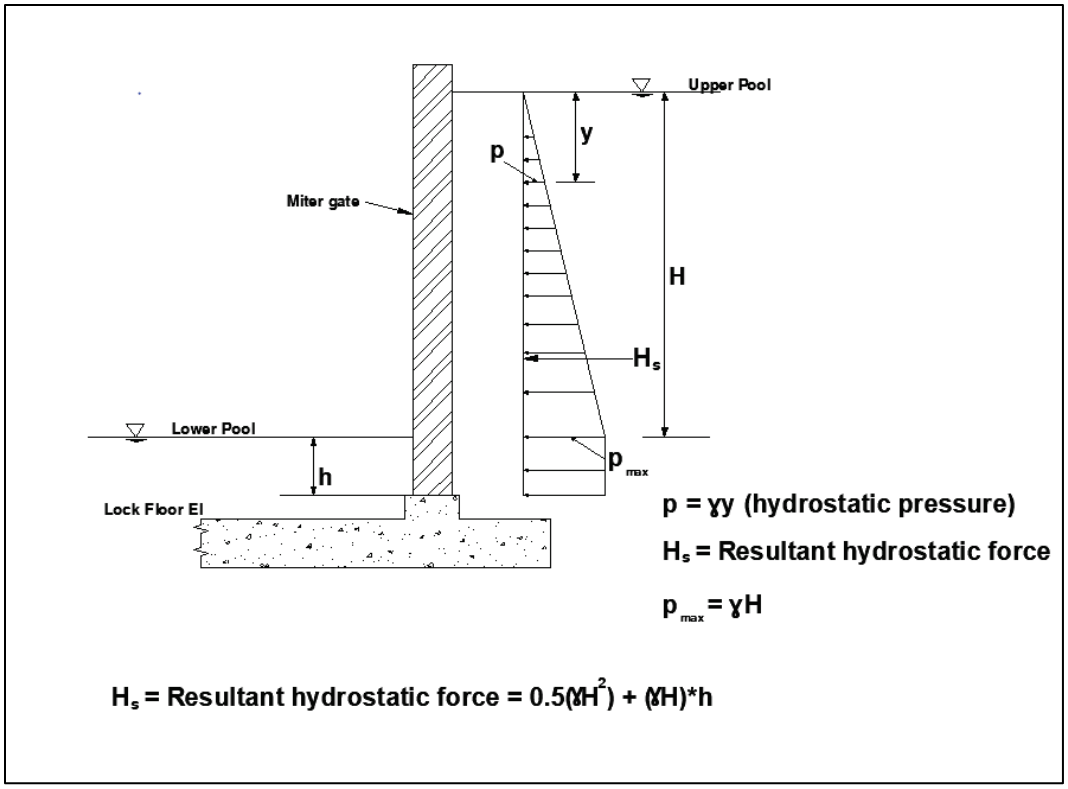

For example, to obtain the total hydrostatic force per foot of gate for the mean head of 42.26 ft,

- H = 42.26 ft,
- Upper pool el = 354.07,
- Lower pool el = 311.81,
- h = lower pool el – lower sill el = 311.81 – 289 = 22.81 ft, and
- $H_s = (0.5(\gamma H^2)) + (\gamma H)h$=(0.5(62.4 lb/ft^3 * (42.26ft)^2) + 62.4 lb/ft^3 * 42.26 ft * 22.81 ft = 115,870 lb/ft.

H_s acts at the centroid of the pressure distribution.

E.5.2 Probabilistic Characterization of the Hydrodynamic Load for the Lower Lock Gate

The dispersion of the hydrodynamic load on the lower lock gate is due to the changes in the lower pool els, which give different values of submergence and the gate opening rate. For the example loads shown in Section E.4, the submergence was 35 ft, and the gate opening rate from the mitered position to the recessed position was 90 sec. A 35 ft submergence

occurs with a TW El of 324, which is 9.22 ft above the mean TW El of 314.78 that was computed from the 31 yr record of TW Els. Using a submergence value of 9.22 ft below the mean TW El is appropriate for establishing the range of TW Els to compute the hydrodynamic loads. The range of gate operating speeds needs to be chosen by the designer performing the LRFD analysis. The effort required to compute the dispersion of the hydrodynamic load for the Barkley lower miter gate is beyond that anticipated in this research work unit.

E.6 Summary of Hydraulic Loads for the BLD Miter Gates

The hydraulic loads on the Barkley lock miter gates consist primarily of the hydrostatic, wave, and hydrodynamic loads. Table E-15 lists example hydraulic loads that were determined for the Barkley Lock project.

Table E-15. Example hydraulic loads for the Barkley Lock miter gates.

Max Estimated Hydraulic Load	Value (kips/ft)
Hydrostatic (upper gate)	55.037 (forebay el of 375)
Hydrostatic (lower gate)	166.265 (73 ft head)
Hydrodynamic	See Table E-13
Wave* (upper gate)	2.974 (wind speed 39.3 mph and direction of 154°, 100 yr wind event + 3σ)
Wave* (lower gate)	3.326 (wind speed 41.5 mph and direction of 340°, 100 yr wind event + 3σ)
Hydrostatic + Wave (upper gate)	58.01
Hydrostatic + Wave (lower gate)	169.576
Hydrodynamic + Wave**	N/A

* Based on a mean forebay el, P_1/P_3 = 12.32 for upper gate and 21.67 for lower gate.

** Gates would not operate in high winds

Some of the loads should be combined to give the maximum loads expected for the miter gate. Table E-15 shows these combined loads.

Appendix F: Example Hydraulic Load Computations for the Ice Harbor Lock Upper Submergible Tainter Gate

In this appendix, the procedures discussed in Chapter 7 of the main report are presented using data from an existing USACE Navigation project. The project being assessed is the Ice Harbor Lock and Dam project on the Snake River in the Walla Walla District. The data needed to quantify the hydraulic loads for the upper submergible tainter gate and example computations are described.

F.1 A 30 yr Record of Hydrologic Data for the Ice Harbor Lock and Dam

The Ice Harbor Lock and Dam project on the Snake River was chosen to illustrate how to determine the hydraulic loads on a submergible tainter gate used as the upper lock gate. USACE-NWW provided a record of hydraulic data from April 1962 through November 2020. The data consisted of a daily value for the forebay el. The pertinent project-specific data for the analysis are listed here:

- Top of gate el = 442
- Upper lock sill el = 422
- Average forebay el = 438.68
- Range of forebay el over period of record = 440.45 to 435.98
- Estimated approach el = 325
- Gate net width = 86 ft
- Gate height = 20 ft

Figure F-1 shows a view of the Ice Harbor submergible tainter gate, and Figure 67 shows a schematic of a cross section of a submergible tainter gate.

Figure F-1. Ice Harbor Lock submergible tainter gate.

The upper pool el, also referred to as the forebay el, is one of the primary variables affecting the load on the submergible tainter gate. Figure F-2 shows a histogram of the forebay el over the 58 yr period. The mean forebay el was 438.68, the maximum el was 440.45, and the minimum el was 435.98. The standard deviation was 0.701 ft. The histogram shown in Figure F-2 represents the number of occurrences of forebay el in the selected range. There are 45 bins, each with a bin width of 0.10 ft in this figure. The area of each bin was computed, and the total area was determined by summing the individual bin areas. These areas were normalized by dividing each individual area by the total area to give the PDF (Figure F-3). A CDF was developed by cumulatively summing the normalized areas of the PDF (Figure F-4).

Figure F-2. Histogram of forebay el from 1962 through 2020.

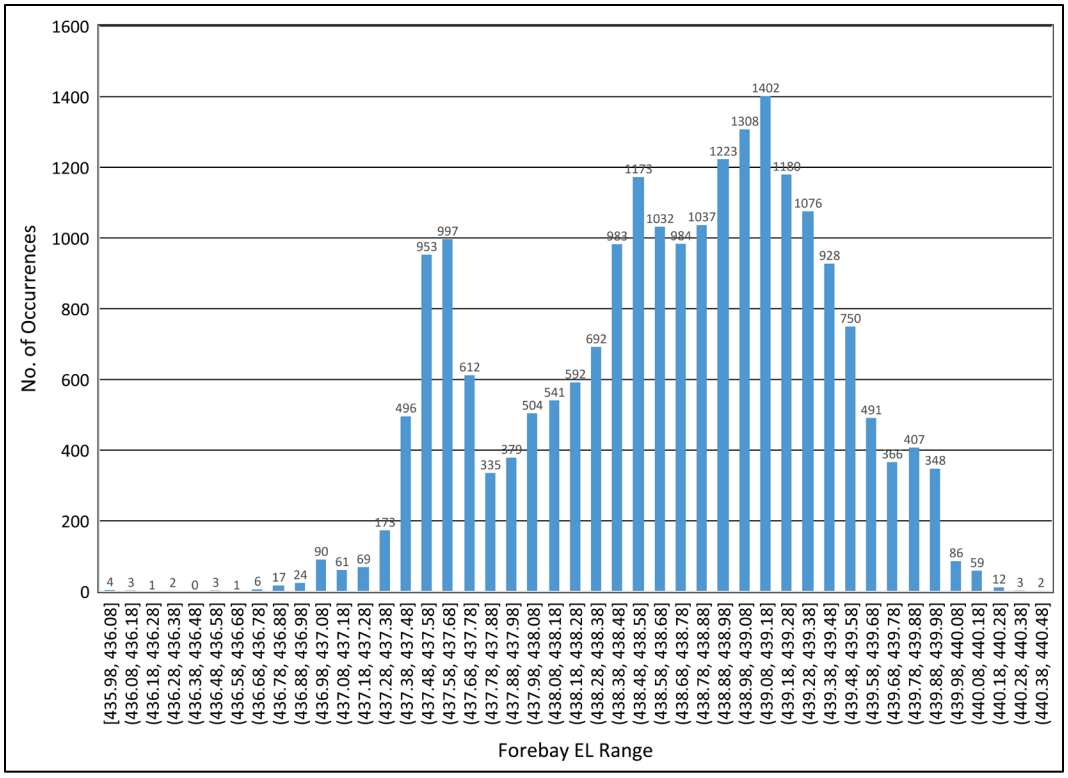

Figure F-3. PDF from histogram of forebay el for the Ice Harbor submergible tainter gate.

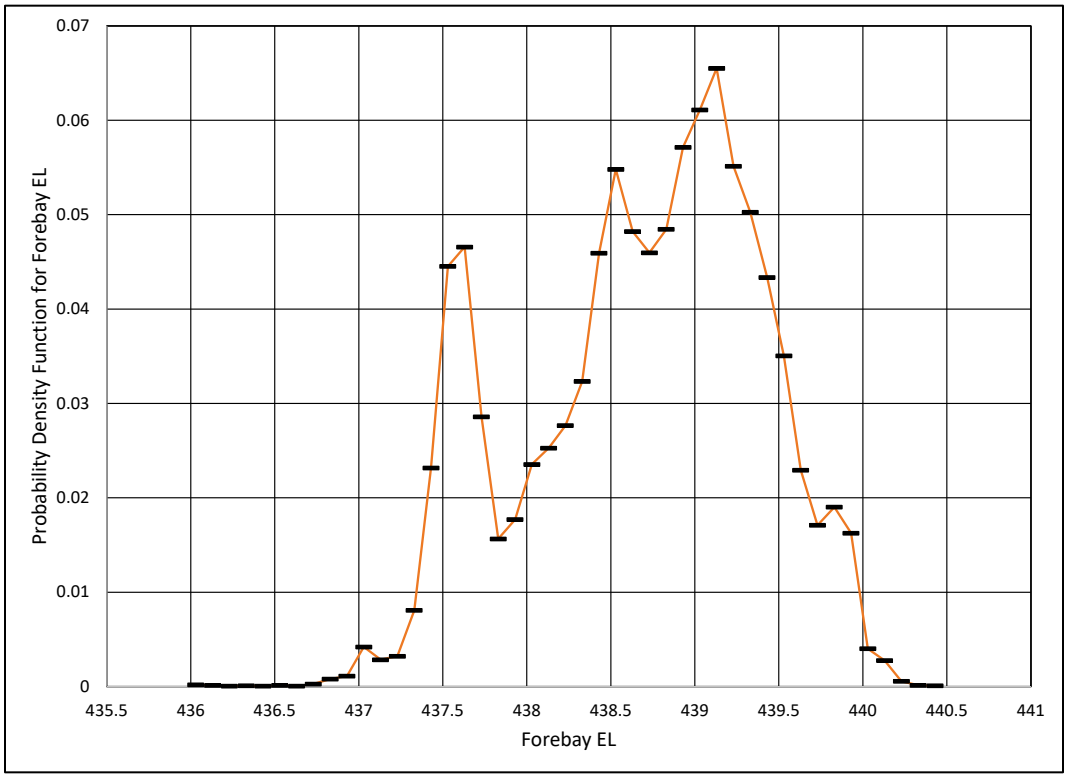

Figure F-4. CDF for forebay el for the Ice Harbor submergible tainter gate.

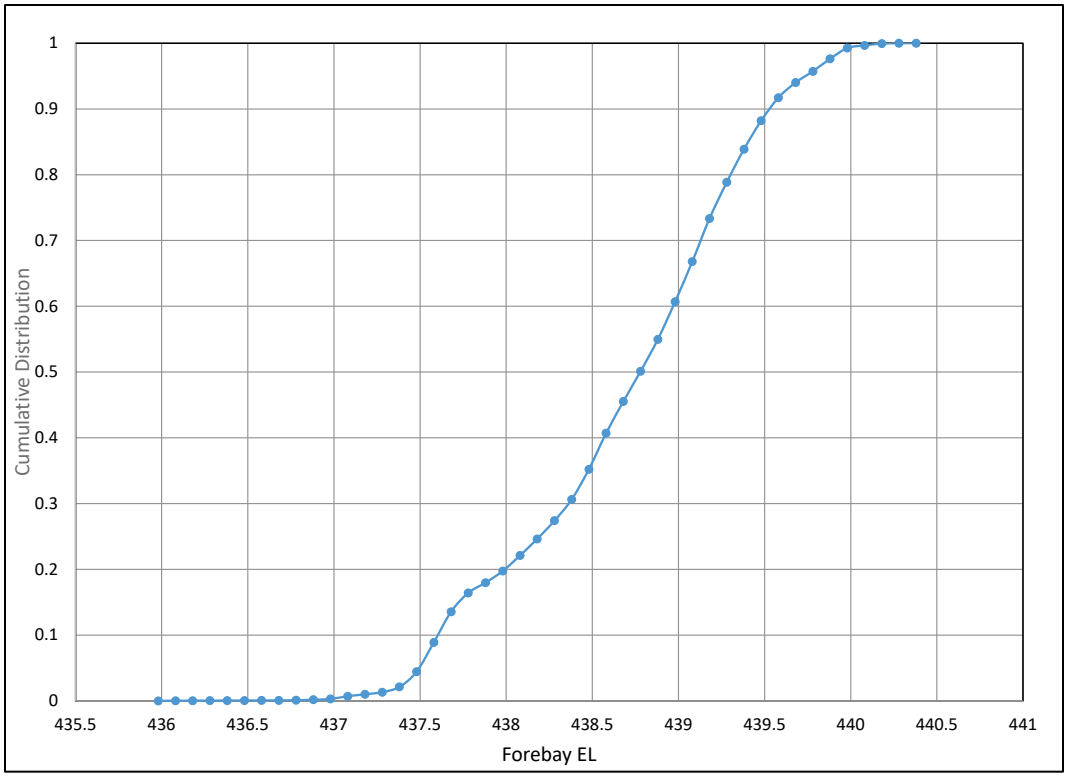

F.2 Hydrostatic Load for the Ice Harbor Submergible Tainter Gate

Equation (10), which is repeated here, is a conventional equation found in many fluid mechanics and hydraulics textbooks and is used to compute the hydrostatic pressure (p). As stated previously, γ is the unit weight of water, and y is the vertical distance from the water surface to the location of the hydrostatic pressure of interest (Figure 14):

$$p = \gamma y.$$

The horizontal hydrostatic pressure on the submergible tainter gate in the raised position is expressed as γH, where γ is the unit weight of water, and H is the total head on the gate. When the gate is closed, H represents the difference between the forebay el and the upper lock sill el. Equation (11), which is repeated here, can be used to calculate the maximum hydrostatic pressure:

$$p_{max} = \gamma H.$$

The hydrostatic force, H_s, per foot of width for the bulkhead is

$$H_s = \frac{1}{2}\gamma H^2,$$

where

γ = the unit weight of water = 62.4 lb/ft^3,
H = the head on the gate = 442 – 422 = 20 ft, and
Max hydrostatic load = 0.5 [62.4 lb/ft^3 * (20 ft)^2]= 12,480 lb/ft.

The maximum hydrostatic load is experienced if the forebay el is at the top of the gate. The head on the gate, H, would be el 442 – el 422, or 20 ft. This load condition represents H_1 (i.e., the maximum net hydrostatic load that will ever occur), which is one of the three hydrostatic loads that are to be considered. The mean hydrostatic load with a forebay el of 438.68 is 8,680 lb/ft.

F.3 Wave Load Based on Wave Height and Period for the Submergible Tainter Gate

The dispersion due to wind-induced wave loading about the mean hydrostatic and hydrodynamic loads needs to be determined. The wave load is one of the main loads that contributes to load fluctuations. The procedures and methods used to determine wave loads for the STGs presented in Chapter 2 and Appendix A were used for the submergible tainter gate. The supporting data and computations to determine the load for the Ice Harbor project are presented in the subsections that follow. As mentioned, developing a wind-induced wave loading requires determining the wind speed, wind direction, and fetch.

F.3.1 Wind Speed and Fetch for the Submergible Tainter Gate

The wind speed and wind direction data were obtained from meteorological data collected over a 30 yr period between 1999 and 2020 at the Pasco / Tri Cities (PSC) airport near Pasco, Washington. PSC is located approximately 11.5 mi west of the project. Figure F-5 shows the wind data collection site in relation to the project.

Figure F-5. Satellite imagery of the wind speed and direction data collection site in relation to Ice Harbor Lock. (Map data: Google Earth 2012.)

Significant data were found for the period of January 2016 to December 2020, with wind speeds and directions reported multiple times per hour. Between 1990 and January 2016, the wind speed and direction were usually reported on an hourly basis.

The latitude of PSC is 46.2647, and the longitude is –119.1190. The data were obtained from Iowa State University (n.d.).

Figure F-6 shows the fetch determined for the Ice Harbor Lock and Dam project. The wind direction that impacts the project perpendicular to the submergible gate is 76°. The fetch is approximately 1.66 mi. The upper lock guard wall prevents much of the wind from reaching the gate from the southeast direction.

Figure F-6. Satellite imagery of the fetch and wind direction determined for the Ice Harbor Lock and Dam project. (Map data: Google Earth 2012.)

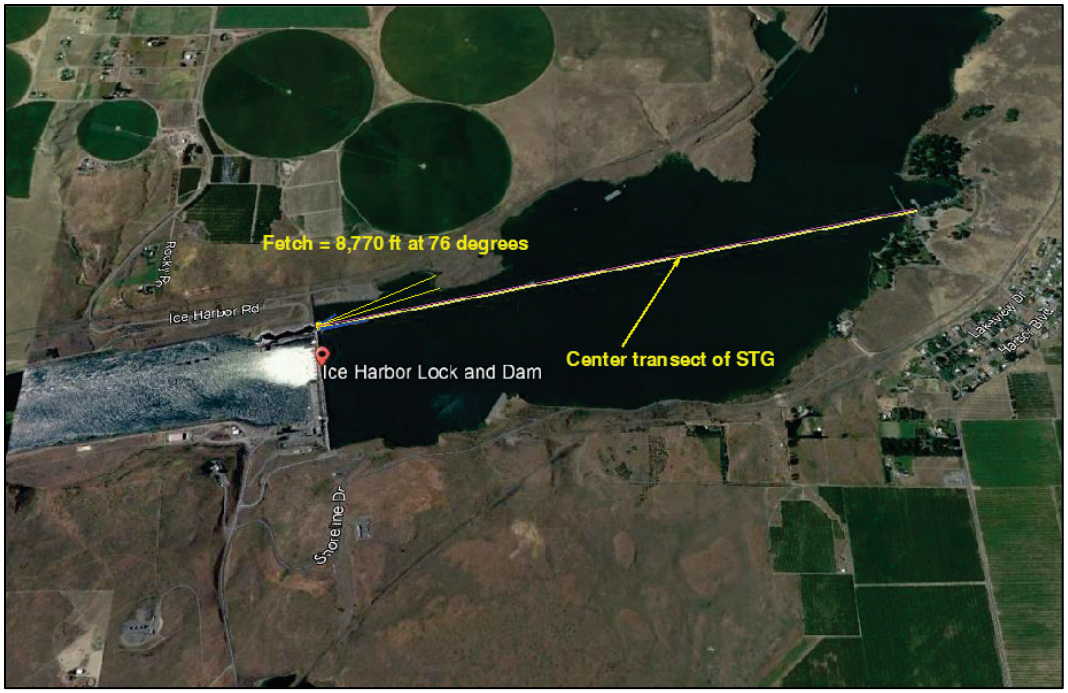

F.3.2 Wind Speed Analyses for the Submergible Tainter Gate

The methods used to determine the appropriate wind speed for the analyses of the wave load developed for the STG were also used for the submergible tainter gate. Based on the fetch length and wind speed, Equation (50), which is repeated here, can be used to determine the time required for full wave growth:

$$t_{\min} = 1.0F^{0.73}U_{10}^{-0.46}.$$

Using an estimated wind speed between 20 and 30 mph and a fetch length of 1.66 mi, the minimum time to reach full wave growth was around 30 min, so a t_{min} value of 0.5 hr was used in the analysis. Equation (50) requires metric units. The wind speed data were then processed to determine the maximum 30 min average wind speed with a wind direction between 50° and 90° per year. Table F-1 shows the wind speed values used in the analyses that follow.

Table F-1. Maximum yearly 0.5 hr average wind speed for wind directions between 50° and 90° at the Pasco / Tri Cities (PSC) airport for the 1990 to 2020 observation period.

Year	Max 0.5 hr Avg Wind Speed (mph)
1990	18.80
1991	17.25
1992	13.80
1993	28.75
1994	24.15
1995	23.00
1996	30.28
1997	29.61
1998	14.38
1999	13.23
2000	16.10
2001	13.80
2002	16.10
2003	27.03
2004	18.40
2005	24.15
2006	16.68
2007	14.95
2008	17.25
2009	28.18
2010	13.80
2011	18.98
2012	18.40
2013	20.13
2014	18.98
2015	20.70
2016	16.10
2017	26.45
2018	16.16
2019	28.37
2020	20.12

F.3.3 Extreme Value Estimation Using Maximum 0.5 hr Average Yearly Values of Wind Speed for the Submergible Tainter Gate

The type 1 Gumbel distribution was used for a GEV analysis. Figure F-7 shows the results from the extreme value estimation using the maximum 0.5 hr average annual values for the PSC data. The 100 yr recurrence

interval wind speed from this analysis was 42.15 mph. The magnitude of the 100 yr recurrence interval for wind speed was considered a suitable frequency for wave height calculations.

Figure F-7. Extreme wind speed estimation for Pasco / Tri Cities (PSC) based on maximum 0.5 hr average annual values of wind speed.

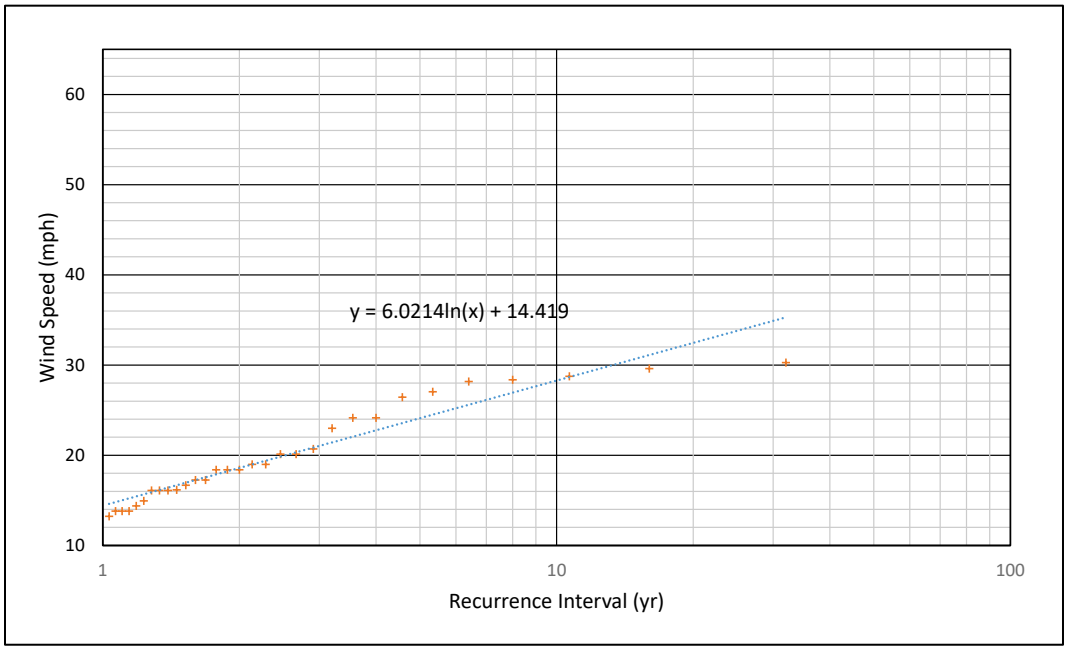

F.3.4 Wind Frequency Based on Gumbel Type 1 Distribution with Gringorten's Method Using Maximum Yearly 0.5 hr Average Values of Wind Speed for the Submergible Tainter Gate

The type 1 Gumbel distribution can be used with Gringorten's (1963) plotting position formula to create another method for evaluating wind speed. A description of this procedure is given in Chapter 2. Figure F-8 shows a plot of the return period versus wind speed determined using this procedure for the data from the PSC. The wind speed for the 100 yr return period was 36.3 mph.

Figure F-8. Wind frequency from Gumbel type 1 distribution with Gringorten's method for the PSC using the maximum 0.5 hr average annual wind speed.

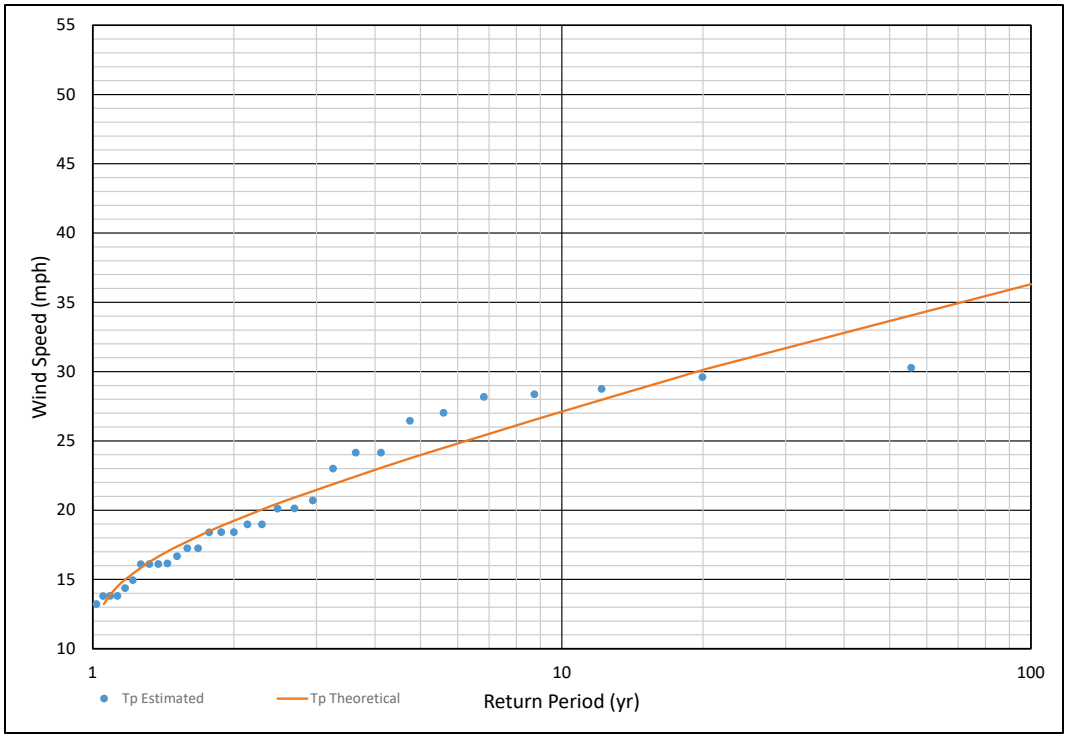

To further investigate the statistics for the wind speed, a formula for determining the standard error (discussed in Appendix A) was used for the data presented in Figure F-8.

Figure F-9 shows the fitted curve bounded by plus and minus 1, 2, and 3 standard deviations (σ) for the PSC wind data (n = 31). Table F-2 shows the values for these statistics. The mean 100 yr return period wind speed was 36.3 mph. The standard deviation was determined to be 1.340 mph. The use of the 100 yr return period plus 3 standard deviations gives a wind speed of 40.3 mph.

Table F-2. Results from wind speed analysis for the Ice Harbor submergible tainter gate.

Statistic	100 yr Wind Speed (mph)
+3σ	40.3
+2σ	39.0
+1σ	37.6
Mean	36.3
−1σ	35.0
−2σ	33.6
−3σ	32.3

Figure F-9. Wind frequency curves based on peak yearly 0.5 hr average wind speed for the PSC data.

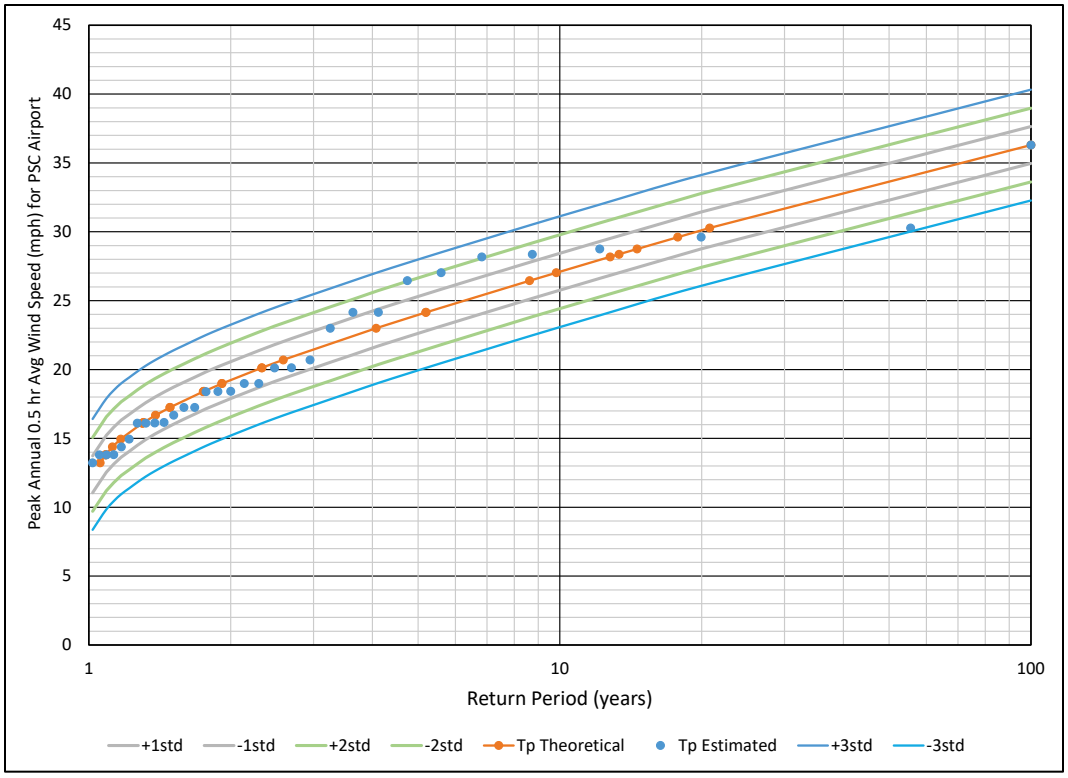

F.3.5 Wave Height and Period from the NARFET Model for the Submergible Tainter Gates

Table F-3 shows the input data and results from using the NARFET program for the Ice Harbor submergible tainter gate. The program input requires the radial lengths of the fetch and the angle increments for resolution of the wind direction, as partially visible in Figure F-6. The radial lengths (a total of 27) determined for an angle increment of 6° are shown in yellow. Not all of the radial lengths are visible in the figure because the ones between the center of the gate and the lock guard wall are very short compared to the ones visible in the figure. The significant wave height and period for the wind speeds determined between −3σ and +3σ for the 100 yr return period shown in Figure F-9 are presented in Table F-3, and the wave heights are plotted in Figure F-10. The wind direction was between 50° and 90° for a duration of 0.5 hr.

Table F-3. Wave height, wave period, and wavelength computed using the NARFET model for the submergible tainter gate.

Wind Speed (mph)	Wave Height (m)	Wave Period (sec)	Wavelength (m)
40.3	0.60	2.50	10.07
39.0	0.59	2.50	9.88
37.6	0.57	2.50	9.53
36.3	0.55	2.40	9.27
35.0	0.53	2.40	9.01
33.6	0.52	2.40	8.72
32.3	0.50	2.40	8.45

Figure F-10. Wave height versus wind speed from Smith's NARFET model for the submergible tainter gate.

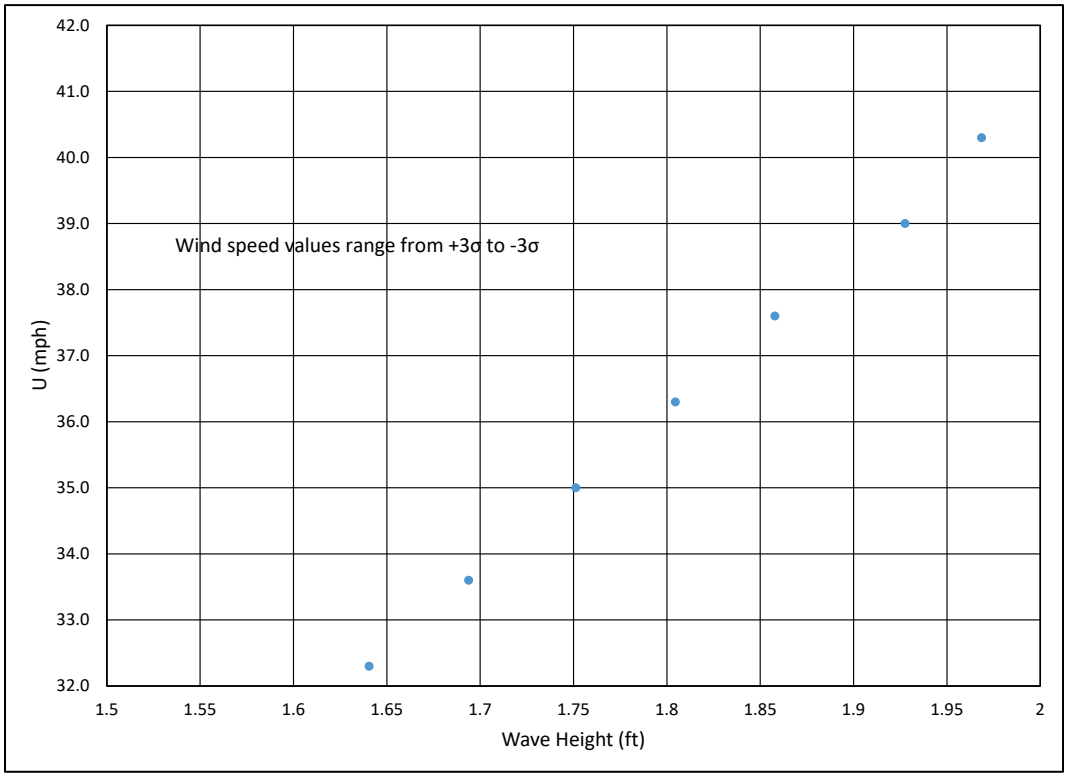

F.3.6 Wave Load for the Ice Harbor Lock Submergible Tainter Gate

Goda (2010) recommended formulations for determining significant wave heights and periods based on wind speed and fetch. The background and supporting equations for his formulations are provided in Chapter 2. This methodology is applicable to the submergible tainter gate.

Table F-4. Significant wave height, wave period, and wavelength using Goda's (2010) formulations for submergible tainter gates.

Wind Speed (mph)	Wave Height (m)	Wave Period (sec)	Wavelength (m)
40.3	0.719	2.53	9.99
39.0	0.705	2.51	9.84
37.6	0.686	2.48	9.60
36.3	0.667	2.46	9.44
35.0	0.649	2.43	9.23
33.6	0.628	2.40	8.99
32.3	0.608	2.37	8.77

Figure F-11 shows a plot of wind speed (U) versus wave height determined from Goda's (2010) recommended formulations from the statistical analysis of the wind speed data for the PSC.

Figure F-11. Wave height versus wind speed from Goda's (2010) procedure for a submergible tainter gate.

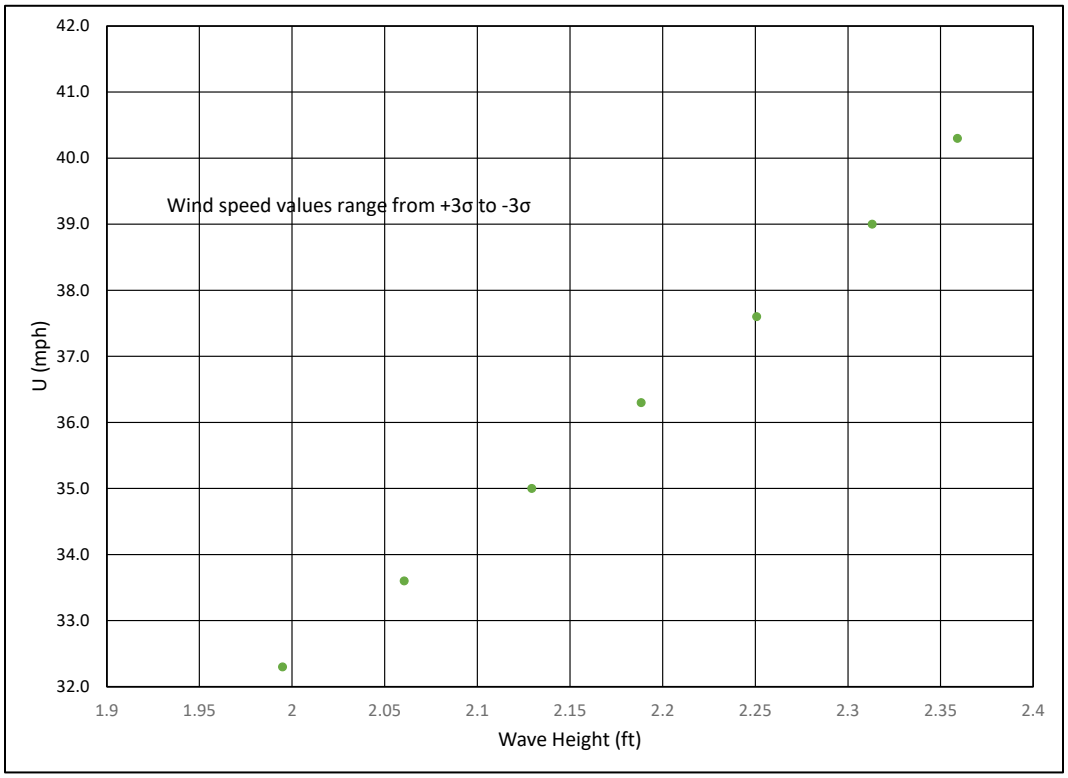

The wave pressure distribution and subsequent wave force for the submergible tainter can now be determined from the significant wave height and wave period. The complete description of this procedure is

shown in Chapter 2, Section 2.3.2.3. Based on the parameters listed in Table F-5 and the Goda (2010) formulations in Section 2.3.2.3, an example solution was reached.

Table F-6 shows the solution in the example wave force calculation (imperial and metric units included). The example uses the average forebay el 438.68, the top of upper lock sill of el 422, and the mean 100 yr return period wind speed of 36.3 mph.

Table F-5. Parameters used in the example wave force calculation (imperial and metric units included) for a submergible tainter gate with a wind speed of 36.3 mph.

Parameter	Value (Imperial Unit)	Value (Metric Unit)	Description
h_c	3.32 ft	1.01 m	Submergible tainter gate height above average forebay el
d (originally d_{SWL})	16.68 ft	5.08 m	Difference between avg forebay el and upper lock sill
h (originally h_{SWL})	113.68 ft	34.65 m	Difference between forebay el and approach channel invert el
tan θ	0	0	Bottom slope toward bulkhead
β_D	0 deg	0 deg	Design incident wave angle
$H_{1/3}$	2.19 ft	0.667 m	Significant wave height for example problem
$T_{1/3}$	2.46 sec	2.46 sec	Significant wave period for example problem
L_D	31.0 ft	9.45 m	Design wave length for example problem
ρ	62.4 lb/ft^3	1,000 kg/m^3	Density of freshwater
g	32.2 ft/sec^2	9.81 m/sec^2	Acceleration due to gravity
h'	16.68 ft	5.08 m	For the submergible tainter gate: $h' = H = d_{SWL}$

The design wave height (H_D) is the minimum of $\alpha_h H_{1/3}$ and H_b, where α_h ranges from 1.6 to 2.0. For the design of nearshore vertical structures, Goda (2010) suggests using a value of 1.8 for α_h. Equations (59) through (61) are repeated here:

$$H_d = H_{Max} = \min\{\alpha_h * H_{1/3}, H_b\},$$

$$H_b = 0.17 * L_D \left\{1 - \exp\left[-1.5\frac{\pi h_b}{L_D}\left(1 + 15 * \tan^{4/3}\theta\right)\right]\right\},$$

where

$$h_b = h + 5 * H_{1/3} * \tan\theta.$$

Therefore,

$$\alpha_h H_{1/3} = 1.8 * 0.667 \text{ m} = 1.2006 \text{ m (3.94 ft)},$$

$$h_b = 34.65 \text{ m} + 5 * 0.667 \text{ m} * \tan(0) = 34.65 \text{ m (113.68 ft)},$$

$$H_b = 0.17 * 9.45 \text{ m} \left\{1 - \exp\left[-1.5 \frac{\pi 34.65 \text{ m}}{9.45 \text{ m}} \left(1 + 15 * \tan^{\frac{4}{3}}(0)\right)\right]\right\}$$
$$= 1.606 \text{ m (5.27 ft)},$$

so,

$$H_d = H_{Max} = \min\{1.2006 \text{ m}, 1.606 \text{ m}\} = 1.2006 \text{ m (3.94 ft)}.$$

Next, we calculate the coefficients of wave pressure (α_1, α_2, and α_3) given in the equations that follow:

$$\alpha_1 = 0.6 + \frac{1}{2}\left[\frac{\frac{4\pi h}{L_D}}{\sinh\left(\frac{4\pi h}{L_D}\right)}\right]^2,$$

$$\alpha_2 = \min\left[\frac{h_b - d}{3h_b}\left(\frac{H_D}{d}\right)^2, \frac{2d}{H_D}\right],$$

$$\alpha_3 = 1 - \frac{h'}{h}\left[1 - \frac{1}{\cosh\left(\frac{2\pi h}{L_D}\right)}\right].$$

The h and d values in the preceding equations are respectively equivalent to the h_{SWL} and d_{SWL} from Table F-5. Substituting the values gives

$$\alpha_1 = 0.60 \text{ (from Equation 56)},$$

$$\alpha_2 = \min\left[\frac{34.65 \text{ m} - 5.08 \text{ m}}{3(34.65 \text{ m})}\left(\frac{1.2006 \text{ m}}{5.08 \text{ m}}\right)^2, \frac{2(5.08) \text{ m}}{1.2006 \text{ m}}\right] = \min[0.0159 \text{ m}, 8.62 \text{ m}]$$
$$= 0.0059 \text{ m (from Equation 57)},$$

and because $h' = d_{SWL} = H$,

$$\alpha_3 = 0.853 \text{ (from Equation 58)}.$$

The lateral pressure components P_1 and P_3 (from Equations 52 and 54) are evaluated here:

$$P_1 = 0.5\,(1 + \cos\beta_D)\,(\alpha_1 + \alpha_2 * \cos^2\beta_D)\,\rho * g * H_D,$$

$$P_3 = \alpha_3 P_1.$$

The solutions to P_1 and P_3 are

$$P_1 = 7{,}254 \text{ N/m}^2 = 7.254 \text{ kN/m}^2 = 151.44 \text{ (lb/ft}^2\text{)},$$

$$P_3 = 6{,}190 \text{ N/m}^2 = 6.190 \text{ kN/m}^2 \text{ (129.22 lb/ft}^2\text{)}.$$

As shown in Section 2.3.2.3, the total lateral force per linear width (F_{Lat}) on the face of the submergible tainter gate is

$$F_{Lat} = 0.5(P_1 + P_3)H + 0.5(P_1 + P_4)h_c',$$

where

$$P_4 = P_1\left(1 - \frac{h_c}{\eta^*}\right), \text{ if } \eta^* > h_c,$$

or

$$P_4 = 0, \text{ if } \eta^* \le h_c,$$

$$\eta^* = 0.75(1 + \cos(\beta_D))H_D,$$

$$h_C' = \min\{\eta^*, h_C\}.$$

Therefore, the solution of the resultant force, F_{Lat}, is given as

$$h_c = 1.01 \text{ m (3.32 ft) (from Table F-5)},$$

$$\eta^* = 1.801 \text{ m (5.91 ft)}.$$

Because $\eta^* > h_c$,

$$P_4 = 3{,}186 \text{ N/m}^2, 3.186 \text{ kN/m}^2 \text{ (66.51 lb/ft}^2\text{)},$$

$$h'_C = \min\{1.801 \text{ m}, 1.01 \text{ m}\} = 1.01 \text{ m (3.32 ft)},$$

$$F_{Lat} = 39.42 \text{ kN/m (2,701 lb/ft)}.$$

The preceding analysis indicates the total lateral wave force per linear width of the submergible tainter gate for a sustained 36.3 mph wind is 2,701 lb/ft.

In Figure A-27 and Figure A-28, the pressure terms P_1, P_3, and P_4 are shown acting on the STG, which is similar to the submergible tainter gate in the raised position. The location of the lateral equivalent force (h_{Lat}) can be determined using the one-third/one-sixth method developed by Ebeling et al. (2018) and presented in Chapter 2, Section 2.3.2.4, of this report. By applying this method for the lateral forces and summing moments about point 3, Equation (A-14), which is repeated here, was developed.

$$h_{Lat} = \frac{(h_4 - h_1)\left(\frac{P_4}{3} + \frac{P_1}{6}\right)h_4 + (h_4 - h_1)\left(\frac{P_4}{6} + \frac{P_1}{3}\right)h_1 + (h_1 - h_3)\left(\frac{P_1}{3} + \frac{P_3}{6}\right)h_1}{F_{Lat}},$$

$$h_{Lat} = \frac{1.02 \text{ m}\left(\frac{3.186 \frac{\text{kN}}{\text{m}^2}}{3} + \frac{7.254 \frac{\text{kN}}{\text{m}^2}}{6}\right)6.10 \text{ m} + 1.02 \text{ m}\left(\frac{3.186 \frac{\text{kN}}{\text{m}^2}}{6} + \frac{7.254 \frac{\text{kN}}{\text{m}^2}}{3}\right)5.08 \text{ m}}{39.42 \frac{\text{kN}}{\text{m}}}$$

$$\frac{+ 5.08 \text{ m}\left(\frac{7.254 \frac{\text{kN}}{\text{m}^2}}{3} + \frac{6.190 \frac{\text{kN}}{\text{m}^2}}{6}\right)5.08 \text{ m}}{39.42 \frac{\text{kN}}{\text{m}}}$$

$$h_{Lat} = 3.004 \text{ m}.$$

Table F-4 shows the wave heights and wave periods used for computing the wave forces and pressure distributions determined from the wind speed analysis at the Ice Harbor submergible tainter gate project. The wave forces and pressure distributions computed from Goda's (2010) procedure for the data in Table F-4 are shown in Table F-6. The definition of Goda's parameters found in Table F-5 and used in the preceding equations are illustrated in Figure 16 and again in Figure A-27.

Table F-6. Wave force and pressure distribution computations using Goda's (2010) procedure for data in Table F-4 for the Ice Harbor project.

Ice Harbor Data	Statistic						
	+3σ	+2σ	+1σ	Mean	−1σ	−2σ	−3σ
Wind Speed (mph)	40.3	39.0	37.6	36.3	35.0	33.6	32.3
η^* (m)	1.941	1.904	1.852	1.801	1.752	1.696	1.642
η^* (ft)	6.37	6.25	6.08	5.91	5.75	5.56	5.39
P_1 (N/m^2)	7,852	7,690	7,472	7,254	7,048	6,810	6,583
P_3 (N/m^2)	6,701	6,563	6,376	6,190	6,015	5,811	5,618
P_4 (N/m^2)	3,767	3,610	3,397	3,186	2,986	2,753	2,533
F_{Lat} (kN/m)	42.83	41.91	40.66	39.42	38.25	36.89	35.60
h_{Lat} (m)	3.015	3.012	3.008	3.004	3.000	2.995	2.990
h_{Lat} (ft)	9.89	9.88	9.87	9.85	9.84	9.82	9.81
P_1 (lb/ft^2)	164	161	156	151	147	142	137
P_3 (lb/ft^2)	140	137	133	129	126	121	117
P_4 (lb/ft^2)	79	75	71	67	62	57	53
F_{Lat} (lb/ft)	2,935	2,872	2,786	2,701	2,621	2,527	2,439

F.4 Probabilistic Characterization of the Hydrostatic Load for the Ice Harbor Lock Submergible Tainter Gate.

The dispersion of the hydrostatic load was determined from the statistics described in Section F.1. The mean upper pool el determined from the historical data was 438.68, and the standard deviation (σ) was 0.701 ft. Table F-7 shows the hydrostatic forces per foot of gate computed for the range of upper pool els from +3σ to −3σ around the mean upper pool el of 438.68. These values will be used for the structural reliability analysis that will be presented in a follow up to this report.

Table F-7. Hydrostatic forces computed for the Ice Harbor Lock submergible tainter gate for the range of upper pool els from +3σ to −3σ around the mean upper pool el of 438.68.

−3σ (lb/ft)	−2σ (lb/ft)	−σ (lb/ft)	Mean (lb/ft)	+σ (lb/ft)	+2σ (lb/ft)	+3σ (lb/ft)
6,630	7,283	7,966	8,681	9,425	10,200	11,007

F.5 Summary of Hydraulic Loads for Submergible Tainter Gates

Hydrostatic and wave loads are the primary hydraulic loads on the submergible tainter used as an upper lock gate. Table F-8 lists example hydraulic loads determined for the Ice Harbor Lock and Dam project.

Table F-8. Example hydraulic loads for the Ice Harbor Lock and Dam submergible tainter gate.

Max Estimated Hydraulic Load	Value (kips/ft)
Hydrostatic	12.48 (8.68 with forebay el of 438.68)
Hydrodynamic	N/A
Wave*	2.935
Hydrostatic + Wave	11.61 (average hydrostatic + wave)
Hydrodynamic + Wave	N/A

* Based on a mean forebay el and 40.3 mph wind speed at 76° (100 yr wind event + 3σ). P_1/P_3 = 1.17.

Some of the loads should be combined to give the maximum loads expected for the gate. Table F-8 shows these combined loads. The wave force results in the table indicate that wind-induced wave forces are significant and need to be included in submergible tainter gate design force computations.

Appendix G: Example Hydraulic Load Computations for the BLD Spillway Bulkhead

In this appendix, the procedures discussed in Chapter 8 of the main report are presented using data from an existing USACE Navigation project. The data needed to quantify the hydraulic loads for the spillway bulkhead and example computations are described.

G.1 A 30 yr Record of Hydrologic Data for the BLD

The BLD project on the Cumberland River was chosen to illustrate how to determine the hydraulic loads on a spillway bulkhead used in a nonemergency operation. USACE-LRN provided a 30 yr record of hydraulic data from January 1989 through August 2020. The data included forebay el, TW El, discharge, and gate settings for the spillway. The Barkley reservoir is held at el 354.0 during the flood season, is filled to el 359.0 in the spring, and is then gradually lowered back to el 354.0 during the summer and fall. Drawdown of the reservoir to as low as 346.0 in advance of an anticipated flood occurs. The pertinent project-specific data for the analysis are listed here:

- Spillway crest el = 325
- Summer and fall normal upper pool el operating range = 354.0
- Range of normal operations = 346.0 to 359.0
- Estimated approach el = 276
- Total number of gates = 12
- Spillway gate width = 55 ft
- Spillway gate height = 50 ft
- Spillway gate top el when gate is closed = 375
- Bulkhead top el with 3 units in place = 361

Figure G-1 shows a cross-section view of the Barkley spillway, and Figure G-2 contains pictures of a 1:15-scale model of the Barkley spillway bulkheads with the lifting frame.

Figure G-1. Barkley Dam spillway section view. (Image reproduced from USACE, Nashville District [USACE-LRN], files.)

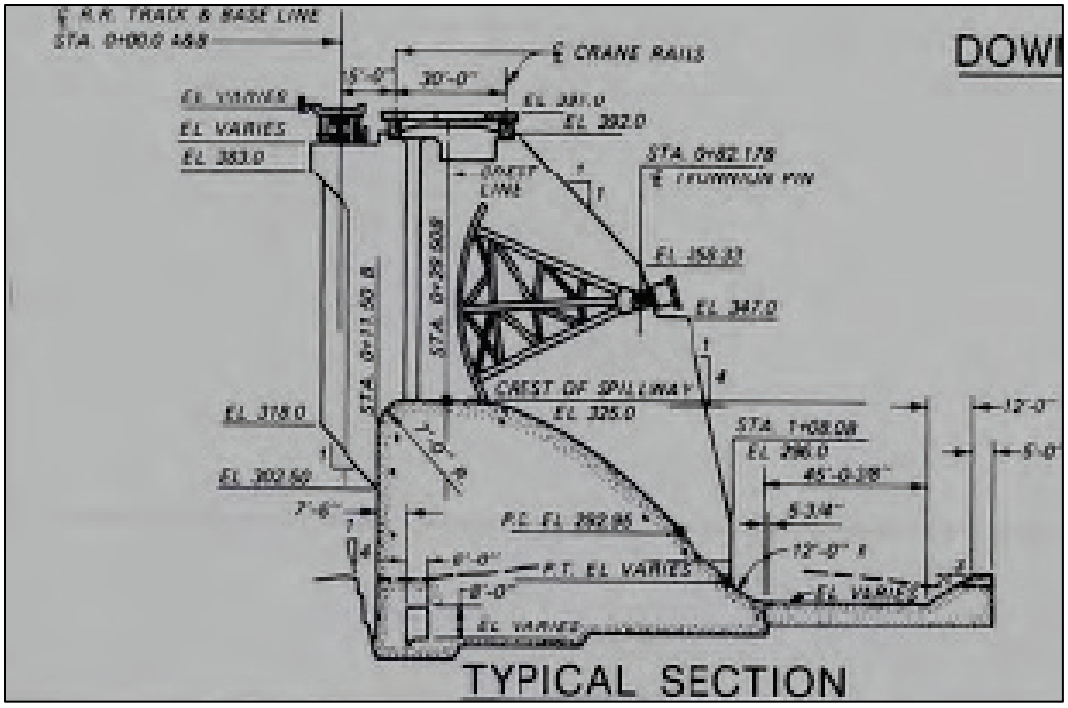

Figure G-2. Pictures of 1:15-scale model of Barkley spillway bulkheads. (Image reproduced from Hite and Pickering 1983, Figure 6. Public domain.)

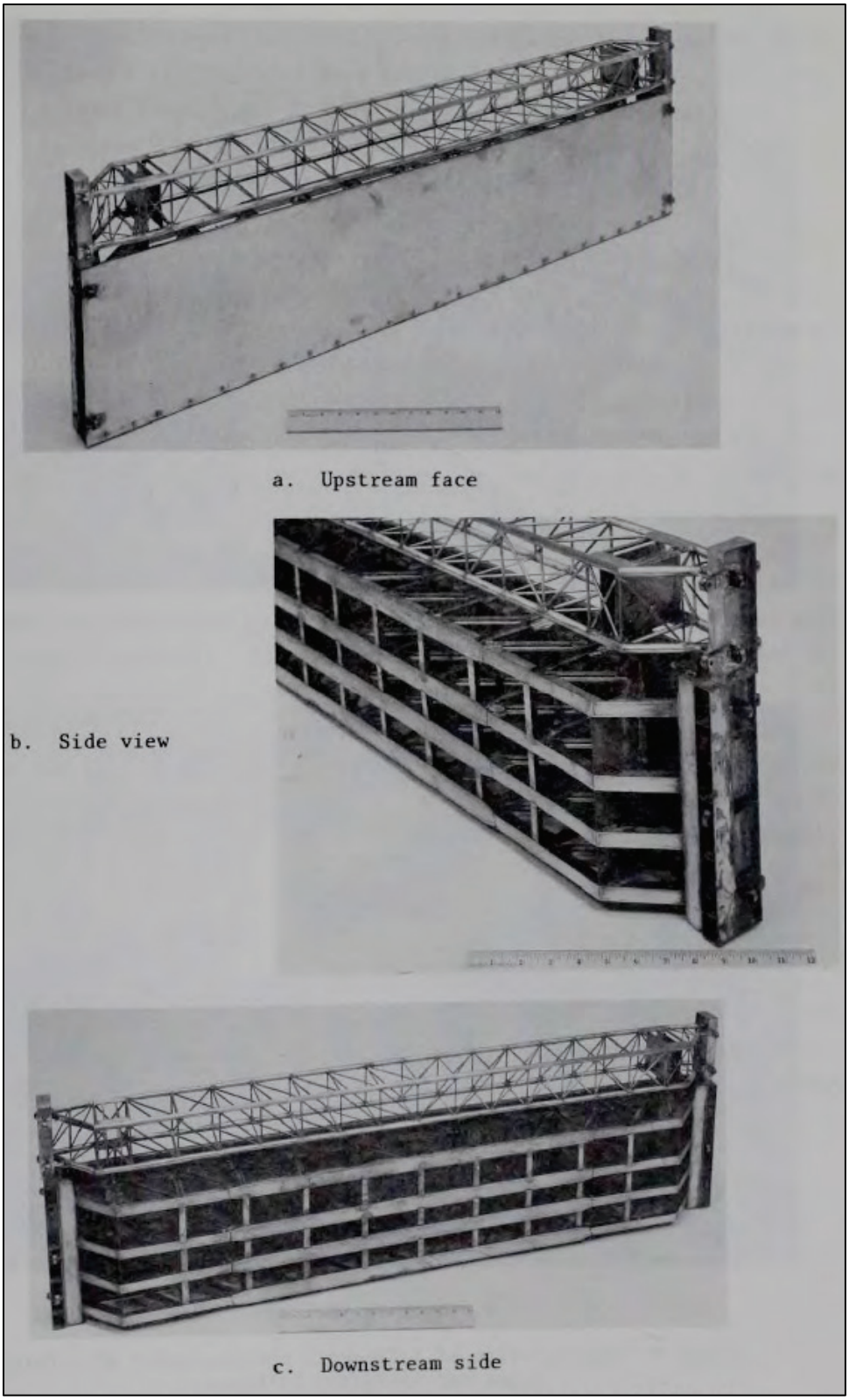

G.1.1 Forebay Statistics for the BLD

The upper pool el, also referred to as the forebay el, is one of the primary variables affecting the load on the spillway bulkhead for most inland navigation projects. Figure G-3 shows a histogram of the forebay el over the 31 yr period. The mean forebay el was 357.04, the maximum el was 372.5, and the minimum el was 353.26. The standard deviation was 2.21 ft. The histogram shown in Figure G-3 represents the number of occurrences of forebay in the selected range.

There are 39 bins, each with a bin width of 0.50 ft. The area of each bin was computed, and the total area was determined by summing the individual bin areas. These areas were normalized by dividing each individual area by the total area to give the PDF shown in Figure G-4. A CDF was developed by cumulatively summing the normalized areas of the PDF, as shown in Figure G-5.

Figure G-3. Histogram of forebay el from 1989 through 2020.

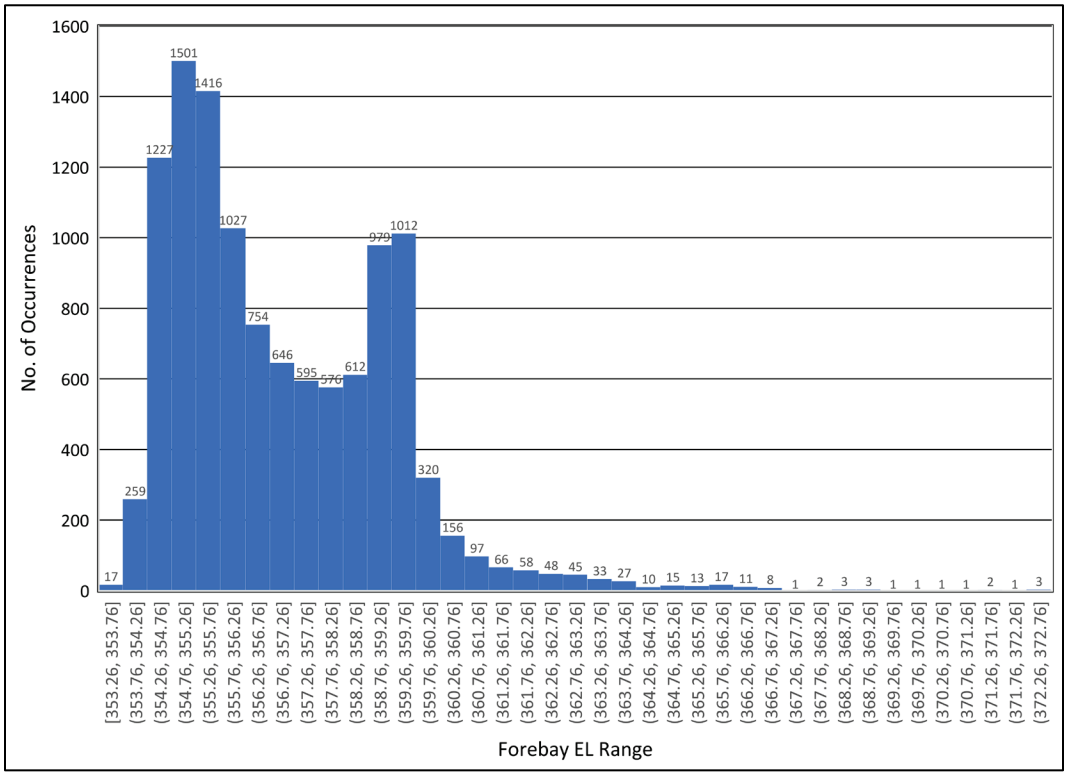

Figure G-4. PDF from histogram of forebay el.

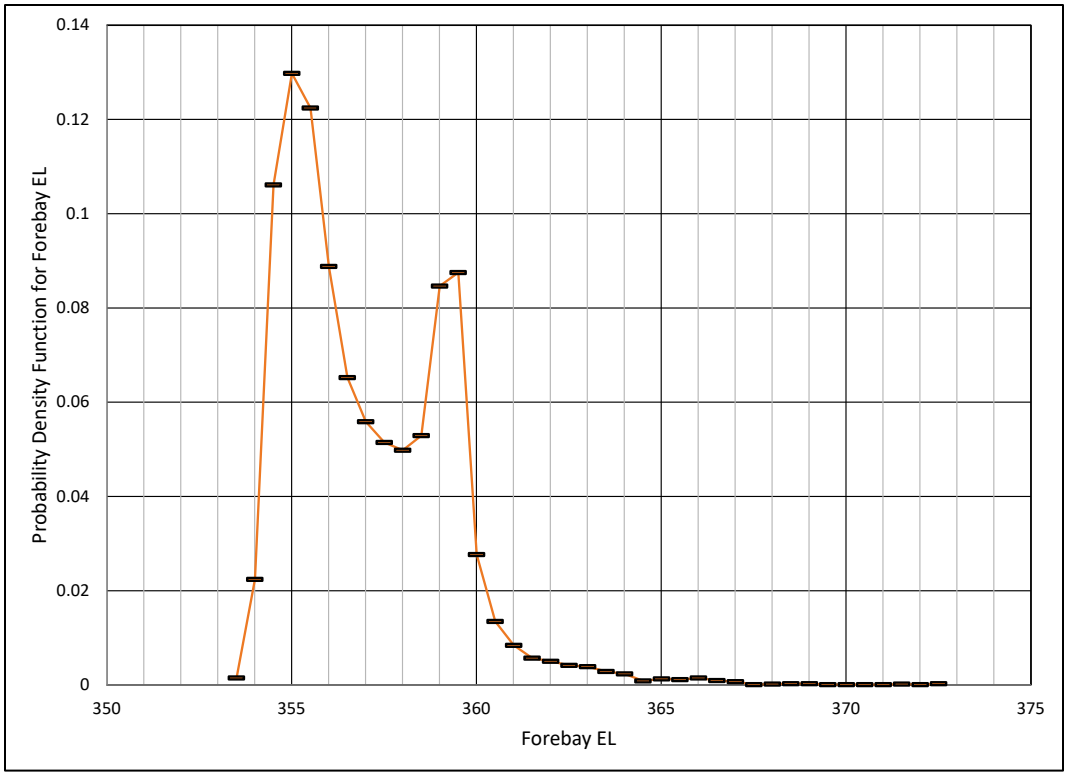

Figure G-5. CDF for forebay el.

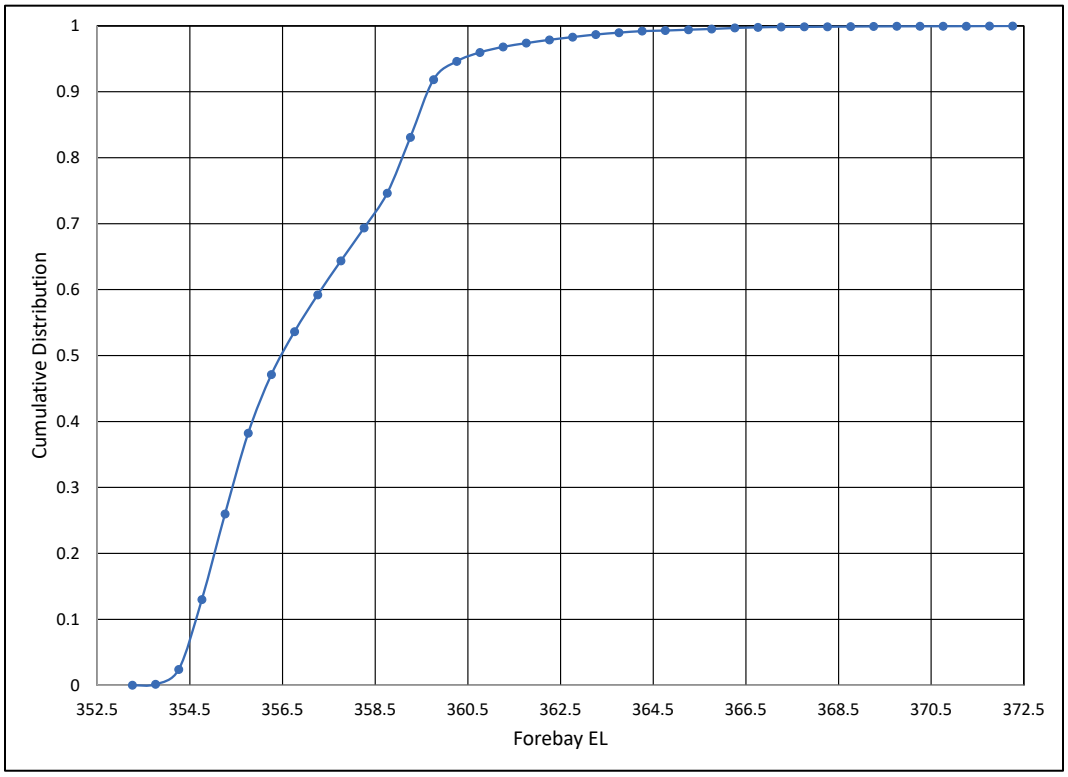

G.1.2 Tailwater Statistics for the BLD

Similar statistics were computed for the TW Els at Barkley Spillway. Figure G-6 shows a histogram of the TW El over the 31 yr period. The mean TW El was 314.78, the maximum el was 350.75, and the minimum el was 300.9. The standard deviation was 9.51 ft.

There are 50 bins, each with a bin width of 1.0 ft. The area of each bin was computed, and the total area was determined by summing the individual bin areas. These areas were normalized by dividing each individual area by the total area to give the PDF shown in Figure G-7. A CDF was developed by cumulatively summing the normalized areas of the PDF (Figure G-8).

Figure G-6. Histogram of TW El between 1989 and 2020.

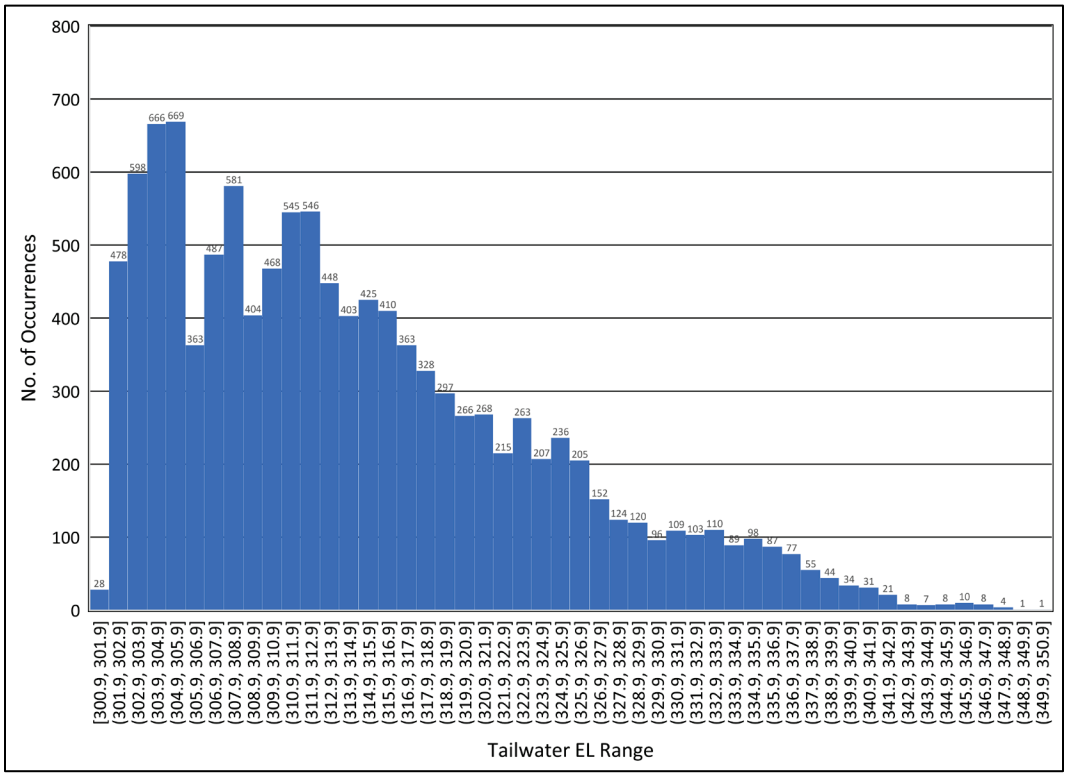

Figure G-7. PDF from histogram of TW El.

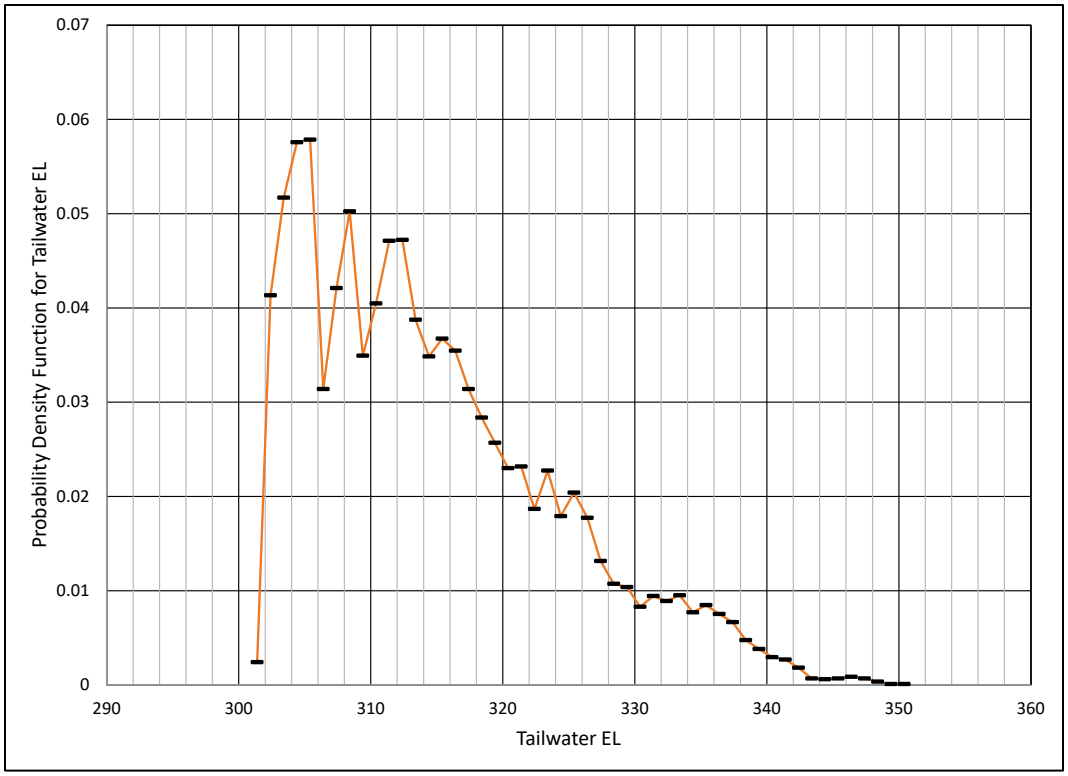

Figure G-8. CDF for TW El.

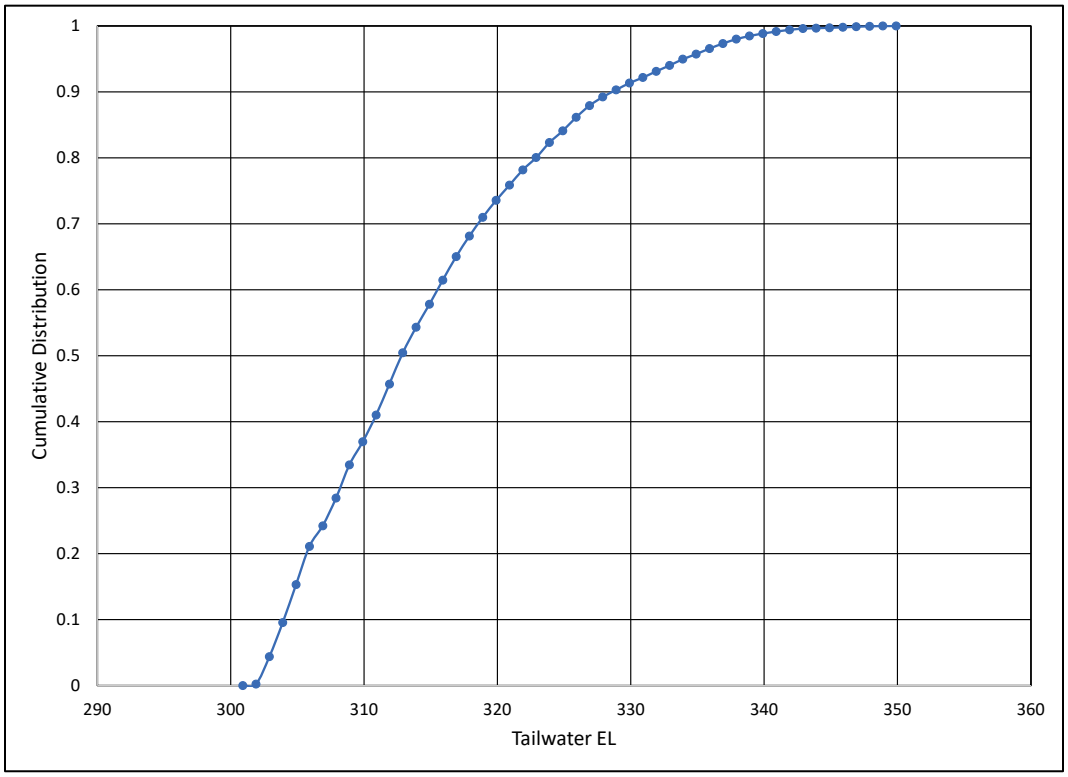

G.2 Hydrostatic Load for the BLD Bulkhead without Tailwater Effects

Equation (10), which is repeated here, is a conventional equation found in many fluid mechanics and hydraulics textbooks and is used to compute hydrostatic pressure (p). As stated previously, γ is the unit weight of water, and y is the vertical distance from the water surface to the location of the hydrostatic pressure of interest (Figure 14):

$$p = \gamma y.$$

The horizontal hydrostatic pressure on the bulkhead is expressed as γH, where γ is the unit weight of water, and H is the total head on the bulkhead. When the bulkhead is closed, H represents the difference between the upper pool el and the spillway crest el when the tailwater is lower than the crest el. Equation (11), which is repeated here, can be used to compute the maximum hydrostatic pressure:

$$p_{max} = \gamma H.$$

The resultant hydrostatic force per foot of width for the bulkhead gate is shown in Equation (12) and is located $H/3$ above the spillway crest (Figure 14):

γ = the unit weight of water = 62.4 lb/ft^3,
H = the head on the gate = 361 – 325 = 36 ft, and
Max hydrostatic load = 0.5 [62.4 lb/ft^3 * (36.00 ft)^2]= 40,435 lb/ft.

The maximum hydrostatic load is experienced if the upper pool is at the top of the top bulkhead unit with the bottom unit seated on the spillway crest. Each unit is 12 ft high, and there are three units, so the maximum head on the bulkheads would be 36 ft (H = 36.0 ft). This load condition represents H_1 (i.e., the maximum net hydrostatic load that will ever occur), which is one of the three hydrostatic loads that are to be considered. The mean hydrostatic load with a pool el of 359 ft is 36,067 lb/ft.

G.3 Wave Load Based on Wave Height and Period for the BLD

The dispersion due to wave load about the mean hydrostatic and hydrodynamic loads needs to be determined. The wave load is a primary load that contributes to load fluctuations. The procedures and methods used to determine wave load for the spillway vertical-lift gate presented in

Chapter 3 and Appendix B were used for the bulkhead. The supporting data and computations for determining the load for the Barkley project are presented in the sections that follow. As mentioned previously, the wind speed, wind direction, and fetch must be determined to develop a wave load.

G.3.1 Wind Speed and Fetch for the BLD

The wind speed and wind direction data were obtained from meteorological data collected over a 24 yr period between 1991 and 2020 at the PAH near Paducah, Kentucky. Wind data were not available for the years 2001–2006. PAH is located approximately 30 mi west of the project. Figure G-9 shows the data collection site in relation to the project.

Figure G-9. Satellite imagery of the wind speed and direction data collection site in relation to the Barkley Spillway. (Map data: Landsat/Copernicus 2002.)

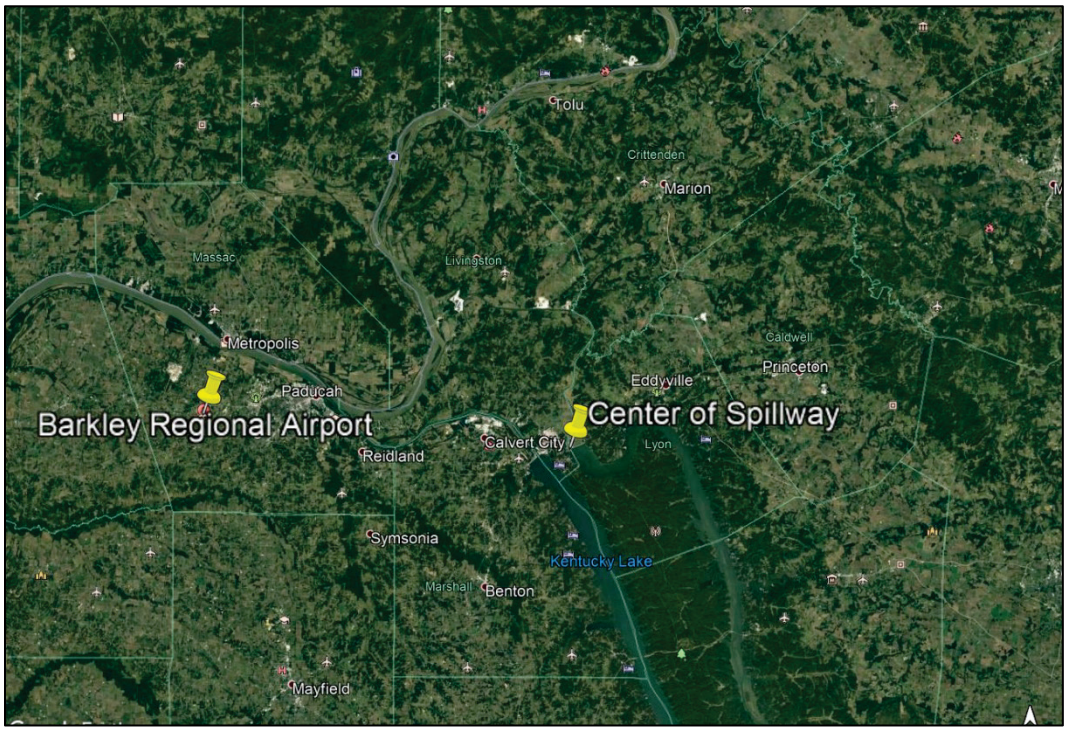

The dataset was fairly complete for the years 2015 to August 2020, with wind speeds and directions reported multiple times per hour. Between 1991 and 2015, the wind speed and direction were usually reported on an hourly basis. The latitude of PAH is 37.0563, and the longitude is −88.7744. The data were obtained from Iowa State University (n.d.).

Figure G-10 shows the fetch determined for the BLD project. The wind direction that impacts the project perpendicular to the spillway axis is 154°. The fetch is approximately 2.22 mi.

Figure G-10. Satellite imagery of the fetch and wind direction determined for the Barkley project. (Map data: Landsat/Copernicus 2002.)

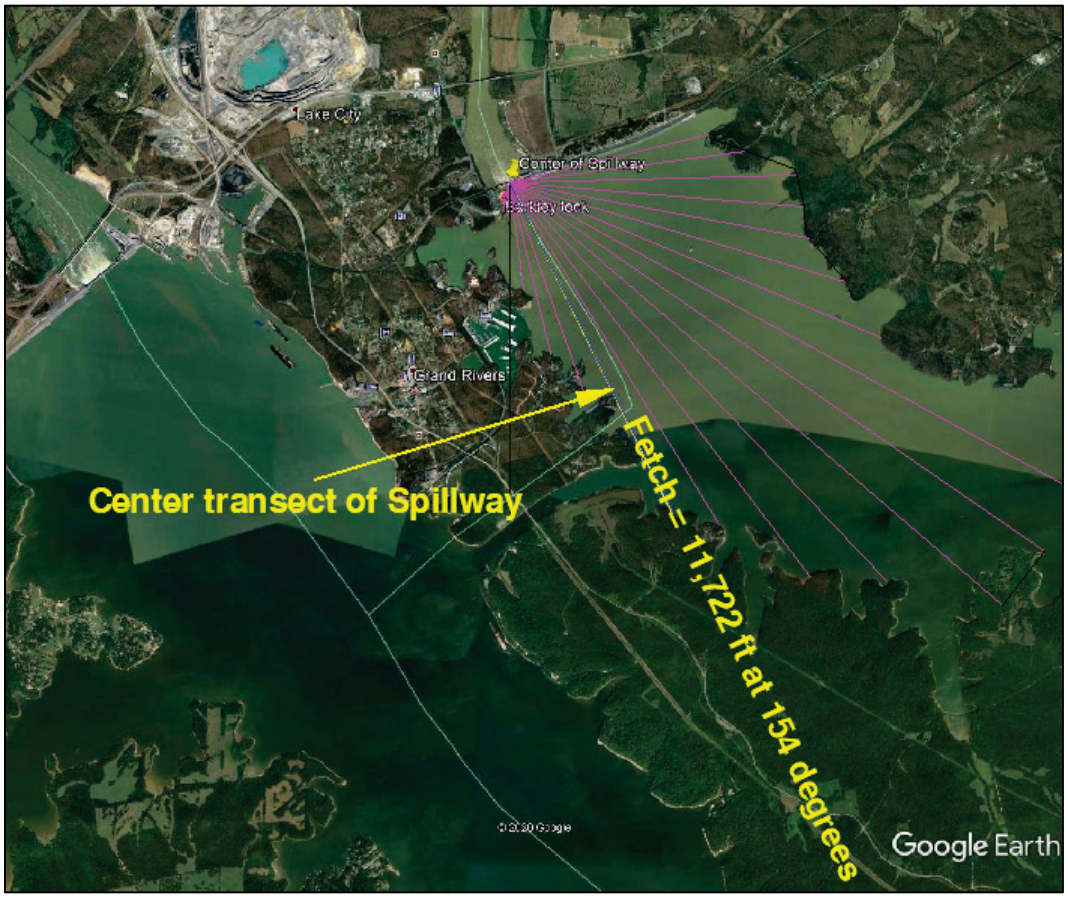

G.3.2 Wind Speed Analyses for the BLD

The methods for determining the appropriate wind speed for the analyses of the wave load developed for the spillway vertical-lift gate were also used for the bulkhead. Based on the fetch length and wind speed, Equation (50), which is repeated here, can be used to determine the time required for full wave growth:

$$t_{min} = 1.0F^{0.73}U_{10}^{-0.46}.$$

Using an estimated wind speed between 30 and 40 mph and a fetch length of 2.22 mi, the minimum time to reach full wave growth was around 1 hr, so a t_{min} value of 1 hr was used in the analysis. Equation (50) requires

metric units. The wind speed data were then processed to determine the maximum 1 hr average wind speed with a wind direction between 140° and 180° per year. Table G-1 shows the wind speed values used in the analyses.

Table G-1. Maximum yearly 1 hr average wind speed for wind directions between 140° and 180° at PAH for the 1991 to 2020 observation period.

Year	Max 1 hr Avg Wind Speed (mph)
1991	26.5
1992	28.2
1993	31.6
1994	25.3
1995	23.9
1996	26.5
1997	23.6
1998	23.6
1999	17.3
2000	16.1
2007	20.1
2008	27.6
2009	27.0
2010	21.0
2011	19.9
2012	20.7
2013	26.8
2014	22.4
2015	26.5
2016	20.3
2017	17.4
2018	18.6
2019	21.7
2020	20.7

G.3.3 Extreme Value Estimation Using Maximum 1 hr Average Yearly Values of Wind Speed for the BLD

The type 1 Gumbel distribution was used for a GEV analysis. Figure G-11 shows the results from the extreme value estimation using the maximum 1 hr average annual values for PAH data. The 100 yr recurrence interval wind speed from this analysis was 39.5. The magnitude of the 100 yr

recurrence interval for wind speed was considered a suitable frequency for wave height calculations.

Figure G-11. Extreme wind speed estimation for PAH based on maximum 1 hr average annual values of wind speed.

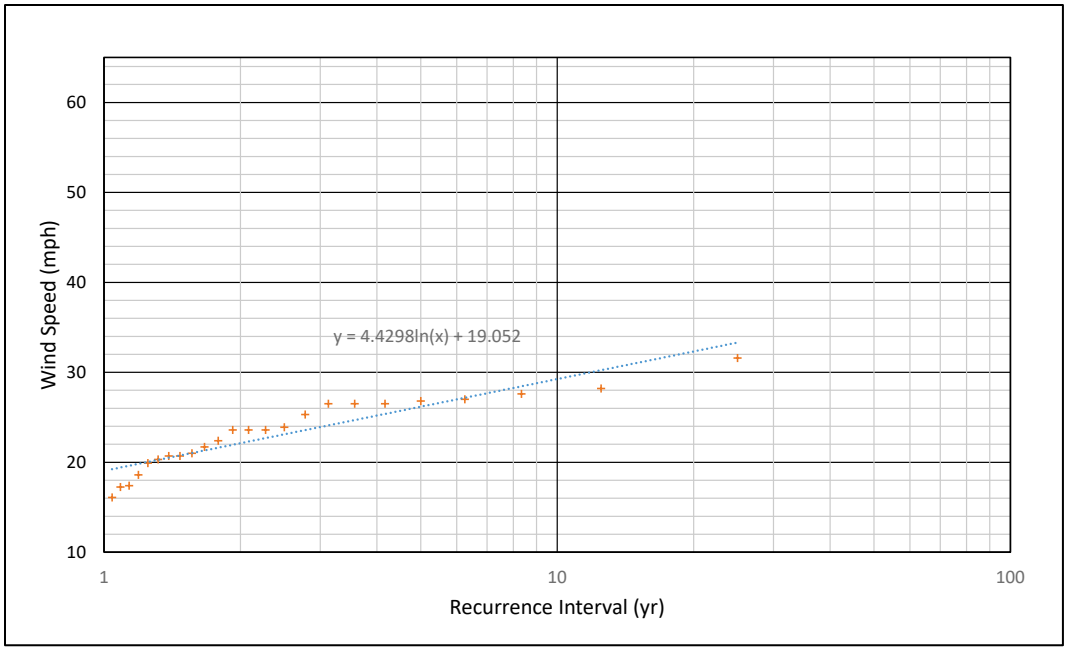

G.3.4 Wind Frequency Based on Gumbel Type 1 Distribution with Gringorten's Method Using Maximum Yearly 1 hr Average Values of Wind Speed for the BLD

The type 1 Gumbel distribution can be used with Gringorten's (1963) plotting position formula to create another method for evaluating wind speed. A description of this procedure is given in Chapter 2. Figure G-12 shows a plot of the return period versus wind speed determined using this procedure for the data from PAH. The wind speed for the 100 yr return period was 36.3 mph.

Figure G-12. Wind frequency from Gumbel type 1 distribution with Gringorten's method for the PAH airport using the maximum 1 hr average annual wind speed.

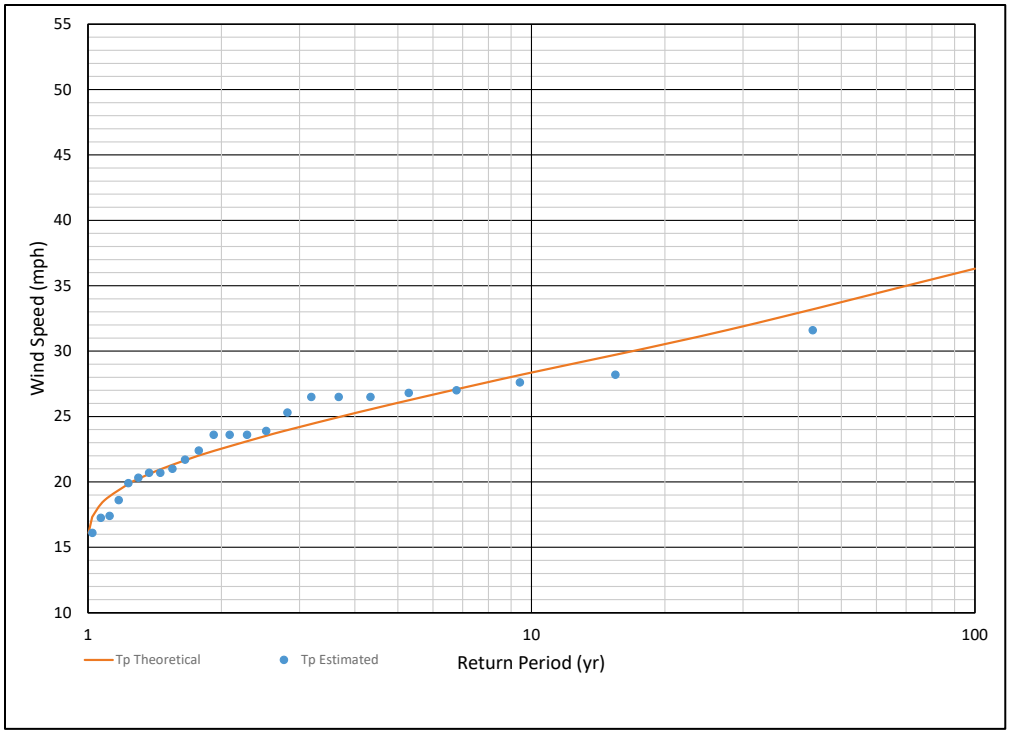

To further investigate the statistics for the wind speed, a formula to determine the standard error (discussed in Appendix A) was used for the data presented in Figure G-12.

Figure G-13 shows the fitted curve bounded by plus and minus 1, 2, and 3 standard deviations (σ) for the PAH wind data (n = 24). Table G-2 shows the values for these statistics. The mean 100 yr return period wind speed was 36.3 mph. The standard deviation was determined to be 1.004 mph. The 100 yr return period plus 3 standard deviations gives a wind speed of 39.3 mph.

Table G-2. Results from wind speed analysis for the Barkley bulkhead.

Statistic	100 yr Wind Speed (mph)
+3σ	39.3
+2σ	38.3
+1σ	37.3
Mean	36.3
−1σ	35.3
−2σ	34.3
−3σ	33.3

Figure G-13. Wind frequency curves based on peak yearly 1 hr average wind speed for the PAH data.

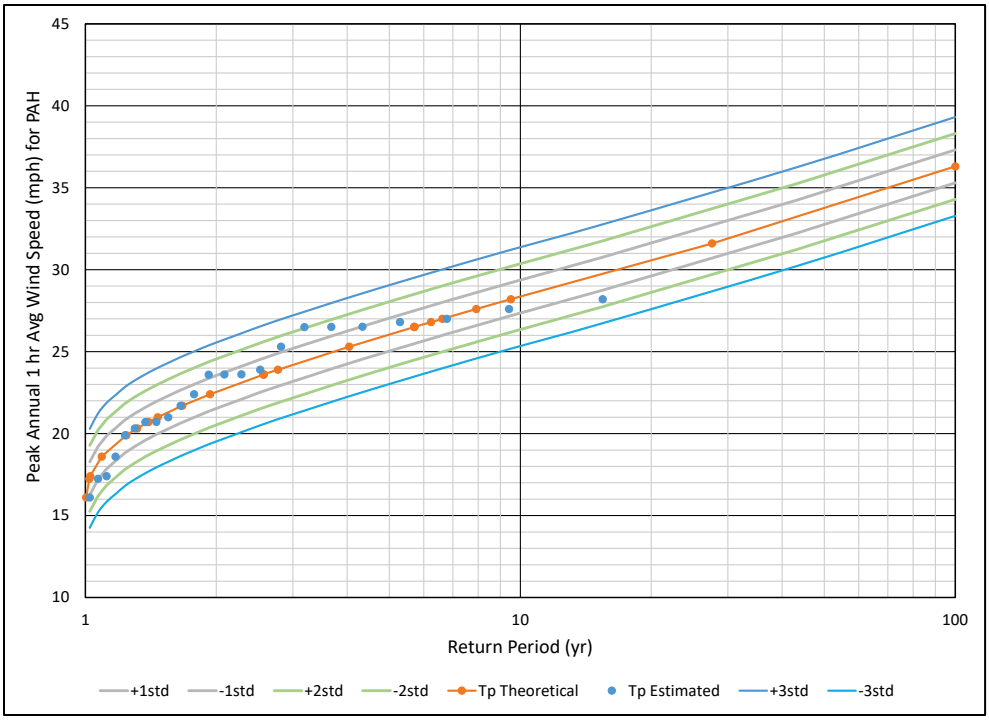

G.3.5 Wave Height and Period from the NARFET Model for the BLD

Table G-3 shows the input data and results from the use of the NARFET program for the Barkley spillway bulkhead. The program input requires the radial lengths of the fetch and the angle increments for resolution of the wind direction. Figure G-10 shows the radial lengths (a total of 22) determined for an angle increment of 6°. Figure G-14 shows the significant wave height and period for the wind speeds determined between −3σ and +3σ for the 100 yr return period for the data shown in Table G-3. The wind direction was between 140° and 180° for a duration of 1 hr.

Table G-3. Wave height, wave period, and wavelength computed using the NARFET model for the Barkley bulkhead.

Wind Speed (mph)	Wave Height (m)	Wave Period (sec)	Wavelength (m)
39.3	1.26	3.87	23.4
38.3	1.23	3.83	22.9
37.3	1.20	3.79	22.5
36.3	1.17	3.75	22.0
35.3	1.14	3.71	21.5
34.3	1.11	3.67	21.0
33.3	1.08	3.63	20.5

Figure G-14. Wave height versus wind speed from Smith's NARFET model for the Barkley bulkhead.

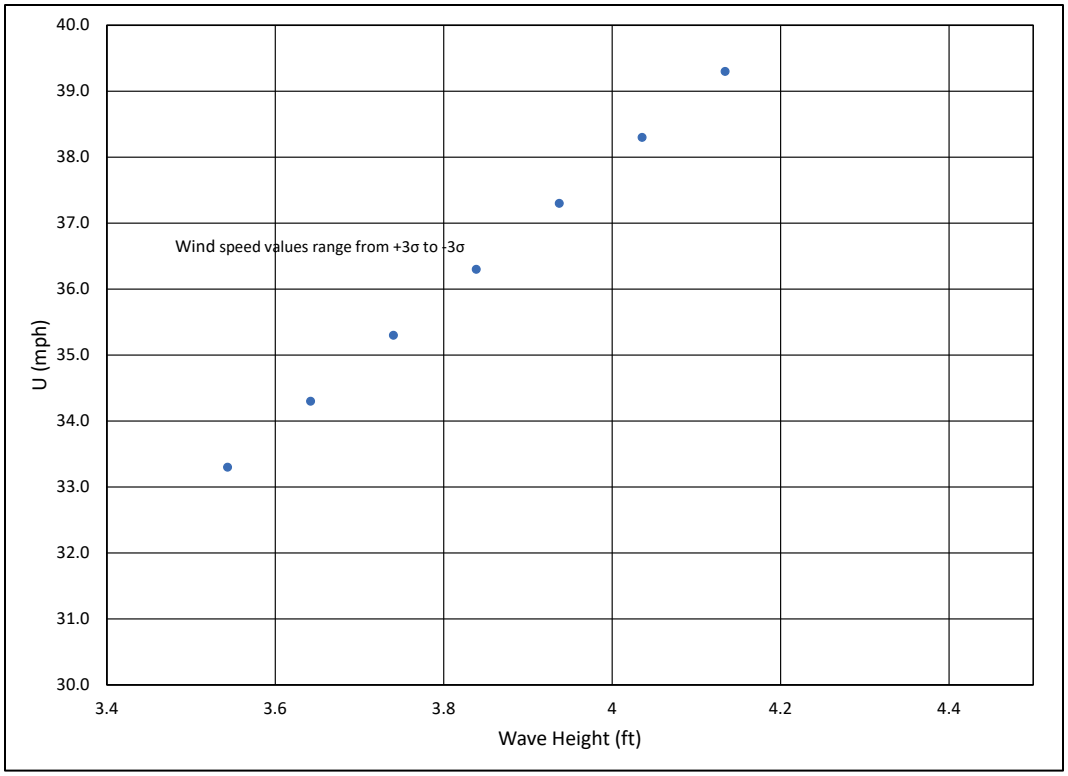

G.3.6 Wave Load from Goda for the BLD

Goda (2010) also recommended formulations for determining significant wave height and period based on wind speed and fetch. The background and supporting equations for his formulations are provided in Chapter 2. This methodology is considered applicable to the spillway bulkhead. Table G-4 contains the significant wave height, wave period, and wavelength for the Barkley bulkhead.

Table G-4. Significant wave height, wave period, and wavelength using Goda's (2010) formulations for the Barkley bulkhead.

Wind Speed (mph)	Wave Height (m)	Wave Period (sec)	Wavelength (m)
39.3	0.814	2.741	11.73
38.3	0.797	2.720	11.55
37.3	0.781	2.700	11.37
36.3	0.765	2.677	11.19
35.3	0.749	2.655	11.01
34.3	0.732	2.632	10.82
33.3	0.715	2.609	10.63

Figure G-15 shows a plot of wind speed (*U*) versus wave height determined from Goda's (2010) recommended formulations from the statistical analysis of the wind speed data for PAH.

Figure G-15. Wave height versus wind speed from Goda's (2010) procedure for the Barkley bulkhead.

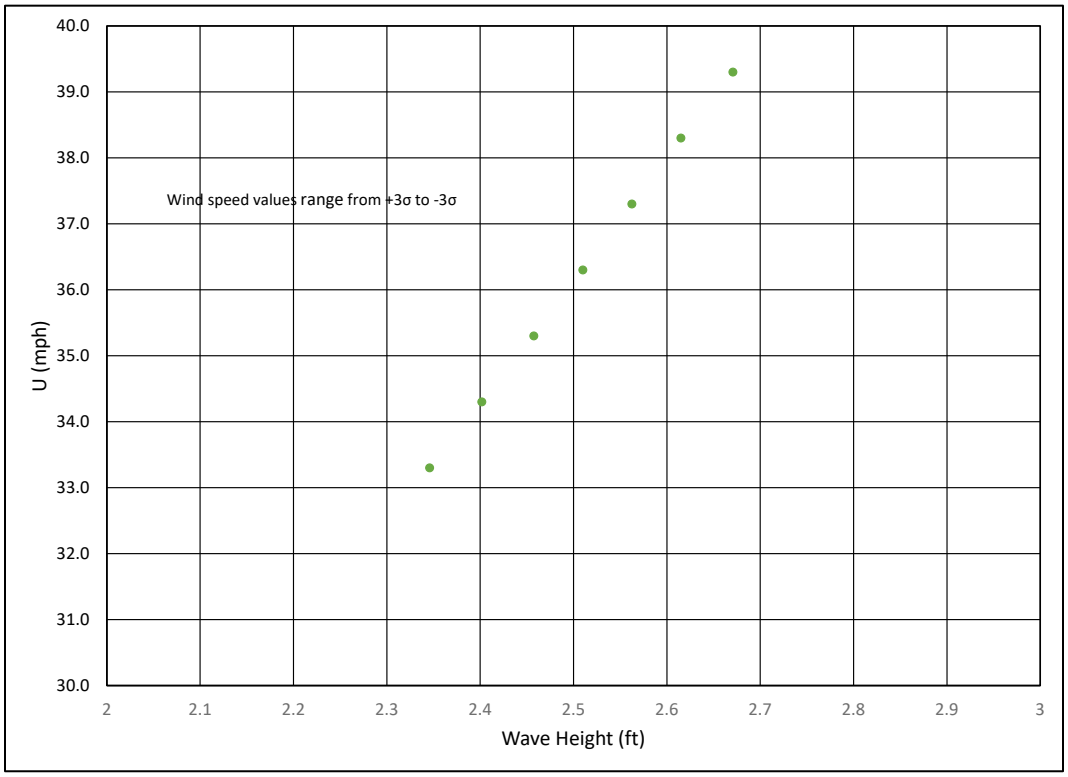

The wave pressure distribution and subsequent wave force for the bulkhead can now be determined from the significant wave height and wave period. The complete description of this procedure is shown Section 2.3.2.3. Based on the parameters listed in Table G-5 and on the Goda (2010) formulations in Section 2.3.2.3, an example solution was reached. Table G-6 lists the parameters used in the example wave force calculation (imperial and metric units included). The example uses the spring upper pool el of 359, the top of bulkhead el of 361, and the mean 100 yr return period wind speed of 36.3 mph.

Table G-5. Parameters used in the example wave force calculation (imperial and metric units included) for the Barkley project for a wind speed of 36.3 mph.

Parameter	Value (Imperial Units)	Value (Metric Units)	Description
h_c	2.00 ft	0.61 m	Bulkhead height above upper pool el
d (originally d_{SWL})	34.0 ft	10.36 m	Difference between upper pool el and spillway crest el
h (originally h_{SWL})	83.0 ft	25.30 m	Difference between upper pool el and approach channel invert el
tan θ	0	0	Bottom slope toward bulkhead
β_D	0 deg	0 deg	Design incident wave angle
$H_{1/3}$	2.51 ft	0.765 m	Significant wave height for example problem
$T_{1/3}$	2.68 sec	2.68 sec	Significant wave period for example problem
L_D	36.7 ft	11.19 m	Design wave length for example problem
ρ	62.4 lb/ft^3	1,000 kg/m^3	Density of freshwater
g	32.2 ft/sec^2	9.81 m/sec^2	Acceleration due to gravity
h'	34.0 ft	10.36 m	For the vertical-lift gate: $h' = H = d_{SWL}$

The design wave height (H_D) is the minimum of $\alpha_h H_{1/3}$ and H_b, where α_h ranges from 1.6 to 2.0. For the design of nearshore vertical structures, Goda (2010) suggests using a value of 1.8 for α_h. Equations (59) through (61) are repeated here:

$$H_d = H_{Max} = \min\{\alpha_h * H_{1/3}, H_b\},$$

$$H_b = 0.17 * L_D \left\{1 - \exp\left[-1.5\frac{\pi h_b}{L_D}\left(1 + 15 * \tan^{\frac{4}{3}}\theta\right)\right]\right\},$$

where

$$h_b = h + 5 * H_{1/3} * \tan\theta.$$

Therefore,

$$\alpha_h H_{1/3} = 1.8 * 0.765 \text{ m} = 1.377 \text{ m (4.52 ft)},$$

$$h_b = 25.3 \text{ m} + 5 * 0.765 \text{ m} * \tan(0) = 25.3 \text{ m (83.0 ft)},$$

$$H_b = 0.17 * 11.19 \text{ m}\left\{1 - \exp\left[-1.5\frac{\pi 25.3 \text{ m}}{11.19 \text{ m}}\left(1 + 15 * \tan^{\frac{4}{3}}(0)\right)\right]\right\}$$
$$= 1.377 \text{ m (4.52 ft)},$$

so,

$$H_d = H_{Max} = \min\{1.377 \text{ m}, 1.377 \text{ m}\} = 1.377 \text{ m (4.52 ft)}.$$

Next, we calculate the coefficients of wave pressure (α_1, α_2, and α_3) given in Equations (56) through (58), which are repeated here:

$$\alpha_1 = 0.6 + \frac{1}{2}\left[\frac{\frac{4\pi h}{L_D}}{\sinh\left(\frac{4\pi h}{L_D}\right)}\right]^2,$$

$$\alpha_2 = \min\left[\frac{h_b - d}{3h_b}\left(\frac{H_D}{d}\right)^2, \frac{2d}{H_D}\right],$$

$$\alpha_3 = 1 - \frac{h'}{h}\left[1 - \frac{1}{\cosh\left(\frac{2\pi h}{L_D}\right)}\right].$$

The h and d values in the preceding equations are respectively equivalent to the h_{SWL} and d_{SWL} of Table G-5. Substituting the values gives

$$\alpha_1 = 0.60 \text{ (from Equation 56)},$$

$$\alpha_2 = \min\left[\frac{25.3 \text{ m} - 10.36 \text{ m}}{3(25.3 \text{ m})}\left(\frac{1.377 \text{ m}}{10.36 \text{ m}}\right)^2, \frac{2(10.36) \text{ m}}{1.377 \text{ m}}\right] = \min[0.0035 \text{ m}, 15.05 \text{ m}]$$
$$= 0.0035 \text{ (from Equation 57)},$$

and because $h' = d_{SWL} = H$,

$$\alpha_3 = 0.591 \text{ (from Equation 58)}.$$

The lateral pressure components P_1 and P_3 are evaluated here:

$$P_1 = 0.5\,(1 + \cos\beta_D)\,(\alpha_1 + \alpha_2 * \cos^2\beta_D)\,\rho * g * H_D,$$

$$P_3 = \alpha_3 P_1.$$

The solutions to P_1 and P_3 are

$$P_1 = 8{,}152 \text{ N/m}^2 = 8.152 \text{ kN/m}^2 = 170.19 \text{ (lb/ft}^2\text{)},$$

$$P_3 = 4{,}814 \text{ N/m}^2 = 4.814 \text{ kN/m}^2 \text{ (100.50 lb/ft}^2\text{)}.$$

As shown in Section 2.3.2.3, the total lateral force per linear width (F_{Lat}) on the face of the spillway bulkhead is

$$F_{Lat} = 0.5(P_1 + P_3)H + 0.5(P_1 + P_4)h_c',$$

where

$$P_4 = P_1\left(1 - \frac{h_c}{\eta^*}\right), \text{if } \eta^* > h_c,$$

or

$$P_4 = 0, \text{ if } \eta^* \leq h_c,$$

$$\eta^* = 0.75(1 + \cos(\beta_D))H_D,$$

$$h_C' = \min\{\eta^*, h_C\}.$$

Therefore, the solution of the resultant force, F_{Lat}, is given as

h_c = 0.61 m (2.00 ft) (from Table G-5),

η^* = 2.065 m (6.77 ft).

Because $\eta^* > h_c$,

P_4 = 5,744 N/m^2, 5.744 kN/m^2 (119.91 lb/ft^2),

h_C' = min{2.065 m, 0.61 m} = 0.61 m (2.00 ft),

F_{Lat} = 71.40 kN/m (4,893 lb/ft).

The preceding analysis indicates the total lateral wave force per linear width of the bulkhead for a sustained 36.3 mph wind is 4,893 lb/ft.

In Figure B-13 and Figure B-14, the pressure terms P_1, P_3, and P_4 are shown acting on the vertical-lift gates, which are similar to the bulkhead. The location of the lateral equivalent force (h_{Lat}) can be determined using the one-third/one-sixth method developed by Ebeling et al. (2018; Section 2.3.2.4). By applying this method for the lateral forces and summing moments about point 3, Equation (A-14), repeated here, was developed:

$$h_{Lat} = \frac{(h_4 - h_1)\left(\frac{P_4}{3} + \frac{P_1}{6}\right)h_4 + (h_4 - h_1)\left(\frac{P_4}{6} + \frac{P_1}{3}\right)h_1 + (h_1 - h_3)\left(\frac{P_1}{3} + \frac{P_3}{6}\right)h_1}{F_{Lat}},$$

$$h_{Lat} = \frac{0.61\text{ m}\left(\frac{5.744\frac{\text{kN}}{\text{m}^2}}{3} + \frac{8.152\frac{\text{kN}}{\text{m}^2}}{6}\right)15.24\text{ m} + 0.61\text{ m}\left(\frac{5.744\frac{\text{kN}}{\text{m}^2}}{6} + \frac{8.152\frac{\text{kN}}{\text{m}^2}}{3}\right)10.36\text{ m}}{104.662\frac{\text{kN}}{\text{m}}}$$

$$+ \frac{10.36\text{ m}\left(\frac{8.152\frac{\text{kN}}{\text{m}^2}}{3} + \frac{4.814\frac{\text{kN}}{\text{m}^2}}{6}\right)14.57\text{ m}}{104.662\frac{\text{kN}}{\text{m}}}$$

$$h_{Lat} = 5.923\text{ m}.$$

Table G-4 lists the wave heights and wave periods used to compute the wave forces and pressure distributions determined from the wind speed analysis at the Barkley project. The wave forces and pressure distributions computed from Goda's (2010) procedure for the data in Table G-4 are shown in Table G-6.

Table G-6. Wave force and pressure distribution computations using Goda's (2010) procedure for data in Table G-4 for the Barkley project.

Barkley Data	Statistic						
	+3σ	+2σ	+1σ	Mean	−1σ	−2σ	−3σ
Wind Speed (mph)	39.3	38.3	37.3	36.3	35.3	34.3	33.3
η^* (m)	2.198	2.152	2.109	2.066	2.022	1.976	1.931
η^* (ft)	7.21	7.06	6.92	6.78	6.63	6.48	6.34
P_1 (N/m^2)	8,681	8,497	8,325	8,152	7,980	7,797	7,614
P_3 (N/m^2)	5,126	5,018	4,916	4,814	4,712	4,604	4,496
P_4 N/m^2	6,271	6,088	5,916	5,744	5,573	5,390	5,208
F_{Lat} (kN/m)	76.08	74.46	72.93	71.40	69.88	68.26	66.64
h_{Lat} (m)	2.324	2.321	2.317	2.314	2.309	2.303	2.298
h_{Lat} (ft)	5.93	5.92	5.92	5.92	5.92	5.92	5.92
P_1 (lb/ft^2)	181	177	174	170	167	163	159
P_3 (lb/ft^2)	107	105	103	100	98	96	94
P_4 (lb/ft^2)	131	127	124	120	116	113	109
F_{Lat} (lb/ft)	5,213	5,102	4,997	4,893	4,788	4,677	4,566

G.4 Hydrodynamic Loads for the BLD

The example in this appendix does not experience hydrodynamic loads. Additional research is needed to develop a method for computing

hydrodynamic loads for an emergency bulkhead. As stated in Chapter 8, the recommended method for determining these loads is full-scale testing at the project site.

G.5 Probabilistic Characterization of the Hydrostatic and Hydrodynamic Loads for the Barkley Spillway Bulkhead

The Barkley bulkhead used during static conditions needs to function during normal pool conditions. The standard deviation for the range of the normal pool is more appropriate than the historical maximum and minimum upper pool els. The top el of the bulkhead (361) is considered a good choice for the maximum allowable upper pool el before the bulkhead is removed from service. The range of the normal upper pool at BLD chosen for the analysis is the top el of the bulkhead, 361, and the historical minimum upper pool el, 353.26. The standard deviation was computed as (maximum – minimum)/6, which gives 1.29 ft. The historical mean upper pool el for the project is 357.04.

Figure G-16 shows a plot of the pressure distributions for upper pools ranging from el 360.91 (+3σ) to el 353.17 (–3σ) and the pressure distribution for the mean upper pool el of 357.04. Figure G-17 shows the resultant hydrostatic force for the range of upper pool els. The magnitude of the resultant hydrostatic force ranged from 24.76 kip/ft to 40.23 kip/ft.

The dispersion of the hydrodynamic loads for the Barkley spillway bulkhead probably need to be estimated using a laboratory or numerical model. Because the dispersion in the hydraulic loads is caused by the changes in the upper and lower pool elevations, the time period over which these changes occur makes field measurements too difficult. The most reliable estimates over the desired range of upper and lower pool els would come from performing laboratory experiments that could be used to validate a numerical model. The numerical model could then be used to compute the hydraulic loads for the range of conditions needed for the LRFD analysis.

Figure G-16. Hydrostatic pressure distributions for the range of upper pool els for the Barkley spillway bulkhead.

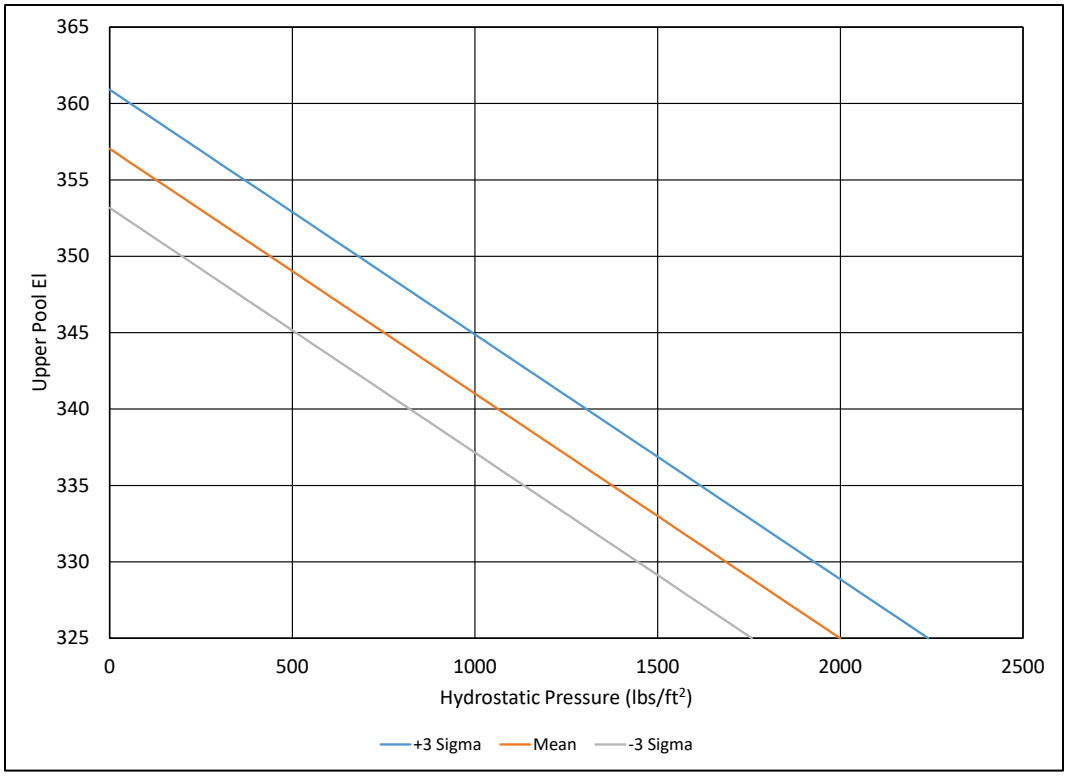

Figure G-17. Resultant hydrostatic force for range of upper pool els for the Barkley spillway bulkhead.

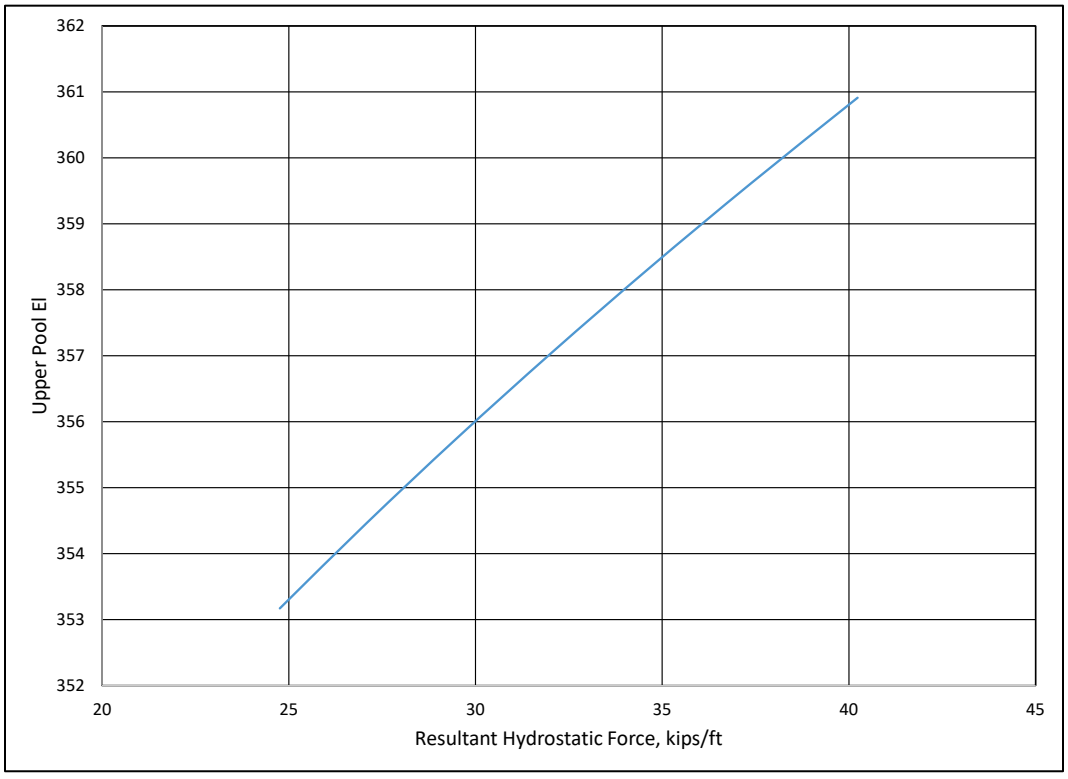

G.6 Summary of Hydraulic Loads for the BLD

Hydrostatic and wave loads are the primary hydraulic loads on the spillway bulkhead used for nonemergency operations. Table G-7 lists example hydraulic loads determined for the BLD spillway bulkhead.

Table G-7. Example hydraulic loads for the Barkley Lock and Dam (BLD) spillway bulkhead.

Max Estimated Hydraulic Load	Value (kip/ft)
Hydrostatic (no tailwater effect)	40.43 (36.07 with forebay el of 359)
Hydrodynamic	N/A
Wave*	5.21
Hydrostatic + Wave	45.64
Hydrodynamic + Wave	N/A

* Based on a mean forebay el and 39.3 mph wind speed at 154° (100 yr wind event + 3σ). P_1/P_3 = 1.69.

Some of the loads should be combined to give the maximum loads expected for the gate. Table G-7 lists these combined loads. The wave force results in the table indicate that wind-induced wave forces are significant and need to be included in spillway bulkhead design force computations.

Appendix H: Example Hydraulic Load Computations for the Williams Boulevard Rolling Gate

In this appendix, the procedures discussed in Chapter 9 of the main report are presented using data from an existing USACE Flood Protection project. This project is different from the previous HSS described in this report because the rolling gate is a flood closure structure, and the other HSS have been associated with navigation projects. The data needed to quantify the hydraulic loads for the rolling gate and example computations are provided.

H.1 Flood Protection System Description

The Williams Boulevard Flood Protection system is located in the City of Kenner, Louisiana. The system was upgraded after Hurricane Katrina to bring the hurricane protection to 100 yr levels. The top el of the previous rolling gate was 14.5, and the new rolling gate has a top el of 16.5 to satisfy the new design criteria. Pertinent information for the rolling gate follows:

- Top of gate el = 16.5
- Bottom of gate el = 10.0
- Gate length = 67.5 ft
- Still water level el = 11.2
- Start station for gate monolith = 143 + 04.78
- End station for gate monolith = 142 + 32.78

An aerial view and plan schematic of the location of the rolling gate taken from the USACE-MVN (2011) report, *Lake Pontchartrain and Vicinity Hurricane Protection Project LPV 18.2–Williams Blvd. Floodgate Jefferson Parish, Louisiana*, is shown in Figure H-1 and Figure H-2. Figure H-3 shows an elevation view of the rolling gate taken from the same report.

The statistics for the rolling gate were determined from the fluctuations in the water level on the flood side of the gate. These fluctuations result from the surge due to an approaching hurricane. If the strength of the hurricane is predicted to cause a surge high enough to reach the gate, then the gate is closed. The flood gate used for surge protection cannot be analyzed in the same manner as the previous HSS discussed in this report. Typical HSS for

navigation projects have historical data for the water surface elevations from which the statistics can be computed. To develop statistics for the rolling gate used as a flood closure structure, data from multiple events would be required; because these events often occur many years apart, these data have to be estimated from simulations. For this design example, the hydrostatic load was determined based on the still-water level (SWL) of el 11.2 and the wind from a 100 yr hurricane event.

Figure H-1. Location of Williams Boulevard Rolling Gate. (Image reproduced from USACE-MVN 2011, sheet G-002. Public domain.)

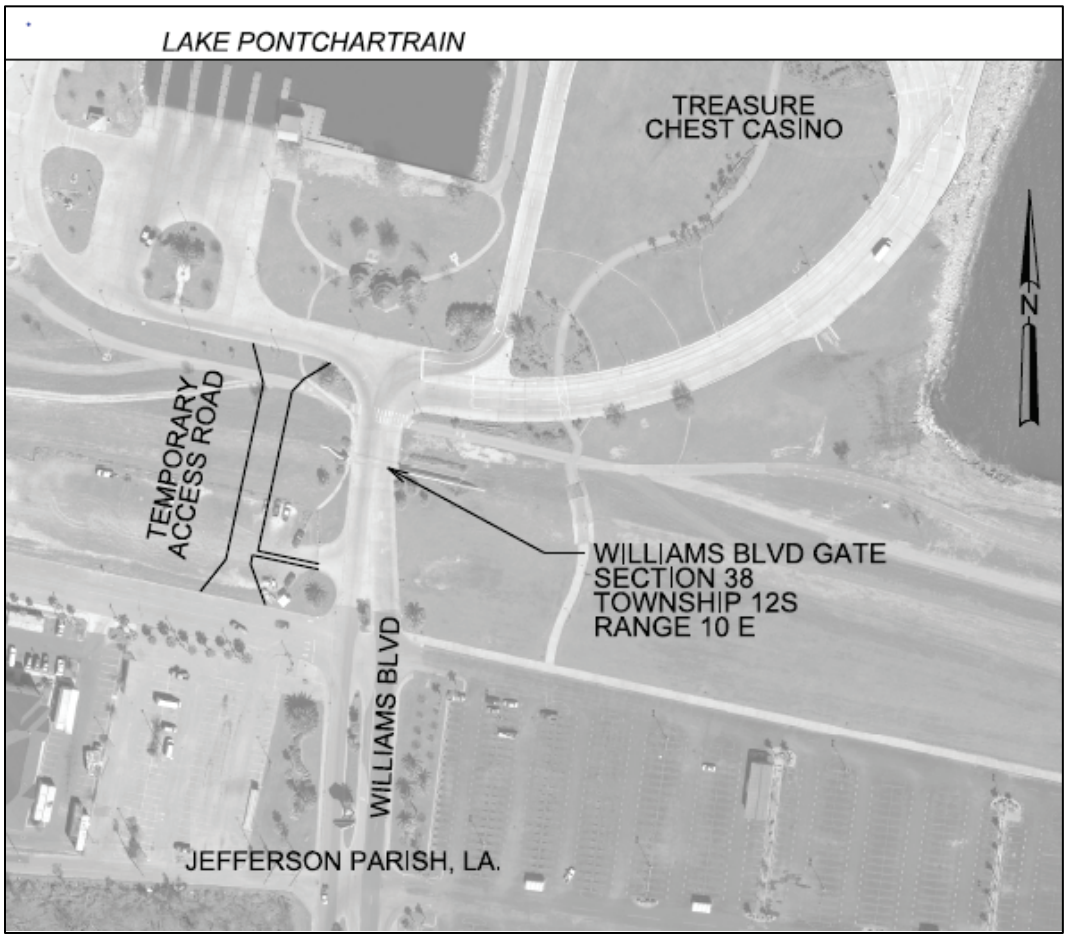

Figure H-2. Plan schematic of rolling gate location. (Image reproduced from USACE-MVN 2011, sheet S-101. Public domain.)

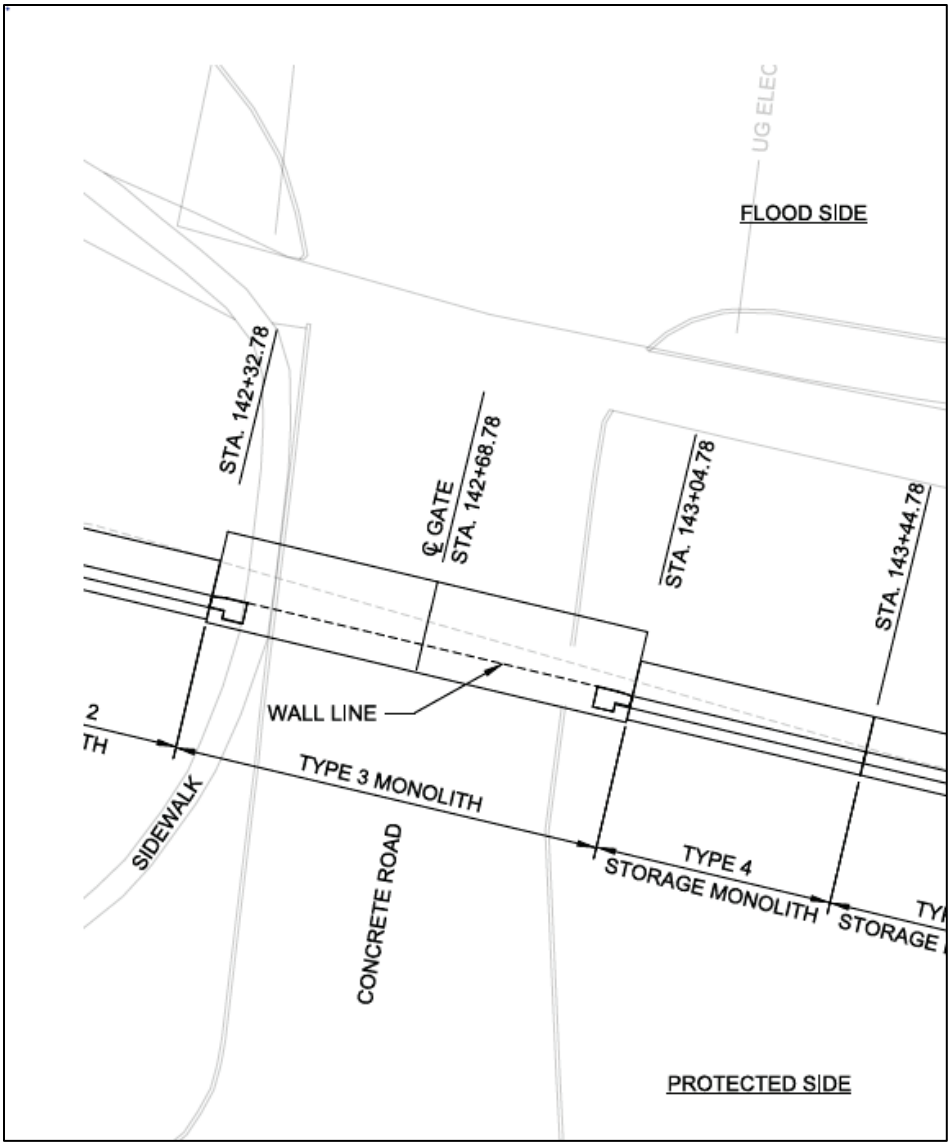

Figure H-3. Partial elevation view of rolling gate. (Image reproduced from USACE-MVN 2011, sheet S-108. Public domain.)

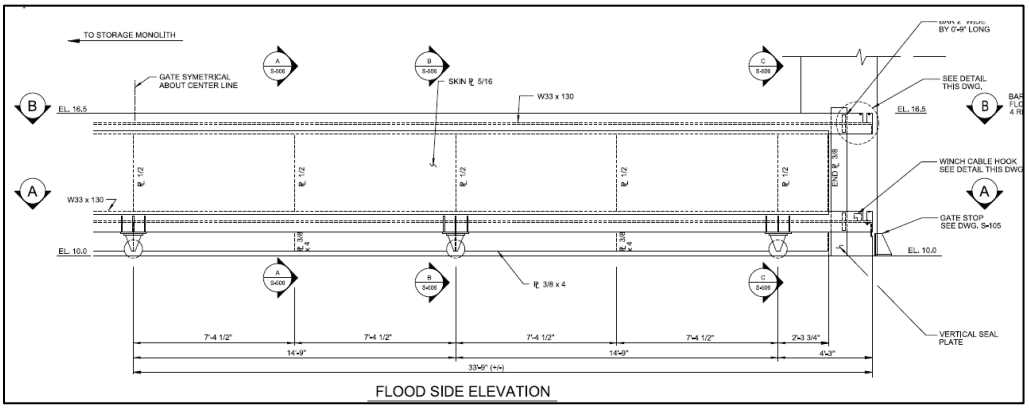

H.2 Hydrostatic Load for Rolling Gates

Equation (10), which is repeated here, is a conventional equation that is found in many fluid mechanics and hydraulics textbooks and is used to compute hydrostatic pressure (p). As stated previously, γ is the unit weight of water, and y is the vertical distance from the water surface to the location of the hydrostatic pressure of interest (Figure 14):

$$p = \gamma y.$$

The horizontal hydrostatic pressure on a closed gate is expressed as γH, where γ is the unit weight of water, and H is the total head on the gate. When the gate is closed, H represents the difference between the surge height el and the bottom of the gate. Equation (11), which is repeated here, is used to compute the maximum hydrostatic pressure:

$$p_{max} = \gamma H.$$

The hydrostatic force per foot of width for the rolling gate is computed from Equation (12), which is repeated here:

$$H_s = \frac{1}{2}\gamma H^2,$$

where

γ = the unit weight of sea water = 64.3 lb/ft^3,
H = the head on the gate = 11.2 – 10.0 = 1.2 ft,
Hydrostatic load at SWL = 0.5 [64.3 lb/ft^3 * (1.20 ft)^2]= 46.3 lb/ft, and
Max hydrostatic load = 0.5 [64.3 lb/ft^3 * (6.5 ft)^2]= 1,358 lb/ft.

The maximum hydrostatic load would be experienced if the surge height el was at the top of the rolling gate. The gate is 6.5 ft high, so the maximum hydrostatic load is 1,358 lb/ft. This load condition represents H_1 (i.e., the maximum hydrostatic load that will ever occur) of the three hydrostatic loads that are to be considered. The hydrostatic load with an SWL of 11.2 ft is 46.3 lb/ft.

H.3 Wave Load Based on Wave Height and Period for Rolling Gates

The wave height and period are required when using the Goda (2010) procedures to determine the wave load for the rolling gate used as a flood closure structure to protect against a hurricane surge. As mentioned, the flood protection system incorporating this rolling gate is designed for 100 yr hurricane level protection. The top of the gate was set at the 100 yr hurricane event, which was el 16.5. The SWL el is 11.2, so a wave height greater than 5.3 ft would overtop the gate. For this example, the significant wave height was arbitrarily selected as 6.56 ft (2 m).

H.3.1 Wind Speed and Fetch for Rolling Gates

A detailed analysis of hurricane events would be necessary to estimate the wind speed and fetch for this project; therefore, the parameters needed to produce a significant wave height of 6.56 ft were chosen. The wind speed was 80 mph, and the fetch was 5 mi.

H.3.2 Wind Speed Analyses for Rolling Gates

Based on the fetch length and wind speed, Equation (50), which is repeated here, can be used to determine the time required for full wave growth:

$$t_{min} = 1.0F^{0.73}U_{10}^{-0.46}.$$

Using a wind speed of 80 mph and a fetch length of 5 mi, the minimum time to reach full wave growth was around 56 min, so a t_{min} value of 1 hr was used in the analysis. This value seems reasonable for a hurricane event. Equation (50) requires metric units.

H.3.3 Wave Load from Goda for Rolling Gates

Goda (2010) also recommended formulations for determining significant wave height and period based on wind speed and fetch. The background and supporting equations for these formulations are provided in Chapter 2. This methodology is considered applicable to the rolling gate used as a flood closure structure for a hurricane event. Table H-1 contains a comparison of wave heights that were determined using Goda's formulations for different wind speeds. The fetch was held constant at 5 mi.

Table H-1. Significant wave height, wave period, and wavelength using Goda's (2010) formulations for a rolling gate with a 5 mi fetch.

Wind Speed (mph)	Wave Height (m)	Wave Period (sec)	Wavelength (m)
60	1.658	3.959	24.47
70	1.869	4.145	26.82
80	2.073	4.311	29.01
90	2.270	4.461	31.08
100	2.461	4.600	33.03

The wave pressure distribution and subsequent wave force for the rolling gate can now be determined from the significant wave height and wave period. The complete description of this procedure is shown in Chapter 2, Section 2.3.2.3. Based on the parameters listed in Table H-2 and on the Goda (2010) formulations in Section 2.3.2.3, an example solution was reached. Table H-3 lists the results of the example wave force calculation (imperial and metric units included). The example uses the SWL at el 11.2, a top of rolling gate el of 16.5, and a wind speed of 80 mph.

Table H-2. Parameters used in the example wave force calculation (imperial and metric units included) for the rolling gate for a wind speed of 80 mph.

Parameter	Value (Imperial Units)	Value (Metric Units)	Description
h_c	5.30 ft	1.62 m	Rolling gate height above SWL
d (originally d_{SWL})	1.2 ft	0.366 m	Difference between SWL and bottom of gate
h (originally h_{SWL})	4.2 ft	1.28 m	Difference between SWL and approach channel invert el
tan θ	0	0	Bottom slope toward bulkhead
β_D	0 deg	0 deg	Design incident wave angle
$H_{1/3}$	6.79 ft	2.07 m	Significant wave height for example problem
$T_{1/3}$	4.311 sec	4.311 sec	Significant wave period for example problem
L_D	95.18 ft	29.01 m	Design wave length for example problem
ρ	64.3 lb/ft^3	1,030 kg/m^3	Density of seawater
g	32.2 ft/sec^2	9.81 m/sec^2	Acceleration due to gravity
h'	1.2 ft	0.366 m	For the rolling gate: $h' = H = d_{SWL}$

The design wave height (H_D) is the minimum of $\alpha_h H_{1/3}$ and H_b, where α_h ranges from 1.6 to 2.0. For the design of nearshore vertical structures, Goda (2010) suggests using a value of 1.8 for α_h. Equations (59) through (61) are repeated here:

$$H_d = H_{Max} = \min\{\alpha_h * H_{1/3}, H_b\},$$

$$H_b = 0.17 * L_D\left\{1 - \exp\left[-1.5\frac{\pi h_b}{L_D}\left(1 + 15 * \tan^{\frac{4}{3}}\theta\right)\right]\right\},$$

where

$$h_b = h + 5 * H_{1/3} * \tan\theta.$$

Therefore,

$$\alpha_h H_{1/3} = 1.8 * 2.07 \text{ m} = 3.726 \text{ m (12.23 ft)},$$

$$h_b = 1.28 \text{ m} + 5 * 2.07 \text{ m} * \tan(0) = 1.28 \text{ m (4.20 ft)},$$

$$H_b = 0.17 * 29.01 \text{ m}\left\{1 - \exp\left[-1.5\frac{\pi 1.28 \text{ m}}{29.01 \text{ m}}\left(1 + 15 * \tan^{\frac{4}{3}}(0)\right)\right]\right\}$$
$$= 0.926 \text{ m (3.04 ft)}.$$

So,

$$H_d = H_{Max} = \min\{3.726 \text{ m}, 0.926 \text{ m}\} = 0.926 \text{ m (3.04 ft)}.$$

Next, we calculate the coefficients of wave pressure (α_1, α_2, and α_3) given in Equations (56) through (58), which are repeated here:

$$\alpha_1 = 0.6 + \frac{1}{2}\left[\frac{\frac{4\pi h}{L_D}}{\sinh\left(\frac{4\pi h}{L_D}\right)}\right]^2,$$

$$\alpha_2 = \min\left[\frac{h_b - d}{3h_b}\left(\frac{H_D}{d}\right)^2, \frac{2d}{H_D}\right],$$

$$\alpha_3 = 1 - \frac{h'}{h}\left[1 - \frac{1}{\cosh\left(\frac{2\pi h}{L_D}\right)}\right].$$

The h and d values in the preceding equations are respectively equivalent to the h_{SWL} and d_{SWL} of Table H-2. Substituting the values gives

$$\alpha_1 = 1.05 \text{ (from Equation 56)},$$

$$\alpha_2 = \min\left[\frac{1.28\text{ m} - 0.366\text{ m}}{3(1.28\text{ m})}\left(\frac{0.926\text{ m}}{1.286\text{ m}}\right)^2, \frac{2(1.28)\text{ m}}{0.926\text{ m}}\right] = \min[1.52\text{ m}, 0.791\text{ m}] = 0.791$$

(from Equation 57).

And because $h' = d_{SWL} = H$,

$$\alpha_3 = 0.989 \text{ (from Equation 58).}$$

The lateral pressure components P_1 and P_3 (from Equations 52 and 54) are evaluated here:

$$P_1 = 0.5\,(1 + \cos\beta_D)\,(\alpha_1 + \alpha_2 * \cos^2\beta_D)\,\rho * g * H_D,$$

$$P_3 = \alpha_3 P_1.$$

The solutions to P_1 and P_3 are

$$P_1 = 17{,}236\text{ N/m}^2 = 17.236\text{ kN/m}^2\ (359.83\text{ lb/ft}^2),$$

$$P_3 = 17{,}052\text{ N/m}^2 = 17.052\text{ kN/m}^2\ (355.99\text{ lb/ft}^2).$$

As shown in Section 2.3.2.3, the total lateral force per linear width (F_{Lat}) on the face of the rolling gate is

$$F_{Lat} = 0.5(P_1 + P_3)H + 0.5(P_1 + P_4)h'_c,$$

where

$$P_4 = P_1\left(1 - \frac{h_c}{\eta^*}\right), \text{if } \eta^* > h_c,$$

or

$$P_4 = 0, \text{ if } \eta^* \le h_c,$$

$$\eta^* = 0.75(1 + \cos(\beta_D))H_D,$$

$$h'_C = \min\{\eta^*, h_C\}.$$

Therefore, the solution of the resultant force, F_{Lat}, is given as

h_c = 1.62 m (5.30 ft) (from Table H-2),

η^* = 1.389 m (4.56 ft).

Because $\eta^* < h_c$,

P_4 = 0 N/m^2, 0 kN/m^2 (0 lb/ft^2),

h'_C = min{1.389 m, 1.62 m} = 1.389 m (4.56 ft),

F_{Lat} = 20.24 kN/m (1,387 lb/ft).

The analysis indicates the total lateral wave force per linear foot of width of the rolling gate for a sustained 80 mph wind is 1,387 lb/ft.

In Figure B-13 and Figure B-14, the pressure terms P_1 and P_3 are shown acting on the vertical-lift gates, which are similar to the rolling gate. P_4 is equal to zero because η* < h_c. The location of the lateral equivalent force (h_{Lat}) can be determined using the one-third/one-sixth method developed by Ebeling et al. (2018) and also presented in Section 2.3.2.4 of this report. By applying this method for the lateral forces and summing moments about point 3, Equation (A-14), which is repeated here, was developed:

$$h_{Lat} = \frac{(h_4 - h_1)\left(\frac{P_4}{3} + \frac{P_1}{6}\right)h_4 + (h_4 - h_1)\left(\frac{P_4}{6} + \frac{P_1}{3}\right)h_1 + (h_1 - h_3)\left(\frac{P_1}{3} + \frac{P_3}{6}\right)h_1}{F_{Lat}},$$

$$h_{Lat} = \frac{1.389\text{ m}\left(\frac{0\frac{\text{kN}}{\text{m}^2}}{3} + \frac{17.236\frac{\text{kN}}{\text{m}^2}}{6}\right)1.755\text{ m} + 1.389\text{ m}\left(\frac{0\frac{\text{kN}}{\text{m}^2}}{6} + \frac{17.236\frac{\text{kN}}{\text{m}^2}}{3}\right)0.366\text{ m}}{104.662\frac{\text{kN}}{\text{m}}},$$

$$h_{Lat}\frac{+ 0.366\text{ m}\left(\frac{17.236\frac{\text{kN}}{\text{m}^2}}{3} + \frac{17.052\frac{\text{kN}}{\text{m}^2}}{6}\right)0.366\text{ m}}{104.662\frac{\text{kN}}{\text{m}}}$$

$$h_{Lat} = 0.547\text{ m}.$$

The wave forces and pressure distributions computed from Goda's (2010) procedure for the data in Table H-2 are shown in Table H-3. The definition of Goda's parameters shown in Table H-2 and used in the preceding equations are illustrated in Figure 16 and again in Figure A-27.

Table H-3. Wave force and pressure distribution computations using Goda's (2010) procedure for data in Table H-2 for the rolling gate example with a wind speed of 80 mph.

Parameter	Value (Metric Units)	Value (Imperial Units)
η^*	1.389 m	4.56 ft
P_1	17,236 N/m^2	360 lb/ft^2
P_3	17,052 N/m^2	356 lb/ft^2
P_4	0 N/m^2	0 lb/ft^2
F_{Lat}	20.25 kN/m	1,387 lb/ft

H.4 Probabilistic Characterization of the Hydrostatic Load for the Williams Boulevard Rolling Gate

The maximum hydrostatic load for the rolling gate occurs when the surge height is at the top of the gate. The minimum hydrostatic load due to surge height would be with no water on the gate. Because data are not available for developing a mean surge height on the rolling gate, a surge height half way up the gate was taken to be the mean. The standard deviation (σ) based on (maximum – minimum)/6 gives 1.083 ft (6.5 ft/6). Table H-4 lists the hydrostatic forces per foot of gate developed from +3σ (surge height el of 16.5) to –3σ (bottom of gate el of 10).

Table H-4. Hydrostatic forces computed for the Williams Boulevard rolling gate for a range of surge heights from +3σ to –3σ around the assumed mean surge height el of 13.25.

–3σ (lb/ft)	–2σ (lb/ft)	–σ (lb/ft)	Mean (lb/ft)	+σ (lb/ft)	+2σ (lb/ft)	+3σ (lb/ft)
0	37	147	330	586	916	1,318

H.5 Summary of Hydraulic Loads for Rolling Gates

Hydrostatic and wave loads are the primary hydraulic loads on the rolling gate used as a flood closure structure. Table H-5 lists the example hydraulic loads determined for the Williams Boulevard project for an SWL el of 11.2 and a wind speed of 80 mph.

Table H-5. Example hydraulic loads for the Williams Boulevard rolling gate.

Max Estimated Hydraulic Load	Value (kip/ft)
Hydrostatic (no tailwater effect)	0.046 (1.358 with water at top of gate, el 16.5)
Wave*	1.387
Hydrostatic + Wave	1.433

* Based on an SWL el of 11.2 and 80 mph wind speed normal to gate. P_1/P_3 = 1.01.

Some of the loads should be combined to give the maximum loads expected for the gate. Table H-5 lists these combined loads. The wave force results in the table indicate that wave forces are significant and need to be included in the rolling gate design force computations.

Appendix I: Example Hydraulic Load Computations for the Chickamauga Lock Needle Dam / Girder Beams (ND/GB)

In this appendix, the procedures discussed in Chapter 10 of the main report are presented using data from an existing USACE Navigation project. The data needed to quantify the hydraulic loads for the needle dam / girder beams (ND/GB) and example computations are described. Because the ND/GB are used as a closure structure for lock dewatering, the hydraulic loads in both the upper and lower lock approaches had to characterized. The upper lock approach is presented in Section I.1, and the lower lock approach is presented in Section I.2.

I.1 Characterization of Hydraulic loads in the Upper Lock Approach for the Chickamauga Lock and Dam ND/GB

I.1.1 A 31 yr Record of Hydrologic Data for the Chickamauga Lock and Dam Forebay El

The Chickamauga Lock and Dam project on the Tennessee River was chosen to illustrate how to determine the hydraulic loads on the ND/GB closure structure. USACE-LRN operates the lock at Chickamauga, and the Tennessee Valley Authority (TVA) operates the powerhouse and dam. The TVA provided a record of hydraulic data from January 1989 through December 2020. The data consisted of hourly values for the forebay el. The pertinent project-specific data for the analysis are listed here.

- Top of ND/GB el = 686
- Upper lock sill el = 663
- Surcharge upper pool el for top of ND/GB = 685
- Average forebay el = 679.80
- Range of forebay el over period of record = 687.13 to 674.72
- Estimated approach el = 661.8 (approach length is about 50 ft)
- Gate net width = 60 ft
- Damming height = 22.17 ft
- Needle dam length = 24 ft

A side view of the Chickamauga ND/GB is shown in Figure 81, and a picture of the ND/GB in the upper approach is shown in Figure 83. Figure I-1 is a picture of a needle being installed in the upper approach.

Figure I-1. Chickamauga needle dam / girder beams (ND/GB) being installed in upper approach (view is looking upstream).

The upper pool el, also referred to as the forebay el, is one of the primary variables affecting the hydraulic load on the ND/GB. Figure I-2 is a histogram of the forebay el over the 31 yr period (i.e., January 1989 through December 2020). The mean forebay el was 679.80, the maximum el was 687.13, and the minimum el was 674.72. The standard deviation was 2.373 ft. Figure I-2 represents the number of occurrences of forebay in the selected range.

There are 34 bins in the histogram, each with a bin width of 0.40 ft. The area of each bin was computed, and the total area was determined by summing the individual bin areas. These areas were normalized by dividing each individual area by the total area to give the PDF shown in Figure I-3. A CDF was developed by cumulatively summing the normalized areas of the PDF (Figure I-4).

Figure I-2. Histogram of forebay el from 1989 through 2020.

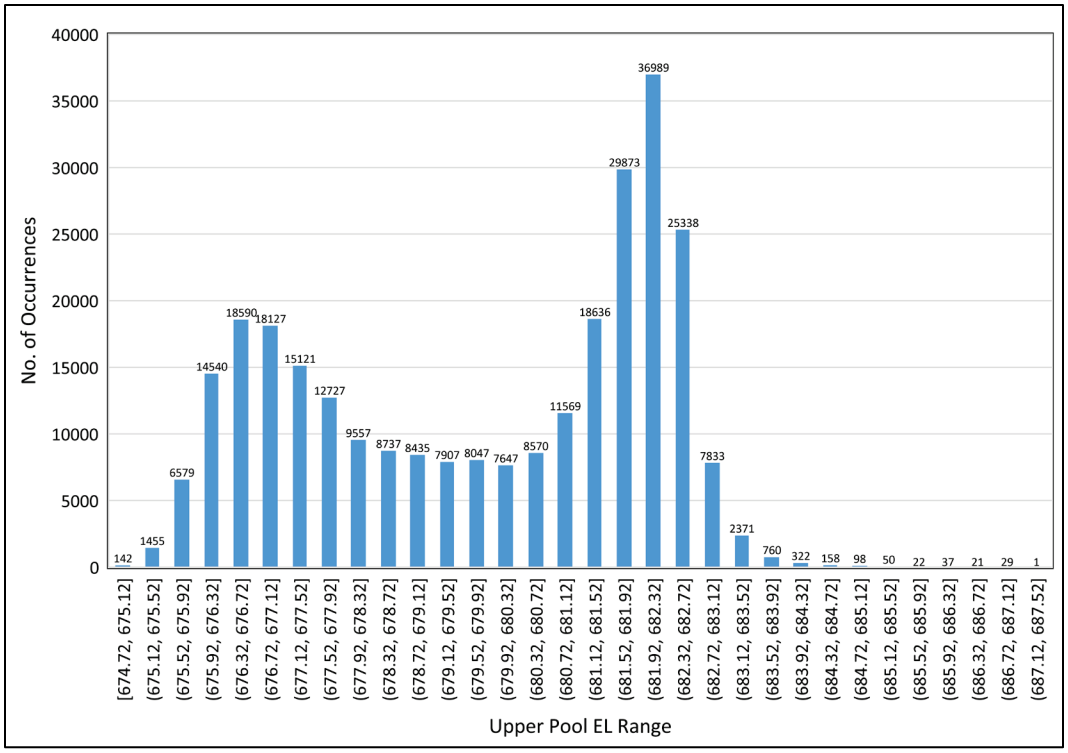

Figure I-3. PDF from histogram of forebay el for ND/GB.

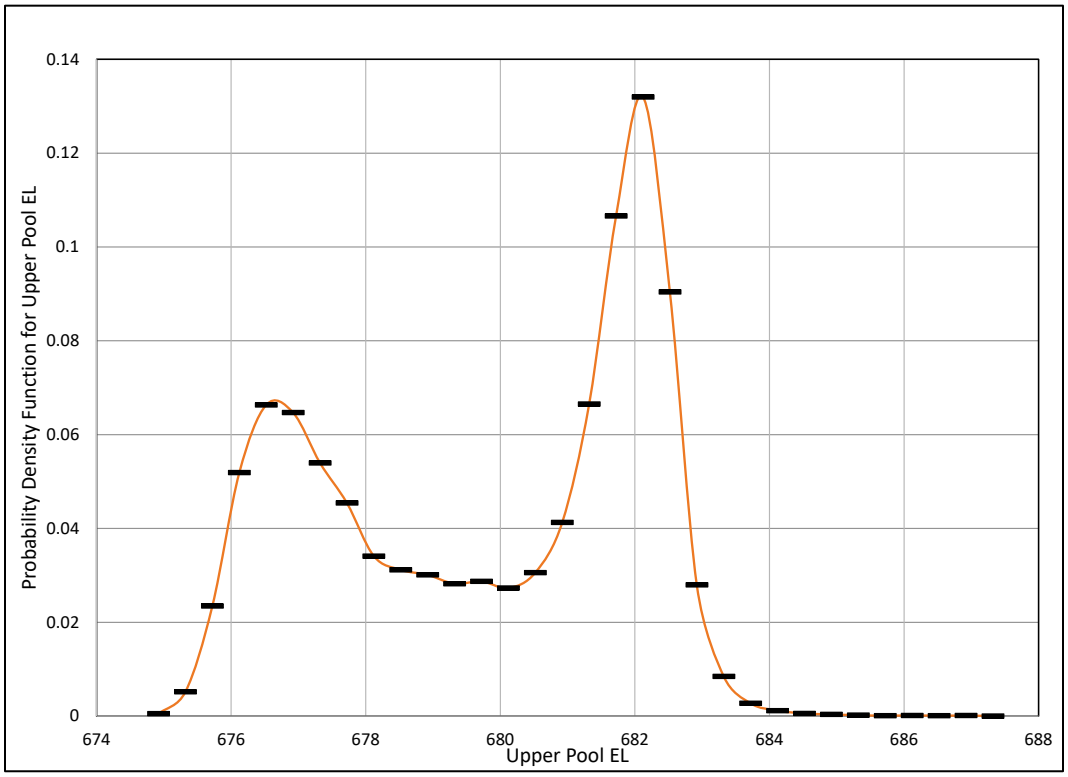

Figure I-4. CDF for forebay el for ND/GB.

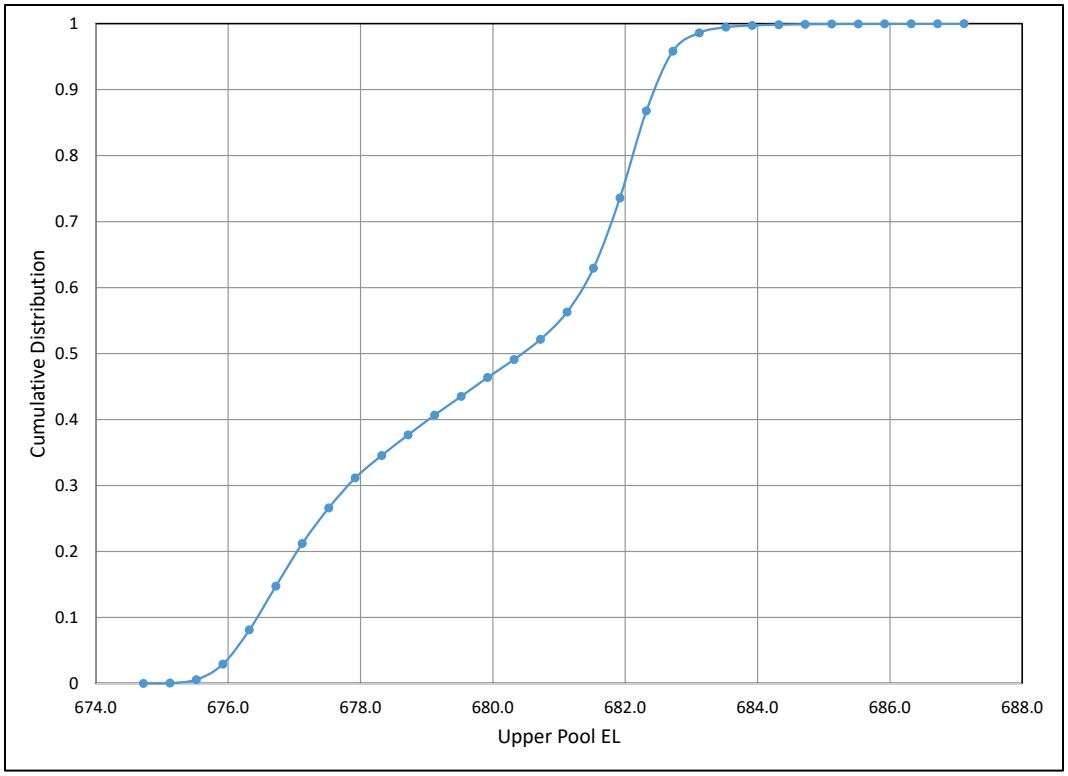

I.1.2 Hydrostatic Load for the Upper ND/GB

Equation (10), which is repeated here, is a conventional equation found in many fluid mechanics and hydraulics textbooks that can be used to compute hydrostatic pressure (p). As stated previously, γ is the unit weight of water, and y is the vertical distance from the water surface to the location of the hydrostatic pressure of interest (Figure 14):

$$p = \gamma y.$$

The horizontal hydrostatic pressure on the ND/GB in the dewatering position is expressed as γH, where γ is the unit weight of water, and H is the total head on the ND/GB. When the lock is dewatered, H represents the difference between the forebay el and the ND/GB lock sill el. The maximum hydrostatic pressure on the gate would be at the bottom of the ND/GB. It can be calculated using Equation (11), which is repeated here:

$$p_{max} = \gamma H.$$

The hydrostatic force (H_s) per foot of width for the ND/GB is calculated using Equation (12), which is repeated here:

$$H_s = \frac{1}{2}\gamma H^2,$$

where

γ = the unit weight of water = 62.4 lb/ft^3,
H = the head on the gate = 685.17 – 663
= 22.17 ft, and
Max hydrostatic load = 0.5 [62.4 lb/ft^3 * (22.17 ft)^2]= 15,335 lb/ft.

The maximum hydrostatic load would be experienced if the forebay el were at the top of the damming surface. The head on the gate, H, would be at el 685.17 – el 663, or 22.17 ft. This load condition represents H_1 (i.e., the maximum net hydrostatic load that will ever occur), which is one of the three hydrostatic loads that are to be considered. The mean hydrostatic load with a forebay el of 679.8 is 8,806 lb/ft. The location of the resultant force is $H/3$ above the upper lock approach when H is the head on the ND/GB (Figure 84).

I.1.3 Wave Load Based on Wave Height and Period for the ND/GB in the Upper Lock Approach

The dispersion due to wave load about the mean hydrostatic and hydrodynamic loads needs to be determined. The wave load is one of the main loads that contributes to load fluctuations. The procedures and methods used to determine wave load for the STG, which were presented in Chapter 2 and Appendix A, were also used for the ND/GB. The supporting data and computations that were used to determine the load for the Chickamauga upper lock approach are presented in the subsections that follow. As mentioned, to develop a wave load, the wind speed, wind direction, and fetch must be determined.

I.1.3.1 Wind Speed and Fetch for the ND/GB in the Upper Lock Approach

The wind speed and wind direction data were obtained from meteorological data collected over a 50 yr period between 1970 and 2020 at the Chattanooga/Lovell Airport (CHA) in Chattanooga, Tennessee. CHA is located approximately 5 mi southeast of the project. Figure I-5 shows the wind data collection site in relation to the project.

Figure I-5. Satellite imagery of the wind speed and direction data collection site in relation to Chickamauga Lock ND/GB. (Map data: Google Earth 2013.)

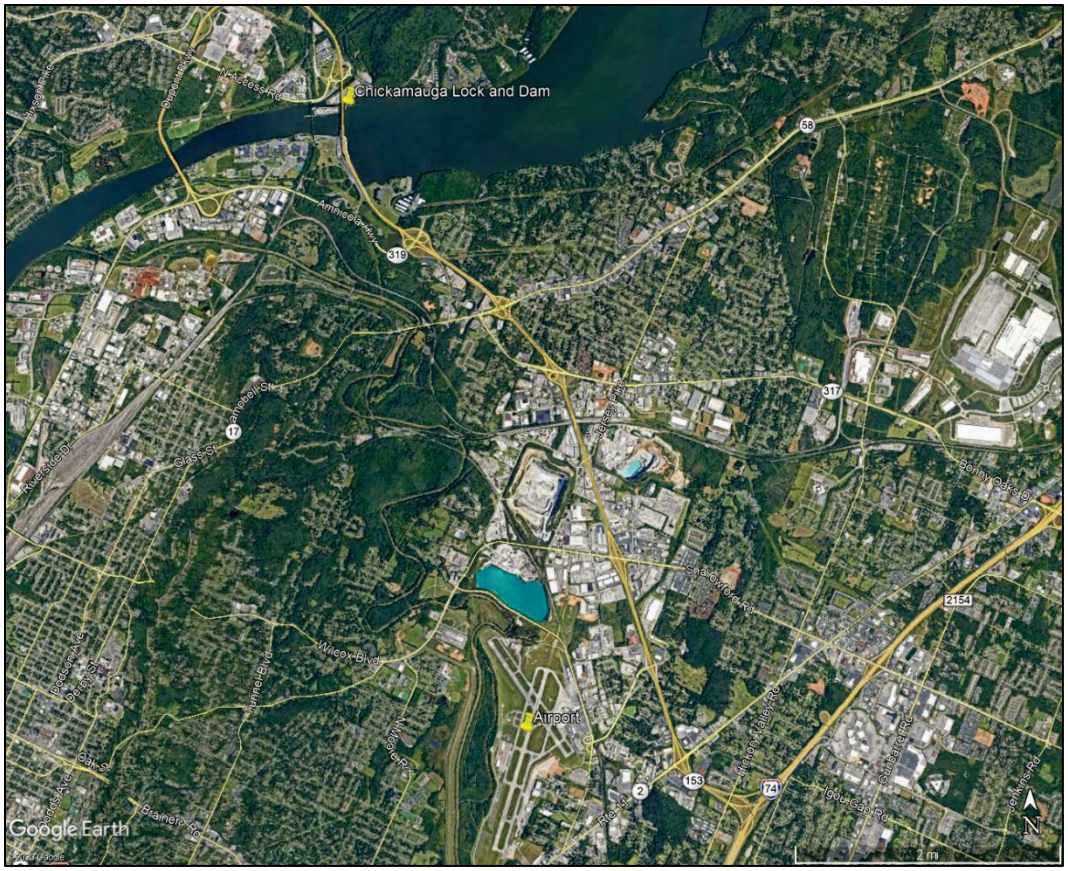

Increased data were found for the period of May 2016 to December 2020, with wind speeds and directions reported multiple times per hour. Between 1970 and May 2016, the wind speed and direction were usually reported on an hourly basis.

The latitude of CHA is 35.0353, and the longitude is –85.2038. The data were obtained from Iowa State University (n.d.).

Figure I-6 shows the fetch determined for the Chickamauga Lock ND/GB project for both the upper and lower lock approaches. The wind direction that impacts the project perpendicular to the upper ND/GB is 88°. The fetch is approximately 2.51 mi (13,253 ft). The upper lock guard wall prevents much of the south wind from reaching the ND/GB.

Figure I-6. Satellite imagery of the fetch and wind direction determined for the Chickamauga Lock ND/GB project. (Map data: Google Earth 2013.)

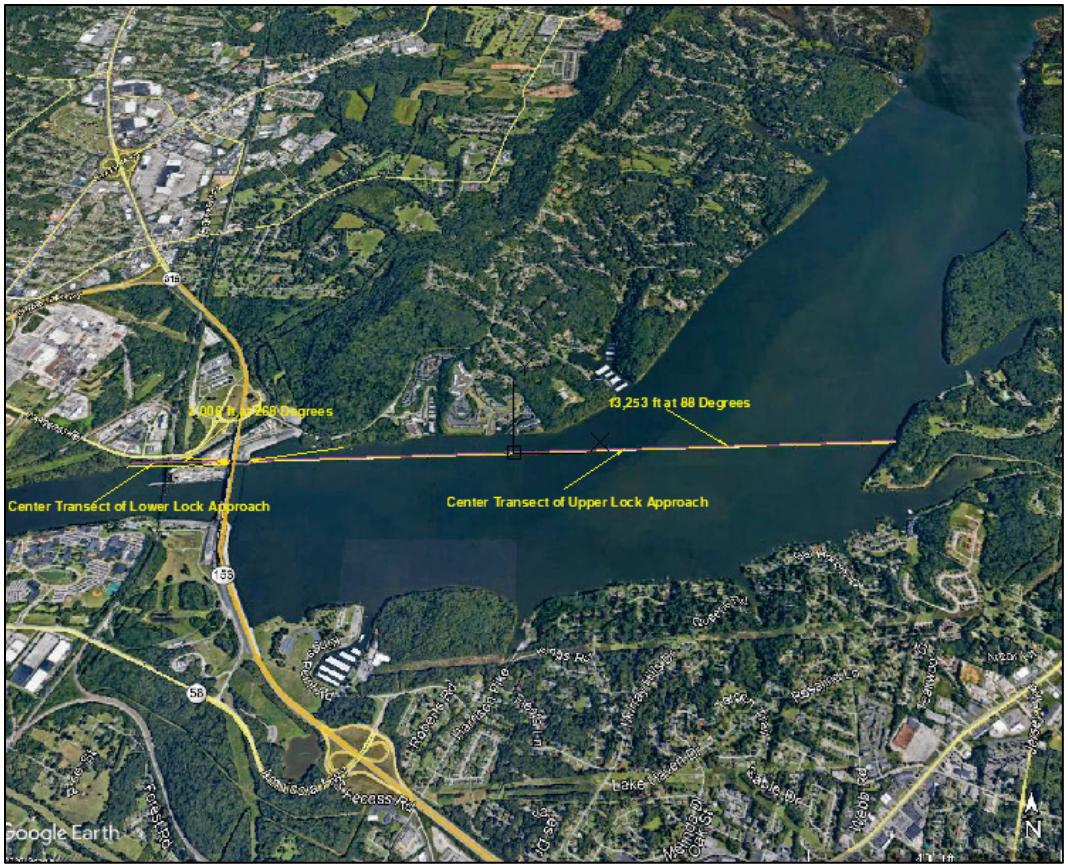

I.1.3.2 Wind Speed Analyses for the Upper ND/GB

The methods used to determine the appropriate wind speed for the analyses of the wave load developed for the ND/GB were also used for HSS discussed in previous appendixes. Based on the fetch length and wind speed, Equation (50), which is repeated here, can be used to determine the time required for full wave growth:

$$t_{min} = 1.0F^{0.73}U_{10}^{-0.46}.$$

Using an estimated wind speed between 20 and 30 mph and a fetch length of 2.51 mi, the minimum time to reach full wave growth was around 50 min, so a t_{min} value of 0.9 hr was used in the analysis. Equation (50) requires the use of metric units. The wind speed data were then processed to determine the maximum 0.9 hr average wind speed with a wind direction between 70° and 110° each year from 1970 to 2020. Table I-1 shows the wind speed values used in the analyses that follow.

Table I-1. Maximum yearly 0.9 hr average wind speed for wind directions between 70° and 110° at Chattanooga/Lovell Airport (CHA) for the upper ND/GB at Chickamauga Lock for the 1970 to 2020 observation period.

Year	Max 0.9 hr Avg Wind Speed (mph)	Year	Max 0.9 hr Avg Wind Speed (mph)
1970	17.25	1996	17.25
1971	11.50	1997	10.35
1972	14.38	1998	16.10
1973	14.38	1999	12.36
1974	25.73	2000	12.07
1975	18.4	2001	12.65
1976	17.25	2002	14.66
1977	17.83	2003	17.16
1978	14.76	2004	13.80
1979	16.87	2005	12.08
1980	16.29	2006	12.65
1981	16.10	2007	16.68
1982	11.50	2008	9.97
1983	20.13	2009	19.84
1984	13.03	2010	13.23
1985	11.50	2011	17.83
1986	9.20	2012	23.00
1987	20.13	2013	16.10
1988	18.40	2014	13.94
1989	14.38	2015	14.66
1990	10.93	2016	17.63
1991	12.65	2017	19.39
1992	10.35	2018	17.48
1993	13.80	2019	11.50
1994	13.80	2020	11.50
1995	29.80	—	—

I.1.3.3 Extreme Value Estimation Using Maximum 0.9 hr Average Yearly Values of Wind Speed for the Upper ND/GB

The type 1 Gumbel distribution was used for a GEV analysis. Figure I-7 shows the results from the extreme value estimation using the maximum 0.9 hr average annual values for the CHA data. The 100 yr recurrence interval wind speed from this analysis was 31.44. Using the magnitude of the 100 yr recurrence interval for wind speed was considered a suitable frequency for wave height calculations.

Figure I-7. Extreme wind speed estimation for Chickamauga Lock Lower ND/GB based on maximum 0.9 hr average annual values of wind speed.

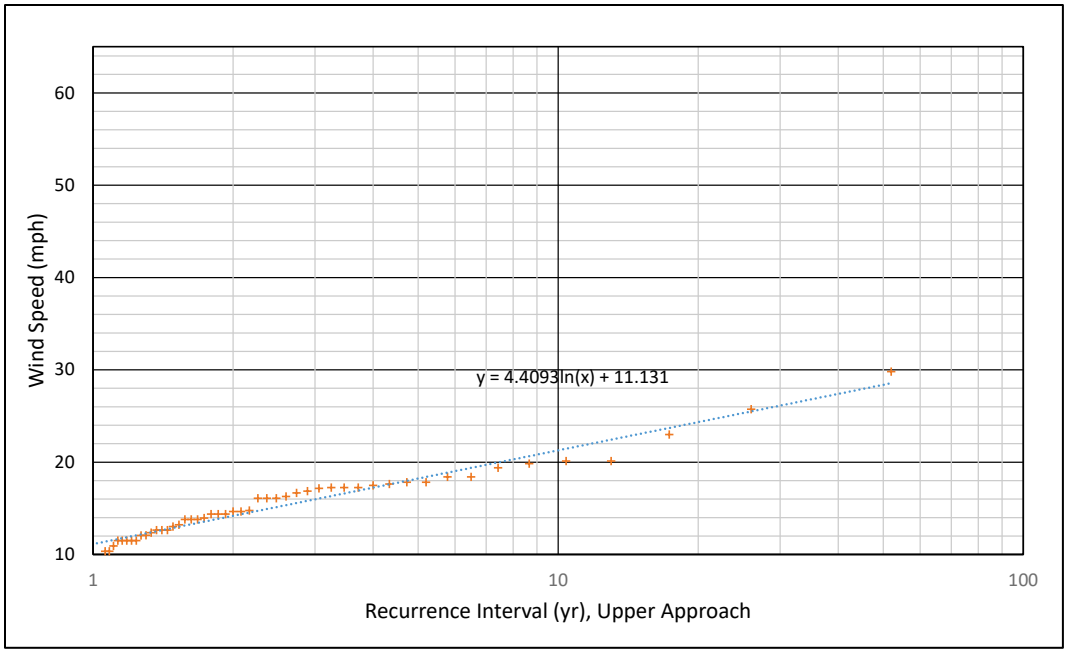

I.1.3.4 Wind Frequency Based on Gumbel Type 1 Distribution with Gringorten's Method Using Maximum Yearly 0.9 hr Average Values of Wind Speed for the Upper ND/GB

The type 1 Gumbel distribution can be used with Gringorten's (1963) plotting position formula to create another method for evaluating wind speed. Chapter 2 contains a description of this procedure. Figure I-8 is a plot of the return period versus wind speed determined using this procedure for the data from the CHA. The wind speed for the 100 yr return period was 28.0 mph.

To further investigate the statistics for the wind speed, a formula to determine the standard error (discussed in Appendix A) was used for the data presented in Figure I-8.

Figure I-8. Wind frequency from Gumbel type 1 distribution with Gringorten's method for the Chickamauga Lock upper lock approach using the maximum 0.9 hr average annual wind speed.

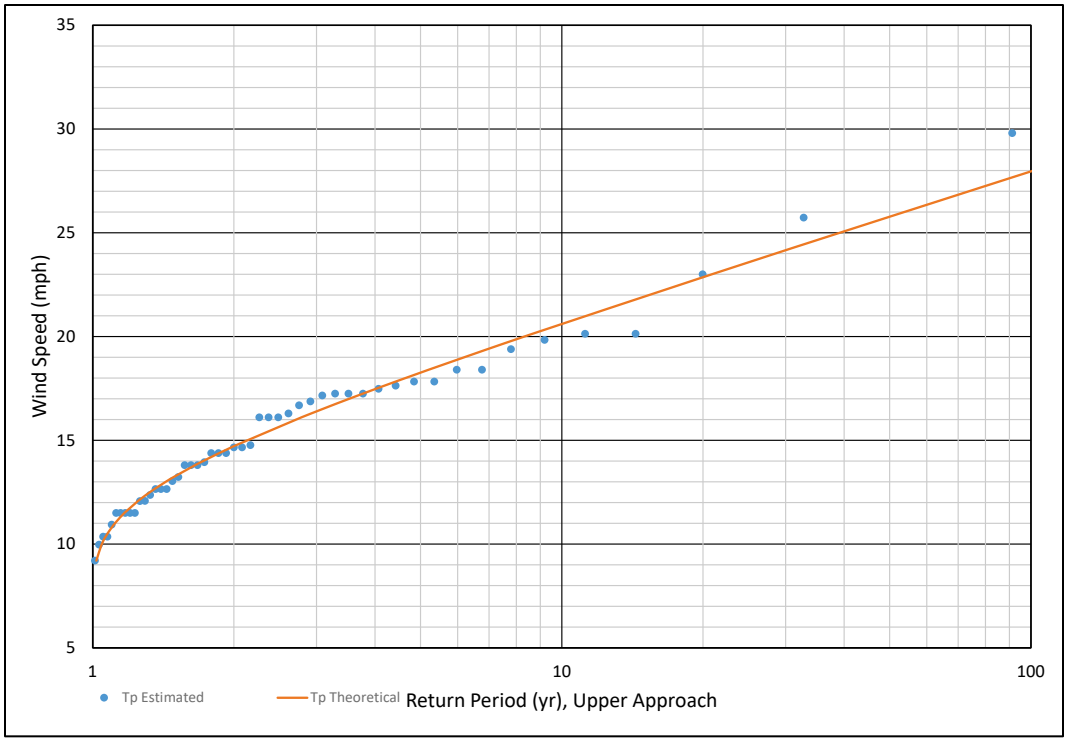

Figure I-9 shows the fitted curve bounded by plus and minus 1, 2, and 3 standard deviations (σ) for the CHA wind data (n = 51). Table I-2 shows the values for these statistics. The mean 100 yr return period wind speed was 28.0 mph. The standard deviation was determined to be 0.569 mph. The use of the 100 yr return period plus 3 standard deviations gives a wind speed of 29.7 mph.

Table I-2. Results from wind speed analysis for CHA for the Chickamauga upper ND/GB.

Statistic	100 yr Wind Speed (mph)
+3σ	29.7
+2σ	29.1
+1σ	28.6
Mean	28.0
−1σ	27.4
−2σ	26.9
−3σ	26.3

Figure I-9. Wind frequency curves based on peak yearly 0.9 hr average wind speed for the Chattanooga/Lovell Airport (CHA) data.

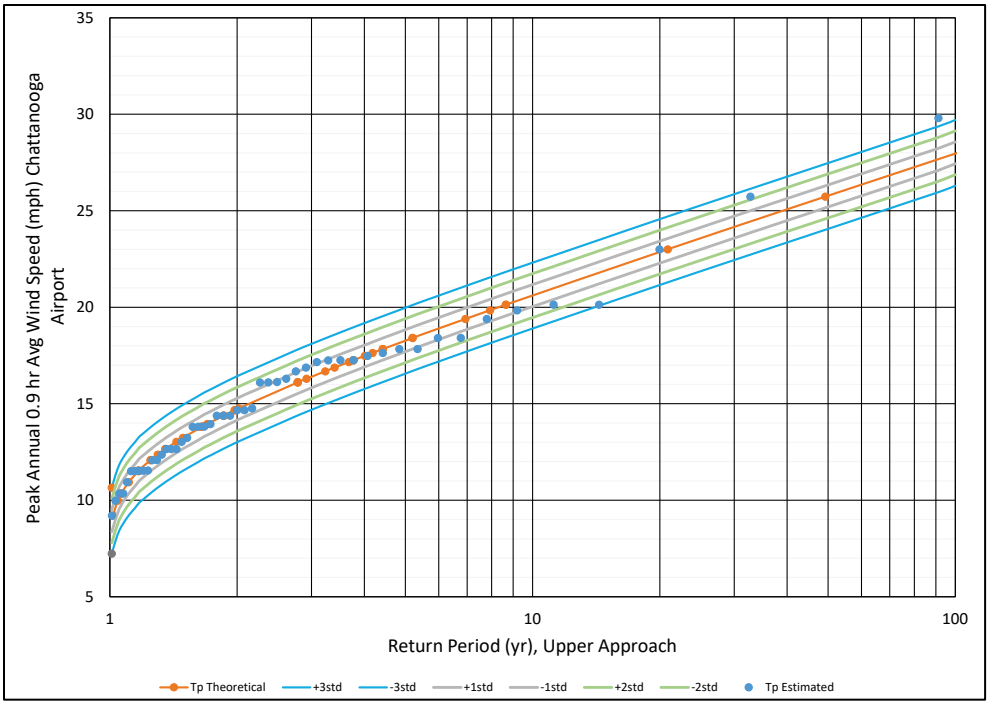

I.1.3.5 Wave Height and Period from the NARFET Model for Upper ND/GB

Table I-3 shows the input data and results from the use of the NARFET program for the Chickamauga Lock upper ND/GB. The program input requires the radial lengths of the fetch and the angle increments for resolution of the wind direction (Figure I-6). Figure I-6 shows the radial lengths (a total of 16) determined for an angle increment of 6°. The significant wave height and period for the wind speeds determined between −3σ and +3σ for the 100 yr return period shown in Figure I-9 are from the data in Table I-3, and the wave heights are shown in Figure I-10. The wind direction was between 70° and 110° for a duration of 0.9 hr.

Table I-3. Wave height, wave period and wavelength computed using the NARFET model for upper ND/GB.

Wind Speed (mph)	Wave Height (m)	Wave Period (sec)	Wavelength (m)
29.7	0.53	2.47	9.5
29.1	0.52	2.45	9.4
28.6	0.51	2.43	9.2
28.0	0.50	2.41	9.1
27.4	0.49	2.39	8.9
26.9	0.49	2.37	8.8
26.3	0.48	2.35	8.6

Figure I-10. Wave height versus wind speed from Smith's NARFET model for Chickamauga Lock upper ND/GB.

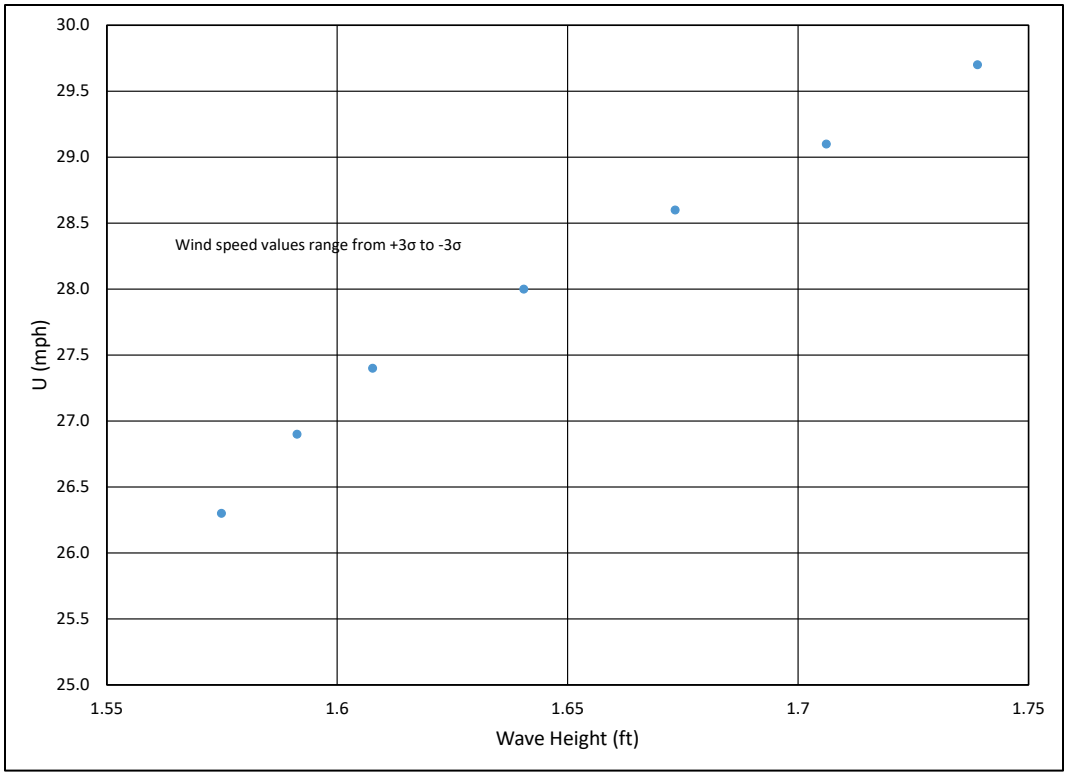

I.1.3.6 Wave Load from Goda for the Upper ND/GB

Goda (2010) also recommended formulations for determining significant wave height and period based on wind speed and fetch. The background and supporting equations for his formulations are provided in Chapter 2. This methodology is considered applicable to the ND/GB. The significant wave height, wave period, and wavelength computed using Goda's formulation are listed in Table I-4.

Table I-4. Significant wave height, significant wave period, and significant wavelength from Goda's (2010) formulations for the upper ND/GB.

Wind Speed (mph)	Wave Height (m)	Wave Period (sec)	Wavelength (m)
29.7	0.692	2.610	10.66
29.1	0.681	2.600	10.53
28.6	0.672	2.583	10.41
28.0	0.661	2.566	10.28
27.4	0.650	2.549	10.14
26.9	0.640	2.534	10.03
26.3	0.629	2.517	9.89

Figure I-11 is a plot of wind speed (U) versus wave height determined from Goda's recommended formulations from the statistical analysis of the wind speed data for the CHA.

Figure I-11. Wave height versus wind speed from Goda's (2010) procedure for the upper ND/GB.

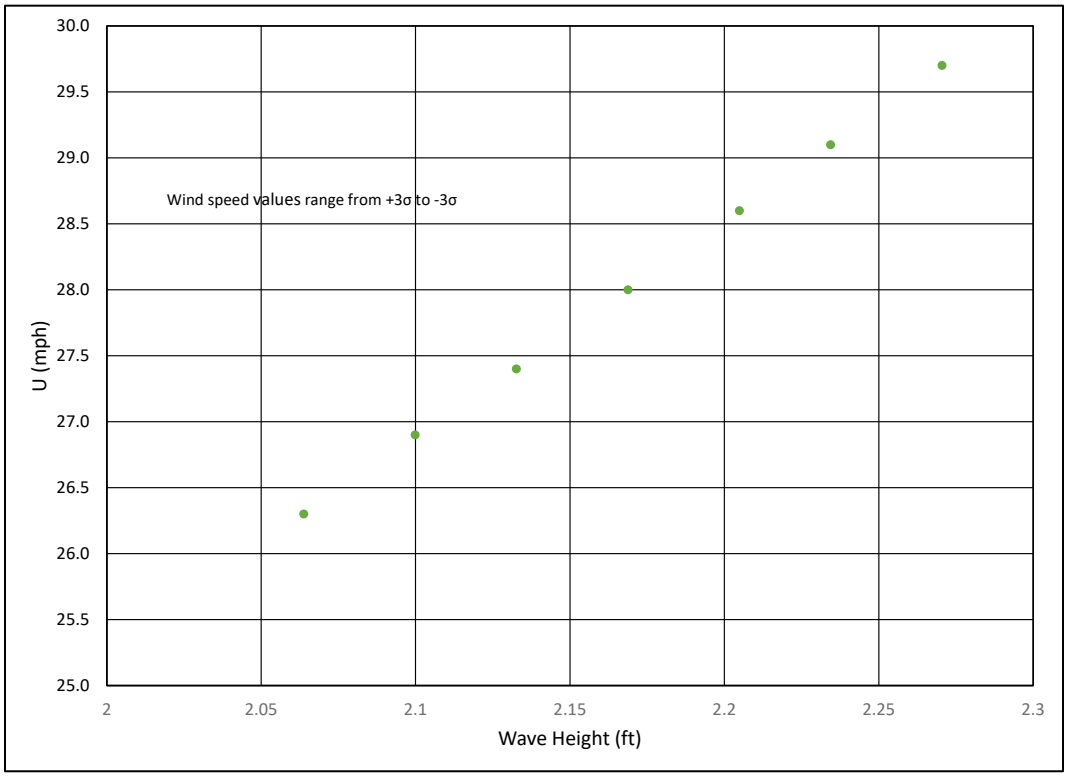

The wave pressure distribution and subsequent wave force for the upper ND/GB can now be determined from the significant wave height and wave period. The complete description of this procedure is shown in Chapter 2, Section 2.3.2.3. Based on the parameters listed in Table I-5 and on the Goda formulations in Section 2.3.2.3, an example solution was reached. Table I-6 shows the solution in the example wave force calculation (imperial and metric units included). The example uses the average forebay el of 679.80, a top of upper lock sill of 663, and the mean 100 yr return period wind speed of 28.0 mph.

Table I-5. Parameters used in the example wave force calculation (imperial and metric units included) for ND/GB for a wind speed of 28.0 mph.

Parameter	Value (Imperial Units)	Value (Metric Units)	Description
h_c	5.37 ft	1.637 m	Top of ND/GB ht above average forebay el
d (originally d_{SWL})	16.80 ft	5.12 m	Difference between avg forebay el and upper lock sill
h (originally h_{SWL})	18.0 ft	5.486 m	Difference between forebay el and approach channel invert el
tan θ	0	0	Bottom slope toward bulkhead
β_D	0 deg	0 deg	Design incident wave angle
$H_{1/3}$	2.17 ft	0.661 m	Significant wave height for example problem
$T_{1/3}$	2.57 sec	2.57 sec	Significant wave period for example problem
L_D	33.73 ft	10.28 m	Design wave length for example problem
ρ	62.4 lb/ft^3	1,000 kg/m^3	Density of freshwater
g	32.2 ft/sec^2	9.81 m/sec^2	Acceleration due to gravity
h'	16.80 ft	5.12 m	For the upper ND/GB: $h' = H = d_{SWL}$

The design wave height (H_D) is the minimum of $\alpha_h H_{1/3}$ and H_b, where α_h ranges from 1.6 to 2.0. For the design of nearshore vertical structures, Goda (2010) suggested using a value of 1.8 for α_h. Equations (59) through (61) are repeated here:

$$H_d = H_{Max} = \min\{\alpha_h * H_{1/3}, H_b\},$$

$$H_b = 0.17 * L_D \left\{1 - \exp\left[-1.5\frac{\pi h_b}{L_D}\left(1 + 15 * \tan^{\frac{4}{3}}\theta\right)\right]\right\},$$

where

$$h_b = h + 5 * H_{1/3} * \tan\theta.$$

Therefore,

$$\alpha_h H_{1/3} = 1.8 * 0.661 \text{ m} = 1.1898 \text{ m (3.90 ft)},$$

$$h_b = 5.486 + 5 * 0.661 \text{ m} * \tan(0) = 5.486 \text{ m (18.00 ft)},$$

$$H_b = 0.17 * 10.28 \text{ m}\left\{1 - \exp\left[-1.5\frac{\pi 5.486 \text{ m}}{10.28 \text{ m}}\left(1 + 15 * \tan^{\frac{4}{3}}(0)\right)\right]\right\}$$
$$= 1.606 \text{ m (5.27 ft)},$$

so

$$H_d = H_{Max} = \min\{1.1898 \text{ m}, 1.606 \text{ m}\} = 1.1898 \text{ m (3.90 ft)}.$$

Next, we calculate the coefficients of wave pressure (α_1, α_2, and α_3) given in Equations (56) through (58) and repeated here:

$$\alpha_1 = 0.6 + \frac{1}{2}\left[\frac{\frac{4\pi h}{L_D}}{\sinh\left(\frac{4\pi h}{L_D}\right)}\right]^2,$$

$$\alpha_2 = \min\left[\frac{h_b - d}{3h_b}\left(\frac{H_D}{d}\right)^2, \frac{2d}{H_D}\right],$$

$$\alpha_3 = 1 - \frac{h'}{h}\left[1 - \frac{1}{\cosh\left(\frac{2\pi h}{L_D}\right)}\right].$$

The h and d values in the preceding equations are respectively equivalent to the h_{SWL} and d_{SWL} in Table I-5. Substituting the values gives

$$\alpha_1 = 0.60 \text{ (from Equation 56)},$$

$$\alpha_2 = \min\left[\frac{5.486 \text{ m} - 5.12 \text{ m}}{3(5.486 \text{ m})}\left(\frac{1.1898 \text{ m}}{5.12}\right)^2, \frac{2(5.12) \text{ m}}{1.1898 \text{ m}}\right] = \min[0.0012 \text{ m}, 8.606 \text{ m}]$$
$$= 0.0012 \text{ m (from Equation 57)},$$

and because $h' = d_{SWL} = H$,

$$\alpha_3 = 0.132 \text{ (from Equation 58)}.$$

The lateral pressure components P_1 and P_3 (from Equations 52 and 54) are evaluated next:

$$P_1 = 0.5\,(1 + \cos\beta_D)\,(\alpha_1 + \alpha_2 * \cos^2\beta_D)\,\rho * g * H_D,$$

$$P_3 = \alpha_3 P_1.$$

The solutions to P_1 and P_3 are, then,

$$P_1 = 7{,}019 \text{ N/m}^2 = 7.019 \text{ kN/m}^2 = 146.53 \text{ (lb/ft}^2\text{)},$$

$$P_3 = 926 \text{ N/m}^2 = 0.926 \text{ kN/m}^2 \text{ (19.33 lb/ft}^2\text{)}.$$

As shown in Section 2.3.2.3, the total lateral force per linear width (F_{Lat}) on the face of the ND/GB is

$$F_{Lat} = 0.5(P_1 + P_3)H + 0.5(P_1 + P_4)h_c',$$

where

$$P_4 = P_1\left(1 - \frac{h_c}{\eta^*}\right), \text{ if } \eta^* > h_c,$$

or

$$P_4 = 0, \text{ if } \eta^* \leq h_c,$$

$$\eta^* = 0.75(1 + \cos(\beta_D))H_D,$$

$$h_C' = \min\{\eta^*, h_C\}.$$

Therefore, the solution of the resultant force, F_{Lat}, is given as

$$h_c = 1.637 \text{ m (5.37 ft) (from Table I-5)},$$

$$\eta^* = 1.785 \text{ m (5.86 ft)}.$$

Because $\eta^* > h_c$,

$$P_4 = 581 \text{ N/m}^2, 0.581 \text{ kN/m}^2 \text{ (12.13 lb/ft}^2\text{)},$$

$$h_C' = \min\{1.785 \text{ m}, 1.637 \text{ m}\} = 1.637 \text{ m (5.37 ft)},$$

$$F_{Lat} = 26.59 \text{ kN/m (1,820 lb/ft)}.$$

The preceding analysis indicates the total lateral wave force per linear width of the ND/GB for a sustained 28.0 mph wind is 1,820 lb/ft.

In Figure B-12 and Figure B-13, the pressure terms P_1, P_3, and P_4 are shown acting on the vertical-lift gates; these are similar to the ND/GB. The location of the lateral equivalent force (h_{Lat}) can be determined using the one-third/one-sixth method developed by Ebeling et al. (2018) and also presented in Chapter 2, Section 2.3.2.4, of this report. By applying this

method for the lateral forces and summing moments about point 3, Equation (A.14) was developed. The equation is repeated here:

$$h_{Lat} = \frac{(h_4 - h_1)\left(\frac{P_4}{3} + \frac{P_1}{6}\right)h_4 + (h_4 - h_1)\left(\frac{P_4}{6} + \frac{P_1}{3}\right)h_1 + (h_1 - h_3)\left(\frac{P_1}{3} + \frac{P_3}{6}\right)h_1}{F_{Lat}},$$

$$h_{Lat} = \frac{1.455\ \text{m}\left(\frac{0.581\frac{\text{kN}}{\text{m}^2}}{3} + \frac{7.019\frac{\text{kN}}{\text{m}^2}}{6}\right)6.757\ \text{m} + 1.455\ \text{m}\left(\frac{0.581\frac{\text{kN}}{\text{m}^2}}{6} + \frac{7.019\frac{\text{kN}}{\text{m}^2}}{3}\right)5.128\ \text{m}}{26.59\frac{\text{kN}}{\text{m}}}$$

$$\frac{+ 5.12\ \text{m}\left(\frac{7.019\frac{\text{kN}}{\text{m}^2}}{3} + \frac{0.926\frac{\text{kN}}{\text{m}^2}}{6}\right)5.12\ \text{m}}{26.59\frac{\text{kN}}{\text{m}}}$$

$$h_{Lat} = 3.798\ \text{m}.$$

Table I-4 contains the wave heights and wave periods used for computing the wave forces and pressure distributions determined from the wind speed analysis at the Chickamauga Lock upper ND/GB. Table I-6 shows the wave forces and pressure distributions computed from Goda's (2010) procedure for the data in the table. The definition of Goda's parameters shown in Table I-5 are illustrated in Figure 2 through Figure 6 and in Figure A-27.

Table I-6. Wave force and pressure distribution computations using Goda's (2010) procedure for data in Table I-4 for the Chickamauga Lock upper ND/GB project.

Chickamauga Lock Data	Statistic						
	+3σ	+2σ	+1σ	Mean	−1σ	−2σ	−3σ
Wind Speed (mph)	29.7	29.1	28.6	28.0	27.4	26.9	26.3
η^* (m)	1.868	1.839	1.814	1.785	1.755	1.728	1.698
η^* (ft)	6.13	6.03	5.95	5.86	5.76	5.67	5.57
P_1 (N/m^2)	7,350	7,233	7,136	7,019	6,901	6,795	6,677
P_3 (N/m$^{2)}$	1,026	997	962	926	891	860	827
P_4 (N/m^2)	910	793	698	581	464	358	241
F_{Lat} (kN/m)	28.20	27.64	27.14	26.56	25.98	25.45	24.87
h_{Lat} (m)	3.015	3.012	3.008	3.004	3.000	2.995	2.99
h_{Lat} (ft)	9.89	9.88	9.87	9.85	9.84	9.82	9.81
P_1 (lb/ft^2)	153	151	149	147	144	142	139
P_3 (lb/ft^2)	21	21	20	19	19	18	17
P_4 (lb/ft^2)	19	17	15	12	10	7	5
F_{Lat} (lb/ft)	1,933	1,894	1,860	1,820	1,780	1,744	1,704

I.1.4 Summary of Hydraulic Loads for Upper ND/GB

The hydrostatic and wave loads are the primary hydraulic loads on the upper ND/GB used as a dewatering structure for the lock. Table I-7 lists the example hydraulic loads determined for the Chickamauga Lock upper ND/GB project.

Table I-7. Example hydraulic loads for the Chickamauga Lock upper ND/GB.

Max Estimated Hydraulic Load	Value (kips/ft)
Hydrostatic	15.335 (8.806 with forebay el of 679.80)
Hydrodynamic	N/A
Wave*	1.933
Hydrostatic + Wave	10.739 (average hydrostatic + wave)
Hydrodynamic + Wave	N/A

* Based on a mean forebay el and 29.7 mph wind speed at 88° (100 yr wind event + 3σ). P_1/P_3 = 7.16.

Some of the loads should be combined to give the maximum loads expected for the upper ND/GB. Table I-7 shows these combined loads. In the table, wave force results indicate that wind-induced wave forces are significant and need to be included in upper ND/GB design force computations.

I.2 Characterization of Hydraulic Loads in the Lower Lock Approach for Chickamauga Lock and Dam ND/GB

I.2.1 A 31 yr Record of Hydrologic Data for Chickamauga Lock and Dam Lower Approach

The TVA provided a record of hydraulic data from January 1989 through December 2020. The data consisted of hourly values for the TW El. The pertinent project-specific data for the analysis are listed here:

- Top of ND/GB el = 641
- Lower lock sill el = 619
- Average TW = 637.02
- Range of TW El over period of record = 660.19 to 631.58
- Estimated approach el = 617.2 (approach length is about 50 ft)
- Gate net width = 60 ft
- Damming height = 21.28 ft
- Needle dam length = 24 ft

Figure 82 shows a side view of the Chickamauga Lock lower ND/GB. Figure I-1 shows a picture of a needle being installed in the upper approach, which is similar to one being installed in the lower approach.

Tailwater is one of the primary variables that affects the hydraulic load on the lower ND/GB. Figure I-12 shows a histogram of the TW El over the 31 yr period. The mean TW El was 637.02, the maximum el was 660.19, and the minimum el was 631.58. The standard deviation was 3.275 ft. The histogram shown in Figure I-12 represents the number of occurrences of forebay in the selected range.

There are 29 bins in the histogram, each with a bin width of 1.0 ft. The area of each bin was computed, and the total area was determined by summing the individual bin areas. These areas were normalized by dividing each individual area by the total area to give the PDF shown in Figure I-13. Figure I-14 shows a CDF that was developed by cumulatively summing the normalized areas of the PDF.

Figure I-12. Histogram of TW El from 1989 through 2020.

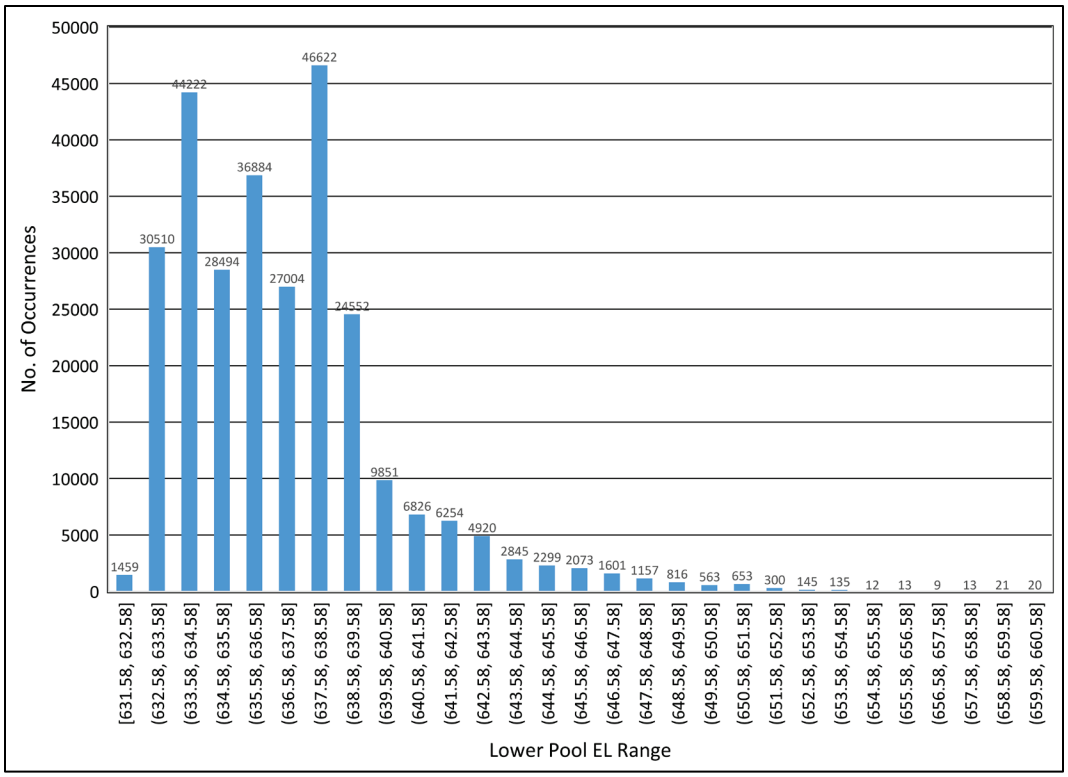

Figure I-13. PDF from the histogram of TW El for the lower ND/GB.

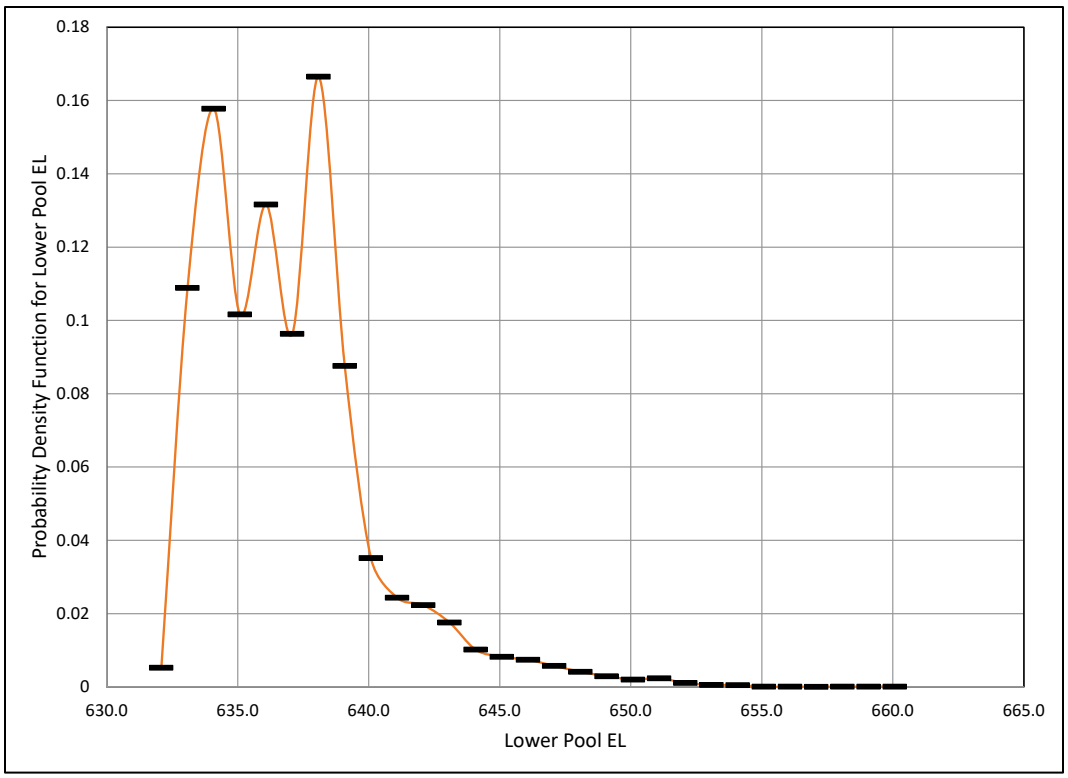

Figure I-14. CDF for TW El for the lower ND/GB.

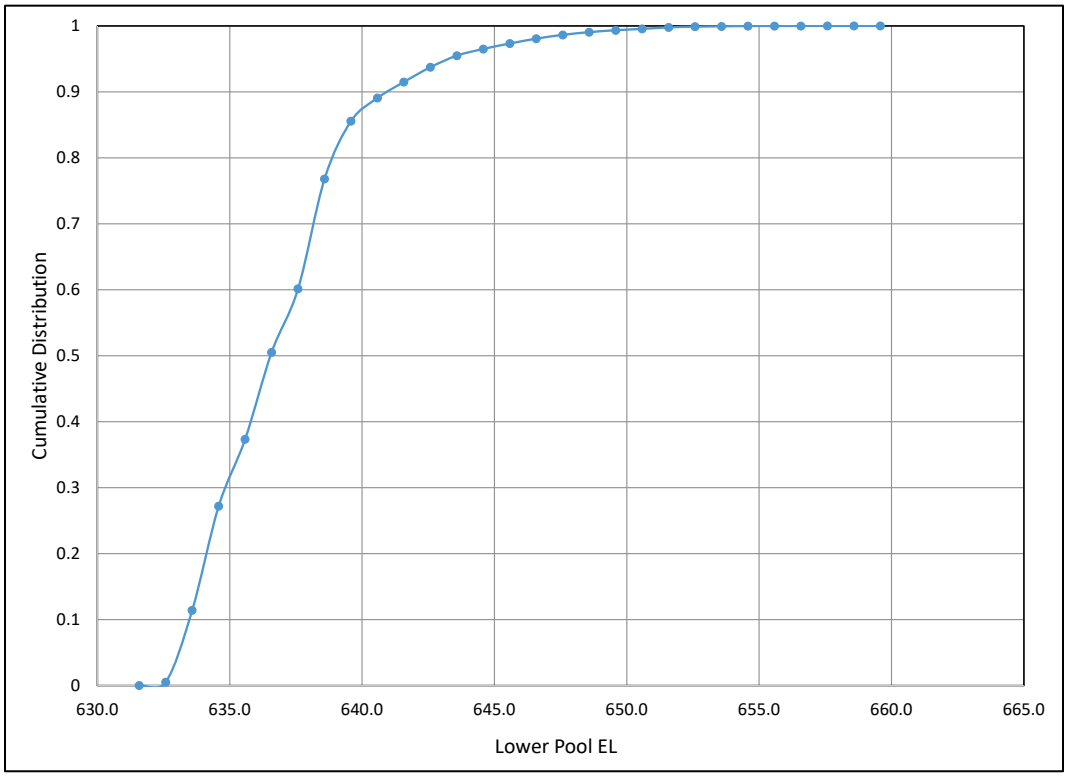

I.2.2 Hydrostatic Load for Lower ND/GB

The horizontal hydrostatic pressure on the ND/GB in the dewatering position is expressed as γH, where γ is the unit weight of water, and H is the total head on the ND/GB. When the lock is dewatered, H represents the difference between the TW El and the ND/GB lock sill el. The hydrostatic force (H_s) per foot of width for the ND/GB is as follows:

$$H_s = \frac{1}{2}\gamma H^2,$$

where,

γ = the unit weight of water = 62.4 lb/ft^3,
H = the head on the gate = 640.28 – 619.0 = 21.28 ft, and
Max hydrostatic load = 0.5 [62.4 lb/ft^3 * (21.28 ft)^2] = 14,129 lb/ft.

The maximum hydrostatic load would be experienced if the TW El was at the top of the damming surface. The head on the gate, H, would be el 640.28 – el 619.0, or 21.28 ft. This load condition represents H_1 (the maximum net hydrostatic load that will ever occur), which is one of the three hydrostatic loads that are to be considered. The mean hydrostatic load with a TW El of 637.02 is 10,131 lb/ft. The location of the resultant force is $H/3$ above the lower lock approach when H is the head on the ND/GB (Figure 84).

I.2.3 Wave Load Based on Wave Height and Period for ND/GB in the Lower Lock Approach

The dispersion due to wave load about the mean hydrostatic and hydrodynamic loads needs to be determined. The wave load is one of the main loads that contributes to load fluctuations. The procedures and methods used to determine wave load for the lower ND/GB, which were presented in Chapter 2 and Appendix A, were used for the lower ND/GB. The supporting data and computations used to determine the load for the Chickamauga lower lock approach are presented in the subsections that follow. As mentioned previously, developing a wave load requires determining the wind speed, wind direction, and fetch.

I.2.3.1 Wind Speed and Fetch for the ND/GB in the Lower Lock Approach

The wind speed and wind direction data were obtained from meteorological data collected over a 50 yr period between 1970 and 2020 at the CHA, which is near Chattanooga, Tennessee. The CHA is located approximately 5 mi southeast of the project (Figure I-5).

The period between May of 2016 and December of 2020 offered a lot of data, with wind speeds and directions reported multiple times per hour. Between 1970 and May of 2016, the wind speed and wind direction were usually reported on an hourly basis. The latitude of CHA is 35.0353, and the longitude is −85.2038. The data were obtained from Iowa State University (n.d.).

Figure I-6 shows the fetch determined for the Chickamauga Lock ND/GB project for both the upper and lower lock approaches. The wind direction that impacts the project perpendicular to the lower ND/GB is 268°. The fetch is approximately 0.4 mi (2,006 ft). The lower lock guard wall prevents much of the south wind from reaching the lower ND/GB.

I.2.3.2 Wind Speed Analyses for the Lower ND/GB

The methods used to determine the appropriate wind speed for the analyses of the wave load developed for the ND/GB were also used for HSS discussed in previous appendixes, except for those discussed in Appendix H (on the rolling gate). Based on the fetch length and wind speed, Equation (50), which is repeated here, can be used to determine the time required for full wave growth:

$$t_{min} = 1.0F^{0.73}U_{10}^{-0.46}.$$

Using an estimated wind speed between 30 and 40 mph and a fetch length of 0.4 mi, the minimum time to reach full wave growth was around 12 min, so a t_{min} value of 0.2 hr was used in the analysis. Equation (50) requires metric units. The wind speed data were then processed to determine the maximum 0.2 hr average wind speed with a wind direction between 250° and 290° each year from 1970 to 2020. Table I-8 shows the wind speed values used in the analyses.

Table I-8. Maximum yearly 0.2 hr average wind speed for wind directions between 250° and 290° at CHA for the lower ND/GB at Chickamauga Lock for the 1970 to 2020 observation period.

Year	Max 0.2 hr Avg Wind Speed (mph)	Year	Max 0.2 hr Avg Wind Speed (mph)
1970	20.56	1996	28.92
1971	23.00	1997	30.52
1972	27.95	1998	22.43
1973	24.61	1999	21.62
1974	20.36	2000	21.85
1975	31.51	2001	23.56
1976	36.07	2002	25.30
1977	27.60	2003	28.75
1978	23.00	2004	23.64
1979	43.01	2005	33.99
1980	27.46	2006	19.93
1981	22.82	2007	24.82
1982	24.96	2008	29.33
1983	19.72	2009	27.26
1984	23.00	2010	28.34
1985	20.24	2011	28.12
1986	18.40	2012	28.75
1987	22.43	2013	18.69
1988	20.36	2014	28.75
1989	22.62	2015	23.84
1990	21.85	2016	26.45
1991	23.14	2017	25.59
1992	24.93	2018	23.58
1993	19.55	2019	23.00
1994	23.69	2020	24.15
1995	29.56	—	—

I.2.3.3 Extreme Value Estimation Using Maximum 0.2 hr Average Yearly Values of Wind Speed for the Lower ND/GB

The type 1 Gumbel distribution was used for a GEV analysis. Figure I-15 shows the results from the extreme value estimation using the maximum 0.2 hr average annual values for the CHA data. The 100 yr recurrence interval wind speed from this analysis was 43.81. The magnitude of the 100 yr recurrence interval for wind speed was considered a suitable frequency for wave height calculations.

Figure I-15. Extreme wind speed estimation for Chickamauga Lock lower ND/GB based on maximum 0.2 hr average annual values of wind speed.

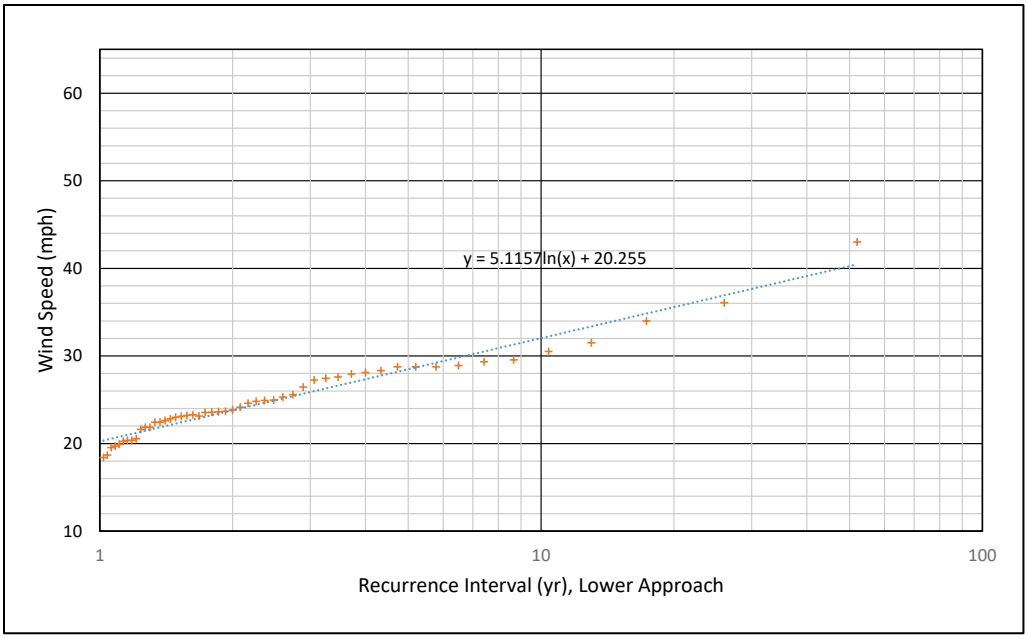

I.2.3.4 Wind Frequency Based on Gumbel Type 1 Distribution with Gringorten's Method Using Maximum Yearly 0.2 hr Average Values of Wind Speed for Lower ND/GB

The type 1 Gumbel distribution can be used with Gringorten's (1963) plotting position formula to create another method for evaluating wind speed. Chapter 2 contains a description of this procedure. Figure I-16 shows a plot of the return period versus wind speed determined using this procedure for the data from the CHA. The wind speed for the 100 yr return period was 39.8 mph.

To further investigate the statistics for the wind speed, a formula for determining the standard error (discussed in Appendix A) was used for the data presented in Figure I-16.

Figure I-16. Wind frequency from Gumbel type 1 distribution with Gringorten's method for the Chickamauga Lock lower ND/GB using the maximum 0.2 hr average annual wind speed.

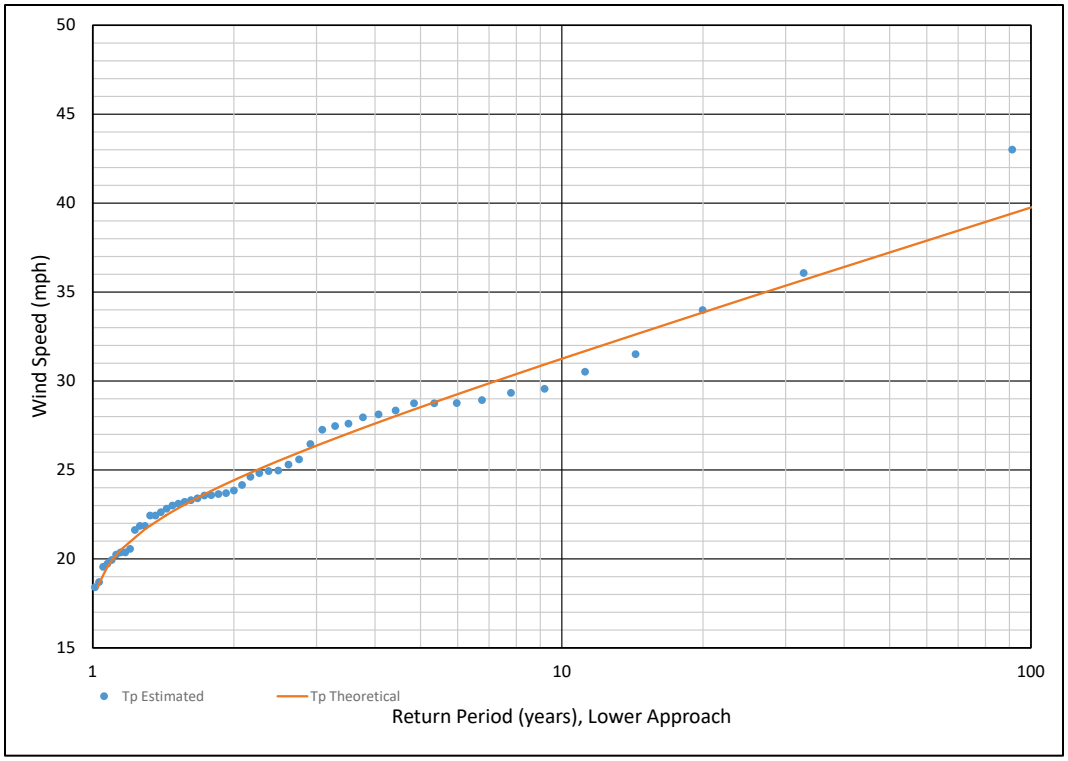

Figure I-17 shows the fitted curve bounded by plus and minus 1, 2, and 3 standard deviations (σ) for the CHA wind data (n = 51). Table I-9 shows the values for these statistics. The mean 100 yr return period wind speed was 39.8 mph. The standard deviation was determined to be 0.715 mph. The use of the 100 yr return period plus 3 standard deviations gives a wind speed of 41.95 mph.

Table I-9. Results from the wind speed analysis for CHA for the Chickamauga lower ND/GB.

Statistic	100 yr Wind Speed (mph)
+3σ	42.0
+2σ	41.2
+1σ	40.5
Mean	39.8
−1σ	39.1
−2σ	38.4
−3σ	37.7

Figure I-17. Wind frequency curves based on peak yearly 0.2 hr average wind speed for the CHA data.

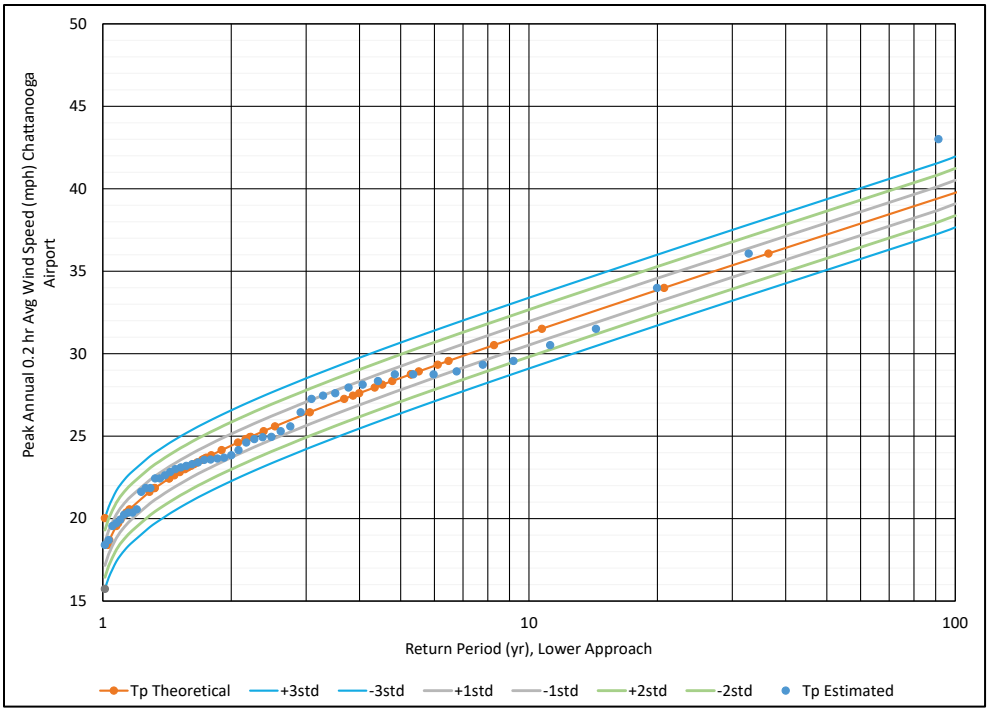

I.2.3.5 Wave Height and Period from NARFET Model for Lower ND/GB

Table I-10 shows the input data and results from using the NARFET program for the Chickamauga Lock lower ND/GB. The program input requires the radial lengths of the fetch and the angle increments for resolution of the wind direction (Figure I-16). Figure I-16 contains the radial lengths (a total of 28) determined for an angle increment of 6°. The significant wave height and period for the wind speeds determined between -3σ and $+3\sigma$ for the 100 yr return period shown in Figure I-17 are shown in Table I-10, and the wave heights are shown in Figure I-18. The wind direction was between 250° and 290° for a duration of 0.2 hr.

Table I-10. Wave height, wave period, and wavelength computed using the NARFET model for lower ND/GB.

Wind Speed (mph)	Wave Height (m)	Wave Period (sec)	Wavelength (m)
42.0	0.63	2.40	9.0
41.2	0.62	2.38	8.8
40.5	0.61	2.37	8.7
39.8	0.60	2.35	8.6
39.1	0.59	2.33	8.5
38.4	0.58	2.32	8.4
37.7	0.57	2.30	8.2

Figure I-18. Wave height versus wind speed from Smith's NARFET model for Chickamauga Lock lower ND/GB.

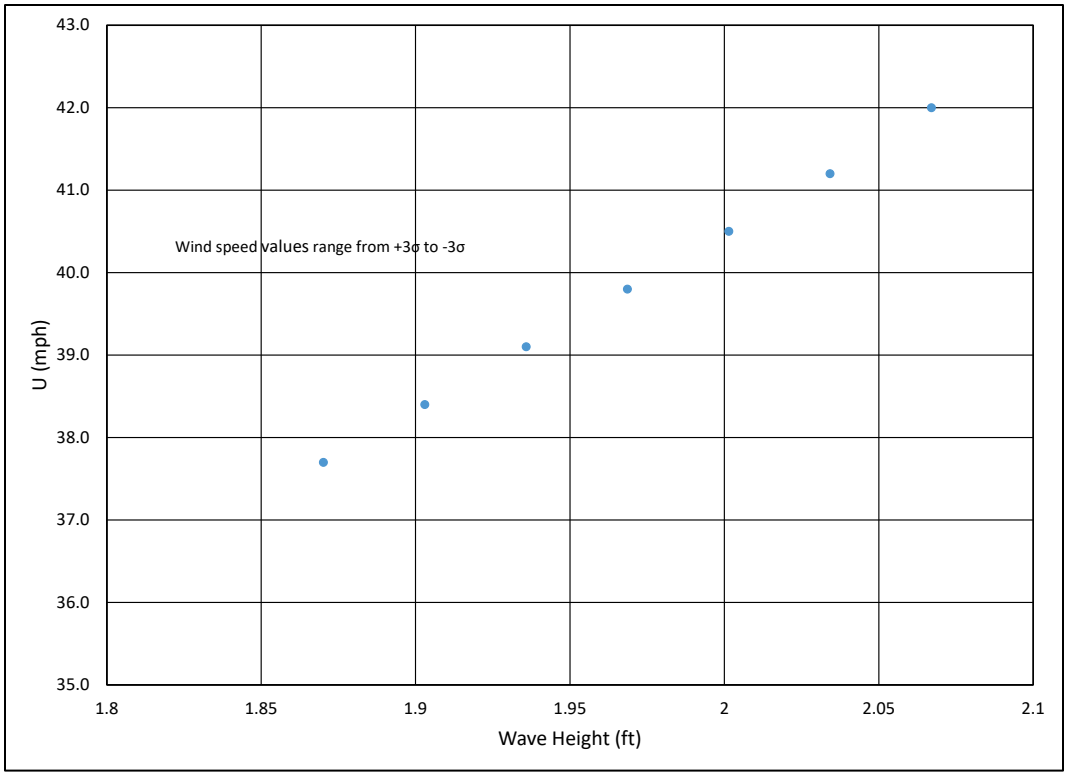

I.2.3.6 Wave Load from Goda for Lower ND/GB

Goda (2010) also recommended formulations for determining significant wave height and period based on wind speed and fetch. The background and supporting equations for his formulations were provided in Chapter 2. This methodology is considered applicable to the ND/GB. Table I-11 lists the significant wave heights, wave periods, and wavelengths that were computed using Goda's formulation.

Table I-11. Significant wave height, wave period, and wavelength computed using Goda's (2010) formulations for the lower ND/GB.

Wind Speed (mph)	Wave Height (m)	Wave Period (sec)	Wavelength (m)
42.0	0.375	1.65	4.26
41.2	0.370	1.64	4.22
40.5	0.365	1.64	4.18
39.8	0.361	1.63	4.14
39.1	0.356	1.62	4.10
38.4	0.351	1.61	4.06
37.7	0.346	1.60	4.01

Figure I-19 shows a plot of wind speed (*U*) versus wave height determined from Goda's (2010) recommended formulations from the statistical analysis of the wind speed data for the CHA.

Figure I-19. Wave height versus wind speed from Goda's (2010) procedure for the lower ND/GB.

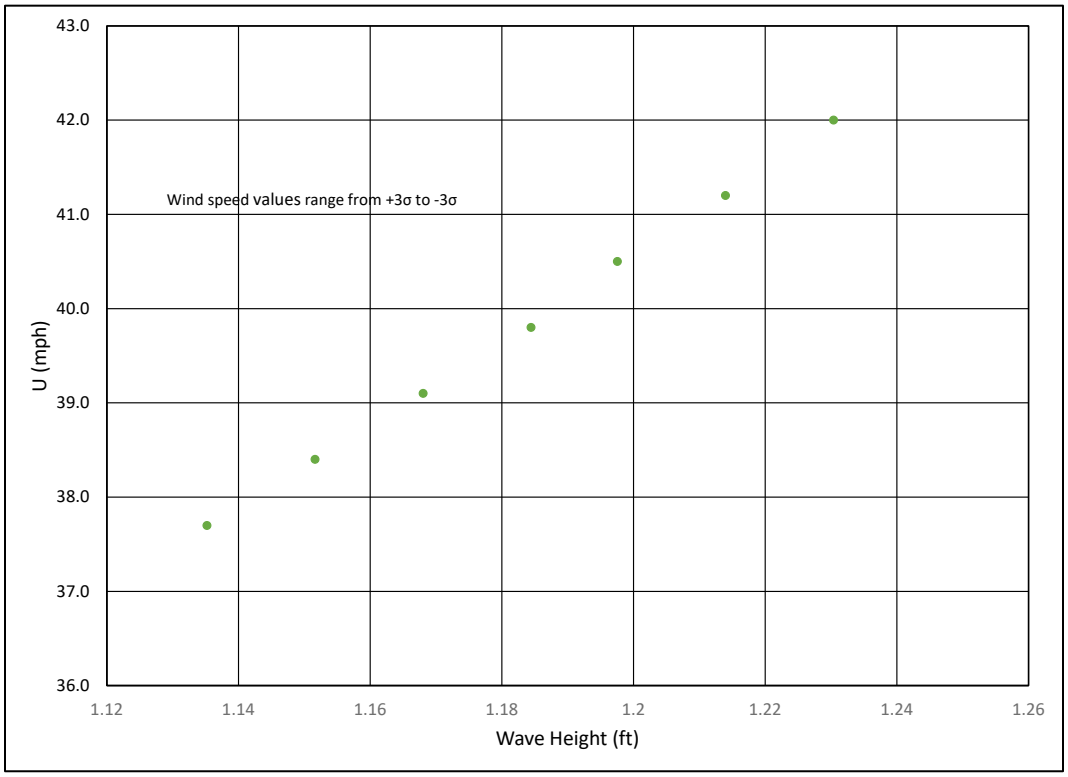

The wave pressure distribution and subsequent wave force for the lower ND/GB can now be determined from the significant wave height and wave period. The complete description of this procedure is in Chapter 2, Section 2.3.2.3. Based on the parameters listed in Table I-12 and on the Goda (2010) formulations in Section 2.3.2.3, a solution was reached. Table I-13 shows the solution in the example wave force calculation (imperial and metric units included). The example uses the average TW El of 637.02, a lower lock sill of 619, and the mean 100 yr return period wind speed of 39.8 mph.

Table I-12. Parameters used in the example wave force calculation (imperial and metric units included) for lower ND/GB for a wind speed of 28.0 mph.

Parameter	Value (Imperial Units)	Value (Metric Units)	Description
h_c	3.26 ft	0.994 m	Top of ND/GB ht above average TW El
d (originally d_{SWL})	18.02 ft	5.492 m	Difference between avg TW El and lower lock sill
h (originally h_{SWL})	19.82 ft	6.041 m	Difference between avg TW El and approach channel invert el
tan θ	0	0	Bottom slope toward bulkhead
β_D	0 deg	0 deg	Design incident wave angle
$H_{1/3}$	1.18 ft	0.361 m	Significant wave height for example problem
$T_{1/3}$	1.63 sec	1.63 sec	Significant wave period for example problem
L_D	13.58 ft	4.14 m	Design wave length for example problem
ρ	62.4 lb/ft^3	1,000 kg/m^3	Density of freshwater
g	32.2 ft/sec^2	9.81 m/sec^2	Acceleration due to gravity
h'	18.02 ft	5.492 m	For the lower ND/GB: $h' = H = d_{SWL}$

The design wave height (H_D) is the minimum of $\alpha_h H_{1/3}$ and H_b, where α_h ranges from 1.6 to 2.0. For the design of nearshore vertical structures, Goda (2010) suggested using a value of 1.8 for α_h. Equations (59) through (61) are repeated here:

$$H_d = H_{Max} = \min\{\alpha_h * H_{1/3}, H_b\},$$

$$H_b = 0.17 * L_D \left\{1 - \exp\left[-1.5\frac{\pi h_b}{L_D}\left(1 + 15 * \tan^{\frac{4}{3}}\theta\right)\right]\right\},$$

where

$$h_b = h + 5 * H_{1/3} * \tan\theta.$$

Therefore,

$$\alpha_h H_{1/3} = 1.8 * 0.361 \text{ m} = 0.650 \text{ m (2.13 ft)},$$

$$h_b = 6.041 + 5 * 0.361 \text{ m} * \tan(0) = 6.041 \text{ m (19.82 ft)},$$

$$H_b = 0.17 * 4.148 \text{ m}\left\{1 - \exp\left[-1.5\frac{\pi 6.041 \text{ m}}{4.148 \text{ m}}\left(1 + 15 * \tan^{\frac{4}{3}}(0)\right)\right]\right\}$$
$$= 0.704 \text{ m (2.31 ft)},$$

so,

$$H_d = H_{Max} = \min\{0.650 \text{ m}, 0.704 \text{ m}\} = 0.650 \text{ m (2.13 ft)}.$$

Next, we calculate the coefficients of wave pressure (α_1, α_2, and α_3) given in Equations (56) through (58), which are repeated here:

$$\alpha_1 = 0.6 + \frac{1}{2}\left[\frac{\frac{4\pi h}{L_D}}{\sinh\left(\frac{4\pi h}{L_D}\right)}\right]^2,$$

$$\alpha_2 = \min\left[\frac{h_b - d}{3h_b}\left(\frac{H_D}{d}\right)^2, \frac{2d}{H_D}\right],$$

$$\alpha_3 = 1 - \frac{h'}{h}\left[1 - \frac{1}{\cosh\left(\frac{2\pi h}{L_D}\right)}\right].$$

The h and d values in the preceding equations are respectively equivalent to the h_{SWL} and d_{SWL} in Table I-12. Substituting the values gives

$$\alpha_1 = 0.60 \text{ (from Equation 56)},$$

$$\alpha_2 = \min\left[\frac{6.041 \text{ m} - 5.492 \text{ m}}{3(6.041 \text{ m})}\left(\frac{0.650 \text{ m}}{5.492}\right)^2, \frac{2(5.492) \text{ m}}{0.650 \text{ m}}\right] = \min[0.0004 \text{ m}, 16.904 \text{ m}] = 0.0004 \text{ m (from Equation 57)},$$

and since $h' = d_{SWL} = H$,

$$\alpha_3 = 0.091 \text{ (from Equation 58)}.$$

The lateral pressure components P_1 and P_3 (from Equations 52 and 54) are evaluated here:

$$P_1 = 0.5\,(1 + \cos\beta_D)\,(\alpha_1 + \alpha_2 * \cos^2\beta_D)\,\rho * g * H_D,$$

$$P_3 = \alpha_3 P_1.$$

The solutions to P_1 and P_3 are

$$P_1 = 3{,}827 \text{ N/m}^2 = 3.827 \text{ kN/m}^2 = 79.90 \text{ (lb/ft}^2\text{)},$$

$$P_3 = 349 \text{ N/m}^2 = 0.349 \text{ kN/m}^2 (7.29 \text{ lb/ft}^2).$$

As shown in Section 2.2.3, the total lateral force per linear width (F_{Lat}) on the face of the ND/GB is

$$F_{Lat} = 0.5(P_1 + P_3)H + 0.5(P_1 + P_4)h_c',$$

where

$$P_4 = P_1\left(1 - \frac{h_c}{\eta^*}\right), \text{if } \eta^* > h_c,$$

or

$$P_4 = 0, \text{ if } \eta^* \leq h_c,$$

$$\eta^* = 0.75(1 + \cos(\beta_D))H_D,$$

$$h_C' = \min\{\eta^*, h_C\}.$$

Therefore, the solution of the resultant force, F_{Lat}, is given as

$$h_c = 0.994 \text{ m } (3.26 \text{ ft}) \text{ (from Table I-12)},$$

$$\eta^* = 0.975 \text{ m } (3.20 \text{ ft}).$$

Because $\eta^* < h_c$,

$$P_4 = 0,$$

$$h_C' = \min\{\text{o.975 m}, 0.994 \text{ m}\} = 0.975 \text{ m } (3.20 \text{ ft}),$$

$$F_{Lat} = 13.37 \text{ kN/m } (916 \text{ lb/ft}).$$

The preceding analysis indicates that the total lateral wave force per linear width of the lower ND/GB for a sustained 39.8 mph wind is 916 lb/ft.

In Figure B-12 and Figure B-13, the pressure terms P_1, P_3, and P_4 are shown acting on a vertical-lift gates, which is similar to the lower ND/GB. The location of the lateral equivalent force (h_{Lat}) can be determined using the one-third/one-sixth method developed by Ebeling et al. (2018) and

also presented in Chapter 2, Section 2.3.2.4, of this report. By applying this method for the lateral forces and summing moments about point 3, Equation (A-14) was developed. The equation is repeated here:

$$h_{Lat} = \frac{(h_4 - h_1)\left(\frac{P_4}{3} + \frac{P_1}{6}\right)h_4 + (h_4 - h_1)\left(\frac{P_4}{6} + \frac{P_1}{3}\right)h_1 + (h_1 - h_3)\left(\frac{P_1}{3} + \frac{P_3}{6}\right)h_1}{F_{Lat}},$$

$$h_{Lat} = \frac{0.994\text{ m}\left(\frac{0\frac{\text{kN}}{\text{m}^2}}{3} + \frac{3.827\frac{\text{kN}}{\text{m}^2}}{6}\right)6.486\text{ m} + 0.994\text{ m}\left(\frac{0\frac{\text{kN}}{\text{m}^2}}{6} + \frac{3.827\frac{\text{kN}}{\text{m}^2}}{3}\right)5.492\text{ m}}{13.37\frac{\text{kN}}{\text{m}}}$$

$$\frac{+ 5.492\text{ m}\left(\frac{3.827\frac{\text{kN}}{\text{m}^2}}{3} + \frac{0.349\frac{\text{kN}}{\text{m}^2}}{6}\right)5.492\text{ m}}{13.37\frac{\text{kN}}{\text{m}}}$$

$$h_{Lat} = 3.838\text{ m}.$$

Table I-11 contains the wave heights and wave periods used for computing the wave forces and pressure distributions determined from the wind speed analysis at the Chickamauga Lock lower ND/GB. The wave forces and pressure distributions computed from Goda's (2010) procedure for the data in Table I-11 are shown in Table I-13. The definition of Goda's parameters shown in Table I-12 are illustrated in Figure 16 and Figure A-27.

Table I-13. Wave force and pressure distribution computations using Goda's (2010) procedure for data in Table I-11 for the Chickamauga Lock lower ND/GB project

Chickamauga Lock Data	Statistic						
	+3σ	+2σ	+1σ	Mean	−1σ	−2σ	−3σ
Wind Speed (mph)	42	41.2	40.5	39.8	39.1	38.4	37.7
η^* (m)	1.013	0.999	0.986	0.975	0.961	0.948	0.934
η^* (ft)	3.32	3.28	3.23	3.2	3.15	3.11	3.07
P_1 (N/m²)	3,976	3,923	3,870	3,827	3,774	3,721	3,668
P_3 (N/m²)	362	357	353	349	344	339	334
P_4 N/m²	0	0	0	0	0	0	0
F_{Lat} (kN/m)	13.89	13.7	13.52	13.37	13.18	13	12.81
h_{Lat} (m)	3.838	3.838	3.838	3.838	3.838	3.838	3.838
h_{Lat} (ft)	12.59	12.59	12.59	12.59	12.59	12.59	12.59
P_1 (lb/ft²)	83	82	81	80	79	78	77
P_3 (lb/ft²)	7.6	7.5	7.4	7.3	7.2	7.1	7
P_4 (lb/ft²)	0	0	0	0	0	0	0
F_{Lat} (lb/ft)	952	939	926	916	903	891	878

I.2.4 Probabilistic Characterization of the Hydrostatic Load for the Chickamauga Lock ND/GB

I.2.4.1 Probabilistic Characterization of the Hydrostatic Load for the Chickamauga Lock Upper Pool ND/GB

The statistics for the ND/GB used on the upstream side of the lock were based on the top el for the damming surface of the ND/GB and the minimum pool el over the period of record presented in Section I.1.1. The structure would be removed before overtopping, so this top el was considered appropriate for the analysis. The top el for the damming surface was 685.17, and the minimum el over the period of record used in this analysis was 674.72. The standard deviation (σ) from (maximum – minimum)/6 was 1.742 ft. Table I-14 provides the hydrostatic loads per foot of gate width computed for the range of upper pool els from +3σ to –3σ.

Table I-14. Hydrostatic forces computed for the Chickamauga Lock needle dam / girder beams (ND/GB) for the range of upper pool els from +3σ to –3σ around the mean upper pool el of 679.80.

–3σ (lb/ft)	–2σ (lb/ft)	–σ (lb/ft)	Mean (lb/ft)	+σ (lb/ft)	+2σ (lb/ft)	+3σ (lb/ft)
4,180	5,530	7,070	8,810	10,730	12,840	15,140

I.2.4.2 Probabilistic Characterization of the Hydrostatic Load for the Chickamauga Lock Lower Pool ND/GB

The statistics for the ND/GB used on the downstream side of the lock were based on the top el for the damming surface of the ND/GB and the minimum lower pool el over the period of record presented in Section I.2.1. Similar to the upper pool ND/GB, the lower structure would be removed before overtopping, so this top el was considered appropriate for the analysis. The top el for the damming surface was 640.28, and the minimum el over the period of record used in this analysis was 631.58. The standard deviation (σ) from (maximum – minimum)/6 was 1.450 ft. The hydrostatic loads per foot of gate width computed for the range of lower pool els from +3σ to –3σ is provided in Table I-15.

Table I-15. Hydrostatic forces computed for the Chickamauga Lock ND/GB for the range of lower pool els from +3σ to –3σ around the mean lower pool el of 637.02.

–3σ (lb/ft)	–2σ (lb/ft)	–σ (lb/ft)	Mean (lb/ft)	+σ (lb/ft)	+2σ (lb/ft)	+3σ (lb/ft)
5,830	7,130	8,570	10,130	11,830	13,650	15,610

I.2.5 Summary of Hydraulic Loads for the Lower ND/GB

Hydrostatic and wave loads are the primary hydraulic loads on the lower ND/GB used as a dewatering structure for the lock. Table I-16 lists the example hydraulic loads determined for the Chickamauga Lock lower ND/GB project. Some of the loads should be combined to give the maximum loads expected for the lower ND/GB. Table I-16 shows these combined loads. The wave force results in the table indicate that wind-induced wave forces are significant and need to be included in lower ND/GB design force computations.

Table I-16. Example hydraulic loads for the Chickamauga Lock lower ND/GB.

Max Estimated Hydraulic Load	Value (kips/ft)
Hydrostatic	14.149 (10.131 with TW El of 637.02)
Hydrodynamic	N/A
Wave*	0.952
Hydrostatic + Wave	11.083 (average hydrostatic + wave)
Hydrodynamic + Wave	N/A

* Based on a mean TW El and 42.0 mph wind speed at 268° (100 yr wind event + 3σ). $P_1/P_3 = 10.98$

Appendix J: Example Design for Determining Hydrostatic Loads for the Dalles Lock Reverse Tainter Valve

In this appendix, some of the procedures discussed in Chapter 11 of the main report are presented using data from an existing USACE Navigation project. The data needed to quantify the hydrostatic loads for the reverse tainter valve are described.

J.1 A 50 yr Record of Hydrologic Data for the Dalles Lock and Dam

The Dalles Lock and Dam project on the Columbia River was chosen to illustrate how to determine the hydraulic loads on a reverse tainter valve. USACE, Portland District (USACE-NWP), provided a 50 yr plus record of hydraulic data, from 1966 through August of 2021. The data included forebay el and TW El. The pertinent project-specific data for the analysis are listed here. Elevations are in feet NGVD 29.

- Normal forebay el = 158.0
- Upper valve seat el = 26
- Valve height = 14 ft
- Valve width = 12 ft
- Maximum lift = 90.5 ft
- Normal lift = 84 ft

Figure J-1 shows an aerial view of the Dalles Lock and Dam project. Figure 88 shows the original double skin plate valve installed at the Dalles Lock that was removed for repairs. The Dalles valves were placed in operation in 1957. Replacement valves that were somewhat similar in design were installed at the Dalles and John Day Locks between 2010 and 2011. USACE-NWP experienced some performance issues with the replacement valves and is planning to replace these reverse tainter valves at the Dalles and John Day Locks. USACE-NWP (2020) provides the history of reverse tainter valve performance, the issues that have been experienced, and alternatives that are being considered to replace the valves.

Figure J-1. Satellite aerial view of the Dalles Lock and Dam. (Map data: Google Earth 2020.)

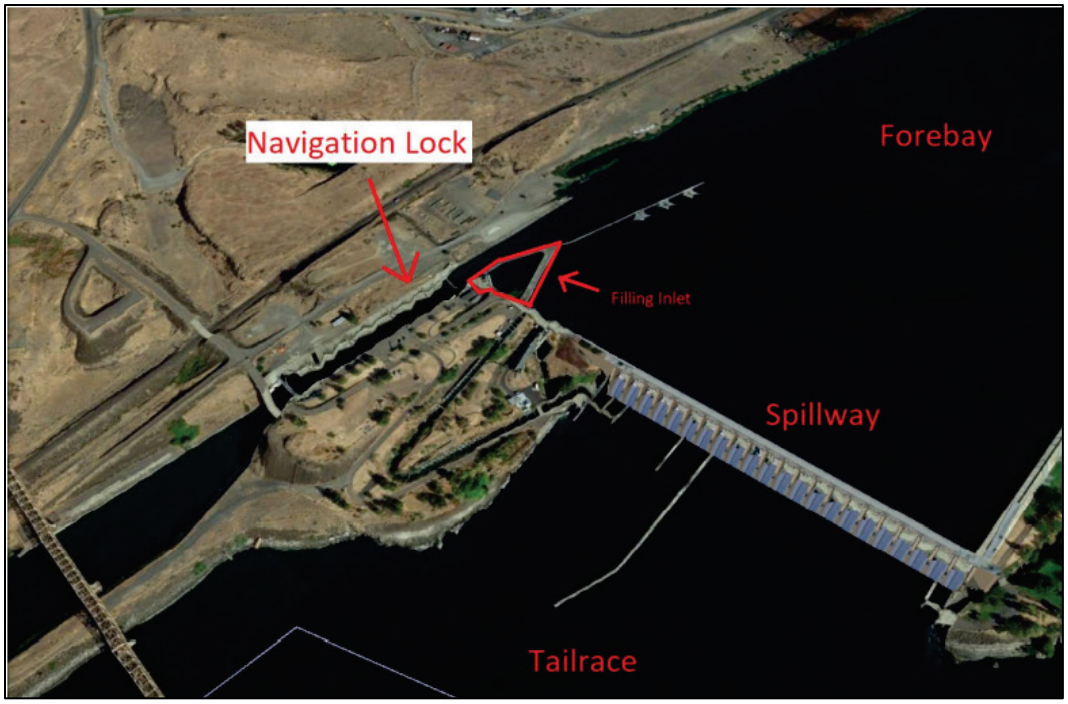

J.1.1 Forebay Statistics for the Dalles Lock Reverse Tainter Valve

The upper pool el, which is also referred to as the forebay el, is one of the primary variables affecting the load on the reverse tainter valve. Figure J-2 is a histogram of the forebay el over the period from 1967 to 2021. The mean forebay el was 158.6, the maximum el was 160.6, and the minimum el was 150.7. The standard deviation was 0.774 ft.

In the histogram, there are 30 bins, each with a width of 0.20 ft. The area of each bin was computed, and the total area was determined by summing the individual bin areas. These areas were normalized by dividing each individual area by the total area to give the PDF shown in Figure J-3. A CDF was developed by cumulatively summing the normalized areas of the PDF (Figure J-4).

Figure J-2. Histogram of the Dalles forebay el from 1967 through 2021.

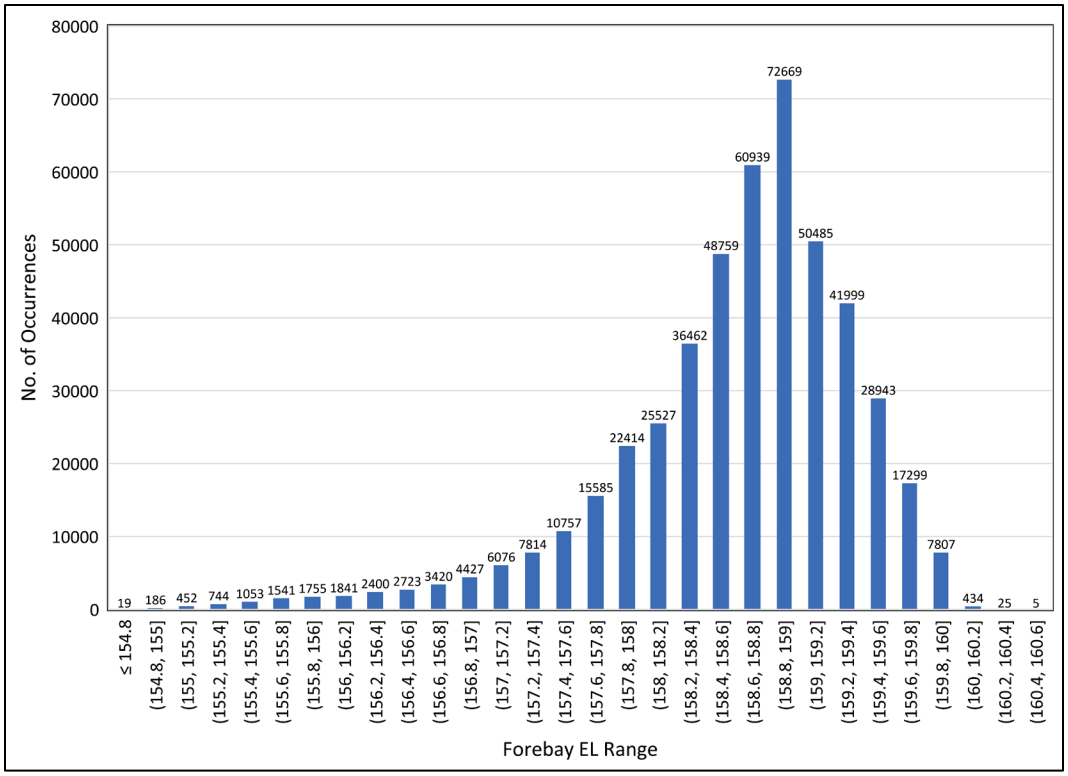

Figure J-3. PDF from histogram of the Dalles forebay el.

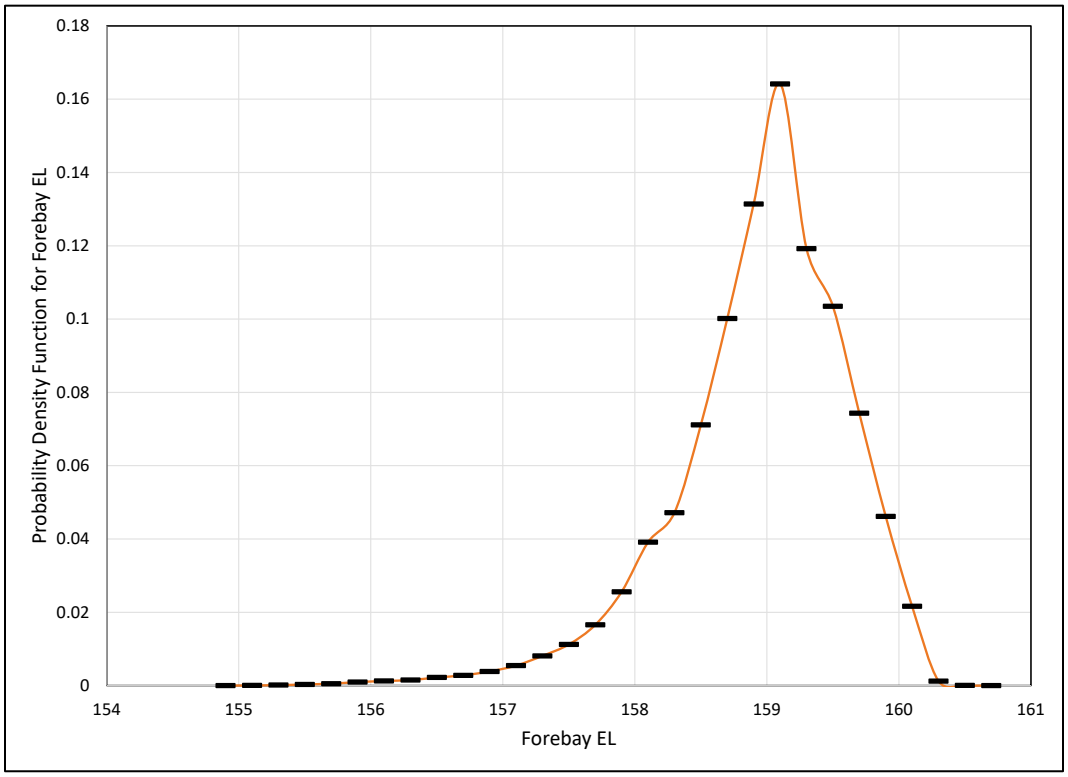

Figure J-4. CDF for the Dalles forebay el.

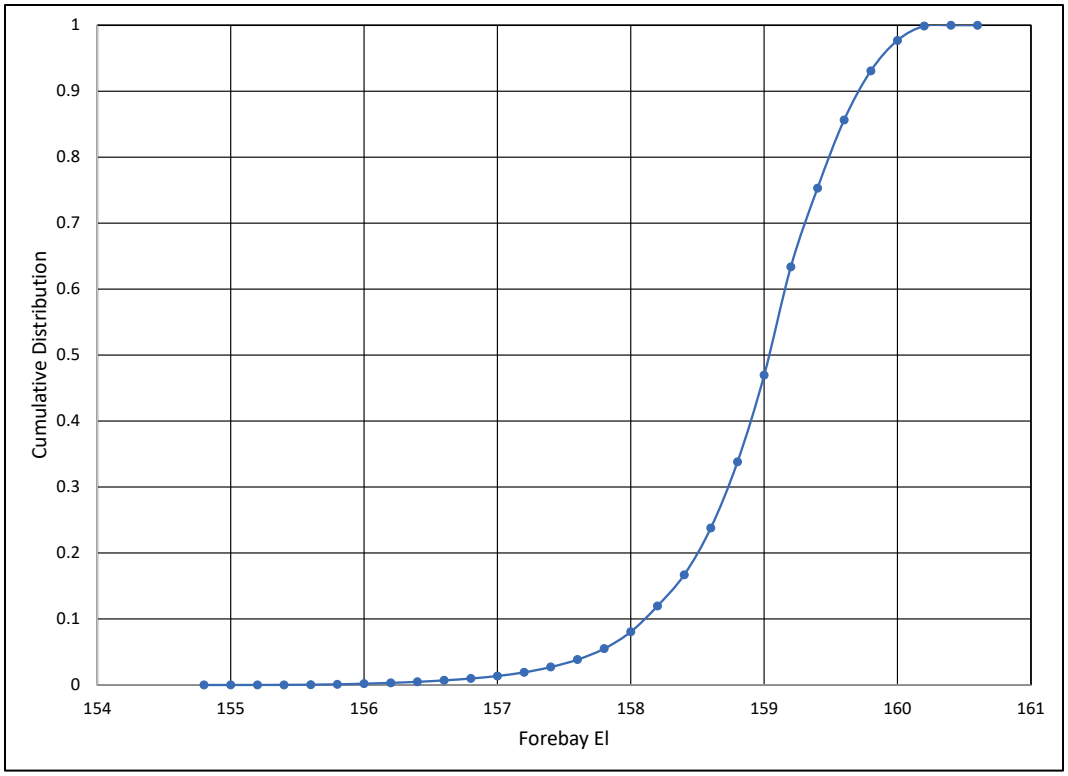

J.1.2 Tailwater Statistics for the Dalles Project

Similar statistics were computed for the TW Els at the Dalles project. Figure J-5 is a histogram of the TW El from December of 1966 to August of 2021. The mean TW El was 78.07, the maximum el was 93.0, and the minimum el was 67.0. The standard deviation was 2.87 ft.

There are 29 bins, each with a bin width of 0.8 ft. The area of each bin was computed, and the total area was determined by summing the individual bin areas. These areas were normalized by dividing each individual area by the total area to give the PDF (Figure J-6). A CDF was developed by cumulatively summing the normalized areas of the PDF (Figure J-7).

Figure J-5. Histogram of the Dalles TW El between November of 1966 and August of 2021.

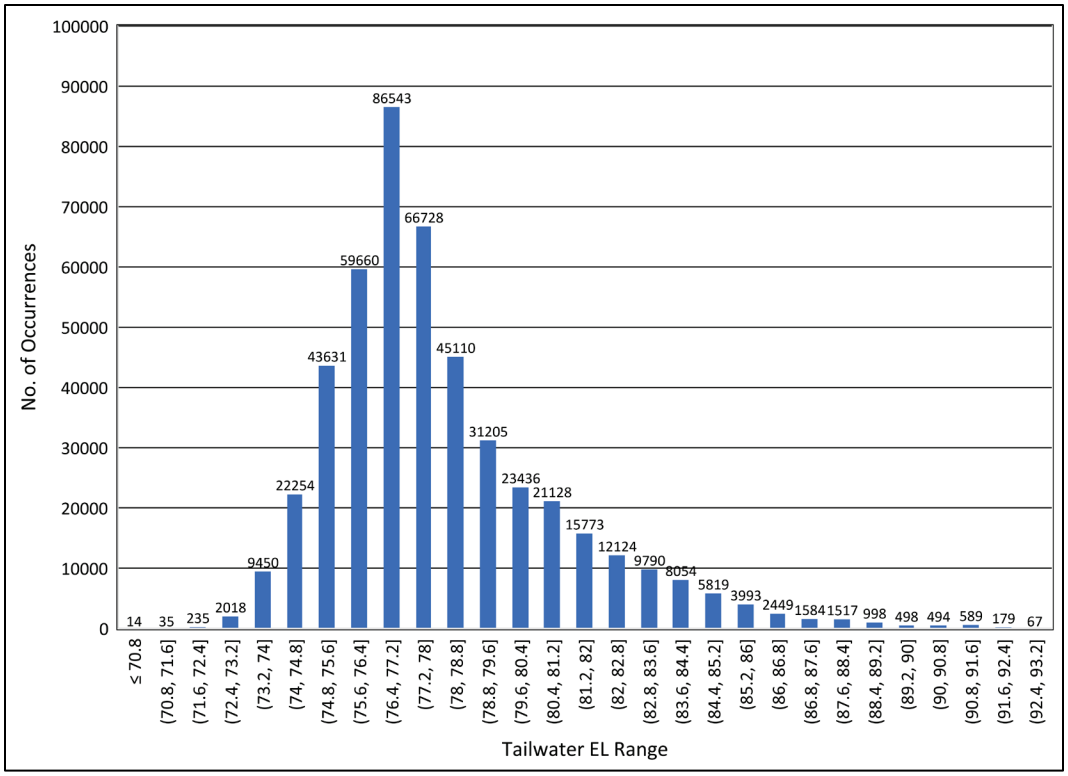

Figure J-6. PDF from histogram of TW El for the Dalles project.

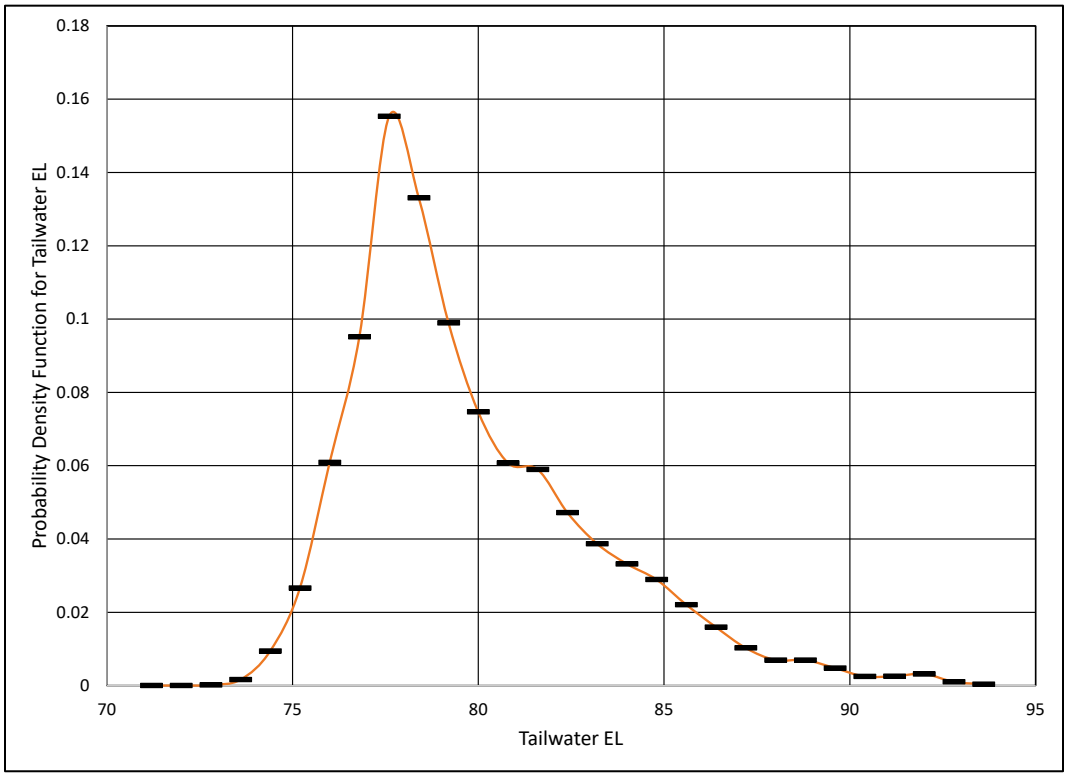

Figure J-7. CDF for TW El for the Dalles project.

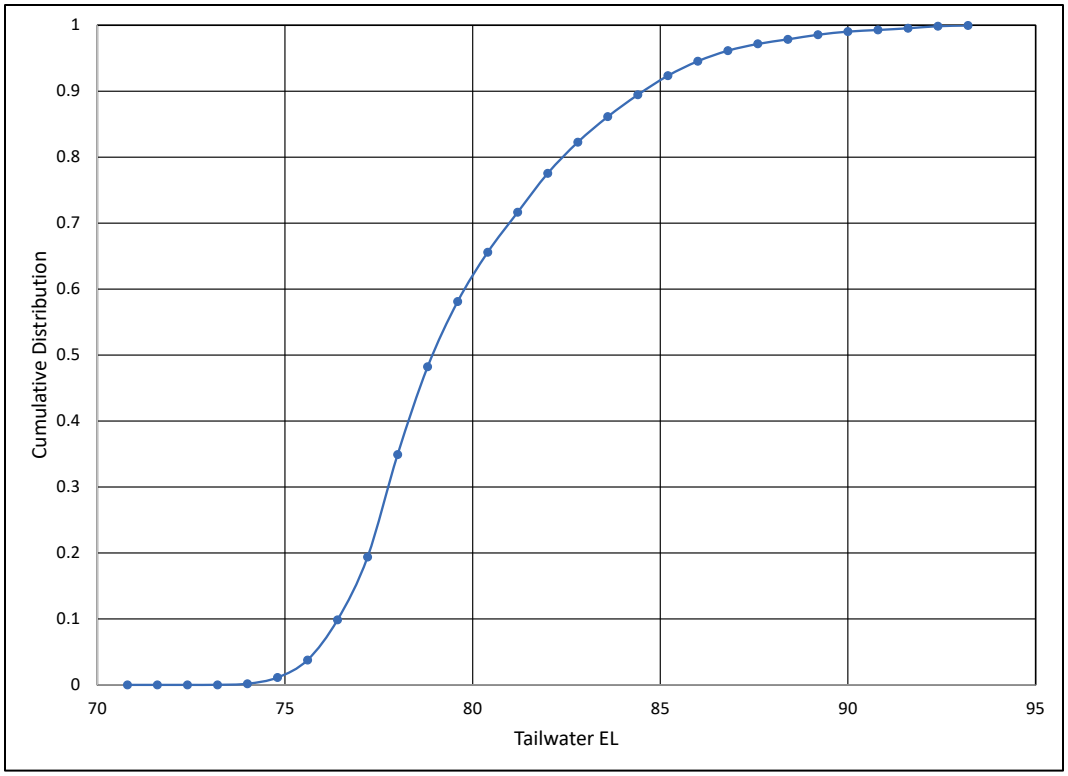

J.2 Hydrostatic Load for the Dalles Reverse Tainter Valve

Equation (10), which is repeated here, is a conventional equation that is found in many fluid mechanics and hydraulics textbooks and can be used to compute hydrostatic pressure (p). As stated previously, γ is the unit weight of water, and y is the vertical distance from the water surface to the location of the hydrostatic pressure of interest (Figure 90):

$$p = \gamma y.$$

The horizontal hydrostatic pressure on the reverse tainter valve gate is expressed as $\gamma \Delta H$, where γ is the unit weight of water, and ΔH is the difference between the forebay el and TW El. To obtain the force, the hydrostatic pressure is multiplied by the area the pressure is acting on. B is the valve height. The hydrostatic force per unit width of reverse tainter valve is given by Equation (110), which is repeated here:

$$H_s = \gamma \Delta H B.$$

The resultant hydrostatic force per foot of width for the reverse tainter valve with the normal lift of 84 ft (see bulleted list in Section J.1) using the following parameters is

- γ = the unit weight of water = 62.4 lb/ft^3,
- ΔH = the head on the reverse tainter valve (normal) = 84 ft,
- ΔH = the head on the reverse tainter valve (maximum) = 90.5 ft,
- Normal hydrostatic load = 62.4 lb/ft^3 * 84 ft * 14 ft= 73,382.4 lb/ft, and
- Maximum hydrostatic load = 62.4 lb/ft^3 * 90.5 ft * 14 ft = 79,061 lb/ft.

The resultant hydrostatic force is located $B/2$ above the culvert floor at the valve (Figure 90).

J.3 Hydrodynamic Load for the Dalles Reverse Tainter Valve

The hydrodynamic loads in this appendix describe the procedures used by USACE-NWP in their investigation of the reverse tainter valves at the Dalles Lock (USACE-NWP 2020). The hydrodynamic loads are the loads that result from moving water. The flow field downstream from the reverse tainter valve is quite complex due to high velocities and continually varying pressures with sometimes extreme fluctuations. Fatigue failures of structural components often result in this type of flow environment.

J.3.1 Dynamic Amplification Factor (DAF)

USACE-NWP is considering using a dynamic amplification factor (DAF) to help evaluate the hydrodynamic loads. This factor is determined using the results of field instrumentation that measures stresses at desired locations on the reverse tainter valve while in operation. USACE-NWP, with the assistance of US Army Engineer Research and Development Center (ERDC), instrumented a reverse tainter valve in 2016. A USACE-NWP contractor installed additional instrumentation in March of 2019. The intended purpose was to determine hydrostatic, hydrodynamic, and vibration loading for analysis of the existing tainter valves and to determine applicable load factors for the design of the new reverse tainter valves.

The DAF was determined by subtracting the minimum average stress from the maximum average stress and dividing this difference by the hydrostatic stress. These stress measurements were obtained at specified gauge locations from an instrumented reverse tainter valve. USACE-NWP was able to obtain this stress data from 14 valve opening tests. A mean value of

1.4 was determined, with a standard deviation of 0.55. USACE-NWP recommended that a DAF of the mean value plus 2 standard deviations, 2.5, be used to determine the hydrodynamic loads.

J.3.2 Vibration and Fatigue Analysis

Due to the standards developed for these designs, it is difficult to analyze the reverse tainter valve using methods intended for bridges and buildings. Limit states and loadings are considerably different for the reverse tainter valve, and additional research is needed to help develop the appropriate standards. USACE-NWP (2020) provided valuable information on their approach to addressing these issues.

J.4 Probabilistic Characterization of the Hydrostatic Load for the Dalles Lock Reverse Tainter Valve

The dispersion of the hydrostatic load on the reverse tainter valve gate is due to the changes in the upper and lower pool els. The maximum load occurs when the upper pool is at maximum el and the lower pool is at a minimum el.

The head on the lower gate was determined for the period of record from 1967 to 2021 for the upper and lower pool els discussed in Sections J.1.1 and J.1.2. The mean head was 80.57 ft, and the standard deviation (σ) was 3.05 ft. The normal upper pool el of 158 was used for the fluctuations of the head. The hydrostatic load on the reverse tainter valve is given by Equation (110) and shown again in Section J.2.

Table J-1 contains the hydrostatic loads per foot of reverse tainter valve for the range of heads between +3σ and −3σ around the mean normal head of 80.57 ft. Figure 90 illustrates the hydrostatic forces on the Dalles Lock reverse tainter valve.

Table J-1. Hydrostatic forces computed for the Dalles Lock reverse tainter valve for the range of heads from +3σ to −3σ around the mean head of 80.57 ft.

−3σ (lb/ft)	−2σ (lb/ft)	−σ (lb/ft)	Mean (lb/ft)	+σ (lb/ft)	+2σ (lb/ft)	+3σ (lb/ft)
62,393	65,057	67,721	70,386	73,050	75,715	78,379

J.5 Summary of Hydrostatic Loads for the Dalles Lock Reverse Tainter Valve

The hydraulic loads on the Dalles Lock reverse tainter valve lock miter gates consist primarily of the hydrostatic, hydrodynamic, vibration, and fatigue loads. The hydrostatic loads are the only loads presented in Table J-2 because the other loads require much more research to determine their values.

Table J-2. Example hydrostatic loads for the Dalles Lock reverse tainter valve.

Estimated Hydraulic Load	Value (kips/ft)
Hydrostatic	73.382 (84 ft lift)
Hydrostatic	79.061 (90.5 ft lift)

Abbreviations

ACE	Annual chances of exceedance
AISC	American Institute of Steel Construction
ASD	Allowable stress design
BLD	Barkley Lock and Dam
CDF	Cumulative distribution function
CFD	Computational fluid dynamics
CHA	Chattanooga/Lovell Airport
DAF	Dynamic amplification factor
DIR	Direction
el	Elevation
EM	Engineer Manual
ERDC	US Army Engineer Research and Development Center
ETL	Engineer Transmittal Letter
GEV	Generalized extreme value
GIWW	Gulf Intracoastal Waterway
GUS	Gust
HDC	Hydraulic Design Criteria
HM	Hermiston Municipal
HSS	Hydraulic steel structures
ITL	Information Technology Laboratory
LCH	Lake Charles
LRFD	Load and Resistance Factor Design

LRH	US Army Corps of Engineers, Huntington District
LRN	US Army Corps of Engineers, Nashville District
MLD	McNary Lock and Dam
MLG	Mean Low Gulf
MODAHRMN	Month, day, hour, minute
MPLD	Melvin Price Locks and Dam
MVN	US Army Corps of Engineers, New Orleans District
MVP	US Army Corps of Engineers, St. Paul District
MVR	US Army Corps of Engineers, Rock Island District
MVS	US Army Corps of Engineers, St. Louis District
NCDC	National Climate Data Center
ND/GB	Needle dam / girder beams
NWP	US Army Corps of Engineers, Portland District
NWW	US Army Corps of Engineers, Walla Walla District
OHB	Oxbow-Hickson-Bakke
PAH	Barkley Regional Airport
PDF	Probability density function
PPA	Point Pleasant Airport
PSC	Pasco / Tri Cities
RCBLD	R. C. Byrd Locks and Dam
SCC	Saint Charles County
SLR	St. Louis Regional
SPD	Speed

SPM	*Shore Protection Manual*
STG	Spillway tainter gate
SWL	Still-water level
TVA	Tennessee Valley Authority
TW El	Tailwater elevation
USACE	US Army Corps of Engineers
WBAN	Weather Bureau Army Navy

REPORT DOCUMENTATION PAGE

1. REPORT DATE	2. REPORT TYPE	3. DATES COVERED	
		START DATE	END DATE
May 2024	Final Technical Report (TR)	FY19	FY24

4. TITLE AND SUBTITLE

Hydraulic Load Definitions for Use in Load and Resistance Factor Design (LRFD) Analysis, Including Probabilistic Load Characterization, of 10 Hydraulic Steel Structures:
Report Number 1

5a. CONTRACT NUMBER	5b. GRANT NUMBER	5c. PROGRAM ELEMENT
5d. PROJECT NUMBER	**5e. TASK NUMBER**	**5f. WORK UNIT NUMBER**

6. AUTHOR(S)

John E. Hite, Jr., Robert M. Ebeling, and Barry C. White

7. PERFORMING ORGANIZATION NAME(S) AND ADDRESS(ES)

US Army Engineer Research and Development Center (ERDC)
Coastal and Hydraulics Laboratory (CHL) and Information Technology Laboratory (ITL)
3909 Halls Ferry Road
Vicksburg, MS 39180-6199

8. PERFORMING ORGANIZATION REPORT NUMBER

ERDC TR-24-11

9. SPONSORING/MONITORING AGENCY NAME(S) AND ADDRESS(ES)

Headquarters, US Army Corps of Engineers
Washington, DC 20314-1000

10. SPONSOR/MONITOR'S ACRONYM(S)

11. SPONSOR/MONITOR'S REPORT NUMBER(S)

12. DISTRIBUTION/AVAILABILITY STATEMENT

Distribution Statement A. Approved for public release: distribution is unlimited.

13. SUPPLEMENTARY NOTES

Funding Account Code U4388265, AMSCO Code 031391

14. ABSTRACT

In the past, allowable stress design (ASD) was used to design steel structures. The allowable stresses used were determined from previous practice, with limited understanding of the reliability and risk performance provided by the structure. Engineering methods based on Load and Resistance Factor Design (LRFD) provide more accurate lifetime models of structures by providing risk-based load factors. Besides improved safety, cost savings can be provided through improved performance and, in some cases, by delaying rehabilitation. This research project develops LRFD-based engineering procedures for the evaluation and design of hydraulic steel structures (HSS).

Hydraulic loads are a key element to the LRFD analysis. This report identifies the primary hydraulic loads and describes procedures that can be used to determine these hydraulic loads. Existing design guidance for HSS is described and presented in the individual chapters. The appendixes to the report provide examples of the procedures used to compute the hydrostatic, wave, and hydrodynamic loads.

A new approach for determining wind-induced wave loads was developed. Design guidance for computing the hydrodynamic load was limited for many of the HSS. Additional research is recommended to improve capabilities for computing hydraulic loads. Details on these recommendations can be found in this report.

15. SUBJECT TERMS

Buildings, structures, etc.--Steel--Structural design; Hydraulics--Loads (Mechanics); Hydraulic structures--Structural design; Load factor design; Strains and stresses

16. SECURITY CLASSIFICATION OF:			17. LIMITATION OF ABSTRACT	18. NUMBER OF PAGES
a. REPORT	b. ABSTRACT	C. THIS PAGE		
Unclassified	Unclassified	Unclassified	SAR	507

19a. NAME OF RESPONSIBLE PERSON	19b. TELEPHONE NUMBER (include area code)